Université Pierre et Marie Curie

Ecole doctorale 398 : Géoscience Ressources naturelles et Environnement

Institut des Sciences de la Terre de Paris (ISTeP)

Tectono-metallogenic model of the Kiggavik uranium deposits, Nunavut, Canada

Par M. Alexis GRARE

Pour obtenir le grade de docteur de l'Université Pierre et Marie Curie dans la discipline des Sciences de la Terre

Dirigée par : Antonio BENEDICTO (directeur de thèse), Olivier LACOMBE (co-directeur de thèse) et Anna TRAVE (co-directrice de thèse)

Thèse soutenue publiquement le 18 janvier 2018

Devant un jury composé de :

Kathryn Bethune, Professeur (Univ. de Regina, SK, Canada)	Rapporteur
Alain Chauvet, Directeur de Recherche au CNRS (Univ. de Montpellier)	Rapporteur
Antonio Benedicto, Maître de Conférence (GEOPS, Univ. Paris Sud Orsay)	Directeur de thèse
Olivier Lacombe, Professseur (ISTeP, Univ. Pierre et Marie Curie)	Co-directeur de thèse
Anna Trave, Professora agregada (Univ. de Barcelona, Spain)	Co-directrice de thèse
Loïc Labrousse, Professeur (ISTeP, Univ. Pierre et Marie Curie)	Examinateur
Julien Mercadier, Chargé de Recherche CNRS (Univ. de Lorraine	Examinateur
Gilbert Stein, Directeur des Géosciences (AREVA)	Examinateur

Remerciements / Acknowledgements

Arrivé au terme de ce travail de thèse, je tiens tout d'abord à citer et remercier les personnes ayant été à l'origine de cette étude qui a été entièrement financée par AREVA. Je remercie Antonio Benedicto qui a assuré mes premiers enseignements en géologie structurale à Orsay avant de prendre la co-direction de mon stage d'alternance à AREVA, puis de m'offrir l'opportunité de commencer un travail de thèse au Canada. Tu as été présent personnellement et professionellement du début à la fin, malgré la longueur de mes écrits.

Ce travail n'aurait pu débuter sans l'appui de Patrick Ledru (VP exploration ARC), que je remercie pour ses conseils et son soutien tout au long de cette thèse.

Je remercie Olivier Lacombe pour avoir accepté de co-encadrer ce travail de thèse alors qu'il ne connaissait rien à l'uranium ni aux gisements de type discordance (ni même le doctorant), tout particulièrement sur ces derniers longs mois de rédaction alors que j'étais rentré du Canada. Merci pour tout.
Merci à Anna Travé d'avoir accepté de co-encadrer ce travail de thèse. Tout comme Olivier, tu connaissais peu ce milieu qu'est l'uranium, merci pour tes conseils, pour m'avoir accueilli à Barcelone et pour avoir joué le rôle de « good cop » (Olivier étant le « bad cop » bien sûr) durant cette thèse.

Je remercie les membres du Jury d'avoir accepté d'examiner et de juger ce travail.

J'ai plaisir à remercier les géologues et autres employés d'AREVA et d'AREVA Resources Canada pour leur accueil et les discussions (géologiques ou non) que j'ai pu avoir avec eux durant mes 3 ans de présence dans les prairies du Saskatchewan : Mario Blains, Régis Roy (à quand un ptit Joe ?), John Robbins, Dave Quirt… et tous les géologues expatriés avec qui j'ai pu discuter.
Je remercie chaleureusement Daniel Hrabok pour avoir relu avec application une bonne partie de ce rapport de thèse.

Merci à Marc Brouand d'AREVA pour m'avoir accueilli l'espace de quelques observations pétrographiques et sur son MEB de poche.

Je remercie les personnes travaillant à Nancy, université de Lorraine/CREGU, qui m'ont accueilli dans le cadre de la caractérisation géochimique et géochronologique de mes échantillons.
Je tiens tout particulièrement à remercier Julien Mercadier pour son aide et ses connaissances sur la géochimie des gisements type discordance, ainsi que pour sa personnalité, sa bonne humeur (assistée par la liqueur de Mirabelle ?) et sa volonté de pousser plus loin les modèles connus.

Je remercie les personnes de Sorbonne Université pour leur accueil durant les derniers mois de rédaction de ce manuscrit de thèse. Merci à Camille pour sa présence durant toute cette période.

Je tiens à remercier les membres de ma famille ainsi que mes amis pour m'avoir soutenu jusqu'au bout.

Résumé

Les bassins Paléo- à Mésoproterozoiques (1750-1500 Ma) de l'Athabasca (Saskatchewan) et du Thelon (Nunavut), ainsi que le socle sous-jacent, présentent des gisements d'uranium de classe mondiale. Néanmoins, malgré son fort potentiel exploratoire, le bassin du Thelon, moins accessible, a été bien moins étudié à ce jour. La zone de Kiggavik, sur la bordure Est de ce bassin, a été intensément explorée par AREVA Resources Canada (ARC) jusqu'en 2016 ; elle abrite des minéralisations à uranium économiquement importantes, présentant un contrôle clair par la fracturation. Préciser la genèse, le contrôle structural et la chronologie de ces minéralisations est crucial pour comprendre le développement et la localisation de ces gisements, et par conséquent pour améliorer les stratégies d'exploration dans ce district.

Ce travail de thèse se focalise sur l'étude du réseau complexe et polyphasé de fractures et de failles associé aux minéralisations à uranium dans la zone de Kiggavik. Il consiste en une étude multi-échelle intégrée combinant des analyses méso- à microstructurales sur le terrain et sur carottes de forages avec des analyses pétrologiques, géochimiques et géochronologiques.

Les données géophysiques et géologiques sur le prospect de Contact récemment découvert, mais aussi celles provenant des autres gisements et prospects de la zone, ont permis de construire un modèle tectono-métallogénique multi-stade à l'échelle de la zone de Kiggavik. Nos résultats montrent que les failles majeures de directions ENE-WSW et NE-SW ont été préalablement formées durant les orogenèses Thelon-Taltson (2100-1900 Ma) et Trans-Hudson (1900-1800 Ma) ; ces failles ont été minéralisées en uranium à quatre stades : U0, U1, U2 et U3, chacun présentant des caractéristiques distincts en terme de fracturation, altération et minéralisation. La minéralisation U0 est interprétée comme étant d'origine magmatique, se déroulant à ~1830 Ma ; elle est liée à une micro-bréchification de la roche encaissante, qui présente une très faible altération. Cet événement tectonique s'est déroulé sous une contrainte encore mal contrainte, avec un raccourcissement de direction WSW-ENE. Cette minéralisation est suivie par un événement tectonique à ~1750 Ma qui a entrainé une forte bréchification siliceuse associée à une hématisation pervasive de la roche encaissante. Cette événement est antérieur au dépôt de la formation du Thelon et est d'origine magmatique-épithermale. Il a entrainé une silicification pervasive des failles précédemment formées, donnant naissance à la « Quartz Breccia » qui a compartimentalisé les événements de fracturation qui ont suivi, contrôlant les fluides minéralisateurs en agissant comme une barrière.

Le stade de fracturation-minéralisation U0 et l'événement silicifiant reflètent l'importance des événements pré-Thelon en lien avec le magmatisme du groupe de Baker Lake, dans le contrôle

de la fracturation et des circulations de fluides postérieures, et par conséquent de la localisation des minéralisations à uranium. U1, U2 et U3 sont postérieures au dépôt de la formation du Thelon : U1 et U2 sont deux minéralisations de type discordance, associées à des stades de fracturation qui se sont produit en réponse à un σ1 de direction WNW-ESE et σ3 de direction NNE-SSW; et à un σ1 de direction NE-SW et σ3 de direction NW-SE, respectivement. U1 et U2 se sont formées entre ~1500 et 1300 Ma et sont liées à la circulation de saumures diagénétiques porteuses d'uranium venant de la formation du Thelon. Postérieurement à U1 et U2, mais antérieurement à la mise en place des dykes de MacKenzie (1267 Ma), une contrainte extensive NE-SW a causé le décalage normal-dextre des corps minéralisés précédemment formés, via la réactivation de failles de directions NNW-SSE et E-W. Cet événement de fracturation a entrainé la circulation de fluides chauds, acides qui ont provoqué la désilicification et l'illitisation de la roche encaissante et à la déstabilisation des oxydes de fer. Ceci a remobilisé une partie de l'uranium présent. La minéralisation U3 est liée à la distribution et à la re-concentration, post-MacKenzie dkes, de l'uranium de U0, U1 et U2 le long de fronts d'oxydo-réduction. La réactivation et la réouverture légère du réseau de fractures a permis la percolation des fluides d'origine météorique à l'origine de cette remobilisation, vers 500-300 Ma.

Notre étude montre que contrairement au bassin d'Athabasca où les gisements d'uranium sont de type discordance et où le halo d'altération argileuse est relié spatialement et génétiquement aux corps minéralisés, dans la zone de Kiggavik : (1) les gisements d'uranium sont de type mixte, évoluant depuis un type a priori magmatique (U0), à un type discordance (U1-U2), et une perturbation finale par la percolation d'eaux météoriques (U3). (2) l'événement à forte altération argileuse est postérieur aux stades de minéralisations principaux (U0 à U2).

Notre étude met aussi l'accent sur la nécessité de combiner une analyse structurale précise avec une étude pétro-géochimique et géochronologique, afin de mieux contraindre la genèse et le contrôle structural responsable de la mise en place d'un gisement. Ceci permet aussi de produire des modèles tectono-métallogéniques plus réalistes et utiles à l'exploration.

Abstract

The Paleoproterozoic to Mesoproterozoic (1750–1500 Ma) Athabasca (Saskatchewan) and Thelon (Nunavut) basins, Canada, host world-class high-grade uranium deposits. However, while being prospective, the Thelon Basin has been much less accessible and studied to date. The Kiggavik area, on the eastern border of the Thelon Basin was intensively explored by AREVA Resources Canada (ARC) until 2016, and hosts significant fracture-controlled uranium resources. Understanding the genesis, structural controls and timing of the mineralization is crucial to better understand the development and location of these deposits, and therefore to improve exploration strategies in this uranium district.

This work focuses on the study of the complex multiphase fault and fracture network associated with uranium mineralization in the Kiggavik area. It consists in an integrated and multiscale study combining meso- and microstructural analyses from field and drill cores with petrological, geochemical and geochronological analyses.

Geophysical and geological data from the recently discovered Contact prospect as well as from other nearby deposits and prospects enabled us to decipher the tectono-metallogenic multi-stage model at the scale of the entire Kiggavik area. Our results show that the main ENE-WSW and NE-SW fault zones formed earlier during the Thelon and Trans-Hudsonian orogenies and were mineralized in four stages, U0, U1, U2, U3, with distinctive fracture, alteration and mineralization patterns. U0, inferred of magmatic origin, likely occurred at ca. 1830 Ma and is related to micro-brecciation and weak clay-alteration under a yet poorly constrained stress, likely a WSW-ENE shortening. This event is followed by intense quartz brecciation, iron oxidation and veining at ca. 1750 Ma. This silicifying event that predates deposition of the Thelon formation is of magmatic epithermal origin; it caused pervasive silicification of former fault zones, giving birth to the so-called Quartz Breccia that compartimentalized subsequent fracturing and behaved as a barrier for mineralizing fluids. Both the U0 mineralization and the subsequent silicifying events reflect the importance of pre-Thelon magmatic-related fracturing/fluid circulation events on controlling the future development and location of later unconformity-type uranium deposits. U1, U2 and U3 postdate deposition of the Thelon formation; U1 and U2 mineralization events are associated with two fracturing stages that occurred in response to a far-field stress that evolved from WNW-ESE σ1 and NNW-SSE σ3 to NE-SW σ1 and NW-SE σ3, respectively; both formed at ~1500-1300 Ma and are related to circulation of Thelon-derived U-bearing basinal brines. A post U1/U2, but pre-MacKenzie dikes, NE-SW oriented extensional stress caused the normal-dextral offset of the orebodies by reactivating NNW-SSE and E-W faults. This fracturing event triggered circulation of hot acidic

fluids, desilicifying, illitizing and bleaching the host-rock, remobilizing and reprecipitating previous uranium stock. U3 is linked to uranium redistribution/reconcentration along redox fronts and occurred through weak reopening of the fracture network enhancing percolation of meteoric fluids at 500-300 Ma.

Our study shows that unlike in the Athabasca Basin where uranium deposits are unconformity-related in type and where clay alteration halos are spatially and genetically associated to ore bodies, in the Kiggavik area (1) uranium deposits are of mixed type evolving from magmatic-related (U0) to unconformity-related (U1-U2), with a final perturbation by meteoric fluid percolation (U3), and (2) the strongest clay alteration event postdates the main stages of mineralization (U0 to U2).

Our study also emphasizes the need of accurate structural analyses combined with petro-geochemical and geochronological studies to better constrain the genesis and the structural plumbing responsible for ore deposits formation and to help provide more realistic tectono-metallogenic models useful for future exploration.

Table of contents

INTRODUCTION

Two-thirds of the uranium world's production comes from three countries, Kazakhstan (the largest producer), Canada (second largest) and Australia (third largest) (OECD/NEA-IAEA 2014) The majority of Canada's production comes from unconformity-related uranium deposits (i.e., Cigar Lake deposit, McArthur River deposit) hosted in the Paleoproterozoic Athabasca basin (Fig. 1), in the Province of Saskatchewan. Unconformity-related uranium deposits formed during the Paleoproterozoic era, during which deposition of important detritic, red-beds sediments were deposed over a wide area, resting unconformably on a metamorphic basement. The Thelon Basin is also a Paleoproterozoic basin in Canada which presents very similar geological characteristics to the Athabasca Basin with significant uranium potential.

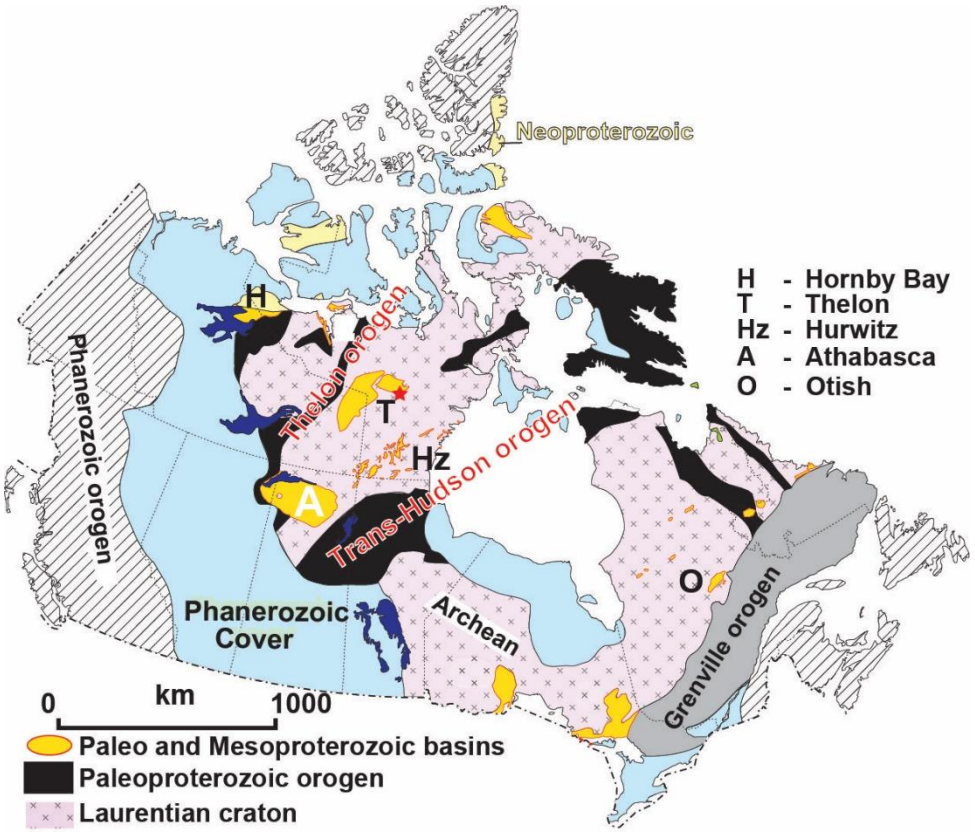

Figure 1: Location of Paleo- to Meso-proterozoic basins in Canada (after Jefferson et al., 2007). Red star locates the Kiggavik area, on the Eastern border of the Thelon basin.

The underexplored Thelon Basin was being explored by AREVA Resources Canada Inc. (ARC) among other companies, until 2015. ARC has discovered several uranium deposits (i.e.,

Kiggavik Main Zone deposit) and prospects in the eastern margin of the basin, within the Kiggavik Uranium Project (also called the Kiggavik area hereafter) which is located 80 km west of Baker Lake, in the territory of Nunavut. The Project property comprises 37 mineral leases for a total of 18,483 hectares (ARC internal data), with ARC being the majority shareholder and operator. Uranium was originally identified at Kiggavik when radioactive frost boils and rock chips were discovered during systematic coverage by an airborne radiometric survey conducted in the mid-1970s by Urangesellschaft Canada Limited (UGC). Drilling commenced in 1977 and led to the discovery of the Kiggavik Main and Centre Zone deposits (Fuchs et al., 1986). Other anomalous areas were identified using intensive airborne and ground surveying (e.g., airborne resistivity, ground VLF, and gravity). The coinciding resistivity and gravity anomalies were drilled, and new uranium mineralization was discovered by UGC at Bong in 1984, End in 1987 and at Andrew Lake in 1988. Jane was discovered in 1988. Delineation of End and Andrew Lake was the focus of drilling up to 1996. From 1998 to 2007, the project was placed in care and maintenance. The geological resources were re-evaluated in 2007 based on the Kiggavik Main Zone, Andrew Lake and End Grid deposits, and were estimated at 56, 413 T @ 0.3% U (Kheloufi, 2007). New exploration drilling started again in 2009. The potential of the known deposits was first reassessed and potential extensions were tested. Discovered in 2014, the Contact prospect is the latest discovery in the district and was found using a multidisciplinary approach combining GIS-based mineral prospectivity analysis of the available airborne and ground geophysical data (Robbins et al., 2015; Roy et al., 2017).

In the Kiggavik, area, uranium mineralization is depicted as unconformity-related type (Weyer et al., 1987; Fuchs and Hilger, 1989; Friedrich et al., 1989; Sharpe et al., 2015) and is hosted within the Archean to Paleoproterozoic metamorphic and granitic basement that underlies the Proterozoic sediments of the Thelon Basin infill. Uranium pods are fracture controlled, located at the intersection between E-W and NE-SW oriented fault arrays (Flotté, 2009), but this structural control remains poorly constrained and understood, as the structural metallotects have not been appropriately identified yet. This study will characterize the structural control on the uranium mineralization in the Kiggavik area.

1 SOME CONSIDERATIONS ON THE GEOLOGY OF URANIUM

1.1 ABOUT URANIUM (U)

Uranium (U) is a lithophile element with a high affinity to oxygen. It is the 92th element of the Mendeleev's periodic table. It has a high ionic radius (1.43 Angstrom) and thus is not easily introduced in crystal structures of common rock-forming minerals. Uranium is not an abundant element; its average crustal abundance is between 2 and 3 ppm (Rogers and Adams, 1969). The lower crust is generally depleted in uranium with an average U content of 0,5 ppm (Barbey and Cuney, 1982). In the upper crust, granites and shales are typically "enriched" in uranium (Table 1). Due to its high ionic radius and valence, U is considered an incompatible element. This is expressed by enrichment of U in felsic melts as a consequence of partial melting and crystal fractionation: granites and rhyolites represent significant primary sources of uranium (Cuney, 2014).

Rock type	U-concentration (ppm)
Basalt	0,8
Sandstone	0.45
Granite	4,4
Shale	3,8

Table 1: Typical abundance of uranium in various rocks (after Krauskopf, 1979).

Uranium possesses 14 radioactive isotopes; the most common ones being ^{238}U, ^{235}U and ^{234}U. ^{238}U represents the most important fraction with 99.27% and is not naturally fissile, unlike ^{235}U. ^{235}U and ^{234}U represent 0.72% and 0.0058%, respectively (table 2). In order to be used in nuclear plants, uranium needs to be enriched in ^{235}U.

Atomic number	Atomic weight	Natural isotopes	Percent fraction	Half-life time
92	238	U234	0.0058%	2.6×10^5
		U235	0.72%	7.3×10^8
		U238	99.27%	4.5×10^9

Table 2: Percent fraction of the three main natural isotopes of uranium (Cuney et al., 1992).

Radioactive decay of uranium produces two types of particles, alpha and beta. The emission of alpha particles destabilizes the mineralogical structure of minerals hosting uranium (monazite, zircon, apatite…). This process of radioactive decay of uranium is used to date geological

events. Age determination is based on the fact that radioactive decay's speed of a radionuclide (a radioactive element) is always constant. ^{238}U and ^{235}U and their descendants (Fig. 2) are used to date geological events using different techniques; among these are Uranium-Lead and Lead-Lead dating, for example. The final stable products of decay chains of ^{238}U and ^{235}U are ^{206}Pb and ^{207}Pb respectively. ^{234}U is a decay product of the ^{238}U chain. ^{206}Pb and ^{207}Pb, with ^{208}Pb coming from ^{232}Th, are called radiogenic Lead. ^{204}Pb, or common Pb, is different because it is not a decay product.

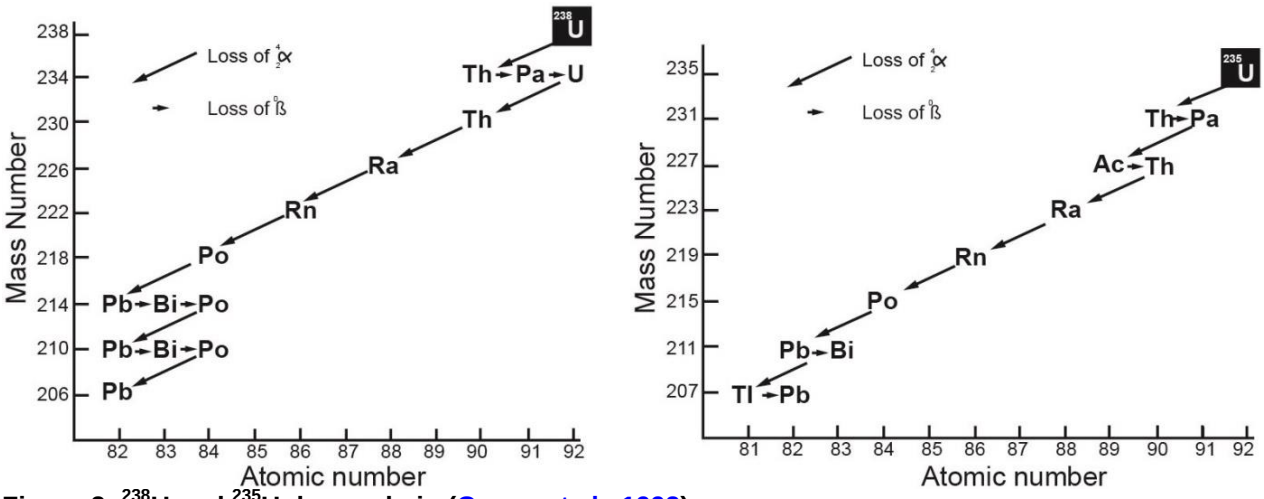

Figure 2: ^{238}U and ^{235}U decay chain (Cuney et al., 1992).

Uranium possesses five valences. Only U^{4+} (tetravalent) and U^{6+} (hexavalent) are important in mineralogy and geochemistry; they are the only two oxidation states stable in natural aqueous solutions. Other oxidation states are rare or stable only in laboratory conditions.

U^{4+} is stable under reducing conditions while U^{6+} is stable under oxidizing conditions. Tetravalent uranium prevails in metamorphic and magmatic environments; the principal ore minerals formed under such conditions are uraninite and pitchblende (UO_2, Fig. 3A and B). The composition of both phases relies mainly on the conditions of the precipitating environment. Uraninite crystallizes at temperatures higher than 300°C and contains commonly high ionic radius elements such as Th or REE. Pitchblende crystallizes usually below 300°C and may contain Ca, Si and Pb.

Hexavalent uranium occurs more frequently as a complex ion (UO_2^{2+}) associated with different elements such as silicon, phosphorus and vanadium, and forms many mineral species in oxidizing environments (more than 400 different species). They usually display bright colours like yellow and green, some of them fluoresce under ultraviolet light (Fig. 3C and D). Uraninite, pitchblende and coffinite ($USiO_4$) are U^{4+} compounds, and are the primary uranium ore minerals.

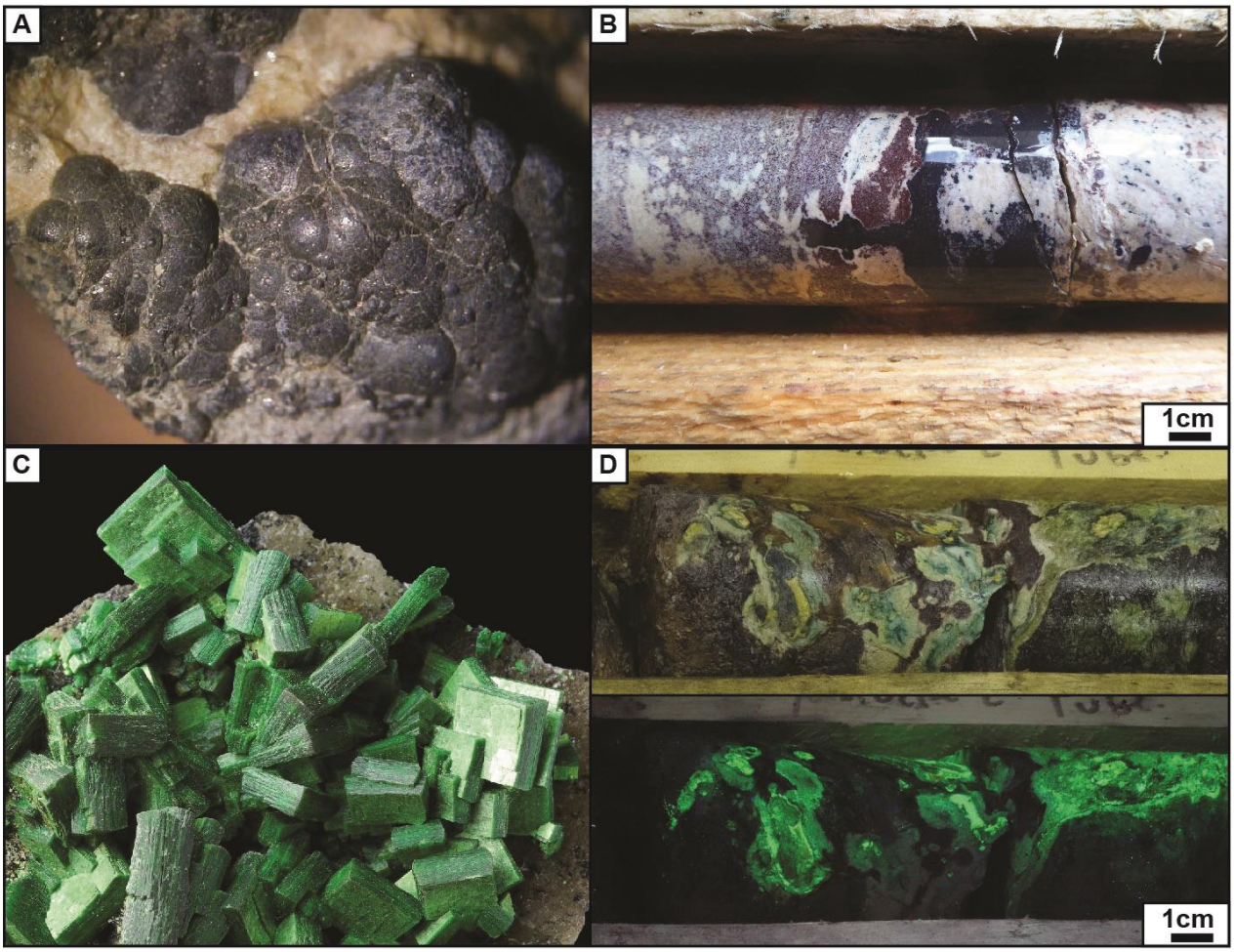

Figure 3: A) Colloform pitchblende concretions. B) Pitchblende in a drill core (black mineral) from the Andrew Lake deposit (Kiggavik area). C) Euhedral crystals of Torbernite ($Cu(UO_2)_2(PO_4)_2 \cdot 12$ H2O). D) Hexavalent uranium (top picture) minerals displaying green fluorescence (bottom picture) in a drill core from the Kiggavik Andrew Lake deposit.

Hexavalent uranium minerals are commonly derived from the "primary" varieties. Hexavalent uranium (mobile under uranyl complexes, transported in aqueous solution) has to be reduced to tetravalent uranium or complexed to precipitate as pitchblende or uraninite (Fig. 4). The major controls on deposition of uranium from aqueous fluids are redox processes, pH increase/decrease, ligand concentration, and change in temperature. Other important processes include adsorption (on clay, organic and other particles or on certain hydroxides such as Ti hydroxides for example) and bacteria-mediated deposition at low temperatures (Lovley et al., 1991; Waite et al., 1994; Fredrickson et al., 2000; Sherman et al., 2008).

.

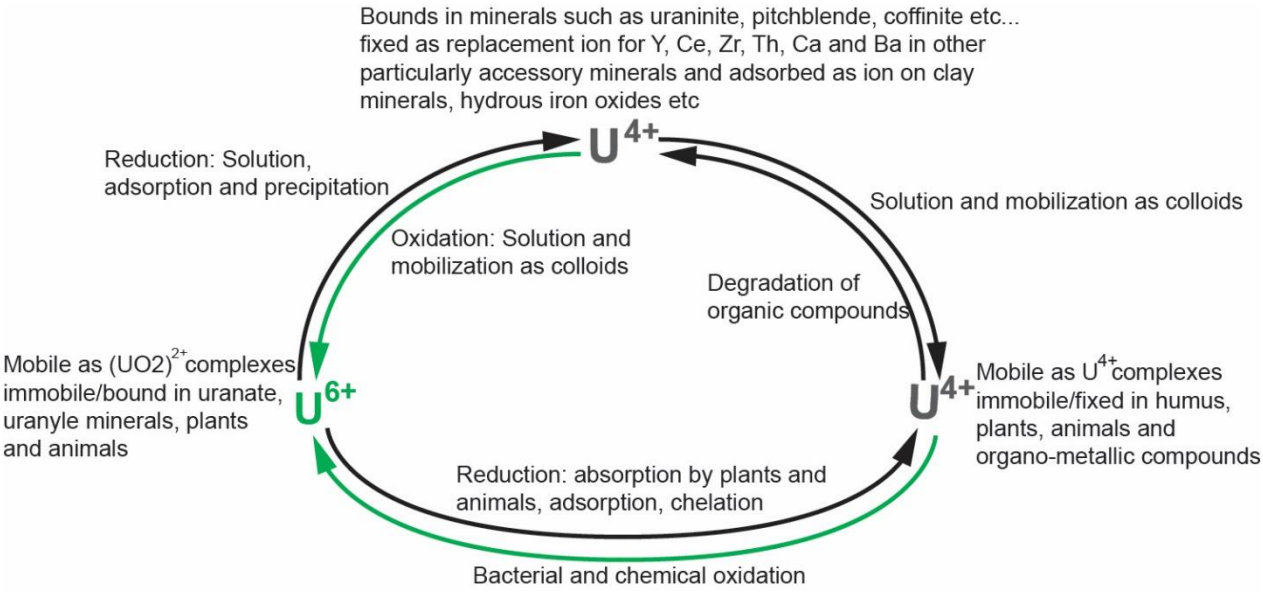

Figure 4: Uranium conversion cycle (after Dahlkamp, 1993).

1.2 TYPOLOGY OF U ORE DEPOSITS

1.2.1 CLASSIFICATION OF U ORE DEPOSITS

There are three general classification schemes.

- Dahlkamp, (1993) and the International Atomic Energy Agency (IAEA) developed a classification scheme for uranium deposits based on the lithology and ore-body morphology of uranium districts listed in the IAEA UDEPO database (15 deposit types and 50 sub-types, http://www-nfcis.iaea.org).
- Plant et al. (1999) and Skirrow et al. (2009) used end-member fluid types to make a genetic classification of uranium deposits, gathering uranium deposits into three end-members mineralizing systems (basin and surface-related uranium systems, metamorphic-related uranium systems and magmatic-related uranium systems). This classification is mainly based on the host rock lithologies. Such an approach may lead to the inclusion of deposits formed by different genetic conditions in the same deposit category and thus may be misleading for exploration (i.e., unconformity-related mineralization hosted in granite and classified as granitic-vein uranium mineralization).
- Cuney and Kyser, (2015) used a genetic classification scheme based on the dominant mechanism responsible of the primary uranium deposition of the deposit. This

classification (Cuney, 2015; modified from Cuney, 2011; 2014) is presented in Table 3. Fifteen categories are regrouped in Table 4 for the IAEA classification; and the Fig. 5 displays a synthetic representation of the geological setting of the various uranium-deposits types.

	Deposit type	size	% U	common ages	type example	Reference
M	**MAGMATIC**					
MCF	Crystal fractionation	small/medium	0.1	2.7 Ga to present	Ilimaussaq	Sorensen, 1974
MPM	Partial melting	large	x 0.01	Neoarch., 1.8 - 1 - 0.5 Ga	Rössing	Berning et al. 1976
H	**HYDROTHERMAL**					
HV	Hydrothermal Volcanic	small/very large	0.05-0.2	mostly post-Silurian, largest Jurassic-Cretac.	Streltsovkoye	Chabiron et al. 2003
HG	Hydrothermal Granitic	small/large	0.1-0.6	Permian, Cretaceous	Niederschlema	Golubev et al. 2000
HD	Hydrothermal Diagenetic					
HDia	*- intraformational redox*					
HDiaTb	** tabular*	small/large	0.1-0.2	Post-Silurian	Grants	Hansley and Spirakis 1992
HDiaTl	** tectonolithologic*	small/large	0.1-0.4	Post-Silurian	Lodève	Mathis et al. 1990
HDiaCb	** collapse breccia*	Small	0.1-0.9	Jurassic	Colorado	Wenrich and Sutphin 1989
HDbb	*- basin/basement redox*	small/very large	0.2-20%	1.7 to 1.3 Ga	McArthur River	Kyser and Cuney 2009
HDir	*- interformational redox*	small/medium	0.1-0.4	2.0 Ga – 1.5 Ga	Oklo	Gauthier-Lafaye 1986
HMp	Hydrothermal-Metamorphic	small/medium	0.5-0.05	1.8 – 0.5	Kawanga	Eglinger et al. 2013
HMt	Hydrothermal-Metasomatic					
HMtNa	*- Na-metasomatism*	small/large	0.1-0.2	1.8 Ga – 0.5 Ga	Michurinka	Cuney et al. 2012
HMtK	*- K-metasomatism*	large	0.1		Elkon district	Boitsov and Pilipenko1998
HMtSk	*- skarns*	small	0.1	1.8 – 1.5 – 1.0 - 0.5 Ga	Mary Katheleen	Maas et al., 1987
M MB MRf	**METEORIC WATER INFILTRATION** ** basal type* ** roll front*	small/large small/very large	0.01-0.1 0.01-0.2	Tertiary –Quaternary Jurassic - Cretaceous	Vitim Wyoming	Kondrat'eva et al. 2004 Adams and Cramer 1985
S	**SYN-SEDIMENTARY**					
SMs	*- mechanical sorting*	large	0.02-0.15	2.9 Ga – 2.4 Ga	Witwatersrand	Frimmel et al. 2005
SRt *SRtM* *SRtC*	*- redox trapping* ** marine (black shales)* ** continental (coal, lignite…)*	 very large small/medium	 0.005-0.3 0.001-0.5	 Paleozoic-Mesozoic Paleozoic-Mesozoic	 Randstatt Kazakhstan	 Andersson et al. 1985 IAEA 2005
SCcr	*- crystal-chemical/redox (phosphates)*	very large	0.005-0.03	Mainly Cretaceous Miocene-Pliocene	Morocoo Florida	IAEA 2001
E	**EVAPOTRANSPIRATION**	small/large	0.014-0.1	Tertiary –Quaternary	Yeleree	Carlisle et al. 1978
O	**OTHERS**	very large	0.01-0.04	Mesoproterozoic	Olympic Dam	Hitzman and Valenta 2005

Table 3: Genetic classification of the uranium deposits (Cuney, 2015).

1.2.2 U ORE DEPOSITS LINKED TO HYDROTHERMAL PROCESSES

In all these classifications, some deposits are linked to hydrothermal processes. Epigenetic deposits are associated with fluid circulation through porous and/or fractured rocks. There are various possible origins for these fluids: meteoric, diagenetic, and metamorphic or a mixing of these different fluids. The following types of deposits (Cuney and Kyser, 2015) are associated with low temperature hydrothermal processes (<300°C):

	Deposit types	#	Deposit sub-types	#	Type locality
1	Intrusive	83	1.1. Anatectic	51	Rossing, Namibia;
			1.2. Plutonic	32	*Quartz monzonite*: Bingham, USA *Peralkaline complexes*: Kvanefjeld Greenland *Carbonatite*: Palabora in South Africa
2	Granite-related	129	2.1. Endogranitic	80	La Crouzille district, France
			2.2. Perigranitic	49	Niederschlema-Alberoda, Germany
3	Polymetallic Fe-oxide breccia complex	15		15	Olympic Dam, Australia
4	Volcanic-related	124	4.1. Structure-bound	103	Streltsov-Antei, Russia
			4.2. Strata-bound	18	Dornod N° 7 ore zone, Mongolia
			4.3. Volcano-sedimentary	3	Anderson Mine, USA
5	Metasomatite	76	5.1. Na-metasomatite	54	*Granite-derived*: Central Ukraine *Metased.-metavolcanic-derived*: Michelin, Canada
			5.2. K-metasomatite	17	Elkon District, Russia
			5.3. Skarn	4	Mary Kathleen, Australia
6	Metamorphite	106	6.1. Strata-bound	5	Forstau in Austria
			6.2. Structure-bound	92	*Monometallic*: Schwartzwalder, USA *Polymetallic*: Shinkolobwe, DRC
			6.3. Marble-hosted phosphate	9	Itataia, Brazil
7	Proterozoic unconformity	84	7.1. Unconformity-contact	36	Cigar Lake, Canada
			7.2. Basement-hosted	43	Jabiluka, Australia
			7.3. Stratiform fracture-controlled	5	Lambapur, India
8	Collapse breccia pipe	16		16	Arizona Strip, USA
9	Sandstone	627	8.1. Basal channel	76	Dalmatovskoye, Russia
			8.2. Tabular	294	*Continental fluvial, intrinsic reductant:* Arlit, Niger *Continental fluvial, extrinsic humate/bitumen:* Grants, USA *Continental fluvial V-U*: Salt Wash type, USA
			8.3. Rollfront	231	*Continental, intrinsic reductant*: Wyoming USA *Continental to marginal marine*, intrinsic reductant: Chu-Saryisu, Kazakhstan *Marginal marine, extrinsic reductant*, Texas, USA
			8.4. Tectonic-lithologic	18	Lodève Basin, France
			8.5. Mafic dykes/sills	8	Westmoreland District, Australia
10	Paleo quartz pebble conglom.	69	10.1. U-dominant	26	Elliot Lake District, Canada
			10.2. Au-dominant	43	Witwatersrand Basin, South Africa
11	Surficial	65	11.1. Peat-bog	2	Kamushanovskoye, Kyrgyzstan
			11.2. Fluvial valley	39	Yeelirrie, Australia
			11.3. Lacustrine-playa	21	Lake Maitland, Australia
			11.4. Karst cavern		Tyuya-Muyun, Kyrgyzstan
			11.5. Pedogenic/fracture-fill	3	Beslet, Bulgaria
12	Lignite-coal	33	12.1. Stratiform	31	Koldzhat, Kazakhstan
			12.2. Fracture-controlled	2	Freital, Germany
13	Carbonate	10	131. Stratabound	1	Tumalappalle, India
			13.2. Cataclastic	7	Mailuu-Suu, Kyrgyzstan
			13.3. Paleokarst	2	Sanbaqi, China
14	Phosphate	49	14.1. Organic phosphorite	7	Mangyshlak, Kazakhstan
			14.2. Phosphorite	38	Phosphoria Formation in the USA
			14.3. Continental phosphate	4	Bakouma district, Central African Republic
15	Black shale	45	15.1. Stratiform	26	Haggan in Sweden
			15.2. Stockwork	19	Roneburg district in Germany

Table 4: Uranium deposit types and sub-types listed in order of economic ranking (Cuney and Kyser, 2015, from IAEA 2014 red book).

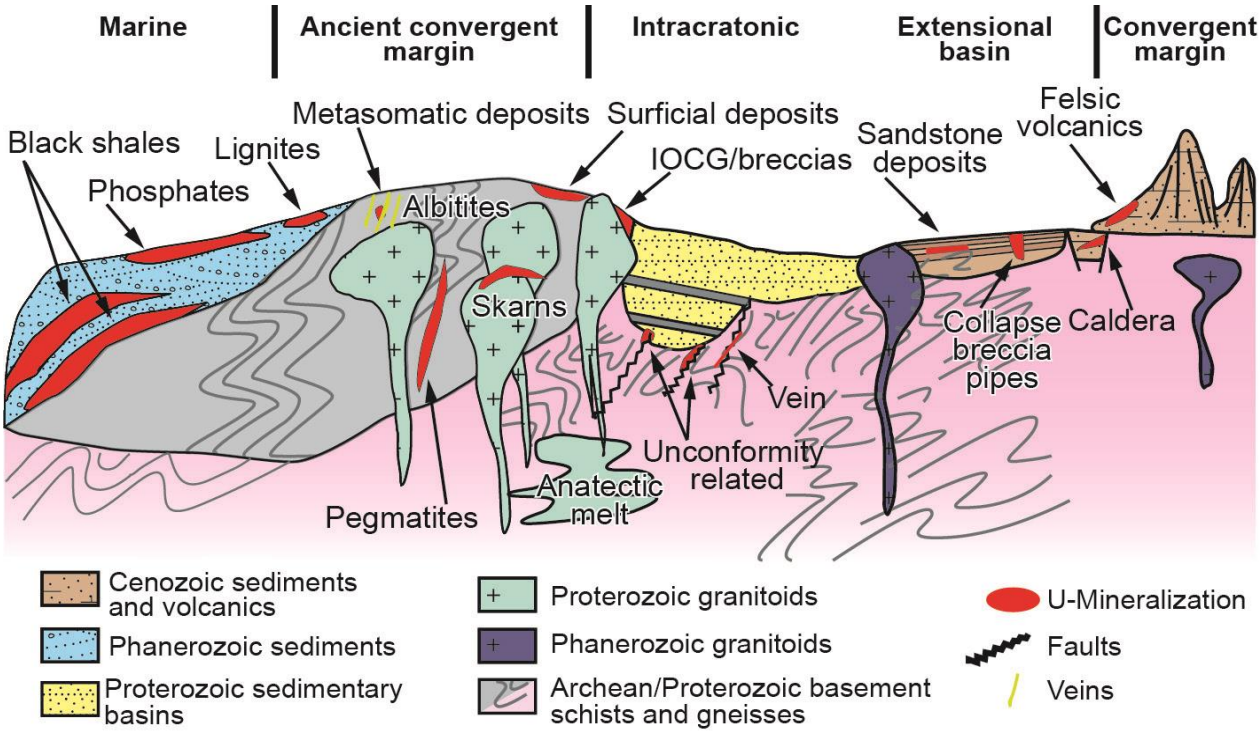

Figure 5: Scheme summarizing the various types of uranium deposits and their environment. The term "Vein-type" deposits has been abandoned and these deposits reclassified (after Cuney and Kyser, 2015).

Volcanic-associated ore deposit: This type, located mainly in continental extensional settings, and in some cases in caldera complexes, occurs with felsic volcanic rocks. These deposits are related to faults and shear zones within volcanic units. They form from uranium enriched felsic magmas that are subsequently enriched by hydrothermal fluids. They range in ages from Proterozoic to Tertiary. Typical examples of these deposits are Streltsovsk caldera in Russia and the McDermitt caldera in Basin and Range in USA.

Sandstone-hosted ore deposits: These occur in medium- to coarse-grained arkosic sandstones deposited in continental fluvial or marginal marine environments (Sanford, 1994). Impermeable layers, typically mudstones, interbedded in the sedimentary sequence, commonly occur above and below the mineralized sandstones. U^{6+} transported by slightly modified basinal brines is reduced to U^{4+} and precipitates as UO_2 when the fluid interacts with a reductant such as carbonaceous material, sulfides or hydrocarbons. Most deposits are younger than 440 Ma, after the time in Earth history when organisms began to invade the continents. Different types of sandstone uranium deposits exist, the three main are:

- Roll-front deposits: arcuate bodies of mineralisation that crosscut sandstone bedding, often in palaeo-channels. Good examples are deposits in Kazakhstan like the Tortkuduk (Mathieu et al., 2015) and Moynkum deposits, and in the USA like the Crow Butte (Hansley et al., 1989) and Smith Ranch ones (Leibold, 2013; WoldeGabriel et al., 2014).

- Tabular deposits: irregular, elongate lenticular bodies parallel to the depositional trend, commonly in palaeo-channels incised into underlying basement rocks. Examples are the Akouta (Turpina et al., 1991), Arlit (Pagel et al., 2005), and Imouraren (Pagel et al., 2005) deposits (Niger).

- Tectonic/lithologic deposits: they occur in sandstones adjacent to permeable faults. Examples are in the Lodève (Laversanne, 1978) District (France) and in the Franceville Basin (Gabon, Diouly-Osso and Chauvet, 1979).

Paleo quartz-pebble conglomerate: The deposits occur as uraninite, brannerite, monazite and thoro-uraninite in basal Paleoproterozoic conglomerates that overlie Archean basement (OECD/NEA-IAEA, 2014). Uranium occurs in seams rich in pyrite and organic matter. The origin of the uranium in these deposits remains contentious, with most models favouring a detrital origin for some of the uranium, with a later hydrothermal remobilization and introduction of additional uranium that reacted with carbonaceous material. Two representative deposits are the Elliot Lake deposits in Canada, mined exclusively for uranium (Ifill et al., 1989) and the Witwatersrand deposit in South Africa (Depiné et al., 2013), where uranium is produced as a by-product of gold mining.

Granite-related deposits: These deposits include veins hosted in granite or adjacent rocks and disseminated mineralization in episyenite bodies where quartz has been hydrothermally dissolved. In the Hercynian belt in Europe (i.e., uranium mineralization in the Bohemian massif, Czech Republic) and other parts of the world, these deposits are generally associated with large, peraluminous, two-mica granite complexes. They are related to crystal fractionation which is a major mechanism leading to uranium enrichment in the Earth. Two subtypes are defined from their location either in the granitic pluton (endogranitic deposits) or in the country rocks (perigranitic deposits), though deposits may straddle the contact. Resources range from small to large and grades vary from low to medium (Kvanefjeld deposit, Greenland, 220 000 tU at 240pp;

Rössing deposit, Namibia, 250 000 tU at 300ppm, Berning et al., 1976; Basson and Greenway, 2004).

Proterozoic unconformity-related uranium (URU) ore deposit: This last type is the most representative deposit type associated with hydrothermal processes. These deposits usually occur where metamorphosed and folded lower Proterozoic graphitic-pelitic sediments and Archean granitic gneiss domes are unconformably overlain by Unmetamorphosed Mesoproterozoic red beds. Uranium ores are associated with a strong clay alteration halo, can be found at or around the unconformity. Two sub-types are observed: i) Clay-Bound (e.g., Cigar-Lake, Canada) and ii) Fracture-Bound (e.g., Eagle Point, Canada), and described more in details hereafter. Major unconformity-related uranium deposits are found in the Athabasca Basin in Canada and other Paleoproterozoic basins in Canada are less explored, but unconformity-related uranium mineralization does exist: e.g., the Otish basin in Quebec, with the Camie River deposit (Beyer et al., 2012) and the Beaver Lake mineralization (Gatzweiler, 1987). The Hornby Bay Basin hosts the Port Radium U-Ag mineralization (Gandhi et al., 2013).

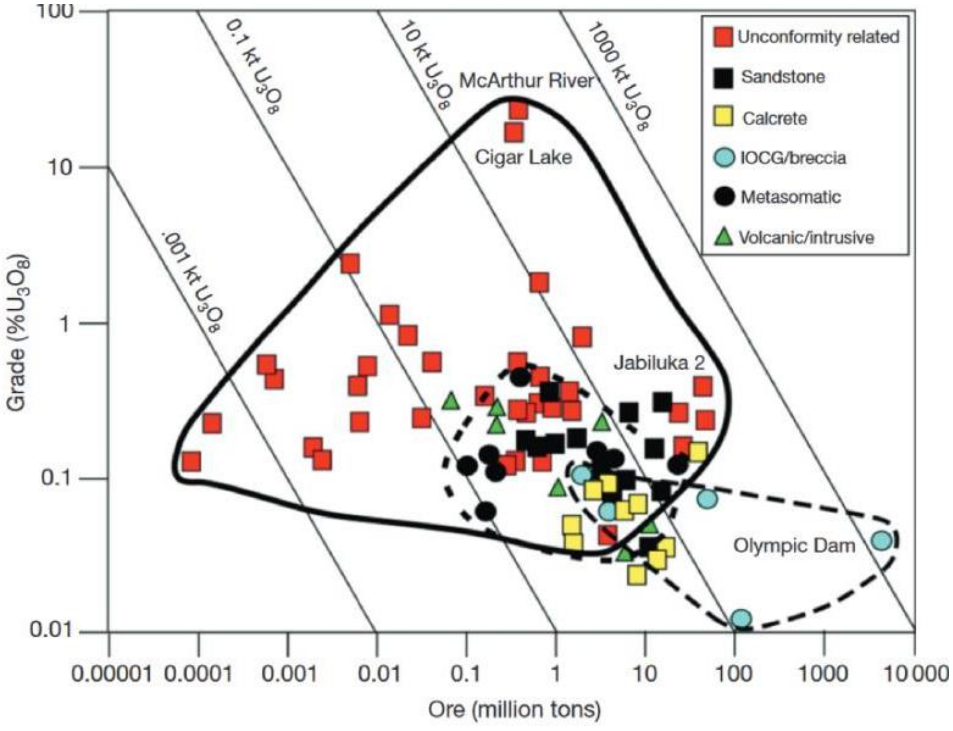

Figure 6: Basin grade versus tonnage for the major types of uranium ore deposits in the world. Unconformity-related uranium deposits (solid line) have the highest worldwide grade and large reserves (Cuney and Kyser, 2009).

URU deposits have the highest grades and large reserves: the average grade of these deposits varies from 1%U to over 15%U (Jefferson et al., 2007). The most spectacular grades and tonnages (Fig.6) are come from Cigar Lake (east and west zones combined ~875 000t of

ore grading at ~15% and containing ~131 000 tonnes U) and McArthur River (1 000 000t of ore grading at ~22.28% and containing ~192 000 tonnes U). In Cigar Lake, the presence of highly radioactive high-grade uranium ore leads to specific mining technique called “block caving”, where the recovery of the ore is mainly made by machines driven by technicians, using remotely-controlled high pressure water (Jamieson, 2000). Within Australia, unconformity deposits account for approximately 20% of the uranium resources with medium to large deposits (40 000 to 180 000 tU) at low to medium grades (~0.2-1.0%). The second and third largest uranium deposits in Australia, Jabiluka and Ranger, are located within the Alligator Rivers ore field (Northern Territory, www.wise-uranium.org, 2013). The Kiggavik area, the subject of this study, hosts deposits which display some characteristic features of URU mineralization. These deposits support economic comparisons with the uranium deposits in the Athabasca Basin, as shown in Fig.7 which compares the Kiggavik (e.g., End, Andrew Lake), Athabasca (e.g., Cigar Lake, Eagle Point, Cluff Lake) and Australian deposits (e.g., Jabiluka, Nabarlek, Ranger).

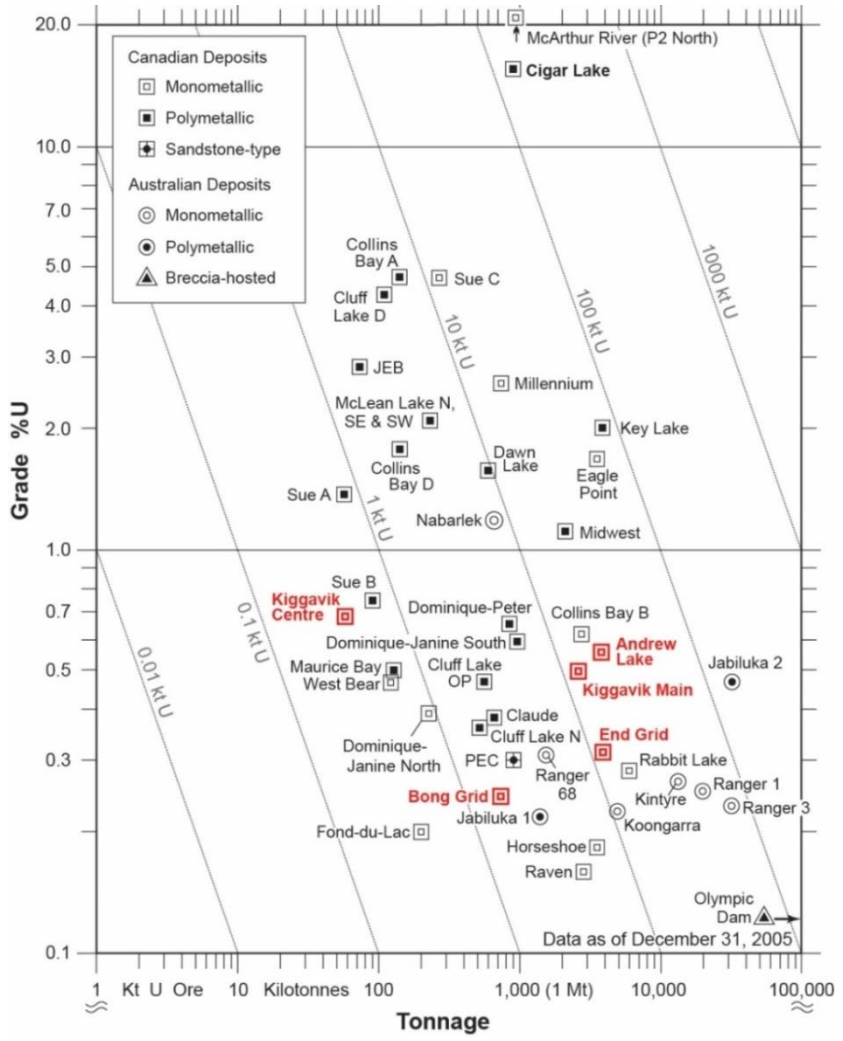

Figure 7: Grade versus tonnage plot of URU and selected other types of uranium deposits in Canada (squares, deposits from Kiggavik area are in red) and Australia (circles). Modified after Jefferson et al., 2007.

In the next section the main processes leading to the formation of URU deposits will be reviewed, in terms of their timing and metallogenic evolution, as background information for better understanding the Kiggavik-related deposits.

1.3 GEOLOGY AND GENESIS OF UNCONFORMITY-RELATED URANIUM MINERALIZATIONS

1.3.1 GENERAL CONCEPTS

The formation of URU deposits is linked to a reduction front near the unconformity between Paleoproterozoic sandstones and underlying metamorphosed basement lithologies (Fig. 8). This redox front is produced from the circulation of basinal brines mixing with a reduced fluid from the basement, or by interaction of the brines with reducing lithologies (e.g., graphitic pelites) of the basement. The deposits are structurally-hosted either in the basement, at the unconformity, or in the sandstone. In all cases clay bounded, massive ore composed of veins, pods and massive accumulation of uraninites develops along, above or immediately below the unconformity or more in the overlying sandstone (perched mineralization, e.g., Shea Creek, Cigar Lake).

As stated previously, unconformity-related uranium deposits can be divided between basement-hosted deposits (monometallic, fracture-bound) and unconformity-basin-hosted deposits (polymetallic, clay-bound). Principal uranium minerals are pitchblende, uraninite, coffinite (uranium oxide silicate), and some amorphous uranium-carbon material.

- Basement-hosted deposits present a more simple mineralogy, with simple Fe and Pb sulfides such as pyrite and chalcopyrite. These deposits are hosted in fractures and faults and therefore are usually narrow in terms of the ore-body and alteration zone.
- Basin-hosted deposits are typically high in grade and tonnage. (Cigar Lake) and characterized by sulfides, arsenides, locally selenides and tellurides. These secondary elements are thought to reflect local variations in geochemistry and metal endowment of lithostratigraphic units, their concentration can vary considerably and in most cases they do not represent economic concentrations.

Current models for the formation of unconformity-related uranium deposits can be divided into two end-members: one involves the basement as the source of the uranium and the basin as the source of the fluids (Cuney et al, 2003) and the other involves the overlying basin as a source for both uranium and fluid (Kyser et al., 2005). Mineralizing fluid circulation can be

characterized by a downward “ingress” circulation, e.g., Rabbit Lake, Eagle Point, in Canada; Jabiluka, Ranger, Nabarlek, in Australia, Jaireth et al., 2016; Skirrow et al., 2016), or by a upward “egress” circulation of fluids, e.g. McArthur River, Cigar Lake, Key Lake, in Canada, Dalkamp, 1993; Jefferson et al., 2007).

Remobilization of uranium is common in all deposits and is associated with an extensive loss of radiogenic lead (Holk et al., 2003; Kister et al., 2004; Uvarova et al., 2012). Uranium is redistributed along redox fronts related to cold and late meteoric fluid infiltration. Such fronts show similar features (mineralogical and geochemical) as Phanerozoic uranium roll-front deposits (Mercadier et al., 2011a).

The extensive circulation of fluids associated with these deposits can produce significant alteration zones in the overlying sandstones or in the basement rocks around the uranium orebodies (Hoeve and Quirt, 1984). Due to differences in fracture-propagation, permeability and porosity, alteration tends to be different in basin-hosted and basement-hosted deposits both in character and extent but the main lines are comparable (see Fig.8).

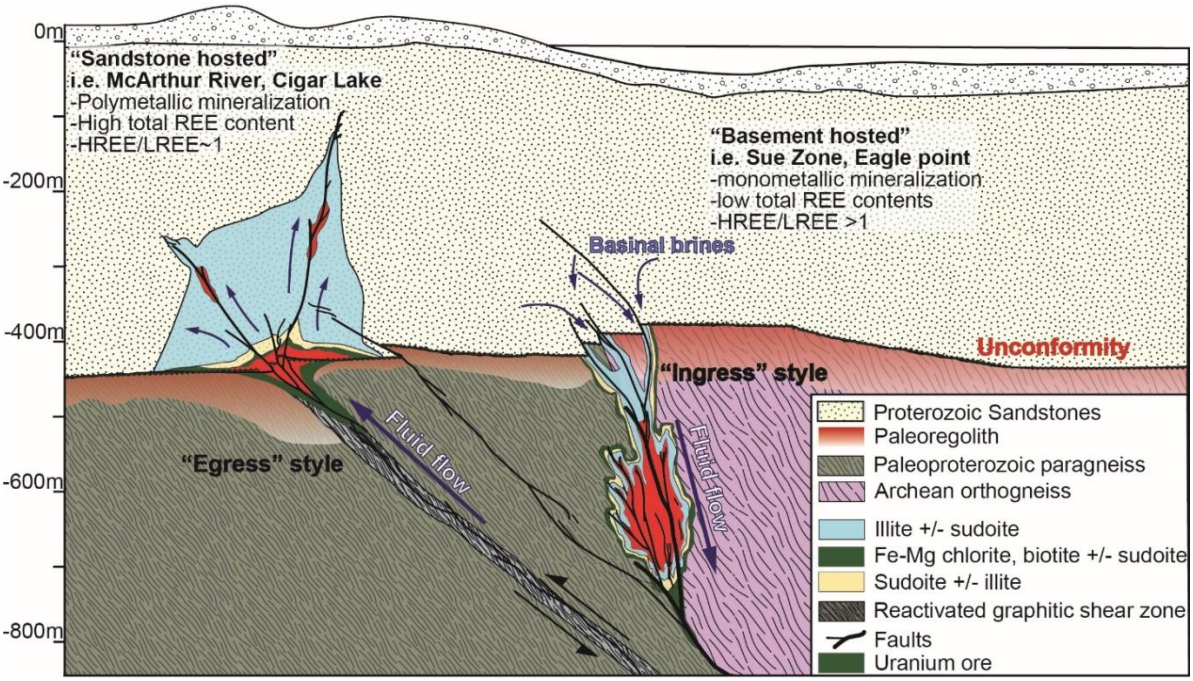

Figure 8: General components and geology of Proterozoic unconformity-related uranium deposits showing basement- and basin-hosted types (After Hoeve and Quirt, 1984; Quirt, 2003 and Jefferson et al., 2007).

Alteration, mineralogy and geochemistry of URU deposits and their host rocks are the most important exploration criteria. A detailed paragenesis of alteration minerals in the Athabasca Group and basement rocks was developed by Hoeve and Quirt (1984), Miller and LeCheminant

(1985), Kotzer and Kyser (1995) and refined by Fayek and Kyser (1997), Wasyliuk (2002), Kister et al., (2005, 2006), Derome et al., (2005) and Alexandre et al., (2005). They set the modern template for exploration of these deposits using clay mineralogy, where uranium orebodies are surrounded by a zoned alteration halo consisting of Fe-Mg trichlorite and di,trichlorite (sudoite) closer to the orebody and sudoite-illite intergrown in the outer zone, in the case of egress type deposits (fluid flow from the basement to the basin, Fig. 8). In ingress-type deposits, relatively unaltered material displays Fe-Mg trichlorite and illite, and strongly altered rocks show illite and sudoite. Riegler et al., (2014) also showed that, in the case of illite, the closer to the orebody -to uranium oxides- the poorer the cristallinity.

1.3.2 PROCESSES CONTROLLING UNCONFORMITY-RELATED URANIUM MINERALIZATIONS

In this section, the three main factors involved in the formation of unconformity related uranium deposits will be reviewed, including: (1) the source(s) of uranium, (2) the mechanisms of uranium transport, and (3) the mineralization place/trap. A synthesis of the current genetic model for unconformity-related uranium mineralization will be presented at the end of this section.

1.3.2.1 Source(s) of uranium

The uranium content of potential sources is one factor among others in generating a uranium-bearing ore fluid. In hydrothermal systems where uranium is leached through fluid-rock interaction, a critical factor in the effectiveness of the mineral system is the availability of uranium for possible transfer from minerals to the fluid. Uranium will be easily scavenged from metamict minerals or from minerals less resistant to alteration, compared to fresh refractory minerals (Fayek et al., 2010; Mercadier et al., 2013a).

In unconformity uranium deposits, current models for the formation of the deposits can be divided into two general end-members. One involves the basement rocks as the source of the uranium (Hecht and Cuney, 2000; Derome et al., 2003b; Richard et al., 2010; Mercadier et al., 2012, 2013a) and the basin as the source of the fluids (Cuney et al., 2003), the other involves the overlying basin as a source for both the uranium (Wilde and Wall, 1987; Fayek and Kyser, 1997; Kyser et al., 2000; Polito et al., 2004, 2005a, 2011) and the fluids.

In the case of the basin as a source, uranium derives from the breakdown of U-bearing refractory heavy minerals of the detrital phases, such as monazite, zircon or phosphates. In the

case, of a basement source, uranium could be leached from monazite, U-enriched mylonite zones or pre-Athabasca mineralization, like the Beaverlodge pitchblende veins (Uranium mineralization in the underlying basement, derived from fertile uranium-bearing basement granites and significantly post-dated by unconformity related uranium deposits; Tremblay, 1972). Another example is the Millenium deposit, where the 1750-1650 Ma ages of uraninite (Cloutier et al., 2009; Beshears, 2010) were the first documented pre-Athabasca ages from an unconformity-type deposit and supported the occurrence of a basement source for unconformity-related uranium mineralization. Mercadier et al., (2013a) showed that there are easily leachable proto-ores consisting of magmatic and metamorphic uraninite of Hudsonian age in the basement rocks on the eastern margin of the Athabasca basin.

Although altered U-bearing minerals have been identified as possible sources in both basin and basement rocks, no studies have so far recognised large-scale basement alteration zones representing the uranium-leached source rocks and definitively linked them genetically to the uranium deposits. The paleoregolith with uraniferous enrichment could also have been a good complementary source of uranium. It occurs regionally and directly beneath the unconformity of the Athabasca Basin (Macdonald, 1980) and in the Australian Alligator River Uranium Field. These two paleoregoliths are uranium-depleted and therefore could represent parts of the uranium mineral systems. Skirrow et al., (2015) reported observations of basinal fluid flow in the paleoregolith zones distal from the Ranger deposit (Australia) and possible intakes of uranium from these zones.

1.3.2.2 Uranium transport

A general consensus has emerged for the fluids responsible in the formation of unconformity-related uranium deposits. These deposits are thought to have formed from basin-scale circulation of basin-derived (basinal) brines at temperatures of 120-200°C that percolated between sedimentary basins and underlying crystalline basement rocks (e.g. the pioneering “diagenetic-hydrothermal” model of Hoeve and Sibbald, 1978, also Derome et al., 2005; Boiron et al., 2010; Richard et al., 2013a; Richard et al., 2015).

Analysis of fluid inclusions genetically linked with the uranium mineralization by fluid inclusions microthermometry, LA-ICP-MS, synchrotron-SRF and XANES have shown that these brines have salinities of 25–35 wt% NaCl equivalent, with highly variable Na/Ca ratios from NaCl-rich to $CaCl_2$-rich end-members (Derome et al., 2005; Richard et al., 2013b), and with U(VI) contents up to 600 ppm (Richard et al., 2010, 2012). These brines are oxidized, with a fO2>-45 in the hematite field (Ruzicka, 1996), owing to the lack of organic matter and the

presence of pervasive hematite in these basins. The oxidized nature of the brine is a critical factor because, as said in Section 2.1, in order to be mobilized in a fluid, uranium has to be oxidized from U^{4+} to the U^{6+} form. Theses oxidized brines display a pH of ~4.5 at 200°C (Cuney et al., 2003). Temperatures during primary mineralization are interpreted in various ways. Pagel et al., (1980), Kyser et al., (2000), and Cuney et al., (2003) interpreted that ore was deposited during peak diagenesis at 180 to 250°C, suggesting a geothermal gradient on the order of 35°C/km.

Early diagenetic brines preserved as inclusions in quartz overgrowths on detrital quartz grains are NaCl-rich and inferred by Cuney et al., (2003) to have been derived from evaporitic layers that once existed in upper strata of the basin (a possible present-day analogue could be the sabkha of the Persian Gulf). Derome et al., (2002, 2003a, b) described fluids enriched in Ca, and inferred them to have resulted from their earlier interaction with Ca-rich basement rocks. High Ca in the mineralizing fluid has been suggested to be of major importance for uranium mobilization from basement source rocks.

If the basinal-derived brines were the carrier of the uranium, they likely travelled through faults that were important for focusing mineralizing fluids in these deposits (Hoeve and Sibbald, 1978). Reactivated faults rooted in the basement and initially associated with Trans-Hudson orogeny offset the unconformity up to 100m, and some are directly associated with mineralization, having acted as conduits for hydrothermal fluid flow in the vicinity of ore deposits (e.g., Hoeve and Quirt, 1984; Baudemont and Pacquet, 1996). In the McArthur River area, ore pods are localized where cross-faults intersect the main “P2” fault (Györfi et al., 2007) with mineralization mainly hosted in reverse faults along graphitic units and quartzites. At the Key Lake deposit, a direct association has been recognized between graphitic fault zones and uranium mineralization (Matthews et al., 1997). The importance of faulting in focusing fluid flow and related mineralization has been reinforced by recent numerical modelling studies (Zenghua Li et al., 2016, among others).

1.3.2.3 Trap/place of deposition of uranium

The final step of the process is the deposition of uranium, by reducing it from its hexavalent mobile form (uranyl ion UO_2^{2+} or associated complexes, usually chloride complex, Dargent et al., 2013) to its tetravalent immobile form (mainly uraninite and pitchblende, UO_2). Therefore, changes in the redox conditions are critical for the deposition of uranium from oxidized basinal brines. Several mechanisms exist (Yeo and Potter, 2010), the reductant can be present in a reduced lithology from the underlying basement (fluid-rock interaction) or the reduction can

proceed from the mixing with a reduced basement-derived fluid (mobile reductant, Fayek and Kyser, 1997).

Unconformity-related uranium can show spatial relationship with graphitic lithologies and faults, and in most deposits, mineralization is associated with carbonaceous matter. Hoeve and Sibbald (1978) hypothesized that CH_4 was the dominant product of hydrothermal alteration of graphite. Bray et al., (1988) proposed that interaction of basinal brines with sulfide-bearing graphitic metasediments could have produced reduced gases (CO_2, CH_4, H_2S, H_2 Cheney, 1985; Ruzicka, 1993; Alexandre et al., 2005a). Traces of these reduced gases were detected by Raman spectroscopy in fluid inclusions (Wilde et al., 1989; Derome et al., 2003a,b, 2005). These gases come from the reaction of the basinal brines with the variably graphitic schists by breaking them down (Alexandre and Kyser, 2005; Pascal et al., 2015).

Also other specific mechanisms exist like electron transfer with Fe^{2+} from pyrite oxidation, chloritization of biotite or illitization of hornblende (Wallis et al., 1985; Alexandre et al., 2005a). This is the Fe-U redox couple, following the reaction:

$$2Fe^{2+} + U^{6+} + 4H_2O + 0.5O_2(aq) \rightarrow \text{hematite} + UO_2 + 8H$$

The products of these processes are commonly preserved in the rock record as zoned alteration mineral assemblages centred on the redox front of the mineral system. Zones recording the passage of oxidized fluids may contain combinations of hematite or goethite replacing magnetite or sulfides; sulfate minerals; high Fe^{3+}/Fe^{2+} ratios in silicates such as chlorite or amphibole; high CO_2 /CH_4 ratios in fluid inclusion. Even if the presence of a reductant, such as graphite, is one of the major indicators of uranium enrichment, some recent discoveries in the basement are not directly connected with graphite-bearing rocks/structures (e.g. the Kiggavik deposits, Haid, 2014).

At the deposit scale, the relationship between fault intersections, inferred fluid flow, and ore locations was illustrated by Baudemont and Federowich (1996) for the Dominique-Peter deposit, Baudemont and Pacquet (1996) for the McClean Lake area, Rippert et al., (2000) for Shea Creek, Harvey and Bethune (2007) for the Deilmann orebody at Key Lake, and Tourigny et al., (2002, 2007) during active mining at Sue C mine. For example, at Cluff Lake, in extensional setting, en-echelon uranium-mineralized veins developed along listric faults as a result of the creation of open space within the hanging wall and the footwall. These kind of studies at the deposit scale, combined with field-work, usually show more detailed and accurate observations of geological features than can be observed only partially in drill cores, due to the strong clay

alteration associated with these alterations types.

In Australia, unconformity-related uranium deposits in the Pine Creek Orogen region are all structurally controlled. Northwest-trending reverse fault/shear zone controls the uranium mineralization at the Nabarlek deposit (Wilde and Wall, 1987). At the Jabiluka deposit, mineralisation is structurally controlled within semi-brittle shear zones sub-conformable to the pre-metamorphic stratigraphy of the basement, and also within breccias developed in the hinge zone of fault-related folds (Polito et al., 2005a, 2005b).

However, the presence of well-developed structures (associated or not with strong alteration) is not a perfect indicator of mineralization. Structural environments identical to those that host known deposits exist, but most of these environments contain no uranium mineralization. Favourable geological features are needed and favourable structures (e.g. ductile shear zones outlined by graphite and re-activated in a brittle manner, crosscutting local structures) is one of them in order to enhance fluid flow to focus uranium deposition.

1.3.2.4 Current genetic models of unconformity-related uranium mineralizations

There are two schools of thought about genetic models for unconformity-related uranium deposits, divided only by differences in the source of the uranium, and by the circulation of the brines. Fig.9 shows the four generalized models of formation.

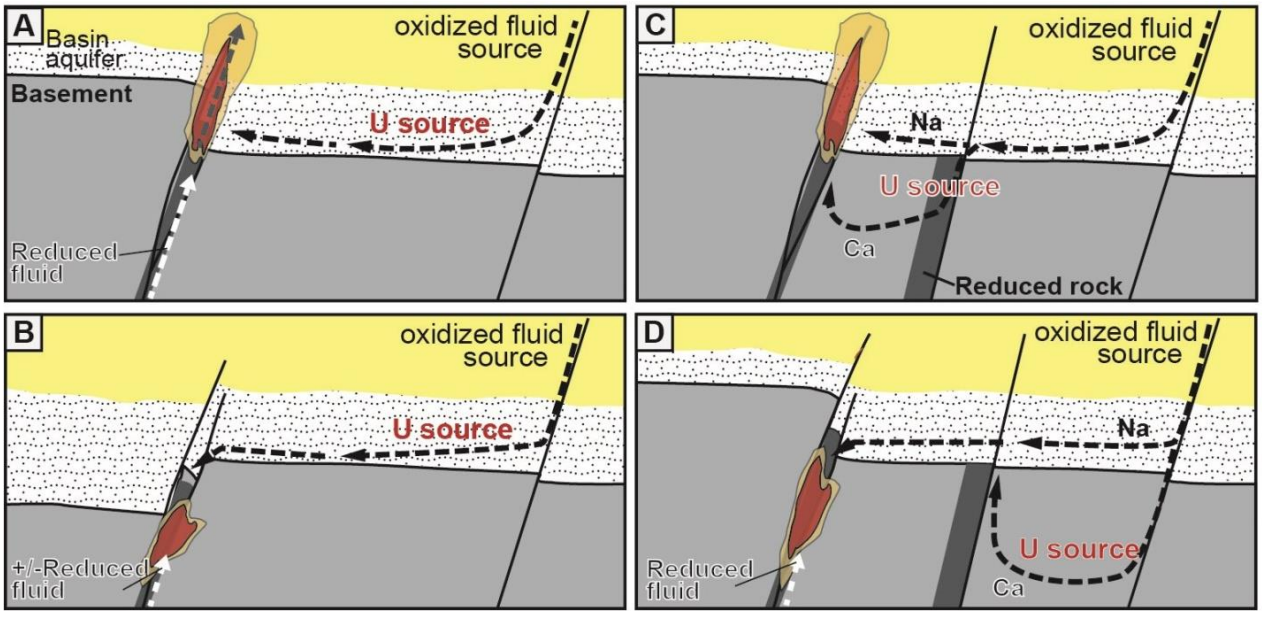

Figure 9: Models for the formation of URU deposits (after Skirrow et al., 2015).

Fig. 9A: Diagenetic-hydrothermal model of Hoeve and Sibbald (1978), the first genetic model developed for URU mineralization. Uranium is leached from heavy detrital minerals in the basin, and oxidized basinal brines mix at and above the unconformity with reduced fluid that was originally basinal fluid (reduction of these fluids proceed from fluid-rock interaction with the reduced basement rocks).

Fig. 9B: Model of basement-hosted mineralization where the basin is the source for the uranium. In this model, basinal brines rich in uranium interact with reduced basement rocks in and around fault zones (Wilde et al., 1989; Jefferson et al., 2007). There is also a possibility for an interaction beneath the unconformity with a more or less reduced, ascending fluid as suggested by Wilde et al. (1989). Reverse faulting setting is the most common case scenario but Cui et al., (2012) also proposed formation of basement-hosted deposits via downflow during normal faulting and extension.

Fig. 9C: Model with the basement as a source for uranium. It involves percolation of basin-derived Na-rich brines into basement, exchange of Ca for Na, leaching of uranium, and then mixing of the Na and Ca–U-rich brines to precipitate uranium (Mercadier et al., 2010, 2012).

Fig. 9D: Model where the basement is the source for uranium. Oxidized basinal brines descend down into fault systems and leach uranium from the basement rocks, becoming Na-Ca brines and precipitate uranium on reaction with reductants or mixing with an ascending, reduced fluid (Derome et al., 2003a).

Despite the critical role played by tectonic structures which are a common feature of most, if not all, URU mineralization models, such faults remain poorly documented in terms of their architecture and characteristics, including description of fault zonation (core zone, damage zone etc.) and related fault rocks present, as well as the relationship of these elements to mineralization.

1.3.2.5 Time constraints on the mineralizing events in some notable Proterozoic basins hosting unconformity-related deposits

Studies on uranium mineralization in the Beaverlodge district (Northwest margin of the Athabasca Basin) yielded uraninite ages for the main uranium-mineralizing stage of ca. 1830 Ma (Koeppel, 1967; Dieng et al., 2013; Dieng et al., 2015). This mineralization is located near the unconformity between basement gneiss and the Martin Group volcano-sedimentary rocks of the Athabasca Group. This mineralizing event is linked with the Trans-Hudson Orogeny and magmatic-volcanic-related systems of the Martin Lake Basin, (Bosman and Ramaekers, 2015)

and is not an unconformity-related mineralization. Sedimentation began in the eastern Athabasca Basin at ca. 1700 Ma (Rammaekers et al., 2007; Rainbird et al., 2007) and slightly earlier in the west (Ramaekers et al., 2007). Age dating on fluorapatite cements of ca. 1630 Ma (Rainbird et al., 2003b) in the Athabasca Basin (Fig. 10) suggests a regional hydrothermal event at about the same time as localized pre-ore alteration minerals developed (1670-1620 Ma; Alexandre et al., 2003).

Athabasca Basin U deposits record two primary hydrothermal ore-related events, synchronous with development of alteration envelopes. The first uranium mineralization event occurred at ca. 1590 Ma -based on U/Pb dating of uraninite and Ar/Ar dating of syn-ore illite- and is obtained in several studies throughout the Athabasca basin in both the basement and basin-hosted deposits (Alexandre et al., 2007; Cloutier et al., 2009, 2010, 2011; Dieng et al., 2013; Chi et al., 2016). The second uranium mineralization event exhibits ages from ca. 1500 to 1300 Ma (McGill et al., 1993; Fayek et al., 2002). This event is thought to correspond to the tectonic inversion of the Athabasca. These two main mineralization events were overprinted by further alteration and U remobilization events at approximately 1176, 900, and 300 Ma (Hoeve and Quirt 1984; Cumming and Krstic 1992; Kyser et al., 2000; Fayek et al., 2002).

In the Thelon Basin, unconformity-related U deposits may have formed at about the same time as the Athabasca Basin, with a first uranium-mineralizing event at ca. 1500 Ma followed by events at ca. 1400, 1300 and 500 Ma (Fuchs et al., 1986; Kyser et al., 2000; Riegler et al., 2014; Sharpe et al., 2015; Chi et al., 2017; Fayek, 2017).

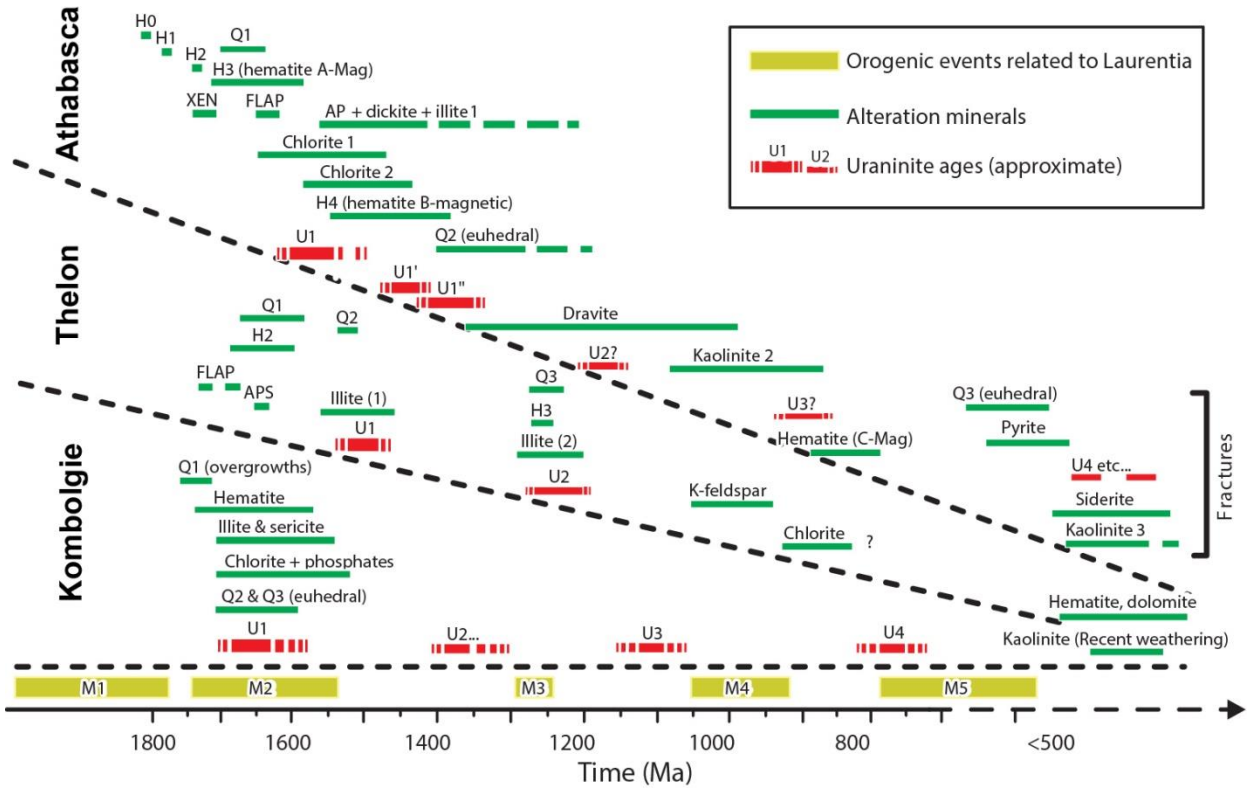

Figure 10: Simplified paragenetic relationships of the Athabasca, Thelon, and Kombolgie Basins with major tectonic events, which may have stimulated mineralizing fluid flow, associated with Laurentia (modified from Kyser et al., 2000; Polito et al., 2004, 2005; Jefferson et al., 2007; Betts et al., 2008; Hiatt et al., 2010; Cui et al., 2012). AP: aluminum phosphate, APS: aluminum phosphate sulfate, FLAP: fluorapatite, H0: primary hematite in the paleoweathered regolith, H1 and H2: early diagenetic hematite in basal red mudstone beds, H3: pervasive hematite, H4: dark, intense hematite cement, Q1, Q2, and Q3: quartz cement, XEN: xenotime. M1: Trans-Hudson Orogeny, M2: orogenic events associated with the accretion of Nena, M3: MacKenzie dikes, M4: Grenville Orogeny, and M5: breakup of Rodinia.

Interestingly, in other Paleoproterozoic basins, U and associated alteration minerals in northern Australia (The Pine Creek Orogen area, PCO) reveal similar punctuated histories (Fig.10) following a primary uraninite deposition at ca. 1700 Ma (Ludwig et al., 1987; Pechmann, 1992; Polito et al., 2005a; Chipley et al., 2007; Jaireth et al., 2016) temporally linked to hydrothermal events recorded in the overlying Kombolgie Subgroup (Polito et al., 2005b). Age-dating studies of alteration, diagenetic minerals and uraninite at various deposits in the PCO usually show younger ages at ca. 1300 Ma, ca. 1190 Ma, and ca. 800 Ma, which can be related to several proximal and distal thermal events, like in Athabasca and Thelon basins.

These Paleoproterozoic basins display similar characteristics in term of lithologies, sequence of

deposition, diagenetic histories and timing of the mineralizing events.

Following this presentation of the main characteristics of the uranium element and URU deposits, we will, in the next chapter of this thesis, address the geological setting of two first-order U-bearing Paleoproterozoic basins (Athabasca and Thelon) in Canada.

2 REGIONAL AND LOCAL GEOLOGICAL SETTING OF THE STUDY

2.1 GEOLOGY OF THE CANADIAN PRECAMBRIAN SHIELD

The study area (ARC's Kiggavik property), is localized within the Laurentian Craton (North American craton, also termed the Canadian Shield) in central Canada (Fig.11). The Pre-Grenville 'Laurentia' (Hoffman, 1988; also termed the Canadian Shield) is itself an aggregate of five Archean cratons, the Superior, Churchill, Wyoming, Slave and Nain (Fig. 11), that are mantled by Paleoproterozoic (2.0-1.8 Ga) orogenic belts. The tectonic history of the Churchill craton (also called Churchill Province) and associated sedimentary sequences and igneous suites is presented in Fig 12A-E).

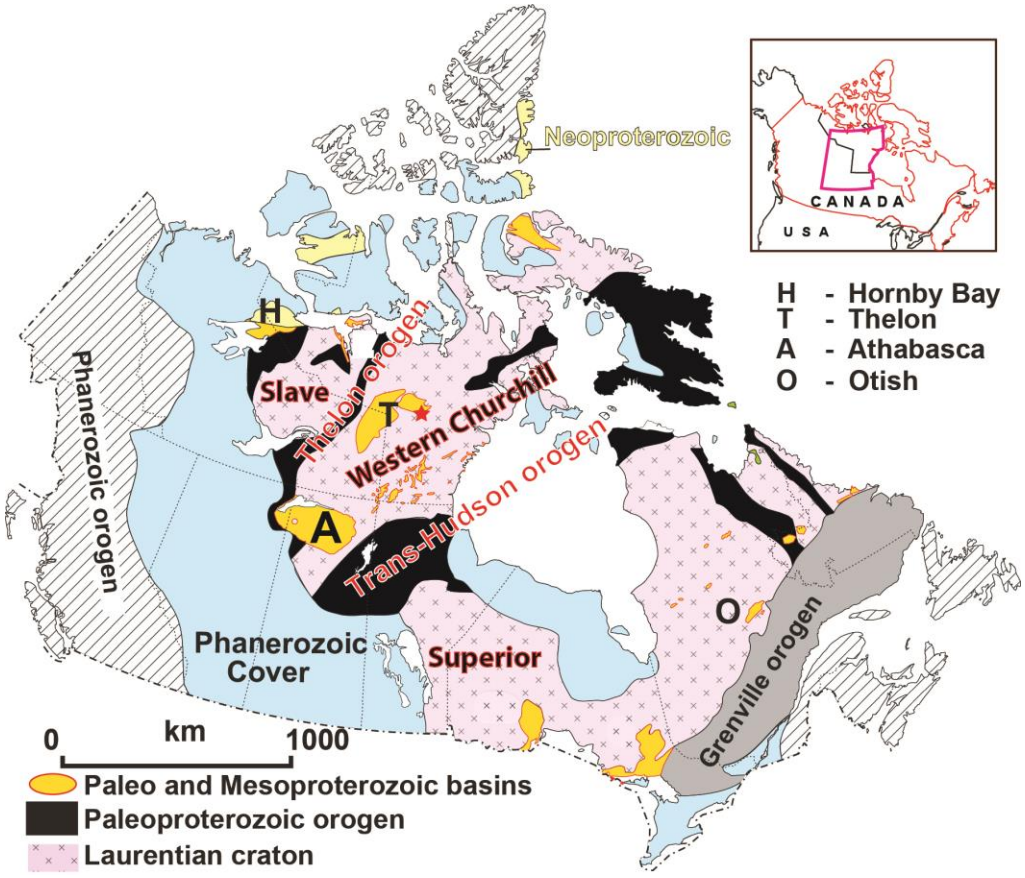

Figure 11: Location and subdivision of the Laurentian craton, and location of Paleo-Mesoproterozoic basins within it. Athabasca and Thelon basin are located within the western Churchill Province

The western part of the Churchill craton is bounded by two major Paleoproterozoic orogenic belts: the Trans-Hudsonian orogenic belt (2.0 to 1.8 Ga) to the southeast and the Thelon-Taltson orogenic belt (2.0 to 1.9 Ga) to the northwest (Fig. 11). These orogenic belts accommodated the convergence (Fig. 12B) of the Slave and Superior Provinces (Hoffman, 1988). Thereafter, the margins of the Laurentian Craton underwent a polyphase and composite tectonic accretion through successive Paleo- to Mesoproterozoic orogenies from ~1.8 to 0.9 Ga; e.g. the Yavipai-Mazatzal (1750-1600 Ma), Central Plains (1500-1300 Ma), followed by the Grenville orogenies (1300-1000 Ma) signalling assembly of Rodinia. The Athabasca (1740-1540 Ma) and Thelon (ca. 1667-1540 Ma) Paleoproterozoic basins (Gall et al., 1992) are located between the eroded remnants of these two orogenic belts (Fig. 12A).

In the northern part of the Churchill Province, the Dubawnt Supergroup, including the Baker Lake and Wharton volcanosedimentary sequences and the Barrensland group (Thelon Formation), were deposited in two rift basins (Late-orogenic and anorogenic) that resulted from the trans-tensional environment during lateral escape that formed in response to crustal thickening of the Trans-Hudson orogeny, followed by thermal sag (Rainbird et al., 2003a).

2.2 MAIN FAULTS AND SUTURE ZONES

The Churchill Province has two Sub-Provinces: Rae and Hearne; Paleoproterozoic collisional amalgamation of Rae and Hearne cratonic blocks is proposed to have occurred along a NE-SW tectonic belt named hereafter the Snowbird Tectonic Zone (STZ).

At the regional scale, the STZ is a prominent feature (Fig.12A) that has given rise to many interpretations, the STZ being either a Paleoptroterozoic suture between Rae and Hearne Sub-Province (Hoffman, 1988; Berman et al., 2007), an intracontinental shear zone (Hanmer et al., 1995) of Paleoproterozoic (Mahan and Williams, 2005) or Archean (Hanmer et al., 1995) age or the suture of a former ocean separating both Sub-Province (Ross et al., 2000; Berman et al., 2007). Recent field observations by Regan et al., (2014) on the Cora Lake Shear Zone support a ca. 2600 Ma intracontinental crustal-scale structure (Fig. 12B) that underwent several later episodes of transpressional reactivation, with sinistral and dextral motions in response to the Trans-Hudsonian orogenies from 2000 to 1930 Ma (Sanborn-Barrie et al., 2001; Mills et al., 2007; Regan et al., 2014).

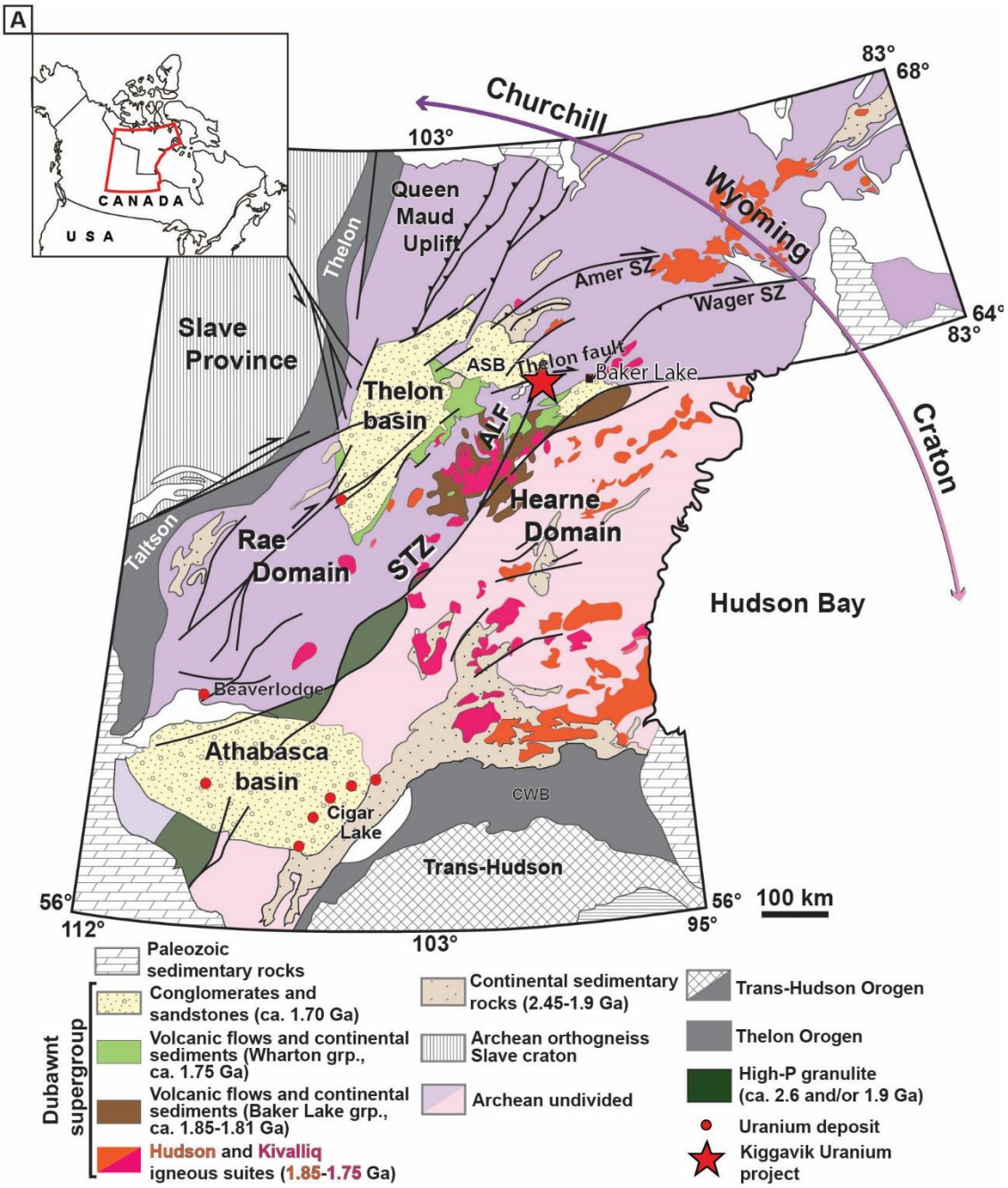

Figure 12: A) Major structural domains of the Western Churchill Province; location of the Athabasca and Thelon basins within the Rae and Hearne Sub-Province. The red star locates the Kiggavik area (modified after Eriksson et al., 2001; Peterson et al., 2002).

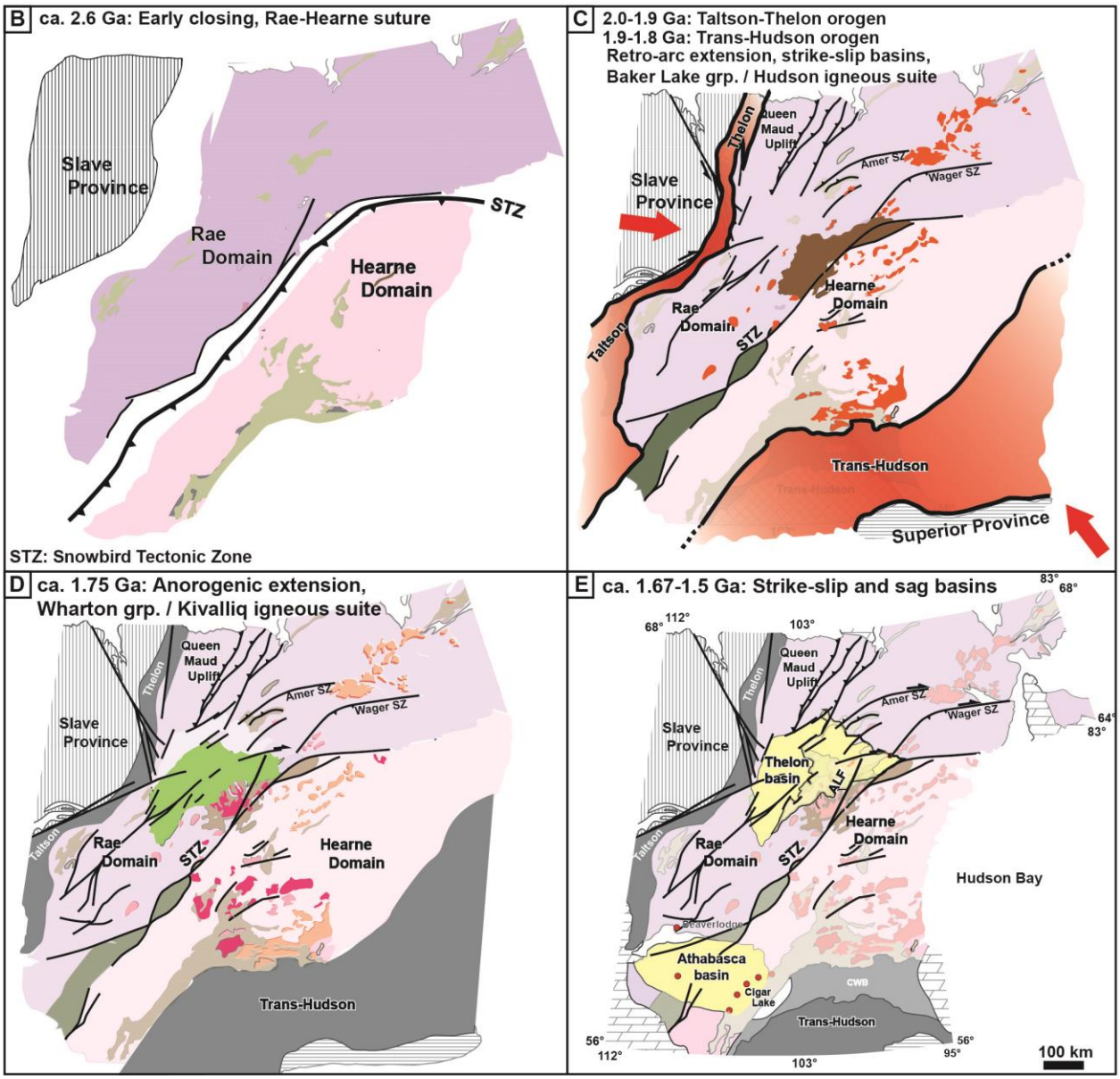

Figure 12 Continued: B) Suturing (still under debate) of the Rae and Hearne Sub-Province occurred at ca. 2.6 Ga. C) Thelon-Taltson orogeny (collision with the Slave Province) to the NW, and Trans-Hudson orogeny (collision with the Superior Province) to the SW. Deposition of the Baker Lake volcanic-sedimentary sequence occurred in a retro-arc setting, with associated late-orogenic Hudsonian intrusive suite. D) Bimodal magmatism of the Kivalliq igneous suite and deposition of the Wharton group in response to post-Trans-Hudsonian anorogenic extension. E) Deposition over a wide area of eolian sediments and conglomerates (red beds) in strike-slip and extensional/transtensional sag basins.

Aeromagnetic mapping shows that a major fault trend in the Kiggavik area, the Andrew Lake Fault (ALF) seems to connect to the STZ (Fig.12A). The STZ system forms two parallel regional trends and numerous Mid-Proterozoic uranium deposits and occurrences are found within this 1200-km long and 150-km wide fault system, from the Shea Creek and the Centennial deposits (Athabasca basin) to the Kiggavik deposits (Thelon basin).

2.3 ARCHEAN AND PALEOPROTEROZOIC SUPRACRUSTAL ASSEMBLAGES OF THE THELON-BAKER LAKE AREA

2.3.1 GEOLOGICAL EVOLUTION OF THE THELON-BAKER LAKE AREA

This thesis is focused in region within Rae Sub-Province, northwest of the STZ where metamorphic formations are dominated by granitic gneisses of greenschist to granulite facies. Early sedimentation in a platform environment is characterized by the Woodburn Lake group and its upper greenschist formations, also locally displaying banded iron formations, bedded carbonates, shales and mafic to felsic volcanic lavas. Five regionally discrete assemblages constitute the Woodburn Lake group (Fig. 13, 14); they are observed at various places (e.g., the N. Meadowbank assemblage described near the Meadowbank mine (Sherlock et al., 2004), or the Pipedream Assemblage hosting the Kiggavik Main Zone deposit).

The Woodburn Lake group and the north-central Rae sub-povince are regionally intruded and capped by the ca. 2600 Ma Snow Island Suite (Davis and Zaleski, 1998; Pehrsson et al., 2004). The exposures of this suite comprise diorite, granodiorite, and quartz-fedspar porphyritic schists, subvolcanic intrusions, tuff and ignimbrite (LeCheminant and Roddick, 1991; Peterson, 2006). Examples of such metavolcanic tuffs, as well as interpreted epiclastic volcanogenic rocks, were recently recognized in the Kiggavik area, from drillcore and outcrops samples (Johnstone et al., 2017). In the region WNW of Baler Lake, the felsic metavolcanic rocks of the SIS seem to be a distinct lithotectonic marker between the Woodburn Lake group metagreywacke (Pipedream assemblage) and the Paleoproterozoic Ketyet River group quartzite.

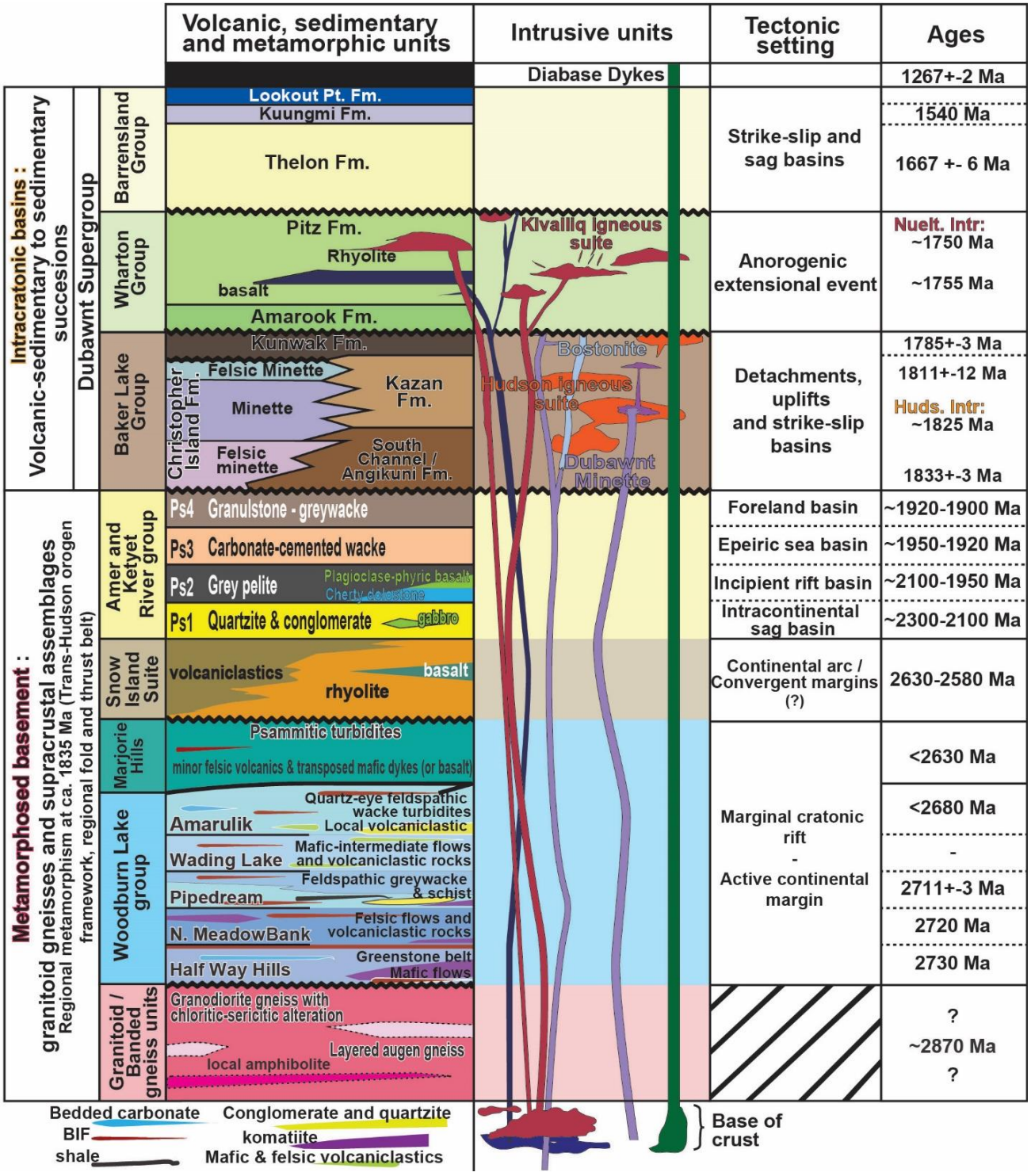

Figure 13: Lithostratigraphic column of the Western Churchill Province (Baker-Lake-Thelon area). Data after Sherlock et al., 2004; Rainbird et al., 2010; Hadlari and Rainbird, 2011; Pehrsson et al., 2010, 2013; Peterson et al., 2015a; Jefferson et al., 2015; Scott et al., 2015).

Four main groups of Paleoproterozoic supracrustal rocks (Amer, Ketyet, Chantry and Montresor) are observed throughout the Rae Sub-Province, predating deposition of the un-metamorphosed, better preserved Dubawnt Supergroup, (Rainbird et al., 2010). Only those of the north-central Rae (Amer and Ketyet) have been extensively studied (McEwan, 2012). The Amer and Ketyet River groups (Krg) of the central Rae craton overlie mainly Neoarchean rocks of the Snow Island Suite and Woodburn Lake Group (Fig. 14), where they display fold and thrust belt style (Rainbird et al., 2010; Pehrsson et al., 2013). To the southeast, the Krg extends 200 km north of Baker Lake and is best exposed in the Whitehills belt (Rainbird et al., 2010, Jefferson et al., 2011).

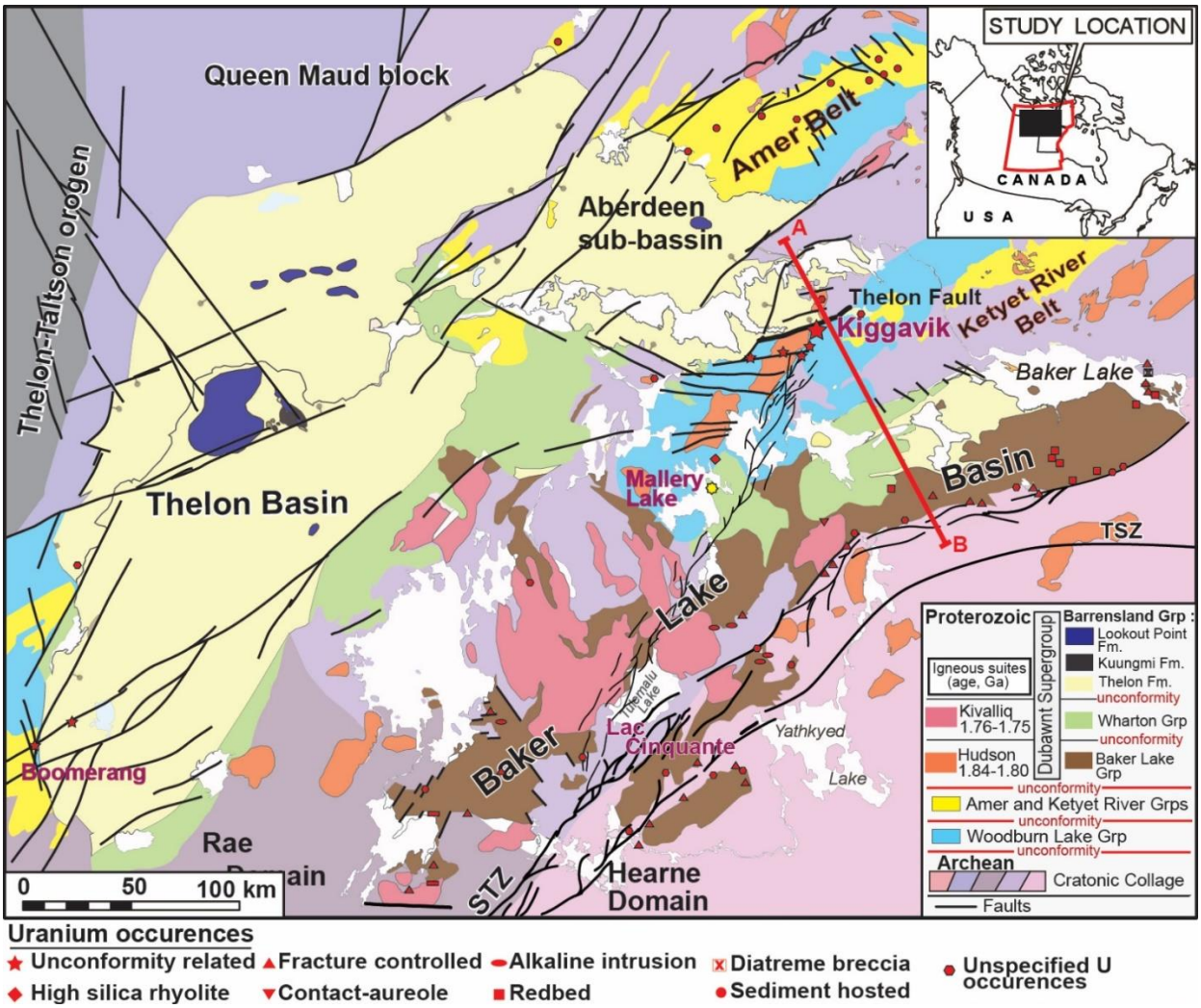

Figure 14: Geology of the Thelon and Baker Lake basins (Thelon-Baker Lake area), distribution of the Dubawnt supergroup rocks and of the Schultz Lake intrusive complex (Nueltin and Hudsonian intrusions). The cross section locates the Kiggavik mineralization in regard to the Thelon formation, controlled by the Thelon fault. (Modified after Jefferson et al., 2011).

The Amer Group consists of eight sedimentary units comprising metaquartzites, metapsammites and metapelites, interpreted to have been deposited mainly in a continental shelf environment during a transgression-regression cycle (Rainbird et al., 2010). The Krg is very similar to the Amer group, as it consists of dominantly quartzites with intervals of volcanics, carbonates and shales. Based largely on geochronological data, Rainbird et al., (2010) grouped the units of the Amer group and the Krg into four discrete stratigraphic assemblages (Ps1, Ps2, Ps3 and Ps4, figure 13). Deposited between 2.40-1.85 Ga, the rocks of these groups are attributed to the initial rifting and break-up (Ps1 and Ps2) followed by a later foreland setting (Ps3 and Ps4) at the beginning of amalgamation of Laurentia (Rainbird et al., 2010).

At 1.84-1.83 Ga (Fig. 12C), the central portion of the Churchill Province underwent extension, in a retro-arc setting as described by Hadlari and Rainbird (2011), in response of the collision between the Superior and the Churchill Province (the Trans-Hudsonian orogeny). This extensional event is recorded by the preservation, in the Churchill Province, of several basins (and sub-basins) filled with sedimentary to volcano-sedimentary and intrusive rocks belonging to the Dubawnt Supergroup (Miller et al., 1986; Peterson et al., 2006, Fig.13; Fig. 14). The Dubawnt Supergroup comprises three second-order sedimentary sequences (Baker Lake, Wharton, and Barrensland sequences) Miller et al., 1986; Rainbird et al., 2003a; that record deposition within a asymmetric strike-slip rift basin (Fig. 15A), a symmetric, anorogenic rift basin (Fig. 15B) and a thermal sag basin (Fig. 15C), respectively (Hadlari and Rainbird, 2011). The two main basins, visible in Fig. 14, are the Baker Lake Basin (1850-1750 Ma) and the Thelon Basin (ca. 1667-1540 Ma).

Figure 15 (next page): Tentative reconstruction of the regional structural evolution along the transect A-B in Fig. 14. A) Retro-arc extension, deposition of volcano-sedimentary succession in a half-graben of the Baker Lake Basin. Emplacement of the late-orogenic hudsonian intrusive suite. B) Anorogenic extension, volcanism and formation of the Wharton basin. Emplacement of the anorogenic Kivalliq igneous suite (Nueltin granite). C) Thermal relaxation and deposition of eolian and clastic sediments of the Thelon formation over a wide area in sag-basins. D) Emplacement of the Kuungmi formation at ca. 1540 Ma over the Thelon formation. The MacKenzie swarm (1267 Ma) is observed throughout the Churchill Province, and diabase dikes crosscut all the previous formations. Legend as in figure 13 and 14. Modified after Jefferson et al., 2011, 2017; Hadlari and Rainbird, 2011; Pehrsson et al., 2013.

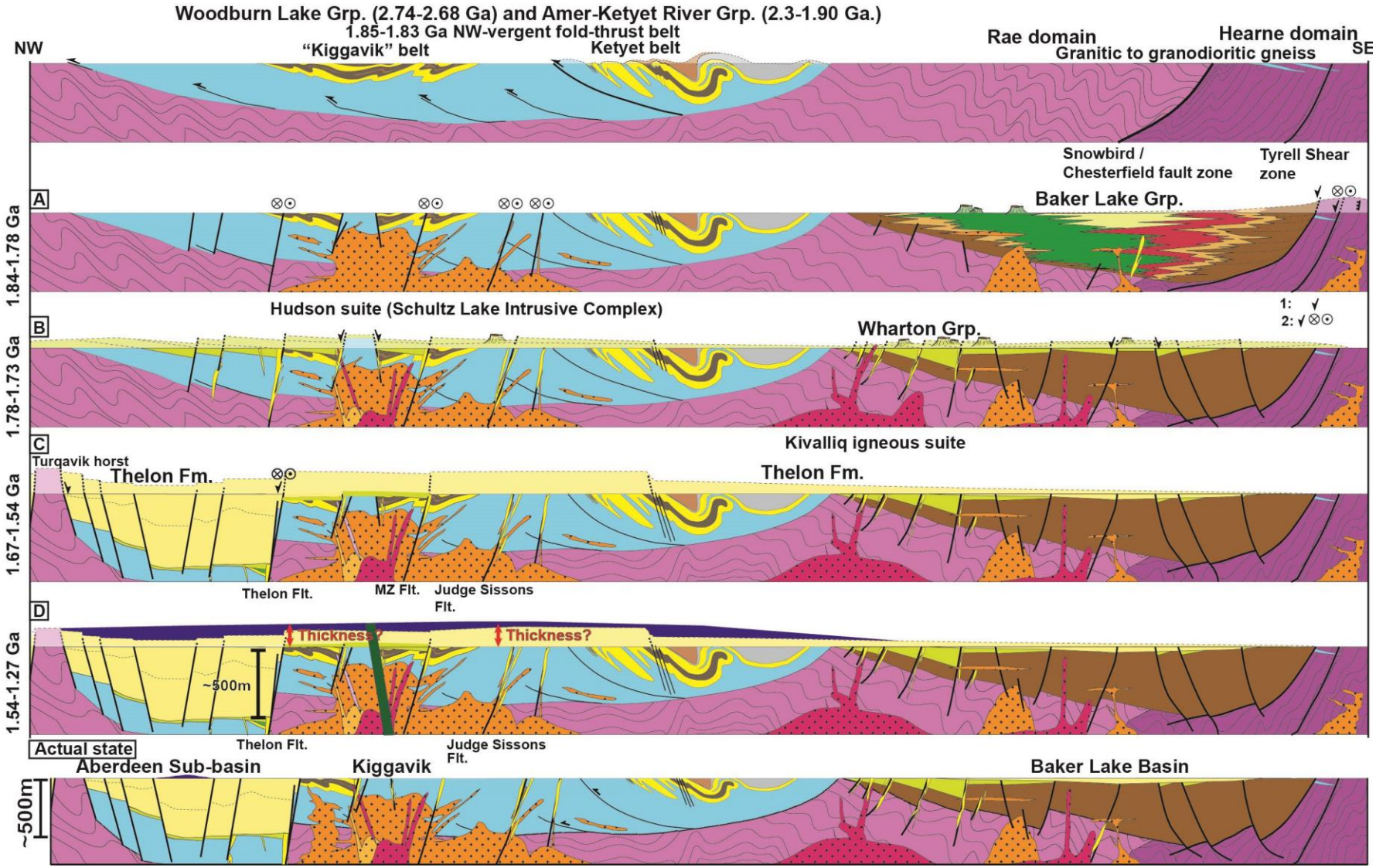
Woodburn Lake Grp. (2.74-2.68 Ga) and Amer-Ketyet River Grp. (2.3-1.90 Ga.)
1.85-1.83 Ga NW-vergent fold-thrust belt
NW
"Kiggavik" belt
Ketyet belt
Rae domain
Hearne domain
Granitic to granodioritic gneiss
SE
Snowbird / Chesterfield fault zone
Tyrell Shear zone
A
1.84-1.78 Ga
Baker Lake Grp.
Hudson suite (Schultz Lake Intrusive Complex)
1:
2:
B
1.78-1.73 Ga
Wharton Grp.
C
Kivalliq igneous suite
Turqavik horst
Thelon Fm.
Thelon Fm.
1.67-1.54 Ga
Thelon Flt.
MZ Flt.
Judge Sissons Flt.
D
Thickness?
Thickness?
~500m
1.54-1.27 Ga
Actual state
Thelon Flt.
Judge Sissons Flt.
Aberdeen Sub-basin
Kiggavik
Baker Lake Basin
~500m

The Baker Lake Basin is mainly filled with the Baker Lake and Wharton formations (Fig. 13, Fig. 14). The Wharton and Baker Lake formations filled up the Baker Lake Basin that developed between ca. 1850 Ma and ca. 1750 Ma. The Baker Lake formation is represented by continental continental siliciclastic redbeds succession and coeval voluminous ultrapotassic mafic to felsic volcanic rocks of the Christopher Island Formation (Rainbird et al., 2003; Peterson, 2002, 2006). The development of the Baker Lake formation was contemporaneous with the Hudsonian intrusive suite at ca. 1830 Ma. The Wharton formation is represented by eolian sandstones and coarse conglomerates in restricted basins and extension-related felsic magmatism (rhyolitic flows). The development of the Wharton formation was contemporaneous with the bimodal Kivalliq igneous suite (rapakivi Nueltin granite) at ca. 1750 Ma.

The development of the Baker Lake Basin was followed by uplift, extensive erosional planation and regolith formation before the development of the Thelon Basin (Rainbird et al., 2003a; Rainbird and Davis, 2007; Hadlari and Rainbird, 2011). Major ENE-trending dextral strike- and oblique-slip faults, including the Thelon fault became active at that time (Anand and Jefferson, 2017).

The Thelon Basin consists mainly of the Thelon Formation (Figs. 13, 14), an 1800 m thick sedimentary sequence of conglomerates and coarse-grained sandstones, deposited over a broad area. The depositional record reflects progressive upward thinning and the first record of marine transgression within the Dubawnt Supergroup. These features suggest that the Barrenlands sequence was deposited over a broad region (Fig. 15) of thermal subsidence, likely related to cooling of a previously shortened continental lithosphere. The Barrenlands sequence may be a remnant of a huge cratonic sand sheet that included the Thelon, Athabasca, Amundsen, and Elu basins, as the Thelon and Athabasca basins display significant similarities in terms of sedimentological and evolutionary records (Miller et al., 1989). Mantle downwelling linked to the late-stage amalgamation of Laurentia is theorized to be the regional subsidence mechanism leading to the formation of these basins (Rainbird et al., 2003a, b). Currently, the Thelon formation is not present over basement rocks of the Kiggavik area but its former presence (Fig. 15) is inferred through the recorded circulation of basinal brines in the basement rocks (Chi et al., 2017), however, the maximum thickness of the cover at the time of the fluid circulation can only be estimated.

The Thelon formation is overlain by the shoshonitic basalts Kuungmi Formation (Fig. 14, 15D) dated at ca. 1540 Ma (Chamberlain et al., 2010) and marine dolomites of the Lookout Point Formation (Gall et al., 1992) of the Barrensland Group. The Thelon Formation. overlies granite,

syenite and lamprophyre of the late syn-orogenic, ca. 1825 Ma Trans-Hudson suite and the ca. 1750 Ma rapakivi-style Nueltin granite of the anorogenic Kivalliq igneous suite (Hoffman 1988; Van Breemen et al., 2005; Peterson et al., 2015a, b; c.f., Scott et al., 2015) that intruded the Archean to Paleoproterozoic rocks in an arcuate pattern from the SW to NE accross the Churchill Province (Fig. 12 and 14). The age of the Thelon Formation is thus bracketed by the age of emplacement of the Nueltin granite (ca. 1750 Ma), the diagenetic fluoro-apatite (ca. 1670 Ma) found in the basal Thelon Formation (Davis et al., 2011) and by the alkali basaltic volcanism of the Kuungmi Formation (ca. 1540 Ma) that caps this formation (Chamberlain et al., 2010). Emplacement of the Kuungmi Formation was followed by marine transgression with deposition of dolomite and stromatolites of the Helikian Lookout Point Formation (Gall et al., 1992). The Lookout Point Formation is thought to be equivalent of marine units observed in the Athabasca, Hornby Bay and Elu basins (Kerans et al., 1981; Ross and Kerans, 1989; Ramaekers, 1981).

The dolerite dikes of the MacKenzie diabase swarm that form prominent linear aeromagnetic features trending NNW-SSE (Tschirhart et al., 2013; 2017) cut across all of the Thelon units (Fig. 13 and 15). The corresponding intrusive event is dated at 1267+-2 Ma (Lecheminant and Heaman, 1989; Heaman and Lecheminant, 1993), and represents the last main regional event.

2.3.2 URANIUM OCCURRENCES IN THE BAKER LAKE-THELON AREA

The uranium potential of volcano-sedimentary rocks of the Baker Lake basin (Nunavut, previously called District of Keewatin, named Thelon-Baker Lake area in this work) was recognized through exploration and mapping in the 1960s and 1970s. Reconnaissance helicopter mapping, sedimentology/sequence-stratigraphy studies and ground exploration by the Geological Survey of Canada produced the initial work. Metallogenic studies provided the first models of uranium mineralization types in the Keewatin District, from syngenetic to epigenetic orebodies (Curtis and Miller, 1980; Miller, 1980; Miller, 1982; Miller and Lecheminant, 1985; Miller et al., 1986; Miller, 1995). The different types are presented in Table 5, highlighted with examples from the Thelon-Baker Lake area. The main uranium association is fracture-controlled mineralization in the Dubawnt Supergroup and underlying basement gneiss.

Type	Sub-type	Area	Name	Mineralisation (metallic minerals and others)	Description
Fracture controlled	Diatrem breccia	Christopher Island (East to Baker Lake)	——	Pitch-chalc-sphal-py-chl Hematized breccia, qtz-carb-bar	Mineralization is linked to ellipsoidal syenite stocks and dikes of the Christopher Island Formation. Hydrothermal fluids were channeled through zones of high permeability within diatreme structures.
Fracture controlled	Granite-related veins or unconformity-related ?	NE Angikuni basin	Lac cinquante	Pitch-hem-chl-cal veins	Tension-gash veins are cemented with carbonate, hematite, chlorite, sulfides and pitchblende and are accompanied by a relative narrow alteration (0.5-0.1m) First stage of mineralization occured at ca. 1830 Ma and is linked to magmatic and tectonic events of the Trans-Hudson orogeny.
Fracture controlled	Unconformity related	Kiggavik	Kiggavik Main and Center zone	Pitch-uran-coff-py-chal-chl minor qtz-carb veins	Fracture controlled uranium pods, the precipitation of which is linked to basinal brines, are hosted in paragneiss of the Woodburn Lake Group, Snow Island Suite and granite of the Hudson intrusive suite. Late alteration features are characterized by meteoric-linked remobilization fronts and supergene uranium minerals such as tristramite.
Fracture controlled	Unconformity related (?)	Christopher Island	——	Pitch-Se-Cu-Ag-Au Hem-chl-calc-qtz	Uranium mineralization occurs in fractures and breccia zones in arkose and intrusive biotite trachyte of Christopher Island formation.
Intrusion related	Granite-related contact aureole	Thirty Mile Lake	——	Pitch-pyr-chal-fluo-cal garn-fluo-epid veinlets	Mineralization is observed close to an epizonal fluorite-bearing granite probably of the Kivalliq igneous suite. It is characterized by fluorite-rich pitchblend veins with minor pyrite and chalcopyrite
Intrusion related	syenitic bostonite	Deep Rose Lake Tulemalu Lake	——	U-Pb oxides (?)	Uranium-thorium are present in syngenetic refractory minerals, hosted by strongly potassic intrusive suites correlated with phlogopite-rich lavas of the Christopher Island Formation.
Intrusion related	Pegmatitic	Nueltin Lake	——	Uranothorite and allanite in Nueltin granite (rapakivi style)	Anomalous occurrences of uranium and thorium are observed in aplite dikes and pegmatitic seams in the Nueltin granite, belonging to the Kivalliq igneous suite (ca. 1750 Ma).
Stratabound	Syngenetic	Amer Belt	Deep rose	Pitch-pyr-chal-moly	Low grade stratabound mineralization in folded quartzititc and pelitic metasediments. The mineralization is locally remobilized along fractures. Pitchblende is observed as a cement between quartz grains and mantles or replaces feldspar grains.
Fracture controlled	Redbeds	Thirty Mile Lake	Kazan type (74-1W)	U-Ti-Se-Cu-Chl and Calcite-Quartz	Epigenetic Ag-Cu-U mineralization concentrated within symmetrical envelopes that surround carbonated and chloritized lamprophyre dikes intruding the Christopher Island Formation. It is characterized by pitchblende and U-Ti compounds accompanied by iron sulfides, native copper and silver.

Table 5: Synthetic table describing exemples of the different types of uranium mineralizations observed in the Thelon-Baker Lake area (mainly within the Baker Lake Basin, see Fig.14. See text for references).

Rocks belonging to the Dubawnt Supergroup were deposed during a period marked by rift tectonics. They host uranium mineralization and alterations with lithological and structural characteristics similar to the Beaverlodge District, the fracture-controlled mineralizations of which are linked with pre-Athabasca to post-Athabasca history (Dieng et al., 2013; 2015). No recent studies characterize uranium mineralization of the Thelon-Baker Lake basins, except in the Kiggavik, described hereafter, and Lac Cinquante deposit area (table 5). The latter display fracture-controlled uranium mineralization in tension gashes, dated at ca. 1830 Ma (Bridge et al., 2013).

2.3.3 GEOLOGY OF THE KIGGAVIK AREA

Uranium deposits in the Kiggavik area are hosted within the Archean and Paleoproterozoic basement rocks marginal to the Aberdeen sub-basin of the Thelon Basin (Jefferson et al., 2011a, 2011b; Fig.16).

In the Kiggavik area, the Archean rocks include Mesoarchean (ca. 2870 Ma) granitic gneisses, the 2730 - 2680 Ma supracrustal Pipedream assemblage of the Woodburn Lake group and the distinctive package of 2620 - 2580 Ma felsic volcanic and related hypabyssal rocks of the Snow Island suite, including newly discovered epiclastic rocks (Jefferson et al., 2017; Johnstone, 2017) (Fig.16). These rocks are overlain by the Paleoproterozoic (2300 - 2150 Ma) orthoquartzite of the Ketyet River group, with possible repetition due to thrusting and faulting in the sequence (McEwan, 2012; Jefferson et al., 2017; Johnstone, 2017).

These various groups were intruded in the area by the Schultz Lake Intrusive Complex (SLIC, in the western part of the Kiggavik area, Fig. 16) (Scott et al., 2015). The SLIC comprises two groups of rocks with contrasting origins but with some overlap in geochemical and petrographic features (Scott, 2012): (i) non-foliated granitoid sills, syenites (Martell syenites) and lamprophyre dikes of the syn- to late-orogenic Hudson intrusive suite. They represent the first pulse of magmatic activity at 1840-1820 Ma in the Kiggavik area. The “Hudson granite” in the area is a non-foliated, medium crystalline rock containing fluorite, magnetite, biotite and sulfide minerals (Fuchs and Hilger, 1989; Scott et al., 2015). Studies on the minimum melt compositions and Nd isotopes indicate that the Hudson grantoids were likely derived by melting of late Archean crust (van Breemen et al. 2005); (ii) Rapakivi granite to rhyolite of the anorogenic bimodal Kivalliq igneous suite (1770-1730 Ma, Peterson et al., 2015a), including the McRae Lake dikes and minor Dubawnt minette intrusives (equivalent of the felsic minette of the Christopher Island Formation, Dubawnt supergroup, Scott et al., 2015) (Fig.13).

The Kivalliq igneous suite represents (1770-1730 Ma) a second pulse of magmatic activity in the area. The “Nueltin granite” is characterized by a non-foliated bimodal basalt-rapakivi granite consisting predominantly of white to pink, megacrystic potassium feldspars with interstitial coarse plagioclases, smoky quartz, and coarse to very coarse biotite (Scott et al., 2015). Dikes of biotite-bearing felsite (bostonites), enriched in rare-earth-elements, uranium and thorium, are observed in the Kiggavik area and were proposed to correlate with the magmatic events happening during the formation of the Baker Lake Basin (Peterson et al., 2011). Mafic dikes of the McRae Lake dike swarm and Thelon River dike swarm also belong to the Kivalliq igneous suite.

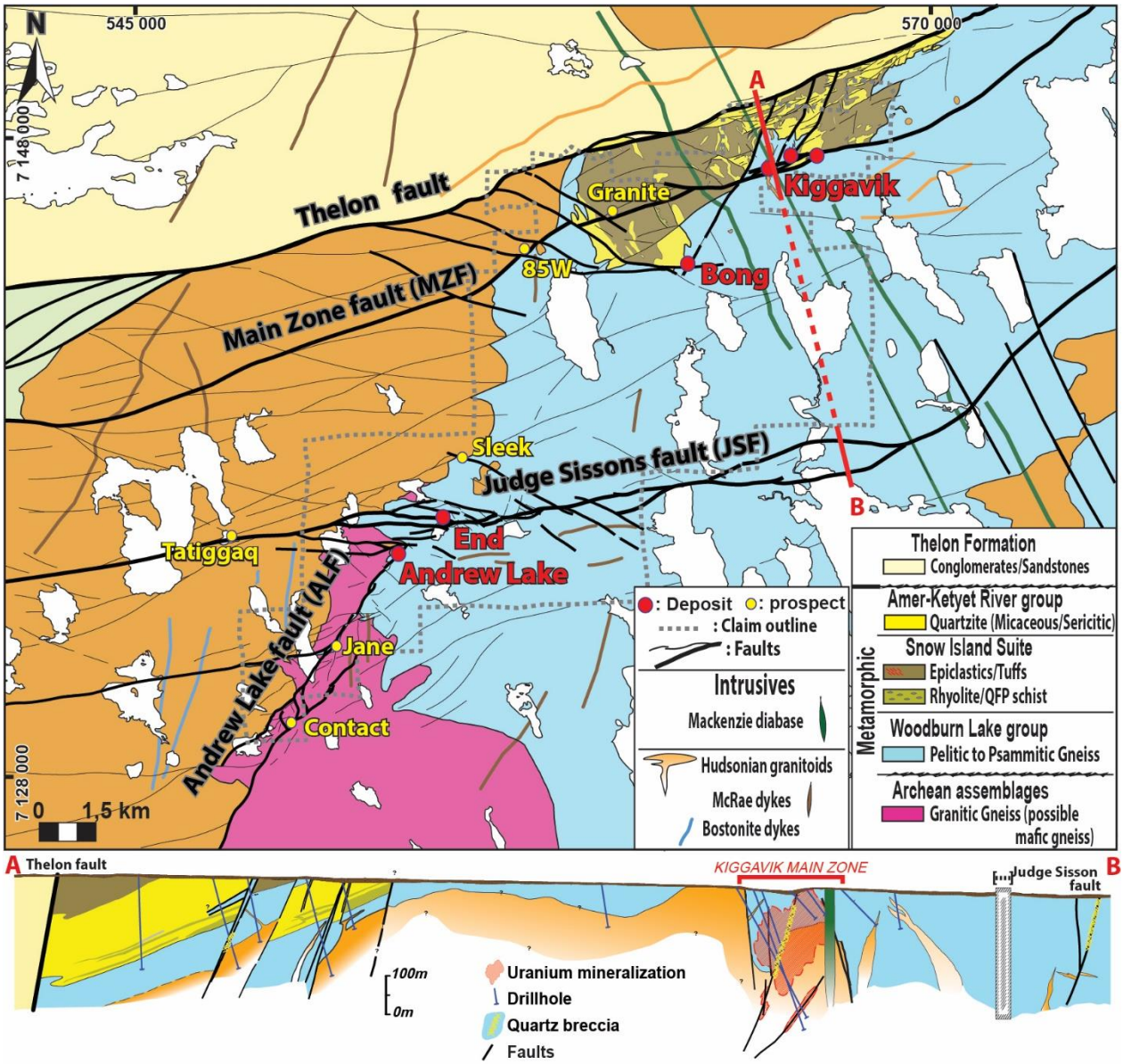

Figure 16: Simplified geological map of the Kiggavik area. Deposits are indicated with red circles, prospects with yellow circles (modified ARC internal document).

All the previously described rock units are unconformably overlain by the Thelon formation, observed in the northern part of the Areva property (Fig.16). The dolerite dikes of the MacKenzie diabase swarm (1267 Ma) cut across all of the previously described lithologies in the Kiggavik area.

3 SCIENTIFIC INTEREST AND OBJECTIVES OF THE STUDY

3.1 THE KIGGAVIK U DISTRICT: STATE OF THE KNOWLEDGE AND PENDING QUESTIONS

Uranium deposits in Kiggavik are commonly classified as unconformity-related due to proximity to the Thelon Basin (i.e. Hiatt et al., 2010, Riegler 2013, Riegler et al., 2014), equivalent to those in the Athabasca Basin. The reason is that they show common features such as a general close relationship to the unconformity, along with similar alteration styles, structural controls and chronologies of mineralization. The Kiggavik deposits possess some unique characteristics, such as the variety of host rocks like granites, granitic gneisses or even epiclastics and locally metagreywacke (Johnstone et al., 2017), the uncertain extent of the mineralized lenses towards the unconformity (unknown thickness of eroded rocks), the general lack of graphite and dravite. The distinguishing characteristics are not well understood yet, but make the Kiggavik area a unique setting.

3.1.1 Uranium mineralization on the Eastern border of the Proterozoic Thelon basin

The history of the Athabasca Basin has been thoroughly studied by many researchers, while the structural and fluid history of the Thelon Basin and associated basement rocks is poorly understood. Since the first work of Donaldson (1965) on the definition of the Dubawnt Supergroup, of which the Thelon sediments are part, much work has been done on the basin fill itself including sequence stratigraphy, diagenesis, and fluid history (Renac et al., 2002; Hiatt et al., 2003, 2010; Rainbird et al., 2003a, 2010). The majority of these studies have a very large scope, generally including the entire basin and the surrounding units.

Some studies dealt with the uranium metallogeny of the Kiggavik deposits (Farkas, 1984; Miller and LeCheminant, 1985; Fuchs et al., 1986; Weyer et al., 1987; Friedrich et al., 1989; Fuchs and Hilger, 1989; Riegler, 2013; Riegler et al., 2014; Sharpe et al., 2015; Shabaga et al.,

2017). These studies have described the uranium mineralization as primary pitchblende and lesser secondary coffinite associated with iron sulfides such as pyrite. Associated alteration minerals include di,trichlorite (sudoite), hematite, and illite. This simple mineral paragenesis is described for the Kiggavik, Bong, End and Andrew Lake (deposits location in Fig.16) and corresponds well with the monometallic mineralization described in the basement-hosted deposits of the Athabasca Basin. Only Reyx (1984) described a more complex paragenesis for the Andrew Lake, End and Kiggavik deposits, with the presence of native gold and silver associated with cryptocrystalline sulfides, arsenides or selenides. It is also at Andrew Lake that secondary, hexavalent uranium minerals have been extensively observed (Fig. 2D).

Various authors also describe several generations of uranium minerals with different associated ore minerals. These uranium generations and assemblages differ between each deposit. It is therefore necessary to study the ore minerals in more detail (polymetallic or monometallic mineralizations?), to understand and characterize the uranium mineralizing events in the Kiggavik area.

3.1.2 Typology of U mineralizations in the Kiggavik area: really unconformity-related?

In the Kiggavik area, all the deposits are basement hosted, and the basement is not covered by the Thelon sandstones (Jefferson et al., 2013). The more recent studies postdating the renewed exploration (after 2008) seem to favour the unconformity-related model for the Kiggavik area, while some of the older studies pointed toward magmatic-derived uranium mineralizations.

Early studies by Weyer et al., (1989) described uranium mineralization at the Kiggavik main zone deposit as temporally and spatially associated to the Hudsonian intrusions, while Fuchs and Hilger (1989) showed that mineralization is closer to the unconformity-related type, without being able to provide a more detailed conclusion. Microprobe analysis on uranium oxides by Weyer (1992) shows thorium values up to several percent, consistent with magmatic-derived fluids. At that time, for F.J Dahlkamp (Weyer et al., 1989), mineralization at Kiggavik Main zone represented a vein-type granite-related deposit overprinted in its upper part by unconformity-related processes. Following more recent studies of geochemical signature of uranium oxides in the Kiggavik area, Lach et al. (2013) analyzed the rare earth element signature of pitchblende

from the End deposit and found a similar distribution (i.e., bell shaped, Mercadier et al., 2011b) to all other URU deposits. They concluded that the End grid deposit represents an URU deposit. Chi et al. (2017) studied fluid inclusions in quartz and calcite at the End deposit and described Na-dominated and Ca-dominated H_2O-NaCl-$CaCl_2$ ± $MgCl_2$ fluids which are commonly found in other unconformity-related uranium deposits, and are consistent with a model where the mineralizing fluids would have been derived from basinal brines of the Thelon Basin.

In the case of the Bong deposit, the alteration-related minerals were characterized by Riegler et al. (2014) as related to a diagenetic-hydrothermal alteration similar to those associated with Athabasca-type URU, and similarly would have originated from a Thelon-derived basinal brine. The ore minerals and timing of the uranium mineralization at Bong were studied by Sharpe et al. (2015). Based on isotopic composition, the mineralizing fluids were inferred to be meteoric-hydrothermal in origin and were recognized to be isotopically different from the basinal brines associated with Athabasca-type uranium deposits. One of Sharpe's conclusions was therefore that basinal brines were not required to form this deposit and, therefore, the unconformity is not a critical factor for the formation of the Bong deposit. In their study on fluid inclusions at the End deposit Chi et al. (2017) demonstrated that quartz and calcite that precipitate before and after uranium minerals, formed from a basinal brine. They concluded that uranium mineralization in the End deposit formed from basinal brines derived from the Thelon basin. Shabaga et al. (2017) determined that the mineralizing fluids at the Andrew Lake deposit were meteoric, oxidizing and acidic but did not discuss their link with the Thelon formation.

3.1.3 Nature of the reductant for uranium precipitation

The question about the nature of the reductant required for the precipitation of uranium is interesting, because in contrast to the Athabasca, there are no graphitic faults or lithology in the basement. Graphite and organic matter is very locally present in the Bong deposit, where it was observed coated with uranium (Sharpe et al., 2015; Riegler et al., 2017). The $\delta^{13}C$ of the graphite and the organic matter displays very similar values (ranging from -48.3% to -21.0%) (Sharpe et al., 2015) to those observed in graphite, bitumen and carbon nodules in the Athabasca Basin (Leventhal et al., 1987; Kyser et al., 1989; Landais et al., 1993; Sangely et al., 2007).

In the search for the reductant, excluding any carbonaceous material, special consideration should be given to the sulfide and mafic mineralogy of basement rocks. Liberation of H_2S from hydrothermal alteration of Fe^{2+} bearing minerals (e.g., retrograde chlorite, sulfide minerals) is a potential reducing agent of U^{6+}; the Fe-U redox couple with iron being the electron acceptor to

convert U^{6+} to U^{4+} (see section 1.3.1.3). Another possibility is a change in pH of the mineralizing fluid. In the deposits of the Kiggavik area, the replacement of ferromagnesian metamorphic minerals (e.g., biotite, Fe-Mg chlorite) by Fe-poor hydrothermal alteration minerals (e.g., sudoite, illite) in the oxidized alteration zone was observed (Riegler, 2014). This indicates that iron was liberated during alteration by the mineralizing fluid.

3.1.4 Alteration products associated with the circulation of fluids, comparison with the Athabasca Basin.

Hasegawa (1990) studied the alteration halo at the Kiggavik Main Zone deposit in order to better calibrate a geophysical model for increasing the accuracy of exploration. Clay minerals are dominated by illite through alteration of feldspar, and Mg-rich chlorite (sudoite) through alteration of Fe-chlorite. Decreased density results from quartz dissolution. Riegler et al. (2014) studied the different alteration minerals associated with the uranium mineralization at the Bong deposit. The alteration halo is analogous to those of the Athabasca Basin with illite-sudoite as a main component. They also showed that at the Andrew Lake deposit, illite crystallinity decreases as you get closer to uranium oxide. Quirt (2017) showed that illite at Bong is similar to illite of Athabasca unconformity-type, with same polytypes (1Mc and 1Mt) and only minor chemical differences. Sudoite also shows similar features but is an Mg-sudoite rather than an Al-Mg-sudoite as in the Athabasca unconformity-deposits. The presence of sudoite was also characterized by Ida (1998) at the End deposit.

The main difference from the Athabasca unconformity-deposits is the absence of Mg-foitite (dravite), which is commonly closely asssociated with orebodies of the Athabasca and Kombolgie basins (Australia). The boron anomalies observed in the uranium deposits of the Athabasca Basin are linked to the presence of dravite (boron-rich tourmaline, McGill et al., 1993; Matthews et al., 1997), so the absence of dravite raises the question of the boron-anomaly halo observed associated with all the uranium deposits in the Kiggavik area. Current research is focusing on the chemistry of the various clay species, some of which might be responsible for this anomaly (D., Quirt, pers. Com., 2017; see also Kandasami, 2015). Alteration and uranium mineralization display the same controls in both basins with the structural geology as a first order, and the lithology as a second order control. The question of why altered zones display significant gravity anomalies (indicating host-rock clay alteration) without any trace of uranium needs to be addressed. This is unexpected as clay alteration is regarded to be part of the uranium mineralizing process. Having a better understanding of the relationship between

alteration products and fault zones would help characterize fracturing events and their relationship to uranium orebodies.

3.1.5 Structural controls on uranium mineralization in the Kiggavik area

A noteworthy characteristic of the Kiggavik mineralization is the obvious control on the mineralization by mainly brittle-style structures imposed on different lithologies from Archean and Paleoproterozoic gneisses (≈2.7 to 2.5 Ga) to Hudsonian granites (≈1.84 to 1.75 Ga). Most recent research on the Kiggavik deposits has employed petrological, geochemical, and geochronological approaches to decipher alteration parageneses and mineralization stages (Riegler 2013, Sharpe, 2013, Sharpe et al., 2015, and Haid, 2014, Chi et al., 2017). These works did not specifically attempt to link between mineralization and structures, such that the plumbing system controlling mineralizing fluid flow remains poorly defined, although it is a key part of any reliable regional metallogenic model. There has been no attempt to connect the findings in each deposit and at proposing an integrated metallogenic model at the project scale. Moreover, none of the studies linked mineralization and structural evolution, including the successive local- to regional-scale fracturing-faulting events.

Fuchs et al., (1986) described the Main and Central Zone deposits as cigar-shaped ore bodies within an ENE striking structure at the intersection with E-W faults. Flotté (2009) and Zerff (2013), demonstrated the geometrical structural control of the mineralization at the End deposit and established the foundations of a 3D structural model for that specific deposit. This model is based on two observed generations of mineralization, related to a local (?) polyphase tectonic and kinematic evolution. All stages of mineralization can be linked to veins and/or fault zones/corridors (Flotté, 2009). The more recent structural model of Zerff (2013) based on the analysis of drill-core oriented data of fractures confirms Flotté's (2009) structural model while somewhat refining fault orientations related to mineralization.

Baudemont and Reilly (1997) and Feybesse (2010) pointed out that uranium deposits are located at the intersection of, or along, E-W and NNE-SSW tectonic trend (e.g., the Andrew Lake Fault and the Judge Sissons Fault). No study has to date focused on detailed characterization of the brittle fault zones that are the main hosts of uranium mineralization in the Kiggavik area. This could be of great interest when looking at classical model of fluid circulation enhanced in fault damage zones, fault relay-zones, releasing vs restraining bends, among other structural features. Before being able to understand fluid-rock interactions leading to U mineralization, we

have to first understand where the fluid-rock interaction happen and is increased, and therefore, where uranium mineralization will likely occur. The characterization of the fault-trap is a critical step in this conceptual process. These uncertainties need to be addressed in order to make a significant step toward better characterization and understanding of the genetic processes leading to U mineralization and guide exploration.

3.2 OBJECTIVES AND ORGANISATION OF THE MANUSCRIPT

The main objective of this PhD is to decipher and reconstruct the faulting/fracturing events, mineralizing or not, that occurred in the Kiggavik area. This characterization of the different fault systems and the establishment of its spatial and temporal relationships with alteration and mineralization will constrain the Kiggavik structural model. The fracturing events characterized in the Kiggavik area will be integrated in the regional setting of pre-, syn- and post-Thelon tectonic evolution. Such an approach is nearly unique to our knowledge when applied to basement hosted (unconformity-related?) uranium mineralizations.

A geochemical identification of the different clay minerals and uranium oxides is also required to characterize the fluids that circulated through the fault systems, and the products resulting of the fluid-rock interaction. This approach should allow for the identification of the successive fracture-related fluid pathways and for a refined definition of fracture-related mineralization traps.

Results will be used to improve and refine the Kiggavik metallogenic model that has undergone several iterations since the beginning of exploration of these deposits by various companies (Urangesellschaft, Cameco, Areva) and in addition studies supported by Areva. This uranium-rich region has been progressively included in the unconformity-related model for the various reasons described above. It is considered that the Kiggavik metallogenic model represents a particular class of uranium deposits in which understanding the superposition of different types of alteration and mineralization stages, controlled by active faults and/or a passive fracture permeability network is a key for the understanding of the genesis of these deposits. The geochemical characterization of clay minerals and uranium oxides will enable assessment of whether uranium mineralization in the Kiggavik area is unconformity-related or not.

A further objective is the definition of new exploration guide lines based on fertile structures and tectonic events. The structural model and succession of alteration types/styles present along fault zones suggest structural control of the successive fluid flow events. Exploration

targets at Kiggavik are today mainly based on low-gravity anomalies that result from the loss in density of the altered/mineralized rocks. However, the high-grade hydrothermal primary mineralization occurs mainly in faults and veins, not always associated with strong host-rock alteration. Validation of this model should open new field for exploration along identified fertile faults, outside of the low-gravity anomalies.

Even if the knowledge has improved in many areas, a number of crucial questions remain unanswered or poorly explored, and will be addressed in this work:

- Can we define precisely the macroscopic and microscopic characteristics and the sequence of the different fracturing/faulting events?
- Which fracturing events are linked the circulation of uranium-bearing fluids, and the precipitation of uranium?
- What are the tectonic stresses behind the mineralizing and non-mineralizing fracturing events; what can we deduce from this, regarding regional-scale events?
- What is the fault architecture associated with uranium orebodies in the Kiggavik area, and how did it evolve before and after uranium mineralization?
- Can we characterize those of the fracture zones which are more favourable for the circulation and trapping of uranium bearing fluids?
- What are the mineralogical and structural characteristics of the mineralization in the Kiggavik area and can we conclude on its nature/type?
- What can we learn through comparison to unconformity-related uranium of the Athabasca Basin?

Manuscript organisation:

Following the presentation of the objectives, the rest of the manuscript is organized as follows:
Chapter 4 presents the methodology/techniques used to address the objectives.

Chapter 5 is dedicated to the results obtained after studying in detail the Contact prospect. The article by Roy et al., (**5.1**) published in the Canadian Journal of Earth Science reports the discovery of the Contact prospect using new geophysical inversion method. I played a role on the geological setting and on the cross-sections presented in the article. The structural architecture and the fracture control on uranium mineralization at the Contact prospect presented in **5.2** with a second article submitted (resubmitted after minor revisions) to Ore

Geology Review as first author. Complementary observations on the main fracturing events observed at the Contact prospect are presented in **5.3**.
Geochemical characterization of main fracturing events through Principal Component Analysis (PCA) is developed in **annexe.**

Chapter 6 presents the integrated structural and genetic model of uranium mineralization in the Kiggavik area, in a third article to be submitted, in which I am first author (**6.1**). In this third article, Marie Guilcher did, during her Master degree at the University of Lorraine, all the measurements concerning the fluid inclusions. A tentative model on a particular feature, the so-called Quartz breccia unit observed throughout the Kiggavik area is reported in part **6.2**.

C**hapter 7** consists of the general conclusions, followed by implications for the exploration and the scientific perspectives.

4 METHODOLOGY

4.1 FIELD CAMPAIGN AND STRATEGY OF SAMPLING/CORING

Two field seasons were conducted at Kiggavik, one during the 2014 summer and the other during the 2015 summer. During the first mission (2014), A. Benedicto took 27 samples from 4 drillholes on the recently discovered Contact showing. This first samples lead to the first relative chronology of the main events taking place at Contact.

During the second season, I was present full time (for seven weeks) at the Kiggavik exploration camp in the context of my PhD with several objectives:

- Analyze drillcore from Contact and 85W.
- Collect oriented measurements on structures.
- Sample drillcore (for petrographic and geochemical analysis)
- Determine ideal location for two control drillholes of the Andrew Lake and Kiggavik Center Zone deposits. Quickly describe and put the core in coreboxes in order to be shipped to the McClean Lake exploration camp for later observations and sampling. The Andrew Lake and Kiggavik Center zone control holes were sampled in April 2016.

It is important to understand the difficulties linked to core drilling, observations and sampling. The quality of the observations, and the possibility to take oriented measurements is highly dependent on the drill hole (orientation and dip, amount of core recovery, etc) because the more fractured and altered the core is (*i.e.* fault damage zone or fault core), the lower the probability of getting drill core suitable for orientation. Figure 17 highlights these issues. Schemes A and B of figure 17 display the situations of 2 drillholes drilling in 2 different directions. The result of the drilling is shown on the right of the cross section. The first problem is the construction of a coherent model of structures and lithology. Drilling sub-parallel to the main structure gives the apparent thickness of mineralization (drillhole A1). Drillhole A2 does not intersect any mineralization, though it is proximal to mineralization. The fact that the main structure was not intersected can cause an over emphasis of minor structures intersected by drillhole A1.

In case B, the main structure has been intersected, as well as the mineralization. Interesting data should be recovered, depending on the following issues: amount of core recovery, quality of this core and availability of an oriented line. The orientation line is marked by the drillers (with a specific tool) at the bottom of a run (a run is 3 meters of core) and provides a reference line to allow the core to be oriented in space with the use of the drill hole survey data. The line is

extended to the length of the run manually (figure D). Without this line, the only orientations possible are relative to foliation, which is only possible with a well-defined and consistent foliation. In case B, drillhole 3 drilled trough an extended damage zone and through the main structure/fault core. The orientation line was not available because of the strong alteration and fracturing of the core (the red line on the left of the drillhole indicates the availability of the orientation line). Therefore the main structures are not oriented in space. Moreover, because of the poor quality of the core, it was not possible to recover 100% of it. Figure C displays an example where approximately 50% of the core was lost, leading to incomplete observations (coupled with un-oriented structures).

In total, 140 drill core samples were collected. 66 were collected from the Contact prospect, 27 from the 85W prospect, 28 from the Andrew Lake deposit, 5 from the End deposit and 14 from the Kiggavik deposit. Two drill holes were completed to allow for more in-depth research and better structural understanding on the Andrew Lake and Kiggavik Center Zone deposits. A triple tube technique was used, allowing for better recovery, less rubbly core in fractured zones and better drill core orientation.

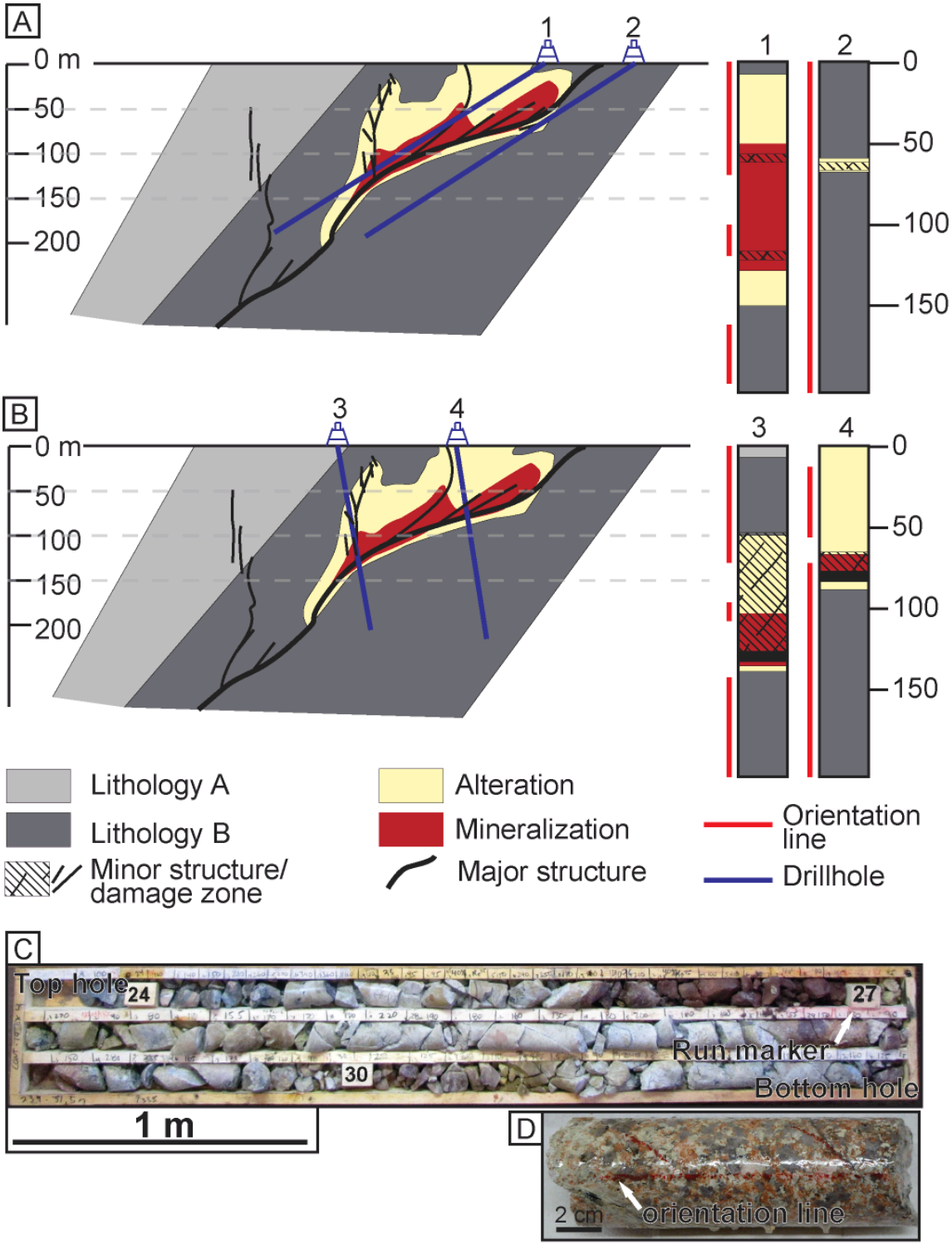

Figure 17: A) and B) Interpretations of two drillholes (on the right) made through the same deposit. The challenge of exploration geologists is to interpret as accurately possible the shape of the structures and the associated mineralization. C) Example of a core box of drillcore from a strongly fractured zone. D) Sample displaying an orientation line used for measuring oriented structures.

Figure 18 shows an example of the sampling done on drill hole CONT-16. Samples from A to G were collected from the core boxes, tagged, consolidated with epoxy resin and then shipped to Saskatoon (Figure 18-H).

Sampling was guided by the primary objective to characterize the fracture network and was limited by:

1) The quality of the drill core. A too rubbly and/or altered drill core is very difficult to observe and sample for structural purposes.
2) If the core was mineralized, the grade of the mineralization was a limiting factor, as special permissions are required to ship and receive samples.
3) By the complexity of the sample in terms of geology. Ideally, a “good” samples display alteration, mineralization and structures/microstructures in order to refine crosscutting relationships.

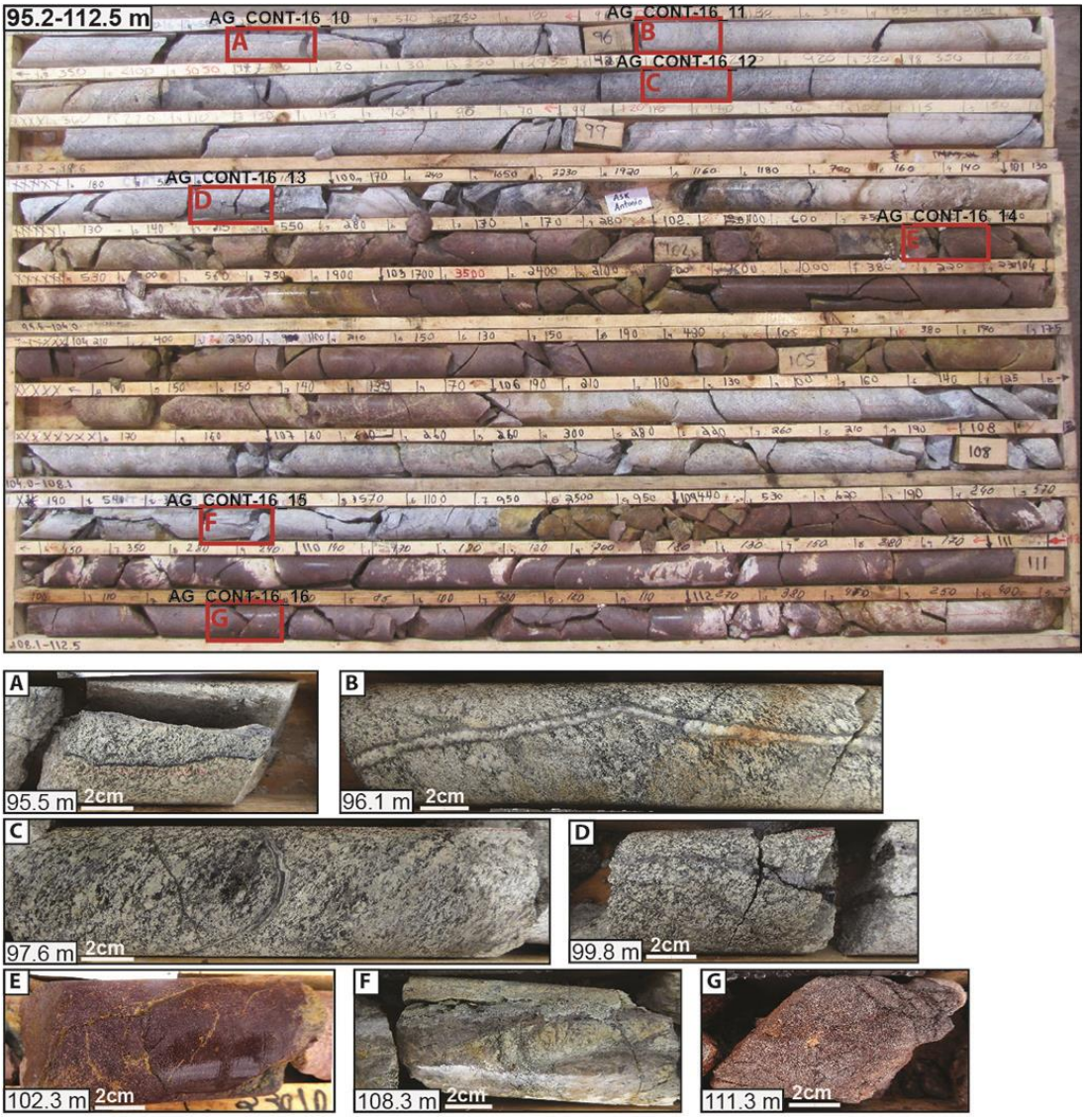

Figure 18: Example detailing sampling procedure on four core boxes of the CONT-16 drillhole.. Samples A to G are steel-tagged, quickly consolidated with e-poxy resin in the field and packed (H) for shipping to the Saskatchewan Research Council (SRC).

4.2 STRUCTURAL MEASUREMENTS

More than 4000 m of drill core have been logged in order to identify mineralization, lithologies, faults and fractures. Fault zones were characterized by identifying the core of the fault and fault damage zones through the presence of fault rocks such as breccias or gouges (Chester and Logan, 1986; Wibberley et al., 2008; Faulkner et al., 2010). Within the damage zones, the focus is on the categorization and timing of the different generations of veins, joints and undifferentiated fractures. Undifferentiated fracture relates to a fracture plane which cannot be unambiguously classified as vein, joint or fault/micro-fault (no evidence of kinematics) at the time of observation). Fracture corridors and isolated veins, joints and fractures were also systematically reported. Drill core was oriented using a Reflex ACT III digital core orientation tool (Bright et al., 2014), and then a protractor was used to measure angles between fractures relative to the core axis (alpha angle). The angle between the down hole apex of the feature and the inflection line (beta angle) was also measured for calculation of true dip/dip direction data. Acoustic televiewer probing ABI40 (Williams et al., 2004) was run through key holes providing accurate oriented data in faulted core intervals. The data were processed to their true orientation and plotted with Dips 6.0 software by Rocscience. Uncertainty on orientation measurements is usually about 10° as estimated from the comparison between oriented core-measurements and acoustic televiewer data.

4.3 OPTICAL MICROSCOPY

In order to characterize fracturing events, crosscutting relationships and fracture related alteration and cement, samples were observed in transmitted and reflected light. Hand-size

samples were cut in a half and observed under a binocular microscope (MOTIC SMZ-161 with the software Motic Images Plus 2.0 for taking pictures). Then, polished thin sections were made on selected samples and areas for examination of mineral composition and microstructures. Thin sections were scanned at the University of Alberta in Edmonton using a Nikon Coolscan 5000, using standard Nikon FH-3 strip film holder. It was possible to scan thin section in plane polarized and cross polarized light, using a polarizing film on both sides of the holder (figure 19).

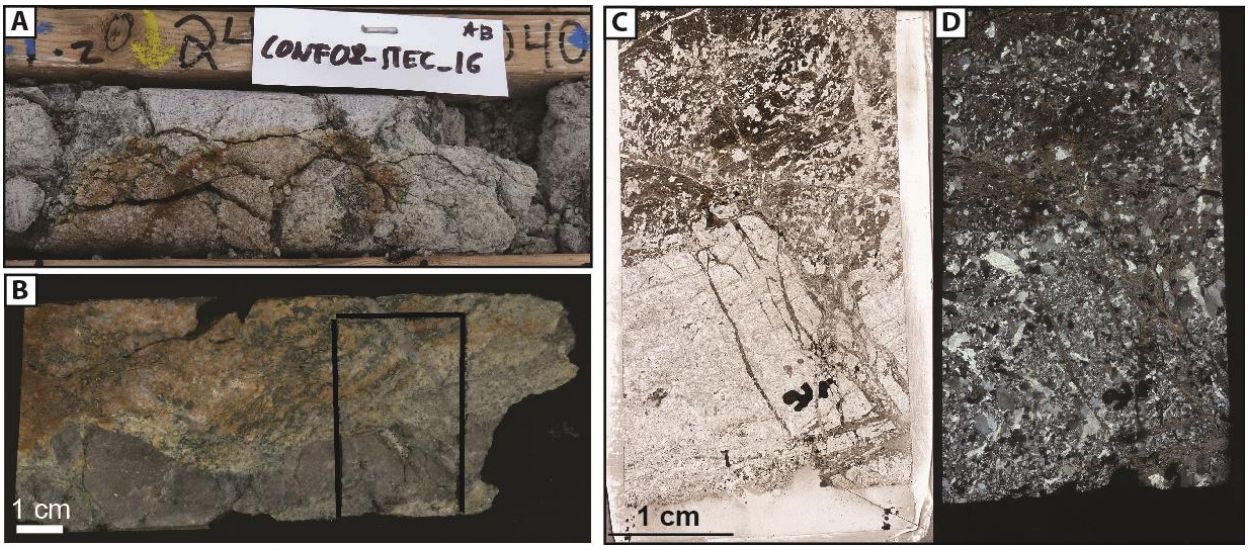

Figure 19: Different views of the same sample (Cont-08_2Petb-16) from the Contact showing, displaying a weakly mineralized fractured quartz vein. A) Sample in core box. B) Scan of the half-cut sample with location of the thin section. C) and D) Plane polarized and cross-polarized light high definition (4000 dpi) scan of the thin section.

Uranium oxides and associated ore minerals alongside with fracture cements were in a first step observed under optical microscopy (Motic BA310 POL Trinocular, using transmitted and reflected light, in the AREVA Resources Canada office).

4.4 CATHODOLUMINESCENCE

Carbonate and quartz cement generations were studied through their variations of luminescence observed under cathodoluminescence. The cathodoluminescence was a Technosyn Cold Cathodoluminescence device (model 8200 MkII), operating between 10 and 12 kV gun potential and between 150 and 350 µA beam current. Observations were carried out at the University of Barcelona, Spain (Departament de Mineralogia, Petrologia i Geologia Aplicada, Facultat de Ciències de la Terra).

4.5 SCANNING ELECTRON MICROSCOPY (SEM)

Thin sections made on fractures and fault rocks were studied under a Motic BA310 POL Trinocular, using transmitted and reflected light, and also under a HIROX SH-3000 Scanning electron microscope (SEM) equipped with a back-scattered electron detector and a nitrogen free Energy Dispersive Spectrometer (EDS) BRK D351-10 with digital mapping capabilities at AREVA la Defense site. The SEM was operated at low accelerating voltage (10 kV), 100 nA filaments current and 600 Å beam width for a working distance between 8 and 39 mm. Complementary observations on mineralogical observations and U mineralization were performed at Service Commun de Microscopie Electronique et de Microanalyses (SCMEM) of GeoRessources lab (Vandoeuvre-lès-Nancy, France), using a JEOL J7600F Scanning electron microscope equipped with an energy dispersive spectrometer.4.6 Electronic microprobe analysis (EMPA)

The exact composition of uranium oxides and clay minerals was obtained through EMPA. This technique allows the concentration of elements to be measured at low level, such as thorium in uranium oxides. Chlorites and white micas (mainly illite) are a common product of host-rock alteration associated with circulation of fluids (with or without uranium). They are also found in fractures as neo-formed minerals, and can be used as geothermometers to constrain the temperature of the altering fluid. Uranium oxides and clay minerals (chlorite and white micas) geochemistry was characterized using a CAMECA SX-100 was operated at up to 30 kV for elements with high atomic number. The calibration used natural and synthetic oxides and/or alloys (orthoclase, albite, LaPO4, CePO4, wollastonite, UO2, PbCrO4, olivine, DyRu2). The analytical conditions at SCMEM were 10-nA current, accelerating voltage of 15 kV, counting time of 10 s (K, Na, Ca), 20s (Ce, U, Si), 40s (Dy,), 50s for Pb, and 60s for La. Observations were performed at Service Commun de Microscopies Electronique et de Microanalyses (SCMEM) in Nancy, France.

Complementary measures on uranium oxides and clay minerals were made on 6 thin sections, with a Cameca SX50 electron microprobe and conducted at the Camparis service in Paris (UPMC).

4.7 AGE-DATING AND TRACE ELEMENTS CONCENTRATION IN URANIUM OXIDES: SECONDARY ION MASS SPECTROMETRY (SIMS)

The U–Pb isotopic composition of uranium oxides were determined using a CAMECA ims 1280-HR Secondary Ion Mass Spectrometer (SIMS) at CRPG-CNRS (Nancy, France). The O− primary ion beam was accelerated at 13 kV, with an intensity ranging between 3.5 and 5 nA. The primary beam was set in Gaussian mode with a raster of 10 µm. The size of the spot on the uranium oxides was ~ 15 µm. Positive secondary ions were extracted with a 10 kV potential, and the spectrometer slits were set for a mass resolving power of ~6,000 to separate isobaric interferences of rare earth element (REE) dioxides from Pb. The field aperture was set to 2,000 µm, and the transfer optic magnification was adjusted to 80. Rectangular lenses were activated in the secondary ion optics to increase the transmission at high mass resolution. The energy window was opened at 30 eV, and centred on the low energy side, 5eV before the maximum value. Ions were measured by peak jumping in monocollection mode using the axial Faraday cup (FC) for 238U and 238UO and the axial electron multiplier (EM) for 204Pb, 206Pb, 207Pb, 208Pb, and 248ThO. Each analysis consisted of 8 successive cycles. Each cycle began with measurement of the mass 203.5 and 203.6 for backgrounds of the FC and the EM respectively, followed by 204Pb, 206Pb, 207Pb, 208Pb, 238U, 248ThO, and 238UO, with measurement times of 4, 4, 10, 6, 20, 4, 4, 3, and 3 s, respectively (waiting time of 1 s).

The beam centering, mass, and energy calibrations were checked before each measurement, after a 60 s presputtering by rastering the primary beam over a 30×30 µm area to clean the gold coating and avoid pollution. Several spot analyses (at least five) were measured on the Zambia reference uraninite (concordant age of 540 ± 4 Ma; Cathelineau et al., 1990) before and after each sample for sample bracketing. To define the relative sensitivity factor for Pb and U used for samples, an empirical linear relationship was defined between UO+/U+ and Pb+/U+ from all the measurements performed on the reference mineral (Zambia). The error on the calibration curve is reported in the error given for each analysis. To achieve good reproducibility, each analysis was preceded by automated centering of the sample spot image in the field aperture and contrast aperture (Schuhmacher et al. 2004) and of the magnetic field values in scanning the 206Pb peak. The 204Pb/206Pb ratio were low (<0.00001), indicating that common lead was not incorporated at the time of crystallization, except sample 9850. A correction for common lead was made for each analytical spot by precisely measuring the 204Pb amount and the common lead composition was calculated at the 207Pb/206Pb measured age, using the Pb isotopic composition calculated from Stacey and Kramers (1975) model at the

age of uranium oxide. Ages and error correlations were calculated using the ISOPLOT flowsheet of Ludwig (1999). Uncertainties in the ages are reported at the 1σ level.

The rare earth element (La, Ce, Pr, Nd, Sm, Eu, Gd, Tb, Dy, Ho, Er, Tm, Yb, Lu) concentrations in the different uranium oxides were quantified using a LA-ICP-MS system composed of a GeoLas excimer laser (ArF,193 nm, Microlas) coupled to an Agilent 7500c quadrupole ICP-MS. The detailed instrumentation and methodology is described in Lach et al. (2013).

4.8 FLUID INCLUSIONS (FI) AND FLUID INCLUSION PLANES (FIP) STUDY

Fluid inclusions (FI) were studied individually in order to characterize salinity, temperature, metal concentration of the fluid that circulated as well as its trapping conditions (i.e. pressure) at a specific time in the host mineral growth. Host minerals like quartz and carbonates are usually transparent so that FIs can be observed in cross-polarized light. Fluid inclusions can be characterized regarding the number of phases present, and by the relative proportion of each phase. Phases can be liquid, gas or solid (i.e. salt cube). The fluid characterizes the mineral from which it formed, or the fluid that circulated in a microfracture network formed after the formation of the crystal.

Petrographically, three types of FIs can be recognized (Roedder, 1984):

- Primary fluid inclusions: the fluid is trapped during the growth of the crystal. These inclusions are observed in planes parallel to the external border of the crystal and at the limit of each growth zone.
- Pseudo-secondary fluid inclusions: these fluid inclusions are trapped during the growth of the crystal. They are observed in planes crosscutting the crystal and possibly its growth zones but are truncated at the external border of the crystal.
- Secondary fluid inclusions: These fluid inclusions are trapped after the growth of the crystal, when it undergoes fracturing. Fluids are trapped as fluid inclusions when the microfractures heal (Fig. 20A). These fractures can possibly cut across several older crystals, making it the best recognition criterion of secondary fluid inclusion planes.

Generally, fluid circulation occurs through the fracture network but also depends on the porosity and permeability of rocks (Lespinasse, 1999; Lespinasse et al., 2005; Mercadier et al., 2010). Porosity and permeability depend partly on the density of microfractures within minerals.

Microfractures can be associated to fractures at various scales. Microfractures can be neoformed or reactivated and used as a pathway for fluids that can be trapped in the form of fluid inclusions (Lespinasse et al., 2005); as a consequence, fluid inclusions planes (FIP) are formed.

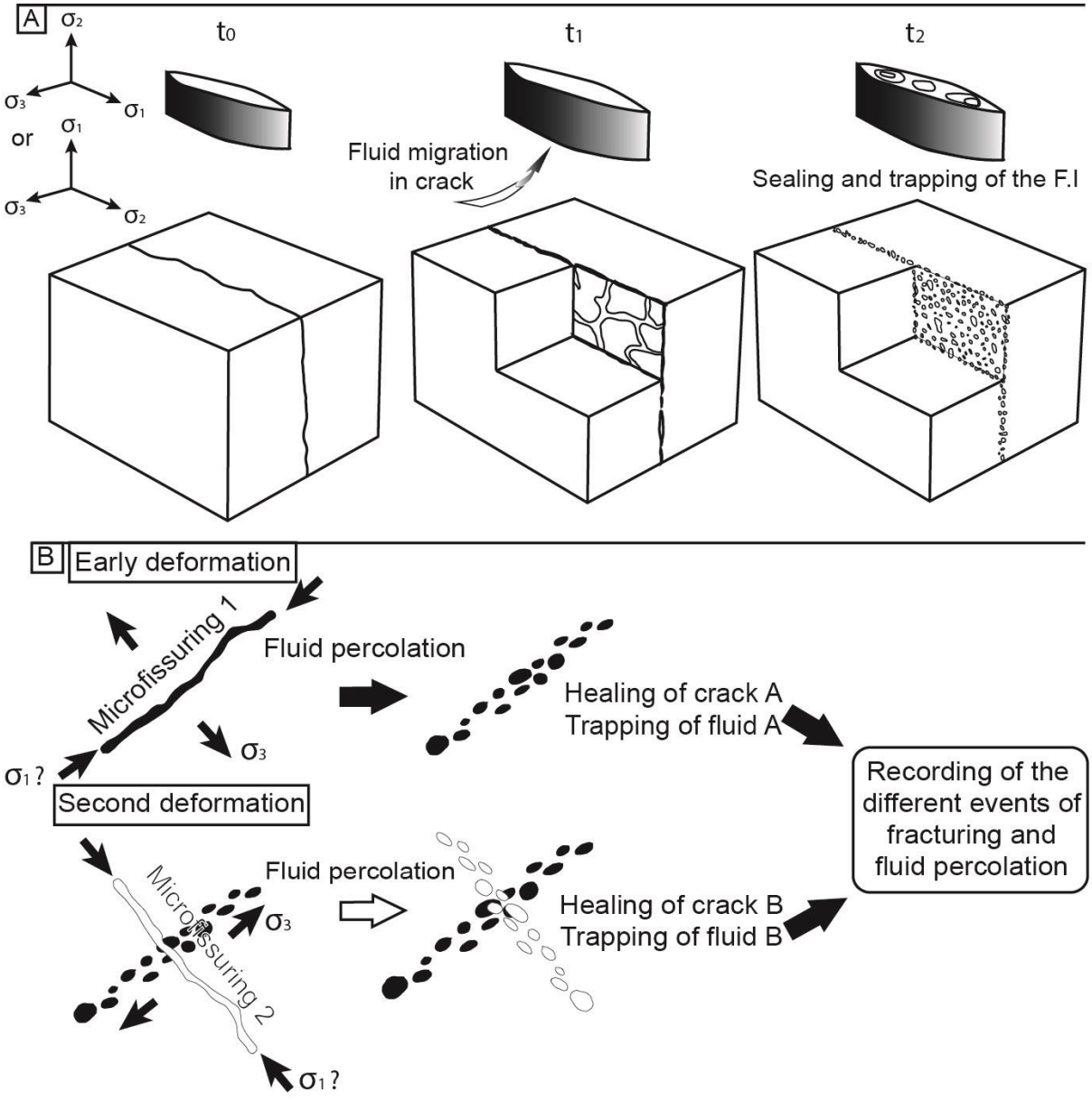

Figure 20: A) Trapping of fluids as fluid inclusions and formation of a fluid inclusion plane (FIP) B) Trapping of successive fluid events that circulated through successive micro-fracturing events, after Lespinasse (1999) and Tuttle (1949).

The orientation of these FIPs provides information on the direction of paleostress during the formation of these microfractures, as the FIP is a mode I fracture (parallel to σ1, Fig. 20B).

Crosscutting relationships between FIPs allow characterization of successive microfracturing events and associated fluid circulation (Fig. 20B). It is therefore possible to identify several groups of FIPs and fluid generations, on the basis of the types of FIs and the crosscutting relationships between FIPs.

When the characteristics (size, phases.) of the FI forming FIP are studied and when the different generations and groups of FIP are determined, Fis are then studied individually through microthermometry (temperature, salinity), Raman spectrometry (salinity, chlorinity, gas characteristics) and LA-ICP MS (trace elements concentrations). Representative oriented samples were collected from the 85W and Contact prospect.

A thin section and a wafer were prepared on a horizontal plane from selected regions of the core. Quantification of the abundance of each FIP type was carried out using a systematic and statistical procedure of the microstructural markers in the quartz within the oriented wafers. FIP orientations were measured under cross-polarized light microscope using the AnIma software (Lespinasse et al., 2005). FIP and fractures orientations are given in the form of rose diagrams, which take into account the cumulative number of cracks for angular section of 10° between 0 and 0° 360°. Microthermometry was carried out on fluid inclusions (FI) using a Linkam® MDS600 heating-cooling stage, adapted to an Olympus® microscope at the GeoRessources laboratory (Nancy, France). The following microthermometric parameters were measured for liquid-dominated FIs: eutectic temperature (Te), melting temperatures of ice and hydrohalite (Tmice and Tmhyd), halite dissolution (TsNaCl), and homogenization temperature (L+V□L or L+V+S□L+S) (Th). The following microthermometric parameters were measured for gas-dominated FIs: halite dissolution (TsNaCl), CO2 melting and clathrate dissociation (TmCO2 and TmCl), CO2 homogenization (ThCO2), and total homogenization temperature (Th).

The temperatures of phase changes have a precision of about ± 5 °C for Te, ±0.1 °C for Tmice, Tmhyd and ±1 °C for TsNaCl and Th. Aqueous carbonic fluid inclusions were classified using the nomenclature of Boiron et al. (1992). A Dilor-Labram Raman microspectrometer was used for the quantitative measurement and characterization of gas species present in the fluid inclusions, following the procedure described by Dubessy et al. (1989).

The quantification of the chemical composition (major, minor and trace elements) of water-rich FI was tempted using the LA-ICP-MS system composed of a GeoLas excimer laser (ArF,193 nm, Microlas) coupled to an Agilent 7500c quadrupole ICP-MS at GeoRessources lab.

The laser beam is focused onto the sample within a low-volume custom-made lozenge-shaped ablation cell dedicated to fluid inclusion analyses that has a Schwarzschild reflective objective (magnification × 25; numerical aperture 0.4) mounted onto an optical microscope (Olympus BX41) equipped with a X–Y motorized stage and CCD camera. NIST610 (Jochum et al., 2011) was chosen as the external standard, with accuracy also accuracy verified using the NIST612 standard. Analysis parameters include a fluence of 14 J/cm² and laser shot frequency of 5 Hz, He = 0.5 L.min-1 as a carrier gas mixed with Ar = 0.7 L.min-1 via a cyclone mixer prior to entering the ICP torch. Spot sizes varied from 24 µm up to 44 µm, depending on the inclusion size. The elemental isotopes analysed were: 23Na, 11B, 24Mg, 39K, 44Ca, 55Mn, 57Fe, 63Cu, 66Zn, 88Sr, 55Cs, 57La, 137Ba, 208Pb, and 238U, using an integration time of 0.01 s per mass channel for a total cycle time of 0.22 s.

System calibration and signal integration were performed using the Matlab®-based SILLS program. Absolute element concentrations can be calculated from analyzed ratios relative to the Na concentration. The Na concentration can be obtained from the salinity estimated from microthermometry (in wt.% NaCl + CaCl2 equiv.) using the charge-balance technique. This method corrects the modelled amount of Na (from the wt.% NaCl equiv.) for contributions from other chloride salts using the analyzed elemental ratios to Na. Limits of detection (LODs) were calculated using the 3σ criterion. The analytical precision of most elements is within 20-30% RSD.

As presented in the methodology, the sampling was conducted mainly on the 85W and Contact prospect at first, then lateron the Andrew Lake and Kiggavik deposit through the two “control drillholes” realized during the 2015 summer field campaign. This second sampling took place when the two drillholes were stored at the McLean Lake mine.

The Contact prospect has been the subject of most of the observations, structural interpretations and sampling. Two articles have been prepared on the Contact propect to date. The first one by R. Roy, focuses on the discovery and modelling of the Contact prospect through geophysical methods, while the second one, presents the structural model of the Contact prospect and how the successive fracturing/faulting events have controlled fluid circulations and shaped the uranium mineralizations.

5 THE CONTACT PROSPECT

5.1 CONTACT PROSPECT 3D GEOPHYSICAL MODELLING

In the following scientific article, I brought informations and precisions on the geological context, cross-sections and other relevant geological informations regarding some structural specificity of the Contact prospect.

Three-dimensional gravity modelling applied to the exploration of uranium unconformity-related basement-hosted deposits: the Contact prospect case study, Kiggavik, northeast Thelon region (Nunavut, Canada)

Régis Roy, Antonio Benedicto, Alexis Grare, Mickaël Béhaegel, Yoann Richard, and Grant Harrison

Abstract: In unconformity-related uranium deposits, mineralization is associated with hydrothermal clay-rich alteration haloes that decrease the density of the host rock. In the Kiggavik uranium project, located in the eastern Thelon Basin, Nunavut (Canada), basement-hosted shallow deposits were discovered by drilling geophysical anomalies in the 1970s. In 2014, gravity data were inverted for the first time using the Geosoft VOXI Earth Modelling™ system to generate three-dimensional (3D) models to assist exploration in the Contact prospect, the most recent discovery at Kiggavik. A 3D unconstrained inversion model was calculated before drilling, and a model constrained by petrophysical data was computed after drilling. The unconstrained inversion provided a first approximation of the geometry and depth of a low-density body and helped to collar the discovery holes of the Contact mineralization. The constrained inversion was computed using density values measured on 315 core samples collected from 21 drill holes completed between 2014 and 2015. The constrained modelling highlights three shallower and smaller low-density bodies that match the geological interpretation and refines the footprint of the gravity anomalies in relation to the current understanding of the deposit. The 3D inversion of gravity data is a valuable tool to guide geologists in exploration of shallow basement-hosted uranium deposits associated with alteration haloes and to assess the deposit gravity geometry.

Résumé : Les minéralisations dans les gisements d'uranium de type discordance sont accompagnées d'halos argileux d'altération hydrothermale qui provoquent une diminution de la densité de la roche encaissante et par conséquent une anomalie gravimétrique. Dans le projet uranifère de Kiggavik, situé à l'est du Bassin du Thelon, Nunavut (Canada), des gisements peu profonds encaissés dans le socle ont été découverts dans les années 1970 en explorant des anomalies géophysiques. En 2014, les données gravimétriques ont été inversées pour la première fois à l'aide du module VOXI Earth Modelling™ de Geosoft et ceci pour générer des modèles en trois dimensions (3D) en support à l'exploration de Contact, la dernière découverte à Kiggavik. Un modèle 3D non contraint et un modèle 3D contraint par des données pétrophysiques ont été construits, respectivement, avant et après les campagnes de forage. Le modèle non contraint a été calculé pour produire un modèle de contraste de densité en 3D sans aucune information a priori. Il fournit une première approximation sur la géométrie et la profondeur du corps de faible densité. Malgré l'incertitude en taille et en profondeur, ce modèle a contribué à localiser les forages qui ont permis de découvrir la minéralisation à Contact. Le modèle contraint a été calculé en utilisant les valeurs de densité mesurées sur 315 échantillons prélevés dans 21 forages réalisés entre 2014 et 2015. Il met en évidence trois corps superficiels de plus faible densité et qui répondent à l'interprétation géologique. Le modèle contraint permet de matérialiser l'empreinte du gisement sur les anomalies gravimétriques. L'inversion 3D des données gravimétriques est un outil qui permet de guider les géologues dans l'exploration de gisements d'uranium peu profonds associées à des halos d'altération et d'évaluer leur géométrie. [Traduit par la Rédaction]

NRC Research Press

ARTICLE

Three-dimensional gravity modelling applied to the exploration of uranium unconformity-related basement-hosted deposits: the Contact prospect case study, Kiggavik, northeast Thelon region (Nunavut, Canada)

Régis Roy, Antonio Benedicto, Alexis Grare, Mickaël Béhaegel, Yoann Richard, and Grant Harrison

Abstract: In unconformity-related uranium deposits, mineralization is associated with hydrothermal clay-rich alteration haloes that decrease the density of the host rock. In the Kiggavik uranium project, located in the eastern Thelon Basin, Nunavut (Canada), basement-hosted shallow deposits were discovered by drilling geophysical anomalies in the 1970s. In 2014, gravity data were inverted for the first time using the Geosoft VOXI Earth Modelling™ system to generate three-dimensional (3D) models to assist exploration in the Contact prospect, the most recent discovery at Kiggavik. A 3D unconstrained inversion model was calculated before drilling, and a model constrained by petrophysical data was computed after drilling. The unconstrained inversion provided a first approximation of the geometry and depth of a low-density body and helped to collar the discovery holes of the Contact mineralization. The constrained inversion was computed using density values measured on 315 core samples collected from 21 drill holes completed between 2014 and 2015. The constrained modelling highlights three shallower and smaller low-density bodies that match the geological interpretation and refines the footprint of the gravity anomalies in relation to the current understanding of the deposit. The 3D inversion of gravity data is a valuable tool to guide geologists in exploration of shallow basement-hosted uranium deposits associated with alteration haloes and to assess the deposit gravity geometry.

Résumé : Les minéralisations dans les gisements d'uranium de type discordance sont accompagnées d'halos argileux d'altération hydrothermale qui provoquent une diminution de la densité de la roche encaissante et par conséquent une anomalie gravimétrique. Dans le projet uranifère de Kiggavik, situé à l'est du Bassin du Thelon, Nunavut (Canada), des gisements peu profonds encaissés dans le socle ont été découverts dans les années 1970 en explorant des anomalies géophysiques. En 2014, les données gravimétriques ont été inversées pour la première fois à l'aide du module VOXI Earth Modelling^{MD} de Geosoft et ceci pour générer des modèles en trois dimensions (3D) en support à l'exploration de Contact, la dernière découverte à Kiggavik. Un modèle 3D non contraint et un modèle 3D contraint par des données pétrophysiques ont été construits, respectivement, avant et après les campagnes de forage. Le modèle non contraint a été calculé pour produire un modèle de contraste de densité en 3D sans aucune information a priori. Il fournit une première approximation sur la géométrie et la profondeur du corps de faible densité. Malgré l'incertitude en taille et en profondeur, ce modèle a contribué à localiser les forages qui ont permis de découvrir la minéralisation à Contact. Le modèle contraint a été calculé en utilisant les valeurs de densité mesurées sur 315 échantillons prélevés dans 21 forages réalisés entre 2014 et 2015. Il met en évidence trois corps superficiels de plus faible densité et qui répondent à l'interprétation géologique. Le modèle contraint permet de matérialiser l'empreinte du gisement sur les anomalies gravimétriques. L'inversion 3D des données gravimétriques est un outil qui permet de guider les géologues dans l'exploration de gisements d'uranium peu profonds associées à des halos d'altération et d'évaluer leur géométrie. [Traduit par la Rédaction]

Introduction

The Kiggavik uranium project is located approximately 80 km west of Baker Lake in Nunavut, Canada (Fig. 1*a*). The Kiggavik deposits, attributed to unconformity-related basement-hosted uranium types (Miller and LeCheminant 1985; Miller et al. 1989; Riegler et al. 2014; Chi et al. 2016), are situated south of the Aberdeen sub-basin of the Paleoproterozoic Thelon Basin (Fig. 1*b*), a contemporaneous analog of the Athabasca Basin in Canada (Jefferson et al. 2007) that hosts the world's most important sources of high-grade uranium ore (OECD 2014). The current calculated measured and indicated resources (NI-43-101 compliant) for four of the deposits at Kiggavik yield 48 953 t of uranium at a grade of 0.47%U (AREVA 2015).

The Kiggavik uranium mineralization consists primarily of pitchblende and lesser secondary coffinite (Miller and LeCheminant 1985; Fuchs et al. 1986; Weyer et al. 1987; Riegler et al. 2014). This mineralization is associated with pervasive hydrothermal alteration haloes around the ore deposits consisting of chlorite, hematite, and illite (Riegler et al. 2014; Sharpe et al. 2015), which extensively alters the original texture of the rock and lowers the electrical resistivity, density, and magnetic susceptibility leading to significant geophysical anomalies (Hasegawa et al. 1990).

Received 21 December 2016. Accepted 4 May 2017.

Paper handled by Associate Editor Randolph Enkin.

R. Roy, A. Benedicto, M. Béhaegel, and G. Harrison. AREVA Resources Canada Inc., P.O. Box 9204, 810 – 45th Street West, Saskatoon, SK S7K 3X5, Canada.
A. Grare. AREVA Resources Canada Inc., P.O. Box 9204, 810 – 45th Street West, Saskatoon, SK S7K 3X5, Canada; Université Paris Pierre et Marie Curie, ISTeP, UMR 7193 UPMC et CNRS, 4 Place Jussieu F-75252 Paris, France.
Y. Richard. AREVA Mines, Geosciences Department, 1 Place Jean Millier, F-92084 Paris La Défense Cedex, France.
Corresponding author: Régis Roy (email: regis.roy@areva.com).

Can. J. Earth Sci. **54**: 869–882 (2017) dx.doi.org/10.1139/cjes-2016-0225

Published at www.nrcresearchpress.com/cjes on 11 May 2017.

Fig. 1. Simplified geological map showing the location of the (*a*) Kiggavik uranium project in (*b*) northeast Thelon region (modified after Peterson et al. 2002). SZ, shear zone. [Colour online.]

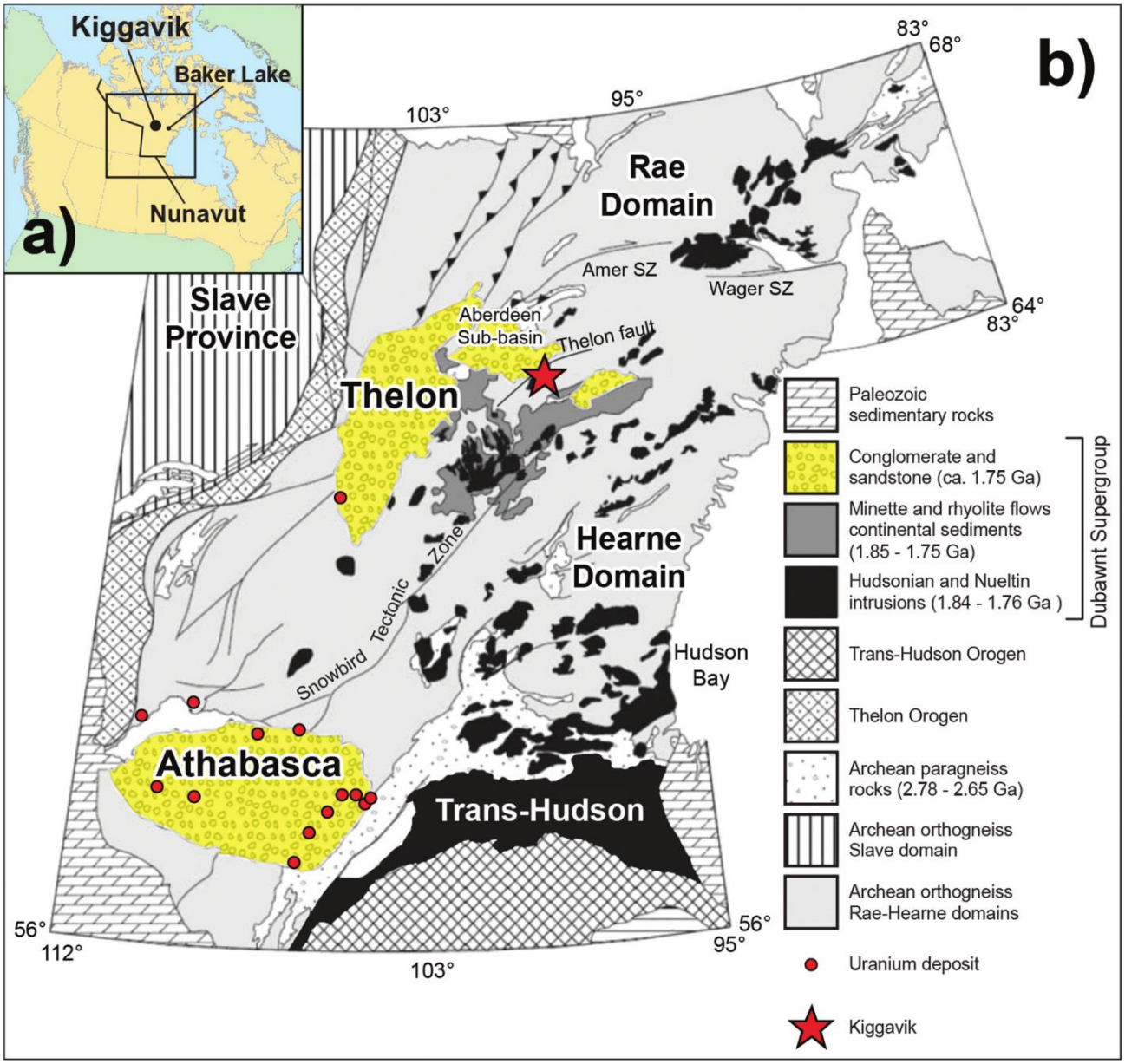

Uranium was originally identified at Kiggavik when radioactive frost boils and rock chips were discovered during systematic coverage by an airborne radiometric survey conducted in the mid-1970s by Urangesellschaft Canada Limited (UGC). Drilling commenced in 1977 and led to the discovery of the Main and Centre Zone deposits (Fuchs et al. 1986). Other anomalous areas were identified using intensive airborne and ground surveying (e.g., airborne resistivity, ground very-low-frequency (VLF-EM), and gravity). The coinciding resistivity and gravity anomalies were drilled, and new uranium mineralization was discovered by UGC at Bong in 1984, at End in 1987, and at Andrew in 1988 (Fig. 2). Genetic models have been proposed recently for the Bong deposit (Riegler 2013; Sharpe et al. 2015), while petrography, fluid inclusion analysis, and geochronology have been published for the End deposit (Chi et al. 2016).

Discovered in 2014, the Contact prospect is the latest discovery of the Kiggavik uranium deposits and prospects. As with the Andrew Lake and the End deposits, the Contact prospect is located along the Andrew Lake fault trend, a structural corridor along a northeast–southwest trend (Fig. 2). The corresponding gravity low was first tested with two drill holes in the early 1990s. Alteration and trace mineralization were intersected in one of the holes. The area was highlighted in 2013 by a GIS-based mineral prospectivity analysis of the available airborne and ground data (Robbins et al. 2015). In 2014, the anomaly was drilled intersecting the initial discovery holes at Contact, and a new ground gravity survey was conducted over the area. The drilling activities continued in 2015 based on the results of a new ground gravity survey. The drill-hole targeting was assisted by unconstrained three-dimensional (3D) gravity modelling that helped localize the discovery holes of the

Fig. 2. Simplified geological map of the southern Kiggavik project (i.e., south of the Judge Sissons fault) showing the location of the Contact prospect and the Andrew Lake and End deposits along the Andrew Lake fault trend. The blue frame highlights the area where gravity data were modelled with the Geosoft VOXI module. SLIC, Schulz Lake Igneous Complex (Jefferson et al. 2011*a*, 2011*b*).

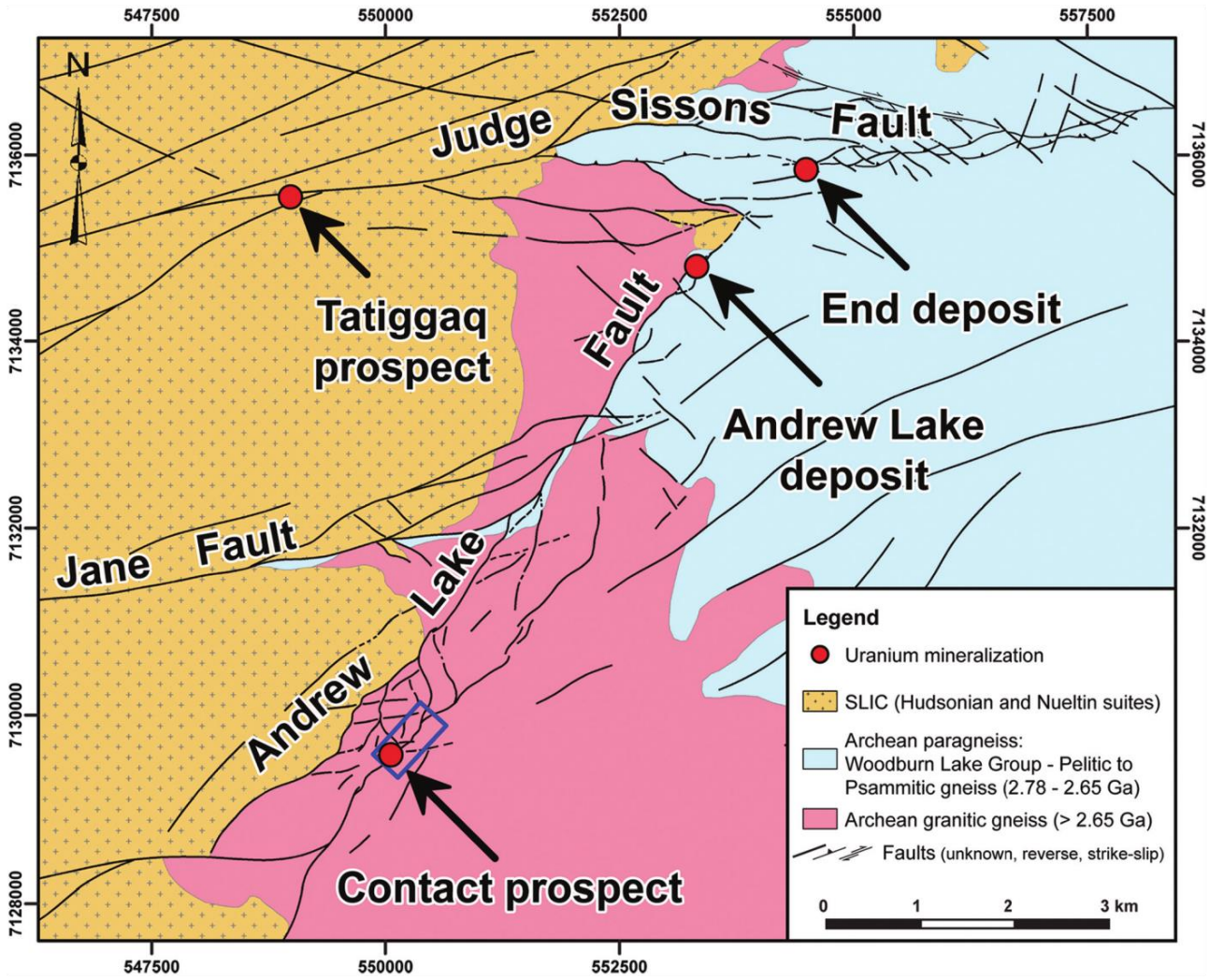

Contact mineralization. This paper presents and discusses the 3D gravity inverse modelling.

The use of 3D modelling of potential fields (e.g., magnetics and gravity) has become an important tool in mineral exploration (Li and Oldenburg 1998; Oldenburg et al. 1998), as it can provide relevant information for target generation (Fitzpatrick and Large 2015). Three-dimensional modelling has been mainly implemented within academic environments (Oldenburg and Pratt 2007; Lelièvre et al. 2009); and its use in mining exploration has been increasing over the last two decades, as the algorithms and the computer calculations have been improved (Vallée et al. 2011). Potential field methods lead to nonunique inverse models. An infinite number of solutions can replicate the observed geophysical field data, and the solutions are not necessarily geologically realistic. Integrating an a priori knowledge in the modelling (Fullagar et al. 2008), for example, rock physical properties measured on samples (McGaughey 2007; Sun and Li 2011), can help the inversion algorithm to converge to a more realistic model better reflecting the deposit geometry.

In the Kiggavik area, a regional-scale study was published on geophysical modelling by integrating detailed gravity, aeromagnetic, and structural geology observations measured along a series of two-dimensional (2D) transects with a petrophysical rock properties database (Tschirhart et al. 2013*a*). This work allowed constraining the geometry of nonmetamorphosed intrusive complexes with respect to the ore-hosting metamorphic rocks and intersecting reactivated fault arrays. Forward modelling, applied to mineral exploration targeting, was attempted at a local scale in the Kiggavik region by AREVA Resources Canada. The 2D gravity models were constructed to define drilling targets based on geological models assuming that the low-gravity anomaly was caused by the overburden, the alteration zones, or a combination of both.

The aim of the present study is to show (*i*) how unconstrained 3D gravity modelling was used in the Kiggavik project to assist successful exploration and (*ii*) how the Contact prospect footprint changes based on constrained 3D gravity modelling.

Geological setting

Regional geology

Uranium deposits in Kiggavik are hosted within the Archean and Paleoproterozoic basement rocks marginal to the Aberdeen sub-basin of the Thelon Basin (Jefferson et al. 2011*a*, 2011*b*; Fig. 1).

The Archean basement rocks include Mesoarchean (~2.87 Ga) granitic gneisses, 2.73–2.68 Ga supracrustal rocks of the Woodburn Lake Group (Pehrsson et al. 2013), and a distinctive package of 2.62–2.58 Ga felsic volcanic and related hypabyssal rocks known as the Snow Island suite (Jefferson et al. 2011*a*, 2011*b*; McEwan 2012; Tschirhart et al. 2013*b*, 2017; Peterson et al. 2015*a*; Johnstone et al. 2016). These rocks, together with overlying Paleoproterozoic (2.30–2.15 Ga) rocks of the Ketyet River Group (Rainbird et al. 2010), including a prominent unit of orthoquartzite, are strongly deformed and in turn unconformably overlain by undeformed sedimentary and minor volcanic rocks of the Wharton and Barrensland groups of the Dubawnt Supergroup (Rainbird et al. 2003; Fig. 1*b*). Deposition of the Dubawnt Supergroup began at ~1.83 Ga and continued into the waning stages of Trans-Hudsonian orogeny. The interior of Rae craton underwent dextral-oblique shortening, accompanied and superseded by local extension, subsidence, and intracratonic basin formation (Hoffman 1988; Rainbird et al. 2003; Corrigan et al. 2009). Major east-northeast-trending dextral strike- and oblique-slip faults, including the Thelon and Judge Sissons faults, and the northeast-trending Andrew Lake fault, became active, and faulting was accompanied by emplacement of the Schultz Lake Intrusive Complex (SLIC). The SLIC comprises ~1.84–1.82 Ga nonfoliated granitoid sills, syenites (Martell syenites), and lamprophyre dykes of the late syn-orogenic Trans-Hudsonian suite and ~1.75 Ga rapakivi-style Nueltin granite of the anorogenic Kivalliq igneous suite (Hoffman 1988; Peterson et al. 2015*b*; cf., Scott et al. 2015). There is evidence to suggest that these faults underwent repeated reactivation during multistage uranium mineralization (e.g., Fuchs and Hilger 1989; Jefferson et al. 2011*a*, 2011*b*; Grare et al. 2016).

The Contact prospect

The Contact prospect is located within the hanging wall of the Andrew Lake fault (Fig. 2). In this location, the Andrew Lake fault is a northeast-trending, northwest steeply dipping fault corridor characterized by tens of metres thick quartz-sealed breccia and forms the lower boundary of the Contact prospect. This quartz-sealed breccia acted as a transversal barrier for fluids that are responsible for mineralization and alteration. This caused a spatial convergence of both mineralizing and alteration fluids and the development of the Contact uranium mineralization within its hanging wall (Grare et al. 2016).

The mineralization is hosted in granitic gneiss of suspected Archean age (Jefferson et al. 2007), locally in Hudsonian granite sills and related lamprophyres dykes and is surrounded by a halo of varying degrees of weak to moderate hematite, chlorite, and illite alteration. Mineralization occurs as primary vein-related and disseminated pitchblende replacing or co-precipitating with minor sulphides (e.g., pyrite, chalcopyrite, and bravoite). Later alteration and remobilization are expressed in the form of nodular–spherulitic pitchblende (rich in goethite) in redox fronts, illite being the dominant alteration clay. In accordance with the metallogenetic model proposed by Sharpe et al. (2015) for the Bong deposit, the strong phase of alteration in the Contact prospect would have occurred during a stage of pervasive argillization and desilicification (i.e., stage 2 of Sharpe et al. 2015), and in a stage of oxidizing fluid remobilization, concentrating the uranium along redox fronts (i.e., stage 3 of Sharpe et al. 2015).

The Contact prospect is covered by a thin glacial till-type overburden. Although the overburden is less than 10 m thick, it can reach up to 20 m in some areas. In the Contact area, the mineralized and (or) altered basement rocks are at shallow depth, between 10 and 180 m.

Dataset and tools

Ground gravity data

Ground gravity surveys were conducted in the Contact area (Fig. 3) using Lacoste & Romberg gravity meters with a resolution of 0.01 mGal (1 Gal = 1 cm/s^2). Gravity stations were measured along profiles separated by 100–200 m. The station separation was approximately 50 m along the lines. Gravity observations were acquired using the looping method, with beginning and ending observations obtained at a temporary gravity base station established on the surveyed grid and tied to the main base station of the Kiggavik exploration camp. The project gravity reference site was the Canadian Gravity Standard Network base in Baker Lake. The position of the observations was established using a Differential Global Positioning System (DGPS).

The ground gravity data were corrected for free-air effect, latitude, Earth's tides, instrument drift, and adjusted to the defined base value. Terrain corrections were calculated to a radius of 750 m for each gravity observation.

The resulting gravity values were corrected to Bouguer anomaly using equations conforming to gravity standards set by the U.S. Geological Survey (Hildenbrand et al. 2002) and the Standards/Format Working Group of the North American Gravity Database Committee (Hinze et al. 2005). The ellipsoid theoretical gravity calculation uses the Somigliana closed-form formula based on the 1980 Geodetic Reference System (GRS80) to predict the gravity at any height and any latitude ( ) (Moritz 1980; Hildenbrand et al. 2002). The gravity dataset used in the 3D modelling was the Bouguer anomaly reduced at a Bouguer density of 2.70 g/cm^3 (Fig. 3). The estimation of this density value was based on the Nettleton method (Nettleton 1939; Nettleton 1976).

Sample density data

A total of 315 drill-core samples (~10 cm long each) were collected from 21 drill holes for density measurements. The samples were collected systematically every 20 m or less when lithological changes were identified. Densities were obtained using the standard Archimedes' principle based on mass and volume measurements (Quirt and Brulé 1990; Blaise 1998).

For the statistical analysis of the density, altered and fresh rocks were grouped into three units: Archean granitic gneisses, Hudson suite intrusives, and fault rocks (Fig. 4). The Archean granitic gneiss unit has a bimodal distribution (Table 1; Fig. 4*a*): the first and largest mode has an average value of 2.61 g/cm^3, while the average value for the second population is 2.28 g/cm^3. According to drill-hole observations, these two populations represent fresh and altered granitic gneisses, respectively (see examples in Figs. 5*a*, 5*b*). The Hudson suite intrusives are dominantly represented by granite, local syenite, and lamprophyre dikes (Table 1; Fig. 4*b*). Fresh Hudsonian granites samples show an average density of 2.55 g/cm^3, although a few samples can reach a density of 2.70 g/cm^3 (see Table 1, Fig. 4*b*, and example in Fig. 5*c*). The large number of altered Hudsonian granite samples (i.e., standard deviation of 0.22 g/cm^3) with densities lower than 2.33 g/cm^3 is related to the exploratory target location of the drill holes in alteration zones (see example in Fig. 5*d*). Density values for fresh syenite samples vary from 2.50 to 2.74 g/cm^3 (Table 1; Fig. 4*b*). The only altered syenite density sample is 2.34 g/cm^3. The density for fresh and altered lamprophyres ranges from 1.97 to 2.81 g/cm^3 (Table 1; Fig. 4*b*). Although fresh samples present an average value of 2.60 g/cm^3, the density for some of them can be as low as 2.03 g/cm^3. Altered lamprophyres show density values lower than 2.40 g/cm^3, with an average of 2.22 g/cm^3 (Table 1; Fig. 4*b*). Two populations of samples were collected from fault zones (Fig. 4*c*): undifferentiated fault samples (e.g., clayey, chlorite and (or) hematized cataclasite) and quartz-sealed breccia samples. Altered samples taken from undifferentiated faults are characterized by an average density value of 2.32 g/cm^3, in agreement with the moderate bleaching and argillization observed in drill core (Table 1; Fig. 4*c*). The fresh faulted samples show higher values, with an average density of 2.55 g/cm^3. In contrast, the quartz-sealed breccia samples show an average density close to 2.60 g/cm^3 in accordance with quartz densities (Table 1; Fig. 4*c*). Argillization and bleaching rarely involve this

Fig. 3. Ground gravity grid acquired in the Contact prospect. The black frame highlights the area where gravity data were modelled with the Geosoft VOXI inversion module. Black lines show the projected surface traces of the inclined holes drilled in the area. *d*, Bouguer density.

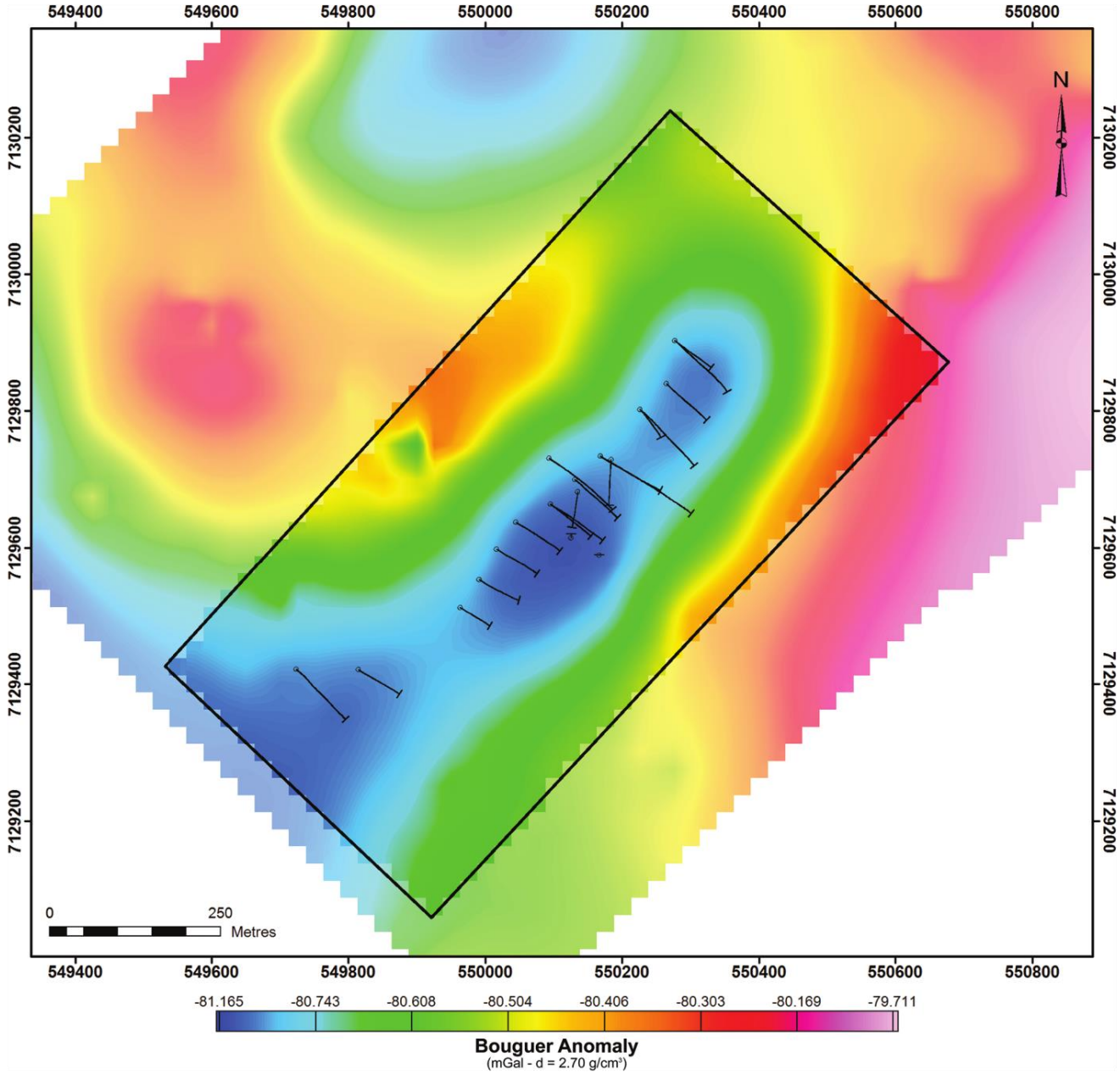

lithology. For the purpose of this study, it is globally assumed as fresh.

For modelling purposes, the lithological units were assigned the density values measured from corresponding samples in each drill hole. If two or more samples were taken from one unit, the average was used. The overburden is not represented, as it could not be sampled owing to its low thickness and cohesiveness. Thus, the quartz-sealed breccia was neglected in the following 3D model.

VOXI inversion software module

VOXI Earth Modelling™ is a Geosoft Oasis Montaj cloud and clustered computing module that allows the inversion of geophysical data (e.g., gravity, magnetics) in 3D (Geosoft 2016). It utilizes a Cartesian Cut Cell (CCC) and an Iterative Reweighting Inversion (IRI) algorithm developed by Ingram et al. (2003). The algorithm has been simplified by Ellis and MacLeod (2013) to represent geological surfaces with greater accuracy. Inversions can be completed as "unconstrained" or "constrained" using drill-hole information (e.g., magnetic susceptibility or density logs) or geological information. Gravity and magnetic data (ground or airborne data, total field or gradient measurements) can be inverted using different methods and sets of constraints or regularizations (e.g., Barbosa and Pereira 2013; Farhi et al. 2016).

3D inversion modelling

Two methods were used to invert gravity data: (*i*) an unconstrained inversion was computed to produce a 3D density contrast model to highlight low-density areas and position drilling targets at the first stage of exploration without any a priori information;

Fig. 4. Calculated density distribution from drill-hole samples of main altered and fresh rocks encountered in the Contact prospect: (*a*) Archean granitic gneiss; (*b*) Hudson suite intrusives; (*c*) fault rocks. To better illustrate the variations, the densities are grouped into classes of 0.05 g/cm³. The frequency of altered and fresh samples has been stacked for each density class. [Colour online.]

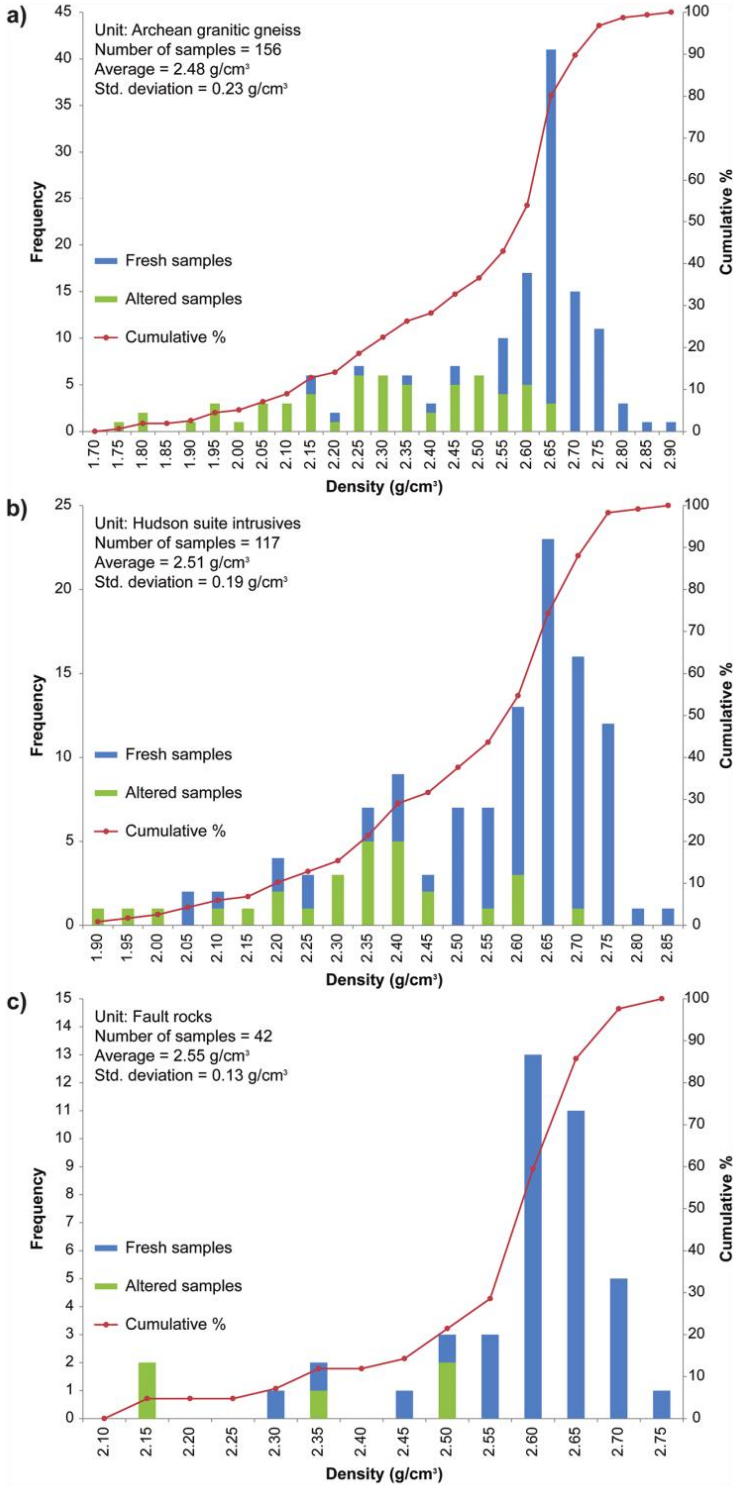

Table 1. Descriptive statistics of density values measured on altered and fresh samples for the three rock units.

		Density (g/cm³)				
Unit	Lithology	Minimum	Maximum	Median	Average	Standard deviation
Altered						
Archean granitic gneisses	Granitic gneisses	1.75	2.64	2.29	2.28	0.23
Hudson suite intrusives	Granite	1.64	2.65	2.33	2.32	0.22
	Syenite	2.34	2.34	2.34	2.34	0.00
	Lamprophyre dykes	1.97	2.40	2.22	2.22	0.15
Fault rocks	Undifferentiated fault	2.13	2.49	2.33	2.32	0.16
Fresh						
Archean granitic gneisses	Granitic gneisses	2.12	2.88	2.63	2.61	0.13
Hudson suite intrusives	Granite	2.05	2.71	2.62	2.55	0.15
	Syenite	2.50	2.74	2.59	2.60	0.08
	Lamprophyre dykes	2.03	2.81	2.68	2.60	0.18
Fault rocks	Quartz-sealed breccia	2.30	2.70	2.60	2.58	0.07
	Undifferentiated fault	2.31	2.67	2.59	2.55	0.13

Note: No altered quartz-sealed breccia samples were encountered.

Fig. 5. Examples: (*a*) fresh granitic gneiss (e.g., 2.65 g/cm³); (*b*) mineralized (black pitchblende) strongly altered granitic gneiss (e.g., 2.25 g/cm³); (*c*) fresh Hudsonian granite (e.g., 2.70 g/cm³); (*d*) strongly altered Hudsonian granite (e.g., 2.10 g/cm³).

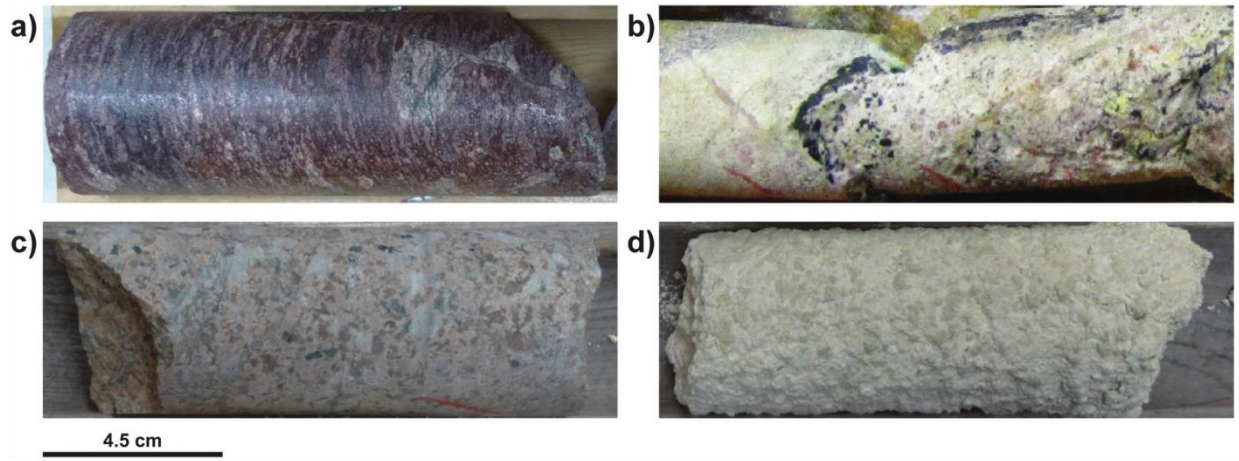

and (*ii*) a constrained inversion was performed after drilling, using available measured density properties.

The thin overburden cover present in the Contact prospect makes this area favourable to invert gravity data, as this layer can be considered as negligible during the modelling process.

Multiple models were tested considering different density backgrounds and density distributions. In this paper, only the 3D constrained inversion model that best fits the geological observations is presented and discussed.

Constrained inversions require a parameter reference model that contains a priori information (e.g., density measured on drill-hole samples). In such a model, each volumetric pixel (i.e., voxel) near a drill hole corresponds to available density information (Fig. 6*a*). In addition to the parameter reference model, a weighted model is used to provide a confidence level associated with the various regions of the parameter reference model (Fig. 6*b*). The degree of confidence for the physical property is high near the drill-hole axis (i.e., along the axis of the blue cylinder) and decreases gradually with distance from the drill hole (i.e., edge of the blue cylinder). The inversion process takes into account these parameters and attempts to find the best model that explains the dataset taking into consideration the imposed constraints.

To improve the models and produce a more geologically reasonable inversion result, an additional IRI constraint was applied. The IRI constraint allows refining the model and emphasizing both positive and negative ends of the density distribution (Geosoft 2016). For this specific study, the positive fresh bedrock anomaly and the negative alteration zone responses are more clearly defined after the IRI process.

The inversion was performed on a 480 168 voxel cells model (i.e., 114 cells in *X*, 117 cells in *Y*, and 36 cells in *Z*). The *X* and *Y* voxel cell sizes have been defined as 10 m. The *Z* voxel cell size follows a logarithmic progression with depth, with 5 m cell size at the surface and larger cell size at depth (maximum 95 m). The acceptable absolute error level for all models was set to 0.02 mGal. A linear trend background was removed from the input gravity grid to facilitate the modelling process and avoid erroneous results and undesirable edge effects. Voxel models represent the density contrasts. Therefore, the average of the density (i.e., 2.55 g/cm³ based on 315 samples) was removed for each sample of the database (i.e., equivalent to removing the background from the observed data). In the present case, the average density value appears to be lower than the one used to reduce the data (i.e., 2.70 g/cm³) because the sampling was done in a low-gravity area characterized by altered rocks. The parameter reference model was empirically gridded to a distance of 40 m (i.e., average mid-distance between all holes drilled in the area) using 3D kriging. It is important to note that a Bouguer density of 2.70 g/cm³ was applied when calculating the Bouguer anomaly used as the input for the inversion. The resulting models present the density variations with

Fig. 6. (*a*) Parameter reference model built using density measurements on drill-core samples (see horizontal colour bar). Blue represents low-density lithologies (i.e., <2.20 g/cm^3), while magenta corresponds to high-density lithologies (i.e., >2.62 g/cm^3). (*b*) Weighted model built using drill-hole database (see horizontal colour bar): high degree of confidence is along the drill-hole axis (i.e., in magenta), while a low degree of confidence extends outward from the core axis (i.e., in blue).

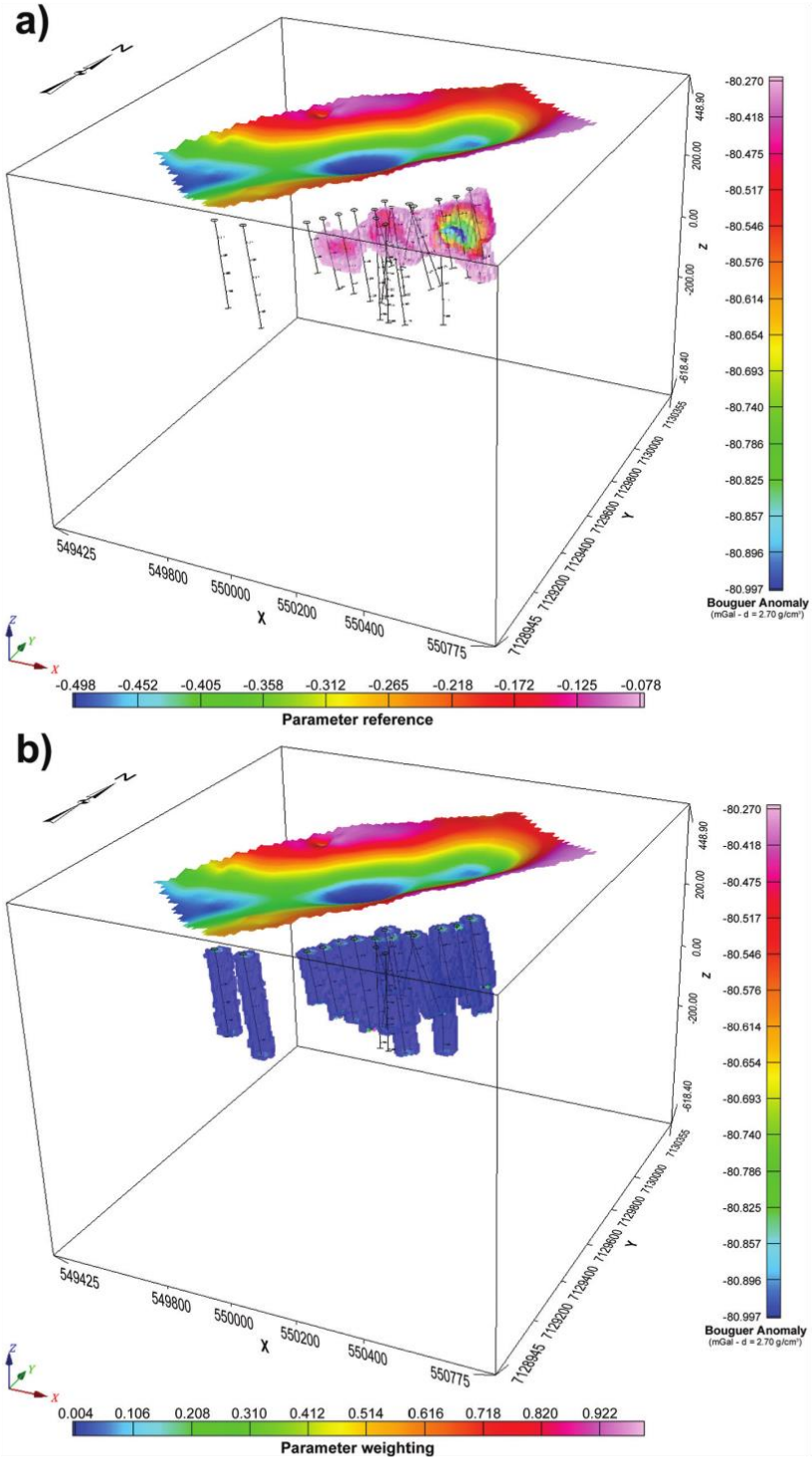

Fig. 7. (*a*) Unconstrained 3D inversion gravity model. (*b*) Constrained 3D inversion gravity model. Data cubes clipped for density contrasts below –0.075 g/cm³. The arrows identify interesting features that are discussed in the text.

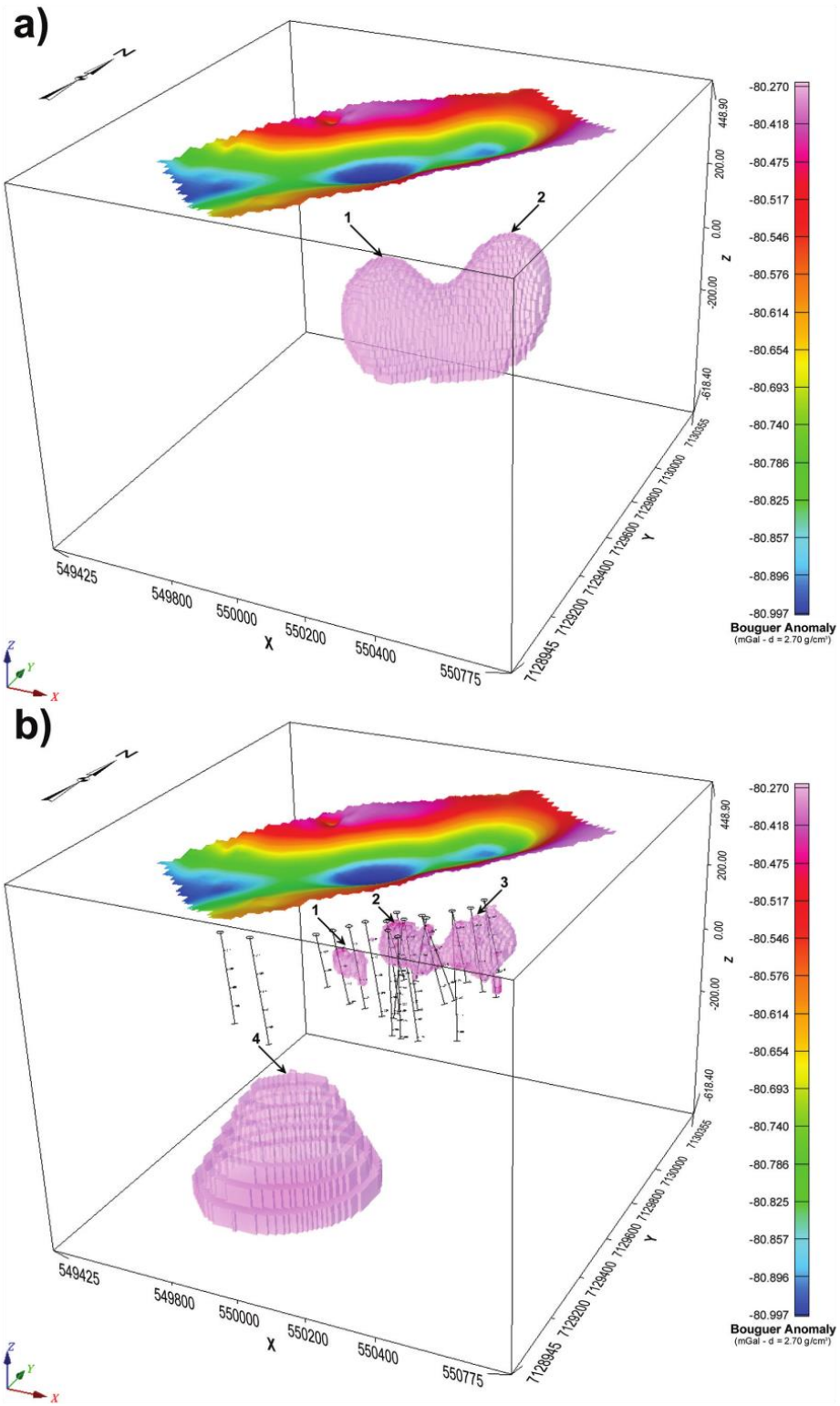

Fig. 8. Comparison of the constrained 3D density model bodies (density contrasts <–0.075 g/cm³ in pink) with (*a*) both clay-altered and bleached zones (in blue) and (*b*) mineralized pods from the gamma-ray probing (in green). The arrows identify interesting features that are discussed in the text.

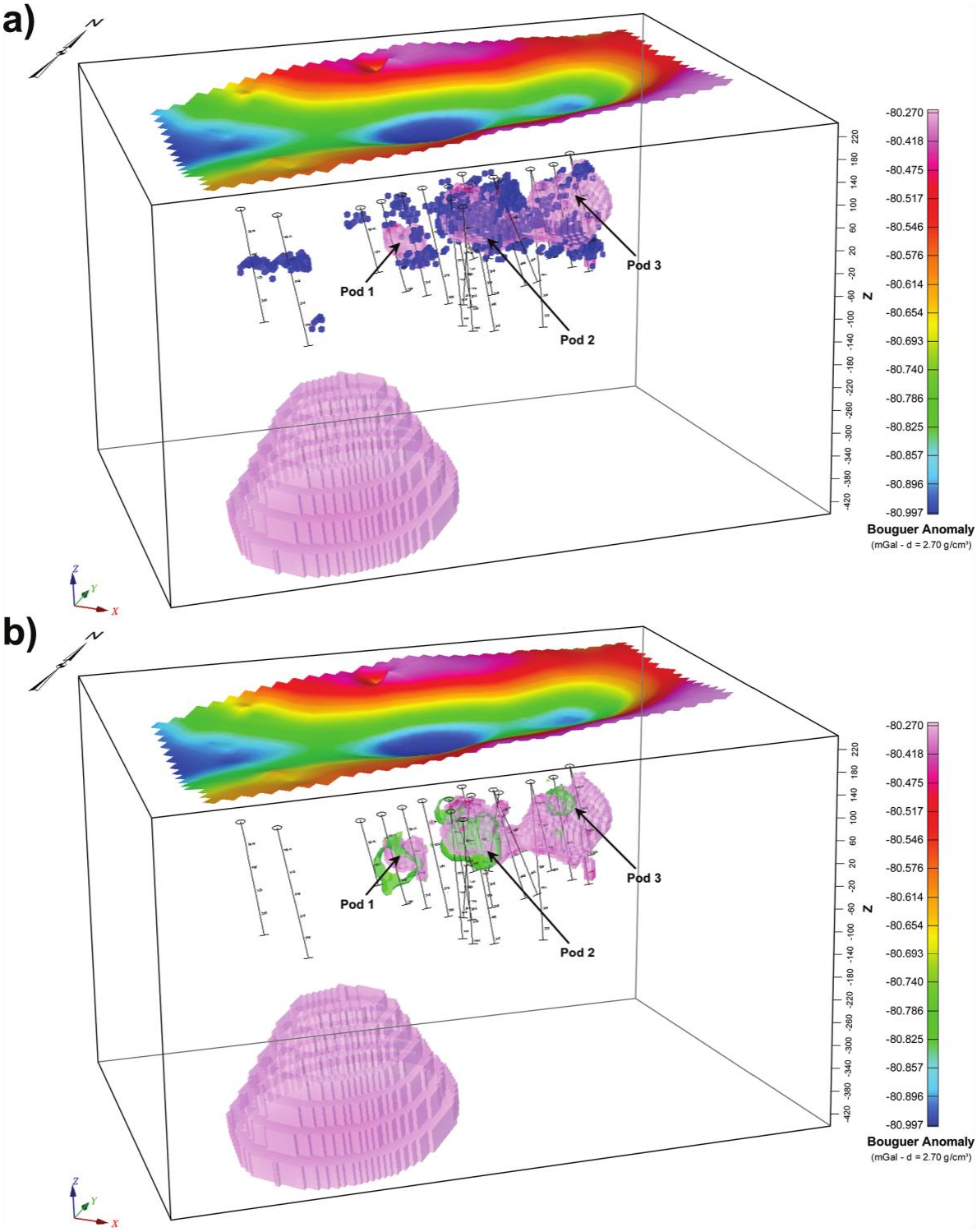

Fig. 9. Northwest–southeast sections through the mineralized pod No. 2 (see Fig. 8): (*a*) section from the constrained inversion results showing density contrast below 0 g/cm^3 (dashed lines delineate the alteration halo in blue in the geological section); (*b*) geological interpretation (mineralization is in dark red, while the altered zone is in blue). See explanations in the text.

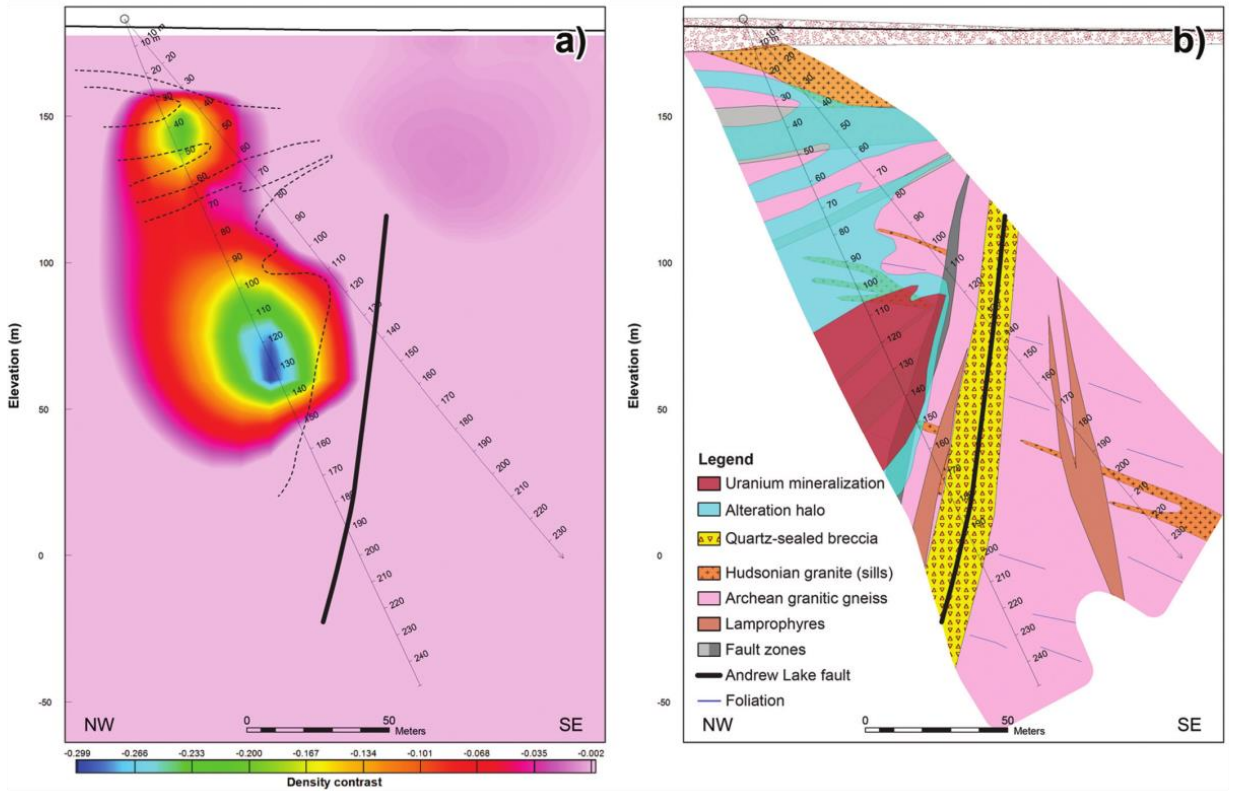

respect to the Bouguer density used (i.e., 2.70 g/cm^3). In Fig. 6*a*, for example, blocks with –0.25 g/cm^3 value represent rocks with a density of 2.45 g/cm^3.

Results

Unconstrained 3D inversion model

The unconstrained 3D inversion of gravity data creates a massive, "bean"-shape, low-density body located beneath the gravity anomaly (Fig. 7*a*). It is oriented along a N045° trend (590 m long and 190 m wide). The depth to the top of the body is about 120 m below the surface in the southwest (arrow No. 1 in Fig. 7*a*) and 150 m deep in the northeast (arrow No. 2 in Fig. 7*a*). The bottom of this body is at 390 m below the surface. This low-density body was first targeted at its shallower southwesternmost apex (indicated by arrow No. 1in Fig. 7*a*), and intersected the main mineralization at a depth of 60 m. A drill-hole fence was then planned based on these results following the N045° trend.

Constrained 3D inversion model

The constrained inversion results shows that the bean-shaped body splits into three smaller and shallower low-density bodies (arrows Nos. 1–3 in Fig. 7*b*). Their size and depth increases from the southernmost body to the northeasternmost body. The isolated body indicated by arrow No. 1 (Fig. 7*b*) is approximately 170 m long by 60 m wide, and its top is at a depth of 60 m. Body No. 1 is constrained by two adjacent holes characterized by fresh granites and granitic gneisses with measured densities between 2.60 and 2.65 g/cm^3. The anomaly generated by the inversion is produced by fractured granitic gneiss and (or) weakly to moderately bleached weakly argillized granite and local syenite (e.g., 2.00 < density < 2.40 g/cm^3). The low-density body indicated by arrow No. 2 (Fig. 7*b*) is located 200 m to the northeast from previously described body. It is approximately 180 m long and 120 m wide. The top of this low-density body nearly outcrops and extends to a depth of 170 m from the surface. This second body is caused by strongly altered (e.g., 1.90 < density < 2.20 g/cm^3) or strongly bleached granitic gneiss (e.g., 2.20 < density < 2.45 g/cm^3). The low-density body shown by arrow No. 3 (Fig. 7*b*) represents the northeastern continuation of the second body. It is approximately 240 m long and 120 m wide. The top of this third body appears to be 40 m below the surface and extends to a depth of 180 m. The density contrast is explained by altered and (or) faulted granitic gneisses (e.g., 1.80 < density < 2.30 g/cm^3) and strongly argillized and friable incompetent granites (e.g., density < 2.00 g/cm^3).

A fourth low-density body (No. 4 in Fig. 7*b*) is generated by the inversion 250 m southwest of the previously described bodies. It has a conical shape, with its apex at 450 m and roots in depth. At 600 m depth (i.e., at the bottom of the modelling workspace), it is approximately 560 m ×470 m.

Reconciliation between geology and 3D gravity inversion models

The consistency of the 3D constrained gravity model was checked against the geological model built from drill-core logging. The unconstrained model explains the observed gravity anomaly, but it does not match the geology from the drill-hole observations; consequently, it will not be discussed.

Fig. 10. (*a*) Simplified geological map of the Contact prospect. (*b*) Top map view of the Contact deposit showing the mineralization and the related alteration halo footprint on the ground residual Bouguer anomaly data.

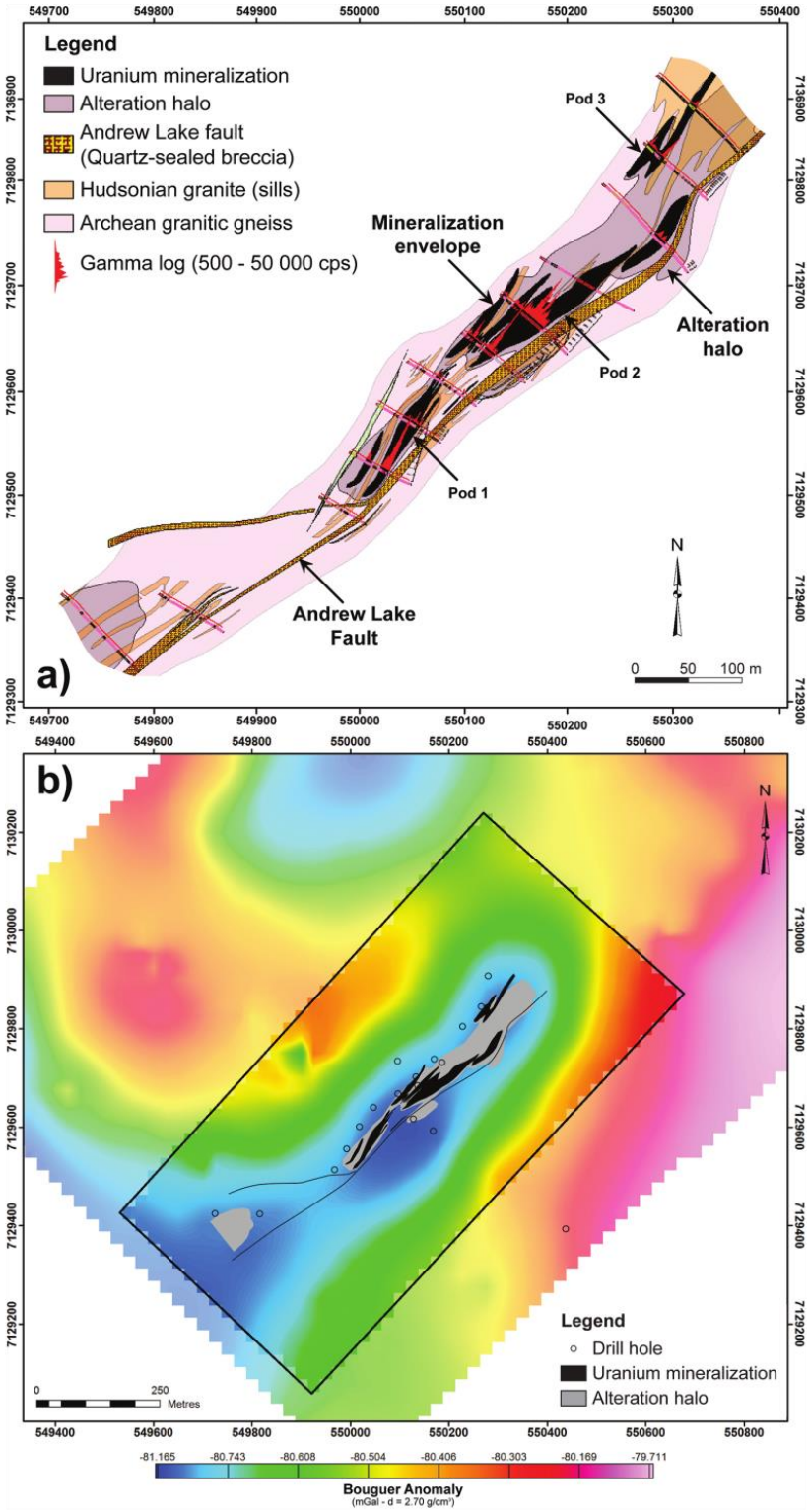

A 3D voxel mesh was generated by combining both clay-rich altered and bleached zones observed from the drill core as the most common sources of the low-density anomalies. The 3D mesh allowed showing the spatial extension of the alteration halo in relation to the modelled bodies. The mineralized envelopes were defined using the Natural Gamma Ray Sonde (NGRS)[1] probing data recorded on drill holes (1500 cps (counts per second) cutoff threshold ≈425 ppm of uranium).

Figure 8*a* shows that the three low-density bodies identified by the constrained gravity model (Fig. 7*b*) fit well with the alteration halo built from drill-core logging (i.e., blue voxels). The best fit occurs for pod No. 2, which is the best constrained by a greater number of drill holes. A section through pod No. 2 (Fig. 9) shows the very good fit between the alteration and the gravity low. In pods Nos. 1 and 3, the alteration mostly surrounds the low-density bodies. The large body located at depth (i.e., body No. 4 in Fig. 7*b*), southwest of the three alteration pods (Fig. 8*a*), can be explained as a response to a strong joint-type fracturing (i.e., fracture corridor) observed on the drill core. The fragmented core prevents systematic sampling and then capturing the low density, which in turn leads to a lack of a priori information coming from these holes. The anomaly is consequently pushed deeper, below the two southernmost drill holes, and does not reflect a geological reality. It is difficult to evaluate the validity of this body, but it is likely an artefact created by the partial gravity coverage (i.e., anomaly truncated to the south), as this falls at the southernmost boundary of the exploration claims (see Fig. 4) and the inversion process (i.e., overestimation of high densities).

Figure 8*b* allows comparison of the mineralization (green envelope) with the low-density bodies. Mineralized pods Nos. 1 and 2 fit well with the low-density bodies, while pod No. 3 shows a much smaller envelope than the altered surrounding rock. This situation is common in most of the uranium deposits where alteration usually extends farther away from the mineralization (Jefferson et al. 2007), or as illustrated in Fig. 9, the alteration may extend along nonmineralized fault zones. Effectively, Fig. 9*a* shows two low-density zones. The deeper one matches the mineralization (see Fig. 9*b*), while the upper one is associated with a fault corridor driving strong alteration.

The interpretation of the drill-hole geology indicates that mineralization forms elongate bodies aligned along the N045°-trending Andrew Lake fault corridor, corresponding to the three pods in the constrained 3D inversion modelling (Fig. 10*a*). The three mineralization pods coincide with the low-density bodies generated by the constrained inversion (Fig. 10*b*), confirming the accuracy and the validity of the constrained inversion versus the unconstrained inversion. Alteration, which in map view surrounds the mineralization, appears to be more widespread than the mineralization; however, it does match quite well with the bodies resulting from the constrained inversion, with the strongest alteration fitting with the low-density body No. 2.

Conclusions

The application of 3D gravity inversion modelling was conducted to assist exploration in the Kiggavik project, as part of a set of tools, helping to collar the discovery holes of the Contact mineralization, and to characterize the 3D geometry (i.e., depth, dip, and size) of the low-density bodies associated with mineralization and related alteration haloes. For this case study, two types of models were tested: unconstrained without any a priori information and constrained by petrophysical data. The unconstrained model is a first approximation that created a low-density body that was not accurate in depth and size; however, it was used for targeting purposes, allowing for targeting of the discovery holes. The model constrained by drill-core density data brings interesting insights about the true deposit footprint. The unconstrained low-density body is split into three shallower and smaller bodies. The location and the geometry of the low-density bodies are more realistic and validated by a geological model built from logging data. The constrained model allows to better locate the follow-up drill holes and to optimize the drill-hole spacing. It can also potentially help to define drilling grid size for resource estimation. The constrained model is sample dependent. Consequently, care has to be taken where altered samples cannot be measured, for instance, when the altered rocks are not cohesive enough or too fractured for appropriate density measurements. The obtained results illustrate that the constrained inversion modelling is a valuable method that improves predicting the location of low-density bodies associated with alteration zones. The spatial distribution of drill holes and the samples selected both systematically and based on the lithology that were used in the constrained 3D inversion modelling play a role when modelling the low-density bodies.

The results suggest that 3D gravity inversions during the drill program could lead to better positioning of drill holes and thus better location of low-density bodies if no alteration zones have been encountered in previous drilled holes. Therefore, it is possible to update the model during the drilling campaign by integrating the a priori information provided by each drill hole and consequently using the updated model to determine the best location for the next drill hole (including its nominal length and dip). This process can be completed in the field because inversions with the VOXI inversion software are fast and require only an internet connection.

This study shows that 3D inversion of gravity data are a valuable tool to guide geologists in exploration of shallow basement-hosted uranium deposits associated with alteration haloes and to assess the deposit gravity geometry.

For future investigations, it is recommended to constrain geophysical models, taking into account (*i*) geological information of lithologies and structural features and (*ii*) a priori information coming from different probing techniques (e.g., borehole gravity, neutron density, and resistivity data).

Acknowledgements

The authors thank Patrick Ledru, John Robbins, Mario Blain, Robert Hearst, and the Kiggavik Team of AREVA Resources Canada for their geological, geophysical, and logistical support. Reviews by Kathryn Bethune and Victoria Tschirhart and the editorial comments by Ali Polat contributed to significantly improve both the geological and the geophysical content of the manuscript and are acknowledged.

References

AREVA. 2015. 2015 Reference document. *Edited by* AREVA, Paris, France.

Barbosa, R.D., and Pereira, J.G. 2013. Inversão 3D de dados Magnéticos na Região de Mara Rosa - Goiás, Brasil, utilizando Geosoft VOXI. *In* Proceedings of the 13th International Congress of the Brazilian Geophysical Society and EXPOGEF, Rio de Janeiro, Brazil, pp. 520–525. doi:10.1190/sbgf2013-109.

Blaise, J.R. 1998. Détermination de la densité sur carottes de sondages. COGEMA Direction des Opérations Minières, RAP98.010.

Chi, G., Haid, T., Quirt, D., Fayek, M., Blamy, N., and Chu, H. 2016. Petrography, fluid inclusion analysis, and geochronology of the End uranium deposit, Kiggavik, Nunavut, Canada. Mineralium Deposita, **52**(2): 211–232. doi:10.1007/s00126-016-0657-9.

Corrigan, D., Pehrsson, S., Wodicka, N., and de Kemp, E. 2009. The Paleoproterozoic Trans-Hudson Orogen: a prototype of modern accretionary processes. Journal of the Geological Society of London, Special Volume "Ancient Orogens and Modern Analogues". *In* Ancient Orogens and Modern Analogues. *Edited by* J.B. Murphy, J.D. Keppie, and A.J. Hynes. Geological Society, London, Special Publications, 327, pp. 457–479.

[1]The NGRS probe uses a sodium iodide scintillation crystal (50 mm long by 28 mm diameter) coupled to a photomultiplier to detect total natural gamma radiation.

Ellis, R.G., and MacLeod, I.N. 2013. Constrained voxel inversion using the Cartesian Cut Cell method. *In* Proceedings of the 23rd International Geophysical Conference and Exhibition, Melbourne, Victoria, Australia, pp. 1–4.

Farhi, W., Boudella, A., Saibi, H., and Bounif, M.O.A. 2016. Integration of magnetic, gravity, and well data in imaging subsurface geology in the Ksar Hirane region (Laghouat, Algeria). Journal of African Earth Sciences, **124**: 63–74. doi:10.1016/j.jafrearsci.2016.09.013.

Fitzpatrick, A., and Large, P. 2015. Magnetic modelling and geological modelling come together at the Kintyre uranium deposit. *In* Proceedings of the 23rd International Geophysical Conference and Exhibition, Perth, Western Australia, Australia, pp. 1–4.

Fuchs, H., and Hilger, W. 1989. Kiggavik Lone Gull: an unconformity related uranium deposit in the Thelon Basin, Northwest Territories, Canada. Uranium Resources and Geology of North American: Inter. Atomic Energy Agency, Tech. Doc. 500, pp. 429–454.

Fuchs, H.D., Hilger, W., and Prosser, E. 1986. Geology and exploration history of the Lone Gull property. Canadian Institute of Mining and Metallurgy, Special Vol. 33, pp. 286–292.

Fullagar, P.K., Pears, G.A., and McMonnies, B. 2008. Constrained inversion of geological surfaces - pushing the boundaries. The Leading Edge, **27**: 98–105. doi:10.1190/1.2831686.

Geosoft. 2016. VOXI Earth Modelling [online]. Available from http://www.geosoft.com/products/voxi-earth-modelling/ [accessed 20 December 2016].

Grare, A., Benedicto, A., Ledru, P., and Quirt, D. 2016. Structural controls on the Kiggaivk basement-hosted unconformity-related uranium deposits (NE Thelon area, Nunavut). Geol. Assoc. Canada-Mineral. Assoc. Canada Conf., June 1–3, Whitehorse, YK, Abstr. Vol. 39, p. 29.

Hasegawa, K., Davison, G.I., Wollenberg, P., and Iida, Y. 1990. Geophysical exploration for unconformity-related uranium deposits in the NE part of the Thelon Basin, Northwest Territories, Canada. Mining Geology, **40**: 83–95.

Hildenbrand, T.G., Briesacher, A., Flanagan, G., Hinze, W.J., Hittelman, A.M., Keller, G.R., et al. 2002. Rationale and Operational Plan to Upgrade the U.S. Gravity Database. U.S. Geological Survey Open-File Report 02-463.

Hinze, W.J., Aiken, C., Brozena, J., Coakley, B., Dater, D., Flanagan, G., et al. 2005. New standards for reducing gravity data: The North American gravity database. Geophysics, **70**: J25–J32. doi:10.1190/1.1988183.

Hoffman, P.F. 1988. United plates of America, the birth of a craton: Early Proterozoic assembly and growth of Laurentia. Annual Review of Earth and Planetary Sciences, **16**: 543–603. doi:10.1146/annurev.ea.16.050188.002551.

Ingram, D.M., Causon, D.M., and Mingham, C.G. 2003. Developments in Cartesian cut cell methods. Mathematics and Computers in Simulation, **61**: 561–572. doi:10.1016/S0378-4754(02)00107-6.

Jefferson, C.W., Thomas, D.J., Gandhi, S.S., Ramaekers, P., Delaney, G., Brisbin, D., et al. 2007. Unconformity-associated uranium deposits of the Athabasca Basin, Saskatchewan and Alberta. *In* Mineral Deposits of Canada: A Synthesis Of Major Deposit Types, District Metallogeny, The Evolution Of Geological Provinces, And Exploration Methods. *Edited by* W.D. Goodfellow. Geological Association of Canada, Special Publication 5, pp. 273–305.

Jefferson, C.W., Chorlton, L.B., Pehrsson, S.J., Peterson, T., Wollenberg, P., Scott, J., et al. 2011*a*. Northeast Thelon Region: 77 Geomapping for Uranium in Nunavut. Geological Survey of Canada, Open File 6862.

Jefferson, C.W., Pehrsson, S., Peterson, T., Chorlton, L., Davis, W., Keating, P., et al. 2011*b*. Northeast Thelon region geoscience framework - new maps and data for uranium in Nunavut. Geological Survey of Canada, Open File 6950. doi:10.4095/288791.

Johnstone, D., Bethune, K., Quirt, D., and Benedicto, A. 2016. Lithostratigraphic and structural controls of uranium mineralization in the Kiggavik East, Centre and Main Zone Deposits, Nunavut. Geol. Assoc. Canada-Mineral. Assoc. Canada Conf., June 1–3, Whitehorse, YK, Abstr. Vol. 39, p. 41.

Lelièvre, P.G., Oldenburg, D.W., and Williams, N.C. 2009. Integrating geological and geophysical data through advanced constrained inversions. Exploration Geophysics, **40**: 334–341. doi:10.1071/EG09012.

Li, Y., and Oldenburg, D. 1998. 3-D inversion of gravity data. Geophysics, **63**: 109–119. doi:10.1190/1.1443968.

McEwan, B. 2012. Structural style and regional comparison of the Ketyet River group northeast of Baker Lake, Nunavut. M.Sc. thesis, University of Regina, Regina, Sask., Canada.

McGaughey, J. 2007. Geological Models, Rock Properties, and the 3D Inversion of Geophysical Data. *In* Proceedings of the 5th Decennial International Conference on Mineral Exploration, Toronto, Ontario (Canada), pp. 473–483.

Miller, A.R., and LeCheminant, A.N. 1985. Geology and uranium metallogeny of Proterozoic supracrustal successions, central District of Keewatin, N.W.T. with comparisons to northern Saskatchewan. *In* Geology of uranium deposits. *Edited by* T.I.I. Sibbald and W. Petruk. Canadian Institute of Mining and Metallurgy, Special Vol. 32. pp. 167–185.

Miller, A.R., Cumming, G., and Krstic, D. 1989. U–Pb, Pb–Pb, and K–Ar isotopic study and petrography of uraniferous phosphate-bearing rocks in the Thelon Formation, Dubawnt Group, Northwest Territories, Canada. Canadian Journal of Earth Sciences, **26**(5): 867–880. doi:10.1139/e89-070.

Moritz, H. 1980. Geodetic Reference System 1980. Journal of Geodesy, **54**: 395–405.

Nettleton, L.L. 1939. Determination of density for reduction of gravimeter observations. Geophysics, **4**: 176–183.

Nettleton, L.L. 1976. Gravity and magnetics in oil prospecting. McGraw-Hill, New York.

OECD 2014. Uranium 2014: Resources, Production and Demand. Joint Report by OECD Nuclear Energy Agency and the International Atomic Energy Agency 7209.

Oldenburg, D.W., and Pratt, D.A. 2007. Geophysical inversion for mineral exploration: a decade of progress in theory and practice. *In* Proceedings of the 5th Decennial International Conference on Mineral Exploration, Toronto, Ontario, Canada, pp. 61–95.

Oldenburg, D.W., Li, Y., Farquharson, C., Kowalczyk, P., Aravanis, T., King, A., and Watts, A. 1998. Applications of geophysical inversions in mineral exploration problems. The Leading Edge, **17**: 461–465. doi:10.1190/1.1437989.

Pehrsson, S., Berman, R., and Davis, W. 2013. Paleoproterozoic orogenesis during Nuna aggregation: a case study of reworking of the Archean Rae craton, Woodburn Lake, Nunavut. Precambrian Research, **232**: 167–188. doi:10.1016/j.precamres.2013.02.010.

Peterson, T.D., Van Breemen, O., and Sandeman, H. 2002. Proterozoic (1.85–1.75 Ga) igneous suites of the Western Churchill Province: granitoid and ultrapotassic magmatism in a reworked Archean hinterland. Precambrian Research, **119**: 73–100. doi:10.1016/S0301-9268(02)00118-3.

Peterson, T.D., Jefferson, C.W., and Anand, A. 2015*a*. Geological setting and geochemistry of the ca. 2.6 Ga Snow Island Suite in the central Rae Domain of the Western Churchill Province, Nunavut. Geological Survey of Canada, Open File 7841, pp. 1–29.

Peterson, T.D., Scott, J.M.J., LeCheminant, A.N., Jefferson, C.W., and Pehrsson, S. 2015*b*. The Kivalliq Igneous Suite: Anorogenic bimodal magmatism at 1.75 Ga in the Western Churchill Province, Canada. Precambrian Research, **262**: 101–119. doi:10.1016/j.precamres.2015.02.019.

Quirt, D., and Brulé, R. 1990. Determination of density and specific gravity on geological materials by the Saskatchewan Research Council. Available from Saskatchewan Research Council, Saskatoon, R-1230-4E-90.

Rainbird, R.H., Hadlari, T., Aspler, L.B., Donaldson, J.A., LeCheminant, A.N., and Peterson, T.D. 2003. Sequence stratigraphy and evolution of the Paleoproterozoic intracontinental Baker Lake and Thelon basins, western Churchill Province, Nunavut, Canada. Precambrian Research, **125**: 21–53. doi:10.1016/S0301-9268(03)00076-7.

Rainbird, R., Davis, W., Pehrsson, S., Wodicka, N., Rayner, R., and Skulski, T. 2010. Early Paleoproterozoic supracrustal assemblages of the Rae domain, Nunavut, Canada: Intracratonic basin development during supercontinent break-up and Assembly. Precambrian Research, **181**: 167–186. doi:10.1016/j.precamres.2010.06.005.

Riegler, T. 2013. Système d'altération et minéralisation en uranium le long du faisceau structural Kiggavik-Andrew Lake (Nunavut, Canada): modèle génétique et guides d'exploration. Ph.D. thesis, Université de Poitiers.

Riegler, T., Lescuyer, J.L., Wollenberg, W., Quirt, D., and Beaufort, D. 2014. Alteration related to uranium deposits in the Kiggavik-Andrew lake structural trend, Nunavut, Canada; new insights from petrography and clay mineralogy. The Canadian Mineralogist, **52**: 27–45. doi:10.3749/canmin.52.1.27.

Robbins, J., Richard, Y., Carter, C., Behaegel, M., Benedicto, A., and Ledru, P. 2015. New guides led to new models - Continuing return of exploration experience, Nunavut, Canada. *In* The AusIMM International Uranium Conference 2015, Abstract volume, p. 2.

Scott, J., Peterson, T., Davis, W., Jefferson, C., and Cousens, B. 2015. Petrology and geochronology of Paleoproterzoic intrusive rocks, Kiggavik uranium camp, Nunavut. Canadian Journal of Earth Sciences, **52**(7): 495–518. doi:10.1139/cjes-2014-0153.

Sharpe, R., Fayek, M., Quirt, D., and Jefferson, C.W. 2015. Geochronology and genesis of the Uranium deposit, Thelon Basin, Nunavut, Canada. Economic Geology, **110**: 1759–1777. doi:10.2113/econgeo.110.7.1759.

Sun, J., and Li, Y. 2011. Geophysical inversion using petrophysical constraints with application to lithology differentiation. *In* Proceedings of the SEG Annual Meeting, San Antonio, Texas, USA, pp. 2644–2648.

Tschirhart, P.A., Morris, W.A., and Jefferson, C.W. 2013*a*. Geophysical modeling of the Neoarchean Woodburn Lake and Paleoproterozoic Ketyet River groups, and plutonic rocks in central Schultz Lake map area, Nunavut. Geological Survey of Canada, Current Research 2013-2, p. 19. doi:10.4095/292116.

Tschirhart, V., Morris, W.A., and Jefferson, C.W. 2013*b*. Framework geophysical modelling of granitoid vs. supracrustal basement to the northeast Thelon Basin around the Kiggavik uranium camp, Nunavut. Canadian Journal of Earth Sciences, **50**(6): 667–677. doi:10.1139/cjes-2012-0149.

Tschirhart, V., Jefferson, C.W., and Morris, W.A. 2017. Basement geology beneath the northeast Thelon Basin, Nunavut: insights from integrating new gravity, magnetic and geological data. Geophysical Prospecting, **65**: 617–636. doi:10.1111/1365-2478.12430.

Vallée, M.A., Smith, R.S., and Keating, P. 2011. Metalliferous mining geophysics - State of the art after a decade in the new millennium. Geophysics, **76**: 31–50. doi:10.1190/1.3587224.

Weyer, H.J., Friedrich, G., Bechtel, A., and Ballhorn, R.K. 1987. The Lone Gull uranium deposit: New geochemical and petrological data as evidence for the nature of the ore bearing solutions. International Atomic Energy Agency Report TC542/19.

Additional remarks: One problem about the link with measuring the gravity of various samples was raised in the article; sampling fault zones and fractured samples can be delicate. Some samples are strongly clay altered but still competent (Fig. 21), however their density can't be measured as the sample is going to completely crumble when plunged in water. Therefore the representative density of specific zones can be underestimated. It also important to point out that some modelled gravity anomalies are not directly linked to the uranium orebody.

Figure 21: Example of a strongly clay altered drill core. The white arrow point a hole left by a pen that when through the entire drillcore.

The structural control of the uranium mineralization was not presented in this article, except for the discussion of the quartz breccia that appears to be crosscut in drillholes at the bottom of the uranium orebody. Fracturing events and the structural control on uranium pods are going to be addressed in the following article.

5.2 MULTI-SCALE, INTEGRATED STUDY OF THE CONTACT PROSPECT: STRUCTURAL STUDY AND GEOCHEMICAL CHARACTERISTICS OF URANIUM MINERALIZATION

5.2.1 The Contact uranium prospect, Kiggavik prject, Nunavut (Canada): tectonic history, structural constraints and timing of mineralization

Re-submitted to Ore geology review after minor revisions

The Contact uranium prospect, Kiggavik project, Nunavut (Canada): tectonic history, structural constraints and timing of mineralization

Alexis Grare[a,b] , Antonio Benedicto[b,c], Olivier Lacombe[a], Anna Trave[d], Patrick Ledru[b], Mario Blain[b], John Robbins[b],

[a] *Sorbonne Universités, UPMC-CNRS-iSTeP, 4 place Jussieu. 75005 Paris. France*

[b] *AREVA Resources Canada Inc. 817-45th St West Saskatoon. SK S7L 5X2. Canada*

[c] *UMR Geops, Université Paris Sud, 91405 Orsay, France*

[d] *Universitat de Barcelona (UB), Departament de Mineralogia, Petrologia i Geologia Aplicada, Facultat de Ciències de la Terra. Carrer de Martí i Franquès s/n. 08028 Barcelona. Spain*

The Contact uranium prospect, Kiggavik project, Nunavut (Canada): tectonic history, structural constraints and timing of mineralization

Alexis Grare[a,b] , Antonio Benedicto[b,c], Olivier Lacombe[a], Anna Trave[d], Patrick Ledru[b], Mario Blain[b], John Robbins[b],

[a] *Sorbonne Universités, UPMC-CNRS-iSTeP, 4 place Jussieu. 75005 Paris. France*

[b] *AREVA Resources Canada Inc. 817-45th St West Saskatoon. SK S7L 5X2. Canada*

[c] *UMR Geops, Université Paris Sud, 91405 Orsay, France*

[d] *Universitat de Barcelona (UB), Departament de Mineralogia, Petrologia i Geologia Aplicada, Facultat de Ciències de la Terra. Carrer de Martí i Franquès s/n. 08028 Barcelona. Spain*

Abstract

Uranium mineralization in the Kiggavik area, on the eastern border of the Thelon basin (Nunavut, Canada), hosts significant uranium resources within the basement and its understanding is critical to comprehending the genesis of unconformity-related deposits' structural controls and therefore exploration of these types of deposits in this prospective district. This article deciphers the complex multiphase fracture network associated with uranium mineralization of the most recently discovered, basement-hosted prospect in the Kiggavik area, named Contact. The Contact prospect is located along the Andrew Lake Fault (ALF), a major NE-SW fault corridor in the area. This study combines field work, drillcore logging, sampling, and macro- to micro- petro-structural analyses. Key results from this study highlight that the NE-trending ALF, along with the ENE-trending Thelon (TF) and Judge Sissons (JSF) faults, formed early during intracratonic rifting and deposition of the Baker Lake and Wharton groups (ca. 1850–1750 Ma) in response to the Thelon and Trans-Hudsonian orogeny. The ALF was affected by a strong silicification-brecciation event that likely developed at ca. 1750 Ma, and partitioned later deformation and fluid circulation. In the Contact prospect, the ALF was reactivated multiple times and mineralized in three stages with distinctive secondary fracture patterns, alteration, and mineralization types. Ten fracture stages have been identified at the Contact prospect, f1 to f10. The first stage of mineralization, coeval with f5, is related to fluids of unconstrained origin that circulated through E-W faults in the area that locally re-activated quartz veins of the brecciation event at the intersection with the ALF. Mineralization at this stage is polymetallic and associated with weak clay alteration. The second stage of uranium

Abreviations: ASB: Aberdeen Sub-Basin. STZ: Snowbird Tectonic Zone. SLIC: Schultz Lake Intrusive Complex. ALF: Andrew Lake Fault. TF: Thelon Fault. MZF: Main Zone Fault. JSF: Judge Sissons Fault. QB: Quartz Breccia.

mineralization occurred coeval with transtensional reactivation of the NE-SW trending ALF (f6c) and in relation to circulation of oxidizing basinal brines within the fault zone. Mineralization at this stage is monometallic and associated with illite and sudoite alteration. Later reactivation of the inherited fracture network (f8) led to strong illitization and bleaching of the host rock, with local reworking of the ore body. Finally, reactivation of the fracture network during f9 and 10 lead to circulation of meteoric fluids that remobilized mineralization in a third stage of uranium re-concentration along redox fronts, with strong illitization and bleaching of the host rock. Unlike the classic unconformity-related uranium deposits in the Athabasca Basin where clay alteration halos occur around the ore bodies related to mineralizing processes, in the Contact prospect the strongest clay alteration event (f8) postdates both main stages of mineralization. Along with uranium remobilization, the basement-hosted Contact prospect is likely a relict of what was once a larger deposit.

Keywords

Uranium deposit; alteration; structural control; fracture; Thelon Basin; Kiggavik.

1. Introduction

Unconformity-related uranium deposits are important because they are among the major uranium metal contributors in the world (OECD, NEA and IAEA, 2016). Such massive and high grade uranium deposits are found close to the unconformity between an Archean to Paleoproterozoic metamorphosed basement rocks and an overlying non-metamorphosed Paleoproterozoic sedimentary basin-infill (Dahlkamp, 1993). Major uranium deposits of this type are found in Canada, in the Athabasca Basin (i.e., the Cigar lake deposit, Dahlkamp, 1993; Jefferson et al., 2007), or in Australia, in the McArthur Basin (i.e., the Ranger deposit, Jaireth et al., 2016; Skirrow et al., 2016). The uranium ore is located within the basement (e.g. Eagle Point, Mercadier et al., 2011), at the unconformity (e.g. Cigar Lake, Bruneton, 1993) or perched within basin sandstones (e.g. Shea Creek, Sheahan et al., 2016). In both the Athabasca and the McArthur basins, the importance of structural control has been recognized (Hoeve and Quirt, 1984; Baudemont and Pacquet, 1996; Baudemont and Federowich, 1996; Tourigny et al., 2007; Jefferson et al., 2007; Kyser and Cuney, 2009). Uranium is linked to ductile to ductile-brittle shear zones in the Eagle Point (Mercadier et al., 2011), Nabarlek (Wilde and Wall, 1987), and Jabiluka (Polito et al., 2005a,b) deposits, to faults in the McArthur and Dominique-Peter deposits (Györfi et al., 2007; and Baudemont and Fedorowich, 1996; respectively), to breccias

in the case of the Shea Creek deposit (De Veslud et al., 2009), and to a complex combination of folding and brecciation in the Jabiluka deposit (Polito et al., 2005a,b).

All this existing literature attributes a major role to shear zones, faults, and breccias in channeling metal-bearing fluids responsible for mineralization in unconformity-related uranium deposits, but none of these studies describes in detail the multi-scale organization of the mineralized fracture network and replaces it into the often long, polyphase and complex tectonic history. For instance, Dieng et al. (2013) reported the most complete review of the tectonic and uranium mineralizing events in the uraniferous Beaverlodge area (north-west of the Athabasca Basin), but they did not focus on the description of the related fracture network to which each stage of mineralization is linked. However, the understanding of the fracture network at different scales is essential to unravel the uranium-bearing fluid plumbing system and uranium trapping in this type of economic deposit, and also in order to help future exploration. The insertion of the uranium-related fracture system in the whole tectonic history of a region is another critical key to define the fertile tectonic episodes and for establishing the right metalotects. In fact, the lack of detailed structural studies in unconformity-related uranium deposits is overall due to the strong clay alteration associated with this type of deposits (Percival et al., 1993; Beaufort et al., 2005; Jefferson et al., 2007).The lack of oriented micro- and meso-structural data and the difficulty to visualize in 3D complex structures that show significant and rapid lateral and vertical changes between available drill holes constitute additional difficulties (Childs et al., 1996; 2009; Van der Zee et al., 2008; Lunn et al., 2008).

The Kiggavik uranium project is located 80 km west of Baker Lake, on the eastern border of the Paleoproterozoic Thelon Basin in the Nunavut territory, northern Canada (Fig. 1). It is currently being explored by AREVA Resources Canada (ARC) as a prospective area for uranium due to the similarities in the geological context between the Thelon and the Athabasca basins (Miller and LeCheminant, 1985, Fuchs et al., 1986, Weyer et al., 1987, Fredrich et al., 1989, Fuchs and Hilger, 1989; Jefferson et al., 2007a). Uranium deposits in the Kiggavik area (Fig. 2) have recently been interpreted to have some characteristics of unconformity-related deposits (Kiggavik Main and Central Zone deposits: Farkas, 1984; Shabaga et al., 2017b; Bong deposit: Riegler et al., 2016; Sharpe et al., 2015; Quirt, 2017; End deposit: Chi et al., 2016; see also Fayek et al., 2017). In contrast to the Athabasca Basin, where ductile deformation involving graphitic and mineralized shear zones are commonly observed, the tectonic style of deformation and mineralization in the Kiggavik area is dominantly brittle, as exemplified by the presence of cataclastic to ultracataclastic fault rocks and mineralized veins. Ductile to ductile-brittle shear zones are rarely observed and their reactivation appears not to be a key process controlling

uranium mineralization there (Johnstone et al., 2017). Previous studies of the various deposits in the Kiggavik area focused on the characterization of mineralizing fluids and their alteration products, through geochemical and isotopic analyses of uranium oxides and clay minerals (Farkas, 1984; Riegler et al., 2016a; Shabaga et al., 2015; Sharpe et al., 2015; Potter et al., 2015; Chi et al., 2016; Fayek et al., 2017; Quirt, 2017; Shabaga et al., 2017a, 2017b). While the knowledge in these various fields has greatly improved in the last years, the tectonic history, the structural controls, and the relative timing of the deposits in the Kiggavik area remain poorly understood. Discovered in 2014, the Contact prospect is the latest discovery in the district and was found using a multidisciplinary approach combining GIS-based mineral prospectivity analysis of the available airborne and ground geophysical data (Robbins et al., 2015; Roy et al., 2017).

The aims of this paper are: (i) to accurately reconstruct the tectonic events and sequence of fracturing (mineralized and non-mineralized) in the Contact prospect, (ii) to decipher the spatial organization of the resulting fracture sets in order to unravel the structural controls and relative timing of uranium mineralization in the Contact prospect, and (iii) and in a more general perspective, to provide better constraints on classic models of mineralized fracture networks for unconformity-related uranium deposits. The identification and characterization of fractures along with the reconstruction of the relative chronology on the basis of observed crosscutting relationships and widespread oriented data allows for accurately determining the structural control of the uranium mineralization and alteration at the Contact prospect for the first time in the Kiggavik area.

2. Geological setting of the Kiggavik area

2.1 Regional setting

The Thelon (ca. 1670–1540 Ma, Hiatt et al., 2003; Davis et al., 2011) and Athabasca (1740–1540 Ma, Ramaekers et al., 2007) basins are Proterozoic intracratonic basins (Gall et al., 1992) hosted by the Churchill-Wyoming craton, which resulted from the Paleoproterozoic collisional amalgamation of the Rae domain to the northwest with the Hearne domain to the SE (Hoffman, 1988; Fig. 1). These basins are located between the eroded remnants of the Trans-Hudson orogenic belt to the SE (ca. 2070-1800 Ma, overall NW-SE shortening) and the Thelon-Taltson orogenic belt to the west (ca. 2020-1900 Ma, overall E-W shortening). At the regional scale, the main structural feature within the Churchill-Wyoming craton is the Snowbird Tectonic Zone (STZ in Fig. 1), a tectonic trend which has given rise to many interpretations (see for example

Hoffman, 1988, Hanmer et al., 1995; Ross et al., 2000; Berman et al., 2007). Recent field observations by Regan et al. (2014) on the Cora Lake Shear Zone lead them to propose an intracontinental crustal-scale structure formed at ca. 2600 Ma, which underwent several later episodes of transpressional reactivation, with sinistral and dextral motions in response to the Thelon and Trans-Hudsonian orogenies from 1900 to 1820 Ma (Sanborn-Barrie et al., 2001; Mills et al., 2007; Regan et al., 2014). Aeromagnetic maps show that a major fault trend in the Kiggavik area, the Andrew Lake Fault (ALF) connects to the STZ (Fig.1).

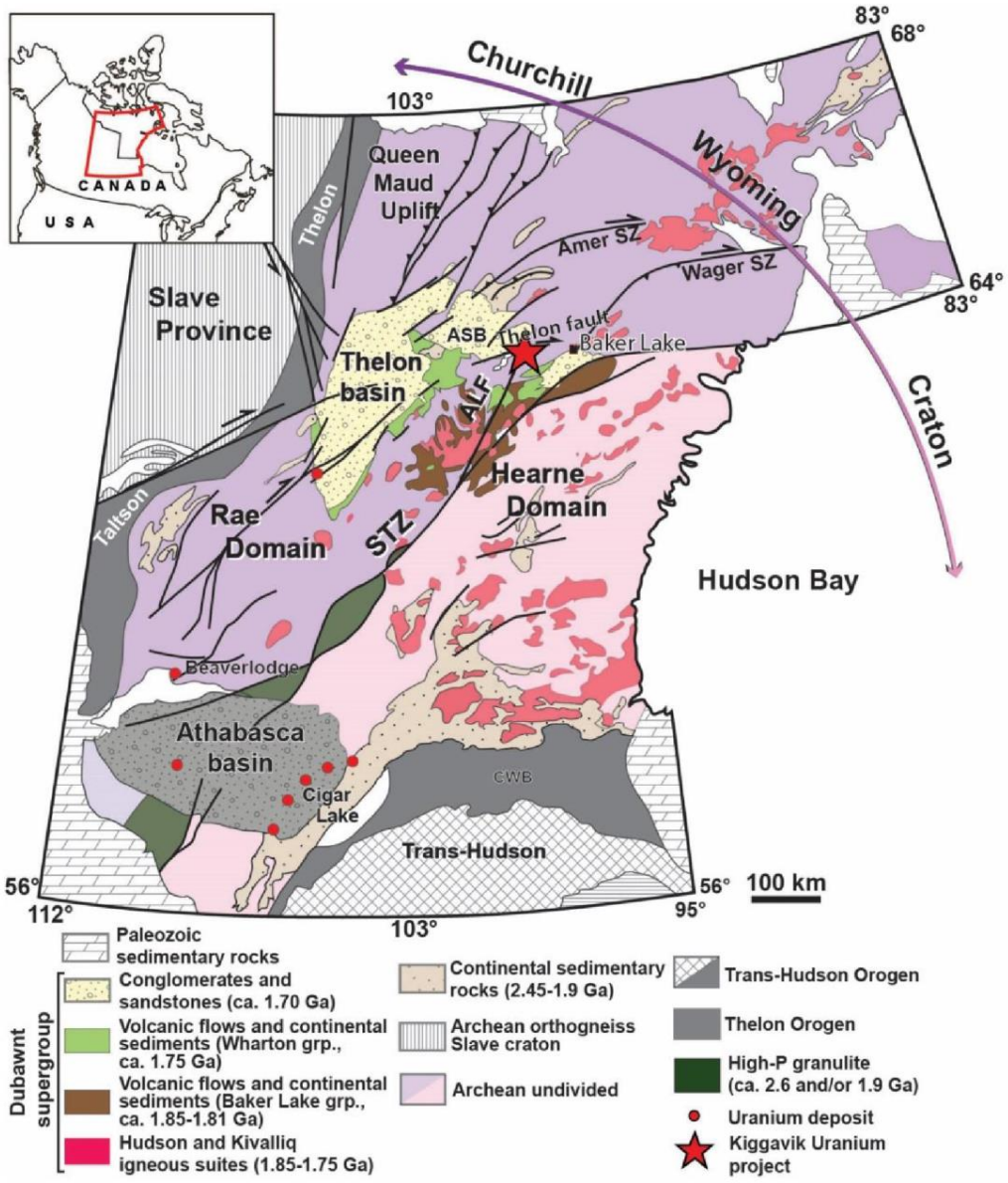

Figure 1: Geological map of the Churchill-Wyoming craton showing the location of the Athabasca and Thelon basins. The Kiggavik area is located between the Thelon fault and the Snowbird

Tectonic Zone (STZ). CWB: Chipewayan-Wathaman batholith, ALF: Andrew Lake Fault, ASB: Aberdeen sub-basin. (modified after Eriksson et al., 2001; Peterson et al., 2002).

The Thelon Basin consists of the Thelon Formation, an 1800 meter-thick sedimentary pile of conglomerates and coarse-grained sandstones, overlain by ca. 1540 Ma shoshonitic basalts of the Kuungmi Formation (Chamberlain et al., 2010) and Lookout Point Formation marine dolomites (Gall et al., 1992) of the Barrensland Group (Fig. 2). The Thelon Formation overlies a complex setup of sedimentary and bi-modal volcanic-sedimentary rocks of the Wharton and Baker Lake groups (Rainbird et al., 2003; Hadlari and Rainbird, 2011), which filled up the Baker Lake Basin that developed between 1850 Ma and 1750 Ma (Rainbird et al., 2006; Rainbird and Davis, 2007). Development of the Baker Lake Basin occurred due to extensional to transtensional rifting tectonics in response to the Thelon-Taltson and Trans-Hudsonian orogenies and was followed by uplifting, extensive erosional planation, and regolith formation linked to thermal subsidence (Rainbird et al., 2003; Rainbird and Davis, 2007; Hadlari and Rainbird, 2011). The Barrensland, Wharton, and Baker Lake groups are parts of the Dubawnt Supergroup (Peterson et al., 2006) (Fig. 2). Major ENE-trending dextral strike- and oblique-slip faults, including the Thelon-Fault (Fig. 1) became active at that time. The Dubawnt Supergroup unconformably overlies the metamorphosed basement consisting of Archean basement rocks that include Mesoarchean (ca. 2870 Ma) granitic gneisses, 2730–2680 Ma supracrustal rocks of the Woodburn Lake Group (Pehrsson et al., 2013), and a distinctive package of 2620–2580 Ma felsic volcanic and related hypabyssal rocks known as the Snow Island suite (Jefferson et al., 2011a, 2011b; McEwan, 2012; Tschirhart et al., 2013, 2017; Peterson et al., 2015a; Johnstone et al., 2016). These rocks, together with overlying Paleoproterozoic (2300–2150 Ma) rocks of the Ketyet River Group (Rainbird et al., 2010), include a prominent unit of orthoquartzite (Zaleski et al., 2000). The Archean to Paleoproterozoic rocks where intruded by felsic to mafic rocks of the late syn-orogenic Trans-Hudsonian suite and ca. 1750 Ma rapakivi-style Nueltin granite of the anorogenic Kivalliq igneous suite (Hoffman 1988; van Breemen et al., 2005; Peterson et al., 2015b; c.f., Scott et al., 2015). The age of the Thelon Formation is thus bracketed by the age of emplacement of the Nueltin granite suite, ca. 1750 Ma, the diagenetic fluoro-apatite in the basal Thelon Formation, ca. 1670 Ma (Davis et al., 2011), and by the alkali basaltic volcanism of the Kuungmi Formation at 1540 Ma that caps the Thelon Formation (Chamberlain et al., 2010).

The diabase dikes of the Mackenzie diabase swarm that form prominent linear aeromagnetic features trending NNW-SSE (Tschirhart et al., 2013; 2017), cut across all of the previous rocks. This intrusive event is dated at 1267±2 Ma (Lecheminant and Heaman, 1989;

Heaman and Lecheminant, 1993), and represents the last magmatic-tectonic event in the region.

2.2 Lithostratigraphy and structural trends in the Kiggavik area

Uranium mineralization in the Kiggavik area are hosted within the Archean and Paleoproterozoic basement rocks marginal to the Aberdeen sub-basin of the Thelon Basin (Jefferson et al., 2011a, b; Fig. 1). The Archean rocks include the Mesoarchean (ca. 2870 Ma, Davis et al., 2006) granitic gneisses, the 2730–2680 Ma (Pehrsson et al., 2010) supracrustal rocks of the Woodburn Lake Group and the distinctive package of 2620–2580 Ma (Rainbird et al., 2010) felsic volcanic and related hypabyssal rocks of the Snow Island suite (metarhyolites, epiclastics, and tuffs in Fig. 3). These rocks are overlain by the Paleoproterozoic (2300–2150 Ma, Rainbird et al., 2010) orthoquartzite of the Ketyet River Group (Fig. 3). These various groups are intruded in the area by the Schultz Lake Intrusive Complex (SLIC) (Scott et al., 2015).

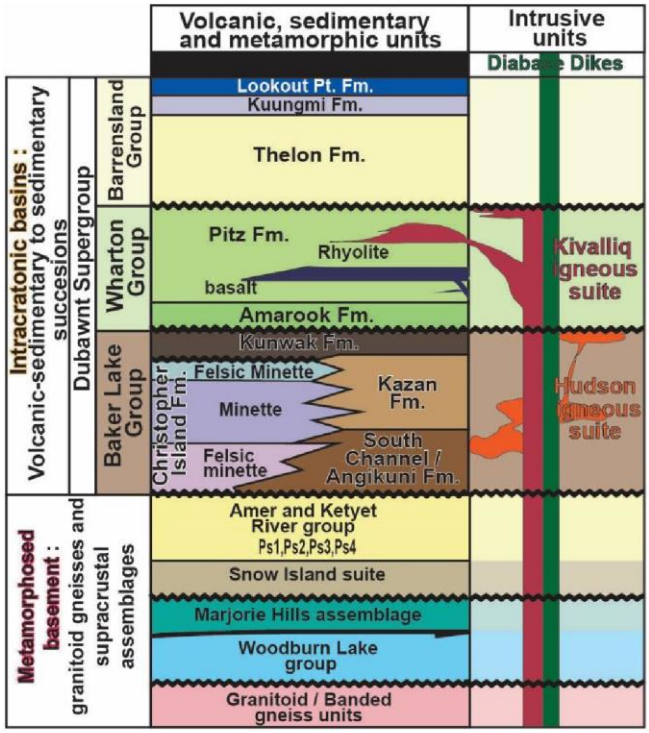

Figure 2: Simplified stratigraphic column of lithological and intrusive units in the Western Churchill Province.

The SLIC comprises two groups of rocks with contrasting origins, but with some overlap in geochemical and petrographic features (Scott et al., 2015): (i) the "Hudson granite" consists in non-foliated granitoid sills, syenites, and lamprophyre dikes of the late syn-orogenic Trans-Hudsonian suite. The Hudson granite represents the first pulse of magmatic activity at 1840–

1820 Ma in the Kiggavik area. (ii) The “Nueltin granite” consists in anorogenic granite to rhyolite of the Kivalliq igneous suite (1770–1730 Ma, Peterson et al., 2015a), including the McRae Lake dikes and minor Dubawnt minette intrusives of the Dubawnt Supergroup (Scott et al., 2015). The Nueltin granite represents a second pulse of magmatic activity in the area dated at 1750 Ma.

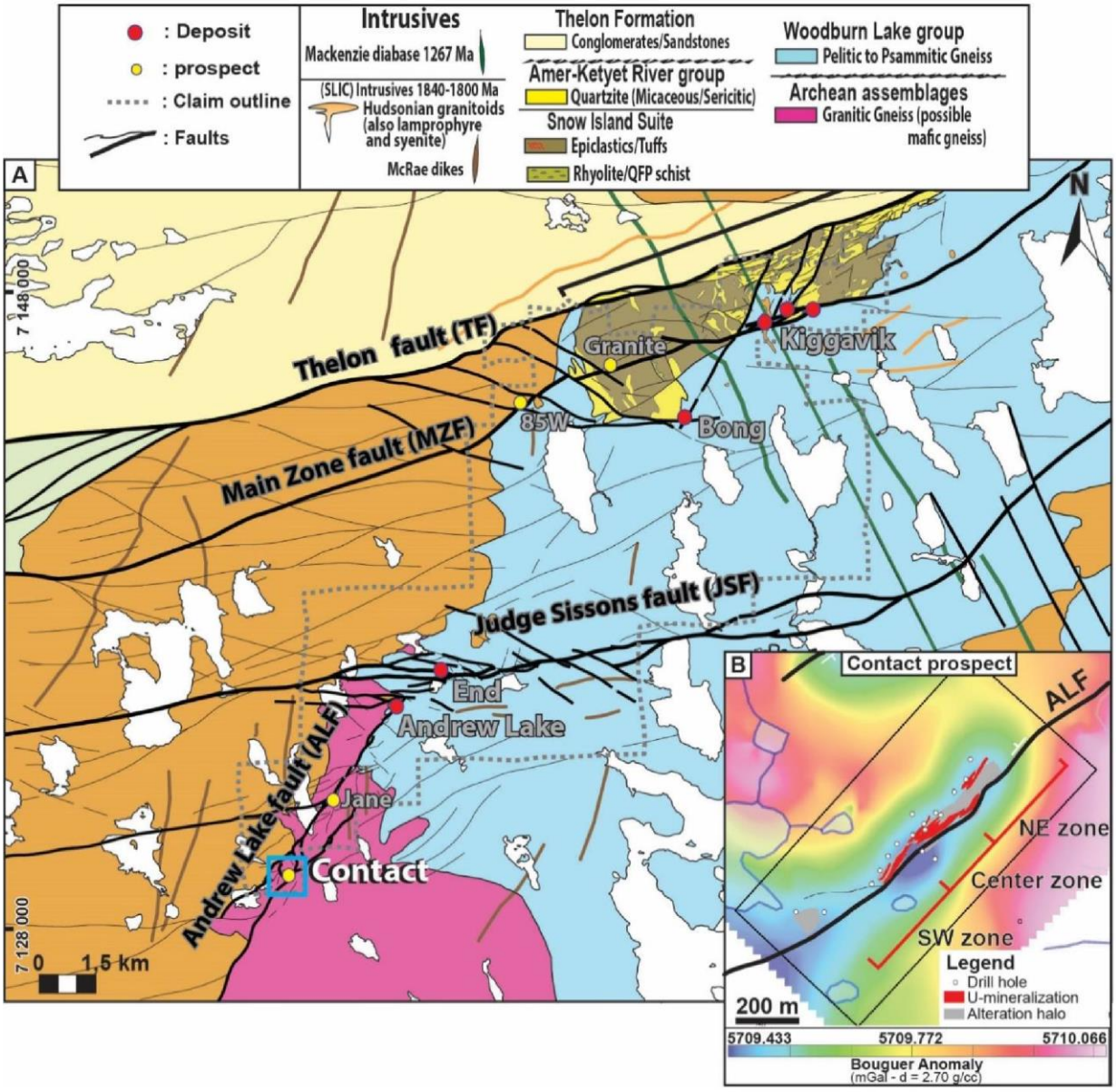

Figure 3: A) Simplified geology map of the Kiggavik area (AREVA internal document). Deposits and prospects are indicated with circles. The Contact prospect is located in the southwest, on the Andrew Lake Fault. The blue square locates B. B) Footprint of the mineralization (>0.0425 %U_3O_8, in red) and the alteration halo (in grey) projected on the Bouguer anomaly map of the Contact prospect distributed into three mineralized zones (NE, Center and SW

zones) (from Roy et al., 2017). The black trend represents the trace of the ALF at the depth of the mineralization.

All the previously described rock units are unconformably overlain by the Thelon Formation, which crops out in the northern part of the Kiggavik property (Fig. 3). The diabase dikes of the Mackenzie diabase swarm cut across all of the previous rocks in the Kiggavik area.

The main structural features in the Kiggavik area are the ENE-trending Thelon fault (TF) and Main Zone fault (MZF) in the north of the permit, the ENE-trending Judge Sisson fault (JSF) in the central part, and the NE-trending ALF in the southwestern part (Fig. 3). The MZF hosts the 85W and Granite prospects and the Kiggavik (Main, Central, and East Zones) deposits. The End deposit is hosted by the JSF, while the Andrew Lake deposit and the Jane and Contact prospects occur along the ALF (Fig. 3). Tectonic initiation of these faults goes back to the accretion of cratonic blocks during the Trans-Hudsonian orogeny. The TF constitutes the boundary between the siliciclastic sedimentary rocks of the Thelon Formation to the north and the metamorphosed basement rocks to the south (Fig. 3). The TF offsets the SLIC Hudson granite of at least 25 km with a right-lateral component (Tschirhart et al., 2013) and its northern hanging-wall is down-thrown by up to 700 m (Davis et al., 2011). South of the TF, magnetic maps show that the SLIC is crosscut by numerous ENE-trending parallel and sub-parallel faults with apparent right-lateral displacement. The second ENE-trending major fault is the JSF (Fig. 3). The JSF dips steeply to the north on discontinuous outcrops and in drill holes. The NE-trending ALF constitutes the mapped boundary between the Hudson granite to the west and the metamorphosed basement rocks to the east (Fig. 3). The ALF is delineated from interpretation of aeromagnetic and ground gravity maps (Tschirhart et al., 2016; Roy et al. 2017), as outcrops are almost non-existent. Its trend is reported on Figure 3. A main feature of both the JSF and the ALF, which is observable on outcrops and systematically intersected by drill holes, is an extensive silicification characterized by a quartz-healed breccia, named in the literature as the Quartz Breccia (QB) and described in detail hereafter.

3. Sampling and methodology

Eighteen inclined –mostly to the SE– drill holes from two exploration campaigns in 2014 and 2015 were examined in this study. The drill holes targeted gravimetric anomalies related to ore and rock alteration (Roy et al., 2017). More than 4000 m of drillcores have been logged in order to identify mineralizations, lithologies, faults, and fractures. Fault zones were characterized by

identifying the core of the fault (fault core) through the presence of fault rocks, such as breccias or gouges whereas fault damage zones (Chester and Logan, 1986; Wibberley et al., 2008; Faulkner et al., 2010) were documented by associated veins (mode I or mixed mode I-mode II), joints (mode I) and undifferentiated fractures; “undifferentiated fracture” in this case relates to a fracture plane which cannot be unambiguously classified as vein, joint or fault/micro-fault (no evidence of kinematics) at the time of observation. Fracture corridors and isolated veins, joints and fractures were also systematically reported. Drillcore was oriented using a Reflex ACT III digital core orientation tool (Bright et al., 2014), and then a protractor was used to measure angles between fractures and the core axis (alpha angle). The angle between the bottom of the hole and the inflection line (beta angle) was also measured for calculation of true dip/dip direction data. Acoustic televiewer probing ABI40 (Williams et al., 2004) was run through key holes providing accurate oriented data in faulted core intervals. The data were processed to their true orientation and plotted with Dips 6.0 software by Rocscience. Uncertainty on orientation measurements is usually about 10° as estimated from the comparison between oriented core-measurements and acoustic televiewer data. Kinematic indicators are rare. Some were identified and measured occasionally, but the amount of collected data appeared to be statistically insufficient to insure proper interpretation. The acquisition of oriented data from exploration drillcores can be limited because the more the rock fractured and altered (i.e. fault damage zone or fault core) the lower the probability of getting drillcore suitable for orientation. Recent drilling in the Kiggavik area was done with NQ 4.5 cm of diameter double tubing. The holes drilled in the Contact prospect provided enough good quality oriented core to collect reasonable statistically representative data of the various fault and fracture sets. Oriented data was also supported by local acoustic televiewer probe.

Ninety-six core samples were collected (10 and 20 cm in length) from fractured zones; forty-nine of which were mineralized. All samples were studied from the macro- to the micro-scale in order to define fracture cross-cutting relationships, mineral paragenesis, and alteration. Sixty-four thin sections were prepared for petrographic and microstructural studies.

Optical microscopy (plane polarized transmitted and reflected light microscope Motic BA310 POL Trinocular, equipped with a 5M pixel Moticam camera), Scanning Electron Microscopy (SEM) JEOL J7600F field-effect coupled with a X-Ray Microanalysis device (EDAX Genesis) and cathodoluminescence (CITL Cold Cathodoluminescence device Model MK5-1) were systematically used for accurate definition of fracture-cementing/coating phases and mineral paragenesis. Clay mineral species and uranium oxides (UO_2) were characterized with an electronic microprobe (CAMECA SX-100) and by SEM performed at the “Service Commun de

Microscopie Electronique et de Microanalyses (SCMEM)" at the University of Nancy-CREGU, in France. The CAMECA SX-100 was operated at up to 30 kV for elements with high atomic numbers. The calibration used natural and synthetic oxides and/or alloys (orthoclase, albite, $LaPO_4$, $CePO_4$, wollastonite, UO_2, $PbCrO_4$, olivine, $DyRu_2$). The analytical conditions at SCMEM were 10-nA current, accelerating voltage of 15 kV, counting time of 10 s (K, Na, Ca), 20s (Ce, U, Si), 40s (Dy), 50s for Pb, and 60s for La. The SEM was operated at low accelerating voltage (10 kV), 100 nA filament current, and 600 Å beam width for a working distance between 8 and 39 mm. The cathodoluminescence microscopy was operated between 10 and 12 kV gun potential and between 150 and 350 µA beam current. Observations were performed at the "Departament de Mineralogia, Petrologia i Geologia Aplicada, Facultat de Ciències de la Terra", at the University of Barcelona, in Spain.

4. Fracturing stages and mineral paragenesis

The Contact prospect is located along the ALF, one kilometer east of the Hudson granite (Fig. 3A). Uranium mineralization is hosted in faults, veins, and other fractures (described in detail hereafter) that occur in moderately foliated, granitic to granodioritic gneiss of inferred Archean age. Granitic sills and dikes, syenites to granites, and lamprophyre dikes of the SLIC are common and are locally mineralized. Interpretation of the newly acquired ground magnetic and gravity data suggests that the ALF is divided in two overlapping fault segments between the Jane and Contact prospects (Fig. 3A) (see also Roy et al., 2017). The southern fault segment dips to the NW and hosts the Contact prospect, while the northern fault segment dips to the SE and hosts further north the Jane prospect and the Andrew Lake deposit (Fig. 3A). As presented by Roy et al. (2017), the mineralization in the Contact prospect is distributed in three pods called SW, Center, and NE zones (Fig. 3B).

The microstructural and petrographic study combining optical, cathodoluminescence microscopy, and SEM observations has allowed for the recognition of ten main fracturing stages. We define "fracturing stage" as the fracture set or group of fracture sets that are associated with the same paragenesis indicating the same step or period of fluid/fracture/rock interaction. A fracture stage can correspond to a well identified and unique tectonic episode, or to one or several episodes of fracture reactivation and mineralization. The various recognized fracture stages in the Contact prospect are presented below by their chronological order based on observed cross-cutting relationships. Three fracture stages are associated with uranium mineralization, of which two are primary mineralizing stages, and one is a remobilizing stage.

The other seven fracture stages are barren and can be indirectly associated with the ore deposit either by having enhanced the permeability of the host rock by micro-fracturing or by having controlled fluids that have reworked uranium mineralizations in late stage.

4.1 Fracturing stage 1: First tectonic activity observed on the Andrew Lake Fault

The first fracturing stage (f1) is represented by the occurrence of cataclastic to ultracataclastic faults observed locally in some drill holes (Fig. 4A-B). Fault zones exhibit cataclasites and breccias of small clasts with weak illitic alteration, cemented with illite and finely crushed grains from the host rock; they are usually pervasively silicified and crosscut by quartz veins (Fig. 4B).

Granitic gneiss and various intrusive rocks (granite, fig. 4A, lamprophyre, syenite) are crosscut by these fault zones and form the breccia clasts. This stage of faulting is the earliest brittle tectonic deformation stage recognized on the ALF. No evidence of ductile or ductile-brittle shearing was observed within the ALF at the Contact prospect. Related faults were observed only in the vicinity and/or within the quartz breccia of the following deformation stage that subsequently silicified and crosscut these faults (Fig. 4C to D). The strong overprinting by quartz veins and quartz breccias prevented the collection of statistically significant oriented data, and "screened" the full recognition of these faults. This fracturing stage is the oldest recognized at the Contact prospect (fig.4 E).

4.2. Fracturing stage 2: quartz breccia (QB) and first stage of oxidation

One of the most remarkable deformation features of the JSF and ALF in the Kiggavik area is the so-called hematitic quartz-rich breccia, first described in the area by Cogema's field geologists in 1994 from outcrops along the JSF (Fig. 5A). This breccia is also called barren quartz breccia by Chi et al. (2016) in their fluid inclusion study at the End deposit and called hereafter the quartz breccia (QB). The QB consists of mosaic quartz-sealed breccia and veins (Fig. 5A-B), and reflects a major regional silicification event (Turner et al., 2001; Hadlari and Rainbird, 2011). Lithologies within and around the QB display a pervasive, red-purple hematization (Fig. 5B and C). This hematization is the first hematization event identified in the Contact prospect and Kiggavik area.

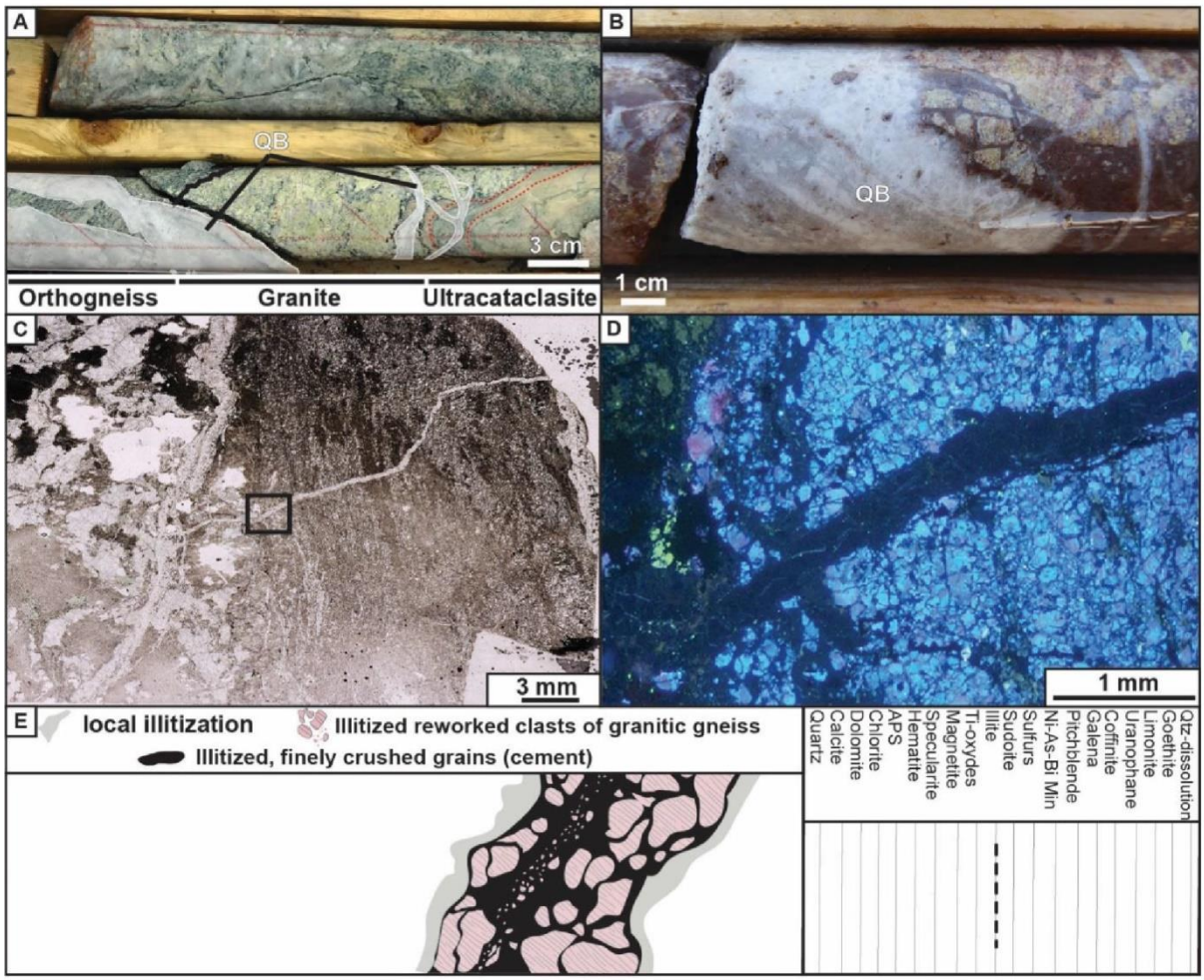

Figure 4: Fracturing stage f1: A) Drillcore box photograph showing an ultracataclastic fault rock in a granite that intrudes a granitic gneiss. Both lithologies are then crosscut by quartz veins from fracturing stage 2. B) Drillcore photograph of a silicified and illitized cataclastic fault rock crosscut by white quartz and grey quartz veins of the second fracturing stage. C) Optical microscopy transmitted light photograph of an ultracataclastic fault rock crosscut by a thin quartz vein of the second fracturing stage. The black square locates picture D. D) Cathodoluminescence microscopy photograph. Zoom in showing the crosscutting relationship between the ultracataclastic fault rock and the quartz vein (dark blue weak luminescence). E) Sketch depicting the textural features with the paragenesis characterizing this fracturing stage.

At the Contact prospect, the QB was intersected by most of the drill holes at the bottom of all mineralized pods discovered to date. The breccia zone displays abundant, pervasively hematized hetero-lithic clasts of various intrusive rocks such as lamprophyre, granite, or syenite and granitic gneiss, and a quartz-healed silicified matrix. The QB can be divided into damage

zones characterized by numerous quartz veins (<5cm thick), and core zones characterized by dominant massive quartz sealed breccias (>50cm thick) over minor quartz veins. The QB crosscuts and postdates the fault of the first brittle tectonic event (f1), the associated fractures of which were re-activated as pathways for the silica-rich fluids. A similar chronology has been recognized at the Andrew Lake (Shabaga et al., 2017a) and End deposits.

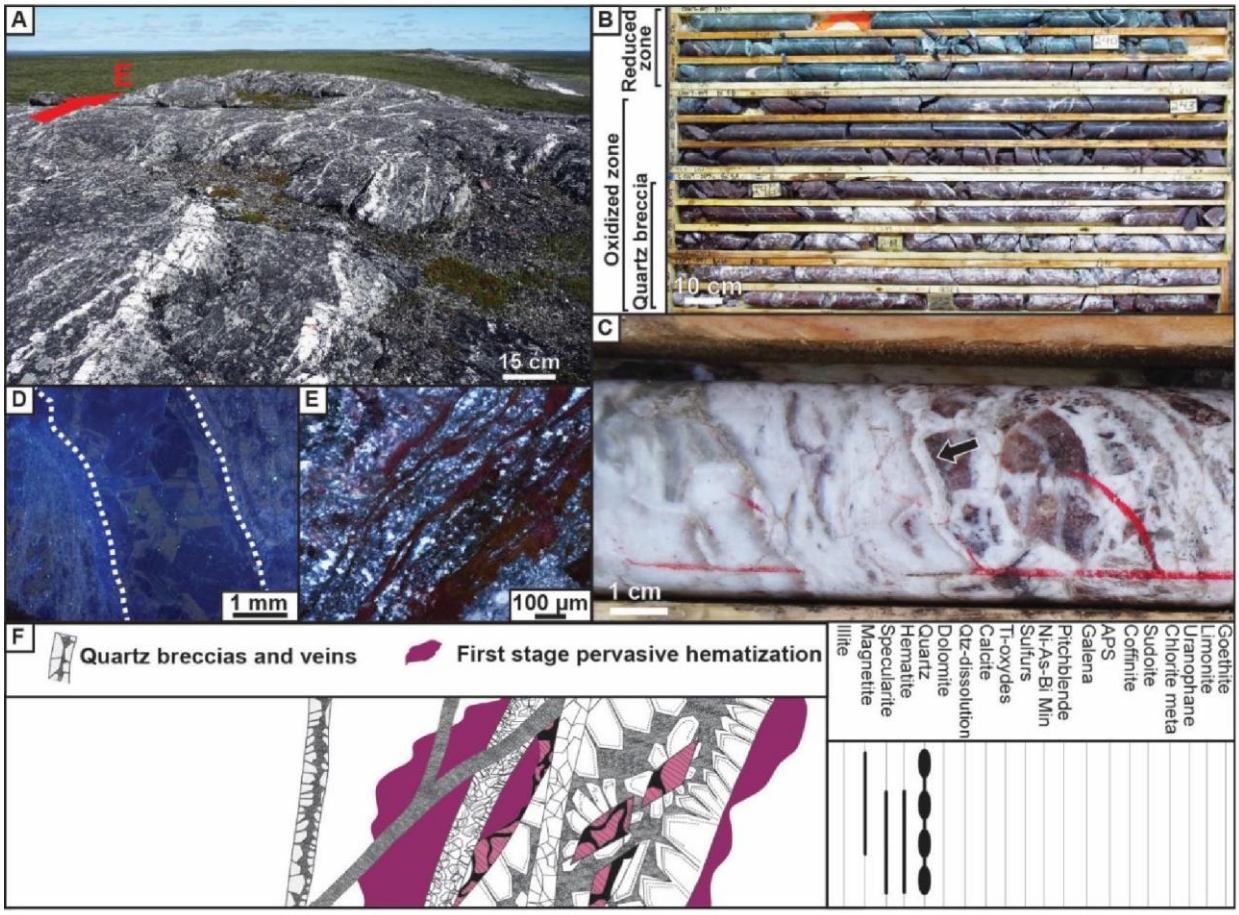

Figure 5: Fracturing stage f2 (QB): A) Outcrop view looking east on the N80-trending steeply dipping to the north JSF underlain by at least 10 meters of white quartz veins. B) Core box photograph showing examples of the quartz breccia and associated deep red to purple red pervasive hematization (Contact prospect). C) Massive white quartz breccia with opaque white quartz, grey microcrystalline quartz and angular granitic gneiss clasts. Colloform quartz texture is visible pointed by the arrow (Contact prospect). D) Cathodoluminescence microscopy photograph showing a vein of zoned quartz (white dot line) crosscutting microcrystalline quartz. E) Microscopy reflected light photograph showing alternating micro-crystalline quartz and hematite in a vein. F) Sketch depicting the textural features with the paragenesis characterizing this fracturing stage.

Numerous generations of quartz veins crosscut each other (Fig. 5D), which makes it difficult to establish a proper chronology between all quartz textures. However, two groups of textures dominate: primary crustiform, comb and zonal growth textures, and secondary microcrystalline mosaic quartz, feathery and ghost sphere growth textures (Bodnar et al., 1985; Dong et al., 1995; Moncada et al., 2012). The most representative quartz texture observed consists of white quartz crystals with alternating growth zones of blue and light brown colors under cathodoluminescence; this is usually observed as a late quartz generation (Fig. 5D). Micro-crystalline quartz is observed in different settings: oriented along planes (stylolite-like), following boundaries of quartz veins or present in the center of quartz veins.

The pervasive purple-red hematization of the breccia host rocks (Fig. 5C) is characterized at the micro-scale by disseminated, fine-grained hematite, magnetite and rare specular hematite (also filling vugs). Veins of crustiform hematite and anhedral microcrystalline quartz (Fig. 5E) attest for synchronous brecciation and oxidation phenomena, which is the second fracturing stage observed at the Contact prospect (fig. 5F).

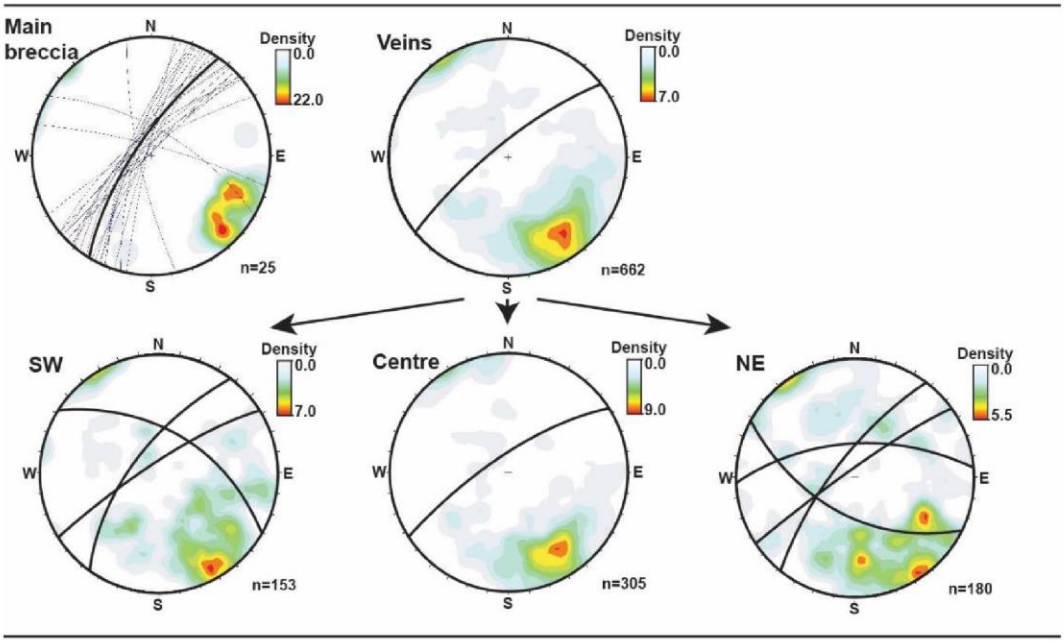

Figure 6: Fracturing stage f2: oriented data of quartz veins and breccia of QB. Bold black great-circles indicate the main trend. Schmidt's lower hemisphere plots.

Veins of the QB are divided into massive quartz veins measured in the breccia core and minor veins measured in damage zones (Fig. 6). Data are separated by location: Southwest (SW), Center, and Northeast (NE) zones. Oriented data plots show that the massive quartz

veins are mainly oriented N035°, with a steep dip to the NW. Minor quartz veins strike on average N060°, with a steep dip to the NW. Minor veins are much more focused along one direction in the Center Zone, compared to the SW and NE zones. The QB is also thicker in the Center Zone where it reaches up to 70 m in drill hole CONT-10, (Fig. 7), with 30 m of fault core zone and a well-developed damage zone up to 40 m thick.

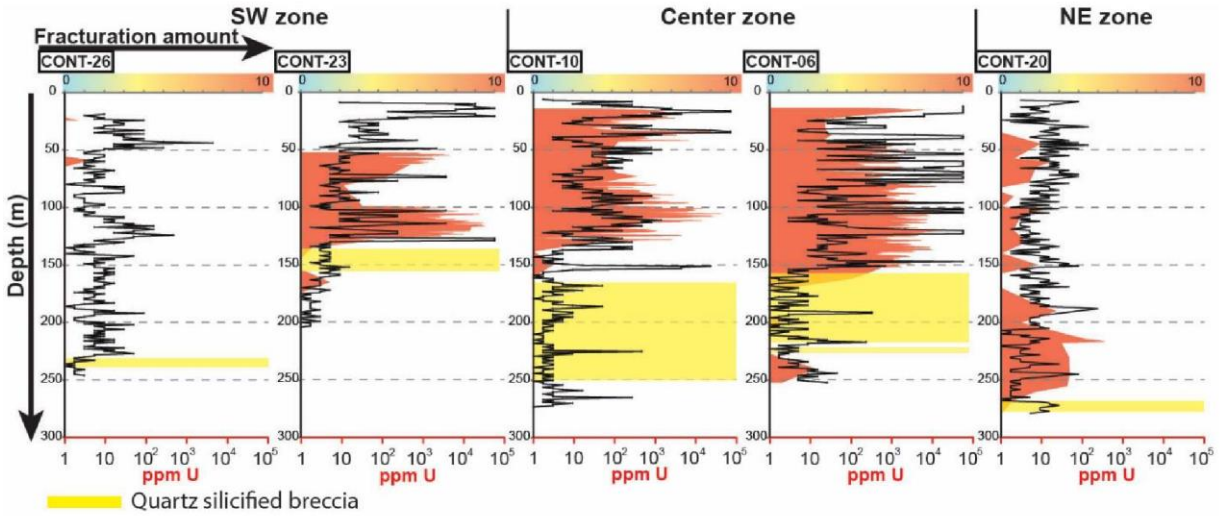

Figure 7: Distribution of fracture density as a function of depth. Fracture density as black lines; 0: non-fractured drill-core, 10: intensely fractured drill-core. Uranium mineralization in red: U in ppm measured by assays, logarithmic scale). The QB is highlighted by a yellow zone including both the core and the damage zone.

4.3. Fracturing stages 3 and 4: carbonate-filled veins

The fracturing stage 3 (f3) is characterized by isolated veins filled by dolomite. Dolomite cement fills newly formed veins and vugs in inherited quartz-filled veins (Fig. 8A). In the latter case, quartz crystals display edges with evidence of corrosion and microcrystalline quartz is replaced by dolomite (Fig. 8B). Dolomite crystals are also disseminated within the host rock.

The fracturing stage 4 (f4) consists of isolated calcite-filled veins that crosscut f1 to f3, including the dolomite veins. Calcite occurs as the main vein cement and also as later cement infilling the remnant voids partially filled by dolomite or locally disseminated within the host rock. Calcite also appears as replacing pre-existing sulfide minerals. Calcite veins display two apparent pseudo-conjugate trends: E-W and NW-SE, with conjugate dip directions (Fig. 8C). Observations under cathodoluminescence confirm that dolomite and calcite veins crosscut quartz veins of the QB event (fig. 8D).

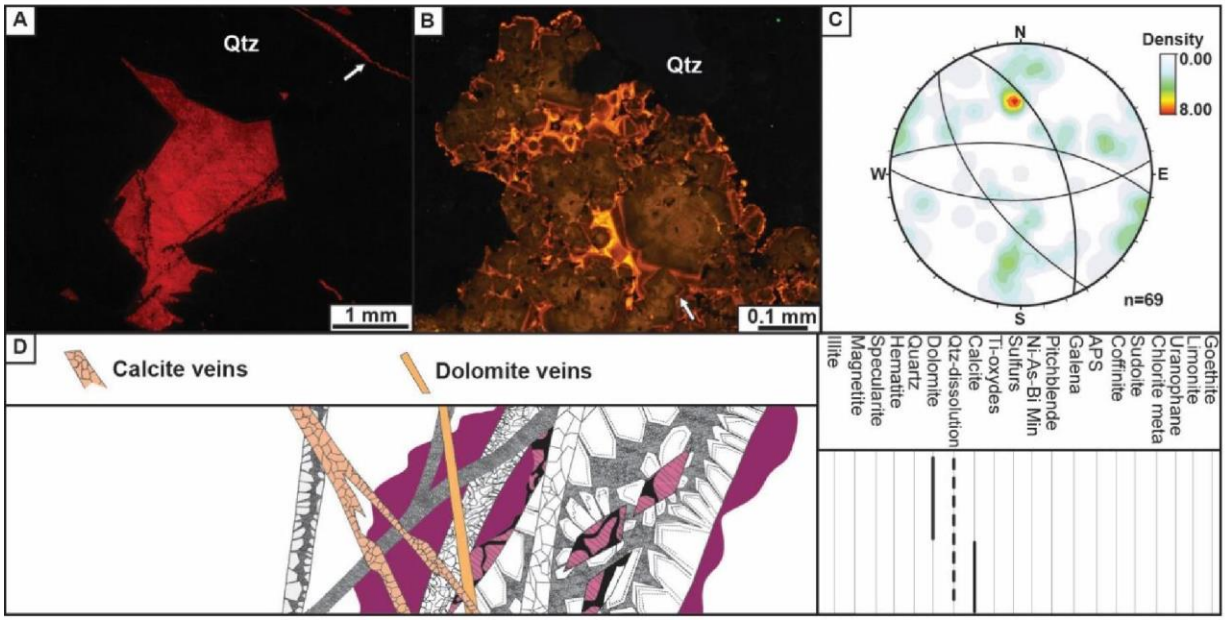

Figure 8: Fracturing stage f3 and f4: A) Cathodoluminescence microscopy photograph showing a vein cemented with dolomite (f3) crosscutting quartz crystals (white arrow, quartz vein of the QB). B) Cathodoluminescence microscopy photograph showing calcite replacing polygonal shaped sulfide mineral phantoms (white arrows). C) Oriented data for calcite filled veins. Schmidt's lower hemisphere plot. D) Sketch depicting the textural features with the paragenesis characterizing this fracturing stage.

4.4. Fracturing stage 5: uranium-related faults (first stage of uranium mineralization)

This fracturing stage (f5) is represented by mineralized faults and veins, and embodies the first stage of uranium mineralization in the Contact prospect. The mineralized fractures crosscut all features of stages f1 to f4, and reactivate and/or cause micro-fracturing of quartz veins of the QB. This initial mineralization with pitchblende and coffinite with other uranium oxides (see hereafter) generated the highest ore grades in the Contact prospect (i.e., 4.76 $\%U_3O_8$ over 50cm), although it is not the largest in terms of spatial extent. Uranium mineralization macroscopically appears in two settings that can coexist: i) in newly formed fault zones, coating undifferentiated fractures and veins, locally observed as disseminated within cataclastic fault rocks, and filling fault damage zone-related fractures with other ore minerals (Fig. 9A-B). ii) in re-opened and mineralized quartz veins of the QB (Fig. 9C-F). Both type of mineralized faults and veins are also characterized by iron oxide removal or bleaching with weak grey-greenish clay alteration and illitization (see table 1 for clay composition).

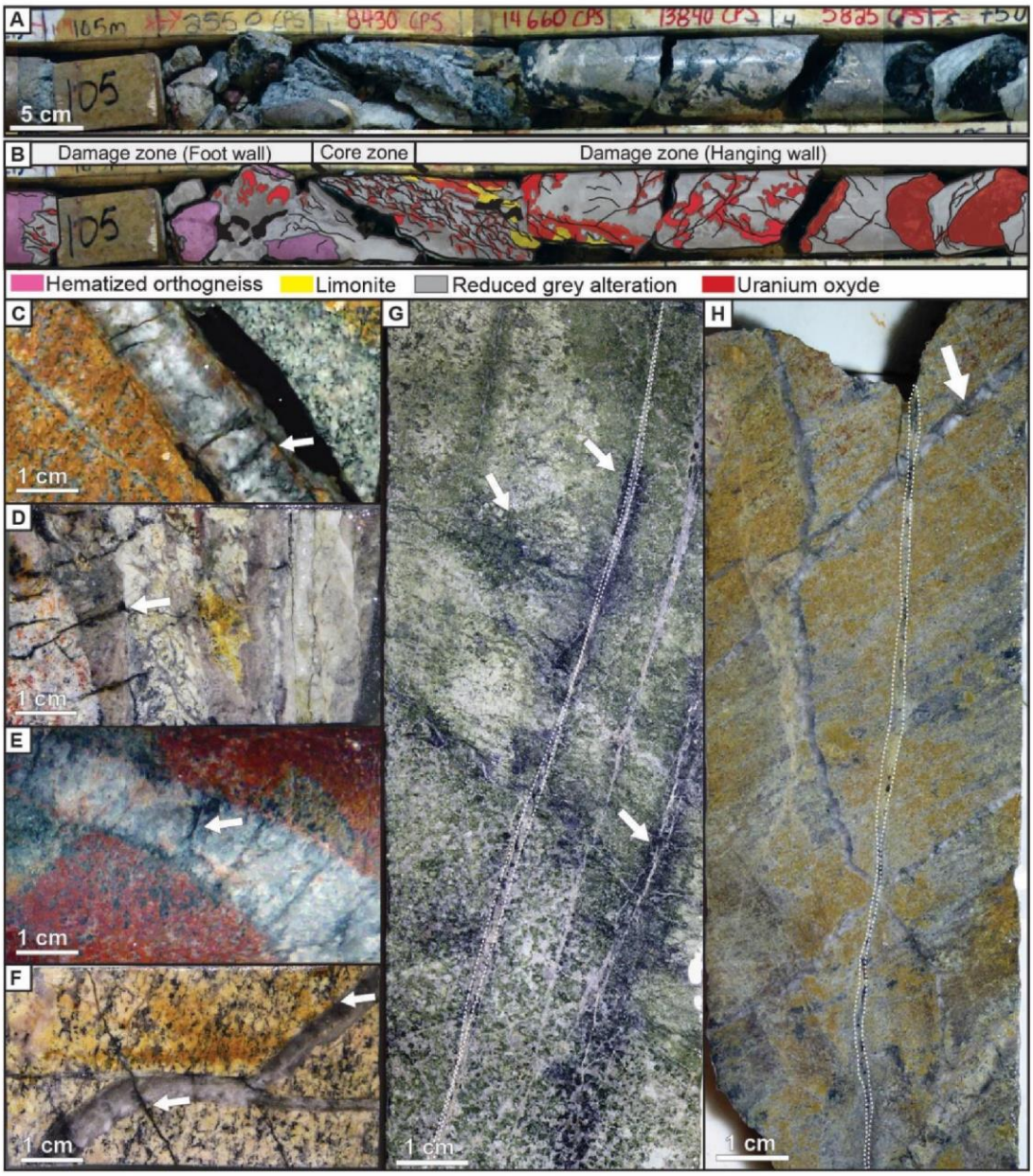

Figure 9: Fracturing stage f5: A-B) Core box photograph and interpretation respectively showing a mineralized cataclastic fault with grey-greenish clay alteration. Mineralization is disseminated within the cataclastic fault core and fills fractures within the fault damage zone. C-F) Core samples exhibiting various examples of quartz veins (QB) with mineralized microveins (pitchblende and sulfide minerals) that orthogonally cut across the vein. G) Core samples displaying mineralized inherited micro-crystalline quartz veins (QB) with haloes of grey-greenish clay alteration. Mineralization (pitchblende) has leaked out into the foliation of the host rock. H) Core sample with mineralized quartz veins (QB) crosscut by a fracture (white dotted line) cemented with ore minerals.

Bleaching varies from light (Fig. 9G) to strong (Fig. 9A and H) and correlates to the amount of uranium mineralization. No oxidation of the host rocks has been observed linked to this stage of mineralization. Dolomite and calcite veins from f3 and f4 can also be locally re-activated and mineralized during this stage.

Quartz veins of the QB contain mineralization along the vein walls and leaking out into the foliation (Fig. 9G and H), or filling micro-veins that orthogonally cut across the veins (Fig. 9C-F). In both occurrences, vein edges show irregular boundaries indicating quartz corrosion or dissolution prior to, or synchronous with, mineralization. The mineralized fractures that orthogonally cut across the quartz veins are a notable macroscopic and microscopic feature of this stage of mineralization, which is still poorly understood. Their geometry varies depending on the texture of the crosscut quartz; microfractures are straight in the case of micro-crystalline quartz, while irregular and along grains boundaries in the case of sub-euhedral quartz (Fig. 10A and B).

Dissolution has also been observed in re-opened and mineralized carbonate veins of the f3 and f4. In this case, dolomite grains display dissolved boundaries where they are in contact with pitchblende, and calcite is observed as a rim between the pitchblende and dolomite (Fig. 10C). This texture suggests that calcite precipitated coevally with uranium mineralization: calcium was remobilized from the dissolved dolomite into calcite precipitated around the pitchblende or in nearby microfractures. Observations under cathodoluminescence microscopy reveal specific pink-yellowish luminescence along the boundaries of quartz grains and along the boundaries of microfractures in quartz (Fig.10B), cemented with uranium oxides.

Uranium minerals at this stage are represented by colloform to xenomorph pitchblende (Fig. 10D) and coffinite, uraniferous titanate, titanium-oxides with pitchblende micro-inclusions (Fig. 10E), iron sulfides (mainly pyrite but also chalcopyrite and bravoite, see Fig. 10D and F-G), and illite (Table 1). Rare occurrences of native bismuth and unidentified As-Ni-Co (±U) xenomorphic minerals are also associated with xenomorphic pitchblende along microfractures (Fig. 10 H-I). Iron sulfides not associated with pitchblende are rare throughout the Contact prospect. The lack of iron sulfides is inferred to be associated to their remobilization (if they were present) due to the pervasive hematization of the QB event along the ALF. This first mineralizing stage which postdates carbonate and quartz veins (fig. 10J) is classified as polymetallic.

Oriented data of the re-openend, orthogonally micro-fractured and mineralized quartz veins show a dominant NE-SW and a minor NW-SE trends (Fig. 11), consistent with the main QB and ALF trends (Fig. 8F), while the newly formed f5 faults and fractures strike nearly perpendicular to the ALF, following the TF trend (Figs. 3, 11).

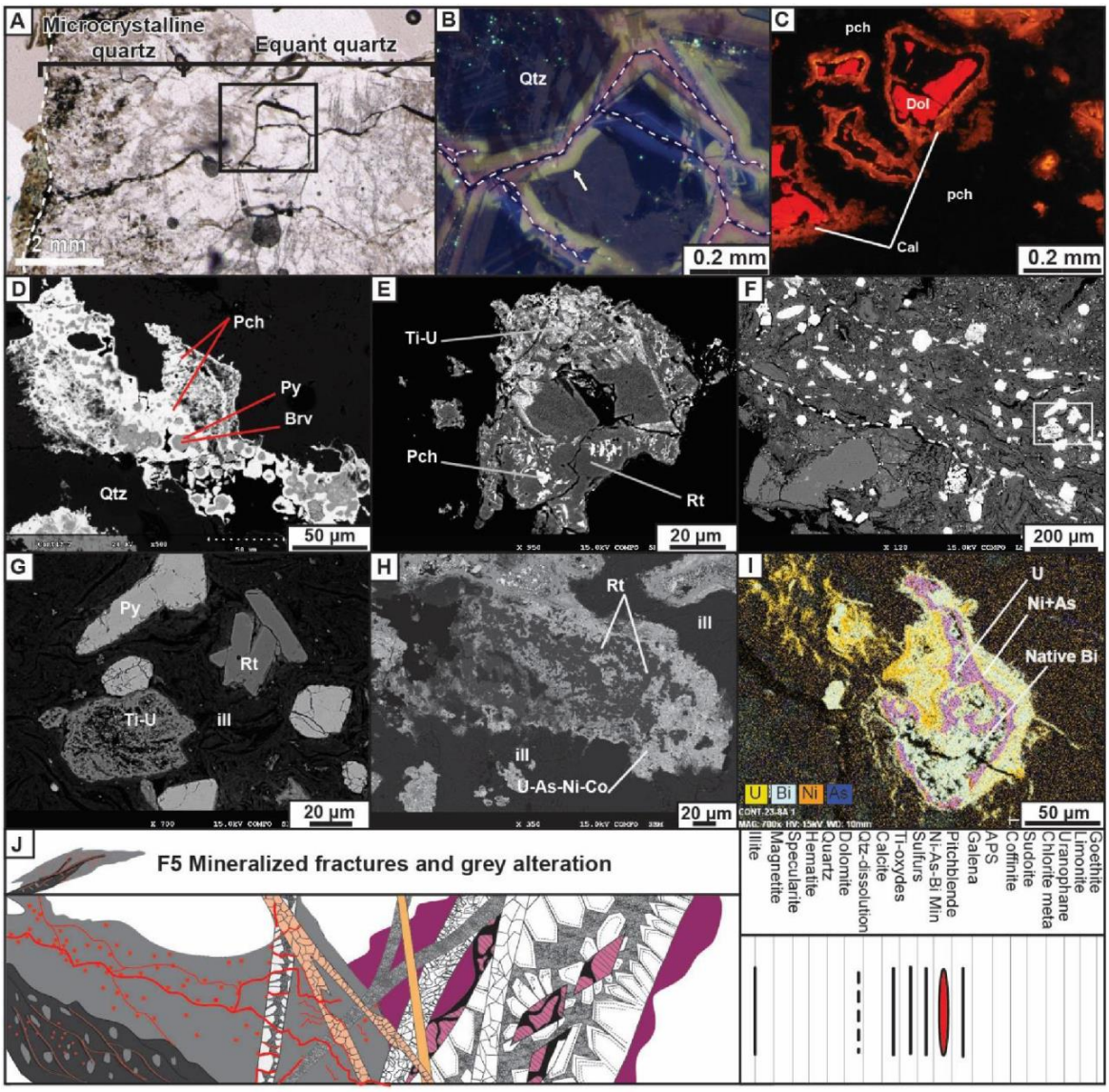

Figure 10: Fracturing stage f5: A) Transmitted light microscopy photograph showing a quartz vein of the QB crosscut orthogonally by mineralized microveins (white dotted line on the left highlights the boundary of the vein). The microvein is filled with pitchblende, pyrite and chalcopyrite. The black square locates photograph B. B) Cathodoluminescence microscopy photograph showing the luminescence irradiation halo surrounding the mineralized microvein traced with the white dot line. C) Cathodoluminescence microscopy photograph showing dissolution of dolomite linked to pitchblende precipitation and carbonate re-precipitation as calcite. D) SEM microphotograph illustrating a microvein crosscutting a quartz vein and cemented with pyrite and bravoite which are coated with anhedral pitchblende. E) SEM microphotograph illustrating rutile with pitchblende micro-inclusions and mixed with uraniferous titanate. F) SEM microphotograph showing a vein (white dot line, from Fig. 10D) cemented with uranium minerals. White square locates photograph

G. G) SEM microphotograph. Zoom into the core of the previous vein showing: rutile, pyrite, uraniferous titanate and illite. H) Subhedral rutile coated with U-As-Ni-Co compounds. I) Anhedral uranium, nickel-arsenide mineral and native bismuth. J) Sketch depicting the textural features with the paragenesis characterizing this fracturing stage.

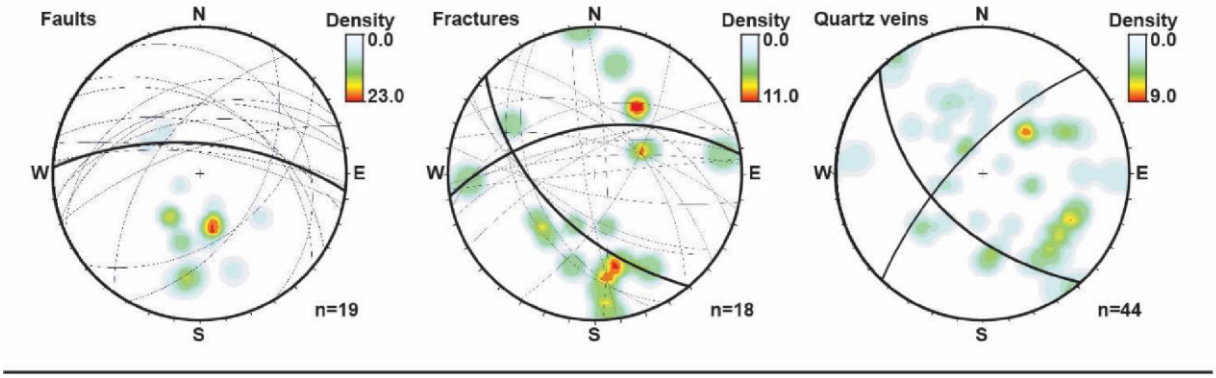

Figure 11: Fracturing stage 5: Oriented data for newly formed mineralized faults, associated fractures (left and middle) and mineralized quartz veins (right). Schmidt's lower hemisphere plot.

4.5. Fracturing stage 6: faulting, second oxidation stage and second stage of uranium mineralization

The fracturing stage 6 (f6a to f6c) is the more complex deformation stage. Two sub-stages (f6a and f6c) displaying strong similarities in fault rocks, alteration type, and oriented data were distinguished on the basis of crosscutting relationships at the micro-scale and on the presence of uranium mineralization since they are separated by a sub-stage of calcite vein formation (f6b). The spatial association of these calcite veins with the oxidized fault rocks is however difficult to establish precisely because of the small size of the calcite veins (<3 mm) and the discontinuous picture of the fault zone given by drilling.

4.5.1 Fracturing stage 6a (f6a): faulting and second stage of oxidation

Faults that characterize f6a were observed both on outcrops and in drillcores. Fault core rocks contain reworked clasts of the QB (Fig. 12A) and of the Thelon Formation (Fig. 12B). These faults display characteristic oxidized and illitized (Table 1) tectonic breccias and cataclasites (Fig. 12C). Calcite veins are fractured and stained with hematite (Fig. 12D, E) and

reworked clasts (Fig. 12F) with remnant minerals like iron sulfide, rutile, and micro-grains of pitchblende of the first mineralization stage are also common (Fig. 12E).

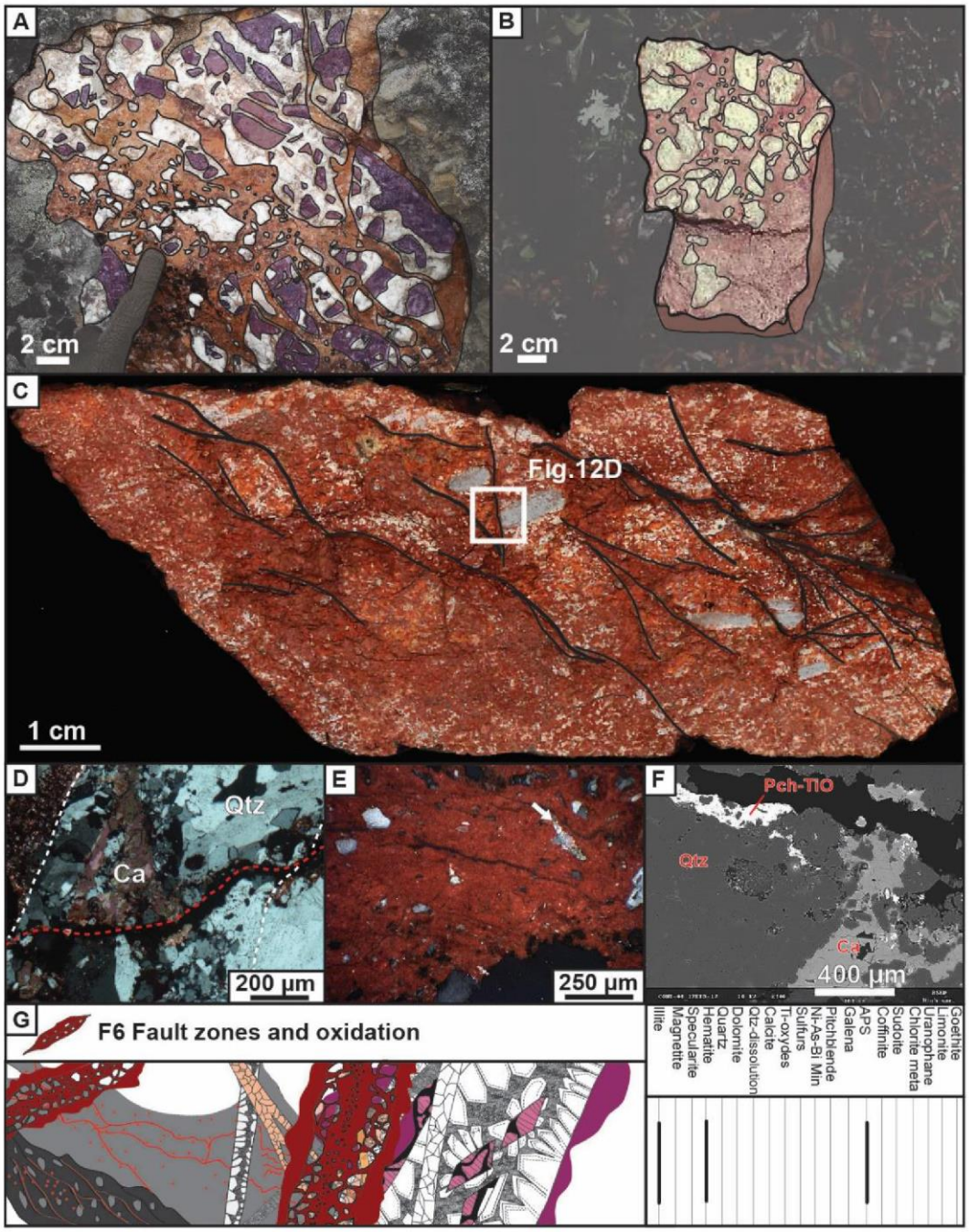

Figure 12: Fracturing stage f6a: A) Tectonic breccia on outcrop in the Kiggavik area embedding heterometric fragments of QB with purple-red hematization (first hematization stage) floating in a matrix consisting of bright red hematized clay (second hematization stage). B) Cataclastic fault

rock displaying yellow clasts of the Thelon Formation in bright red hematized clay matrix (second hematization stage). Sample from an outcrop 30km west of the Kiggavik area. C) Protocataclastic hematized fault rock. Brecciation of a quartz vein (QB) is visible (white arrow). D) Transmitted light microscopy photograph. Closer view of the hematized fault rock of picture C: brecciated (red dot line) quartz vein (white dot line) with vugs filled by calcite (f4). E) Reflected light microscopy photograph showing a hematized ultracataclastic fault rock with microclasts of calcite and quartz. F) SEM photograph. Zoom in a hematized fault rock with reworked quartz vein with calcite-cemented fractures hosting remnant xenomorphic pitchblende and rutiles. G) Sketch depicting the textural features with the paragenesis characterizing this fracturing stage.

This stage postdates the first stage of uranium mineralization (Fig. 12G). Fine-grained crushed aluminum-phosphate-sulfate (APS) minerals were observed in one sample of hematized ultracataclastic fault rock.

The f6a event is associated with a second oxidation event of the host rock. This oxidation is more closely spatially associated with fault zones and the hematization is less penetrative (centimetre scale) into the host rocks than in the case of the first hematization event linked with the QB (metre scale). It is characterized by fine-grained hematite that imparts the bright reddish color to the fault (Fig. 12E).

Oriented data of f6a (Fig. 13A) needed specific sorting as fracture directions vary with depth and from the Center Zone to the outer zones (SW and NE zones). In the Center Zone, above 170m, faults orientations are scattered in three different trends (Fig. 13B).

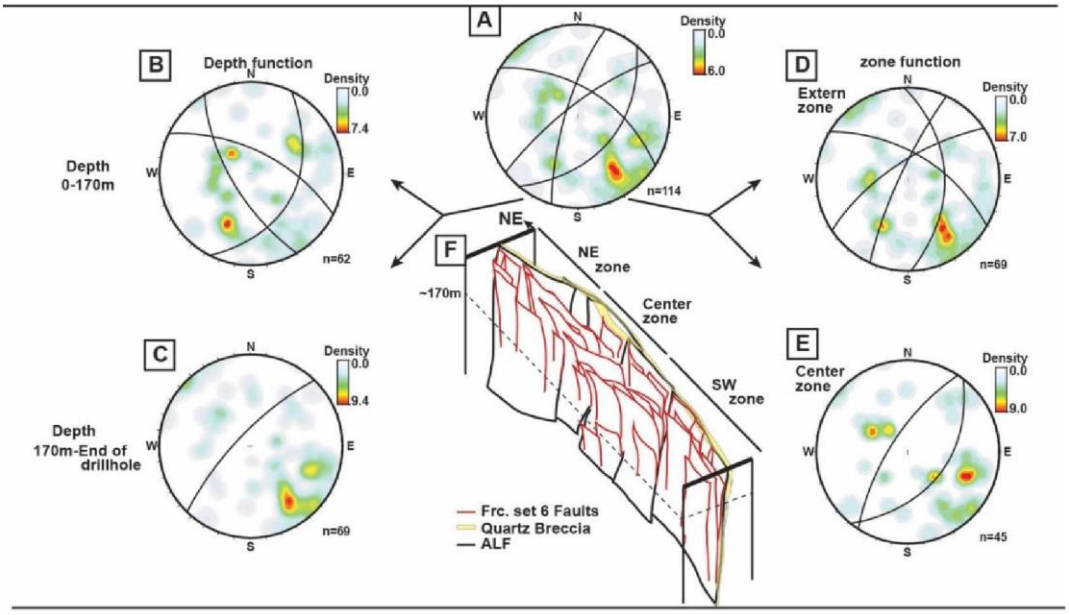

Figure 13: Fracturing stage f6a. A) All oriented fault data sets. B) Depth selection for oriented data. Faults above 170m display two directions, NE-SW and NW-SE; C) faults below 170m have a dominant N040° trend, steeply dipping to the NW. D) Zone selection for oriented data. Faults in the outer zones are dominantly subvertical or dip steeply to the NW; E) Faults in the Center Zone display synthetic dip directions, one to the SE, and a steeper one to the NW. Outer zones correspond to northwest and southeast zones. F) Simplified sketch of the inferred spatial organization of f6a faults, flower type fault geometry. Schmidt's lower hemisphere plot.

Below 170 m, the dominant fault set is better defined along a NE-SW trend, with steep dip to the NW (Fig. 13C). Faults in the Center Zone display opposing dips (Fig. 13E), while in the outer zones faults are dominantly sub-vertical or dip steeply to the NW. This complex arrangement is sketched in figure 13F.

4.5.2. Fracturing stage 6b: second generation of calcite veins

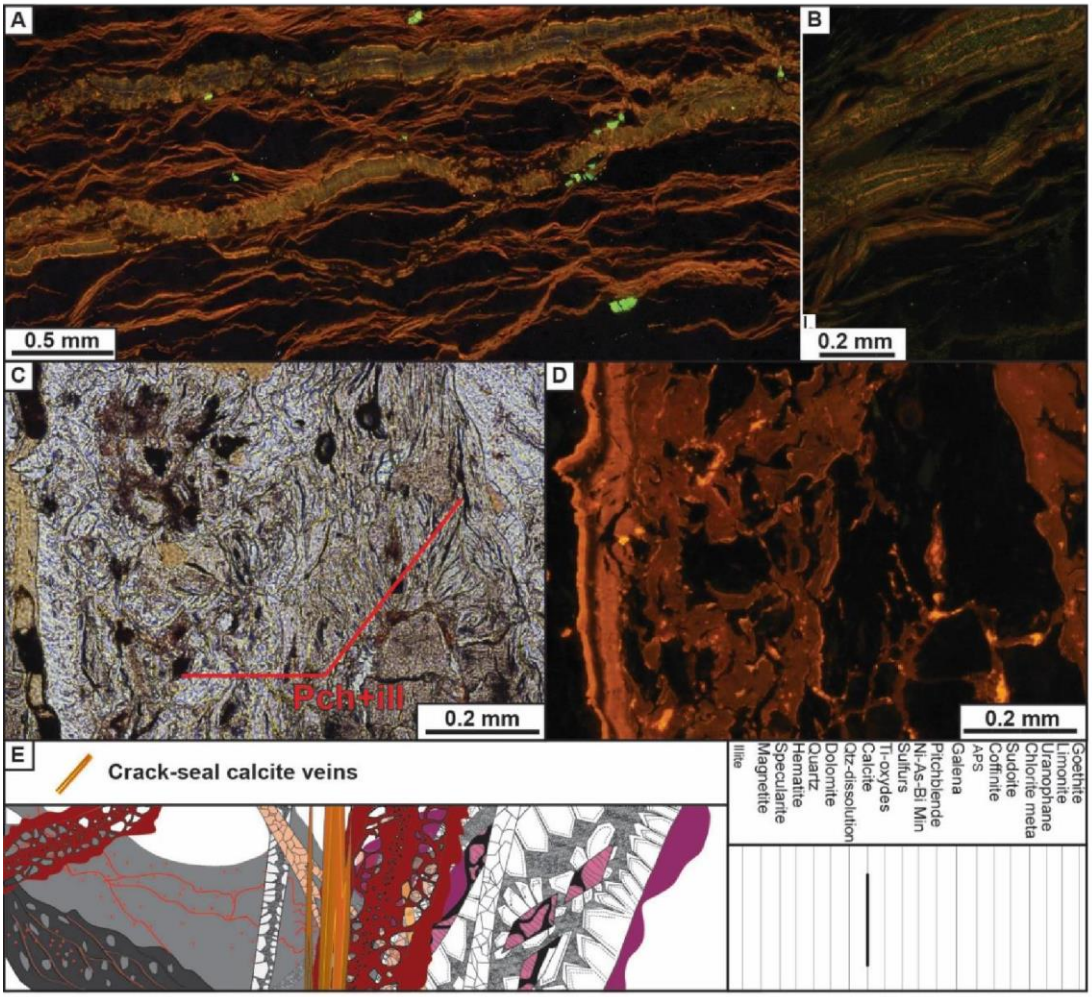

Figure 14: Fracturing stage f6b: A) Cathodoluminescence microscopy photograph showing crack-seal calcite fractures. B) Cathodoluminiscence microscopy photograph. Zoom in a crack-seal fracture exhibiting calcite banding. C-D) Optical and cathodoluminescence photographs respectively of vein in D. Reworked pitchblende is observed as micro-clasts. E) Sketch depicting the textural features with the paragenesis characterizing this fracturing stage.

This fracturing event (f6b) is characterized by a second generation of calcite veins. These veins are anastomosed and the calcite is dark orange to yellowish (Fig. 14A). Cathodoluminescence microscopy observation reveals calcite crack-seal (as defined by Bons et al., 2012) (Fig. 14B). The crack-seal mechanism, together with the orthogonal to the vein edges growth of calcite crystals support a dominant opening mode (mode I). These calcite veins crosscut hematized cataclastic faults of the f6a (Fig. 14C) and locally contain reworked micro-clasts of the mineralized veins of the first stage of mineralization (f5) (Fig. 14D, E). No oriented data are available for these veins that were only observed microscopically and characterized under cathodoluminescence.

4.5.3. Fracturing stage 6c: second stage of uranium mineralization

At this stage (f6c), uranium mineralization occurs in faults of the f6a stage after the calcite event f6b (Fig. 15A). Mineralization is associated with a phase of illite and sudoite alteration (Fig. 15 and 16, Table 1), and is medium grade (i.e. 3.06 %U_3O_8 over 4m). Macroscopically, the mineralization consists of spherulitic pitchblende within fault cataclasites, coating fractures, and leaking out into the foliation in altered host rocks associated with clay alteration (Fig. 15A-C). The spherules of pitchblende are typically rimed by a halo of iron removal or bleaching (Fig. 15B and C). This characteristic rim of bleaching is linked to the pitchblende precipitation process itself with transfer of electrons between Fe^{2+} and U^{6+}: Fe^{3+} travelled very locally and re-precipitated as hematite (Wallis et al., 1985; Alexandre et al., 2006). Microscopically, the spherules are made by pitchblende (clay-shaped) co-precipitated and/or impregnated by fine-grained illite (Fig. 16A-B, Table 1). Although sudoite (Table 1) has been observed associated with this pitchblende, illite remains the dominant clay mineral. The ore mineralogy is made of pitchblende, coffinite, and rare occurrences of galena. Locally, pitchblende displays cubic habit, indicating probable replacement of pyrite (Fig. 16B). The arrangement of ore minerals within some fractures often displays anastomosed textures possibly indicating syn-kinematic precipitation (Fig. 16C and D).

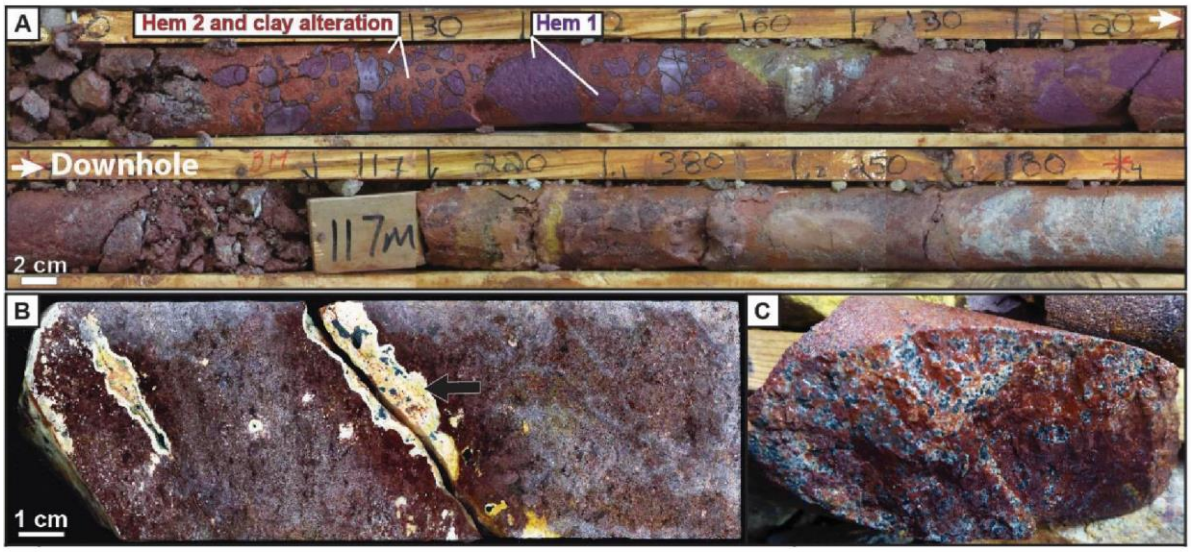

Figure 15: Fracturing stage f6c: A) Drillcore example of a uranium-mineralized cataclastic to ultracataclastic fault rock with reworked purple hematized clasts of the QB, matrix-supported by red hematized clay. B) Core sample photograph showing a mineralized fracture. Pitchblende (black spherulites) is altered to secondary yellow crystals of uranophane (black arrow). The white bleaching halo is characteristic of this mineralization stage (see text for explanation). C) Core sample photograph showing a fracture coated with numerous small spherulitic pitchblende rimed with the halo of bleaching.

In comparison with the first stage of uranium mineralization, this second stage shows three main differences: (i) where quartz veins from the QB are locally re-opened and mineralized, quartz dissolution is more intense (Fig. 16E); (ii) mineralization lacks iron sulfides or other metallic minerals, it is monometallic; and (iii) mineralization spreads far from faults into the host rock (at metre scale) with spherulitic pitchblende, making of this type of mineralization the most extensive ore type in the Contact prospect. Within the mineralized faults f6b, anastomosed calcite veins are locally brecciated and cemented by pitchblende indicating that this mineralization episode postdates f6b (Fig. 16F, G).

Oriented data of mineralized f6c faults display expected similar trends and dip directions (Fig. 17) than non-mineralized f6a faults (Fig. 13), with the same NW-SE and NE-SW two dominant trends. The fracture set 6c and the related uranium mineralization are better developed in the Center Zone where the composite fault zone is wider (Fig. 17).

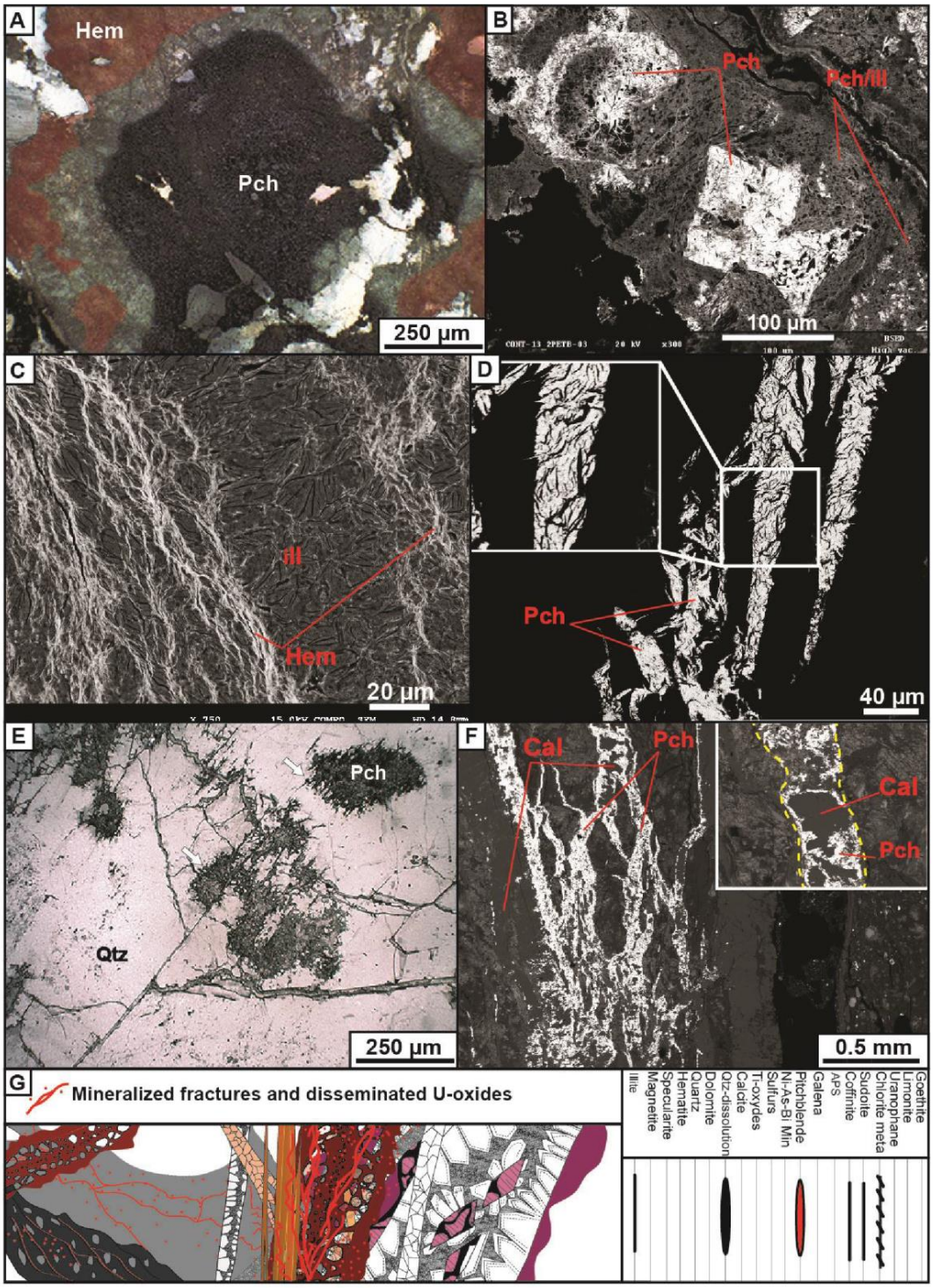

Figure 16: Fracturing stage f6c: A) Transmitted light microscopy photograph. Spherulitic pitchblende surrounded by a halo of bleached hematite. B) SEM photograph showing xenomorphic to cubic pitchblende wrapped by illite. C) SEM photograph showing the anastomosed texture of fractures with hematite and illite typical of the second stage of uranium

mineralization (6c). D) SEM photograph showing the anastomosed texture of pitchblende infill of anastomosed fractures. E) Transmitted light microscopy photograph showing corroded quartz in a QB vein (white arrows) with pitchblende infilling. F) SEM photograph showing brecciated f6b calcite veins cemented by pitchblende. G) Sketch depicting the textural features with the paragenesis characterizing this fracturing stage

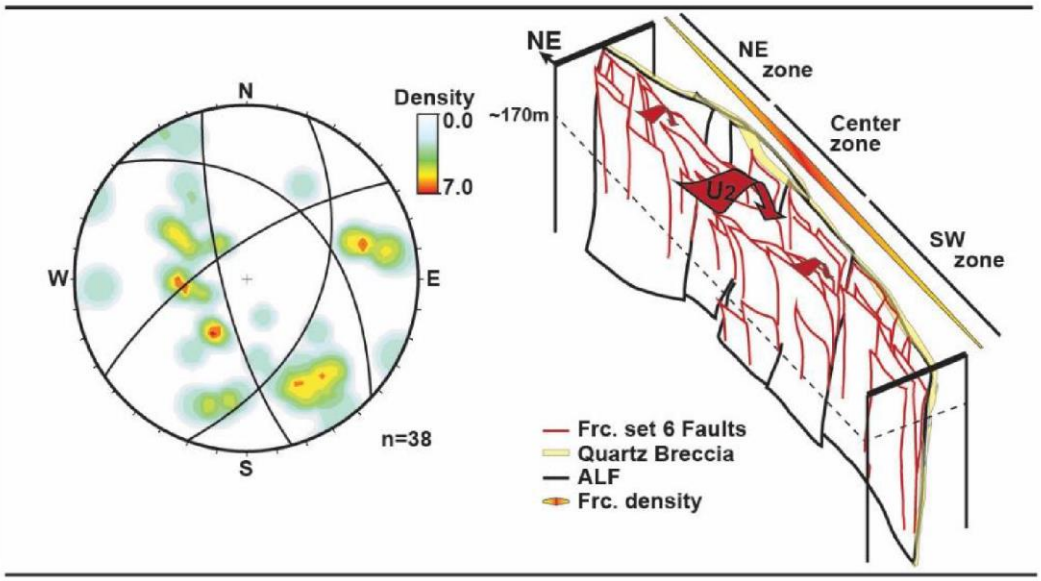

Figure 17: Fracturing stage f6c. Left: Oriented data of f6c mineralized faults and fractures, second stage of uranium mineralization. Dominant trend is NE, with a secondary NW one. Schmidt's lower hemisphere plot. Right: synthetic cartoon showing the spatial arrangement of the composite f6. Red arrows indicate dominant second stage uranium mineralization better developed in the Center Zone where the composite fault zone is larger.

4.6. Fracturing stages 7 and 8: cataclastic faults and post-primary uranium mineralization alteration

These two faulting stages (f7 and f8) represent the latest major tectonic events observed at the Contact prospect, and both are accompanied by strong clay alteration and removal of iron oxides (bleaching).

The f7 stage is characterized by faults that principally re-activated f6a faults. Fault zones exhibit multi-episodic cataclastic fault rocks with reworked clasts from previously formed fault rocks. Fault reactivation is easily recognizable because fault cores are typically greenish colored as a result of the presence of mint green colored clay (Fig. 18A), in strong contrasts with the

reddish color of the previously formed iron oxides (Fig. 19A and B). Clay alteration is usually moderate and is characterized by illitization.

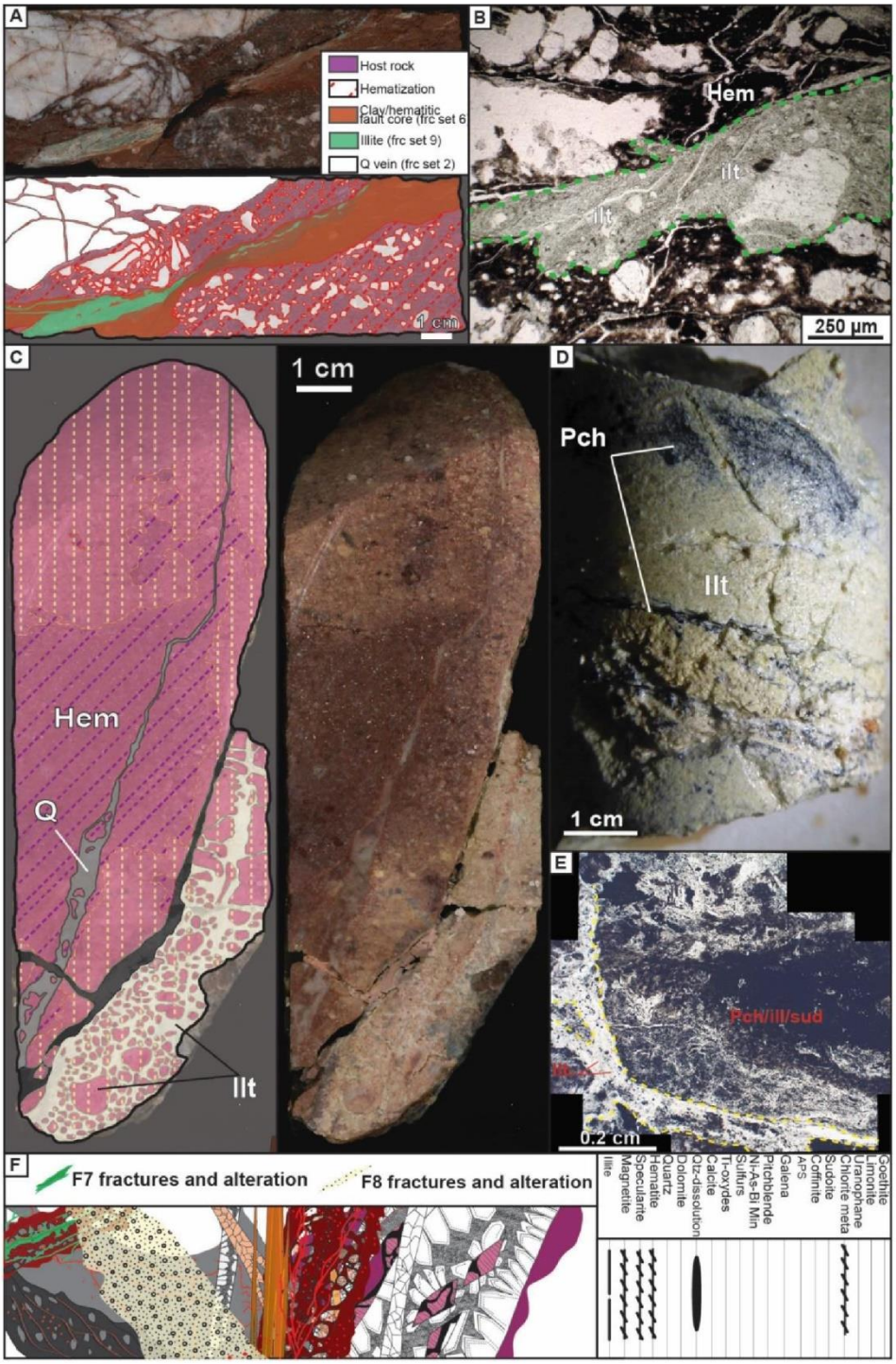

Figure 18: Fracturing stage f7 (A-B) and f8 (C-E): A) Core sample photograph and interpretation showing the typical aspect of a f6 type fault (cataclastic to ultracataclastic fault, light brown)

reactivated during stage f7 (mint green ultracataclastic fault rock at the fault core). B) Transmitted light microscopy photograph at the core of the mint green ultracataclasite formed by illite. C) Core sample photograph and interpretation. Typical protocataclastic fault rock with its characteristic white clay alteration (illitization) and bleaching of iron oxides of f6. D) Same as in picture C but involving a mineralized zone. Note that mineralization (black pitchblende) is crosscut by fracture cemented with illite. E) Transmitted light microscopy photograph. Closer view on a reworked clast (yellow line) of second stage mineralization (pitchblende, illite and sudoite), crosscut by fractures cemented with illite. Thin section was made from sample shown in picture D. F) Sketch depicting the textural features with the paragenesis characterizing this fracturing stage

Chlorite minerals were not observed, suggesting that the particular mint greenish alteration color of f7 might be the result of fine crushing of retrograde metamorphic chlorite (Table 1, f7, relict of chlorite analyzed in a greenish cataclastic fault rock). In addition, the greenish color could also be due to a fine intergrowth of sudoite and illite. The f8 stage is characterized by strongly clay altered protocataclastic (Fig. 18C) to cataclastic fault rocks that crosscut and rework previously formed fractures and ore-bodies (Fig. 18D and E). Fluids driven by these fractures destabilized and removed earlier iron oxides and dissolved and illitized (table 1) other minerals such as chlorite and quartz, thus giving a completely bleached aspect to the rock (Fig. 18D). The whitening illitic clay alteration accompanying f8 is observed as the strongest alteration in the Contact area like in all other Kiggavik deposits, producing destabilization and desilicification of most minerals of the host rock, even leading to a complete argillization of the rock. Therefore it is placed chronologically after the greenish illitic alteration of f7.

The relative chronology between f7 and f8 is unconstrained because crosscutting relationships were not observed at any scale, but both crosscut, thus postdate, the second mineralization stage (Fig.18F). Both fracture sets are similar in clay mineralogy with strong illitization.

Oriented data for f7 and f8 are shown in Figure 19. Mint greenish illite faults (f7) are oriented NE-SW in the NE Zone, and NW-SE to N-S in the SW Zone (Fig. 19A). Strongly whitening clay altered fractures (f8) are oriented N-S and NW-SE in the Center Zone, and NE-SW to E-W in the NE Zone (Fig. 19B).

4.7. Fracturing stage 9: uranium remobilization and supergene alteration (third stage of uranium mineralization)

This stage (f9) is characterized by the local re-concentration of earlier mineralization along reduction–oxidation (redox) fronts marked by the separation between two zones (Fig. 20A-B): one oxidized, reddish to orange, with hematite and goethite (low-temperature iron oxide) minerals and the other reduced, grey, with pitchblende and pyrite. This episode constitutes the third uranium mineralization stage. Mineralization is low to high grade, depending on the remobilized uranium stage, and is only locally present at the Contact prospect. This stage is also characterized by alteration of tetravalent pitchblende and uraninite to secondary hexavalent uranium minerals, like uranophanes and autunite (Fig. 20C) and by alteration of iron oxides with the formation of dusty, yellow limonite coating fractures (Fig. 20D). Although this stage of mineralization is often observed spatially related to limonitic joint corridors, no reliable oriented data could be obtained. Nevertheless, the scattering of oriented data for limonitic joints (Fig. 20E) reflects the reactivation of preexisting fractures as passive conduits for a likely downward flow of oxidizing supergene fluids (Fig. 20F).

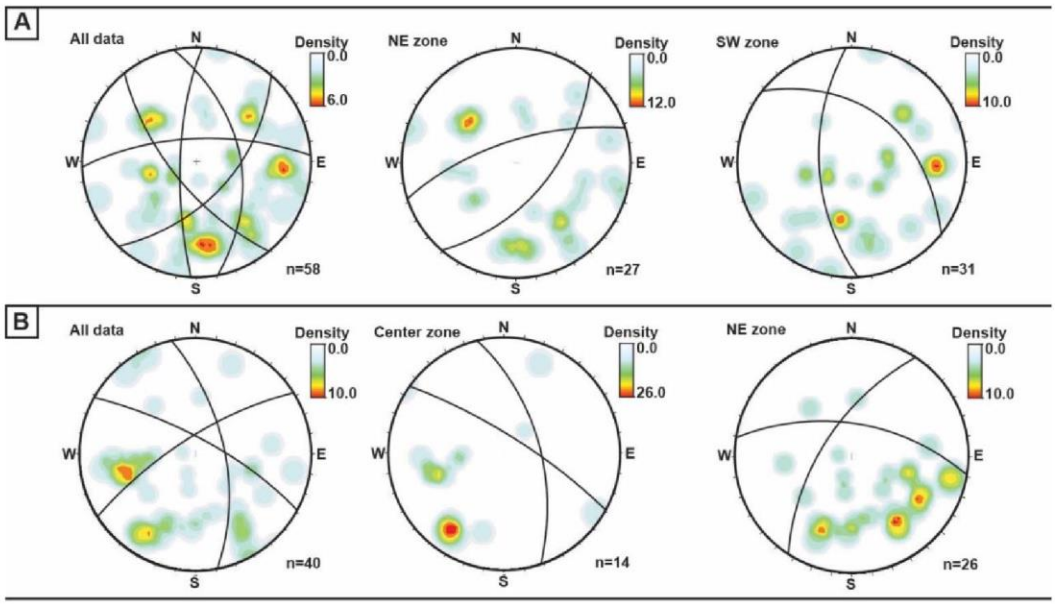

Figure 19: A) Oriented data for faults of f7. No oriented data are available for the Center zone. B) Oriented data for faults of f8. No oriented data are available for the SW zone. Schmidt's lower hemisphere plot.

4.8. Fracturing stage 10: weak fracture reactivation and latest recognizable alteration (bleaching)

The f10 stage is characterized by a weak bleaching of the host rock (Fig. 20A). This bleaching is fracture-controlled, spreads out along the foliation and produces local zones where

iron oxides oxides were destabilized, remobilized and likely re-precipitated locally (orange goethite). This stage is the latest stage of fracturing and alteration observed at the Contact prospect (Fig. 20F).

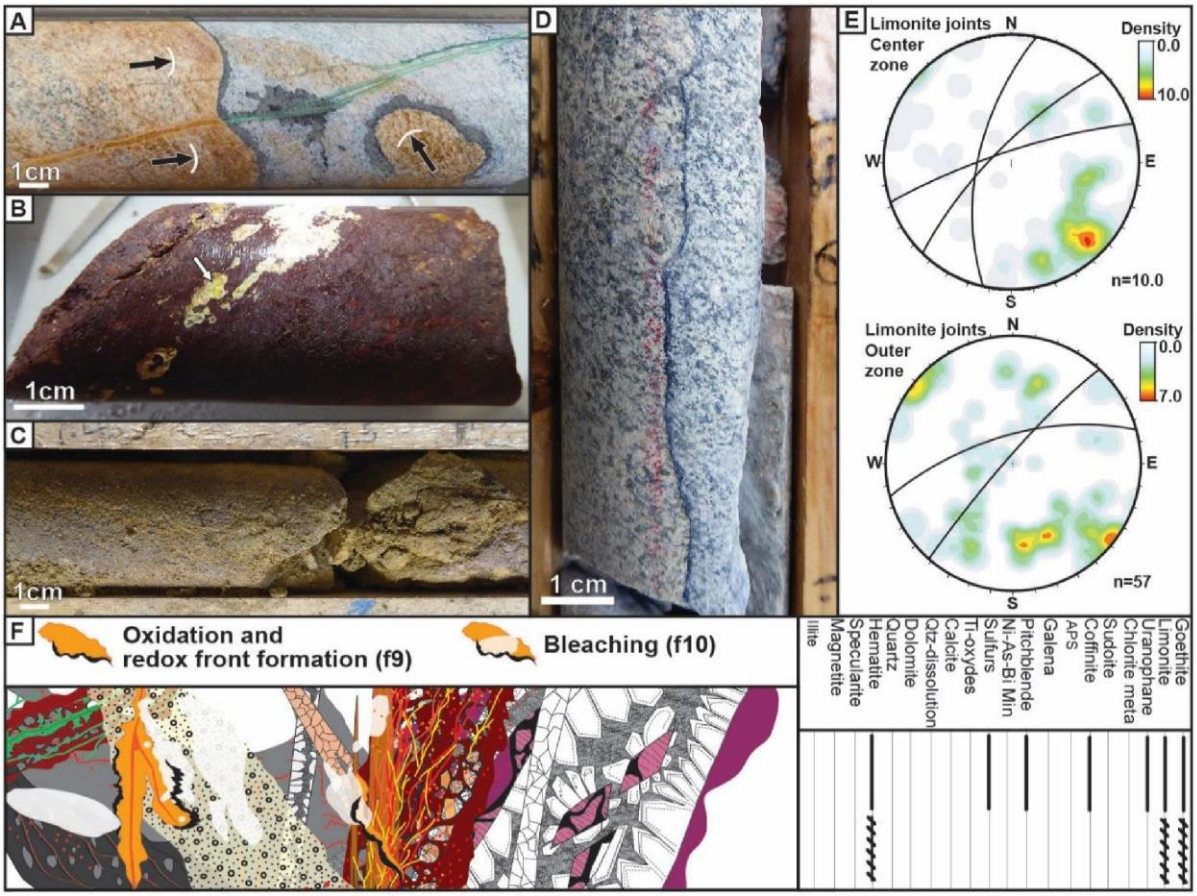

Figure 20: Fracturing stage f9 and f10: A) Drillcore showing redox fronts inducing remobilization of uranium from the first mineralizing stage (stage 5) and re-concentration at the front boundary between the orange oxidized zone (goethite) and the grey reduced zone. Uranium mineralization is in dark grey. B) Drillcore displaying supergene alteration of spherulitic pitchblende (the second stage of mineralization here) to uranophane. C) Drillcore showing supergene alteration of the granitic gneiss characterized by dusty limonite spreading out from fractures. D) Drillcore showing a bleached redox front with remobilized pitchblende but without iron oxides. E) Oriented data for joints (fracture set 9) coated with limonite. Schmidt's lower hemisphere plot. F) Sketch depicting the textural features with the paragenesis characterizing this fracturing stage.

5. Discussion

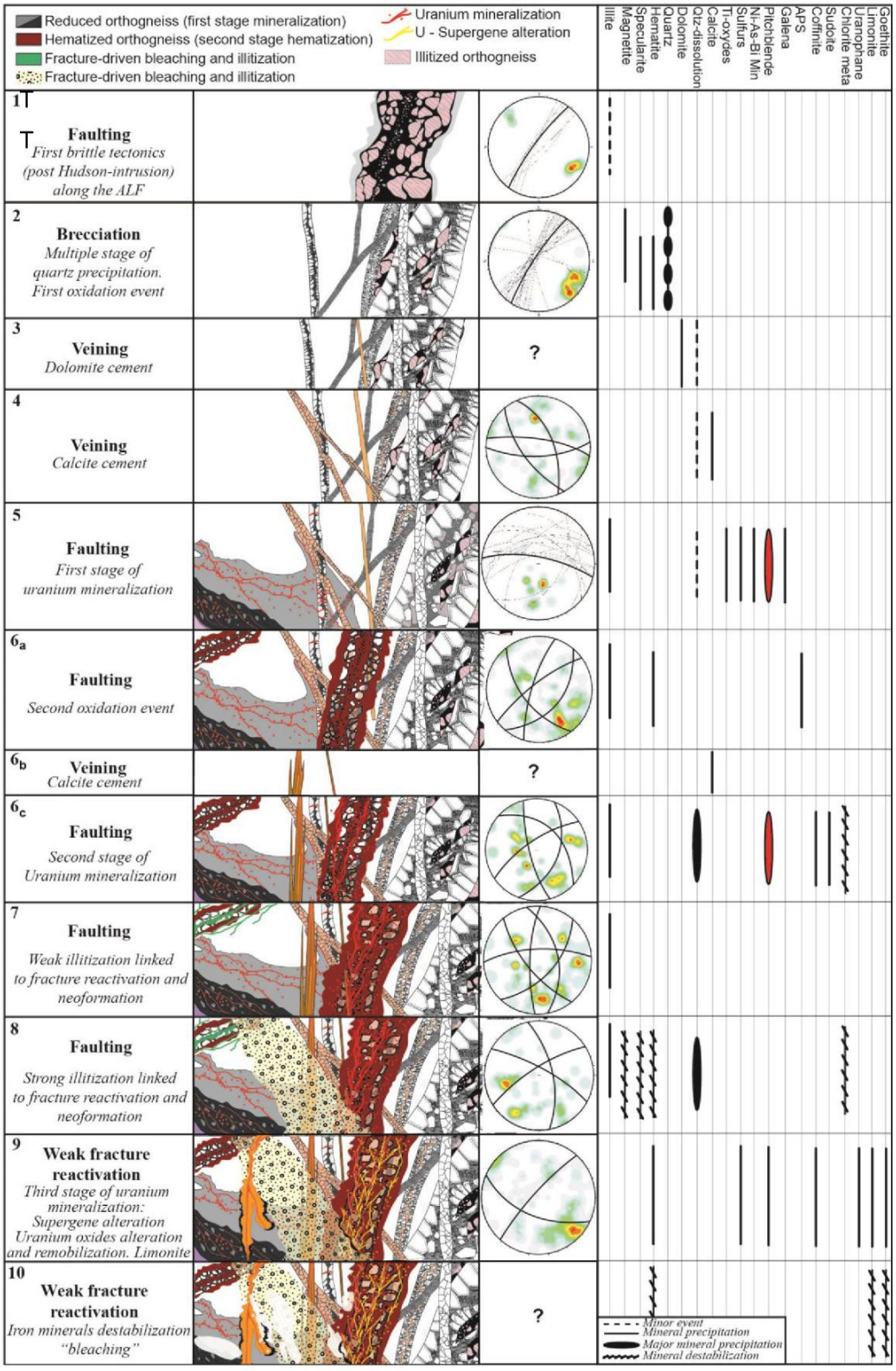

Figure 21: Sequence of structural/microstructural events at the Contact prospect recognized from macroscopic, microscopic, cathodoluminescence and SEM observations. Oriented fracture data in the third column are plotted on Schmidt's lower hemisphere, equal area projection. Mineral paragenesis associated with either mineral precipitation or destabilization is indicated on the last right column.

The identifying characteristics of fracture sets, mineralization and alteration along with the reconstruction of relative chronology (fig. 21) on the basis of observed crosscutting relationships among oriented data allows for the first time in the Kiggavik region to accurately determine the structural controls of uranium mineralization and alteration at the Contact prospect. The synthesis of the fracturing events at the Contact prospect is summarized chronologically in Figure 21, along with oriented data and mineralogical paragenesis. Figure 22 summarizes the main lithological and structural characteristics of the prospect, both in map view (Fig. 22A) and in serial cross sections (Fig. 22C).

As shown on the interpretation of the airborne and ground magnetic maps (Fig. 22B), the ALF is the major structural trend in the area. It runs along the eastern edge of the Hudsonian granite (Fig. 2) and hosts, among others, the Contact prospect (Fig. 2). The Contact prospect is located in the relay zone between the two overlapping AFL fault segments (Fig. 22B). No evidence of ductile or ductile-brittle shear zones was found within the ALF in the Contact prospect.

Furthermore, the ALF likely corresponds to a crustal-scale discontinuity as on the western side of the Kiggavik area the SLIC (Hudson and Nueltin granites) displays a clear NE-trending ellipsoidal shape on aeromagnetic maps (Tschirhart et al., 2013; 2016), which suggests that its emplacement was controlled by a structural discontinuity probably reactivated during the rift episode and deposition of the Baker Lake and Wharton groups. This first fracturing stage is probably linked to the extensional to transtensional tectonics that controlled deposition of these formations between 1850 Ma and 1750 Ma (Hadlari and Rainbird, 2011).

5.1 Role and timing of the QB

The QB is a regional feature that has been recognized in the Contact prospect in all drill holes along the ALF (Fig. 22). The silicification-brecciation event is a key element in the structural analysis which additionally constrains the timing of fracturing and mineralizing events. The fact that (i) quartz fractures of the QB were reactivated at the two main mineralizing

fracturing stages f5 and f6; (ii) fracturing stages f5 to f10 have only been recognized within the hanging wall of the QB, and the mineralization as well (Fig. 22); and (iii) the prospect footprint is parallel to the NE-trending ALF, as depicted in Fig. 22A, supports the role of the QB as a mechanical pre-existing discontinuity that has been tectonically reactivated several times, has strongly partitioned deformation and focused mineralizing fluid flow, leading to greater uranium concentrations at the Contact prospect. On the basis of drillcore oriented data from the QB veins (Fig. 6) and outcrop observations (Fig. 5A), the QB appears to underline a complex fault zone made of major NE-trending fault segments and step overs with complex fractured relay zones in which veins are oriented ENE-WSW, indicating apparent transtensional right-lateral motion. Segmentation and step overs are responsible for along-strike local changes in directions and thickness of the QB: the breccia is much thicker in the Center Zone where the mineralization is better developed than in the outer zones (Fig. 22C). The role played by the QB as a mechanical discontinuity is also attested by the fact that most of the E-W trending mineralized f5 faults stop eastwards and turn toward a NE trend when connecting to the ALF (Fig. 22A). Such a re-orientation of E-W trending faults is also clear at the regional scale south of the JSF (Fig. 2), whereas north of the JSF all E-W faults delineated from magnetic maps extend farther eastwards parallel to the TF (Fig. 2). The QB therefore behaved both as a mechanical discontinuity and as a transversally impermeable but longitudinally permeable barrier, and therefore exerted the first structural control on Uranium mineralization at the Contact prospect (Fig. 23).

On top of that, the QB constrains the maximum age of the observed mineralization in the Contact prospect. As observed on drillcores, the QB cross-cuts Hudson and Nueltin granites dated ca. 1750 Ma (Peterson et al., 2015b), and on outcrops, the QB is covered by the Thelon Formation, thus bracketing the brecciation / silicification event between 1750 Ma and 1667 Ma. The recognition in the QB of microcrystalline mosaic quartz, feathery and ghost sphere growth textures (indicating rapid silica boiling) and crustiform, comb and zonal growth textures (indicating non-boiling fluid conditions) (Bodnar et al., 1985; Dong et al., 1995; Moncada et al., 2012) is typical of geothermal systems (Simmons and Christenson, 1998; Moncada et al., 2012). All these textures show multiple crosscutting relationships indicating that they formed alternatively during the same tectonic phase, and point to an epithermal origin of the QB at the Contact prospect, and more generally in the Kiggavik area. This epithermal origin is also supported by the presence of two groups of fluid inclusions with low temperature-high salinity and high temperature-low salinity, respectively (Chi et al., 2016) as observed in the same type of quartz textures by Turner (2000) and Turner et al., (2001) in the Mallery Lake epithermal Au-

Ag deposit, 50km south of Kiggavik. The QB occurrence at the Contact prospect thus reflects a major silicification event in the region that predated deposition of the Thelon sandstones at ca. 1750 Ma (Turner et al., 2001; Hadlari and Rainbird, 2011) in a transtensional right-lateral tectonic setting. The first pattern of deformation identified in this work -the f1 brittle faulting that is observed along the ALF- therefore occurred after the Hudsonian intrusive event at 1850 Ma and before the quartz-sealed breccia at ca. 1750 Ma.

5.2 Structural controls and timing of uranium mineralizations

Three stages of uranium mineralization have been recognized at the Contact prospect. Their timing is inferred from crosscutting relationships and complementary information from the existing literature about uranium deposits at Kiggavik.

5.2.1 First stage of uranium mineralization

The oldest stage of uranium mineralization, the fracturing stage f5 (Fig.21), is structurally controlled by faults and related fractures, as well as by micro-fracturing and re-activation of QB veins. Oriented data indicate a dominant E-W strike for the mineralized faults and a NW-SE and E-W strike for the associated fractures; secondary directions are ENE-WSW and ESE-WNW (Fig. 11). Re-activated, orthogonally micro-fractured and mineralized quartz veins of the QB show dominant NE-SW and minor NW-SE trends (Fig. 11), consistent - as expected- with oriented data for quartz veins of the QB along the ALF (Fig. 8C). Locally, mineralization is associated with dolomite-calcite veins, which display NW-SE and E-W trends; complementary observations in drillcores from other deposits in the Kiggavik area, for instance occurrence of stepped calcite veins with similar orientations (Grare et al., 2017), allows the interpretation of this set of fractures as right-lateral shear veins (mixed mode I-mode II veins). The E-W trending, Thelon-type faults are the second structural control in the Contact prospect. They formed as right-lateral strike-slip faults in response to a compressional stress oriented approximately WNW-ESE (Anand and Jefferson, 2017; Johnstone et al., 2017). Such kinematics was also recorded in the ENE-WSW Thelon fault, during and after deposition of the Thelon Formation (Anand and Jefferson, 2017). As already mentioned in Section 5.1, most of these E-W trending mineralized f5 faults stop eastwards and connect to the ALF, while turning toward a NE trend (Fig. 22A), which explains the reactivation of the QB veins and the change in orientation of part of the fractures moving NE-ward.

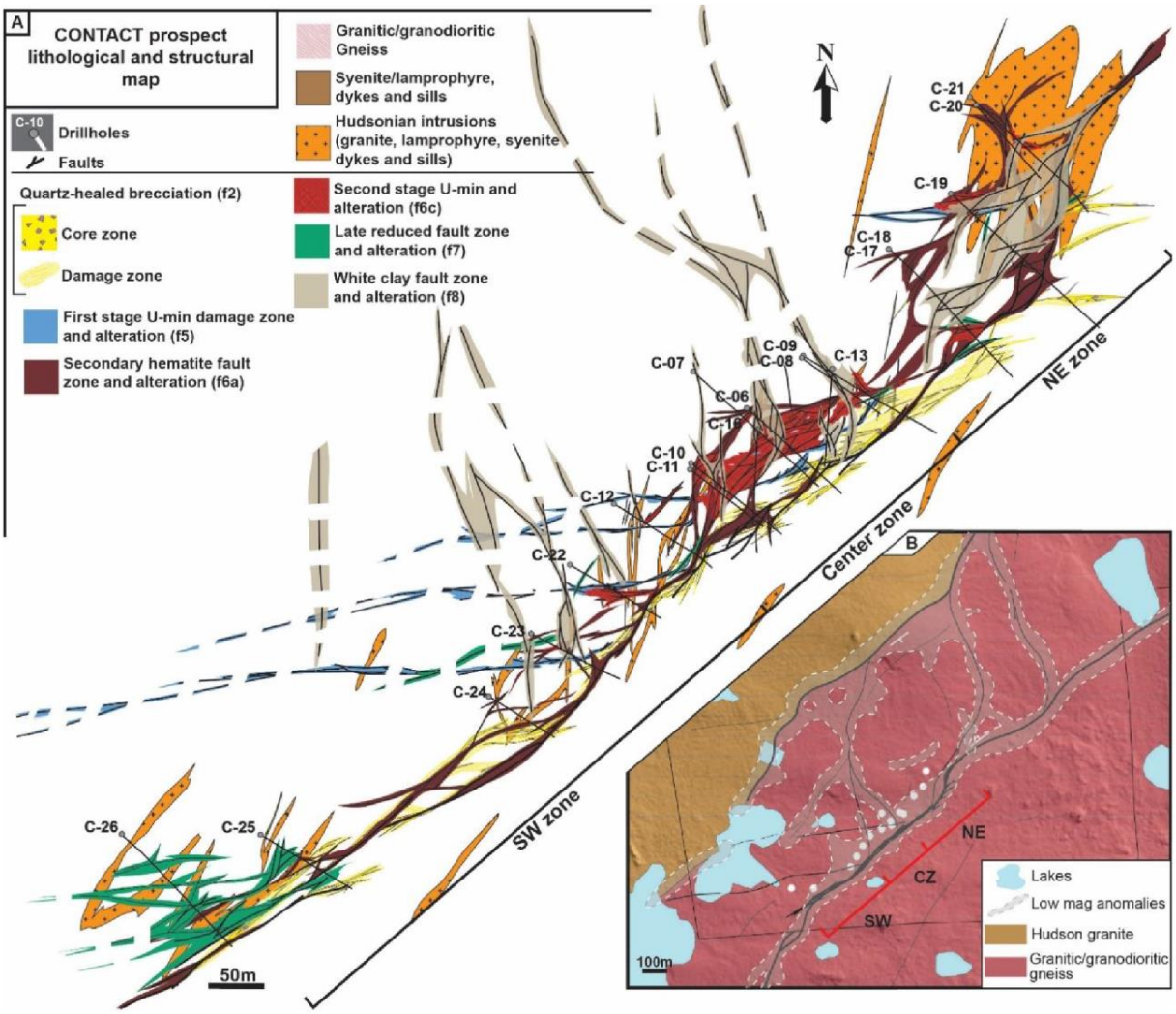

Figure 22: A) Lithology and structural map of the Contact prospect. Fractures sets f1, f5, f6, f7 and f8 are represented, including the two stages of primary uranium mineralization (f5, f6c); the other fractures sets are not represented due to the small scale of related fractures or because they could not be linked to any major fault. B) Insert map of the local cartographic organisation of the ALF, location of the drillholes (white dots) and connections between the northern and southern branches of the ALF. C) Serial NW-SE oriented sections across the Contact prospect. Holes Cont-04 and Cont-05 were drilled by former company exploring the Kiggavik area, they are vertical and do not display any oriented data. Furthermore, they do not crosscut any uranium mineralization. Set f8, which drives white clay alteration, consists of NNW faults steeply dipping to the East and NE in the Center zone, so they appear with an apparent shallow dip on NW cross-sections.

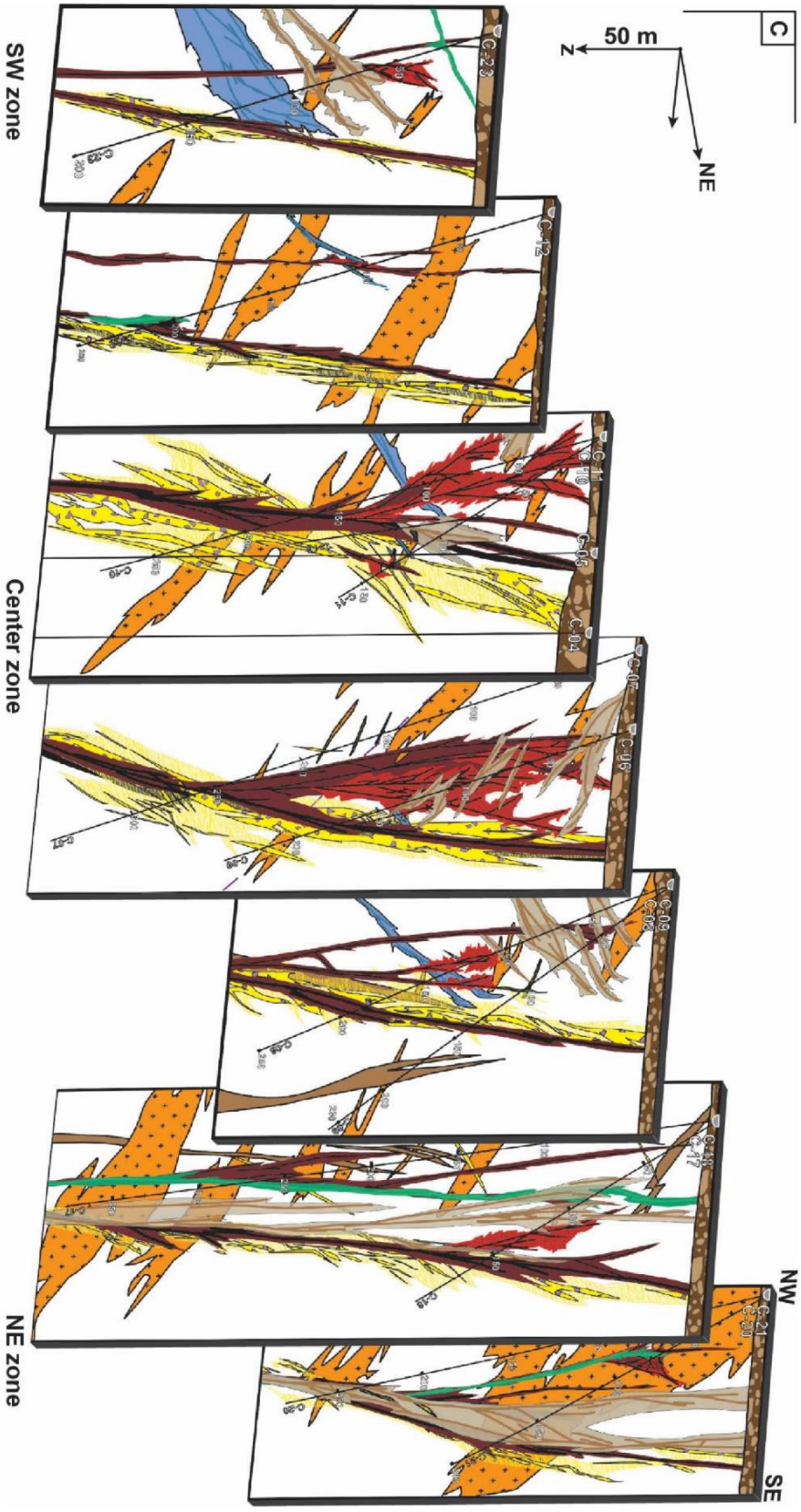
C
50 m
N
NE
SW zone
Center zone
NE zone
NW
SE

At the Contact prospect, the first stage of uranium precipitation (f5) corresponds to a polymetallic mineralization with pitchblende, coffinite, uraniferous titanate, titanium-oxides with pitchblende micro-inclusions, sulfides (pyrite, chalcopyrite and bravoite), occurrences of native bismuth and unidentified As-Ni-Co (+-U) compounds, whereas the second (f6c) and third stages (f9) correspond to monometallic mineralization with pitchblende, coffinite, rare occurrences of galena and pyrite. Rutile, brannerite-like and uraniferous titanium-bearing minerals are not common minerals in unconformity type mineralization in the Athabasca Basin deposits (e.g., Jefferson et al., 2007). Furthermore, the polymetallic mineralization described in the Athabasca uranium deposits are sandstone-hosted (e.g., Cigar Lake and Midwest deposits), while mineralization hosted in basement are predominately monometallic (e.g., McArthur River and Eagle Point deposits; Ruzicka, 1989; 1996; Jefferson et al., 2007). Brannerite is described as related to pre-Athabasca mineralizing events in the Beaverlodge District (Dieng et al., 2013), in the Baker Lake Basin (Miller, 1980), and at the Karpinka uranium prospect in the southern Athabasca Basin (Williams-Jones and Sawiuk, 1985). By analogy, the presence of brannerite minerals in the first stage of mineralization at the Contact prospect may therefore reflect a pre-Thelon uranium source, probably an evidence of relict “magmatic” uranium mineralization present at Contact, described in other deposits of the Kiggavik area (Grare et al., 2017), and remobilized by hydrothermal fluids during the first mineralizing stage. F5 postdates the formation of the QB, which is bracketed between 1750 Ma and 1667 Ma, and thus constrains this mineralization to be younger than 1667 Ma. Pitchblendes within quartz veins reveal U-Pb isotopic ages of 1403±10 Ma (Farkas, 1984) at the Kiggavik Main Zone and of 1520±79 Ma at the Bong deposit (Sharpe et al., 2015). The age of ca. 1500 Ma is the age of the emplacement of the Kuungmi lavas over the Thelon Basin (1540±30 Ma, Chamberlain et al., 2010). This age was obtained in several studies throughout the Western-Churchill province (Turner et al., 2003; Bridge et al., 2013; Gandhi et al., 2013; Dieng et al., 2013; Sheahan et al., 2015) and is possibly linked to a regional thermal event possibly reflecting a craton-scale process. If this thermal event has reset the U-Pb isotopic system (Davis et al., 2011; Peterson et al., 2015b), then the ages of the first stage of faulting and mineralization could be bracketed between ca. 1667 Ma and 1420 Ma; although this remains speculative to date.

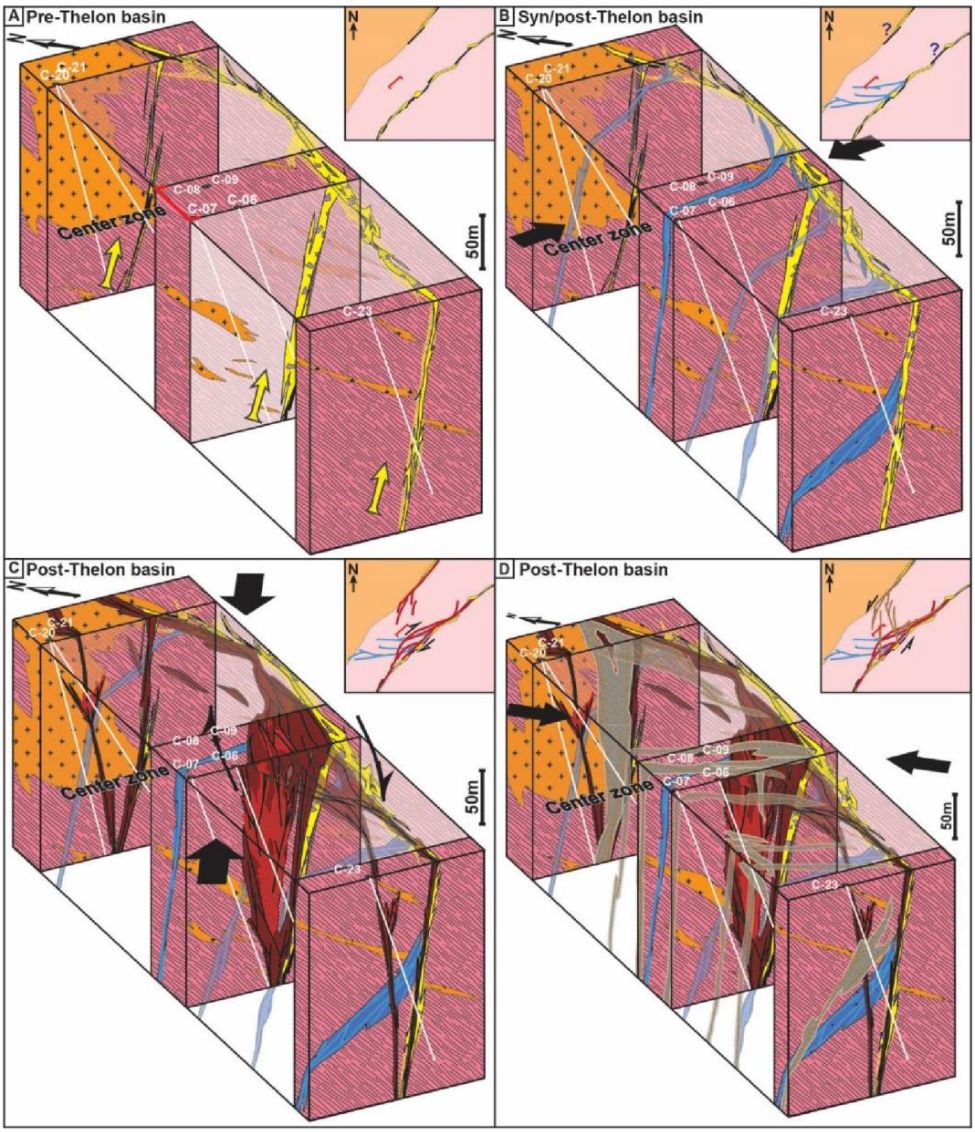

Figure 23: 3D synthetic blocks of the Contact prospect with the main fracturing stages depicted. A) Quartz breccia (f2) along the NE-SW ALF. B) First stage of uranium mineralization (f5). C) Second stage of uranium mineralization (f6). D) Late clay alteration (f8), reworking uranium mineralization of stages 1 and 2.

5.2.2 Second stage of uranium mineralization

Stage f6 corresponds to a new tectonic event responsible for the second stage of mineralization at Contact. This event can be divided into three sub-stages, f6a to f6c, because of the close spatial relationships and the same typological characteristics of the fracture sets (Figs. 12 and 15). As explained above, the sub-stages f6a and f6c display strong similarities in fault rocks, alteration type and oriented data (Figs. 13 and 17), but are separated by a sub-stage

of calcite vein formation, f6b, and mineralization only occurs in f6c veins (Fig. 15). Although a NE trend of f6 fracture set is dominant (Fig. 13), this fracture stage displays a more complex spatial architecture than the f5 that drove the first stage of mineralization, with conjugate NW-trending fractures (Fig. 17), conjugate dip directions particularly in the Center Zone, and anastomosing fault arrangement mimicking the anastomosed geometries observed at the micro-scale (Fig. 16C and D). On the basis of drillhole correlation and oriented data, we deduce that faults become vertical at depth, whereas all fracture sets turn to the NE and connect at depth to the ALF (QB) zone (Figs. 22C and 23). This occurs specifically in the Center Zone, making it a wider fractured zone, which likely enhanced fluid circulation and uranium precipitation. As fractures density decreases when moving from the Center to the outer zones, mineralization does too (Fig. 22). We consider that sub-stages f6a, b and c are synchronous of the same tectonic phase, corresponding to successive tectonic pulses. The lack of kinematic indicators prevents any determination of the precise kinematics for this fracture stage. Nevertheless, the cartographic organisation suggests it has occurred under right-lateral strike-slip kinematics of the ALF (fig. 23) enhancing local fluid circulation. This would be consistent with the NE-SW oriented compression prevailing at this stage (Grare et al., 2017) as deduced from other places in the Kiggavik area, causing dextral motion along the reactivated ALF. This tectonic phase and the related reactivation of the ALF are considered as the third structural control of mineralization at the Contact prospect.

Other studies of the Kiggavik deposits have described and dated pitchblende with characteristics similar to those of the second stage of uranium mineralization (f6c) in Contact; U-Pb isotopic ages range between ca. 1200 and 1300 Ma with various episodes of pitchblende precipitation (Shabaga et al., 2017a, b; Ashcroft et al., 2017). Additionally, at the Kiggavik Main Zone deposit, the orebody is cut by the 1267±2 Ma Mackenzie dikes (Fuchs et al., 1980; Lecheminant and Heaman, 1991). Therefore this second mineralizing stage would be older than the Mackenzie intrusive event, being therefore bracketed between ca. 1500 Ma and 1270 Ma. The presence of sudoite (Table 1) in the mineralogical association with uranium minerals within f6c fractures fingerprints the circulation of basinal brines (Percival et al., 1989; Renac et al., 2002; Beaufort et al., 2005). Unfortunately, our study does not allow determining whether this basinal fluid introduced more uranium into the system or just remobilized the pre-existing mineralization due to the oxidizing nature of brines (Fayek and Kyser, 1997; Cuney, 2005). However, basinal brines would have likely leached uranium from the various stocks available in the Kiggavik area: metamorphosed epiclastic rocks of the Puqik Lake Formation (Johnstone et al., 2017), rhyolitic flows of the Wharton group (Blake, 1980; Peterson, 2015), fluorapatite-

cemented breccia at the base of the Thelon Formation (Davis et al., 2011), and/or much more probably the uranium concentrated during the first stage of mineralization.

Cathodoluminescence observations on quartz in mineralized zones reveal haloes with distinct colors (yellow-red) around fracture-bearing ore minerals. This phenomenon, known as irradiation halo, is due to the structural modification of quartz linked with the travel of an alpha particle through the crystal lattice (Meunier et al., 1990; MacRae et al., 2013), inferred as being due to uranium remaining in contact with quartz crystal or uraniferous fluid flow through the fracture. As such, even when uranium minerals are no longer observable (i.e., due to later remobilization), this interaction between quartz and uranium allows assessing whether or not uranium was present in the host rock or in fluids that circulated through a fault zone.

5.3 Post-primary ore fracturing and alteration

Two faulting stages occurred after fracturing stages f7 and f8. They represent the latest major tectonic events observed at the Contact prospect, and both are accompanied by strong clay alteration and iron oxides bleaching. Oriented data for f8 display NE-SW and NNW-SSE set trends. The first trend is interpreted as related to the reactivation of the previously formed f6 faults, while the second would correspond to newly formed faults. N-S faults highlight the formation of a hard-linked overlapping step over through the final branching of both fault segments of the ALF leading to the present-day architecture of the relay fault zone array (Fig. 22A, regional insert-map). We speculate that this fault relay zone developed in response to left-lateral strike-slip kinematics, favoring connection of the two branches of the ALF and enhancing circulation of acidic, reducing fluids. Such kinematics could have occurred in response to a NNW-SSE oriented compression (Fig. 23).

Interestingly, the reducing fluids that circulated thanks to fault reactivation and new rock fracturing at stage f8 caused intense desilicification, illitization, and bleaching of the host rocks through dissolution and destabilisation of iron-bearing minerals (mainly chlorite and hematite). This strong argillization altered the original texture of rocks and lowered their electrical resistivity, density and magnetic susceptibility leading to significant geophysical anomalies that facilitated the discovery of the uranium deposits in Kiggavik, including the Contact prospect (see Roy et al., 2017 and references therein). Nevertheless, unlike the classic unconformity-related uranium deposits in the Athabasca Basin where clay alteration haloes around the ore bodies are associated with mineralizing stages (Hoeve and Quirt, 1984; Fayek and Kyser, 1997; Jefferson

et al., 2007), the strongest clay alteration event (f8) in the Contact prospect clearly postdates the second stage of mineralization (fig. 23).

The presence of goethite (that usually forms at low temperature), limonite (that usually results from supergene alteration of iron oxides), along with the presence of redox fronts, characterizes the in-coming of supergene, oxidizing, low temperature fluids of meteoric origin (Devoto, 1978; Mercadier et al., 2011) circulating through f9 fractures. It is unknown whether there was only remobilization or also new uranium input at that stage. However, the nature of the circulating fluids, which is very different in terms of chemistry (chlorinity, pH, NaCl content) from basinal brines (Richard et al., 2011), makes it unlikely that a new significant uranium input occurred. Moreover, the supergene mineralization is observed locally at the Contact prospect, which indicates that this fluid circulation did not have a significant impact on the grade and extension of the uranium ore body. Although this stage of mineralization is observed often spatially related to limonitic joint corridors, no reliable oriented data could be obtained. Nevertheless, the scattering of oriented data for limonitic joints (Fig. 20E) reflects the re-activation of previously formed fractures and utilisation of other fracture zones as passive conduits for an inferred downward penetration of oxidizing supergene fluids. This stage is considered the fourth structural control in the Contact prospect. The supergene fluid-related mineralization (redox front type) of stage f9 has been dated in other deposits of the Kiggavik area at ca. <1200 Ma, with various episodes of uranium precipitation between ca. 850 and 500 Ma, as also at ca. 300 and 100 Ma (Farkas et al., 1984; Sharp et al., 2015; Shabaga et al., 2017a, b; Ashcroft et al., 2017).

A final fracturing event associated with f10, occurred at Contact and is responsible for post-redox front bleaching. The origin and the nature (fluid or gas?) of the reducing fluid remain unconstrained. This bleaching stage does not seem to be associated with any clay alteration, but only with iron-bearing minerals destabilization. Contrary to this, at the Eagle Point uranium deposit in Athabasca, Mercadier et al., (2011) proposed that this bleaching post-redox front was associated with kaolinization and linked to renewed circulation of meteoric-derived fluids.

Conclusions

This work describes in detail the multi-scale organization of the mineralized fracture network at the Contact uranium prospect and places it into the long polyphase tectonic history of

the Kiggavik area. This is the first time such a mineralized and non-mineralized fracture network is decrypted and described in unconformity-related uranium deposits hosted within the metamorphosed basement. The identification and characterization of the nature and kinematics of fracture sets along with the reconstruction of the relative chronology on the basis of observed crosscutting relationships, mineral paragenesis, and widespread oriented data allows for identifying four major structural controls. These structural controls can help and guide future exploration in the Kiggavik uranium province to help find new deposits.

Ten fracturing stages (f1 to f10) were identified with three stages directly controlling mineralization. Each of them is characterized by distinct fault rocks, fracture infill, and host rock alteration. The key conclusions are summarized as follows:

1- There is a long lived and polyphase brittle tectonic history in the Kiggavik area, spanning from the emplacement of the Hudsonian Schultz Lake Intrusive Complex at ca. 1850 Ma, to the later stages of circulation of supergene meteoric fluids, which has been recorded by various fracture generations overprinting the Andrew Lake Fault (ALF) and before the emplacement of the Mackenzie dikes at 1267 Ma. The most significant event that exerted the strongest structural control was the formation of the quartz breccia (QB) at ca. 1750 Ma. The QB acted as a mechanical barrier that partitioned deformation and favored later fracturing within its hanging wall. The silicified AFL was also a transverse impermeable barrier for fluids, focusing fluid flow longitudinally (or vertically) dominantly within the hanging wall. This tectonic episode was critical in preparing the impermeable metamorphic gneissic basement for later fluid circulation and uranium entrapment, constituting the first structural control.

2- Three stages of uranium mineralization were determined.

   a. Mineralization precipitated during the first stage (f5) is the highest grade (e.g., 4.76 % U3O8 over 50cm) and is polymetallic with colloform to xenomorph pitchblende and coffinite, uraniferous titanate, titanium-oxides with pitchblende micro-inclusions and sulfides (pyrite, chalcopyrite, and bravoite). Mineralization is associated with quartz dissolution in veins and weak grey clay alteration of the host rock. The uranium-bearing fluids are of unconstrained origin. In this first stage, mineralization is controlled by E-W faults and reactivated, micro-fractured quartz veins of the QB (f2). As the QB is inferred to be bracket between 1750 Ma and 1667 Ma, this mineralizing event postdating the QB, has to be younger than 1667 Ma. F5 mineralized faults formed in response to a compressional stress oriented approximately WNW-ESE

leading to right-lateral strike-slip motion along these faults which constitute the second structural control.

b. The second stage of mineralization is controlled by NE-trending, faults and fractures (f6c), which drove oxidizing fluids and partially reactivated, likely under right-lateral strike-slip kinematics, and overprinted the ALF. They constitute the third structural control. Mineralization is low to medium grade (e.g., 3.06 % U_3O_8 over 4m) and is essentially monometallic with pitchblende and coffinite. Spherulitic pitchblende is disseminated within fault cataclasites, nearby host lithologies or coating fractures. The spherules of pitchblende are typically rimmed by a halo of iron bleaching and are formed by pitchblende (clay-shaped) co-precipitating with fine-grained illite, locally associated with sudoite. This stage of mineralization is linked to oxidizing basinal brines, following an episode of hematization, and is the most penetrative outward from faults into the host rock. It has not been determined whether the brines remobilized preexisting mineralization or brought new uranium into the system. This tectonic and mineralization event likely occurred between ca. 1500 Ma and 1270 Ma.

c. In the third stage, mineralization was remobilized by supergene oxidizing fluids circulating though pre-existing fractures of various orientations and re-concentrated uranium along redox fronts. Mineralization is low to high-grade with secondary uranium minerals, such as uranophane and alteration of iron oxides to limonite. The exploitation of the pre-existing fractures networks as conduits for downward permeating supergene fluids is considered to be the fourth structural control in the Contact prospect. By association with other dating of Kiggavik deposits, this mineralization occurred at ca. <1200 Ma, with various episodes of uranium precipitation between ca. 850 and 500 Ma, as also at ca. 300 and 100 Ma.

3- Unlike the classic unconformity-related uranium deposits in the Athabasca Basin, in which clay alteration extends as haloes around the ore bodies associated with mineralizing stages, the strongest clay alteration of event f8 postdates the two stages of primary uranium mineralization in the Contact prospect, and seems to have caused significant uranium remobilization. This suggests that the basement-hosted Contact prospect is a relict of what was once a bigger deposit, and that a part of uranium ore could have been remobilized toward the now eroded overlying Thelon sandstones.

Acknowledgements

The authors thank AREVA and AREVA Resources Canada for the full financial support and access to the Kiggavik camp and exploration data. Special thanks to Senior geoscientist D. Quirt and geologists R. Zerff, R. Hutchinson, K. Martin, and D. Hrabok for their help and enriching discussions during field work and data interpretation. The detailed reviews by Dr. Stefan Kruze, two anonymous reviewers, and Associate Editor David Lentz, have greatly improved the quality of this paper.

References

Adams, S.S., and Saucier, A.E., 1981. Geology and recognition criteria for sandstone uranium deposits in mixed fluvial-shallow marine sedimentary sequences, south Texas. Final report, US-DOE, GJBX-2(81)

Alexandre, P., Kyser, K., Polito, P., Thomas, D., 2006. Alteration Mineralogy and Stable Isotope Geochemistry of Paleoproterozoic Basement-Hosted Unconformity-Type Uranium Deposits in the Athabasca Basin, Canada. Econ. Geol. 100, 1547 LP-1563

Alexandre, P., Uvarova, Y., Kyser, T.K., 2012. Origin of uranous and uranyl minerals at the Centennial deposit, Athabasca basin, Northern Saskatchewan, Canada. Can. Mineral. 50, 693–704. doi:10.3749/canmin.50.3.693

Annesley, I.R., Madore, C., Portella, P., 2005. Geology and thermotectonic evolution of the western margin of the Trans-Hudson Orogen: evidence from the eastern sub-Athabasca basement, Saskatchewan. Can. J. Earth Sci. 42, 573–597. doi:10.1139/e05-034

Ashcroft, G.S., Fayek, M.F., Quirt, D., Camacho, A., Jefferson, C.W., 2017. The geochemistry and geochronology of the End Deposit, NE Thelon region, Nunavut Canada: An insight to the Athabasca basin's closest relative. Poster presented at 2017 GAC MAC.

Baudemont, D., Fedorowich, J., 1996. Structural control of uranium mineralization at the Dominique-Peter Deposit, Saskatchewan, Canada. Econ. Geol. 91, 855–874. doi:10.2113/gsecongeo.91.5.855

Baudemont, D., and Pacquet, A., 1996. The Sue D and E Uranium Deposits, Northern Saskatchewan: Evidence for structurally controlled fluid circulation in the Athabasca Basin. MinExpo'96 Symposium. Adv. in Saskatchewan Geol. and Min., 85–94

Baudemont, D., and Reilly, B., 1997. Thelon Project – 1997 Reconnaissance mapping and structural geology. Cogema internal report. 97-CDN-100-01. 43p.

Beaufort, D., Patrier, P., Laverret, E., Bruneton, P., Mondy, J., 2005. Clay Alteration Associated with Proterozoic Unconformity-Type Uranium Deposits in the East Alligator Rivers Uranium

Field, Northern Territory, Australia. Econ. Geol. 100, 515–536. doi:10.2113/gsecongeo.100.3.515

Berman, R.G., Davis, W.J., Pehrsson, S., 2007. Collisional Snowbird tectonic zone resurrected: Growth of Laurentia during the 1.9 Ga accretionary phase of the Hudsonian orogeny. Geol. 35, 911–914. doi:10.1130/G23771A.1

Bodnar, R.J., Reynolds, T.J. and Kuehn, C.A. 1985. Fluid inclusion systematics in epithermal systems. In Geology and Geochemistry of Epithermal Systems (B.R. Berger & P.M. Bethke, eds.) Society of Economic Geologists, Reviews in Economic Geology, 2, 73-98

Bons, P.D., Elburg, M.A., Gomez-Rivas, E., 2012. A review of the formation of tectonic veins and their microstructures. J. Struct. Geol. 43, 33–62. doi:https://doi.org/10.1016/j.jsg.2012.07.005

Bridge, N.J., Banerjee, N.R., Pehrsson, S., Fayek, M., Finnigan, C.S., Ward, J., and Berry, A., 2013. The Lac Cinquante uranium deposit, western Churchill Province, Nunavut Canada. Exploration and Mining Geology, 21: 27–50; doi 0964-1823/00

Bright, S., Conner, G., Turner, A., Vearncombe, J., 2014. Drillcore, structure and digital technologies. Appl. Earth Sci. 123, 47–68. doi:10.1179/1743275814Y.0000000051

Bruneton, P., 1993. Geological environment of the Cigar Lake uranium deposit. Can. J. Earth Sci. 30, 653–673. doi:10.1139/e93-054

Chamberlain, K.R., Schmitt, A.K., Swapp, S.M., Harrison, T.M., Swoboda-Colberg, N., Bleeker, W., Peterson, T.D., Jefferson, C.W., Khudoley, A.K., 2010. In situ U–Pb SIMS (IN-SIMS) micro-baddeleyite dating of mafic rocks: Method with examples. Precambrian Res. 183, 379–387. doi:10.1016/j.precamres.2010.05.004

Chester, F.M., Logan, J.M., 1986. Implications for mechanical properties of brittle faults from observations of the Punchbowl fault zone, California. Pure Appl. Geophys. 124, 79–106. doi:10.1007/BF00875720

Childs, C., Watterson, J., Walsh, J.J., 1996. A model for the structure and development of fault zones. J. Geol. Soc. London. 153, 337–340. doi:10.1144/gsjgs.153.3.0337

Childs, C., Manzocchi, T., Walsh, J.J., Bonson, C.G., Nicol, A., Schöpfer, M.P.J., 2009. A geometric model of fault zone and fault rock thickness variations. J. Struct. Geol. 31, 117–127. doi:https://doi.org/10.1016/j.jsg.2008.08.009

Chi, G., Haid, T., Quirt, D., Fayek, M., Blamey, N., Chu, H., 2016. Petrography, fluid inclusion analysis, and geochronology of the End uranium deposit, Kiggavik, Nunavut, Canada. Miner. Depos. 1–22. doi:10.1007/s00126-016-0657-9

Cuney, M.L., 2005. World-class unconformity-related uranium deposits: Key factors for their genesis, in: Mao, J., Bierlein, F.P. (Eds.), Mineral Deposit Research: Meeting the Global Challenge: Proceedings of the Eighth Biennial SGA Meeting Beijing, China, 18-21 August 2005. Springer Berlin Heidelberg, Berlin, Heidelberg, pp. 245–248. doi:10.1007/3-540-27946-6_64

Dahlkamp, F., J., 1993. Uranium ore deposits. Springer-Verlag, Berlin, 460 p.

Davis, W.J., Hanmer, S., Tella, S., Sandeman, H., Ryan, J.J., 2006. U–Pb Geochronology of the MacQuoid supracrustal belt and Cross Bay plutonic complex: key components of the northwestern Hearne subdomain, Western Churchill Province, Nunavut, Canada. Precambrian Research 145, 53–80.

Davis, W.J., Gall, Q., Jefferson, C.W., Rainbird, R.H., 2011. Fluorapatite in the Paleoproterozoic Thelon Basin: Structural-stratigraphic context, in situ ion microprobe U-Pb ages, and fluid-flow history. GSA Bull. 123, 1056–1073. doi:10.1130/B30163.1

De Veslud, C.L.C., Cuney, M., Lorilleux, G., Royer, J.-J., Jébrak, M., 2009. 3D Modeling of Uranium-bearing Solution-collapse Breccias in Proterozoic Sandstones (Athabasca Basin, Canada)-Metallogenic Interpretations. Comput. Geosci. 35, 92–107. doi:10.1016/j.cageo.2007.09.008

Devoto, R.H., 1978. Uranium in Phanerozoic sandstone and volcanic rocks. Short course in uranium deposits; their mineralogy and origin. Mineralogical Association of Canada, Short Course Handbook 3, 293-305

Dieng, S., Kyser, K., Godin, L., 2013. Tectonic history of the North American shield recorded in uranium deposits in the Beaverlodge area , northern Saskatchewan , Canada. Precambrian Res. 224, 316–340. doi:10.1016/j.precamres.2012.09.011

Dong, G., Morrison, G., Jaireth, S., 1995. Quartz textures in epithermal veins, Queensland; classification, origin and implication. Econ. Geol. 90, 1841–1856. doi:10.2113/gsecongeo.90.6.1841

Eriksson, P.G., Martins-Neto, M.A., Nelson, D.R., Aspler, L.B., Chiarenzelli, J.R., Catuneanu, O., Sarkar, S., Altermann, W., Rautenbach, C.J.D.W., 2001. An introduction to Precambrian basins; their characteristics and genesis; The influence of magmatism, tectonics, sea level change and paleo-climate on Precambrian basin evolution; change over time. Sediment. Geol. doi:10.1016/S0037-0738(01)00066-5

Farkas, A., 1984. Mineralogy and host rock alteration of the Lone Gull deposit: Urangesellschaft internal report, 44 p.

Faulkner, D.R., Jackson, C.A.L., Lunn, R.J., Schlische, R.W., Shipton, Z.K., Wibberley, C.A.J., Withjack, M.O., 2010. A review of recent developments concerning the structure, mechanics and fluid flow properties of fault zones. J. Struct. Geol. 32, 1557–1575. doi:10.1016/j.jsg.2010.06.009

Fayek, M., Kyser, T.K., 1997. Characterization of multiple fluid-flow events and rare-earth-element mobility associated with formation of unconformity-type uranium deposits in the Athabasca Basin, Saskatchewan. Can. Mineral. 35, 627–658

Fayek, M., Quirt, D., Jefferson, C., Camacho, A., Ashcroft, G., Shabaga, B., Sharpe, R. 2017. The Kiggavik-Andrew Lake structural trend uranium deposits: an overview. In SGA Extended Abstract proceedings. SGA 2017 Conference Quebec City, August 20-23. In press.

Friedrich, G., Weyer, H.J., and Bechtel, A. 1989. The Lone Gull uranium deposit – New geochemical and petrological data as evidence for the nature of the ore-bearing solutions. In: Proceedings of an IAEA Technical Committee Meeting on Metallogenesis of Uranium Deposits, March 9-12 1987, IAEA TC-542/19, p. 293-306

Fuchs, H., and Hilger, W., 1989. Kiggavik (Lone Gull): An unconformity related uranium deposit in the Thelon basin, Northwest Territories, Canada: International Atomic Energy Agency Technical Committee Meeting, Saskatoon, 1–3 September 1987, IAEA TECDOC-500, p. 429–454

Fuchs, H.D., Hilger, W., and Prosser, E., 1986. Geology and exploration history of the Lone Gull property, in Evans, L., ed., Uranium Deposits of Canada: Canadian Institute of Mining and Metallurgy Special Volume 33, p. 286-292

Gandhi, S.S., Potter, E.G., and Fayek, M., 2013. Polymetallic U-Ag veins at Port Radium, Great Bear magmatic zone, Canada: main botryoidal pitchblende stage cuts 1.74 Ga diabase dykes and has REE signatures diagnostic of unconformity-type deposits; Geol. Surv. Canada, Open File 7493

Grare, A., Benedicto, A., Lacombe, O., Trave, A., Ledru, P., Robbins, J., and Blains, M., 2017. Structural controls on uranium mineralization at the Kiggavik Project (NE Thelon area, Canada). In SGA Extended abstract proceedings of the 14th Biennial SGA Meeting, Quebéc, Canada, Volume 2. p739. SGA 2017 Conference in Quebec City, August 20-23. ISBN: 978-2-9816898-0-1

Györfi, I., Hajnal, Z., White, D.J., Takacs, E., Reilkoff, B., Annesley, I.R., Powell B., and Koch, R., 2007. High resolution seismic survey from the McArthur River region; contributions to mapping the complex P2 uranium ore zone, Athabasca Basin Saskatchewan, EXTECH IV:

Geology and Uranium Exploration Technology of the Proterozoic Athabasca Basin, Saskatchewan and Alberta, Edit. C. W. Jefferson, and G. Delaney; GSC Bull. 588; SGS Special Pub. 18; GAC (Mineral Deposits Division) Special Pub. 4; 397-412

Hadlari, T., and Rainbird, R.H., 2011. Retro-arc extension and continental rifting: a model for the Paleoproterozoic Baker Lake Basin, Nunavut1Geological Survey of Canada Contribution 20100436. Can. J. Earth Sci. 48, 1232–1258. doi:10.1139/e11-002

Hanmer, S., Williams, M., Kopf, C., 1995. Striding-Athabasca mylonite zone: implications for the Archean and Early Proterozoic tectonics of the western Canadian Shield. Can. J. Earth Sci. 32, 178–196. doi:10.1139/e95-015

Heaman, L.M., LeCheminant, A.N., 1993. Paragenesis and U-Pb systematics of baddeleyite (ZrO2). Chem. Geol. 110, 95–126. doi:http://dx.doi.org/10.1016/0009-2541(93)90249-I

Hiatt, E.E., Palmer, S.E., Kurt Kyser, T., O'Connor, T.K., 2010. Basin evolution, diagenesis and uranium mineralization in the Paleoproterozic Thelon Basin, Nunavut, Canada. Basin Res. 22, 302–323. doi:10.1111/j.1365-2117.2009.00415.x

Hoeve, J., and Sibbald, T.I.I., 1978. On the genesis of Rabbit Lake and other unconformity-type uranium deposits in Northern Saskatchewan, Canada. Econ. Geol. 73, 1450–1473

Hoeve, J., and Quirt, D., 1984. Mineralization and host-rock alteration in relation to clay mineral diagenesis and evolution of the Middle-Proterozoic, Athabasca Basin, northern Saskatchewan, Canada, Saskatchewan Research Council Technical Report, 187 pp.

Hoffman, P.F., 1988. United Plates of America, the Birth of a Craton: Early Proterozoic Assembly and Growth of Laurentia. Annu. Rev. Earth Planet. Sci. 16, 543–603. doi:10.1146/annurev.ea.16.050188.002551

Jaireth, S., Roach, I.C., Bastrakov, E., Liu, S., 2016. Basin-related uranium mineral systems in Australia: A review of critical features. Ore Geol. Rev. 76, 360–394. doi:https://doi.org/10.1016/j.oregeorev.2015.08.006

Jefferson, C.W., Thomas, D.J., Gandhi, S.S., Ramaekers, P., Delaney, G., Brisbin, D., Cutts, C., Quirt, D., Portella, P., and Olson, R.A., 2007. Unconformity-Associated Uranium Deposits of the Athabasca Basin, Saskatchewan and Alberta. In: Goodfellow, W.D. (Ed.), Mineral Deposits of Canada: A Synthesis Of Major Deposit Types, District Metallogeny, The Evolution Of Geological Provinces, And Exploration Methods. Geological Assoiciation of Candada, Special Publication 5, pp. 273–305

Jefferson, C.W., Chorlton, L.B., Pehrsson, S.J., Peterson, T., Wollenberg, P., Scott, J., Tschirhart, V., McEwan, B., Bethune, K., Calhoun, L., White, J.C., Leblon, B., LaRocque, A., Shelat, Y., Lentz, D., Patterson, J., Riegler, T., Skulski, T., Robinson, S., Paulen, R.,

McClenaghan, B., Layton-Matthews, D., MacIsaac, D., Riemer, W., Stieber, C. and Tschirhart, P. 2011a. Northeast Thelon Region: 77 Geomapping for Uranium in Nunavut. Geological Survey of Canada, Open File 6862

Jefferson, C.W., Pehrsson, S., Peterson, T., Chorlton, L., Davis, W., Keating, P., Gandhi, S., Fortin, R., Buckle, J., Miles, W., Rainbird, R., LeCheminant, A., Tschirhart, V., Tschirhart, P., Morris, W., Scott, J., Cousens, B., McEwan, B., Bethune, K., Riemer, W., Calhoun, L., White, J., MacIsaac, D., Leblon, B., Lentz, D., LaRocque, A., Shelat, Y., Patterson, J., Enright, A., Stieber, C., Riegler, T. 2011b. Northeast Thelon region geoscience framework - new maps and data for uranium in Nunavut. Geological Survey of Canada, Open File 6950. doi:10.4095/288791

Jefferson, C.W., Pehrsson, S., Peterson, T., Wollenberg, P., Tschirhart, V., Riegler, T., McEwan, B., Tschirhart, P., Scott, J., Chorlton, L., Davis, W., Bethune, K., Riemer, W., Patterson, J., Morris, W.A., Anand, A., and Stieber, C. 2013. Bedrock geology of the western Marjorie-Tehek supracrustal belt and Northeast Thelon Basin margin in parts of NTS 66A and 66B, Nunavut; Geological Survey of Canada, Open File 7241

Jefferson, C.W., White, J.C., Young, G.M., Patterson, J., Tschirhart, V.L., Pehrsson, S.J., Calhoun, L., Rainbird, R.H., Peterson, T.D., Davis, W.J., Tella, S., Chorlton, L.B., Scott, J.M.J., Percival, J.A., Morris, W.A., Keating, P., Anand, A., Shelat, Y., and MacIsaac, D. 2015. Outcrop and remote predictive geology of the Amer Belt and basement beside and beneath the northeast Thelon Basin, in parts of NTS 66-A, B, C, F, G and H, Kivalliq Region, Nunavut. Geological Survey of Canada, Open File 7242, 1 sheet. doi:10.4095/296825

Johnstone, D., Bethune, K.M., Quirt, D., Benedicto, A. 2017. Lithostratigraphic and structural controls of uranium mineralization in the Kiggavik East, Centre and Main Zone deposits, Nunavut. In Proceedings of the Geological Association of Canada-Mineralogical Association of Canada, Joint Annual Meeting, Whitehorse Yukon, June 1-3 2016

Kyser, K. and Cuney, M., 2015. Geology and geochemistry of uranium and thorium deposits. Edited by Michel Cuney, Kurt Kyser (2015) 362 pp. ISBN 978-0-921294-57-3

LeCheminant, A.N., Heaman, L.M., 1989. Mackenzie igneous events, Canada: Middle Proterozoic hotspot magmatism associated with ocean opening. Earth Planet. Sci. Lett. 96, 38–48. doi:http://dx.doi.org/10.1016/0012-821X(89)90122-2

Lesperance, J., 2012. The Qavvik-Tatiggaq Trend: an evolving unconformity uranium corridor of the northeast Thelon Basin. Presentation at Nunavut Mining Symposium, April 16-19 2012. 36p.

Lunn, R.J., Willson, J.P., Shipton, Z.K., Moir, H., 2008. Simulating brittle fault growth from linkage of preexisting structures. J. Geophys. Res. Solid Earth 113, n/a--n/a. doi:10.1029/2007JB005388

McEwan, B. 2012. Structural style and regional comparison of the Ketyet River group northeast of Baker Lake, Nunavut. M.Sc. Thesis, University of Regina

MacRae, C.M., Wilson, N.C., Torpy, A., 2013. Hyperspectral cathodoluminescence. Mineral. Petrol. 107, 429–440. doi:10.1007/s00710-013-0272-8

Mercadier, J., Cuney, M., Cathelineau, M., Lacorde, M., 2011. U redox fronts and kaolinisation in basement-hosted unconformity-related U ores of the Athabasca Basin (Canada): late U remobilisation by meteoric fluids. Miner. Depos. 46, 105–135. doi:10.1007/s00126-010-0314-7

Meunier, J.D., Sellier, E., Pagel, M., 1990. Radiation-damage rims in quartz from uranium-bearing sandstones. J. Sediment. Res. 60, 53–58. doi:10.1306/212F910B-2B24-11D7-8648000102C1865D

Miller, A.R., 1980. Uranium geology of the Eastern Baker Lake basin, district of Keewatin, Northwest Territories. Geological survey of Canada, bulletin 330, 63p.

Miller, A.R. and LeCheminant, A.N., 1985. Geology and uranium metallogeny of Proterozoic supracrustal successions, central District of Keewatin, N.W.T., with comparisons to northern Saskatchewan. Special Volume - Canadian Institute of Mining and Metallurgy 32: 167-185

Miller, A.R., 1996. Geology and petrology of the Schultz Lake Intrusive Complex and its relationship to unconformity related uranium deposits Schultz Lake, NTS 66A/5 and Aberdeen Lake 66B/8, western Churchill Province. Geological Survey of Canada, internal document

Mills, A.J., Berman, R.G., Davis, W.J., Tella, S., Roddick, C., S. Carr, S.H., 2007. Thermobarometry and geochronology of the Uvauk complex, a polymetamorphic Neoarchean and Paleoproterozoic segment of the Snowbird tectonic zone, Nunavut, Canada. Can. J. Earth Sci. 44, 245–266. doi:10.1139/e06-080

Moncada, D., Mutchler, S., Nieto, A., Reynolds, T.J., Rimstidt, J.D., Bodnar, R.J., 2012. Mineral textures and fluid inclusion petrography of the epithermal Ag–Au deposits at Guanajuato, Mexico: Application to exploration. J. Geochemical Explor. 114, 20–35. doi:https://doi.org/10.1016/j.gexplo.2011.12.001

OECD NEA & IAEA, 2016. Uranium 2016: Resources, Production and Demand A Joint Report by the OECD Nuclear Energy Agency and the International Atomic Energy Agency English,

504 p, available online at : https://www.oecd-nea.org/ndd/pubs/2016/7301-uranium-2016.pdf

Percival, J.B., Kodama, H., 1989. Sudoite from Cigar Lake, Saskatchewan. Can. Mineral. 27, 633–641

Percival, J.B., Bell, K., Torrance, J.K., 1993. Clay mineralogy and isotope geochemistry of the alteration halo at the Cigar Lake uranium deposit. Can. J. Earth Sci. 30, 689–704. doi:10.1139/e93-056

Pehrsson, S., Jefferson, C.W., Peterson, T., Scott, J., Chorlton, L., Hillary, B., Patterson, Judith, Lentz, D., Shelat, Y., and Bethune, K., 2010. Basement to the Thelon Basin, Nunavut - Revisited. Special Session on Geological Environments hosting Uranium Deposits, GeoCanada 2010 - Working with the Earth, Calgary, May 10-14th, 4 p. abstract

Pehrsson S., Berman, R., Davis, W. 2013. Paleoproterozoic orogenesis during Nuna aggregation: a case study of reworking of the Archean Rae craton, Woodburn Lake, Nunavut. Precambrian Research, 232: 167-188. doi: 10.1016/j.precamres.2013.02.010

Peterson, T.D., Breemen, O. Van, Sandeman, H., Cousens, B., 2002. Proterozoic (1.85–1.75 Ga) igneous suites of the Western Churchill Province: granitoid and ultrapotassic magmatism in a reworked Archean hinterland. Precambrian Res. 119, 73–100. doi:https://doi.org/10.1016/S0301-9268(02)00118-3

Peterson, T.D., 2006. Geology of the Dubawnt Lake area, Nunavut-Northwest Territories. Geological Survey of Canada, Bulletin 580

Peterson, T.D., Scott, J.M.J., LeCheminant, A.N., Jefferson, C.W., Pehrsson, S.J., 2015a. The Kivalliq Igneous Suite: Anorogenic bimodal magmatism at 1.75 Ga in the western Churchill Province, Canada. Precambrian Res. 262, 101–119. doi:https://doi.org/10.1016/j.precamres.2015.02.019

Peterson, T.D., Scott, J.M.J., Lecheminant, A.N., Tschirhart, V.L., Chorlton, L.B., Davis, W.J., Hamilton, M.A., 2015b. Nueltin granites and mafic rocks in the Tebesjuak Lake map area, Nunavut: new geochronological, petrological, and geophysical data. Geological Survey of Canada, Current Research (Online) 2015-5, 2015; 23 pages, doi:10.4095/296163

Polito, P.A., Kyser, T.K., Rheinberger, G., and Southgate, P.N., 2005a. A paragenetic and isotopic study of the proterozoic Westmoreland uranium deposits, Southern McArthur Basin, Northern Territory, Australia. Econ. Geol. 100, 1243–1260

Polito, P.A., Kyser, T.K., Thomas, D., Marlatt, J., and Drever, G., 2005b. Re-evaluation of the petrogenesis of the Proterozoic Jabiluka unconformity-related uranium deposit, Northern Territory, Australia. Mineral. Deposita 40, 257–288

Potter, E. G., Sharpe, R., Girard, I., Fayek, M., Gammon, P., Quirt, D., and Robbins, J. 2015. Fe and Mg Signatures of the Bong Uranium Deposit, Thelon Basin, Nunavut. In Targeted Geoscience Initiative 4: unconformity-related uranium systems. Edited by E.G. Potter and D.M. Wright. Geological Survey of Canada, Open File 7791, pp. 52–60

Quirt. D. 2017. Clay mineral host-rock alteration at the Bong basement-hosted uranium deposit, Kiggavik area, Nunavut. In SGA Extended Abstract proceedings. SGA 2017 Conference Quebec City, August 20-23. In press

Rainbird, R.H. and Hadlari, T., 2000. Revised stratigraphy and sedimentology of the Dubawnt Supergroup at the northern margin of the Baker Lake Basin, Nunavut; Geological survey of Canada, Current Research 2000-C8, 9p.

Rainbird, R.H., Hadlari, T., Aspler, L.B., Donaldson, J.A., LeCheminant, A.N., Peterson, T.D., 2003. Sequence stratigraphy and evolution of the paleoproterozoic intracontinental Baker Lake and Thelon basins, western Churchill Province, Nunavut, Canada. Precambrian Res. 125, 21–53. doi:10.1016/S0301-9268(03)00076-7

Rainbird, R.H., Davis, W.J., 2007. U-Pb detrital zircon geochronology and provenance of the late Paleoproterozoic Dubawnt Supergroup: Linking sedimentation with tectonic reworking of the western Churchill Province, Canada. GSA Bull. 119, 314. doi:10.1130/B25989.1

Rainbird, R.H., Davis, W.J., Pehrsson, S.J., Wodicka, N., Rayner, N., Skulski, T., 2010. Early Paleoproterozoic supracrustal assemblages of the Rae domain, Nunavut, Canada: Intracratonic basin development during supercontinent break-up and assembly. Precambrian Res. 181, 167–186. doi:https://doi.org/10.1016/j.precamres.2010.06.005

Ramaekers, P., 1980. Stratigraphy and tectonic history of the Athabasca Group (Helikian) of Northern Saskatchewan, in Christopher, J.E. and MacDonald, R., eds, Summary of Investigations 1980: Sask. Geol. Survey Misc. Rept. 80-4, pp. 99-106

Ramaekers, P., Jefferson, C.W., Yeo, G.M., Collier, B., Long, D.G.F., Drever, G., et al. 2007. Revised geological map and stratigraphy of the Athabasca Group, Saskatchewan and Alberta. In EXTECH IV: Geology and Uranium Exploration TECHnology of the Proterozoic Athabasca Basin, Saskatchewan and Alberta. Edited by C.W. Jefferson and G. Delaney. Geological Survey of Canada, Bulletin 588, (also Geological Association of Canada, Mineral Deposits Division, Special Publication 4; Saskatchewan Geological Society, Special Publication 18). pp. 155–192

Regan, S.P., Williams, M.L., Leslie, S., Mahan, K.H., Jercinovic, M.J., Holland, M.E., 2014. The Cora Lake shear zone, Athabasca granulite terrane, an intraplate response to far-field

orogenic processes during the amalgamation of Laurentia. Can. J. Earth Sci. 51, 877–901. doi:10.1139/cjes-2014-0015

Renac, C., Kyser, T.K., Durocher, K., Dreaver, G., O'Connor, T., 2002. Comparison of diagenetic fluids in the Proterozoic Thelon and Athabasca Basins, Canada: implications for protracted fluid histories in stable intracratonic basins. Can. J. Earth Sci. 39, 113–132. doi:10.1139/e01-077

Richard, A., Rozsypal, C., Mercadier, J., Banks, D. a., Cuney, M., Boiron, M.-C., Cathelineau, M., 2011. Giant uranium deposits formed from exceptionally uranium-rich acidic brines. Nat. Geosci. 5, 142–146. doi:10.1038/ngeo1338

Riegler, T., Quirt, D., Beaufort, D., 2016a. Spatial distribution and compositional variation of APS minerals related to uranium deposits in the Kiggavik-Andrew Lake structural trend, Nunavut, Canada. Miner. Depos. 51, 219–236. doi:10.1007/s00126-015-0595-y

Riegler, T., Beaufort, M.-F., Allard, T., Pierson-Wickmann, A.C., Beaufort, D., 2016b. Nanoscale relationship between uranium and carbonaceous material in alteration haloes around unconformity-related uranium deposits of the Kiggavik camp, Paleoproterozoic Thelon Basin, Nunavut, Canada. Ore Geol. Rev. 79, 382-391. doi:https://doi.org/10.1016/j.oregeorev.2016.04.018

Robbins, J., Richard, Y., Carter, C. Behaegel, M., Benedicto, A. and Ledru, P. 2015. New guides led to new models - Continuing return of exploration experience, Nunavut, Canada. In The AusIMM International Uranium Conference 2015, Abstract volume, p. 2

Ross, G.M., Eaton, D.W., Boerner, D.E., Miles, W., 2000. Tectonic entrapment and its role in the evolution of continental lithosphere: An example from the Precambrian of western Canada. Tectonics 19, 116–134. doi:10.1029/1999TC900047

Roy, R., Benedicto, A., Grare, A., Béhaegel, M., Yoann, R., Grant, H. 2017. 3D gravity modelling applied to the exploration of uranium unconformity-related basement hosted deposits: the Contact prospect case study, Kiggavik, NE Thelon region (Nunavut, Canada) Can. J. Earth Sci. doi: 10.1139/cjes-2016-0225

Ruzicka, V.R., 1989. Monometallic and polymetallic deposits associated with the sub-Athabasca unconformity in Saskatchewan, in Current Research: Geological Survey of Canada, Paper 89-1C, p. 67-79

Ruzicka, V.R., 1996. Unconformity-associated uranium, Chapter 7 in Eckstrand, O.R., Sinclair, W.D., and Thorpe, R.I., 1995. Geology of Canadian Mineral Deposit Types: Geological Survey of Canada, Geology of Canada, v, 8, p. 197-210

Sanborn-Barrie, M., Carr, S., Thériault, R., 2001. Geochronological constraints on metamorphism, magmatism and exhumation of deep-crustal rocks of the Kramanituar Complex, with implications for the Paleoproterozoic evolution of the Archean western Churchill Province, Canada. Contrib. to Mineral. Petrol. 141, 592–612. doi:10.1007/s004100100262

Scott, J.M.J., Peterson, T.D. and McCurdy, M.W., 2012. U, Th, and REE occurrences within Nueltin Granite at Nueltin Lake, Nunavut: Recent Observations. Geological Survey of Canada, Paper 2012-1, pp. 1–11

Scott, J.M.J., Peterson, T.D., Jefferson, C.W., Cousens, B.L., 2015. Petrology and geochronology of Paleoproterozoic intrusive rocks, Kiggavik uranium camp, Nunavut. Can. J. Earth Sci. 518, 1–80. doi:10.1139/cjes-2014-0153

Shabaga, B., M., Fayek, M., Quirt, D., Davis, B., Pesja, T., Jefferson, C., 2015. Geochemistry and Geochronology of the Andrew Lake deposit, Thelon Basin, Nunavut, Canada. Poster presented at 2015 GAC MAC

Shabaga, B., M., Fayek, M., Quirt, D., Jefferson, C.W., Camacho, A., 2017a. Geochronology and genesis of the Andrew Lake uranium deposit, Thelon Basin, Nunavut, Canada. Poster presented at 2017 GAC MAC

Shabaga, B.M., Fayek, M., Quirt., D., Jefferson, C. 2017b. Geochronology of the Kiggavik uranium deposit, Thelon Basin, Canada. In SGA Extended Abstract proceedings. SGA 2017 Conference Quebec City, August 20-23. In press

Sharpe, R., Fayek, M., Quirt, D., Jefferson, C.W., 2015. Geochronology and genesis of the bong uranium deposit, Thelon Basin, Nunavut, Canada. Econ. Geol. 110, 1759–1777. doi:10.2113/econgeo.110.7.1759

Sheahan, C., Fayek, M., Quirt, D., Jefferson, C.W., 2015. A Combined Ingress-Egress Model for the Kianna Unconformity-Related Uranium Deposit, Shea Creek Project, Athabasca Basin, Canada. Econ. Geol. 111, 225. doi:10.2113/econgeo.111.1.225

Simmons, S.F., Christenson, B.W., 1994. Origins of calcite in a boiling geothermal system. Am. J. Sci. 294, 361–400. doi:10.2475/ajs.294.3.361

Skirrow, R.G., Mercadier, J., Armstrong, R., Kuske, T., Deloule, E., 2016. The Ranger uranium deposit, northern Australia: Timing constraints, regional and ore-related alteration, and genetic implications for unconformity-related mineralisation. Ore Geol. Rev. 76, 463–503. doi:https://doi.org/10.1016/j.oregeorev.2015.09.001

Tourigny, G., Quirt, D.H., Wilson, N.S.F., Wilson, S., Breton, G., and Portella, P., 2007. Geological and structural features of the Sue C uranium deposit, McClean Lake area,

Saskatchewan, inJefferson, C.W., and Delaney, G., eds., EXTECH IV: Geology and Uranium EXploration TECHnology of the Proterozoic Athabasca Basin, Saskatchewan and Alberta: Geological Survey of Canada, Bulletin 588, p. 229–247 (also Geological Association of Canada, Mineral Deposits Division, Special Publication 4; Saskatchewan Geological Society, Special Publication 18)

Tschirhart, V., Morris, W.A., Jefferson, C.W., 2013. Framework geophysical modelling of granitoid vs. supracrustal basement to the northeast Thelon Basin around the Kiggavik uranium camp, Nunavut. Can. J. Earth Sci. 50, 667–677. doi:10.1139/cjes-2012-0149

Tschirhart, V., Jefferson, C.W., Morris, W.A. 2017. Basement geology beneath the northeast Thelon Basin, Nunavut: insights from integrating new gravity, magnetic and geological data. Geophysical Prospecting, 65: 617-636. doi: 10.1111/1365-2478.12430

Turner, W.A. 2000. Geology and geochemistry of the Mallery Lake precious metal-bearing epithermal system, Nunavut, Canada. MSc Thesis, Univ Alberta, 176 pp.

Turner, W.A., Richards, J., Nesbitt, B., Muehlenbachs, K., Biczok, J., 2001. Proterozoic low-sulfidation epithermal Au-Ag mineralization in the Mallery Lake area, Nunavut, Canada. Miner. Depos. 36, 442–457. doi:10.1007/s001260100181

Turner, W.A., Heaman, L.M., Creaser, R.A., 2003. Sm–Nd fluorite dating of Proterozoic low-sulfidation epithermal Au–Ag deposits and U–Pb zircon dating of host rocks at Mallery Lake, Nunavut, Canada. Can. J. Earth Sci. 40, 1789–1804. doi:10.1139/e03-061

Van Breemen, O., Peterson, T.D., Sandeman, H.A., 2005. U–Pb zircon geochronology and Nd isotope geochemistry of Proterozoic granitoids in the western Churchill Province: intrusive age pattern and Archean source domains. Can. J. Earth Sci. 42, 339–377. doi:10.1139/e05-007

Van der Zee, W., Wibberley, C.A.J., Urai, J.L., 2008. The influence of layering and pre-existing joints on the development of internal structure in normal fault zones: the Lodève basin, France. Geol. Soc. London, Spec. Publ. 299, 57–74. doi:10.1144/SP299.4

Wallis, R.H., Saracoglu, N., Brummer, J.J., and Golighltly, J.P.1985. The geology of the McClean uranium deposits, northern Saskatchewan; inSibbald, T.I.I. and Petruk, W. (eds.), Geology of Uranium Deposits, CIM Spec. Vol. 32, p. 101-131

Wibberley, C.A.J., Yielding, G., Di Toro, G., 2008. Recent advances in the understanding of fault zone internal structure: a review. Geol. Soc. London, Spec. Publ. 299, 5–33. doi:10.1144/SP299.2

Wilde, A.R., and Wall, V.J., 1987. Geology of the NabarlekUranium Deposit, NorthernTerritory. Australia. Econ. Geol. Vol. 82, 1152–1168

Williams, J.H., Johnson, C.D., 2004. Acoustic and optical borehole-wall imaging for fractured-rock aquifer studies. J. Appl. Geophys. 55, 151–159. doi:https://doi.org/10.1016/j.jappgeo.2003.06.009

Weyer H..J, Friedrich G., Bechtel A., Ballhorn R.K., 1987. The Lone Gull uranium deposit—new geochemical and petrological data as evidence for the nature of the ore bearing solutions. Metallogenesis of uranium deposits: Proceeding of a technical committee meeting, Vienna, p. 9–12

Zaleski, E., Pehrsson, S., Duke, N., Davis, W.J., L'Heureux, R., Greiner, E., Kerswill, J.A., 2000. Quartzite sequences and their relationships, Woodburn Lake group, western Churchill Province, Nunavut. Geological Survey of Canada, Current Research (Online) no. 2000-C7, 2000; 10 p., doi:10.4095/211098

5.2.2 Complementary macroscopic and microscopic observations on fracturing events at the Contact prospect

The following observations are presented here to support paragenetic sequence and the structural model of the Contact prospect presented in the previous section limited by the size of the research article. These observations were made prior to the article for the construction of the paragenetic table and to understand the architecture of the fault zones. Naming for the fracturing events, their order and abbreviations are the same as in the article.

Fracturing stage 1 (f1): First tectonic activity observed on the Andrew Lake Fault

Fault rocks are intersected in drillholes at depth and are interpreted to represent brittle tectonic activity on the Andrew Lake fault (ALF). They are usually silicified and crosscut by white quartz veins and breccias (Figure 22C-E). Altered granite, likely belonging to the Hudson intrusions and porphyric granite (possibly rapakivi), likely belonging to the Kivalliq igneous suite, are crosscut by fractures and quartz veins and breccias (Fig. 22A-E).

Cataclastic to ultra-cataclastic fault rocks (Fig. 23A-D) with centimetric to millimetric illitized clasts are observerd in fault zones usually completely overprinted by white to grey quartz veins and breccias network of the QB event (Fig. 23C-E). Cements of these fault rocks can be green (chlorite-rich) red (hematite-rich) or brown (possibly finely crushed, illitized material). These different textures can be dependent on the lithology present before faulting (granitic gneiss or lamprophyre, granite, syenite…. of the two intrusive suites). Considering the overprinting by the quartz breccia (QB), this pre-QB fracturing event is observed more easily on the edges of the QB, where veining is less intense.

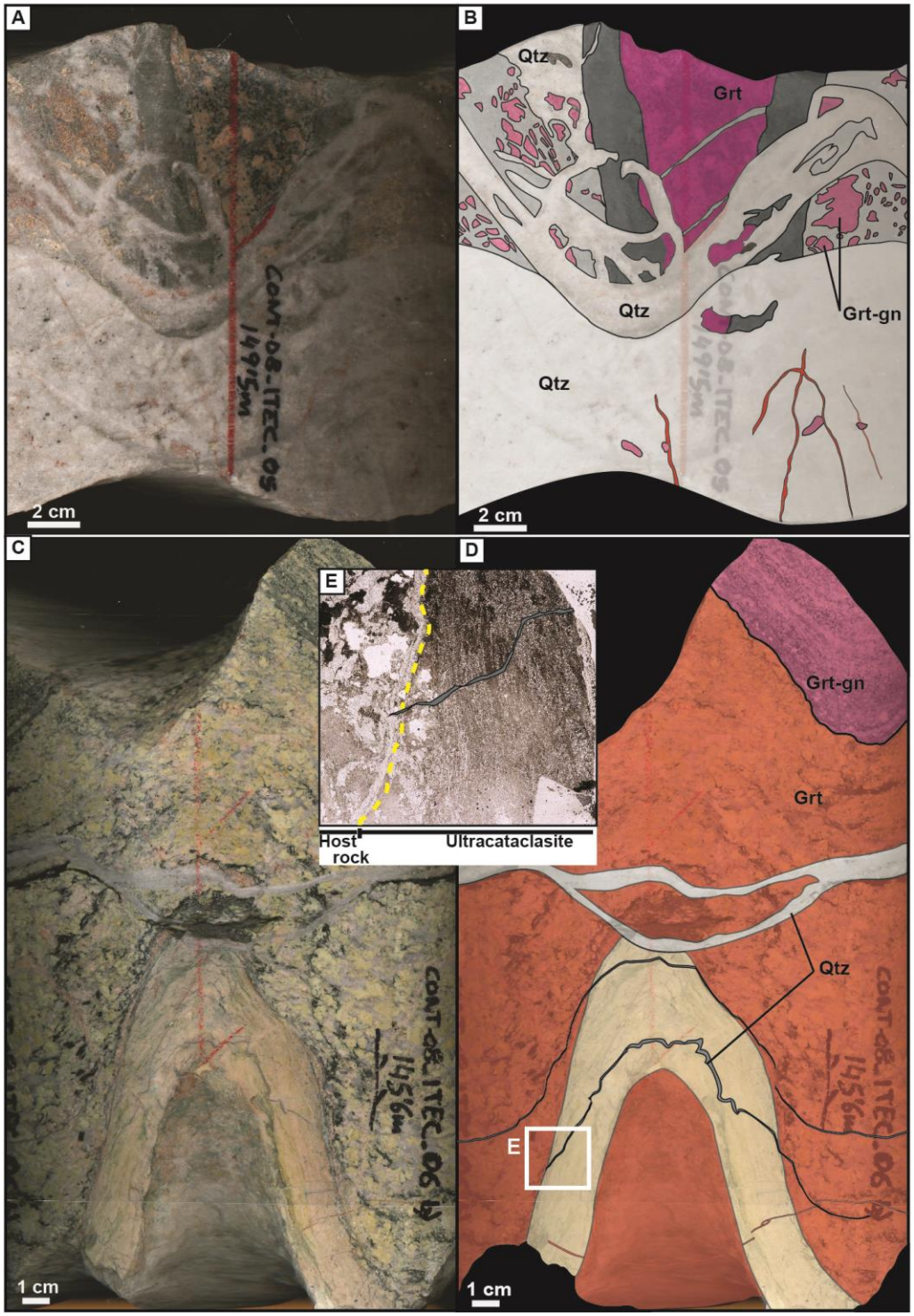

Figure 22: A) Drill-core 360° scan and B) interpretation scheme. Granitic intrusion (Grt) likely belonging to the Kivalliq igneous suite, intruded a proto cataclastic fault rock and is crosscut by quartz veins and protobreccias cemented by several generations of white quartz. C) Drill-core 360° scan and D) interpretation scheme. Clay altered and bleached granite intrudes granitic gneiss. Ultracataclastic fault rock is observed in the granite and crosscut by quartz veins. E) Detailed microscopic picture, plane polarized light (PPL) of picture D.

Fracturing stage 2: quartz breccia (QB) and first stage of oxidation

The quartz breccia, characterized by white (possibly grey –micro crystalline- quartz) quartz veins and massive breccias (Fig. 23F, G), is observed throughout the Contact prospect. It predates deposition of the Thelon formation and is linked to syn-rift magmatism (ca. 1750 Ma, The Kivalliq igneous suite). There is a great variety of quartz textures (Fig. 24A-C in example), mutually cross-cutting each other, defining multiple pulses of silica-rich fluids. Two distinct generations of euhedral white quartz can be distinguished, one characterized by dense arrays of monophase fluid inclusions, usually at the tip of the quartz crystals (Fig. 24C). The second generation is usually observed as a late quartz generation (Fig. 23D, Fig. 24D) and displays vugs. This complex network of quartz veins is associated with a pervasive iron-oxidation of the host rock (Fig. 24B). Iron oxides are mainly represented by disseminated fine grains of hematite, possibly observed in banded veins synchronous with quartz. Sub-euhedral specular hematite is observed filling quartz vugs and disseminated in the host rock (Fig. 24E). The specular hematite could be responsible for the dark-red to purplish colour of the oxidized host rock. Rare anhedral magnetite was observed mixed with (replaced by?) hematite (Fig. 24F) in quartz veins and likely represents changes in the chemistry (redox) of the fluid. These observations alongside with the spatial association of iron oxidation and quartz brecciation, attests for the synchronicity of the two events.

Figure 25 summarizes observations made systematically on the quartz breccia, in each drillhole. The damage zone of the QB (blue in Fig. 25) is represented by a dense to scarce network of quartz veins. The core zone (red in Fig. 25) of the QB is represented by massive quartz breccia and intense quartz vein network, where the host rock is barely observable. Thickness of the damage and core zones and oriented data for the quartz veins and breccias are reported in Fig.25. Fig. 23G is the kind of outcrop that helps to understand the complexity of such structure: the “true” orientation of the breccia is given by the more massive veins and breccias. Where visible, the minor quartz veins are more randomly oriented.

Main orientation of the QB at the Contact prospect is N30°, sub-vertical dip to the NW. The QB displays important changes in the thickness and minor changes in the direction. Dip of the structure is quite constant. Minor quartz veins are mainly trending N70-80°, steeply dipping to the NNW, but measurements returned a variety of orientations, from N10° to N-110°.All these observations were used to understand this fracturing event and reconstruct the architecture of the quartz breccia at the Contact prospect.

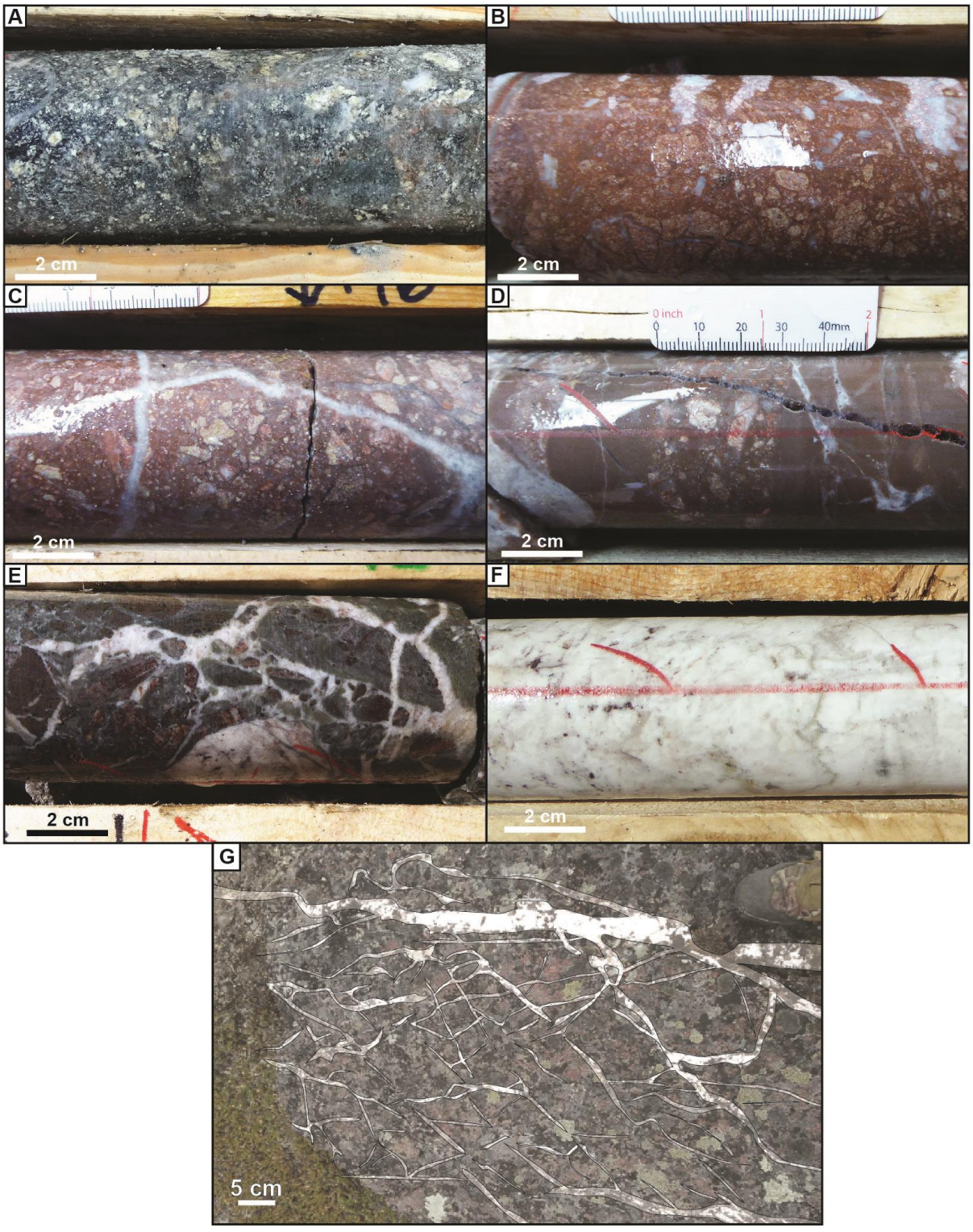

Figure 23: A) Protobreccia cemented with chlorite and crosscute by protobreccia cemented by grey quartz. Clasts are illitized. B) Silicified and hematized cataclastic fault rock. C) Silicified and hematized cataclastic fault rock crosscut by white quartz veins D) Silicified cataclastic to ultracataclastic fault rock crosscut by white quartz and euhedral quartz veins. E) Lamprophyre crosscut by white quartz-cemented breccia. F) Massive white quartz vein. G) Outcrop of a small relay zone of the quartz breccia.

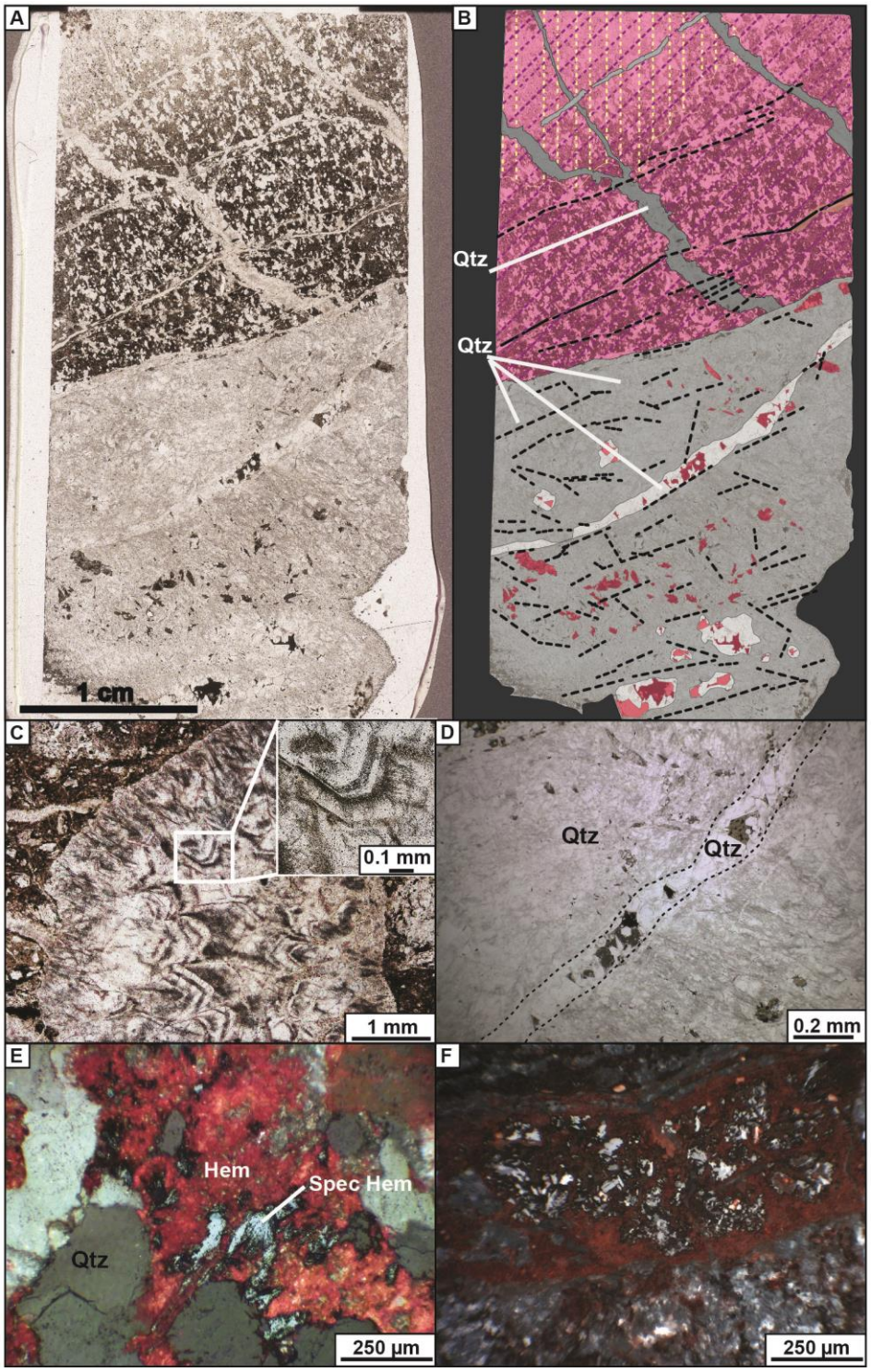

Figure 24: A) Thin section scan and B) interpretation scheme. Several generations of quartz veins crosscut each other in hematized granitic gneiss. C) PPL. Euhedral quartz crystals and arrays of dense monophase fluid inclusions. D) PPL. Detail of scan showed in A: Euhedral clear quartz cement a fracture. E) Reflected light (RFL). Fine grains of hematite and specular hematite. F) RFL. Anhedral magnetite and fine grained hematite in banded quartz vein.

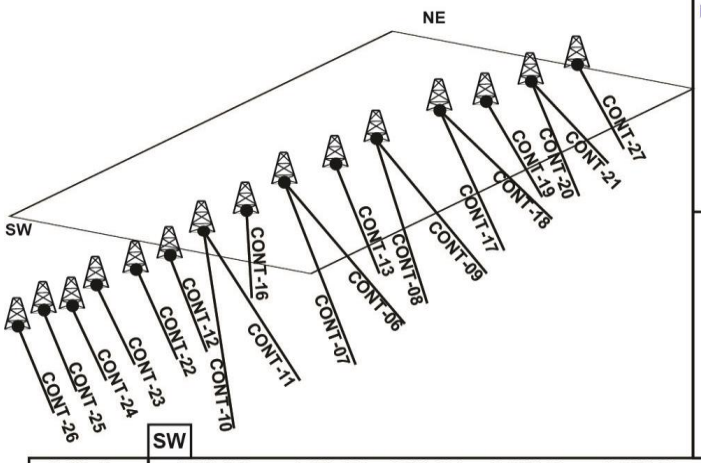

Drillhole	CONT-10	CONT-07	CONT-08	CONT-17	CONT-20
Damage zone-core zone distribution	158-176 176-190 190-210 227-233 240-242 242-243 243-251	247-266 266-291	144-161 171-186 186-188 188-208	148-150	255-260 267-279
Brecciation intensity	4	4	3	4	2
notes	3 branches chloritic breccia hematitic breccia	chloritic breccia (?)		grey breccia	white quartz not dominant hematitic breccia grey breccia
Veins orientation	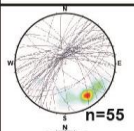 n=55	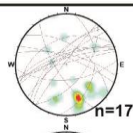 n=17	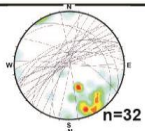 n=32		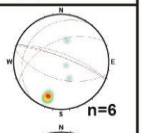 n=6
Breccia orientation	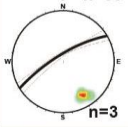 n=3	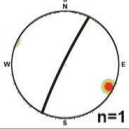 n=1	 n=1		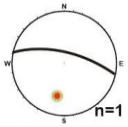 n=1

Drillhole	CONT-26	CONT-25	CONT-24	CONT-23	CONT-22	CONT-12	CONT-11	CONT-16	CONT-06	CONT-13	CONT-09	CONT-18	CONT-19	CONT-21	CONT-27
Damage zone-core zone distribution	227-234 234-238 238-245	144-148 160-161 190-192 269-290	105-114 114-125 126-128 2 veins 50cm 136-140 140-end	132-144 144-149 149-153 153-160	180-186 188-191 192-196 226-227	216-220 220-237 237-241	131-155	201-213 213-216 216-238 238-243 243-255	161-168 168-171 171-175 175-183 183-187 187-194 224-228	148-175 175-176	103-126 126-139 139-145	151-162 162-183	165-185 185-198 198-205	187-195 195-200 200-204	189-220 227-251 251-257
Brecciation intensity	2	1	4	2	2	4	1	2	4	4	3	2	2	2	2
notes	grey breccia		2 branches chloritic breccia hematitic breccia		hematitic breccia	chloritic breccia grey breccia		2 branches chloritic breccia hematitic breccia	2 branches chloritic breccia hematitic breccia	not complete hematitic breccia chloritic breccia (?)	hematitic breccia	white quartz equal other cement hematitic breccia brown breccia	white quartz not dominant hematitic breccia chloritic breccia brown breccia	white quartz not dominant hematitic breccia	
Veins orientation	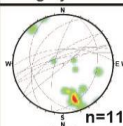 n=11	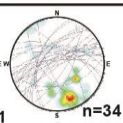 n=34	?	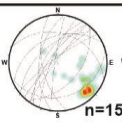 n=15	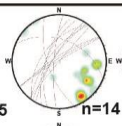 n=14	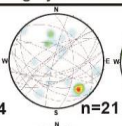 n=21	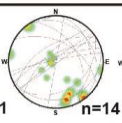 n=14	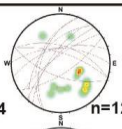 n=12	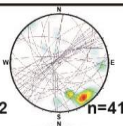 n=41	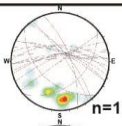 n=18	?	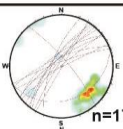 n=17	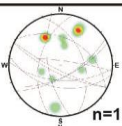 n=11	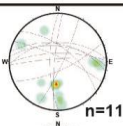 n=11	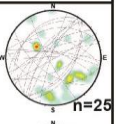 n=25
Breccia orientation	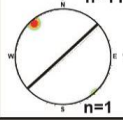 n=1	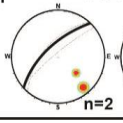 n=2	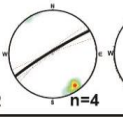 n=4	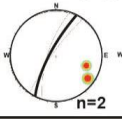 n=2	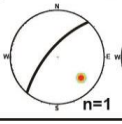 n=1	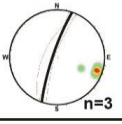 n=3	?	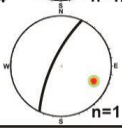 n=1	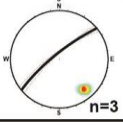 n=3	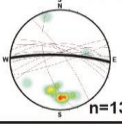 n=13	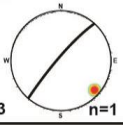 n=1	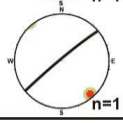 n=1	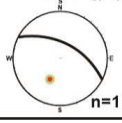 n=1	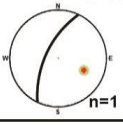 n=1	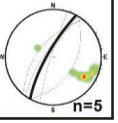 n=5

Figure 25: Table summarizing several observations systematically made for each of the drillholes at the Contact prospect Including: Presence and thickness of fault core and damage zones; Intensity of the brecciation; Texture(s) of the quartz breccia; Orientated data for minor veins and massive breccias.

Fracturing stage 5: uranium-related faults (first stage of uranium mineralization)

First stage of uranium mineralization (f5, U1) at the Contact prospect is characterized by narrow fault zones and grey-greenish (reduced) fault rocks (figure 26). Iron oxides from the first stage of oxidation linked to the QB are removed by the circulation of uranium bearing fluids associated with f5. Ore minerals (mainly pitchblende and sulfides) can be observed filling veins with illite (Fig. 26A-C), in cataclastic fault rocks (Fig. 26D), disseminated in damage zones (Fig. 26E) or filling fractures crosscutting quartz veins, possibly staining euhedral quartz crystals (Fig. 26F-G). Evidence of late remobilization of uranium can sometime be clearly observed (Fig. 26H).

F5 mineralized fractures are spatially associated with quartz veins of the QB. Veins can be re-opened (ore minerals along the edges of the vein) or orthogonally micro-fractured (ore minerals cementing micro-fractures usually not propagating outside of the vein). Examples of this spatial association are presented in figure 27A-J.

Ore minerals were rarely observed associated with carbonates (Fig. 28A-D). Dolomite veins crosscut quartz veins and both are crosscut by calcite veins. Calcite is locally observed associated with pitchblende cementing the microfractures orthogonal to quartz veins (Fig. 28E-F).

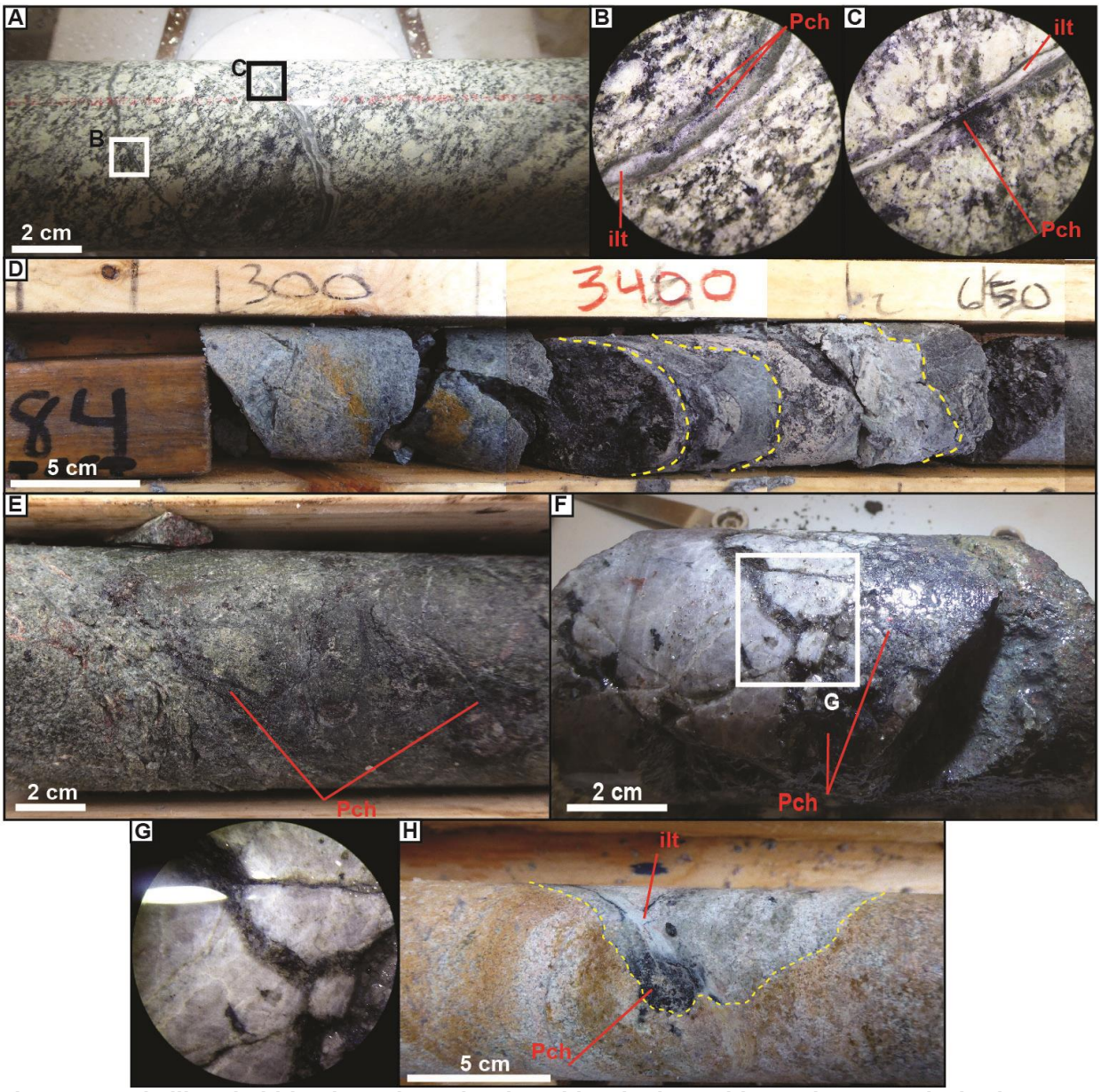

Figure 26: A) Illite-pitchblende-pyrite veins in a bleached granitic gneiss. B and C) Close-up of veins showed in A. Ore minerals are observed at the boundary of the veins and weakly disseminates in the host rock. D) Uranium-mineralized core zone. E) Uranium-mineralized damage zone F) Uranium mineralized cataclastic fault rock. G) Quartz stained with uranium. H) Remobilization of uranium from an illite-pitchblende-pyrite vein.

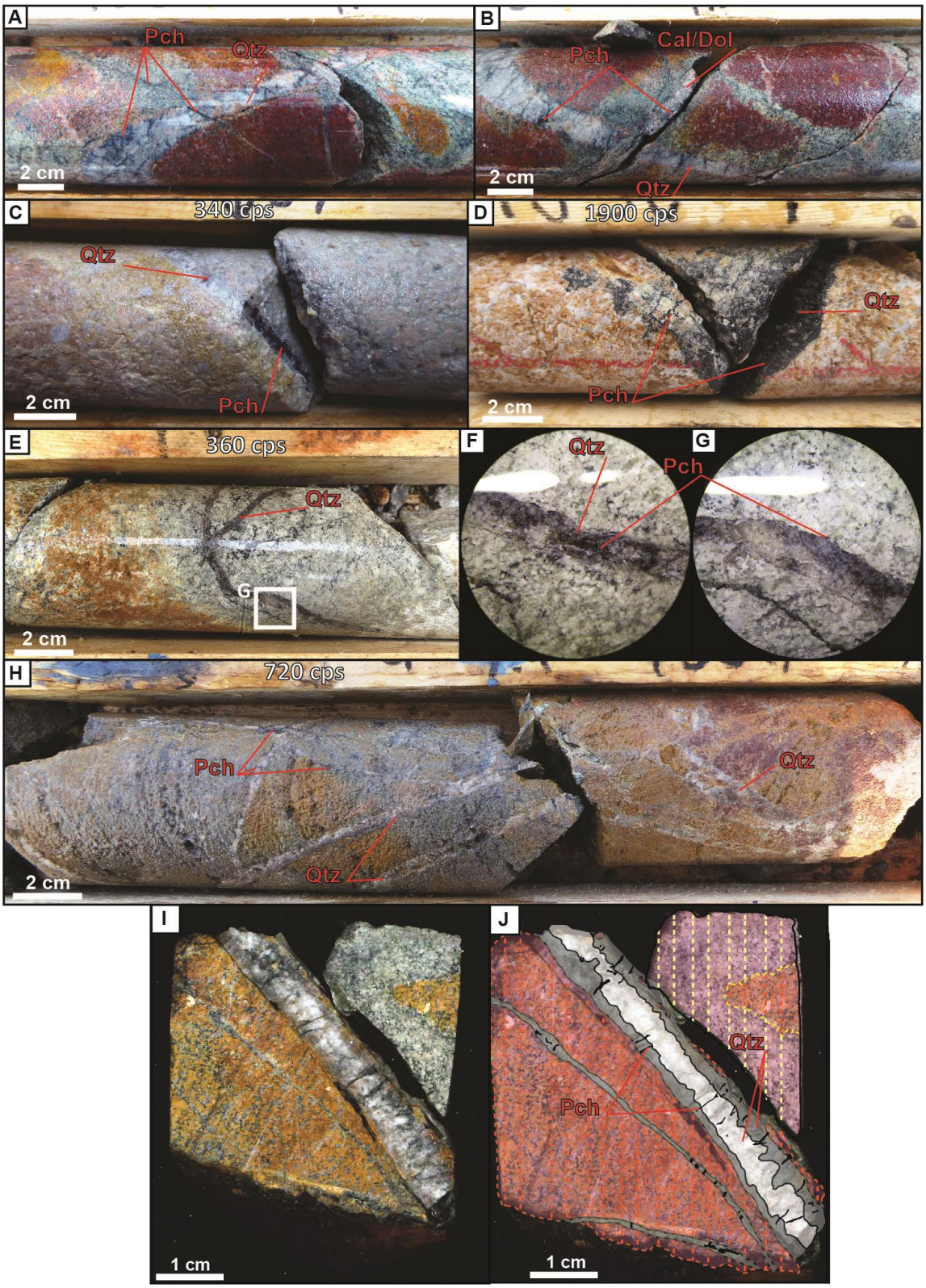

Figure 27: A-J) Several examples of quartz veins bearing ore minerals along edges or in orthogonal microfractures. Open fractures displaying drusy quartz stained with uranium (picture D) are rare.

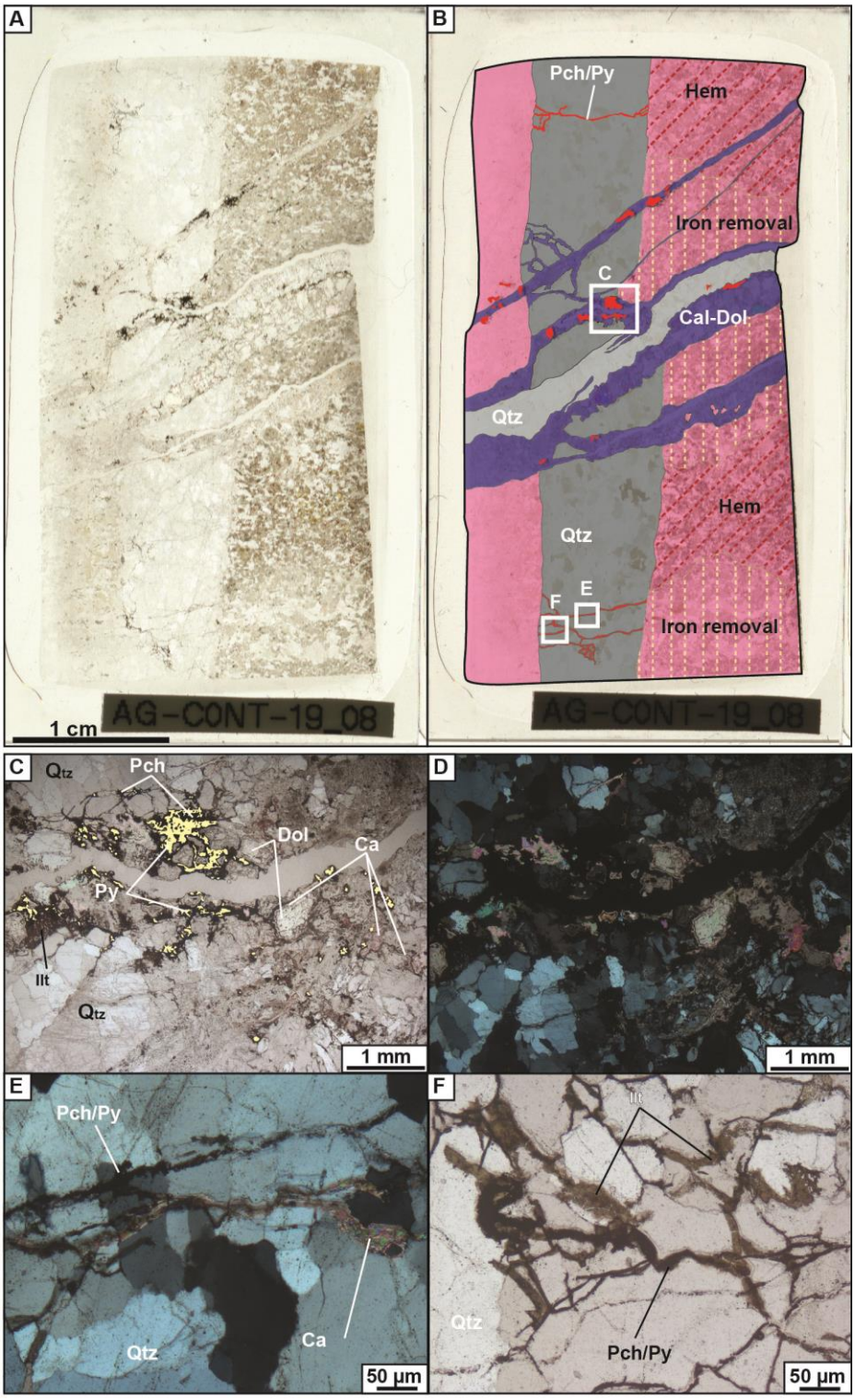

Figure 28: A, thin section scan and B, interpretation scheme: Quartz vein crosscut by dolomite/calcite vein. Quartz vein is orthogonally crosscut by microfractures cemented with ore minerals; pitchblende and sulfurs, minor illite. C) PPL. Pitchblende, sulfides within Dolomite and calcite. Sulfides are highlighted in yellow. D) XPL, of C. E and F) PPL and XPL. Details on orthogonal microfracture cemented with ore minerals and minor calcite.

Fracturing stage 6: faulting, second oxidation stage and second stage of uranium mineralization

Second stage of uranium mineralization (f6, U2) is associated with the second stage of oxidation of the host rock. This light red colour of the mineralized host rock, characterized by fine grains of hematite, characteristic of this fracturing stage. Purplish reworked clasts of QB are observed in reddish cataclastic fault rocks (Fig. 29A-B). After observations made throughout the Contact prospect, it appears that tectono-hydraulic breccias (Fig. 29C-F) and strongly clay altered fault zones of f6 are usually not uranium-mineralized.

In mineralized fault zones, spherulitic pitchblendes (Fig. 30 and 31) surrounded by a millimetric halo of iron-removal is one visual characteristic of this mineralizing stage. Ore minerals mainly represented by pitchblende are observed disseminated in the host rock, or cementing fractures in damage zones (Fig. 30C). Anastomosing shapes of the microfractures were presented in the article. Mineralized joints were observed to be crosscut by post-ore faults as presented in the article and also in Fig. 30C.

Spatial association of this mineralizing stage with quartz veins is usually not observed as the desilicification is strong. However, when observed, the quarz veins don't display orthogonal microfractures and they are more strongly dissolved, along edges and in vugs filled with pitchblende and illite (Fig. 31A-E).

Anastomosed crack-seal calcite veins were observed crosscutting the first stage of uranium mineralization and are micro-brecciated by pitchblende of U2 (altered partly to uranophane in the example of Fig. 32A-G). It is possible that these thin calcite veins could be synchronous with this mineralizing stage. Spatial associations are hard to confirm due to the small size of these veins, and the restricted view we have of fault zones in drill core.

Hematite is the only iron oxide associated with this mineralizing stage, goethite (characterising lower temperatures) is linked to later alteration (probably meteoric) of the iron oxides. Late alteration is also characterized by alteration of U^{4+} minerals (pitchblende) to U^{6+} minerals (uranophane in exemple).

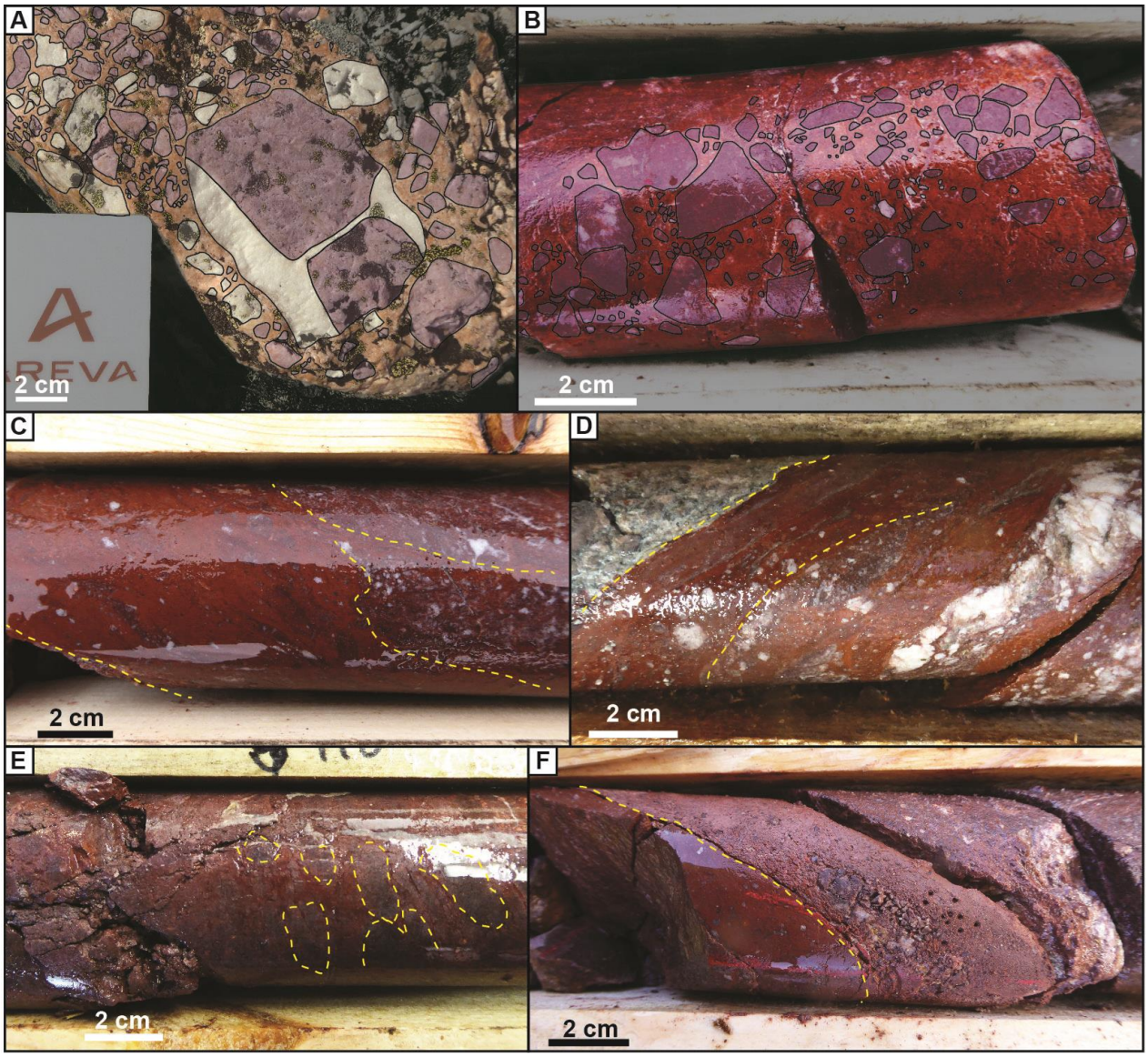

Figure 29: A) Reworked purple clasts (first stage of oxidation) bearing quartz vein in a reddish (second stage of oxidation) silicified matrix. B) Reworked purple clasts in a reddish silicified matrix. C) Hematized tectono-hydraulic breccia. D) Hematized tectono-hydraulic breccia. E) Hematized tectono-hydraulic breccia. F) Hematized tectono-hydraulic breccia, crosscut by a more clay altered ultracataclastic hematized fault rock.

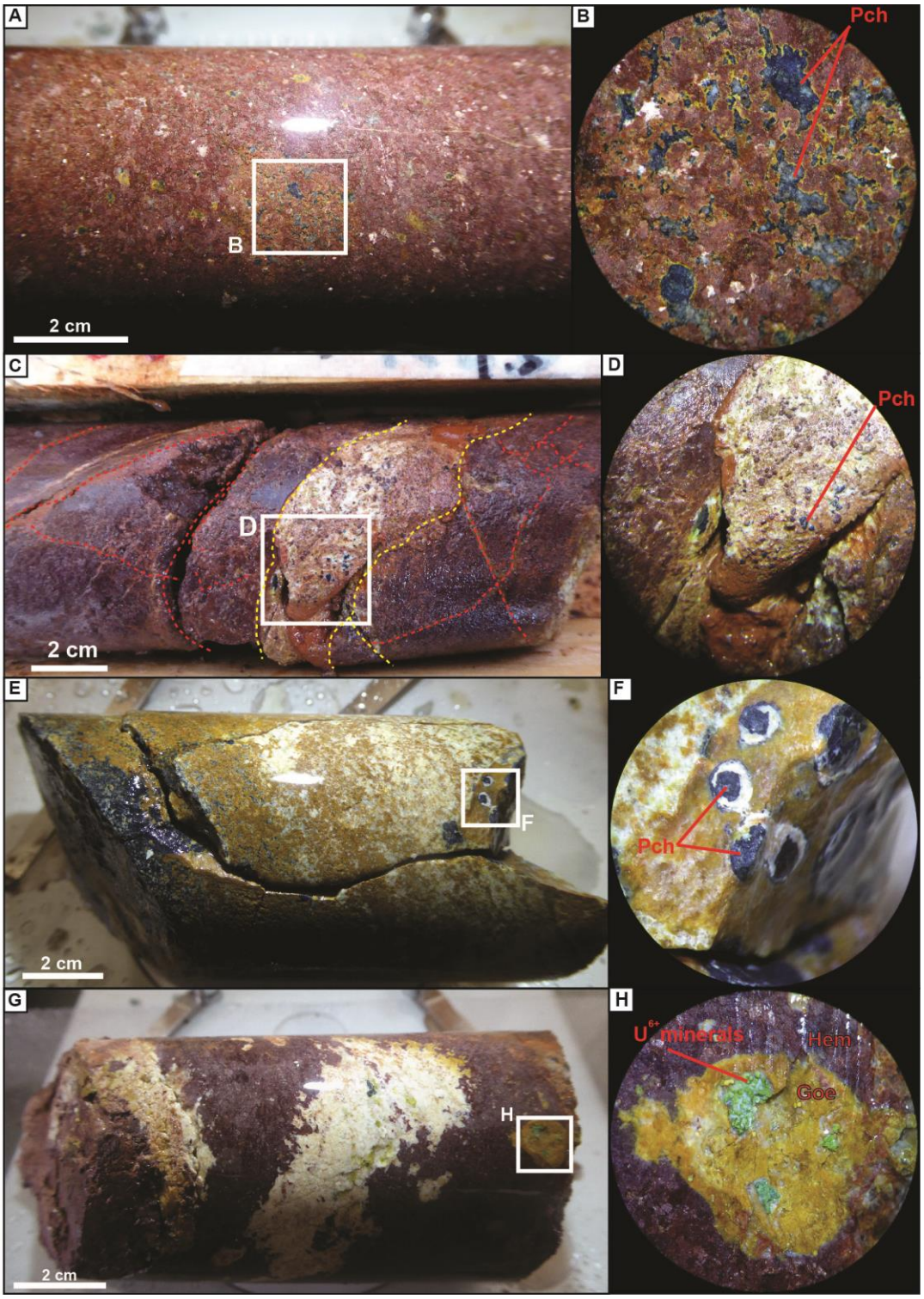

Figure 30: A) Spherulitic pitchblende in a bright red oxidized host rock. B) Detail of the mineralization. C) Mineralized damage zone (some fractures are highlighted in red) crosscut by a post-ore microfault. D) Relict pitchblende in the cement of the microfault. E) Spherulitic pitchblende. Orange/yellow iron oxide is goethtite. F) Detail of the spherulitic pitchblende with the iron removal halo (white). G) Local iron removal linked to pitchblende precipitation. H) Former spherulitic pitchblende altered to uranophane.

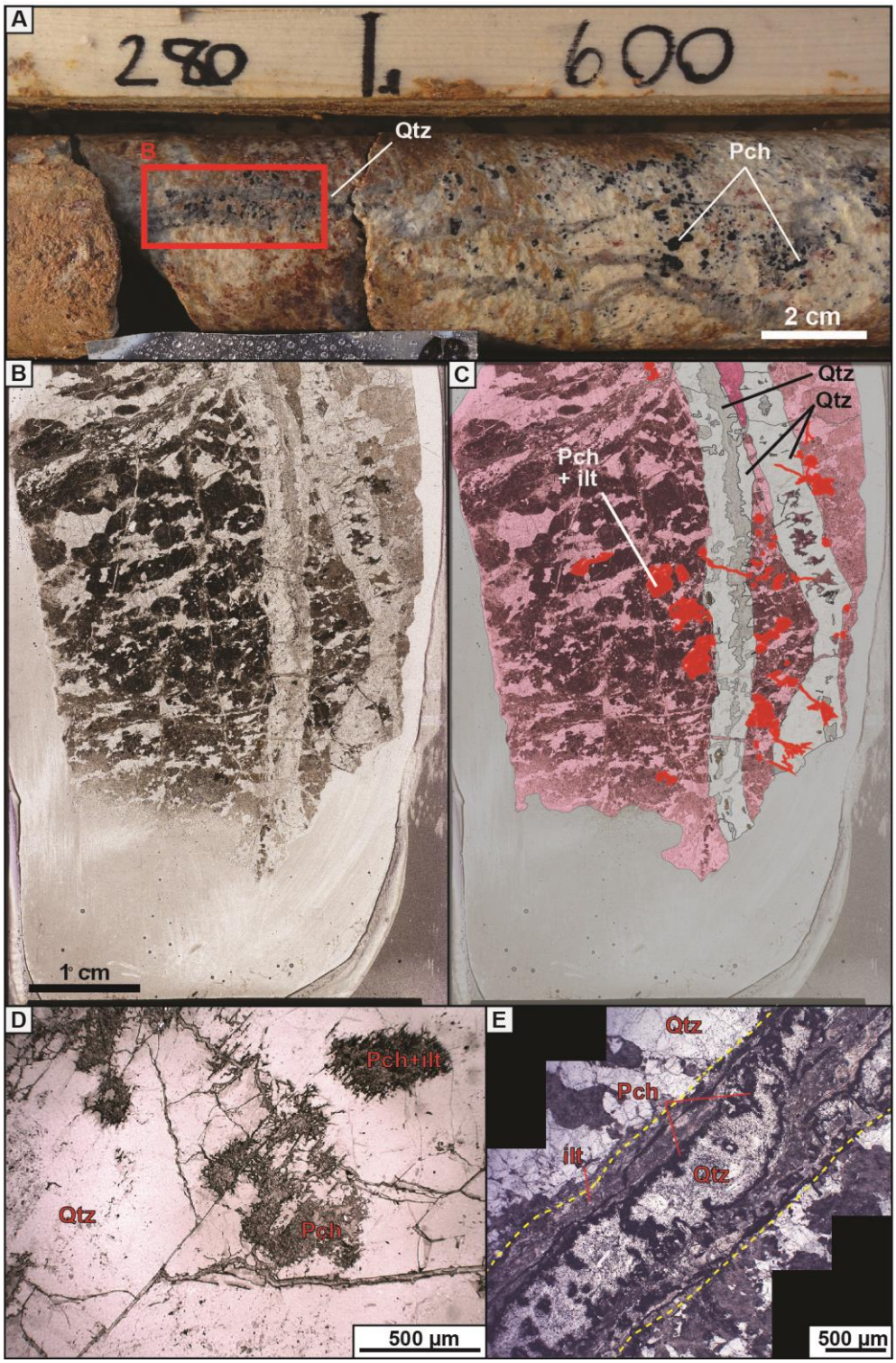

Figure 31: A) Spherulitic pitchblende in bright red oxidized rock, with iron removal halo. Pitchblende is associated to quartz veins. The red rectangle shows the location of the thin section. B and C) Thin section scan and interpretation scheme. D) PPL. Quartz dissolution in quartz vugs filled with pitchblende and illite. E) PPL. Re-opened quartz veins and quartz dissolution (irregular boundaries). Texture is different compared to the first stage of uranium mineralization (no orthogonal microfractures for example).

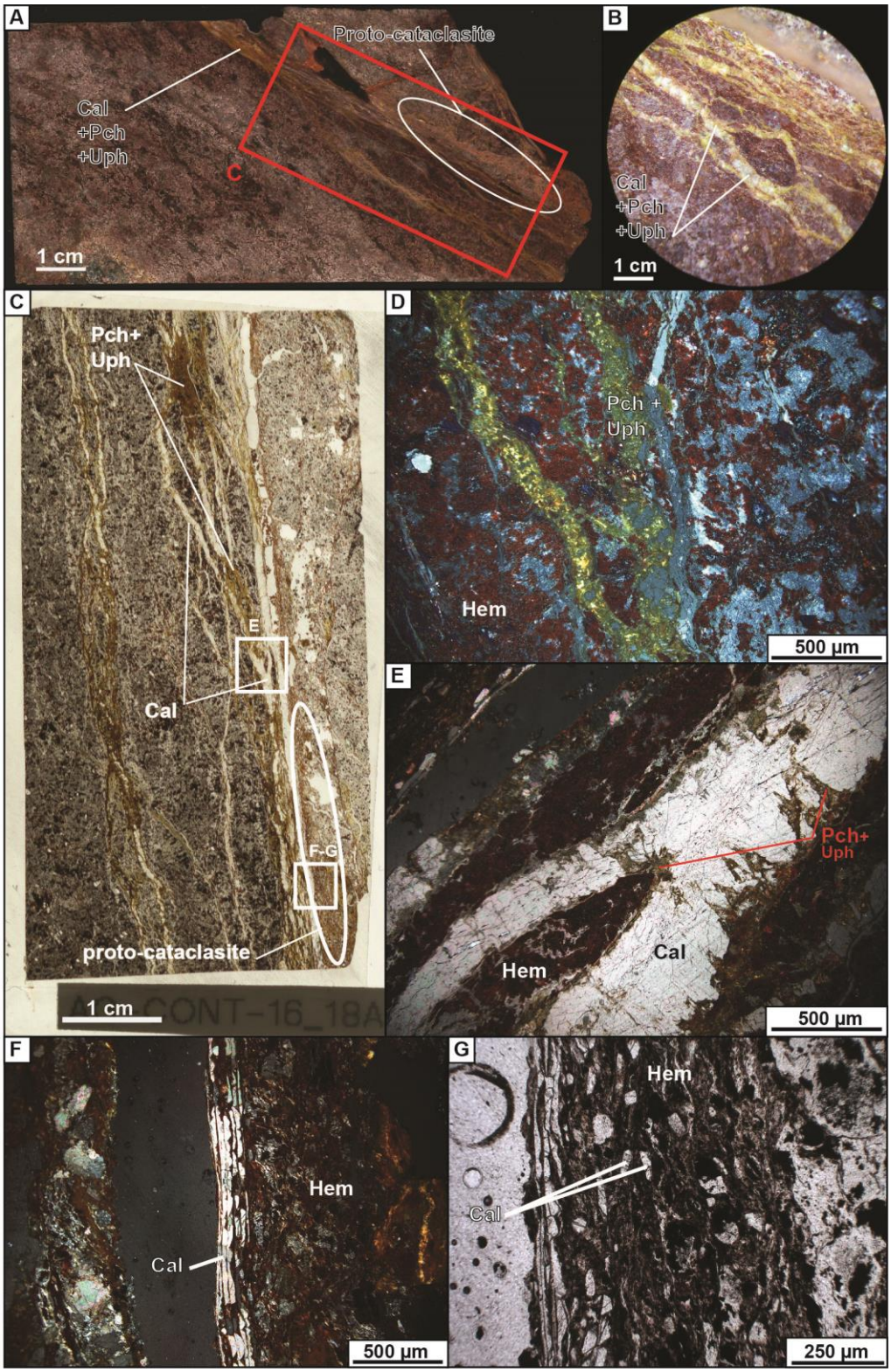

Figure 32: A-G) Anastomosed calcite veins with pitchblende altered to uranophane along the boundaries and in microfractures. The calcite vein network is fractured by a post-ore microfault (proto-cataclasite). Red rectangle locates the thin section. Micro-clasts of post-ore cataclastic fault rock is more detailed in pictures F and G.

Fracturing stages 7 and 8: cataclastic faults and post-primary uranium mineralization alteration

Post-ore alteration is characterized by white and greenish coloured fault rocks (Fig. 33), usually displaying strong illitization and desilicification. The greenish colour (Fig. 33A-D) can be due to a host rock rich in retrograde metamorphic chlorite, that has been reduced in size by the tectonic comminution and mixed with illite. This fracturing stage re-activates previously formed fractures, this is clearly observed when f6 faults are reactivated due to the contrasting colours. Reworked clasts characterized several fracturing events (Fig. 33B-F).

Examples of uranium mineralization being crosscut by these post-ore faults and other examples are presented in figures 34 and 35.

In figure 34, the mineralized quartz vein network (U1) is crosscut by a non-mineralized microfault cemented with illite. Micro clasts of rutile and sulfides (U1 ore minerals) are observed within the microfault. Figures 35A-D show a quartz vein orthogonally crosscut by microfractures cemented with pitchblende, sulfurs and calcite, is crosscut by a microfaults cemented with illite. Small offset of the quartz vein is observable and as in figure 34, microclasts of quartz, pitchblende and sulfides are observed within the microfault. Figures 35 E-F also show similar micro-scale evidence of such crosscutting relationships.

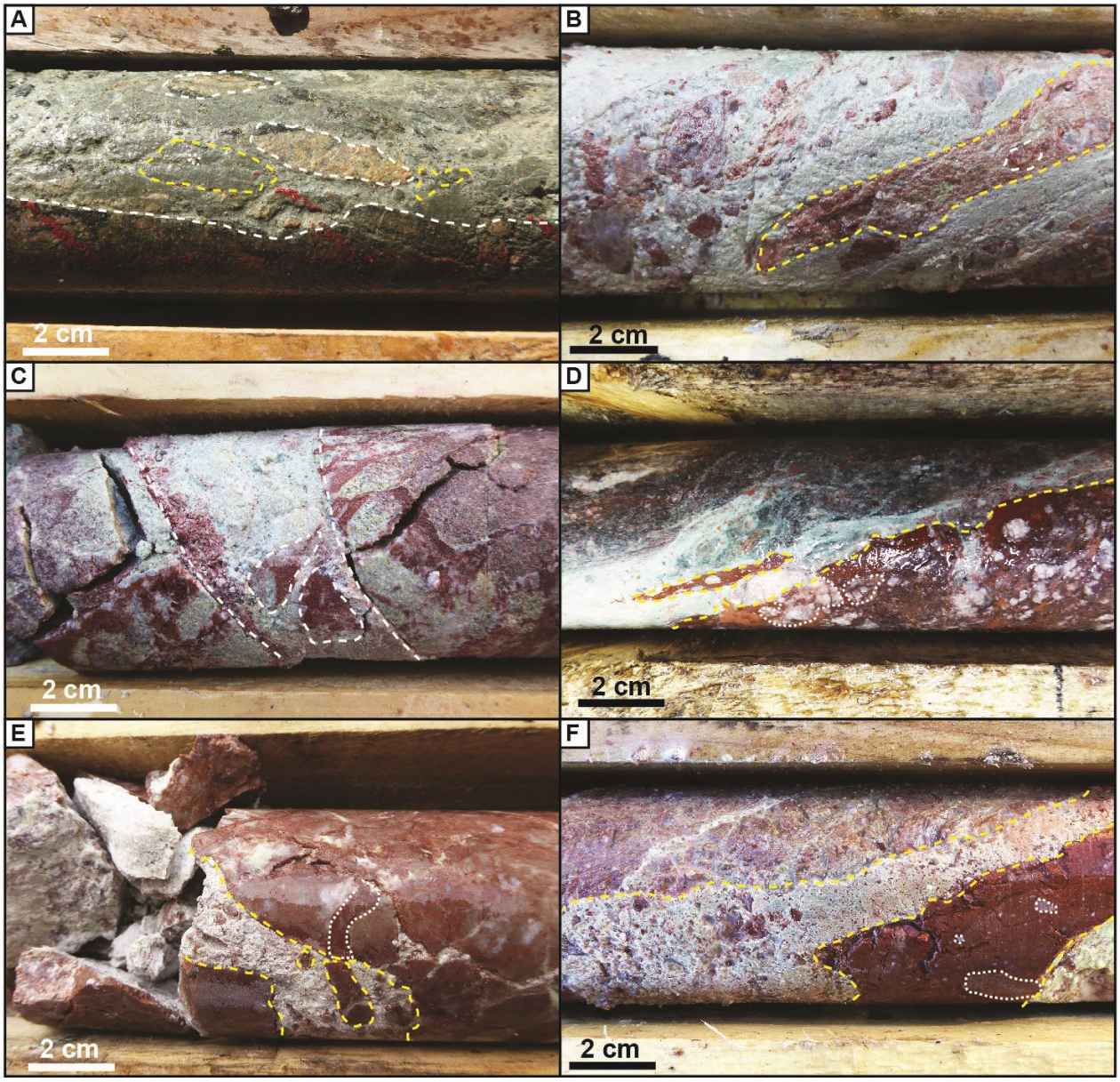

Figure 33: A-F) Several drill holes pictures of reactivated f6 faults. Several generations of clasts are observed. White dotted outline highlights the older clasts, yellow dotted line highlight the younger clasts.

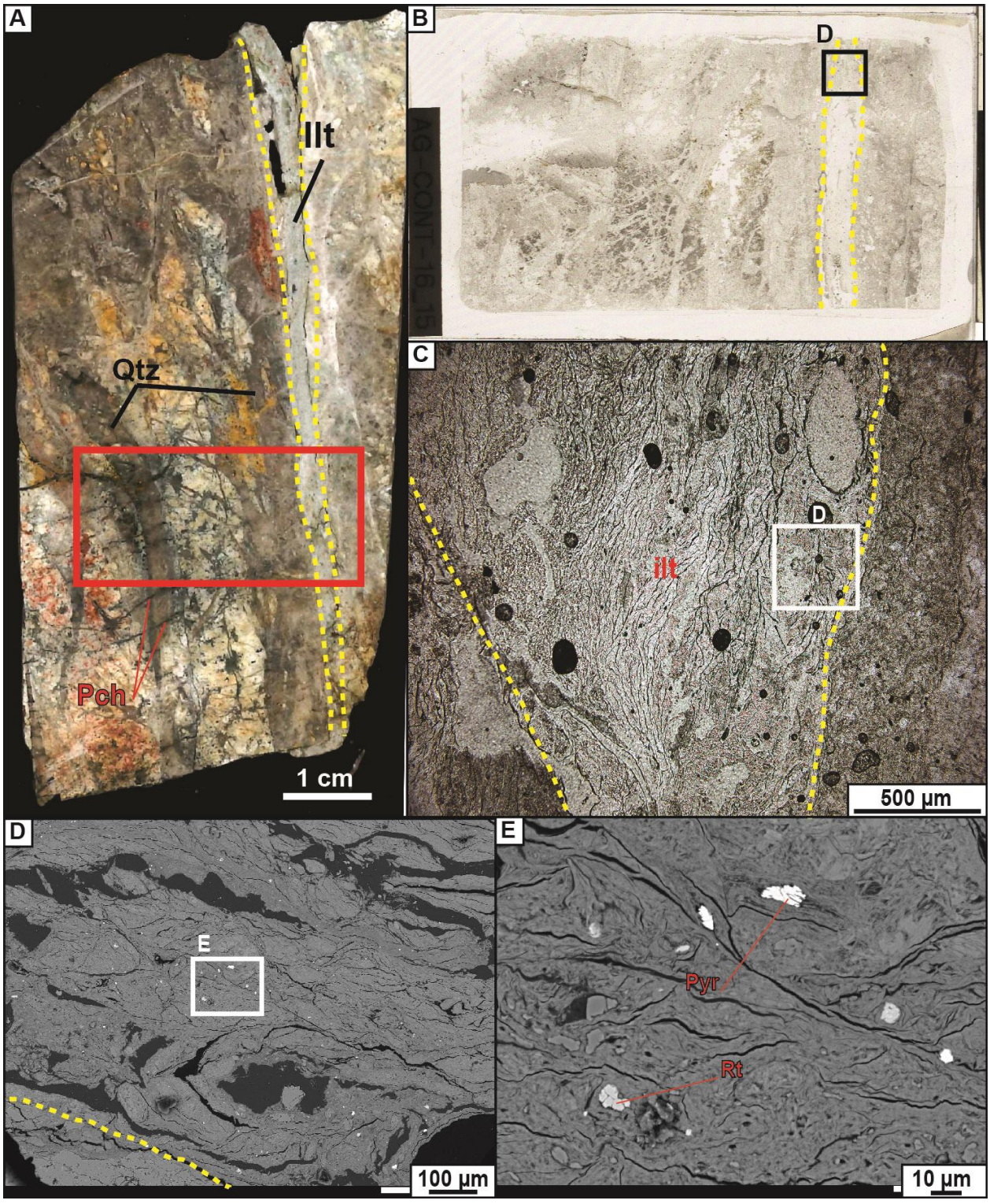

Figure 34: A-E) Macroscopic (drill core sample) to microscopic (transmitted light, picture B and C, SEM, picture D and E) observations of a mineralized (U1) quartz vein network being crosscut by a post-ore microfault, cemented with illite. Relicts of ore minerals are visible in E.

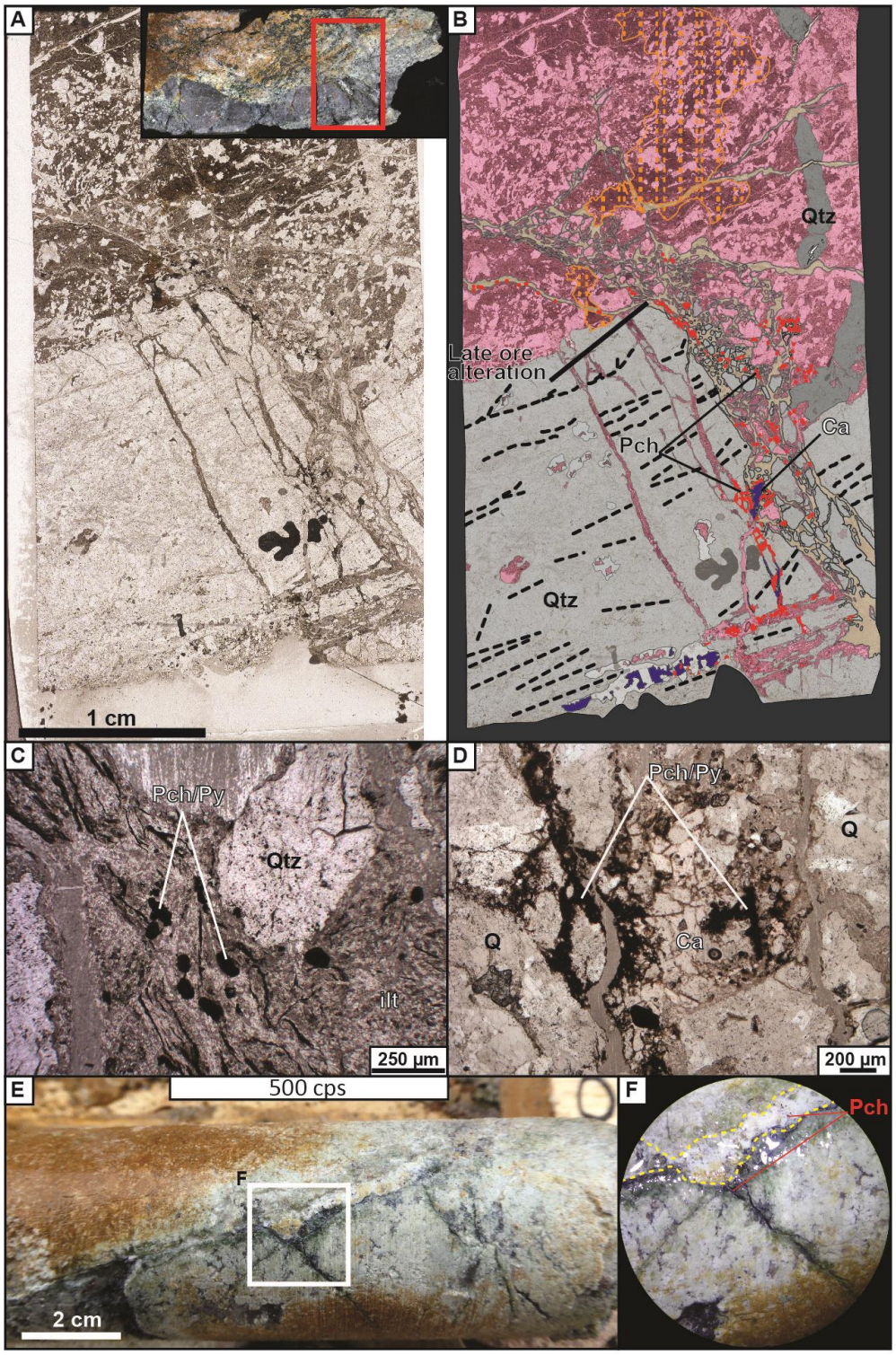

Figure 35: A-D) Thin section scan and interpretation schemes: Microfractured and mineralized quartz vein crosscut by post-ore microfault, cemented with illite. C-D) details of thin section in picture A: micro-reworked clasts within the post-ore microfault. E-F) Uranium-mineralized quartz vein crosscut by a post ore (white illite cement) microfault.

6 UP-SCALING OF THE STRUCTURAL MODEL MADE ON THE CONTACT PROSPECT

6.1 STRUCTURAL CONTROLS AND METALLOGENIC MODEL OF URANIUM MINERALIZATIONS IN THE KIGGAVIK AREA

To be submitted

Alexis Grare[a,b] , Antonio Benedicto[b,c], Julien Mercadier[d], Olivier Lacombe[a], Anna Trave[e], Marie Guilcher[d], Antonin Richard[d], Patrick Ledru[b], Mario Blain[b], John Robbins[b],

[a] *Sorbonne Universités, UPMC-CNRS-iSTeP, 4 place Jussieu. 75005 Paris. France*

[b] *AREVA Resources Canada Inc. 817-45th St West Saskatoon. SK S7L 5X2. Canada*

[c] *Université Paris Sud, UMR GEOPS, 91405 Orsay. France*

[d] *Université de Lorraine, CNRS, CREGU, GeoRessources lab, Campus Aiguillettes, Faculté des Sciences et Technologies, rue Jacques Callot, Vandoeuvre-lès-Nancy, 54506 France*

[e] *Universitat de Barcelona, Departament de Mineralogia, Petrologia i Geologia Aplicada, Facultat de Ciències de la Terra. 08028 Barcelona. Spain*

Abstract

The Kiggavik area is located on the eastern border of the Paleoproterozoic Thelon Basin (Nunavut, Canada), it hosts major uranium mineralization in its archean basement lithologies, displaying a strong structural control and many similarities with unconformity-related uranium deposits of the Athabasca Basin. Our results show that the polyphased, dominantly brittle fracture network with main ENE-WSW and NE-SW fault zones formed earlier during the Thelon and Trans-Hudsonian orogenies and were mineralized in four stages, U0, U1, U2, U3. These stages yield distinctive fracture, alteration and mineralization patterns. U0, inferred of magmatic origine, likely occurred at ca. 1830 Ma and is related to micro-brecciation and weak clay-alteration under a WSW-ENE compressional stress. This event is crosscut by intense quartz brecciation, iron oxidation and veining at ca. 1750 Ma. This silicifying event that predates deposition of the Thelon formation is of magmatic epithermal origin; it caused pervasive silicification of former fault zones, giving birth to the so-called Quartz Breccia that compartimentalized subsequent fracturing and behaved as a barrier for mineralizing fluids. Both the U0 mineralization and the subsequent silicifying events reflect the importance of pre-Thelon magmatic-related fracturing/fluid circulation events on controlling the future development and

location of later unconformity-type uranium deposits. U1, U2 and U3 postdate deposition of the Thelon formation; U1 is characterized by polymetallic reduced narrow fault zones and U2 is characterized by monometallic oxidized wider fault zones. These mineralization events occurred in response to a far-field compressional stress that evolved from WNW-ESE to NE-SW /ENE-WSW; both formed at ~1500-1300 Ma and are related to circulation of Thelon-derived U-bearing basinal brines. A post U1/U2, but pre-Mackenzie dikes, NE-SW extensional stress caused normal-dextral offset of the orebodies by reactivating NNW-SSE and E-W faults. This fracturing event triggered circulation of hot acidic fluids, desilicifying, illitizing and bleaching the host-rock, remobilizing and reprecipitating previous uranium stock. U3 is linked to uranium redistribution/reconcentration along redox fronts and occurred through weak reopening of the fracture network enhancing percolation of meteoric fluids at 500-300 Ma.

Our study shows that unlike in the Athabasca Basin where uranium deposits are unconformity-related in type and where clay alteration halos are spatially and genetically associated to ore bodies, in the Kiggavik area (1) uranium deposits are of mixt type evolving from magmatic-related (U0) to unconformity-related (U1-U2), with a final perturbation by meteoric fluid percolation (U3), and (2) the strongest clay alteration event postdates the main stages of mineralization (U0 to U2).

Keywords

Uranium deposit; alteration; structural control; fracture; Thelon Basin; Kiggavik.

1. introduction

Numerous uranium occurrences have been discovered since the 1970s in the Thelon-Baker Lake area in the Nunavut Territory, northern Canada (Curtis and Miller, 1980; Miller, 1980; Miller, 1982; Miller and Lecheminant, 1985; Miller et al., 1986; Miller, 1995). In this area, the Paleo- to Mesoproterozoic Thelon Basin presents direct similarities whether in term of sedimentology, geological and structural evolution, and diagenetic history with the Athabasca Basin (Saskatchewan, Canada) which concentrates the largest number of high grade unconformity-related uranium (URU) deposits in the world (Miller and LeCheminant, 1985, Fuchs et al. 1986, Weyer et al. 1987, Fredrich et al. 1989, Fuchs and Hilger, 1989; Jefferson et al. 2007a). Based on this knowledge, the Thelon Basin and its related basement have been considered as prospective for the discovery of URU deposits and thus have been explored for several decades. Among the different prospective zones, the Kiggavik area, located on the eastern border of the Thelon's Aberdeen sub-basin (Fig. 1), has been explored since the 1980s and several uranium mineralized bodies of economic interest have been discovered: Kiggavik

(Main Zone, Center Zone, East Zone), Bong, Andrew Lake, End, which are deposits, and Granite grid, 85W, Sleek, Jane and Contact, which are prospects (Fig. 2; Fuchs and Hilger, 1989; Riegler et al., 2014; Chi et al., 2017).

Various scientific studies have been carried out on these deposits to characterize the specific key parameters which controlled the formation of these U mineralization, with the objective to compare them with those controlling the formation of the URU deposits in the Athabasca Basin. In contrast to the Athabasca Basin, where ductile tectonics involving graphitic-rich shear zones were a major structural control on the formation of the deposits, the tectonic style of deformation and mineralization in the Kiggavik area is dominantly brittle, as exemplified by prevailing cataclastic to ultracataclastic fault rocks (Grare et al., 2018). Ductile to brittle-ductile sub-vertical shear zones, especially graphitic-rich, are rarely observed in the Kiggavik area and thus their reactivation appear to be only a secondary process controlling the location and formation of uranium mineralization in some cases (Johnstone et al., 2017). In contrast to the U deposits of the Athabasca Basin for which carbon is considered to be a major player (whether for structural and reducing controls), carbonaceous matter is only noted at Bong, as poorly crystallized hydrothermal graphite (or bitumen?) and organic matter pellets (Sharpe et al., 2015; Riegler et al., 2016). In the Kiggavik area, uranium mineralization is hosted in the basement of various compositions (granitic gneiss, psammo-pelitic gneiss, granite…) which crop out throughout the exploration permit in this area, as it is uncovered by the basin sandstones. This allows for the implementation of 3-D observations on outcrops and of the fracture networks intersected by drill holes.

Previous studies on the Kiggavik area deposits have focused on the characterization of mineralizing fluids and their alteration products throughout geochemical analysis and age-dating of uranium oxides and clay minerals (Farkas, 1984; Riegler et al., 2014; Shabaga et al., 2015; Sharpe et al., 2015; Chi et al., 2016; Fayek et al., 2017; Quirt, 2017; Shabaga et al., 2017a, 2017b; Grare et al., 2017). The tectonic history, related structural controls and the relative timing of the deposits have not been looked at in details and are consequently weakly understood. Recent work on the Contact prospect (Grare et al., 2018), however, has brought the first detailed picture of the successive pre- and syn/post-Thelon fracturing/faulting events at different scales and their role in uranium mineralization.

U in the Kiggavik area is related to different fluid circulation events, active between ca. 1.5 Ga and the present time. Based on the study of fluid inclusions in quartz-carbonate veins spatially associated with the (interpreted) first stage of U mineralization, Chi et al. (2017) proposed that the U mineralization at End initially formed from high-salinity 190-250°C basinal

brines derived from the Thelon Basin, in accordance with the nature of the diagenetic fluids defined within the Thelon Basin (Renac et al., 2002). These brines theoritically mixed with low-salinity and higher T (140-340°C) fluids at the time of primary U deposition. Although information is lacking, the properties of the basinal brines are similar to the basinal brines of the Athabasca Basin (Pagel, 1975; Derome et al., 2005; Richard et al., 2010; 2016; Chu and Chi, 2016) and which are considered as the mineralizing fluids in the URU deposits. For the Andrew Lake deposit, Shabaga et al. (2017) proposed that different mineralizing fluids followed one another over time (from ca. 1000 Ma up to now) and are responsible for the different generations of U mineralization. Those fluids were dominantly meteoric, oxidizing and acidic. Their precise characteristics (T, salinity, etc…) and their link with the Thelon Basin are not known. For the Bong deposit, Sharpe et al. (2015) proposed that primary U mineralization occured at ca. 1500 Ma (U1, oldest age obtained yet, for uranium in the Kiggavik area), followed by different U mineralizing stages for which the controlling parameters are poorly known. The mineralizing fluids are unknown for U1 and those related to the second stage of mineralization (at 1100 Ma) are isotopically closer to meteoric fluids rather than basinal brines. The alterations linked to the U mineralization are diverse, potentially linked with the different type of fluids and of physico-chemical conditions that followed one another in the Kiggavik area. An illite-uranium oxide association is commonly observed (Sharpe et al., 2015; Chi et al., 2016; Shabaga et al., 2017) for the primary stage of mineralization in different zones. A chlorite-uranium oxide was also proposed for the Kiggavik-Andrew Lake trend (Riegler et al., 2013) and at Bong for U2 (Sharpe et al.,2015), the chlorite having a sudoitic composition, as observed for the hydrothermal chlorite linked to U mineralization in the Athabasca Basin (Hoeve and Quirt, 1984; Kotzer and Kyser, 1995).

Based on these previous informations, the nature of the uranium mineralization of the Kiggavik area and their controls (structural and geochemical) remain therefore open, and despite the work by Anand and Jefferson (2017) that provides insights into the succession of regional tectonic events, the link between the macroscale and the microscale fractures and uranium mineralization, and the 3D architecture of faults zones in the Kiggavik area remains unconstrained. These points need to be understood to build a reliable metallogenic model of uranium mineralization in Kiggavik area. The specific work on the evolution of the structural trap for the U mineralization in the Kiggavik area must be coupled to mineralogical and geochemical observations to fully depict the U system in this zone facilitating comparison with world-class URU mineralization from the Athabasca Basin.

The aims of this paper are thus:

(1) To accurately depict the brittle stages of the fracture network that controls the uranium deposits in the whole Kiggavik area and its spatial-temporal evolution. Our work focuses in the characterization of the sequence of brittle structural events established at the Contact prospect (Grare et al., 2018) that also apply to the other deposits and prospects in the Kiggavik area. For this purpose, the entire long-life and polyphase brittle tectonic history of the Kiggavik area, predating and postdating tectonics of the Thelon Basin, has been deciphered and reconstructed on the basis of multi-scale observations from a review of the existing drill-core information, completed with new samples from various deposits, structural analysis of oriented data from both drill-core and outcrops.

(2) To accurately establish the nature and the age(s) of circulation of the paleo-fluids that circulated through the identified fracture network, by analysing the fracture infill products (cements, alteration clays and mineralisation) and the resulting fluid-rock interactions, i.e. uranium mineralization, in relation to the tectonic evolution. To this aim, new mineralogical observations were made, coupled with chemical characterization of both alteration products and U oxides. New U/Pb isotopic measurements on uranium oxides were also performed to define ages for comparison with published uranium oxide ages to complete the timing of the mineralizing events.

By this multi-faceted approach, we aim to propose an integrated structural and metallogenic model for the formation of the basement-hosted uranium deposits in the Kiggavik area that includes pre-Thelon and post-Thelon Basin uranium ore formation. Comparisons with the main characteristics of uranium deposits of the Athabasca Basin are made at the end of this article, and the model for the Kiggavik U deposits is questioned.

2. Geological setting

2.1 Regional setting

The Thelon Basin (ca. 1670–1540 Ma, Hiatt et al., 2003; Davis et al., 2011) and the Athabasca Basin (1740–1540 Ma, Ramaekers et al., 2007) are Proterozoic intracratonic basins (Gall et al., 1992) hosted by the Churchill Province, which resulted from the collisional amalgamation of the Rae and Hearne craton along the STZ, either in the neoarchean or during the Snowbird orogenesis at ~1.9 Ga (Hoffman, 1988; Corrigan et al., 2009; Fig. 1). These basins are located between the eroded remnants of the Trans-Hudson orogenic belt to the Southeast (ca. 2070-1800 Ma, overall NW-SE shortening) and the Thelon-Taltson orogenic belt to the west (ca. 2020-1900 Ma, overall E-W shortening). The Thelon Basin mainly consists of the Thelon

Formation, an 1800 meter-thick sedimentary pile of conglomerate and coarse-grained sandstone, overlain by the ca. 1540 Ma shoshonitic basalts of the Kuungmi Formation (Chamberlain et al., 2010) and marine dolomites of the Lookout Point Formation (Gall et al., 1992) of the Barrensland Group (Fig. 2).

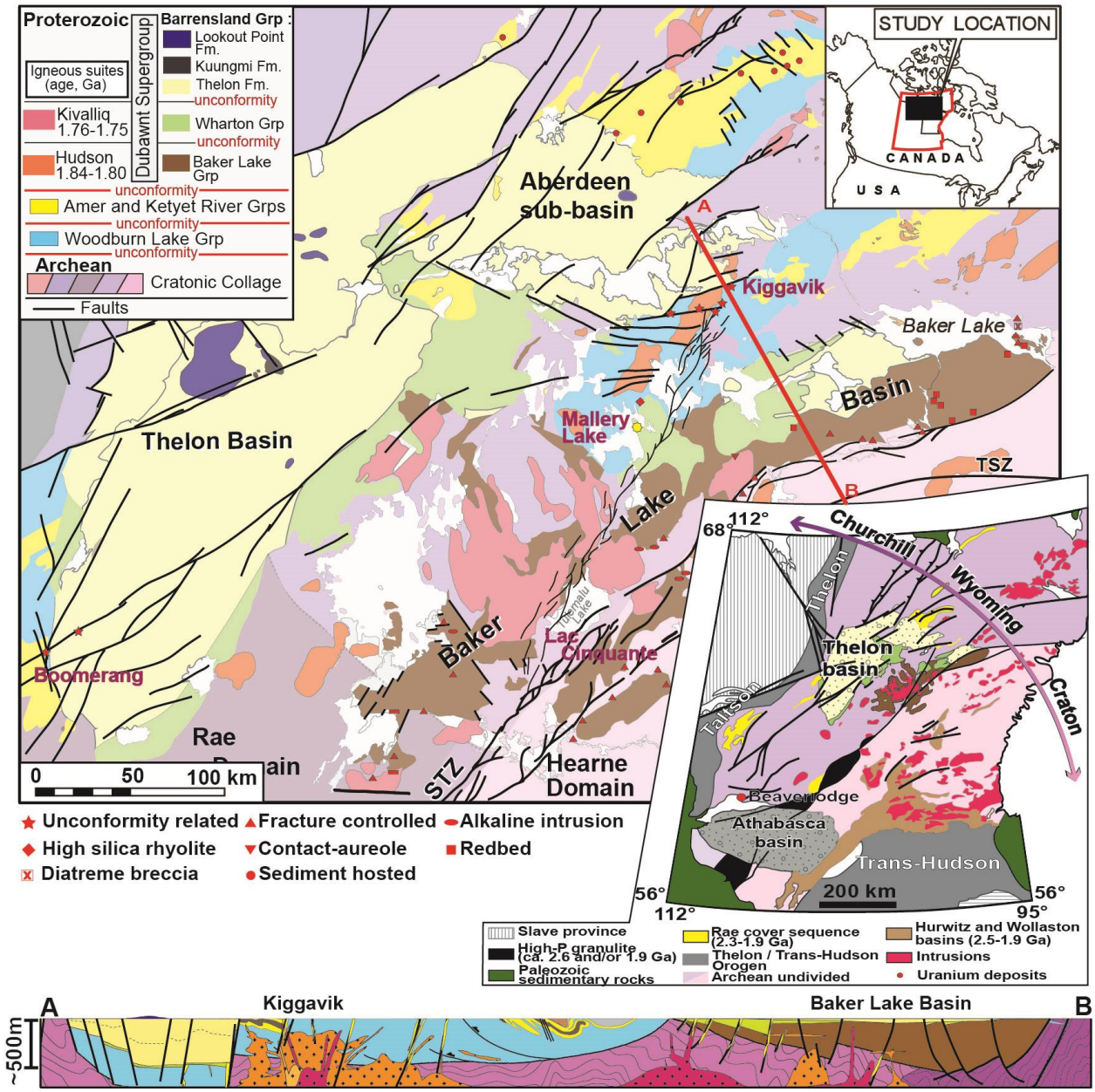

Figure 1: Geological map of the Thelon-Baker Lake area (after Curtis and Miller, 1980; Rainbird et al., 2003). The Kiggavik area is located on the south-eastern border of the Aberdeen sub-basin. Small insert depicts the main geological units of the Churchill-Wyoming craton and location of the Thelon Basin within the Rae Domain, east to the Taltson-Thelon orogeny (cross section built and modified after Jefferson et al., 2011, 2017; Hadlari and Rainbird, 2011; Pehrsson et al., 2013).

The Thelon Formation overlies a complex set of sedimentary and bi-modal volcanic-sedimentary rocks of the Wharton and Baker Lake groups (Rainbird et al., 2003; Hadlari and Rainbird, 2011), that filled up the Baker Lake Basin which developed between 1850 Ma and 1750 Ma (Rainbird et al., 2006; Rainbird and Davis, 2007). The Baker Lake Basin developed as a result of (retro-arc) extensional to transtensional rifting tectonics related to the pre/syn-collision between the Churchill province and the Superior province (the Trans-Hudsonian orogeny). It was followed by uplifting, extensive erosional peneplanation and regolith formation, over which deposited the Thelon formation, linked to thermal subsidence (Rainbird et al., 2003; Rainbird and Davis, 2007; Hadlari and Rainbird, 2011). Major ENE-trending dextral strike- and oblique-slip faults, including the Thelon fault (Fig.1) became active at that time.

The Barrensland, Wharton and Baker Lake groups are parts of the Dubawnt Supergroup (Peterson et al., 2006) (Fig. 2). The Dubawnt Supergroup unconformably overlies the metamorphosed basement consisting of Archean basement rocks that include Mesoarchean (ca. 2870 Ma) granitic gneisses, 2730–2680 Ma supracrustal rocks of the Woodburn Lake Group (Pehrsson et al., 2013) and a distinctive package of 2620–2580 Ma felsic volcanic and related hypabyssal rocks known as the Snow Island suite (Jefferson et al., 2011a, 2011b; McEwan, 2012; Tschirhart et al., 2013, 2017; Peterson et al., 2015a; Johnstone et al., 2016). These rocks, together with overlying Paleoproterozoic (2300–2150 Ma) rocks of the Ketyet River Group (Rainbird et al., 2010) include a prominent unit of orthoquartzite (Zaleski et al., 2000).

The Archean to Paleoproterozoic rocks of the Churchill province where intruded by three intrusive suites: (i) the late syn-orogenic (ca. 1830 Ma) Hudson suite (Peterson et al., 2002), (ii) Dubawnt minette suite (contemporaneous of the Hudson suite), with ultrapotassic rocks, minette dikes and lamprophyres, and (iii) ca. 1750 Ma rapakivi-style Nueltin granite of the anorogenic Kivalliq igneous suite (Hoffman 1988; Van Breemen et al., 2005; Peterson et al., 2015b; c.f., Scott et al., 2015). The diabase dikes of the giant Mackenzie diabase swarm that form prominent linear aeromagnetic features trending NNW-SSE (Tschirhart et al., 2013; 2017) cut across all of the previous rocks. This intrusive event is dated at 1267±2 Ma (Lecheminant and Heaman, 1989; Heaman and Lecheminant, 1993) and represents the last magmatic-tectonic event in the region.

As presented above, the rocks belonging to the Dubawnt Supergroup were deposited during a period marked by rift tectonics. They host uranium mineralization and alteration which display lithological and structural characteristics similar to the Beaverlodge District, the fracture-controlled mineralization of which are linked with pre-Athabasca to post-Athabasca history (Dieng et al., 2013; 2014). The uranium potential of volcano-sedimentary rocks of the Baker

Lake basin (Nunavut, previously called District of Keewatin, named Thelon-Baker Lake area in this work) was recognized through uranium exploration in the 1960s-1970s. Reconnaissance helicopter mapping, sedimentology/sequence-stratigraphy studies and ground exploration by the geological survey of Canada produced the initial work. Metallogenic studies permit to have a good picture and first models of the uranium mineralization types in the Keewatin district, from syngenetic to epigenetic orebodies (Curtis and Miller, 1980; Miller, 1980; Miller, 1982; Miller and Lecheminant, 1985; Miller et al., 1986; Miller, 1995). Except the study of Bridge et al. (2013) on the Lac Cinquante deposit (Fig. 1) and the work done in the Kiggavik area, there were neither recent studies on uranium occurrences in the Thelon Baker Lake area, nor even attempts at characterizing them in light of new conceptual models.

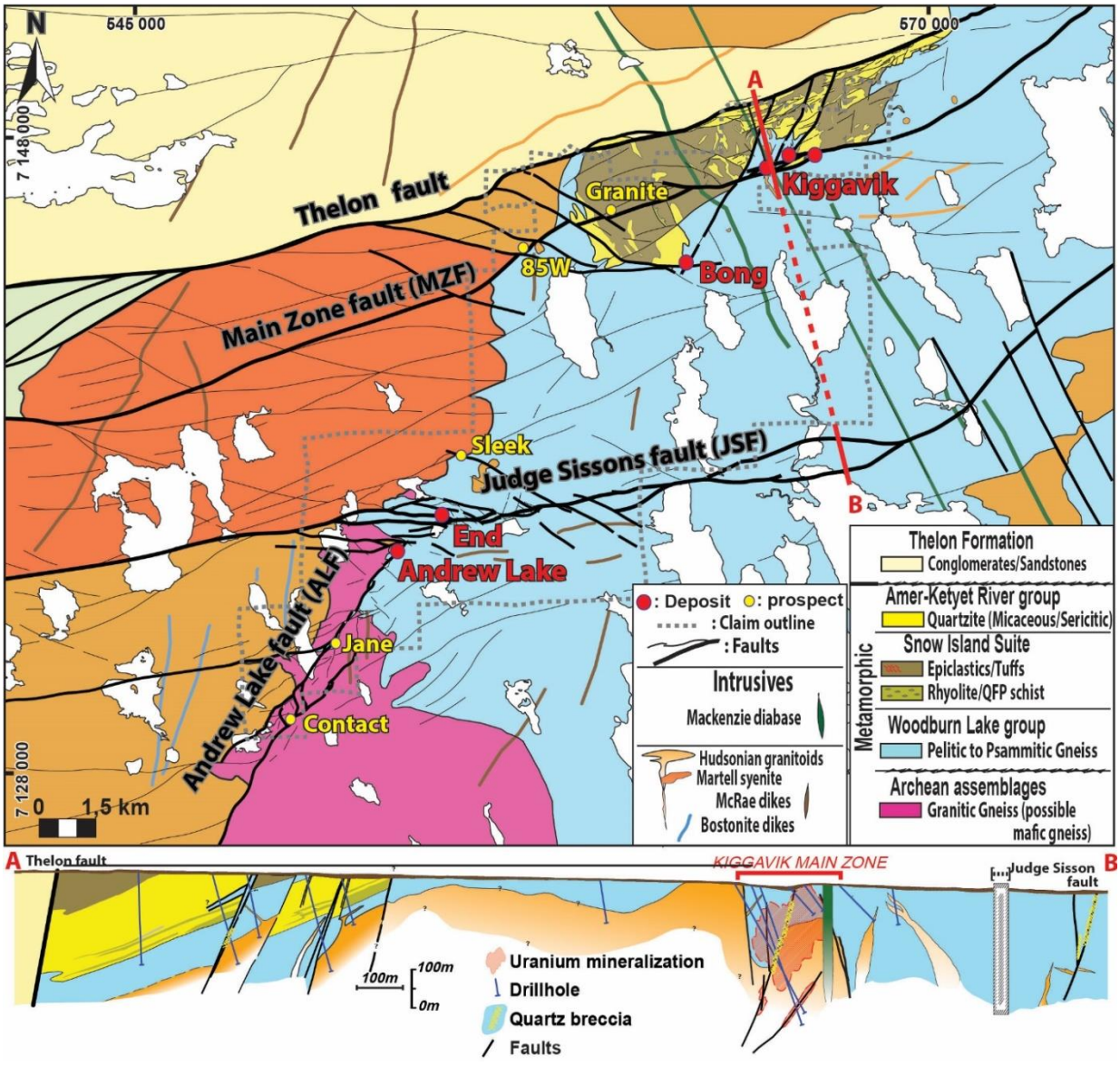

Figure 2: Simplified geological map of the Kiggavik area (AREVA internal document) and cross section from the Thelon fault to the Judge Sisson fault. Deposits and prospects are indicated with red and yellow circles, respectively.

In this scientific article, the term “pre-Thelon” (pre-Thelon formation, which constitutes the biggest part of the Thelon Basin) refers to a period before deposition of the Thelon formation (before ca. 1667 Ma) but after the peak of Trans-Hudson orogenies (i.e. after 1810 Ma), to the onset of rifting and basin development (ca. 1750 Ma). Post-Thelon refers to a period after the deposition of the Thelon formation (usually the lower bracket is used, so post-ca. 1540 Ma). Syn-Thelon refers to a period bracketed at 1667-1540 Ma.

2.2 Local Geologic setting

Uranium mineralization in the Kiggavik area is hosted within Archean and Paleoproterozoic basement rocks marginal to the Aberdeen sub-basin of the Thelon Basin (Jefferson et al., 2011a, 2011b; Fig. 1). The Archean rocks include Mesoarchean (ca. 2870 Ma, Davis et al., 2006) granitic gneisses, the 2730–2680 Ma (Pehrsson et al., 2010) supracrustal rocks of the Woodburn Lake Group and a 2620–2580 Ma (Rainbird et al., 2010) felsic volcanic and related hypabyssal rocks of the Snow Island suite (Peterson et al., 2015; metarhyolites, epiclastics and tuffs in Fig. 1). These rocks are overlain by the Paleoproterozoic (2300–2150 Ma, Rainbird et al., 2010) orthoquartzite of the Ketyet River Group (Fig. 2). Basement rocks are intruded in the area by the Schultz Lake Intrusive Complex (SLIC) (Scott et al., 2015). The SLIC comprises two groups of rocks with contrasting origins but with some overlap in geochemical and petrographic signatures (Scott et al., 2015): (i) the “Hudson granite” consist of non-foliated granitoid sills, syenites and lamprophyre dikes of the late syn-orogenic Hudson suite. The Hudson granite represents the first pulse of magmatic activity at 1840–1820 Ma in the Kiggavik area. (ii) The “Nueltin granite” comprises anorogenic granite to rhyolite of the Kivalliq igneous suite (1770–1730 Ma, Peterson et al., 2015a). Other elements of these suites include the McRae Lake dikes and minor Dubawnt minette intrusives of the Kivalliq igneous suite (Scott et al., 2015) which is a second pulse of magmatic activity in the area dated at 1750 Ma. Uranium and thorium primary enrichment were described to be associated with bostonite dikes (Peterson et al., 2011) and pegmatites attributed to emplacement of the Dubawnt minette (ca. 1830 Ma) and Kivalliq igneous suite, respectively. Such a bostonite dike was observed near the Kiggavik Main Zone (Anand and Jefferson, 2017).

All the previously described rock units are unconformably overlain by the Thelon Formation, which crops out in the Northern part of the Kiggavik property (Fig. 2). The diabase dikes of the 1267 Ma Mackenzie diabase swarm cut across all of the previous rocks in the Kiggavik area.

2.3 Main structural trends in the Kiggavik area

The main structural features in the Kiggavik area are the ENE-trending Thelon fault (TF) and the Main Zone fault (MZF) in the northern part of the property, the ENE-trending Judge Sisson fault (JSF) in the central part, and the NE-trending Andrew Lake Fault (ALF) in the southwestern part (Fig. 2). The MZF hosts 85W, Granite grid and Kiggavik (Main, Central and East Zones). The Kiggavik Main Zone deposit is partly hosted (Fig. 2) by the “Lone Gull granite” which comprises Hudsonian granite, partly mixed with magmas of the Dubawnt suite and lately intruded by Nueltin granites. End is hosted by the JSF, while Andrew Lake, Jane and Contact occur along the ALF (Fig. 2) (see also Grare et al., 2017).

Tectonic initiation of these faults goes back to the convergence of cratonic blocks during the latest stage of Trans-Hudsonian orogeny. The TF constitutes the boundary between the siliciclastic sedimentary rocks of the Thelon Formation to the north and the metamorphosed basement rocks to the south (Fig. 2). The TF offsets the SLIC Hudson granite of at least 25 km with a right-lateral component (Tschirhart et al., 2013) and its northern hanging-wall is down-thrown by up to 700 m (Davis et al., 2011). South of the TF, magnetic maps show that the SLIC is crosscut by numerous ENE-trending parallel and sub-parallel faults with apparent right-lateral displacement. The second ENE-trending major fault is the JSF (Fig. 2). The JSF dips steeply to the north on discontinuous outcrops and in drill holes. The NE-trending ALF constitutes the mapped boundary between the Hudson granite to the west and the metamorphosed basement rocks to the east (Fig. 2). The ALF is delineated from interpretation of aeromagnetic and ground gravity maps (Fig.2) (Tschirhart et al., 2016; Roy et al. 2017), as outcrops are almost non-existent. Studies of the Contact prospect (Grare et al., 2017) gave better insights into the structural evolution of the ALF, an evolution which also included a post-Thelon uranium mineralizing event. Recent observations by Grare et al. (2017) highlighted the presence of an extensive silicification event characterized by a quartz-healed breccia, termed the Quartz Breccia (QB, Grare et al., 2017) in the literature. This structure is a main feature of both the JSF and the ALF: it is observable on outcrops (Anand and Jefferson, 2017) and systematically intersected by drill holes, and is probably linked to silicifying fluids of magmatic origin and related

to the emplacement of the Kivalliq igneous suite. Such structure appears to have played a first-order role in the formation of uranium mineralization.

2.4 Previous work on fracturing/faulting events in the Kiggavik area

As reported before, previous studies in the Kiggavik area were focused on establishing mineral parageneses and geochemical signatures of fluids, uranium oxides and alteration products associated with their precipitation. Anand and Jefferson (2017) recently released a valuable structural synthesis on the Kiggavik area, built mainly after field data; their approach contrasts with the detailed sequence of fracturing/faulting events published by Grare et al. (2018) for the Contact prospect that was reconstructed on the basis of both macroscopic (drill core and field) and microscopic (optical microscopy and SEM) observations. The structural study presented in the present article integrates data from map-scale to micro-scale, without omitting outcrops observations throughout the Kiggavik area. Grare et al.,'s (2018) sequence is summarized in fig. 3; the main recognized fracturing events have been related to brittle tectonic activity along the Andrew Lake fault (fracturing stage 1 or f1), development of the quartz-cemented breccia (QB, f2), the first stage of uranium mineralization (f5), the second stage of uranium mineralization (f6), faulting associated with strong clay alteration and bleaching of the host rock (f8), and late supergene uranium mineralization alteration (f9).

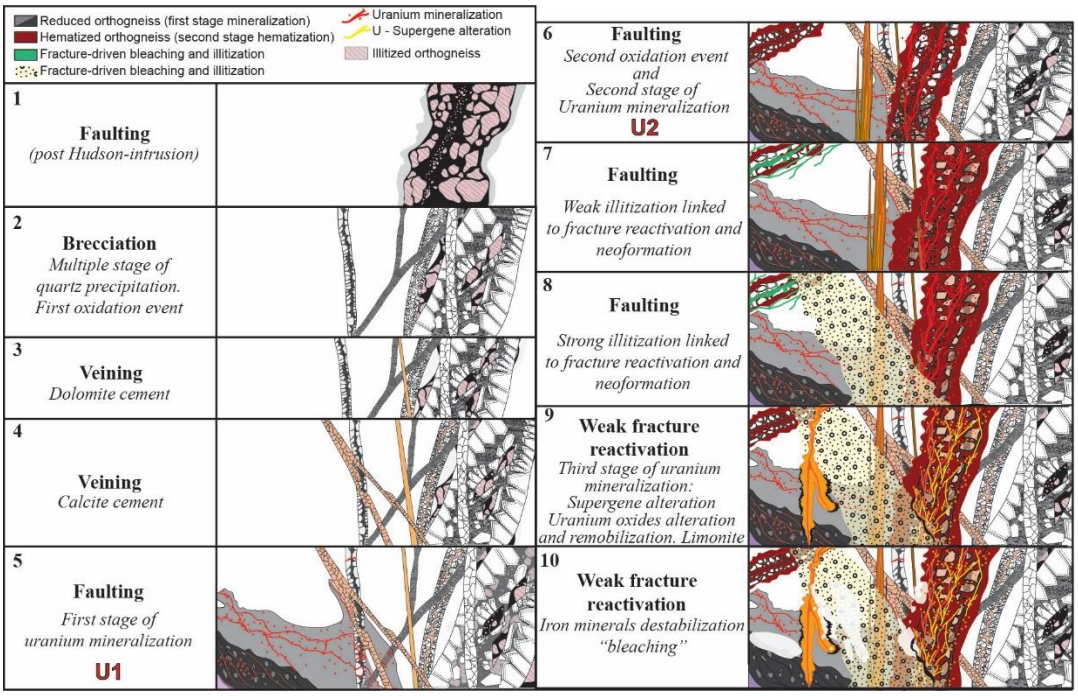

Figure 3: Sequence of fracturing events recognized at Contact (modified after Grare et al., 2017).

3. Methodology

Collection of data from field and drill core

The 140 samples examined in this work were collected from cores drilled during 2014 and 2015 field campaigns; 28 samples come from Andrew Lake, 5 from End, 14 from Kiggavik Center Zone, 66 from Contact and 27 from 85W (see location of deposits and prospects in fig. 2). In addition to classical drilling during exploration campaigns, two double tubing exploration drillholes were realized and studied, allowing for a better preservation of the drill core. One was drilled to reach the Andrew Lake deposit and the other to reach Kiggavik Center Zone. Many other drillholes (~50) from previous campaigns were also re-examined and oriented data from the AREVA Resources Canada (ARC) database were processed.

Field observations of faults, joints and veins were made on outcrops and, when possible, compared and combined with previous field observations made by ARC geologists. Fault zones were characterized in drill core by the identification of fault cores with the presence of fault rocks such as breccias or gouges. Fault damage zones (Chester and Logan, 1986; Wibberley et al., 2008; Faulkner et al., 2010) were documented by the associated veins (mode I or mixed mode I-mode II), joints (mode I) and undifferentiated fractures; an "undifferentiated fracture" in this case relates to a fracture plane which cannot be unambiguously classified as vein, joint or fault/micro-

fault (no kinematic indicator) at the time of observation. Fracture corridors and isolated veins, joints and undifferentiated fractures were also systematically reported.

Orientations of ~2000 fractures and foliation planes were measured from oriented drill core. The drill core were oriented using a Reflex ACT III digital core orientation tool (Bright et al., 2014), and then a protractor was used to measure angles between fractures and the core axis (alpha angle). The angle between the bottom of the hole and the inflection line (beta angle) was also measured for calculation of true dip/dip direction data. Acoustic televiewer probing ABI40 (Williams et al., 2004) was run through key holes providing accurate oriented data in faulted core intervals. The mesostructural data were processed to their true orientation and plotted with Dips 6.0 software by Rocscience. Uncertainty on orientation measurements is usually about 10° as estimated from the comparison between oriented core-measurements and acoustic televiewer data. It should be kept in mind that the acquisition of oriented data from exploration drill core remains usually limited because the more the rock fractured and altered (i.e. fault damage zone or fault core), the lower the probability of getting intact drill core suitable for orientation.

Optical microscopy observations and scanning electron microscope (SEM) analysis

Microscopic observations were carried out to bring new insight into the genetic link between fractures and U mineralization, but also to complete and synthesize the mineralogical observations made by previous authors about the deposits of the Kiggavik area. Thin sections made on fractures and fault rocks were studied under a Motic BA310 POL Trinocular, using transmitted and reflected light, and also under a HIROX SH-3000 Scanning electron microscope (SEM) equipped with a back-scattered electron detector and a nitrogen free Energy Dispersive Spectrometer (EDS) BRK D351-10 with digital mapping capabilities at AREVA la Defense site. The SEM was operated at low accelerating voltage (10 kV), 100 nA filaments current and 600 Å beam width for a working distance between 8 and 39 mm. Complementary observations on mineralogical observations and U mineralization were performed at Service Commun de Microscopie Electronique et de Microanalyses (SCMEM) of GeoRessources lab (Vandoeuvre-lès-Nancy, France), using a JEOL J7600F Scanning electron microscope equipped with an energy dispersive spectrometer.

Cathodoluminescence

Carbonates were observed at the various deposits of the Kiggavik area as filling vugs and cementing veins. The different generations of carbonate cements were distinguished and characterized using a Technosyn Cold Cathodoluminescence device (model 8200 MkII),

operating between 10 and 12 kV gun potential and between 150 and 350 µA beam current. Observations were carried out at the University of Barcelona, Spain (Departament de Mineralogia, Petrologia i Geologia Aplicada, Facultat de Ciències de la Terra).

Electron microprobe analysis (EMPA) and geothermometry of clay minerals

The chemical composition for major elements in uranium oxides and clay minerals (chlorites and white micas) were measured using a CAMECA SX-100 Electron Microprobe Analyser at Service Commun de Microscopie Electronique et de Microanalyses (SCMEM) of GeoRessources lab (Vandoeuvre-lès-Nancy, France). The analytical conditions were an accelerating voltage of 15 kV and 10 nA current. The calibration used natural and synthetic oxides and/or alloys (orthoclase, albite, LaPO4, CePO4, wollastonite, UO2, PbCrO4, olivine, DyRu2). The counting times were 10 s (K, Na, Ca), 20s (Ce, U, Si), 40s (Dy), 50s for Pb, and 60s for La. Complementary measures on uranium oxides and clay minerals were made on 6 thin sections with a Cameca SX50 electron microprobe and conducted at the Camparis service in Paris (UPMC), based on the same analytical conditions as used at SCMEM.

In the Kiggavik area, chlorites and white micas are a common product of host-rock alteration. They are also found in fractures as neo-formed minerals (see descriptions hereafter). Variations in the chemical composition (Tschermark, di-tri-octahedral, Fe-Mg exchange, Fe^{3+}/Fe^{2+} ratio) of chlorites are a useful tool for estimating the crystallization temperature of the clay mineral, which is referred to as chlorite geothermometry. Another type of geothermometer for chlorite, related to the polytype structure (Hayes, 1970; Walker, 1993), will not be considered here. The easiest method of temperature estimation (applied in empirical case) was first exemplified by Cathelineau and Nieva (1985) and Cathelineau (1988), in which a correlation is observed between chlorite tetrahedral Al occupancy (noted Al^{IV}) and temperature. Subsequent refining of the method was made by taking into account the chlorite Fe and Mg contents (Kranidiotis and McLean, 1987; Jowett, 1991; Zang and Fyfe, 1995; Xie et al., 1997). The Structural formulae were calculated on the basis of 14 oxygen atoms with K, Na and C assigned to the interlayer. Analyses with atomic K, Ca or Na > 0.4 or total of oxides < 85% were excluded as numerical criteria applied to exclude poor-quality and/or contaminated analyses (for example by mixing with illite).

White mica crystals were selected from the main altering and/or mineralizing stages for electron microprobe analysis, and the determined major element compositions (site occupancy and end-member mineral data) were used to calculate the formation temperatures. Temperatures were calculated following the equation of Cathelineau (1988). The structural formulae were calculated

on the basis of 11 oxygen atoms. Micas coating or cementing fractures and filling pores were selected rather than replacement micas in order to minimize the influence of precursor minerals, hence to ensure their representativity of the selected fracturing stages

Secondary ion mass spectrometry (SIMS) and LA-ICP-MS for U-Pb and geochemical tracing of uranium oxides

The U–Pb isotopic composition of uranium oxides were determined using a CAMECA ims 1280-HR Secondary Ion Mass Spectrometer (SIMS) at CRPG-CNRS (Nancy, France). The O^- primary ion beam was accelerated at 13 kV, with an intensity ranging between 3.5 and 5 nA. The primary beam was set in Gaussian mode with a raster of 10 µm. The size of the spot on the uranium oxides was ~ 15 µm. Positive secondary ions were extracted with a 10 kV potential, and the spectrometer slits were set for a mass resolving power of ~6,000 to separate isobaric interferences of rare earth element (REE) dioxides from Pb. The field aperture was set to 2,000 µm, and the transfer optic magnification was adjusted to 80. Rectangular lenses were activated in the secondary ion optics to increase the transmission at high mass resolution. The energy window was opened at 30 eV, and centred on the low energy side, 5eV before the maximum value. Ions were measured by peak jumping in monocollection mode using the axial Faraday cup (FC) for ^{238}U and ^{238}UO and the axial electron multiplier (EM) for ^{204}Pb, ^{206}Pb, ^{207}Pb, ^{208}Pb, and ^{248}ThO. Each analysis consisted of 8 successive cycles. Each cycle began with measurement of the mass 203.5 and 203.6 for backgrounds of the FC and the EM respectively, followed by ^{204}Pb, ^{206}Pb, ^{207}Pb, ^{208}Pb, ^{238}U, ^{248}ThO, and ^{238}UO, with measurement times of 4, 4, 10, 6, 20, 4, 4, 3, and 3 s, respectively (waiting time of 1 s). The beam centering, mass, and energy calibrations were checked before each measurement, after a 60 s presputtering by rastering the primary beam over a 30×30 µm area to clean the gold coating and avoid pollution. Several spot analyses (at least five) were measured on the Zambia reference uraninite (concordant age of 540 ± 4 Ma; Cathelineau et al., 1990) before and after each sample for sample bracketing. The error on the calibration curve is reported in the error given for each analysis. To achieve good reproducibility, each analysis was preceded by automated centering of the sample spot image in the field aperture and contrast aperture (Schuhmacher et al. 2004) and of the magnetic field values in scanning the ^{206}Pb peak. The $^{204}Pb/^{206}Pb$ ratio were low (<0.00001), indicating that common lead was not incorporated at the time of crystallization, except sample 9850. A correction for common lead was made for each analytical spot by precisely measuring the ^{204}Pb amount and the common lead composition was calculated at the $^{207}Pb/^{206}Pb$ measured age, using the Pb isotopic composition calculated from Stacey and

Kramers (1975) model at the age of uranium oxide. Ages and error correlations were calculated using the ISOPLOT flowsheet of Ludwig (1999). Uncertainties in the ages are reported at the 1σ level.

The rare earth element (La, Ce, Pr, Nd, Sm, Eu, Gd, Tb, Dy, Ho, Er, Tm, Yb, Lu) concentrations in the different uranium oxides were quantified using a LA-ICP-MS system composed of a GeoLas excimer laser (ArF,193 nm, Microlas) coupled to an Agilent 7500c quadrupole ICP-MS. The detailed instrumentation and methodology is described in Lach et al. (2013).

Fluid inclusions (FI) analyses and orientation of fluid inclusions planes (FIP)

Primary to Secondary fluid inclusions (trapped after the formation of the quartz host crystals) were studied when possible to define the properties of the different fluids which circulated in the Kiggavik area and their structural conditions of circulation. The directions of the different FIPs were measured, FIPS being considered as (σ1- σ2) planes which are interpreted as mode I fractures that contain fluid inclusions. They formed perpendicular to the least principal compressive stress axis σ3, i.e. in the plane that favours the maximal decrease of the total energy of the system (Lespinasse and Pécher, 1986; Gueguen and Palciauskas, 1992; Lespinasse, 1999; Lespinasse et al., 2005). The characterization of the type of FIP, which relies on the characterization of the FI constituting the FIP, allows to directly link a fluid circulation event to a fracturing event and its driving tectonic stress. Characterizing FIs also gives information on the salinity, temperature and nature of the volatile and aqueous phase that represent the trapped fluid. Sampling for FI studies was carried out from cores drilled during the 2014 and 2015 summer field campaign. Cores were oriented during drilling in inclined drill holes through use of the EZT-Mark tool. A selection of four representative oriented samples was collected from the 85W and Contact prospects. A thin section and a wafer were prepared on a horizontal plane from selected region of the core in order to have “map view” of the FIPs. Quantification of the abundance of each FIP type was carried out using a systematic and statistical procedure of the microstructural markers in the quartz within the oriented wafers. FIP orientations were measured under transmitted light microscope using the AnIma software (Lespinasse et al., 2005).

Microthermometry was carried out on fluid inclusions (FI) using a Linkam® MDS600 heating-cooling stage, adapted to an Olympus® microscope at the GeoRessources laboratory (Nancy, France). The following microthermometric parameters were measured for liquid-dominated FIs: eutectic temperature (Te), melting temperatures of ice and hydrohalite (Tmice and Tmhyd), halite dissolution (TsNaCl), and homogenization temperature (L+V→L or L+V+S→L+S) (Th).

The following microthermometric parameters were measured for gas-dominated FIs: halite dissolution (TsNaCl), CO2 melting and clathrate dissociation ($TmCO_2$ and TmCl), CO_2 homogenization ($ThCO_2$), and total homogenization temperature (Th).

The temperatures of phase changes have a precision of about ± 5 °C for Te, ±0.1 °C for Tmice, Tmhyd and ±1 °C for TsNaCl and Th. Aqueous carbonic fluid inclusions were classified using the nomenclature of Boiron et al. (1992). A Dilor-Labram Raman microspectrometer was used for the quantitative measurement and characterization of gas species present in the fluid inclusions, following the procedure described by Dubessy et al. (1989).

The quantification of the chemical composition (major, minor and trace elements) of water-rich FI was tempted using the LA-ICP-MS system composed of a GeoLas excimer laser (ArF,193 nm, Microlas) coupled to an Agilent 7500c quadrupole ICP-MS at GeoRessources lab. The laser beam is focused onto the sample within a low-volume custom-made lozenge-shaped ablation cell dedicated to fluid inclusion analyses that has a Schwarzschild reflective objective (magnification × 25; numerical aperture 0.4) mounted onto an optical microscope (Olympus BX41) equipped with a X–Y motorized stage and CCD camera. NIST610 (Jochum et al., 2011) was chosen as the external standard, with accuracy also accuracy verified using the NIST612 standard. Analysis parameters include a fluence of 14 J/cm² and laser shot frequency of 5 Hz, He = 0.5 L.min-1 as a carrier gas mixed with Ar = 0.7 L.min-1 via a cyclone mixer prior to entering the ICP torch. Spot sizes varied from 24 µm up to 44 µm, depending on the inclusion size. The elemental isotopes analysed were: 23Na, 11B, 24Mg, 39K, 44Ca, 55Mn, 57Fe, 63Cu, 66Zn, 88Sr, 55Cs, 57La, 137Ba, 208Pb, and 238U, using an integration time of 0.01 s per mass channel for a total cycle time of 0.22 s.

System calibration and signal integration were performed using the Matlab®-based SILLS program (Guillong et al., 2008). Absolute element concentrations can be calculated from analyzed ratios relative to the Na concentration (Longerich et al., 1990). The Na concentration can be obtained from the salinity estimated from microthermometry (in wt.% NaCl + CaCl2 equiv.) using the charge-balance technique (Allan et al., 2005). This method corrects the modelled amount of Na (from the wt.% NaCl equiv.) for contributions from other chloride salts using the analyzed elemental ratios to Na. Limits of detection (LODs) were calculated using the 3σ criterion (Longerich et al., 1996). The analytical precision of most elements is within 20-30% RSD (Allan et al., 2005).

4. Results

4.1 Fracturing events

4.1.1 Macroscopic observations

Grare et al. (2018) recognized 10 structural events at the Contact prospect among which three resulted in fracture-controlled uranium mineralization. The present work has followed the Grare et al. (2018) approach and methods and for the sake of clarity, the presentation of the results follows the sequence of fracturing events defined by Grare et al. (2018), with the aim of establishing whether or not the events and timing recognized in the Contact prospect can be recognized in the other deposits and prospects and whether the chronology of events remains the same; so the structural model can be enlarged to the whole Kiggavik area. Macro/meso-scale observations of fault zones in each deposit and prospect allowed deciphering and characterizing the various fracturing events as follows:

Fracture stage 0 (f0) and first stage of uranium mineralization (U0): This stage is named f0 and U0 in order to respect the annotation from f1 to f10 presented in Grare et al. (2018) and to avoid confusion because this stage f0 predates the stage f1 observed at the Contact prospect. Effectively, a first fracturing event, unrecognized at the Contact prospect was identified mainly at End, but also at Andrew Lake, Kiggavik Main Zone and Bong deposits. This fracturing event is characterized by uranium-mineralized protobreccia usually displaying a dense network of millimetric greenish microfractures (Fig. 4C), over a 10m-thick breccia zone. Uranium mineralization is observed within the microfractures and is weakly disseminated within the host rock.

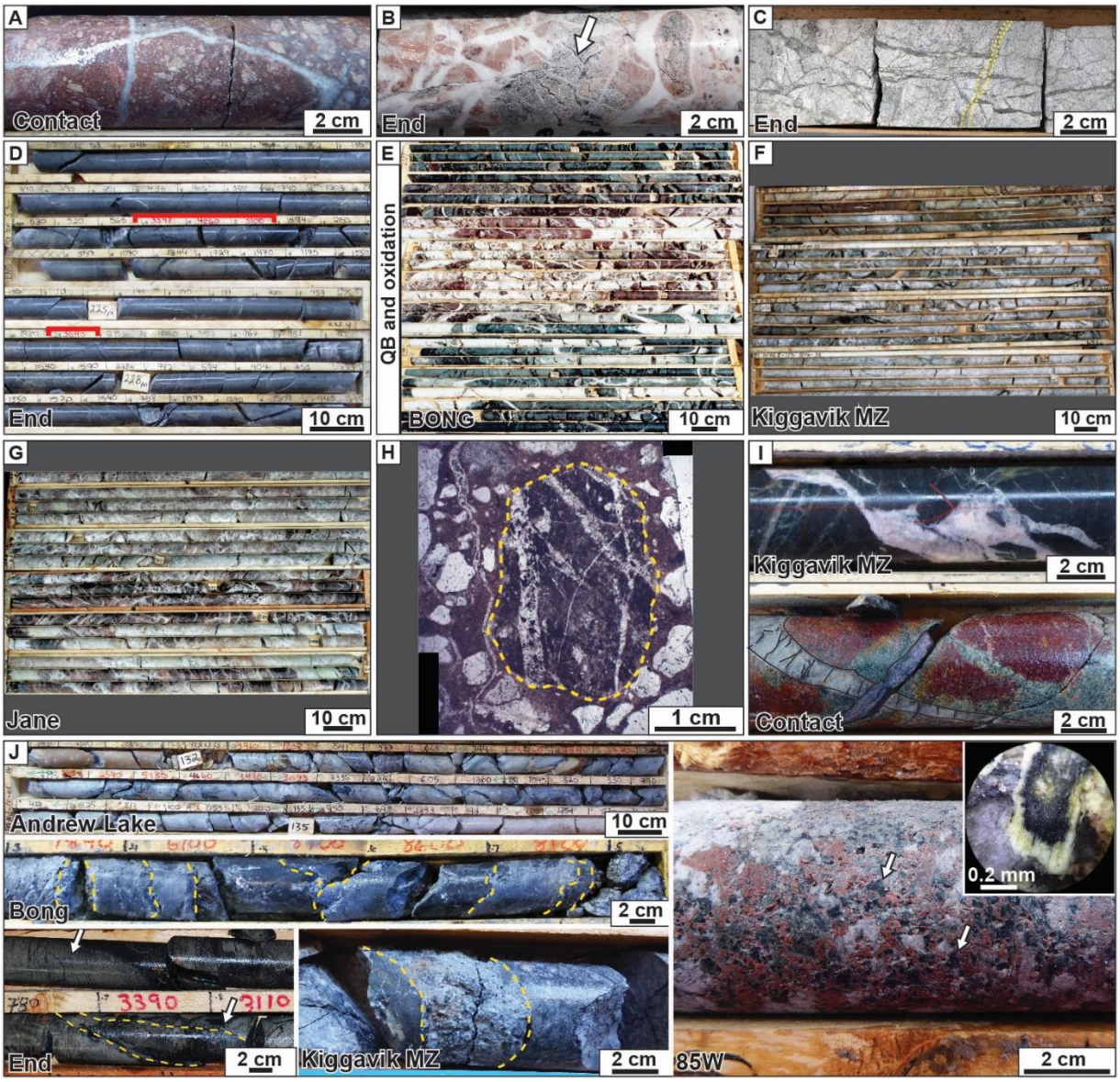

Figure 4: Drill core photographs (DCP) except H. A) Silicified cataclastic fault rock crosscut by white quartz veins of the quartz breccia (QB). B) Microfractures crosscut by QB. C) Uranium mineralized microbreccia crosscut by quartz vein (yellow outline) of the QB. D) Microbrecciated, uranium mineralized and unaltered psammo-pelitic gneiss of the Woodburn Lake Grp. E, F and G) White QB and associated pervasive purple hematization. H) Optical microscopy photograph (OMP). Reworked clast (yellow outline) bearing quartz vein of QB in sandstone of the Thelon formation (exploration drillhole in the Thelon formation). I) Two examples of calcite veins (first generation of calcite-Ca1). J) Various examples of uranium mineralized, grey-greenish altered fault zones of the first stage of uranium mineralization from deposits and prospects in the Kiggavik area.

The mineralization is usually weak but can reach several thousands of counts per seconds (CPS) in some small more brecciated zones (Fig. 4D). Independently of the grade, the

brecciated and mineralized host rock is barely clay altered. Uranium-mineralized microbreccias were not observed within the quartz breccia (QB, Fig. 4B, C), and timing regarding brittle tectonic pre-QB is still unclear (Fig. 4A). This mineralized event is crosscut and likely overprinted by the QB.

Stage f1: This is a pre-Thelon fracturing event. At the Contact prospect, it is formed by faults with proto- to ultra-cataclastic fault rocks related to brittle activity along the ALF (Grare et al., 2018), and later silicified and crosscut by white quartz veins and mosaic breccia related to the QB (Fig. 4A). This type of faulting was also observed along the JSF, at End, where white quartz mosaic breccias crosscut fault rocks (Fig. 4A, B), and at Kiggavik Main Zone and Bong.

Stage f2: This stage is represented in all deposits and prospects by the QB with its characteristic mosaic white quartz-sealed veins and breccia, along major fault zones and silicifying them: at Bong (Fig. 4E), at Kiggavik Main Zone along the ENE-WSW trending, N-dipping MZF (Fig. 4F; note that this fault also controls the steeply-dipping boundary of the Lone Gull granite, see cross-section in Fig. 2), at the Jane prospect along the NE-SW trending, SE-dipping section of the ALF (Fig. 4G) and at End along the ENE-WSW trending, N-dipping JSF (Fig. 4B). The QB can display variable thickness from meters to tens of meters and is recurrently associated with a distinctive red-purple pervasive hematization of the host rock (a first stage of oxidation of the host rock in the Kiggavik area, sometimes misinterpreted as paleo-weathering profile). In these deposits, uranium mineralization is nearly always found in the hanging wall and footwall of the QB. Reworked clasts bearing quartz veins of the QB are observed within the sandstones of the Thelon formation (Fig. 4H).

Stage f4: This stage is represented by calcite veins that crosscut, thus postdate emplacement of the QB (Fig. 4I bottom). Described by Grare et al (2018) as mixed mode-I mode-II shear fractures; they are observed at each deposit of the Kiggavik area (Fig. 4I top), sometimes close to uranium-mineralized fault zones (f5), and may exhibit calcite-cemented steps and proto-breccia textures (Fig. 4I top).

Stage f5: This mineralizing event is the first uranium mineralizing event (also called U1, Fig. 4J) postdates deposition of the Thelon formation. It is characterized by grey-greenish coloured, clay-altered (illite mainly and chlorite) narrow fault zones (Fig. 4J-Andrew Lake) which were also observed in all deposits and prospects of the Kiggavik area. These fault zones show strongly mineralized faults with protocataclastic to cataclastic fault rocks (Fig. 4J-Bong and Kiggavik MZ) and re-opened, micro-fractured quartz veins from which the mineralization leaks

into the foliation (Fig. 4J-End deposit; see also Chi et al., 2017). At the 85W prospect, the uranium mineralization is completely hosted in Hudsonian-age granitoids, mainly granites. As a consequence of the absence of foliation and of coarser size of the minerals there, the control by fractures is stronger and easier to observe. In strongly mineralized fault zones, where the mineralization is disseminated in the host rock (Fig. 4J-85W), biotite is coated with uranium (Fig. 4J-85W small insert), which expands along the mineral cleavage. Like what was observed at the Contact prospect (Grare et al., 2018), clay alteration (illitization mainly, but also chloritization) of the host rock is weak to moderate.

Stage f6: This stage is represented by deep red hematized fault zones and the second stage of uranium mineralization (U2, fig. 5A-C). It has been recognized at each deposit of the Kiggavik area. Cataclastic, strongly clay altered (illite and chlorite) fault cores (Fig. 5A-top) and tectonic breccias are usually not mineralized. Hematite veins (Fig. 5A-bottom), millimetric-thick calcite veins (Fig. 5B, top) and microfaults host the mineralization which spreads out into the host rock as blebs surrounded by a halo of bleaching (Fig. 5B-top and bottom, Fig. 5C-top) in wide fracture networks of bright red oxidized damage zones (Fig. 5C-bottom). Alteration of the host rock is stronger compared to the previous stage of uranium mineralization.

Stages f7-f8: These stages represent the strongest clay alteration events in the Kiggavik area is characterized by illization, desilicification and bleaching of the host rock. They are observed at each deposit and prospect. Multiple, un-mineralized, white clay altered fault cores were observed at Kiggavik Main Zone (Fig. 5D-top). These faults crosscut mineralized fault zones (Fig. 5D-bottom) and reworked clasts bearing uranium oxides are observed within cataclastic fault rocks (Fig. 5E-top and bottom). This fracturing stage, recognized at each deposit and prospect but with variable intensity, has been extensively observed at the Bong deposit. The greenish colour of some fault zones is likely due to a different mineralogy (basement rocks richer in retrograde metamorphic chlorite) and therefore does not reflect a different fracturing process; additionally, white clay fault zones are much more frequent compared to greenish clay fault zones; as a consequence in contrast to the sequence reported by Grare et al (2017), we propose to group these two fracturing events on the basis of these new observations.

The Mackenzie dikes were observed only at Kiggavik Main Zone but these intrusions provide strong constraints on the timing of fracturing events. Indeed, diabase dikes crosscut the altered and mineralized fault zones (Fig. 5F) and are barely fractured and altered, and can therefore be considered as sealing the main tectonic history.

Stage f9: This stage is represented by uranium redox fronts (U3) as described at Bong and Andrew Lake by Sharpe et al. (2015) and Shabaga et al. (2017); they have also been recognized at End,

Figure 5: DCP. A) Strongly clay altered, hematized but un-mineralized fault rock from Sleek (top). Vein cemented with hematite and uranium oxides (second stage of uranium mineralization-U2, bottom). B) Spherulitic pitchblende (U2) leaking out calcite veinlet (second generation of calcite-Ca2) in a bleached host rock. C) Spherulitic pitchblende (U2) in hematized, clay altered microgranite (Top). U2 mineralized, hematized fault damage zone (bottom). D) Strongly clay altered and bleached fault zones (pointed out in yellow). Top: unmineralized fault zone. Bottom: white clay altered fault zone crosscutting a U2 mineralized fault zone. E) Top and bottom: White clay altered cataclastic fault rock bearing small relict of spherulitic pitchblende (white arrow). F) Mackenzie diabase dike (black outline) crosscutting a uranium mineralized fault zone (red outline). The fresh diabase dike is not mineralized and weakly fractured. G) Three examples of redox front remobilizing uranium oxides. H) Top and bottom: bleached redox front remobilizing uranium

oxides. I) Top: late supergene alteration of spherulitic and foliation parallel uranium mineralization. Bottom: late supergene alteration of redox front.

Kiggavik Main Zone and at 85W (Fig. 5G). These remobilization fronts display the typical succession with an oxidized (goethite), un-mineralized zone, a thin black layer where uranium oxides are concentrated and a grey, non-oxidized (reduced) and mineralized zone. These redox fronts are bleached by a later event described at the Contact prospect (f10) which removed iron oxides from the goethite-rich zone and therefore modified the visual aspect of the redox front. Secondary uranium oxides minerals (hexavalent uranium minerals), proceeding from the alteration of primary uranium oxides (tetravalent uranium mineral: U0, U1 and U2), observed at the Contact prospect, were also observed in other deposits but are much more observed at Andrew Lake (Fig. 5I).

Macroscopic re-examination of deposits and prospects in the Kiggavik area confirm the structural stages defined thus leads to extend observation on fracturing events made at Contact by Grare et al. (2018), such that the sequence of fracturing events is representative of the whole area at the Contact prospect although changes in lithologies can induce differences in the mineralogy of fault rock cements between deposits and prospects. In addition, this approach has allowed for the identification of a new stage of deformation and mineralization (f0 and U0) that predates all those described in contact and therefore also the formation of the QB, inferred to be a pre-Thelon fracturing event. This initial mineralizing stage is hereafter characterized more in detail with microscopic observations and geochemical data.

4.1.2 Optical microscopic and SEM observations

Because the related mineralizing event has not been previously recognized at the Contact prospect, samples of the uranium mineralized microbreccia (f0, U0) from End were studied more in detail at the micro-scale. A characteristic feature is the presence of multiple irregular microstructures with interlocking pegs and sockets (Fig. 6A), usually surrounded with a millimetric halo of quartz dissolution, somewhat similar to solution seams. These microstructures connect to microbreccias, within which millimetric clasts display irregular boundaries reflecting dissolution patterns (Fig. 6B). These micro-structures are cemented by dark green chlorite, ore minerals and are sharply crosscut by quartz veins of the QB (Fig. 6C-D). Dark green chlorite displays evidence of alteration into a light green chlorite. SEM observations and microprobe characterization show that microfractures are cemented with iron-rich clinochlore, pitchblende (containing up to several percentages of thorium), brannerite, titanium oxides and sulfide minerals (mainly pyrite). These minerals are observed as subhedral minerals or as anhedral

mixed phases (Fig. 6E-F). Microprobe characterisation shows that the iron-rich clinochlore is altered into an Al-rich chlorite, the composition of which is close to sudoite (Fig. 6D).

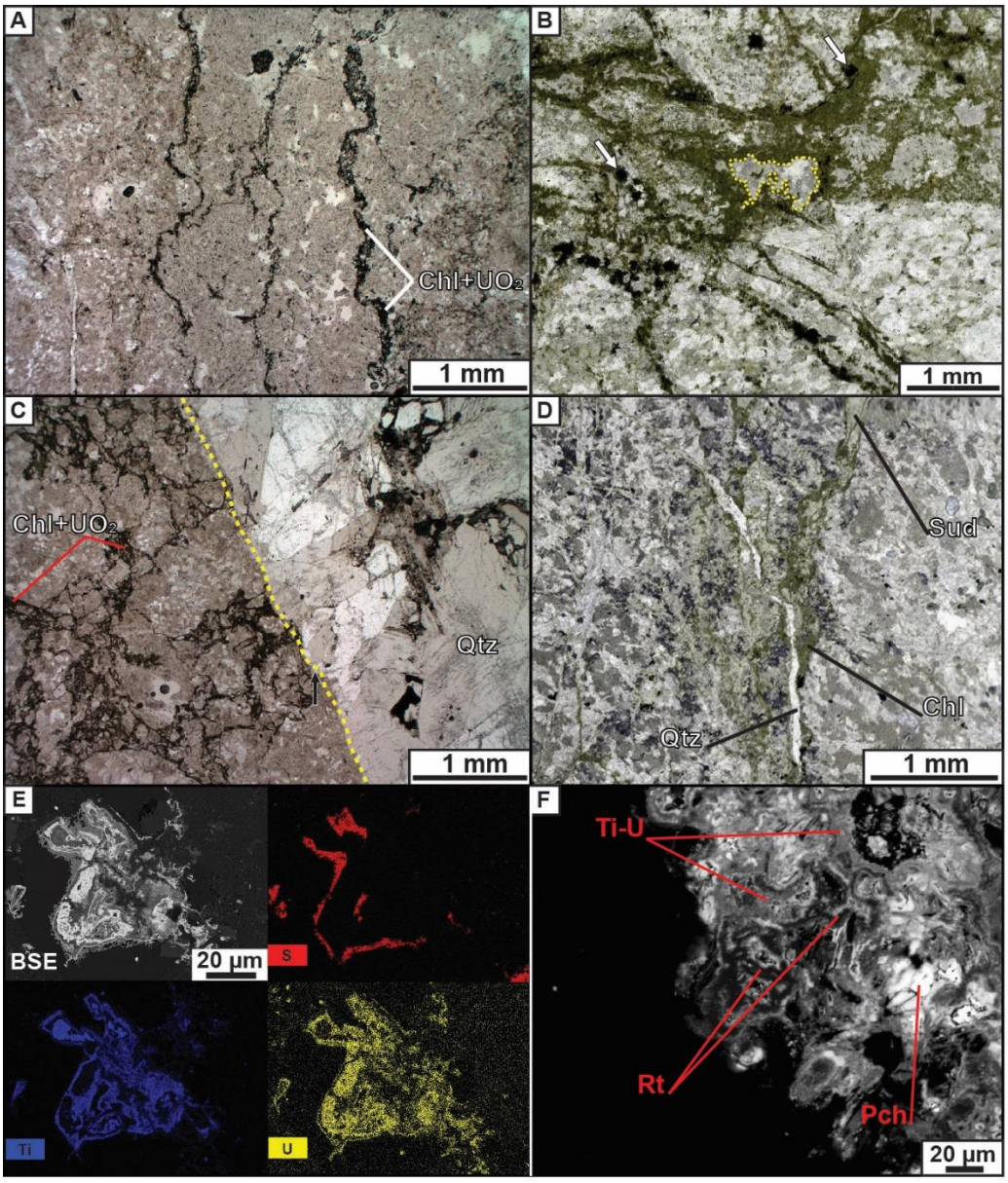

Figure 6: Micro-scale observations of pre-QB uranium mineralized breccia. A-D: OMP. A) Undulating microfractures cemented with chlorite and uranium oxides. B) Mineralized microbreccia: dissolved clasts (yellow outline) cemented by chlorite and opaque minerals (sulfides, uranium oxides and rutiles indicated by white arrow). C) Mineralized microbreccia crosscut by quartz vein of QB. D) Microbreccia with chlorite (dark green) crosscut by quartz vein of QB and altered to sudoite (light green). E) SEM microphotograph and element mapping of anhedral U-S-Ti compounds. F) SEM microphotograph. Anhedral rutile (Rt), uraniferous titanate (Ti-U) and pitchblende (Pch).

Subhedral crystals of brannerite were observed on samples from Kiggavik Main Zone, associated with pitchblende-cemented microbreccia (Fig. 7A). Rutile with micro-inclusions of uranium oxide and coated with anhedral U-Ti phases were observed on samples from Andrew Lake (Fig. 7B). Microfractures within magmatic quartz crystals, cemented with rutile and colloform pitchblende were observed on samples from the 85W prospect (Fig. 7C).

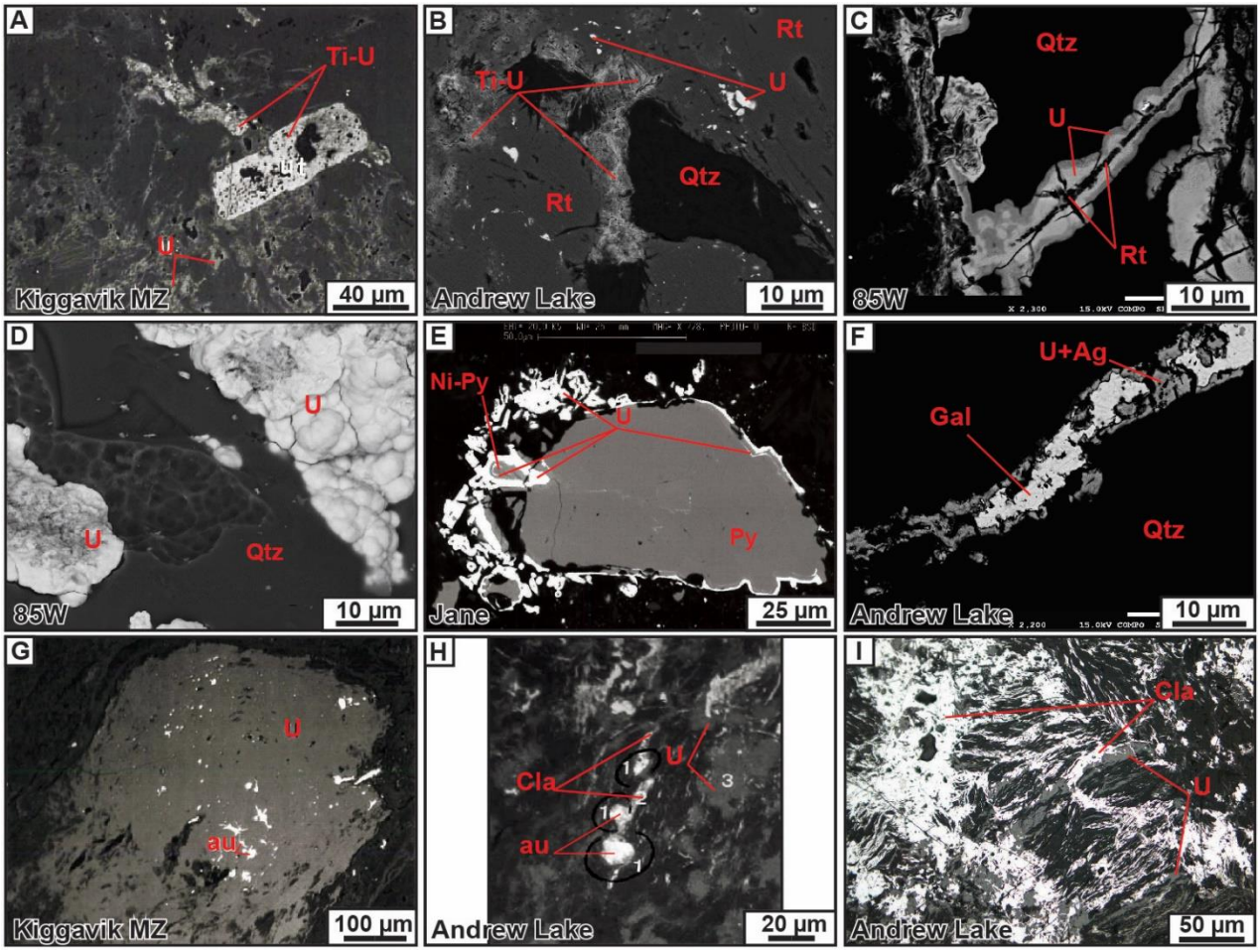

Figure 7: SEM microphotographs, except I: A) Microbreccia cemented with uranium oxides and subhedral brannerite and uraniferous titanate (Ti-U). B) Anhedral uraniferous titanate coating rutile grains with pitchblende micro-inclusions. C) Magmatic quartz displaying a micro-fracture cemented with colloform pitchblende and anhedral rutile. D) Quartz vein showing traces of dissolution linked to colloform pitchblende precipitation. E) Ni-bearing pyrite (bravoite) and pyrite with concentric uranium growth zone. F) Quartz vein crosscut by Galena-Ag-U cemented microfracture. G) Pitchblende with micro-inclusions of native gold. H) Pitchblende crosscut by microfracture cemented with clausthalite. I) OMP in reflected light: Microbreccia cemented with clausthalite and crosscutting pitchblende.

For fracture stage f5 and associated U1, re-opened quartz veins display colloform pitchblende along the edges, with uranium oxides “eating away” quartz crystals (e.g from the

85W prospect, Fig. 7D). Bravoite-pyrite coated with pitchblende (Fig. 7E) was observed on samples from the Jane prospect, a mineralogical association also described at Contact for U1 (Grare et al., 2018). Silver, gold and selenium phases were observed on samples from Andrew Lake, End and Kiggavik Main Zone. Anhedral Ag-U phases with galena were observed cementing microfractures (Fig. 7F), and gold is usually present as micro-inclusions within pitchblende (Fig. 7G) or cementing microfractures that crosscut uranium oxides (Fig. 7H). Clausthalite (PbSe) is observed cementing microfractures that crosscut low reflectivity uranium oxides (Fig. 7I).

Except for f0 which is described for the first time in the present study, these new observations under optical microscopy and SEM confirm and complement previous observations made by Chi et al. (2017), Shabaga et al. (2017) and Weyer et al. (1989) at End, Andrew Lake and Kiggavik Main Zone, respectively.

4.1.3 Carbonate cements characterization under cathodoluminescence: link with uranium mineralization

Numerous calcite veins and microbreccias were observed both macroscopically and by optical microscopy. Two generations of calcite veining are observed. The first, Ca1, is likely formed by mixed mode I/mode II fracturing, prior to U1, and the second, Ca2, displays crack and seal textures; it crosscuts U1 and was likely formed by mode I opening. The calcite veins associated with mineralization stages U1 (f5) and U2 (f6), respectively.

Observations made on centimetric calcite veins and microbreccias (Ca1) associated with the first stage of uranium mineralization (U1) described at the Contact prospect reveal calcite with a yellowish-orange luminescence and a darker tint when closer to uranium oxides. At the Contact and 85W prospects, colloform pitchblende occupies the edge of re-opened quartz-dolomite veins: dolomite and quartz display irregular boundaries in contact with calcite which separates them from uranium oxides (Fig. 8A-B). Calcite is observed cementing microbreccia on samples from 85W and End; uranium oxides are coating the edges of calcite crystals (Fig. 8C) or as subhedral colloform shapes intergrown with the calcite breccia (Fig. 8D-E), thus indicating synchronous precipitation of calcite and uranium oxides. A similar observation was made at Kiggavik Main Zone.

Ca2 veining also occurred during f6 and is spatially associated with U2, likely synchronous with this fracturing event. The millimetric crack-seal calcite veins (Ca2) observed at Contact and

associated with the second stage of uranium mineralization were also observed at End, crosscutting uranium oxides of U1. The calcite of these veins displays a dark orange luminescence (Fig. 8H-I).

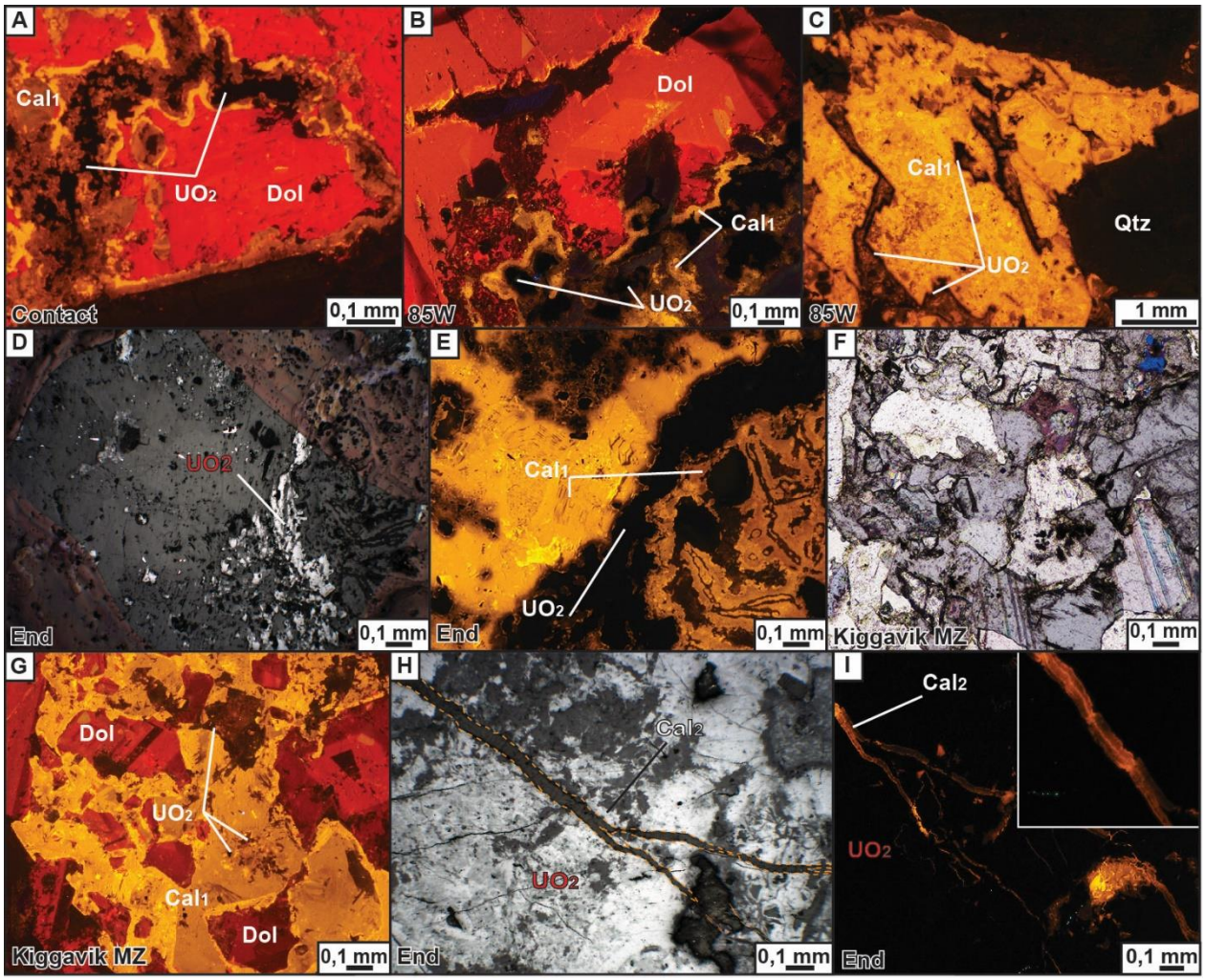

Figure 8: A) Cathodoluminescence microphotograph (CLMP). Within a dolomite vein. Dolomite is corroded and coated with pitchblende and calcite (Ca1). B) CLMP. Same observation, the calcite (Ca1) cements a distinct area separating pitchblende and dolomite. C) CLMP. Microbreccia cemented with calcite (Ca1) and synchronous pitchblende. D) OMP in reflected light. Pitchblende within a matrix of calcite (Ca1) E) Same picture as E observed under cathodoluminescence. F) OMP. Dolomite brecciated and cemented by calcite (Ca1) and synchronous pitchblende. G) CLMP. Same picture as G observed under cathodoluminescence. H) OMP in reflected light. Pitchblende crosscut by calcite micro veinlet. I) CLMP. Same picture as H observed under cathodoluminescence, the typical crack-seal texture of Ca2 is observable.

4.2 Geometry of fault zones from fracture orientation measurements and kinematics data

4.2.1 Oriented data from drill core

A column summarizing the successive fracturing events (adding U0 to the column presented in Fig. 3) and crosscutting relationships (left column) is displayed on the left of Fig. 9 for reference. Prospects and deposits are displayed from left to right, from deposits to the SW of the Kiggavik area (Contact, Jane and Andrew Lake, located on the Andrew Lake fault) to deposits in the center (End, Sleek) and north of the Kiggavik area (Bong, 85W, Kiggavik Main Zone). The frequency of the fracturing event for each deposit and prospect is shown by coloured bars; for example f8 (white clay altered fault zones) is dominant at Bong.

Oriented data for the mineralized microbreccia (f0, Fig. 9 line 0) are rare; however, major fractures from End collected within the mineralized microbreccia display a NE-SW trend and a steep dip to the NW. The numerous micro-“stylolites” observed at the micro-scale display a NW-SE to NNW-SSE orientation (not displayed in Fig. 9). Similarly, oriented data collected from the pre-QB brittle fracturing event (f1, Fig. 9-line 1) in other deposits and prospects, although still observable, are usually strongly silicified and overprinted by the quartz breccia (f2) precluding any reliable collection of oriented data. ENE-WSW striking faults, steeply dipping to the N (mimicking the orientation of the QB, like at the Contact prospect) would be expected for this fracturing stage that characterize the primary orientations of the JSF and the MZF, e.g., at Contact (f1, Fig.9-row 1).

The QB (f2, Fig. 9-row 2) overprints main fault zones in the Kiggavik area, and as such, it displays a NE-SW trend at the Contact and Jane prospects and at Andrew Lake. Secondary ENE-WSW strikes are also observed at Jane and Andrew Lake. The QB displays a main ENE-WSW trend with a steep dip to the North at End and Kiggavik Main Zone. Sleek, which is not located along a major fault zone, shows more diverse orientations, from NNE-SSW to E-W directions, with conjugate dip-directions. At Bong, the QB is characterized by a NNE-SSW direction, steeply dipping mainly to the W and a secondary E-W direction, steeply dipping to the N. At 85W, mainly small white quartz veins were observed, displaying dominant E-W directions with steep dip to the N.

Like at Contact, measurements of oriented data for calcite veins (f4) were mainly taken from the first stage of calcite veining (Ca1), as the second stage (Fig. 9-row 6b, no oriented data) usually displays veins too thin to be measured or to be unambiguously differentiated from those of the first stage calcite veins. Two directions are observed: E-W and NW-SE, with conjugate dip-directions.

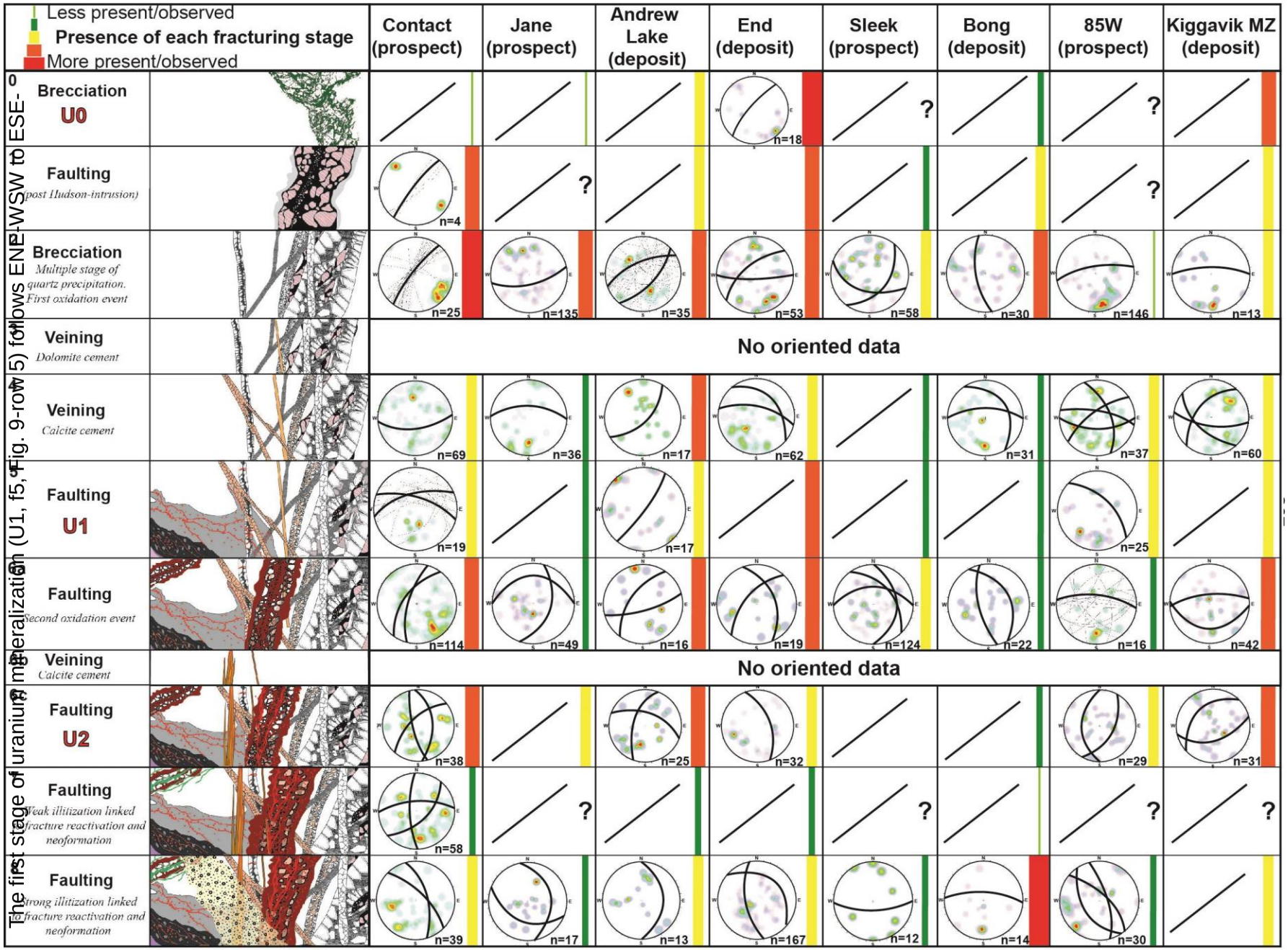

The first stage of uranium mineralization (U1, f5, Fig. 9-row 5) follows ENE-WSW to ESE-

Figure 9: Orientations of faults and breccias for each fracturing stage and for each deposit and prospect, where available. The chronology of the fracturing events was presented by Grare et al. (2017). Schmidt's lower hemisphere stereoplots.

WNW faults at Contact, dipping to the N. At Andrew Lake, mineralization is found within N-S and E-W faults, but also within reopened and/or microfractured quartz veins trending NE-SW (f2, QB stage, like at Contact). At 85W, faults and minor fractures show an ESE-WNW direction, steeply dipping mainly to the N.

Bright red hematized faults (f6, usually associated with U2, Fig. 9-row 6a) are well observed throughout the Kiggavik area. At Contact, Jane and Andrew Lake, they display N-S to NE-SW directions (i.e., the direction of the ALF). Contact is located on a W-dipping segment of the ALF, while Jane and Andrew Lake are located on E-dipping segment of the ALF. Looking at the map organisation (Fig. 2), End is likely hosted within an important relay zone of the JSF; there, oxidized fault zones are trending mainly NNW-SSE to NE-SW (Fig. 9-row 6a). At Sleek, the three main faults trends are N-S, E-W and NW-SE, the latter two being visible on maps. At Bong, 85W and Kiggavik Main Zone, the fault trends are similar to those of the QB, however at Kiggavik Main Zone, like for the Contact prospect, an E-W trend with a shallow dip to the S is also recognized. F6 is also characterized by tectono-hydraulic breccia and strongly clay altered fault zones which are both usually not mineralized (Fig. 5A).

The mineralizing stage U2 (f6c), as presented in Fig. 9-row 6c, was also observed in other deposits and prospects; it is better represented at Contact, Andrew Lake and Kiggavik Main Zone. At Andrew Lake, the third stage uranium mineralization is characterized by ESE-WNW to NW-SE microfaults and by NE-SW millimetric calcite veins (i.e., Ca2, measured precisely only at Andrew Lake). At End, the second stage of uranium mineralization is guided by NW-SE to NNW-SSE faults that mainly dip to the E. At 85W, this mineralizing stage is guided mainly by W-dipping NNE-SSW faults and by NW-SE faults as a second direction. At Kiggavik Main Zone, hematized, mineralized faults are trending either ENE-WSW or NW-SE to WNW-ESE.

Fault zones displaying greenish clay alteration (f7) described at Contact were only scarcely observed at Andrew Lake and End. The same crosscutting relationships (with other stages) and textural observations were confirmed. Nevertheless, oriented data are unfortunately not statistically reliable to be displayed (Fig. 9-row 7).

Finally, late white clay alteration has also been recognized (f8, Fig. 9-row 8) in deposits and prospects of the Kiggavik area. It is usually associated with NW-SE and E-W trending fault

zones (i.e., 85W and End). This fracturing stage is widely encountered and dominant at Bong where it is characterized by E-W trending, N-steeply dipping fault zones.

4.2.2 Kinematic indicators from outcrops and drill core

A statistically significant number of kinematic indicators on veins and faults were gathered mainly from outcrops located in different part of the Kiggavik area, usually not very far from a known deposit or prospect, and also from drill core.

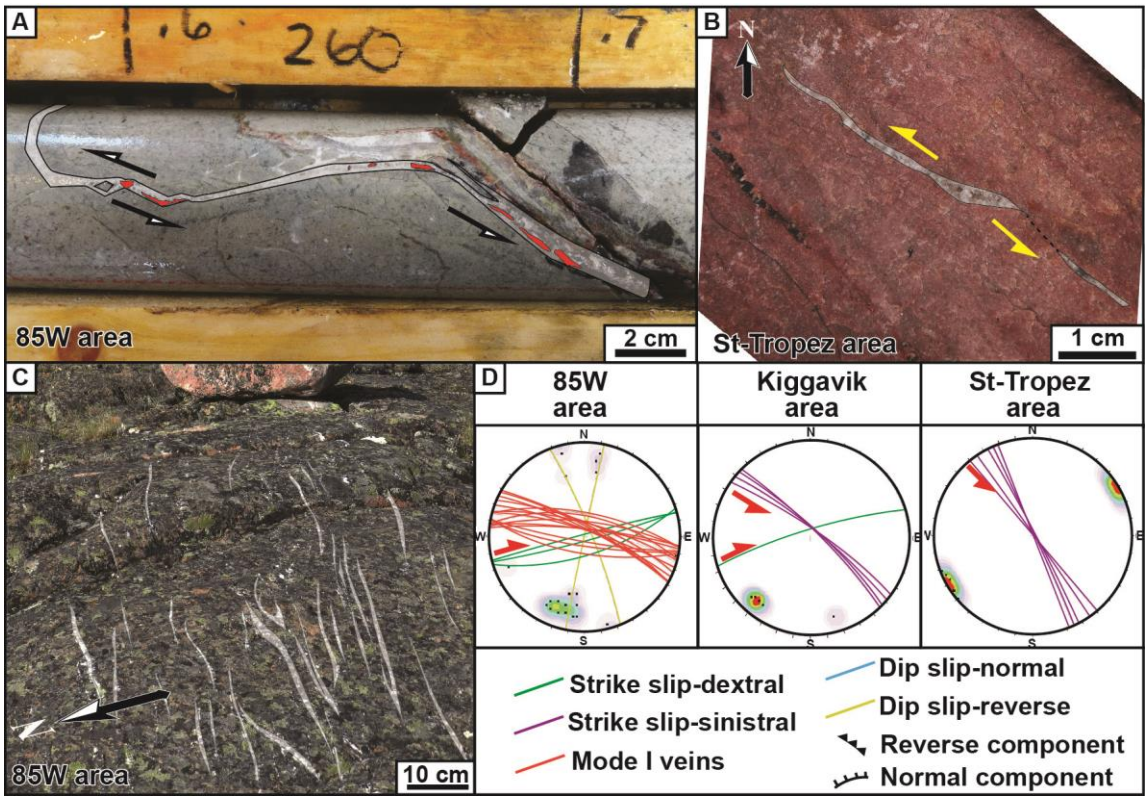

Figure 10: A) DCP. Stepped subvertical, ENE-WSW quartz vein coated with uranium oxides showing evidence of dextral motion. B) Field picture (FP). Stepped subvertical, NW-SE quartz vein displaying evidence of sinistral motion. C) FP. Network of Mode I quartz vein trending ESE-WNW. D) Oriented data and kinematic of quartz veins, collected on outcrops. The St-Tropez area is located 20 km to the NNE of Kiggavik Main Zone. Schmidt's lower hemisphere stereoplots.

Quartz veins (from QB, f2) display stepped veins, associated (Fig. 10A) or not (Fig. 10B) with uranium oxides and arrays of mode I opening fractures (Fig. 10C). Stepped veins are usually trending ENE-WSW and NW-SE, while mode I opening veins display a dominant ESE-WNW direction (Fig. 10D). Stepped veins cemented with Ca1 (f4) and synchronous uranium oxides (U2) were observed only in drill core (Fig. 11A).

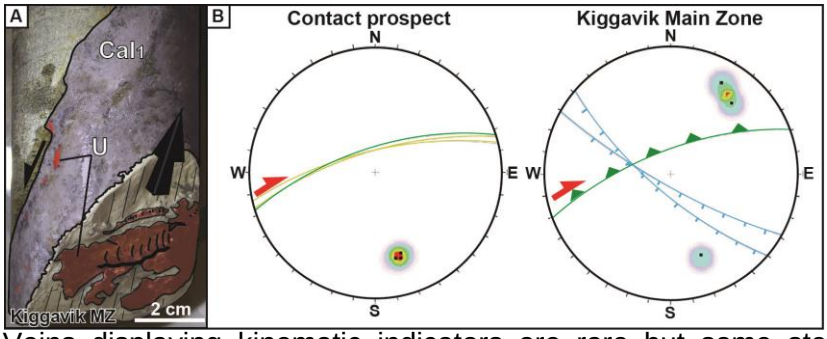

Figure 11: A) DCP. Stepped first generation of calcite veins coated with uranium oxides. B) Oriented data and kinematics of veins from drillcores. Legend as in Fig. 10. Schmidt's lower hemisphere plots.

Veins displaying kinematic indicators are rare but some stepped veins were observed and measured (see locations in Fig. 10); they display ENE-WSW and NW-SE directions (Fig. 11B). Bright red oxidized faults and tectonic breccias of f6 were observed in the field associated with radioactive anomalies. Study of relay zones allowed for the interpretation of the kinematics of the fault zone (Fig. 12A-B). Kinematic indicators were observed in the field and in drill core and are presented in fig. 12C; faults with dominant E-W to ENE-WSW orientation show evidence for reverse and/or sinistral motion. Other faults with dextral indicators were also observed in the St-Tropez area (Fig. 12A and C), which is located 20 km to the NNE of Kiggavik Main Zone.

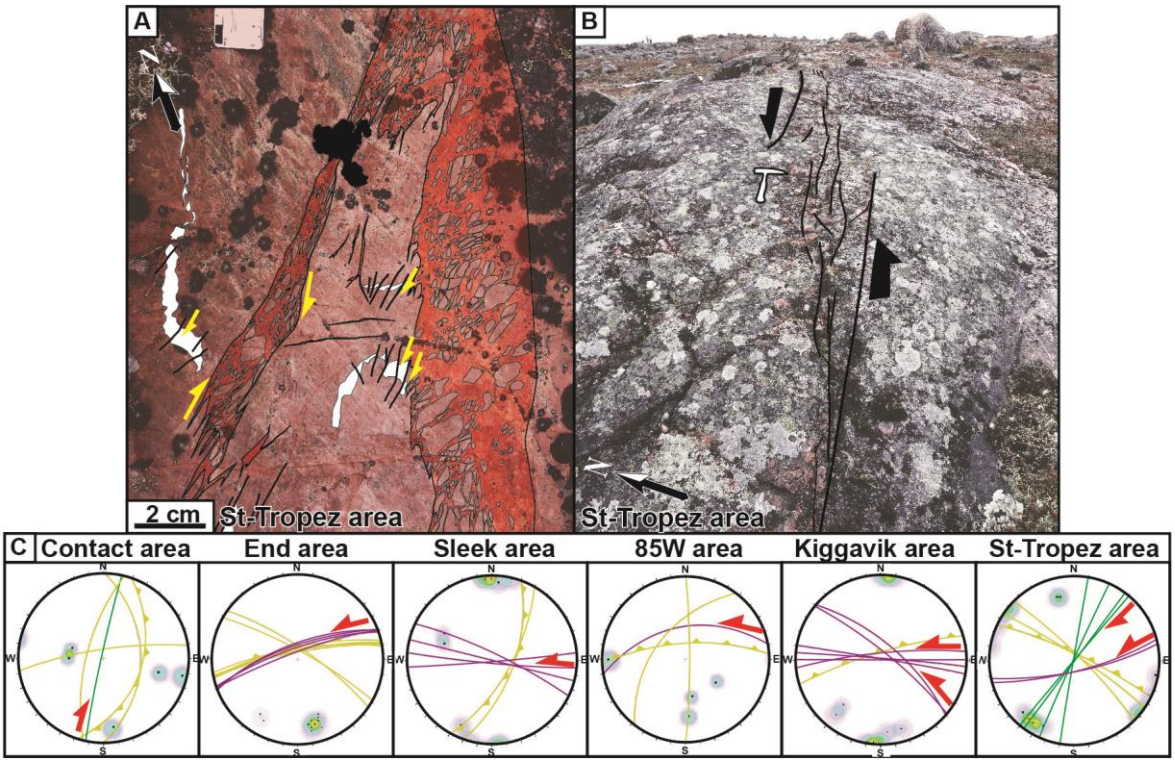

Figure 12: A) FP. NE-SW hematized fault zone displaying dextral kinematics. B) FP. ENE-WSW hematized fault-relay zone displaying evidence of sinistral strike-slip kinematics. C) Oriented data and kinematic of faults and microfaults, mainly from field observations but also collected on drillcores (i.e. Contact, Sleek and 85W). Legend as in Fig. 10.

The JSF, trending ENE-WSW, displays a reverse-sinistral component (Fig. 12C), which is observed as a late reactivation after the main dextral normal component responsible of the Hudsonian granite major offset (SLIC, Fig. 2, see also Anand and Jefferson, 2017).

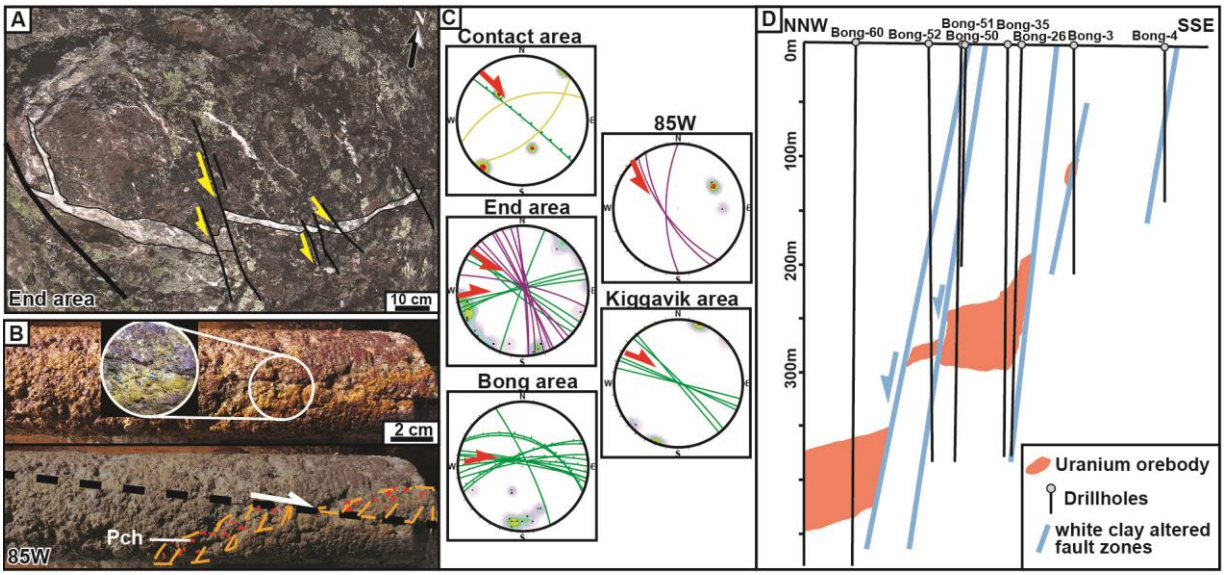

Figure 13: A) FP: Quartz veins of the QB being crosscut and offset (senestral motion) by late NNW-SSE to NW-SE microfaults. B) Drill core picture (top) and interpretation (bottom) of a uranium oxides and clay-cemented vein (orange outline) being crosscut and offset by a NW-SE microfault. Host rock is strongly altered. C) Oriented data and kinematic of faults and microfaults, mainly from field observations but also from drillcores (i.e. Contact and 85W). Legend as in Fig. 10. D) Simplified NNW-SSE cross-section of the Bong deposit, depicting dip-slip offset of the ore body by E-W oriented faults also driving fluids that strongly clay altered and bleached the host rock.

Finally, post-ore fault zones (f8), clay altered, display NNW-SSE direction with strike-slip sinistral motion in End and 85W areas (Fig. 13A-C); these faults also display dip-slip normal kinematics with E-W to WNW-ESE orientation, steeply dipping to the N. At 85W, microfaults offset uranium mineralized fractures (f6, Fig. 13B) while at Bong the orebody is offset by E-W striking fault (Fig. 13D). The dip-slip displacement of the uranium orebodies (metric to decametric) appears to be greater than the strike-slip component (centimetric to metric).

4.3 Nature and timing of the fracture-controlled fluids: chemical compositions of clays and uranium oxides and U-Pb dating of uranium oxides

4.3.1 Composition and crystallisation temperatures of illite and chlorite

Chlorite

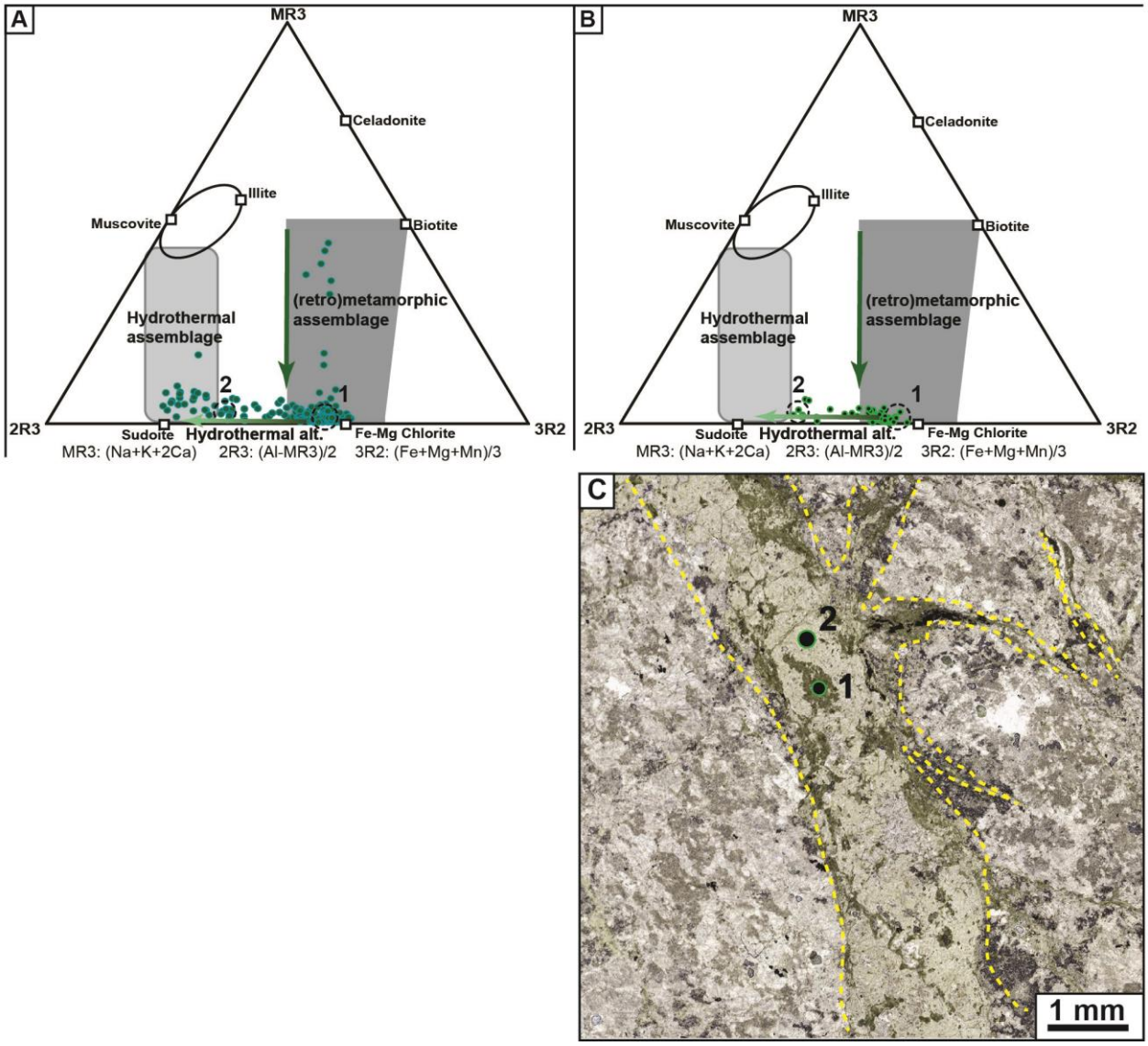

Figure 14: A) Chemiographic representation of chlorite analysed from different locations in the Kiggavik area (Jane, Contact, 85W, Andrew Lake). B) Chemiographic representation of chlorite grains formed during pre-QB mineralizing stage and their later hydrothermal alteration. Structural formulas of chlorites were plotted in a MR3-2R3-3R2 diagram (Velde, 1977). C) OMP of a U0 microbreccia cemented with unaltered dioctahedral chlorite (dark green), altered to light green di-trioctahedral chlorite (sudoite). Opaque minerals are ore minerals. Numbers localize the point analysed under EMPA, which results are plotted in B.

Chlorites in the Kiggavik area fall into three types: retrograde metamorphic chlorite, chlorites (altered and unaltered) associated with the mineralizing stage U0, and chlorites associated with the mineralizing stages U1 and U2, the latter being sudoitic chlorites (the chemical compositions of chlorite for different deposits and prospects, and stages of uranium mineralization are displayed in Table 1 and chemiographically presented in ternary MR3-2R3-

3R2 diagram (Velde, 1977, fig. 14A). Representative structural formulae of several chlorite associated with U1 and U2, in various locations, plot toward the sudoitic pole (di-trioctahedral chlorite).

Representative compositions of analysed chlorite from uranium mineralized microbreccia samples (f0, U0) are presented in Fig. 14B. Analyzed chlorites are cementing the microbreccia (Fig. 14C). Representative compositions of fresh and altered chlorite associated with U0, with calculated temperatures, are presented in Table 2. Chemical analyses and structural formulae of unaltered chlorite linked to U0 indicate an iron-rich species of trioctahedral chlorite. Their octahedral occupancy is close to 6 atoms when the structural formulae is calculated with total Fe in the ferrous state and their XFe is generally close to 0.5. Structural formulae of altered chlorite linked to U0 plot toward the sudoitic pole (di-trioctahedral chlorite), characterized by an Al-Mg rich composition and an octahedral occupancy close to 5 atoms. Numerous analyses of chlorites characterize a mixture of variable amount of iron-rich chlorite and sudoite, showing that a neoformed dioctahedral chlorite was altered to di-trioctahedral chlorite. This is consistent with petrographic observations (Fig. 14C) showing dark green chlorite surrounded by light green chlorite (sudoite).

Location	Contact U2	Jane U1	Jane U2	End	Kiggavik MZ U2	85W U1
SiO2 (wt. %)	36.97	36.02	35.23	36.49	34.59	35.29
Al2O3	34.45	33.98	35.74	30.09	35.17	32.31
K2O	0.88	0.74	0.25	0.27	1.96	0.92
CaO	0.15	0.17	0.02	0.04	0.15	0.18
FeO	0.96	0.12	0.17	2.24	0.5	0.86
MgO	12.28	14.72	15.04	17.13	13.41	15.87
MnO	0.02	0	0	0.06	0	0.03
TiO2	0	0	0	0	0	0
Na2O	0.04	0	0.04	0.08	0	0.06
Total	85.81	85.75	86.49	86.46	85.78	85.52

Table 1: selected representative sudoite analysis from different deposits and prospects of the Kiggavik area.

Temperature calculations were done by several methods (Table 2) for the Fe-rich chlorite variety linked to U0, as the geothermometers generally do not work with low-T° chlorites (i.e. sudoite). The Cathelineau (1988) and Jowett (1991) thermometer returned temperatures ranging from 295 to 333 °C whereas Kranidiotis (1987) and Zang and Fyfe (1995) thermometers returned temperatures ranging from 130 to 159 °C. The Temperature results from each method differ considerably, and the estimation of the possible temperature range needs to be done keepingtextural relationships, as discussed hereafter in the interpretation section.

	Unaltered (U0) chlorite					altered (U0) chlorite			
Sample	8561-9	8561-9	8561-9	8494-8	8548-14	8494-8	8549-6	8549-6	8549-6
Al2O3	18,61	17,72	19,53	19,07	19,96	24,63	27,13	28,81	26,97
SiO2	25,77	26,47	24,43	25,98	26,78	32,79	37,19	36,33	36,09
TiO2	0,09	0,05	0,10	0,00	0,04	0,06	0,00	0,00	0,00
Na2O	0,27	0,00	0,12	0,00	0,03	0,00	0,23	0,02	0,16
MgO	16,33	18,00	14,68	14,76	14,95	15,46	16,45	16,93	16,24
MnO	0,34	0,25	0,21	0,44	0,51	0,22	0,04	0,03	0,13
FeO	24,26	23,18	26,59	26,00	23,17	16,79	3,82	4,17	5,15
K2O	0,05	0,02	0,02	0,04	0,06	0,49	0,49	0,54	0,66
CaO	0,08	0,02	0,01	0,03	0,07	0,02	0,24	0,10	0,17
Cr2O3	0,16	0,00	0,04	0,01	0,01	0,04	0,04	0,03	0,04
Total	86,01	85,76	85,89	86,35	85,58	90,53	85,68	86,96	85,68
Na	0,06	0,00	0,03	0,00	0,01	0,00	0,04	0,00	0,03
K	0,01	0,00	0,00	0,01	0,01	0,06	0,06	0,06	0,08
Ca	0,01	0,00	0,00	0,00	0,01	0,00	0,02	0,01	0,02
Si	2,77	2,83	2,67	2,80	2,86	3,13	3,45	3,33	3,38
Al_{total}	2,36	2,23	2,52	2,42	2,51	2,77	2,97	3,11	2,98
Al^{IV}	1,23	1,17	1,33	1,20	1,14	0,87	0,55	0,67	0,62
Al^{VI}	1,13	1,07	1,19	1,22	1,37	1,89	2,42	2,44	2,36
Mg	2,62	2,87	2,39	2,37	2,38	2,20	2,27	2,31	2,27
Fe	2,18	2,08	2,43	2,34	2,07	1,34	0,30	0,32	0,40
Mn	0,03	0,02	0,02	0,04	0,05	0,02	0,00	0,00	0,01
Ti	0,01	0,00	0,01	0,00	0,00	0,00	0,00	0,00	0,00
Cr	0,01	0,00	0,00	0,00	0,00	0,00	0,00	0,00	0,00
Occ	5,94	6,02	6,01	5,94	5,82	5,43	4,99	5,07	5,04
XFe: Fe/(Fe+Mg)	0,45	0,42	0,50	0,50	0,47	0,38	0,12	0,12	0,15
T°C									
Cathelineau, 1988	333	314	366	324	306				
Jowett, 1991	322	303	355	313	295				
Kranidiotis, 1987	148	142	159	145	139				
Zang & Fyfe, 1995	137	134	143	130	127				

Table 2: Electron microprobe analysis of chlorites from the pre-QB mineralized microbreccia, and calculated temperatures after several techniques.

Illite

Selected representative compositions for white mica associated with pre-ore alteration, with the second U stage (U1, f5), third mineralizing U stage (U2, f6), and late clay alteration micas (f8) are presented in Table 2 and plotted on ternary diagrams representing the average compositional fields of dioctahedral mica-like phases (Dubacq et al., 2010) (Fig. 15A). Pre-ore alteration (Fig. 15B-C) is characterized by interlayered illite/smectite and smectite. Most of the white mica characterizing the alteration of the first mineralizing stage (Fig. 15B) is illite, as for

late ore clay alteration (Fig. 15D). White mica characterising the second stage of uranium mineralization (Fig. 15C) is represented by Illite and interlayered illite/smectite. The repartition of the data points in the diagram likely indicates an inheritance of the illite data from muscovite/sericite.

Temperatures calculated using the equation of Cathelineau (1988) return an average of 224°C for pre-ore alteration, 289°C for U1, 282°C for U2 and 305°C for late ore alteration (Table 2). The method of calculation of Battaglia (2004) returns similar temperatures.

	U1			U2		Late clay alteration			Pre ore	
Sample	**85W-09-1**	**CT-12-02**	**CT-23-06**	**CT-16-18B**	**C-T13-03**	**85W-11-04**	**CT-13-1**	**CT-16-20**	**CT-23-8A**	**CT-16-15**
Na2O	0,22	0,06	0,21	0,07	0,15	0,03	0,19	0,07	0,06	0,10
MgO	2,74	5,33	3,40	2,65	3,09	4,46	2,73	2,41	4,10	2,86
Al2O3	27,28	22,63	25,71	29,78	27,64	24,55	29,15	29,61	21,94	26,92
SiO2	44,82	53,11	53,49	49,81	51,38	54,75	49,25	48,64	51,17	51,82
K2O	10,45	5,74	8,72	8,31	8,50	9,53	9,57	8,40	6,05	7,31
CaO	0,12	0,20	0,32	0,16	0,27	0,05	0,02	0,28	0,69	0,27
TiO2	0,39	0,02	0,00	0,00	0,01	0,03	0,01	0,00	0,00	0,02
FeO	6,26	2,50	1,31	0,21	1,64	0,98	0,97	0,19	5,86	2,15
MnO	0,09	0,04	0,00	0,01	0,08	0,00	0,00	0,00	0,02	0,00
Total	92,38	89,68	93,21	91,13	92,84	94,40	91,95	90,22	90,01	91,50
Na	0,03	0,01	0,03	0,01	0,02	0,00	0,03	0,01	0,01	0,01
K	0,95	0,50	0,74	0,72	0,73	0,80	0,83	0,74	0,54	0,63
Ca	0,01	0,01	0,02	0,01	0,02	0,00	0,00	0,02	0,05	0,02
C,I,	1,00	0,54	0,82	0,75	0,79	0,81	0,86	0,79	0,65	0,68
Si	3,18	3,65	3,57	3,38	3,46	3,62	3,36	3,36	3,59	3,51
Al	2,28	1,83	2,02	2,38	2,19	1,91	2,34	2,41	1,81	2,15
Al (IV)	0,82	0,35	0,43	0,62	0,54	0,38	0,64	0,64	0,41	0,49
Al (VI)	1,47	1,48	1,60	1,77	1,65	1,53	1,70	1,78	1,40	1,66
Fe	0,37	0,14	0,07	0,01	0,09	0,05	0,06	0,01	0,34	0,12
Mg	0,29	0,55	0,34	0,27	0,31	0,44	0,28	0,25	0,43	0,29
Mn	0,01	0,00	0,00	0,00	0,00	0,00	0,00	0,00	0,00	0,00
Ti	0,02	0,00	0,00	0,00	0,00	0,00	0,00	0,00	0,00	0,00
Occ	2,13	2,17	2,01	2,05	2,05	2,02	2,04	2,03	2,18	2,07
Pyr	0,01	0,47	0,21	0,26	0,23	0,19	0,14	0,23	0,40	0,34
Cel	0,17	0,17	0,37	0,12	0,22	0,43	0,22	0,13	0,19	0,18
Ms+Pg	0,82	0,35	0,43	0,62	0,54	0,38	0,64	0,64	0,41	0,49
T°	**307**	**274**	**302**	**293**	**285**	**350**	**314**	**294**	**199**	**246**
Ave (n)		**289(15)**			**282(38)**		**305(24)**			**224(17)**

Table 3: Electron microprobe analysis of various generations of white micas. (CT: Contact prospect).

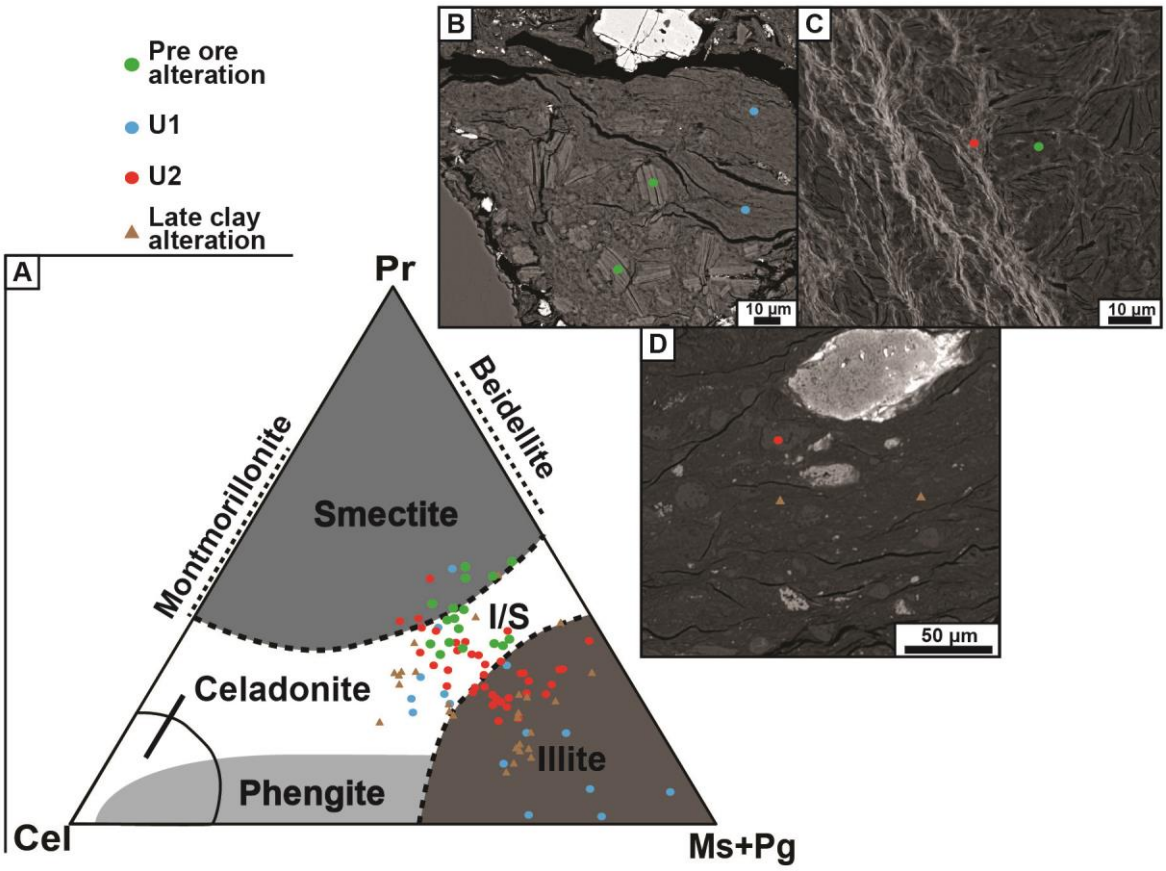

Figure 15: A) Analyzed white mica plotted on a ternary diagram of the average compositional fields of dioctahedral mica-like phases, after Dubacq et al., (2010). Pr: pyrophillite; Cel: celadonite; Ms: muscovite; Pg: paragonite. B) Pre-ore white mica in a fracture cemented by white mica in link with stage 1 U-mineralization. C) Pre-ore white mica in a micro-fracture reopened and cemented by white mica in link with stage 2 U-mineralization. D) Reworked clasts of ore minerals with second stage white mica, in a matrix cemented by late ore white mica.

4.3.2 Composition and age of uranium oxides

REE signatures of uranium oxides

The various generations of fracture-cementing uraninite and pitchblende were studied under LA-ICP-MS for their Rare Earth Element (REE) contents (Table 4), as chondrite-normalised REE patterns are considered as dependant of the geological conditions of uranium oxide formation (Mercadier et al., 2011; Frimmel et al., 2014; Alexandre et al., 2015). Fig. 16 displays the chondrite-normalized patterns for samples from Andrew Lake and End. These represent the first (U1, samples 9850, 9568-38, 9568-39 and 9568-08) and second stage of uranium mineralization (U2 samples 9851, And-15-01-05), and from late uranium remobilization fronts (U3, sample And-

15-01-04). Pre-QB uranium oxides (U0), could not be analyzed due to their small size, anhedral shape and mixing with Ti-U phases. Both the first stage (U1) and second stage (U2) samples display bell-shaped chondrite-normalized patterns centered on Tb with a small anomaly in Eu (Fig. 16).

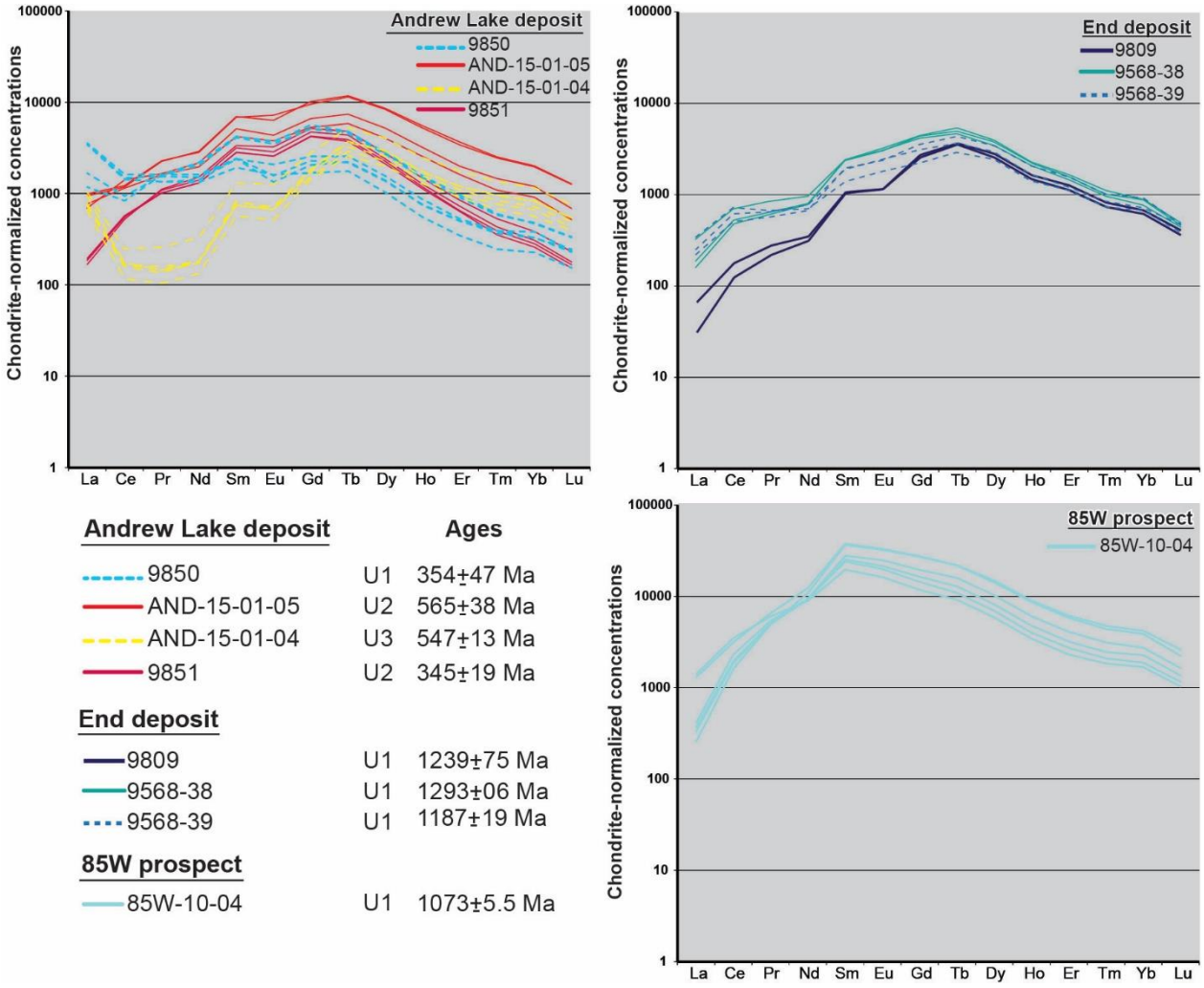

Figure 16: Chondrite-normalized REE patterns for pitchblende and uraninite from 8 different samples of Andrew Lake (Top left), End (Top right) and 85W (bottom right). Each curve corresponds to an in situ SIMS or LA-ICP-MS REE analysis in a selected U-oxide of the studied samples. Ages for the samples were obtained in this study (Fig. 16), except for sample 9568-38 and 9568-39, obtained by Lach, (2011). Classification of the mineralization as U1 (f5) / U2 (f6) /U3 (redox fronts post MacKenzie event) were made prior to age dating and REE measurements, based on the macroscopic character and mineralogy of the samples.

Samples are enriched in intermediate REE (Sm to Dy) compared with light rare earth elements (LREE) and heavy rare earth elements (HREE), except for sample 9850 which is

enriched in LREE compared to HREE. Samples of U1 are characterized by an HREE/LREE ratio around 1 (9568-38 and 39) or higher (sample 9568-08). Samples of U2 are slightly depleted in LREE and their HREE/LREE ratio is therefore higher. Sample AND-15-01-05 from the second stage of mineralization is more enriched in REE compared to other samples.

Sample And-15-01-04, which comes from a redox front (U3), displays a stronger negative anomaly in Eu, higher concentrations in La compared to other LREE and a high LREE/HREE ratio (~2), comparable to sample 9850. Samples 9850, AND-15-01-05 and AND-15-01-04 display enrichment in HREE (slight in the case of AND-15-01-05) characterizing alteration of the uranium oxides by the circulation of meteoric water (Mercadier et al., 2011), which is consistent with macroscopic observations on AND-15-01-04 which is a sample displaying a redox front with goethite, inferred to have formed in such conditions.

Sample 85W-10-04 displays a somewhat different shape pattern compared to the bell shape. The total concentration of REE is also much higher (up to a factor 10 for each element) compared to the other samples. The pattern displays a positive trend from La to Sm, is centered on Sm and displays a negative pattern from Sm to Lu, it is observed for only one of our samples and is described for the first time in the Kiggavik area.

Age dating on uranium oxides (ionic probe)

Uranium oxides from the same six samples that were analysed for REEs were also analyzed with SIMS for U-Pb isotopic dating. The dated samples come from Andrew Lake (4), End (1) and from 85W (1). Samples 9850, 9568-39, 85W-10-04 are of U1, samples 9851, And-15-01-05 of U2 and sample And-15-01-04 of U3. Isotope ratios are listed in a complementary table provided as supplementary material.

In the $^{206}Pb/^{238}U$-$^{207}Pb/^{235}U$ concordia diagrams (Fig. 17), data plot along or below the discordia suggesting that the samples either lost Pb or gained U. Electron microprobe analysis shows that studied uraninites and pitchblende display relatively high U contents but low Pb contents, especially for U1 and U2; indicating a loss of Pb. Based on the U–Pb geochronology, three samples from Andrew Lake yield upper intercept ages at 554 ± 71 Ma (sample 9850) for U1, 565 ±38 Ma (sample And-15-01-05) for U2 and 547 ± 13 Ma (sample And-15-01-04) for U3. Sample 9851 yielded an upper intercept age of 345 ± 19 Ma. The scattering of the data for sample 9850 possibly indicates the analyses of multiple generations of uranium oxides, altered and less altered. Analyses for this sample were corrected for common Pb, thus giving intercepts at 354 ± 47Ma. The oldest upper intercept ages obtained for U1 comes from 9568-39 from the End

deposit (1239 ± 75 Ma), and from sample 85W-10-04 (1073 ± 5 Ma) from the 85W prospect.

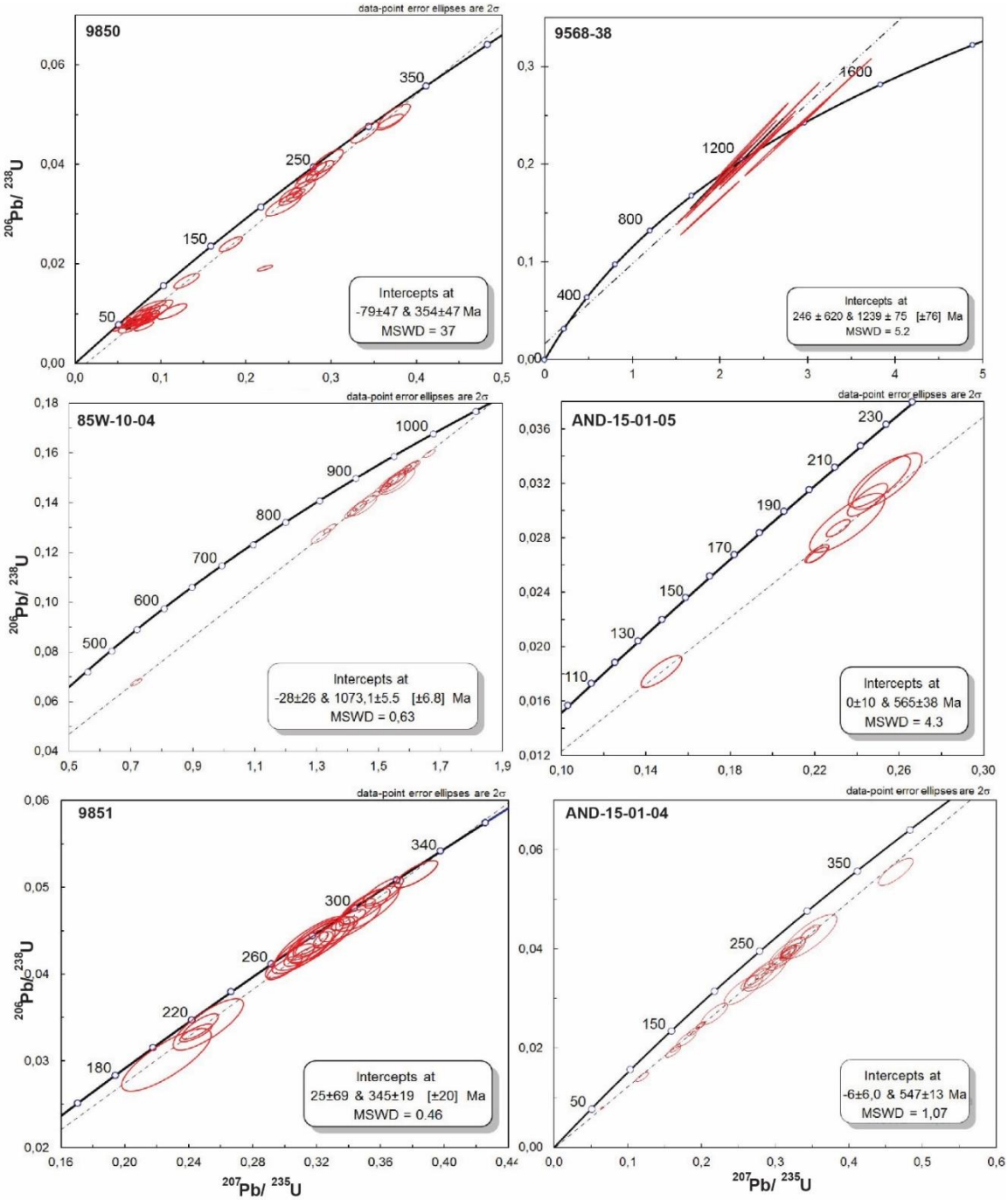

Figure 17: $^{206}Pb/^{238}U$- $^{207}Pb/^{235}U$ Concordia diagram showing the isotopic composition of uranium oxides (pitchblende and uraninite) from six samples coming from End (9568-39), Andrew Lake (9850, 9851, And-15-01-04, And-15-01-05) and 85W (85W-10-04). Analytical data are available as complementary material.

4.3.3 Fluids characterization (secondary Fluid Inclusion Planes)

Fluid inclusions types and microthermometry

Different types of secondary fluid inclusions were observed as FIPs in quartz, mainly magmatic in origin but also from hydrothermal quartz (from the QB) in some cases, within thin sections coming from 85W and Contact. Some primary fluid inclusions were studied in a quartz vein from 85W. A total of 99 secondary fluid inclusions from FIPs were studied for microthermometry. Homogenization temperatures (Th) and ice-melting temperatures (Tm-ice) were determined for liquid-dominated biphase fluid inclusions with relatively low vapour percentages (mostly <20 %). FIs were classified following Derome et al. (2005). No carbonic fluid inclusions were observed and three types of fluid inclusions were identified, belonging to two different types of FIPs, called monophase FIPs and biphase and triphase aqueous FIPs hereinafter (Fig. 18A).

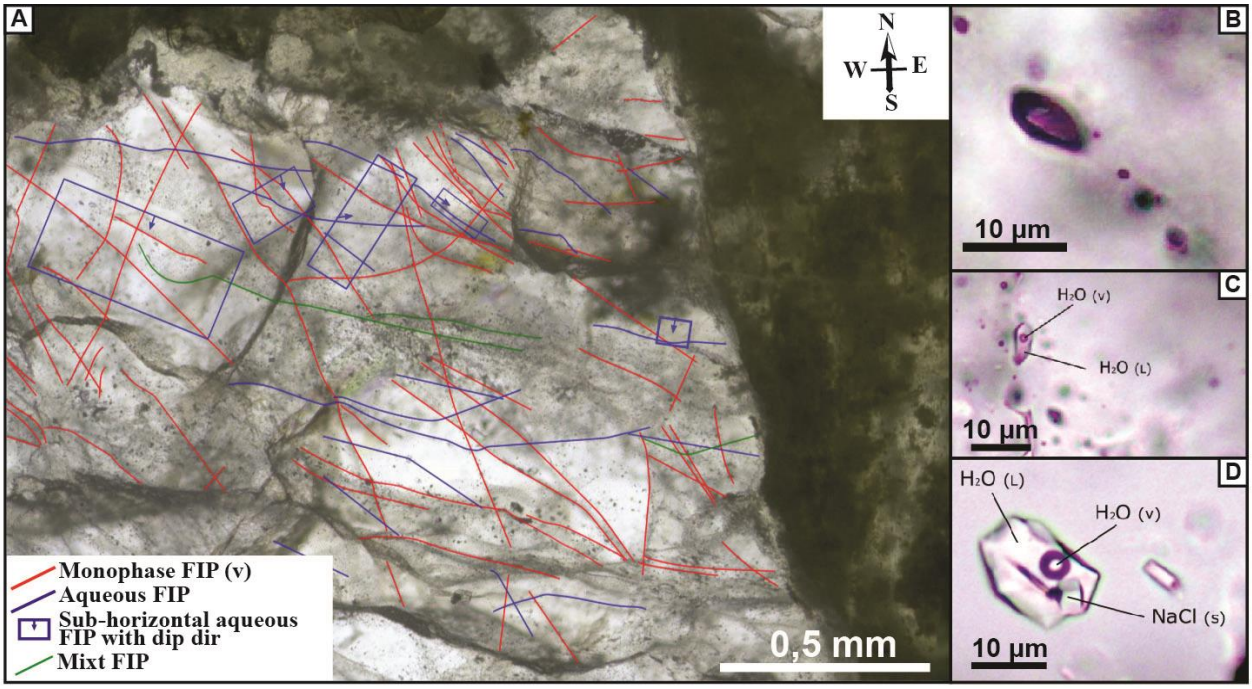

Figure 18: A) Magmatic quartz from the granite of 85W displaying monophase FIPs (red) crosscut by aqueous FIPs (blue). B) Monophase fluid inclusions displaying negative crystal shape. C) Biphase aqueous fluid inclusions. D) Triphase aqueous fluid inclusions with halite crystal.

Monophase, vapour only FIPs were easy to observe as they display a dark fluid inclusions. They display rounded shapes and possibly border's effects termed "negative crystal shape" (Fig. 18B). Their sizes vary from 3 to 10 µm. No phase change was observed for these FIs even when they were cooled to -190°C. Analysis of the gas phase by Raman spectroscopy indicates H_2O at the vapour state, no other gases were detected (Fig. 19A). These inclusions constitute the first type of FIPs.

Biphase and triphase FIs can be observed together in certain FIPs and constitute the second type of FIPs (called “aqueous FIP”). Biphase aqueous FIs are characterized by a dominant liquid phase with a vapour phase representing 10 to 20% of the FI by volume (Fig. 18C, liquid phase is H_2O, fig. 19B). They have variable shapes with a size varying from 3 to 20 µm. They comprise two types; Lw’ and Lw1. Except for H^2 and O^2, no other gas was detected through Raman spectroscopy. Triphase aqueous FIs display a cube of halite (Fig. 18D, indicating oversaturation in NaCl), belonging to Lwh’ type. They have variable shapes and their size range from 6 to 20 µm. Liquid and vapour phases were analyzed under Raman spectroscopy; like biphase aqueous FIs, non-aqueous volatiles such as CO_2, CH_4, H_2S and N_2 were not detected in the inclusions (Fig. 19C).

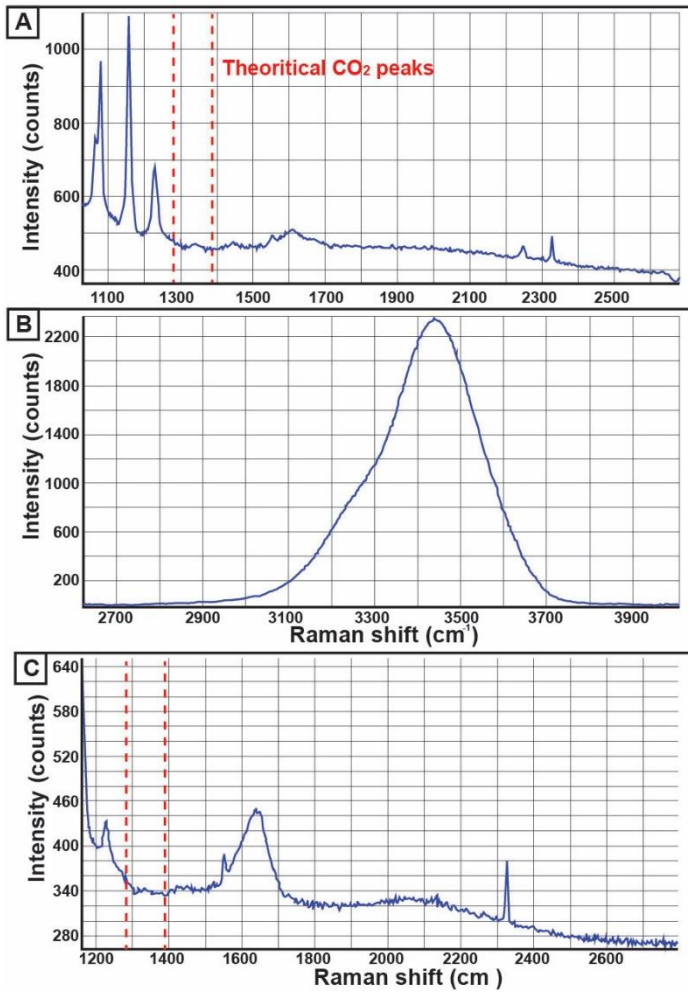

Figure 19: Raman spectra of fluid inclusions. A) Liquid phase of monophase FI. B) Liquid phase of aqueous FI. C) Gas phase of aqueous FI.

A summary of microthermometric data obtained for the analysis of biphase and triphase FIs is presented in table 5B. Inclusions showing a halite cube at room temperature are denoted as Lwh′ or Lwh according to the nature of their last phase to melt during cooling-heating (ice or hydrohalite respectively). Inclusions free of halite cube whose last phase to melt is ice are referred to as Lw′ (−45.4 °C < Tm ice < −30.6 °C), Lw1 (−28.9 °C < Tm ice < −25.9 °C) or Lw″ (−23.9 °C < Tm ice < −1.4 °C). Except for Lw″ inclusions, the observed Te ranges from −85 to −60 °C, which is typical of the H_2O–NaCl–$CaCl_2$ ± $MgCl_2$ system. For Lw″ inclusions, the observed Te range from −65 to −38 °C and may be related to the H_2O–NaCl (± another unknown salt) system. Considering all Lw′ and Lw1 inclusions, Tm ice displays a continuous trend from −45.4 to −25.9 °C. Tm ice of Lw″ inclusions range from −23.9 to −1.4 °C. Total

homogenization of all Lw and Lwh inclusions occurs to the liquid phase ((L–V)→L). Th varies from 62.3 to 244.7 °C. Ts NaCl ranges from 121 to 222 °C for Lwh′ inclusions and is systematically higher than Th (L+V+ NaCl→L+NaCl→L).

A

Nature of last phase to melt after freezing then heating of IF	IF with NaCl cube	IF without NaCl cube			
Ice	Lwh'	Lw'	Lw1	Lw''	Aqueous fluid with NaCl as main component
Tm_{ice} (°C)		-45 to -30	-30 to -24	-15 to -1	
Hydrohalite	Lwh	Lw2			
Doesn't freeze	Lwh'	Lw'			Aqueous fluid with $CaCl_2$ as main component

B

	FI type		% vapor phase	Microthermometric data				Salinitiy (Wt% NaCl+CaCl2)
				Te	Tm ice	Ts NaCl	Th	
85W	Lw'	Range	10-50	-85 to -66	-45.4 to -30.6	207 to 223	99.9 to 215.0	25.0 to 29.3
		Mean		-72	-38		144	28
		n		5	6	2	6	6
	Lwh'	Range	5-40	-80 to -60	-45.8 to -22.8	121 to 222	62.3 to 135.5	24.4 to 29.4
		Mean		-71	-38	190	106	27
		n		17	19	11	8	19
	Lw''	Range	5-90	-65 to -38	-23.9 to -1.4		207.6 to 244.7	2.3 to 22.3
		Mean		-53.6	-13.0		230.9	14.4
		n		9	16		3	16
Contact	Lw1	Range	10-30	-77	-28.9 to -25.9			23.2 to 24.4
		n		1	2			2
	Lw'	Range	10	-75	-31.4		92.0	25.3
		n		1	1		1	1
	Lwh'	Range	10			155 to 168	81.8 to 117.7	
		n				3	4	
	Lw''	Range	30		-16.6			19.8
		n			1			1

Table 4: A) Classification of fluid inclusions (after Derome et al., 2005) for aqueous biphase and triphase inclusions. B) Summary of microthermometric fluid inclusions data obtained in this study for aqueous biphase and triphase fluid inclusions. Te: Temperature of eutectic. Tm ice: melting temperature of the last crystal of ice. Ts NaCl: Fusion temperature of the crystal of halite.

The concentrations of several metals in selected aqueous fluid inclusions were measured through LA-ICP-MS, as presented in the methodology section. Results are presented in Fig. 20 and compared to metal concentration of aqueous FIs from one deposit in the Athabasca Basin (Richard et al., 2010). Aqueous FIs from the Kiggavik area are much less concentrated in

metals, usually by a factor 10 (Zn, Rb, Sr, Cs, Ba, B and Pb). Concentrations in B are also less enriched in the Fis of the Kiggavik area. Concentrations in U are comparable to those obtained for $CaCl_2$-rich brines in the Athabasca Basin deposits.

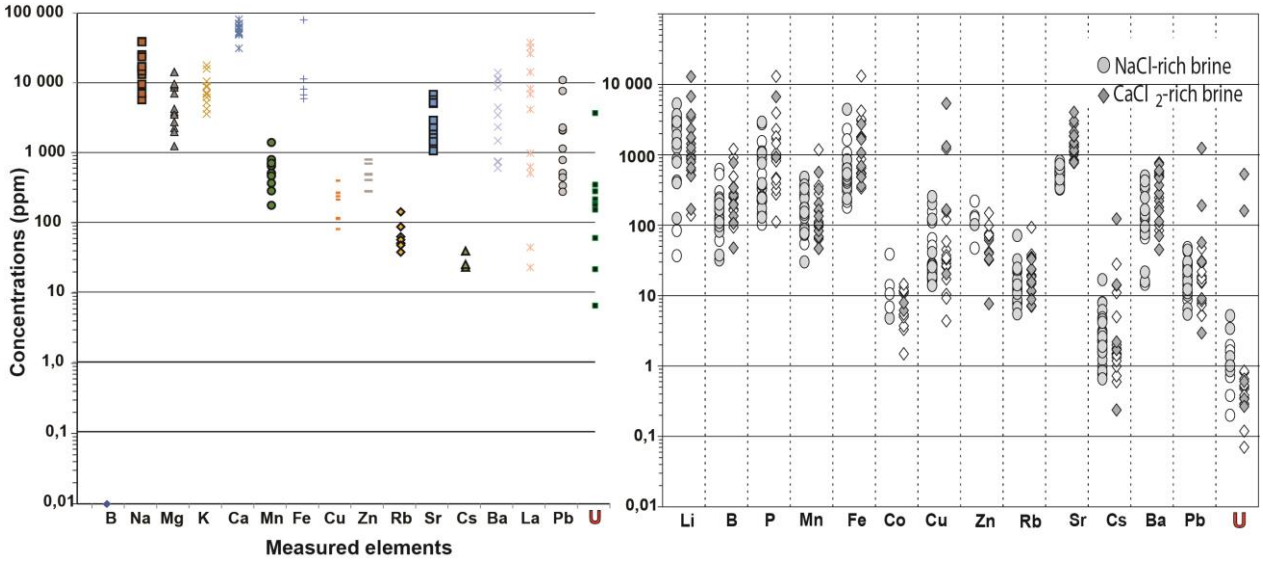

Figure 20: Concentration (µg.g^{-1}) in several metals for selected secondary fluid inclusions in the Kiggavik area (Left) in this study. Obtained data are compared to concentration in several metals in fluid inclusions from the McArthur River unconformity-related deposit in the Athabasca basin (right, after Richard et al., 2010).

Fluid inclusions planes orientation (FIP)

Monophase FIPs within magmatic quartz grains are crosscut by aqueous FIPs (Fig. 21). This indicates the occurrence of at least two episodes of fluid circulation. FIPs of each type were counted and the results plotted in rose diagrams as a function of the planes strike (Fig. 22, top right part).

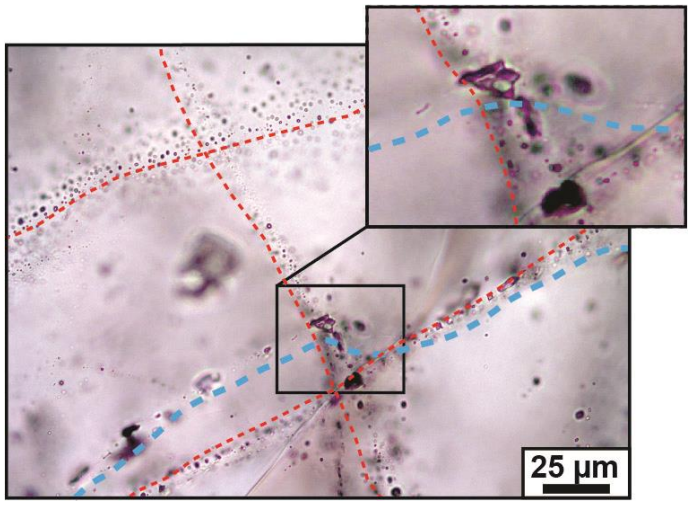

Figure 21: Monophase FIPs (red dotted lines) and aqueous FIP (blue dotted line). Monophase FIs are obliterated at the intersections between monophase and aqueous FIPs.

FIPs at 85W are mainly by monophase (186 FIP measurements). In 85W-09 (samples 85W-09-07 and 85W-09-04), monophase FIPs display main directions of N100-110. Secondary directions are N10-30 and N120-140. For aqueous FIPs, studied samples returned a main direction of N110-

120 and secondary directions around N120-130 and N40-60. For 85W-10 (sample 85W-10-04B), monophase FIPs display main directions around N350-10, N140-160 and N110-130. Aqueous FIPs have main directions around N60-80 and N120-140. At the scale of 85W (Fig. 22, bottom part), there are therefore three main directions for monophase FIPs: N350-10, N110-120 and N140-160, and a minor one: N30-50. Some sub-horizontal FIPs were observed at 85W; they are mainly composed by triphase FIs. Aqueous FIPs show two directions: N110-140, N40-80.

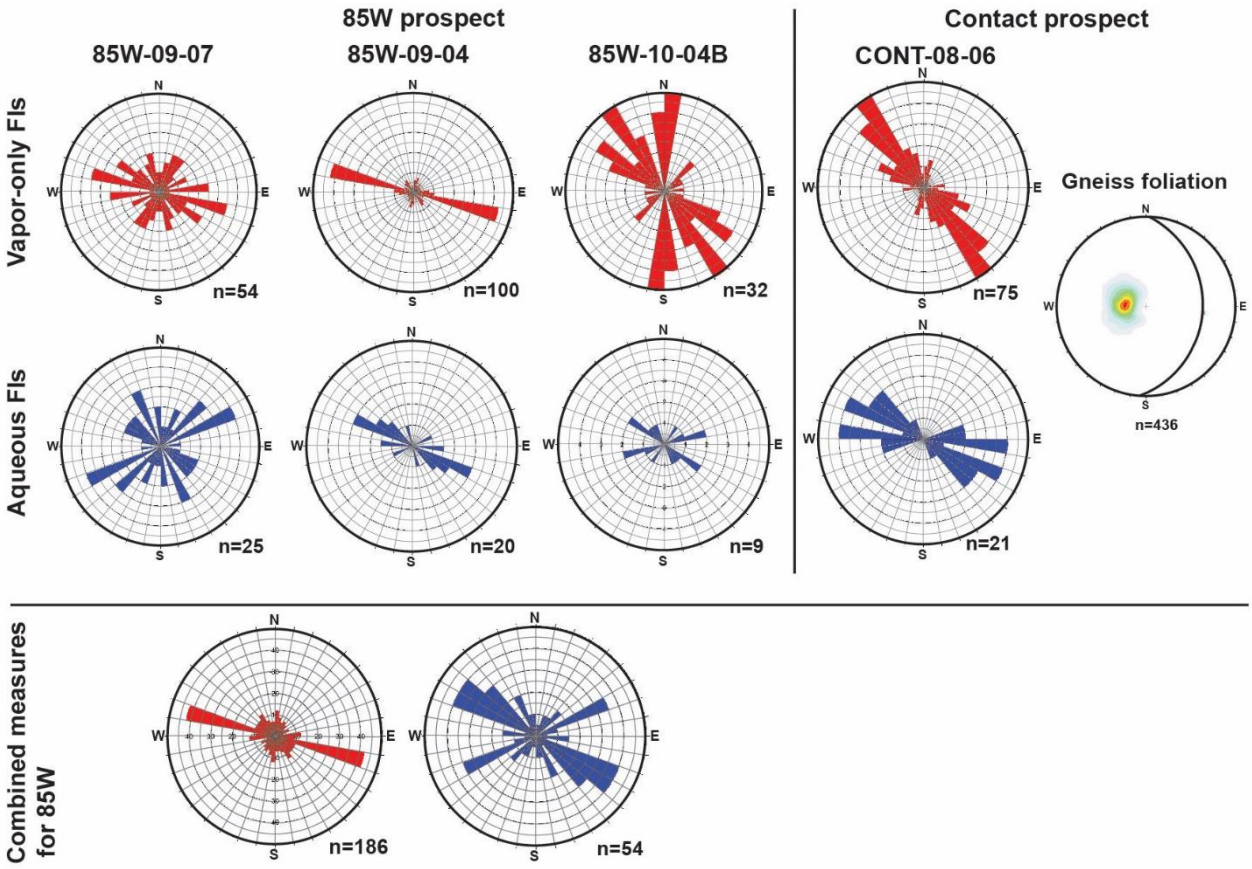

Figure 22: FIPs directions for monophase (red) and aqueous (blue) FIs, for 85W (left) and Contact (right). Mean granitic gneiss foliation at Contact is given. The general dip for the FIPs is sub-vertical.

At Contact, monophase FIPs are also the most represented type (74 FIP measurements), these FIPs display a main N130-150 direction and secondary N110-130 direction. N0-20 is observed as a minor direction. Aqueous biphase and triphase FIPs overprint monophase FIPs like at 85W. Aqueous FIPs display two directions: N110-120 and N80-N100. FIPs directions were also compared with reference to the orientation of the foliation of the granitic gneiss, which is sub-constant at Contact (N10/10°E).

5. Interpretation of the results

5.1 Main fracturing/mineralization events in the Kiggavik area

We have shown that the fracturing events observed at Contact (Grare et al., 2017) were recognized in other deposits and prospects in the Kiggavik area, and that the sequence of events established at Contact is confirmed and valid for the whole Kiggavik area. In addition, the present work determined a first fracturing and mineralizing stage, best preserved at the End deposit, which predates all the fracturing stages. In what follows, macro- to micro-scale observations made throughout the Kiggavik area are gathered and interpreted to propose a comprehensive metallogenic model for this area.

Pre-Thelon fracturing and mineralizing/mineralization events in the Kiggavik area

Stage U0

This first stage of uranium mineralization (termed “U0”) is characterized macroscopically by microbrecciation (f0) of the host rock in zones up to 10 m wides; clasts typically display corroded rims. This brecciation event was observed for all the major deposits in the Kiggavik area, but is better preserved at depth, for example at End, below the QB (f2), where fracturing and associated alteration events are less well represented. Undulating microstructures observed at the micro-scale are another characteristic feature of this fracturing event. We interpret these microstructures as micro-stylolites, Although such features are traditionally observed in sedimentary environments (e.g. Rutter, 1983; Benedicto and Schultz, 2010), they have also been described in igneous rocks; for example in rhyolite and welded tuffs (Bloss, 1954; Burma and Riley, 1955; Golding and Conolly, 1962). Oriented data are lacking for this fracturing event making it difficult to draw a clear picture of the orientations of the associated structural feature. A few of the data from End display ENE to NE, striking NNW, orientations fractures. The observation that this mineralizing stage is more represented in deposits controlled by major ENE faults highlights the role played by the major fault zones in focusing both fracturing and fluid circulation over the entire evolution of the Kiggavik area. The host rocks surrounding the mineralized breccia, despite local significantly mineralized zones, are only weakly to non- clay-altered. This is an unusual pattern in URU deposits and also in the Kiggavik area in general, where mineralization is usually associated with moderate to strongly clay-altered host rocks (Fuchs and Hilger, 1989; Riegler et al., 2014; Sharpe et al., 2015; Shabaga et al., 2017). Such characteristics that U0 was formed in conditions differing from those controlling URU mineralization. Again, oriented data are scarce and come mainly from observations at End.

Fractures strike NE-SW to ENE-WSW fractures, and dip NW, reflecting orientations of the JSF at this location. Sub-vertical micro-stylolites display one main trend, NNW-SSE.

The cement of the microfractures is characterized by hydrothermal rutile, Fe-rich clinochlore and sulfide minerals. U-bearing minerals are pitchblende and brannerite with Th contents of up to 7%. This mineralogy and the Th content of U-bearing minerals is also unusual for URU mineralization, for which all analyzed uranium oxides have Th contents < 1000 ppm (Frimmel et al., 2014; Alexandre et al., 2015). Such mineralogy and high [Th] content for uranium oxides have been recognized in association with magmatic/volcanic-related U ore systems, like those in the Beaverlodge area (Dieng et al., 2013), the Poços de Caldas peralkaline complex (Fraenkel et al., 1985) and the Witwatersrand deposit (Depiné et al., 2013), which are all related to relatively high temperature (>350°C) compared to URU oxides (100-200°C). The f0 mineralized microbreccia predates veins of the QB event (ca. 1750 Ma) and is inferred to predate deposition of the Thelon Formation (1667 Ma, Davis et al., 2011). The U0 mineralizing is thus considered to have formed before the deposition of the Thelon Basin, in relatively high-T conditions.

QB event

The QB event (f2) is characterized by breccias cemented with numerous generations of quartz within oxidized/hematized host rocks and is present throughout the Kiggavik area in close association with the main fault trends (MZF, JSF, ALF). In fact, these faults were likely first active before the brecciation event, and subsequently focused the circulation of Si-rich fluids (probably meteoric fluids interacting with fluids of igneous origin) that caused hydraulic fracturing and repeated reactivation of these faults. The QB is usually several meters thick, and can reach 10 m or more in thickness in rare cases such as in the Center zone of Contact (Grare et al., 2017). The core zones are usually less fractured and altered compared to damage zones and uranium orebodies are observed within its hanging or footwall, always out of the breccia core. This supports the inference that, at the deposit scale, the QB played a role in partitioning fracturing and fluid flow (Grare et al., 2017) depending on its local thickness (Fig. 23). In addition, there is a clear spatial association at the meso/micro-scale between quartz veins and uranium mineralization as quartz veins are reopened and/or orthogonally microfractured and re-cemented by ore minerals. These positions suggest that the QB was a transversale barrier for fluids but enhanced along-strike migration and entrapment. Major faults in the Kiggavik area were the locus of polyphase brittle tectonic activity and again, acted as major drains for fluids, should they be mineralizing or non-mineralizing. The timing of the QB event is well constrained

as pre-Thelon, since clasts bearing quartz veins have been observed in the sandstones of the Thelon formation and the QB is overlain by the Thelon formation. Grare et al. (2017) showed that the quartz generations are characteristic of epithermal Si-rich fluids, the circulation of which was likely triggered by magmatism of the Kivalliq igneous suite (ca. 1750 Ma). U0, predating the QB, is not directly observed in core zones of the QB, as brecciation along with epithermal fluid circulation likely completely overprinted and removed the uranium mineralized microbreccia.

U1 is hosted by f5 fractures characterized in all deposits by “narrow” fault zones (5 to 20 m, damage core zones included) with grey-greenish altered fault rocks (mainly illite, but sudoite was also characterized by XRD by Pacquet, 1993). Fault core zones are much more mineralized than damage zones. Oriented data are scarce and except for Contact, they reflect the orientation of the main fault zone in which they are hosted (NE-SW for the Andrew Lake deposit, WNW-ESE for the 85W prospect).

U1 is usually of high grade and mainly monometallic and is the most commonly described mineralization in the Kiggavik area (Sharpe et al., 2015; Shabaga et al., 2017). It is mainly monometallic, characterized by pitchblende and sulfide minerals (pyrite, chalcopyrite, bravoite, sometime intergrown with pitchblende) but polymetallic (pitchblende, sulfide minerals and Mo-Ni-As-Co-Ag-Au) mineralized fault zones with the same macroscopic features were also described at Contact, Andrew Lake and Kiggavik Main Zone. U1-cemented fractures and calcite veins (Ca1) crosscut dolomite veins and the various quartz generations of QB and both U1 and Ca1 are commonly spatially associated. Moreover, the observation of subhedral uranium-minerals in calcite cement attests for the synchronicity of the two fracturing events, which could therefore be regrouped.

(Syn ?) post-Thelon fracturing events in the Kiggavik area and related U mineralization

U2 is characterized by wider, reddish oxidized f6 fault zones (several tens of meters, extended damage zones) associated with stronger clay alteration of the host rock (illite and sudoite). These types of wide oxidized fault zones were well observed at Contact and Andrew Lake, and also recognized at End and Kiggavik Main Zone. As already observed by Grare et al. (2018) at Contact, these oxidized faults are not always mineralized and fault cores that display strong clay alteration, alongside with tectono-hydraulic breccia that displays weaker alteration, are usually not mineralized.

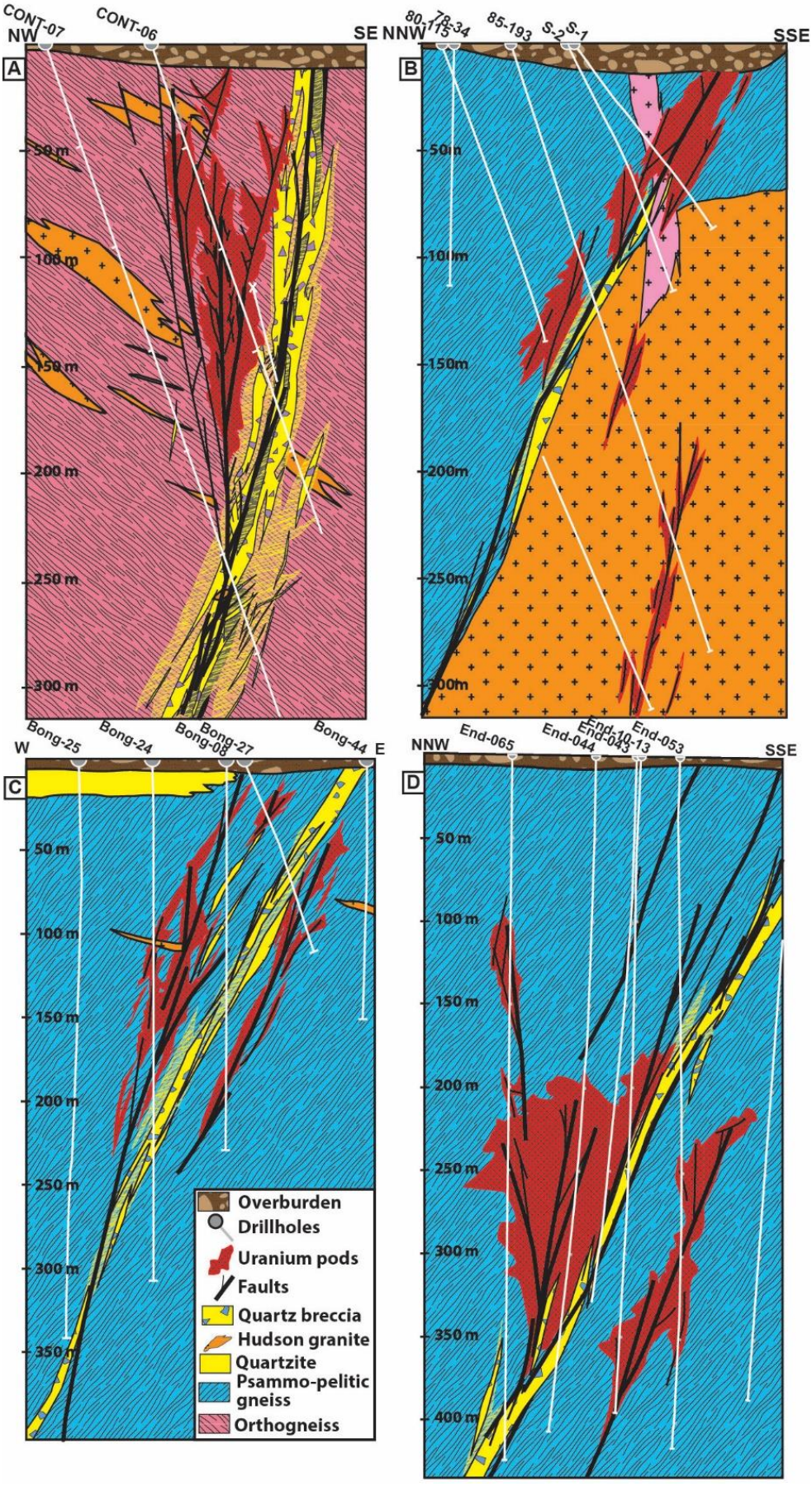

Figure 23: Simplified cross sections of Contact (A), Kiggavik Main Zone (B), Bong (C) and End (D). These cross sections only show the QB, uranium orebodies (without distinction of U-stages) and main faults.

Uranium mineralization is stronger in well-developed, moderately clay-altered damage zones, coating joints and microfaults, along reopened foliation and disseminated within the host rock. These observations are in line with the classical view of fault zones (Chester and Logan, 1986; Kim et al., 2004; Faulkner et al., 2010) where fracturing and fluid flow are more important in damage zones than in core zones.

The U2 stage is mineralogically characterized by pitchblende, rare sulfide minerals (pyrite coated by pitchblende) are observed and relict ore minerals from previous stages can be observed where U1 fault zones are crosscut by U2 fault zones. U2 can therefore be classified as a monometallic uranium mineralizing stage. Along with the hematization of the host rock, these mineralogical differences highlight that the uranium-bearing fluid had a different chemistry compared to the U1 mineralizing event, with slightly more elevated fO2 and pH (see Pourbaix diagram in Romberger, 1984). The orientations of U2 faults do not necessarily reflect the orientations of the main fault that hosts the deposit/prospect. The orientation of the latter fault is better shown by non-mineralized oxidized faults (for example at Contact, Andrew Lake, End and Bong), whereas mineralized faults display a more complex range of directions, sometimes antithetic to the main fault (for example, NNW-SSE fractures at End, NE-SW to N-S fractures at Kiggavik). This kind of variable orientations is typical within damage zones linking main faults and has been described in a variety of settings (Kim et al., 2004; Rotevatn and Bastesen, 2015; Fossen and Rotevatn, 2016).

Overall, the differences (fracture orientations, strength of clay-alteration, reduced vs. oxidized fault zones, polymetallic vs. monometallic) between mineralizing events U1 and U2 could be linked to the differential response of prexisting and reactivated faults to the evolving regional tectonic stress field (i.e., different directions and intensity), inducing a maturation of the fault zones and a change in the pathway of the fluids, thus a different fluid-rock interaction.

The main post-ore (also called “late clay alteration”) fracturing event (f8) is characterized by fault zones showing numerous narrow fault cores and strongly clay altered (illite. sudoite were not observed under optical microscope and SEM), desilicified and completely bleached fault rocks. The fracturing/faulting is spatially and temporally dissociated of uranium mineralization; however it has a significant impact on the 3D organization of the deposits because these faults offset uranium orebodies with a significant dip-slip component and a minor strike-slip component. This is observed especially at Bong where the orebody is offset by E-W to ESE-WNW dip-slip normal faults, but also at End where the orebody is offset by NW-SE to NNW-SSE faults. The reworking of uranium mineralization (U0, U1 and U2) by this fracturing stage was observed in all deposits and prospects of the Kiggavik area. Moreover, observed U1 and U2

fault zones are also less mineralized when they are crosscut by white-clay altered faults, indicating remobilization of the uranium oxides at this stage. As this event corresponds to one of the latest fracturing stages, it makes difficult to process oriented data in order to retrieve the "true" orientation of faults, as we are facing neoformation and re-activation of fractures in complex and polyphase fault zones. An ESE-WNW to NNW-SSE trend and a steep dip to the NW appear to be the main orientation of these faults in the Kiggavik area. Reactivation of faults during this stage is illustrated by NE-SW white clay-altered faults at Contact, initially belonging to the f6 stage (Grare et al., 2017), such similarities in orientations between f8 and other fracturing stages is also observed at other deposits and prospects (End deposit for example, Fig. 9). This observations that most of the faults for this post-ore fracturing stage appear to be inherited is consistent with models in which reactivation of faults is easier compared to neoformation (e.g. Roberto et al., 1997).

To summarize, the fracture/fluid circulation/mineralization history of the Kiggavik area are as follows:

- f0/U0, f1, followed by the brecciation-silicification event that cracked the so-called Quartz Breccia (QB-f2), are all pre-Thelon Basin fracturing stage.
- f3 to f8, including two stages of uranium mineralization (U1-f5 and U2-f6), are all syn to post/post-Thelon Basin event. Among these syn/post-Thelon events a clay barren alteration and fracturing stage (f8) was the latest event. These fracturing/mineralization events predate emplacement of the late NNW-SSE trending Mackenzie dikes swarm that crosscut orebodies, display little to no alteration and show no offset on geophysical maps (Tschirhart et al., 2017).
- Postdating Mackenzie diking in the Kiggavik area, we observe late uranium remobilization-reconcentration (U3) along redox fronts and supergene alteration that ultimately shaped the orebody distribution, If these events can have a significant economic impact on ore redistribution, they are likely linked to (weak) fracturing, and don't correspond to a main fracturing stage that significantly alter the structural architecture of deposits and prospects.

5.2 Temperatures of (mineralizing) fluids

Chlorite geothermometry

U0 is associated with crystallization of medium-temperature chlorite (130-159°C and 295-333°C), depending on the chosen geothermometer. The evaluation of iron valence, thus the

amount of Fe^{3+}, impacts the temperature calculation and has always been an analytical challenge. However, Bourdelle and Cathelineau (2015) demonstrated that the lower the temperature, the lower the impact of Fe^{3+} and a model based solely on Fe^{2+} is suitable in terms of practicability and simplicity while still giving reliable results. In our study, considering the alteration of di-octahedral chlorite to sudoite (a mineral characteristic of basinal brine circulations linked to U1 and/or U2)) and also considering the mineralogy and composition of uranium oxides associated with U0, the high temperatures (295-333°C) obtained by Cathelineau (1988) and Jowett (1991) for dioctahedral chlorite of this stage, are coherent with the high thorium content of pitchblende and brannerite observed in the f0 stage of uranium mineralization. This is because incorporation of thorium (Th^{4+}) into the uraninite structure is mainly a function of temperature and is commonly observed in metamorphic or magmatic uraninite (Mercadier et al., 2013; Depiné et al., 2013; Frimmel et al., 2014; Cuney and Kyser, 2015). The calculated temperature, coherent with late-metamorphic fluids (Dieng et al., 2013) is, however, somewhat lower than the temperatures reported for magmatic-derived fluids (Cuney, 1978; Leroy, 1978), which could be explained by either a limitation of the calculation method or simply by cooling of the fluid before precipitation of the mineral. The pre-Thelon high-temperature dioctahedral chlorites cementing f0 fractures would have likely been altered at a later point, probably after the deposition of the Thelon Formation, by the circulation of Thelon-derived basinal brines thus crystallizing low temperature (~100-200°C) di-trioctahedral chlorites. Such fluid circulation, linked to the formation of sudoite, is considered as the one related to the formation of U1 and/or U2, which have been temporally and spatially linked with Thelon-derived basinal brines. Calculating the temperatures of formation of sudoite is not possible, therefore preventing comparisons with temperatures obtained by illite geothermometers.

Illite geothermometery

Pre-U1-f5, white mica (also called pre-ore, even if crosscutting relationships with U0 were not observed) that crystallized at low temperatures (~200-240°C) could either represent early localized alteration along fault zones (f1) during development of the Baker Lake and Wharton basins (i.e., brittle faulting and illitization prior to QB event, Grare et al., 2017), or diagenetic fluid circulation during development of the Thelon Basin (diagenetic quartz with temperatures of homogenisation of 100-160°C, peak diagenetic illite crystallized at ca. 200 °C, Renac et al., 2002). White micas synchronous with U1 and U2 returned temperatures of ca. 280-290 °C, but slightly higher in the case of U1. These temperatures are higher than those typically obtained in the Athabasca Basin (200-260°C, Chu and Chi, 2016), which could indicate

crystallisation of illite and URU oxides at greater depth and/or an abnormally higher thermal gradient. A higher thermal gradient, produced by a deep-seated heat source, is a preferred hypothesis linked to magmatism associated with emplacement of the Kuungmi lavas at 1540±30 Ma (Chamberlain et al., 2010).

Post-ore (U0/U1/U2) alteration illite, observed in f8 fractures, returned slightly higher temperatures of 290-350°C; this increase of the temperature could be linked to the emplacement of the large volumes of magmas associated with the giant dike swarm of the Mackenzie event. This event could have triggered the circulation of "hot" hydrothermal fluids shortly before emplacement of the diabase dikes and "sealing" of the faults, which would also be consistent with illite Ar-Ar ages obtained at ca. 1300 Ma at End, Andrew Lake, Kiggavik Main Zone and Bong (Ashcroft et al., 2015; Shabaga et al., 2017; and others, see Fig. 24).

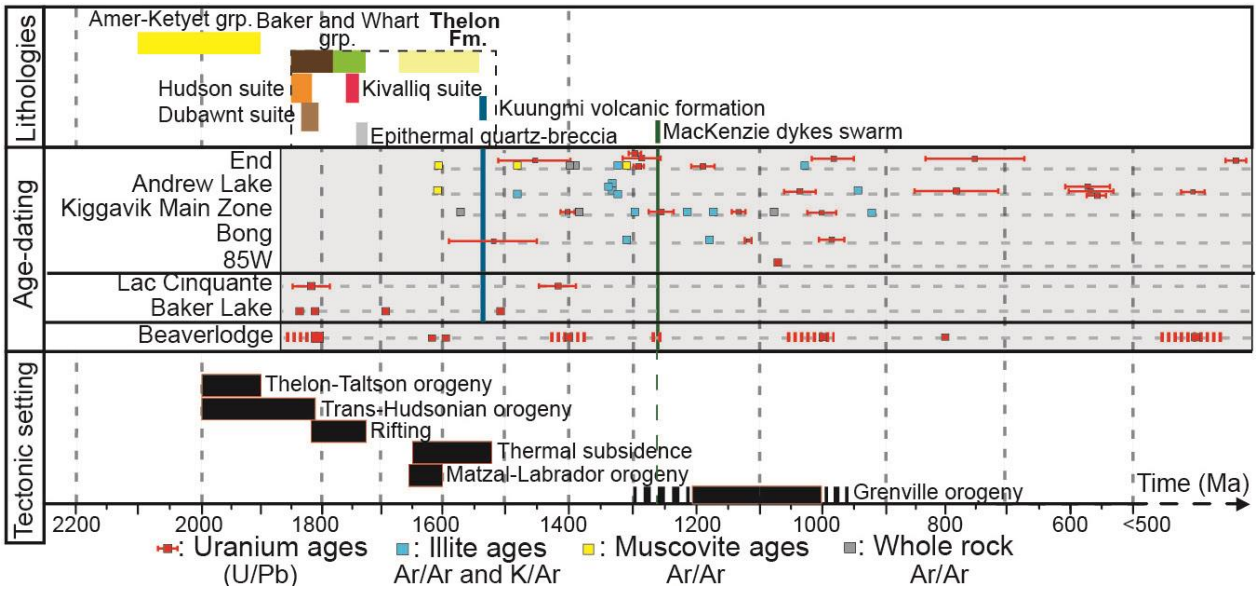

Figure 24: Synthetic scheme summarizing ages obtain within the Thelon-Baker Lake area, through U-Pb isotopes on uranium oxides (Farkas, 1984; Miller, 1986; Bridge et al., 2013; Lach et al., 2013; Sharpe et al., 2015; Chi et al., 2017; Shabaga et al., 2016, 2017; This study), Ar-Ar ages on illite (Weyer, 1992; Riegler, 2013; Ashcroft et al., 2017; Shabaga et al., 2017), Ar-Ar on muscovite (Shabaga et al., 2017; Ashcroft et al., 2017), K-Ar on illite (Weyer, 1992) and whole rock analysis (Hunt and Roddic, 1988, 1991, 1992).

Fluid inclusions

Finally, temperatures obtained with microthermometry on secondary aqueous FIPs (Syn-/post-Thelon event) observed in magmatic quartz (granites and orthogneiss) range from 81°C to 240°C, with an average of 140°C. These temperatures are comparable to those obtained in the Athabasca Basin for diagenetic-hydrothermal fluids (Richard et al., 2012), and at End (100-

200°C, Chi et al., 2017) for fluid inclusions in quartz associated (probably not genetically but at least spatially) with post-Thelon formation uraninite.

The shift of ~100°C between temperatures given by fluid inclusions and those given by illite geothermometry has already been reported in the Athabasca Basin by Chu and Chi. (2016) and could support a need for pressure correction of the fluid inclusion data. Such a difference is also related to the fact that the T^h measured for the fluid inclusions represents the minimum temperature at the time of entrapment (i.e., at the time of fluids circulation).

5.3 Types of Uranium mineralization in the Kiggavik area

REE signature

The REE patterns of uranium oxides are considered as specific to each uranium deposit type (Mercadier et al., 2011a; Frimmel et al., 2014) and these patterns directly reflect their conditions of formation (temperature, redox conditions, fluid composition, REE source(s)). REE patterns were not obtained for U0, but the high Th content of U0 and its relationship with brannerite indicate rather high T conditions in potential metamorphic/magmatic conditions, i.e. before Thelon Basin deposition. Several uranium oxides from End (U1) and Andrew Lake (U2) display a bell-shape pattern centered on Tb which has been described to be typical of uranium mineralization which precipitated in conditions of URU systems (Bonhoure, 2007; Mercadier et al., 2011a; Eglinger et al., 2013; Martz et al., 2017), i.e., from basinal brines in at the vicinity of the unconformity between a sedimentary basin and a basement. Such a pattern was also obtained by Fayek et al. (2017) at Kiggavik Main Zone. Post-crystallization Interaction of uranium oxides with a fluid of different origin and composition than a basinal brine (considering the case of unconformity-related systems) is reflected in REE patterns modified from their initial bell shape, with enrichment in LREE, while concentrations of other rare earth elements (HREE) remain the same. This modified bell-shape REE pattern is clearly observed for uranium oxides located in a remobilization front in a sample from Andrew Lake (U3, sample And-15-01-04, fig. 16A) and was also described by Mercadier et al., (2011b) for uranium oxides in a remobilization front at Eagle Point in the Athabasca Basin. This remobilization would have occurred through interaction with low-T (<50°C) and meteoric fluids. Samples from End return a slight enrichment in LREE, possibly indicating such a weak alteration of uranium oxides through interaction with meteoric fluids.

The shape of the REE patterns for the sample from 85W is quite different compared to the traditional bell-shaped pattern: The pattern displays comparable positive slope for LREE and negative slope for HREE, but is centered on SM and the REE concentrations are increased by a

factor of 10. A similar shape was described in one case for altered URU in Zambia (Eglinger et al., 2013). Such a pattern is not characteristic of URU oxides, as observed for nearly all deposits in the Athabasca and McArthur basins. This shape and the age (post-Mackenzie dyke) could indicate that the conditions for the crystallization of this mineralization were possibly different than U1.

To summarize, U1 and U2 display REE patterns comparable to those found in the Athabasca Basin. The other REE patterns indicate possible post-crystallization interactions with fluids of different origins, likely meteoric (U3), or new precipitation of uranium oxides by meteoric fluids, following dissolution of the uranium oxides crystallized in unconformity-related conditions (U1 and U2). Such phenomenon is possibly marked by the MREE and HREE concentrations of U3 that could be inherited from initial URU oxides (Mercadier et al., 2011). The compilation of the isotopic U-Pb ages and trace element concentrations for the different mineralization observed in the Kiggavil area indicate that the U system was polyphaze and that U was potentially mobilized at ~1000 Ma. Such observations and interpretations were already proposed for the Athabasca Basin. Additionally, these similarities between the Athabasca and Thelon Basins demonstrate that the two basins had rather close evolution through time, in terms of their U systems.

Fluid inclusion compositions

In monophase and aqueous fluid inclusions characterized in this study, no gases were observed except H_2O vapour, and H^2 and O^2 in some fluid inclusions of quartz cementing veins (indicating radiolysis of H_2O, thus presence of U). Optical characteristics of monophase fluid inclusions (dense arrays of small, dark monophase FIs) are very similar to retro-metamorphic (CO_2 bearing mainly, with some other gases) fluid inclusions observed in the Athabasca Basin (Mercadier et al., 2010). The absence of CO_2 and CH_4 in our monophase fluid inclusion could be explained by:

- the fact that graphite-rich lithologies and fault zones would be the source of CO_2 and CH_4 observed in monophase FIs and for the minor amount observed in aqueous FIs (Martz et al., 2017) in Athabasca. Such lithologies and fault zones are absent in the Kiggavik area.
- An epithermal event, which has been characterized in the Kiggavik area (this study, Grare et al., 2017) and close to the Kiggavik area (Turner et al., 2001): a demixion at great depth would induce trapping of CO_2-rich liquid phase. Such event, considered to be linked to the QB has not been described in the vicinity of the Athabasca Basin.

Aqueous biphase and triphase fluid inclusions observed at 85W and Contact display salinity between 24 to 29wt% NaCl, and homogeneization temperatures between 81 and 240°C. Temperatures and salinity obtained for aqueous fluid inclusions are similar to those obtained by Chi et al. (2017) at End. They also made similar observations (absence of gases) for monophase fluid inclusions. These observations, along with melting temperature of NaCl higher than homogeneization temperatures and the fact that most of FIs do not freeze, indicate that aqueous biphase and triphase fluid inclusions are representative of a high salinity calcic brine (Bodnar et al., 2003; Derome et al., 2005). Such brines have been hypothesized throughout the Athabasca Basin for all the studied U deposits, mixed with primary diagenetic sodic brines, and are thought to derive from interaction with the basement (Derome et al., 2005; Richard et al., 2010; Richard et al., 2016).

Because a sodic brine evolves into calcic brine through interactions with basement rocks, the sole occurrence of calcic brine in the Kiggavik area would reflect a sufficiently long interaction of the brine with basement rocks, hence a downward circulation deeper into the basement, as proposed for the Athabasca Basin. The probable higher temperatures measured for the calcic brines in the Thelon Basin compared to the Athabasca Basin could indicate a higher thermal gradient or a deeper percolation of brines within the basement. This could have well be the case in the Kiggavik area where the studied mineralized samples were located at a still unconstrained depth in the basement rocks, at the time of brine circulations (1500-1267 Ma), below a formerly overlying and now eroded cover of unknown thickness.

5.4 Timing of mineralizing events

As presented above, U0 is a pre-Thelon mineralizing event, likely associated with peralkaline magmatism of the Dubawnt minette suite; An age of ~1830 Ma for the emplacement of this mineralizing stage is therefore plausible. Absolute age-dating wasn't possible on our samples due to the small size of U-oxides, but ages of ca. 1830 Ma were obtained on pitchblende within the Baker Lake Basin by Miller et al. (1986) and Bridge et al. (2013) (Fig. 24).

Observations on U1 show that fractures associated with this mineralizing event (f5) crosscut dolomites veins which precipitated from a basinal brine (Riegler et al., 2013) inferred to be derived from the Thelon Basin. U2 oxidized faults (f6) crosscut sandstones of the Thelon Formation (Grare et al., 2017).

In the present study, absolute ages obtained for U1 are 1239±75 Ma for sample 9568-39 from End. U2 display ages much younger, at 565±38 Ma and 345±19 Ma, for samples coming from Andrew Lake. However, the fracturing events that triggered circulation of mineralizing fluids

through the basement rocks for these two stages occurred prior to the emplacement of the Mackenzie diabase dikes at 1267±2 Ma (Lecheminant and Heaman, 1989; Heaman and Lecheminant, 1993). However, these younger ages obtained at Andrew Lake (ca. 550 and 350 Ma) and 85W (1073±5 Ma) do not reflect a reset of the U/Pb system, since for instance the 85W uranium oxides return a very precise age with very low common-Pb. Instead, this would indicate resetting U-Pb system of uranium oxides at these periods of time, after the emplacement of Mackenzie dikes.

To conclude on the timing of uranium mineralizing event on the basis of the results obtained in this study, U0 occurred prior to the deposition of the Thelon formation, likely at ca. 1830 Ma. U1 and U2 postdate deposition of the Thelon formation and predate emplacement of the Mackenzie dikes. They probably happened between 1500 and 1267 Ma. The younger radiometric ages likely reflect recrystallization of uranium oxide through renewed circulation of oxidizing fluids during three distinct events precisely dated at 1073±5 Ma, 550 Ma and 300 Ma. Dissolution of U0/U1/U2 and remobilization by meteoric fluids led to reconcentration of uranium oxides (U3) along redox fronts.

5.5 Tectonic stresses driving fracturing events in the Kiggavik area

Fig. 25 displays a synthesis of all oriented data that exhibit kinematic indicators. Data are separated by macro/meso-scale observations (field, drill core) and micro-scale observations (FIPs and micro-“stylolites”, both observed under optical microscope). This allowed to tentatively derive the tectonic stresses prevailing during fracturing/faulting events and the related fluid circulations.

Macro scale

Stepped quartz veins (f2) and Mode-I quartz veins (f2), along with organisation of relay zones in outcrops of the QB, indicate a WNW-ESE trending σ1. This direction remains the same whether we try to differentiate quartz vein of the QB event (observed throughout the Kiggavik area) that occurred prior to deposition of the Thelon formation, and quartz veins that precipitated from Thelon-derived basinal brines (described by Chi et al. 2017), therefore at a post-Thelon stage. This observation would mean that a WNW-ESE trending σ1 prevailed from a pre-Thelon stage (i.e., when main Thelon fault developed) to a post-Thelon stage, ultimately until precipitation of the second stage of uranium mineralization (U1), as stepped calcite veins displaying E-W to NW-SE directions would have developed under a similar tectonic stress. Linked to the Thelon-Taltson (2100-1930 Ma) and Trans-Hudsonian orogeny (1900-1800 Ma), the whole Churchill craton was under compression from both “sides”; the roughly E-W

shortening associated with these two orogenies could be a good candidate for driving such tectonic stress during a long period of time. It is also not incompatible with observations made by Anand and Jefferson (2017) who concluded that re-activation of ENE-WSW, N-dipping extensional faults (such as the TF or the JSF), formed initially during the deposition of the Baker Lake and Wharton Groups, occurred under a ~N110-140° trending maximum horizontal stress. They proposed the younger Racklan orogeny (to the west of the Kiggavik area) to be at the origin of the WNW-ESE trending shortening. The first shortening episode associated with the Racklan orogeny is bracketed at 1663-1267 Ma (Cook, 1992).

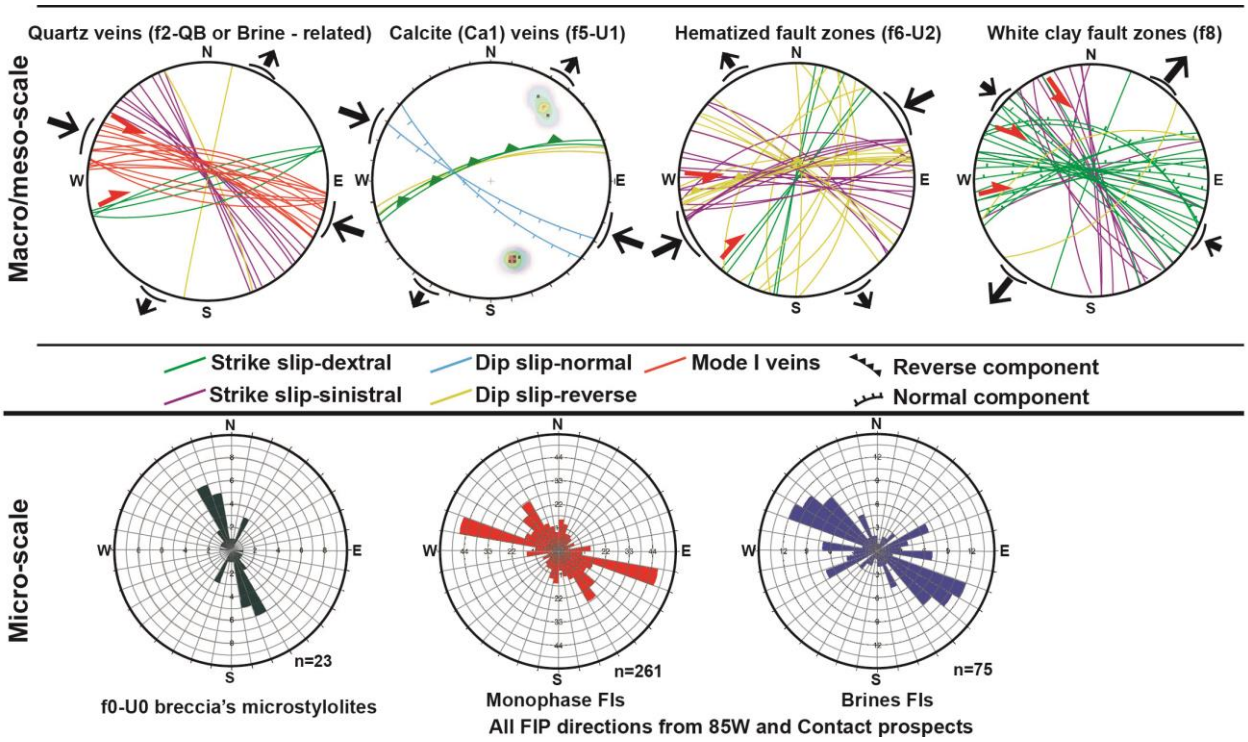

Figure 25: Synthesis of oriented data displaying kinematic indicators and derived paleostress orientations (black arrows).

The neoformed and reactivated hematized fault zones (f6) underwent either strike-slip sinistral and/or reverse movements) (Fig. 25). A sinistral motion was for example observed on the ENE-WSW JSF, as a later event compared to the main dextral motion on this fault that offset the Schultz Lake Intrusive Complex (observed at the map scale, Fig. 2). These orientations combined with ~N30° dextral and reverse fault zones (f6), and NE-SW crack-seal calcite (Ca2) veins (f6) coated with U2 spherulitic pitchblende support a NE-SW to ENE-WSW trending σ1 for this tectonic event associated with the second stage of uranium mineralization. The significance of this NE-SW compression/shortening direction is still unconstrained.

The late- to post-U1 and U2 faulting (f8) faults which drove hot, likely acidic fluids that strongly clay altered and bleached host rocks and uranium mineralisation trend WNW-ESE with dextral to dextral-normal kinematics and NNW-SSE with sinistral kinematics. Combined with the dominant dip-slip component observed on some WNW-ESE faults observed at Bong, we infer a transtensional stress regime with σ1 trending NW-SE and σ3 trending NE-SW. This faulting event would be responsible for "compartmentation" of the uranium orebody at Bong, End and Kiggavik Main Zones: this down-drop offset of orebodies was observed clearly in 3D modelling of the mineralized envelopes (ARC unpublished data); an example is shown in the simplified cross-section of Fig. 13D. The NW-SE trending σ1 would also explain the latest sinistral offset of the Judge Sisson fault and Thelon fault by NNW-SSE faults, observed in the field and on aeromagnetic maps (Tschirhart et al., 2017).

Such NNW-SSE faults were likely reopened and used as a pathway during the emplacement of the Mackenzie dikes. The inferred NW-SE trending σ1 and main NE-SW trending σ3 is consistent with a regional-scale compressive stress active on the southeast margin of the Canadian Shield (Hou et al., 2010).

Micro scale

Kinematic indicators associated with f0/U0 can be represented by the microstylolites oriented NNW-SSE (fig. 25, bottom). This likely indicates an ENE-WSW trending main tectonic stress (□1); such direction was already noted by Hadlari and Rainbird (2011) in their study of the formation of the Baker Lake Basin, at a timing consistent with the one proposed in this study (ca. 1830 Ma). However we have to keep in mind that the number of oriented data is very low and come from few samples, from a single deposit (End), which makes it hard to conclude on the tectonic stress even if the result obtained makes sense.

Monophase FIPs show a WNW-ESE major direction indicating a NNE-SSW to NE-SW trending σ3 for the emplacement of the QB. These oriented data in addition to E-W to ENE-WSW relay zone in the QB observed in the field and indicating a dextral strike-slip kinematics, would indicate a WNW-ESE trending σ1. Secondary directions of monophase FIP (NW-SE, N-S and WSW-ENE) can either reflect an influence of the ~NW-SE trending shortening related to the Trans-Hudsonian (for NW-SE, N-S directions) and Thelon (for WSW-ENE direction) orogeny, or characterize a vertical σ1 as a response to an uplifting prior to the deposition of the Thelon formation, as proposed by Hadlari and Rainbird (2011).

Aqueous FIPs also return a dominant WNW-ESE trend (Fig. 25, bottom) at Contact and 85W, therefore indicating NNE-SSW trending σ3 for an episode of basinal brine circulation consistent with stepped calcite veins associated with U1 (Fig. 25) indicating a WNW-ESE

trending σ1. NE-SW to ENE-WSW directions are observed for aqueous FIPs within magmatic quartz of 85W; they appear to reflect a statistically minor direction compared to WNW-ESE aqueous FIPs, but nevertheless imply a NW-SE to NNW-SSE trending σ3 indicating a second episode of circulation of basinal brines coherent with σ1 deduced from macro/meso-scale kinematic indicators measured for fractures associated with U2.

Differences of 10-20° observed on FIPs could result from a poor orientation of the drill core or from sampling close to a fault zone, resulting in a local stress reorientation and therefore scattered FIPs directions (Rispoli, 1981). The few directions of FIPs with no obvious link with regional events could be explained by a vertical σ1 as a response to exhumation (Benk et al., 2014) in a post-Thelon deposition stage, or by uncharacterized minor tectonic events.

6. Discussion and metallogenic model of the Kiggavik area

Fracturing events in the Kiggavik area

The combination of all structural and geochemical characteristics of uranium deposits and prospects in the Kiggavik area allow proposing a structural related metallogenic model of uranium mineralization in the Kiggavik area. The main fracturing events, their associated tectonic stress and fracture network evolution are presented in block diagrams for Bong, Kiggavik Main Zone (both located on ~ENE-WSW faults), Andrew Lake deposits and Contact prospect (both located on ~NE-SW faults). These block diagrams were built after drill core observations, oriented data and serial cross-sections in order to support discussion and synthesis of the data.

Pre-Thelon Basin fracturing events and the first stage of uranium mineralization

(f0, U0): the first uranium mineralizing event, characterized for the first time in this study, was observed in all major deposits in the Kiggavik area (hydrothermal rutiles cementing microfractures and coated with pitchblende at the Contact prospect (Grare et al., 2017) could represent relict of this first mineralizing stage). It is crosscut by quartz veins of the QB and is usually better preserved in deep-seated, least altered parts of the deposits (like in the End deposit, below the QB). Structural discontinuities (ALF, JSF, MZF, probably TF) were at that time active, basement host-rocks were fractured along these discontinuities by a uranium-mineralized microbreccia (Fig. 26).

Analyzed U-bearing minerals for this stage under EMPA come from the End deposit; nevertheless, the same chemistry (several percent of thorium) was also described by Weyer (1992) at the Kiggavik Main Zone deposit. Thorium content in pitchblende and brannerite

characterize a high temperature fluid, alongside with hydrothermal rutile and temperatures data returned by chlorite geothermometer. Mineralized microfractures and the characteristic micro-stylolites were also described by Miller, (1980) and Lecheminant et al. (1979) in study of the Kazan Fall uranium mineralization, and like unaltered chlorite observed within the cement of the mineralized microbreccia in the Kiggavik area, the chlorite in the Kazan Fall microbreccia returned temperatures around 300-350 °C.

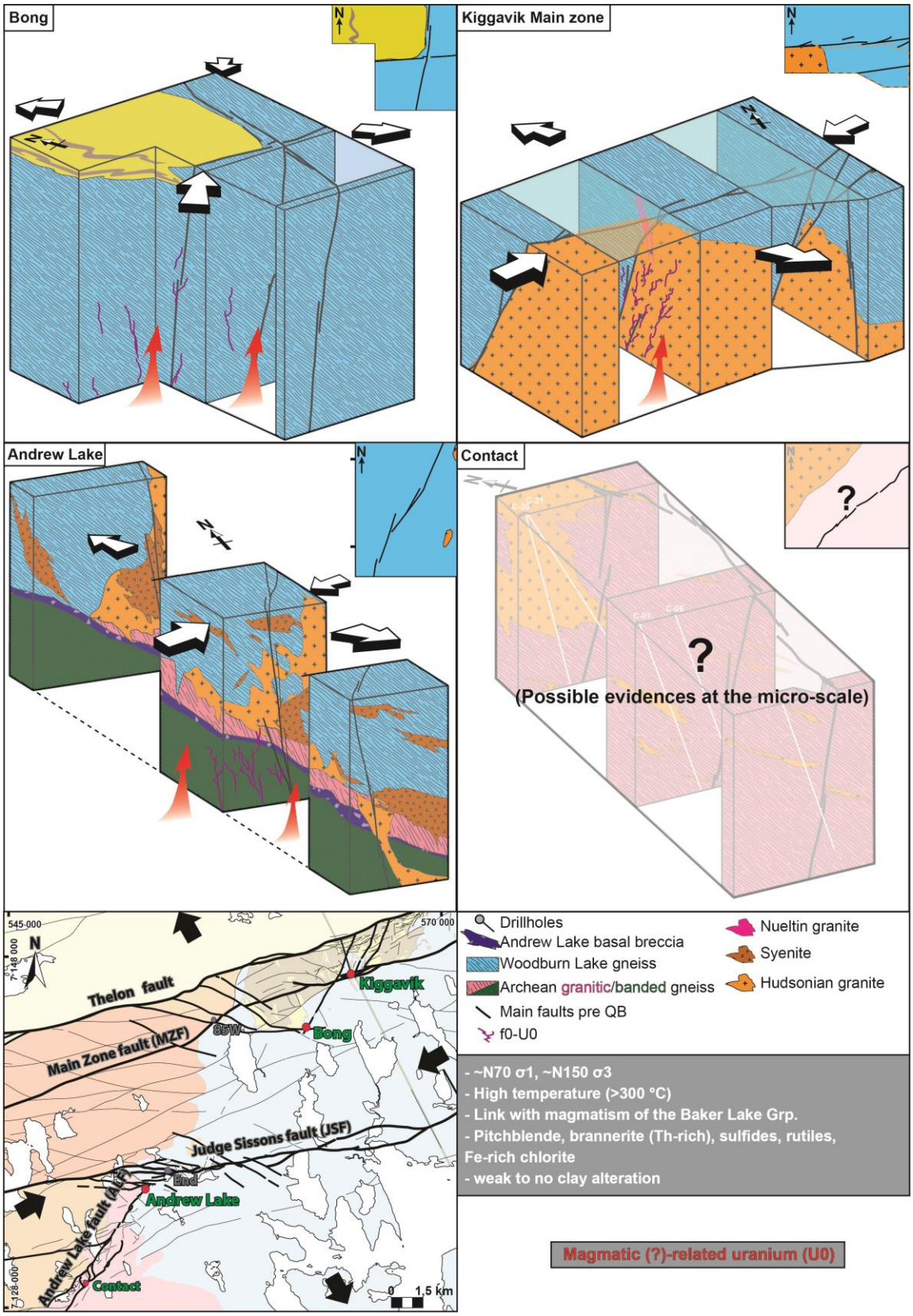

Figure 26: First stage of uranium mineralization U0 in the Kiggavik area.

These observations characterize a global uranium mineralizing event that likely happened in the Thelon-Baker Lake area at the end of the Trans-Hudsonian orogeny (ca. 1830 Ma), with formation of a half-graben as a response to retro-arc extension, deposition of the Baker Lake formations and peralkaline magmas of the Dubawnt igneous suite, such magmas being enriched in U (Cuney et al., 2014 ; Cuney and Kyser, 2015). Such mineralizing event is plausible in the Kiggavik area even if it is located far from the formations of the Baker Lake Basin, as a breccia pipe of the Christopher Island formation (ca. 1827 Ma) was observed in the eastern part of the Kiggavik area, alongside with ultrapotassic minette and bostonite dikes (Anand and Jefferson, 2017) of the Dubawnt igneous suite (ca. 1830 Ma). These rocks are enriched in U (Lecheminant et al., 1987; Miller and Blackwell, 1992; Peterson et al., 2011) and could also represent a good source of U.

This mineralizing event predates deposition of the Thelon formation, is the first mineralizing event in the Kiggavik area and, considering the observations is likely of magmatic-origin type, even if this denomination actually lacks a finer characterization of the fluids or uranium oxides, like what was done for other mineralizing stages in this study. Mineralisation occurred within major fault zones forming a first significant “stock” of uranium oxides associated to a fracturing event that increased porosity and permeability of the basement rocks, facilitating later fluid circulation.

(QB, f2): Intense quartz brecciation and pervasive hematization of the fault rock is recognized at all deposits and prospects of the Kiggavik area, on major fault zones, and South of the Kiggavik area (Baudemont and Reilly, 1997; Turner et al., 2001). FIs in quartz of the QB were characterized by several authors (Pagel et al., 1995; Turner et al., 2001; Riegler, 2013; Chi et al., 2017; this study). Most of the quartz belongs to the QB event, as characterized by cathodoluminescence and textural observations on quartz by Grare et al. (2017) they are characterized by monophase, high temperature/low salinity fluids. One generation of quartz could be link with the circulation of basinal brines (low temperature/high salinity), but such drusy quartz veins display similar orientations to other quartz veins of the QB, and both are crosscut by U1 and U2 fractures, thus not changing the chronology of fracturing events. QB emplacement postdates emplacement of ca. 1750 Ma Nueltin granite’s Kivalliq igneous suite and predates deposition of the Thelon formation. This observation coupled with textural characteristics and fluid inclusion data from different locations in the Kiggavik area attest to a regional magmatic

event associated with massive and likely repeated influx of silica rich fluids, occurring between 1750 and 1667 Ma.

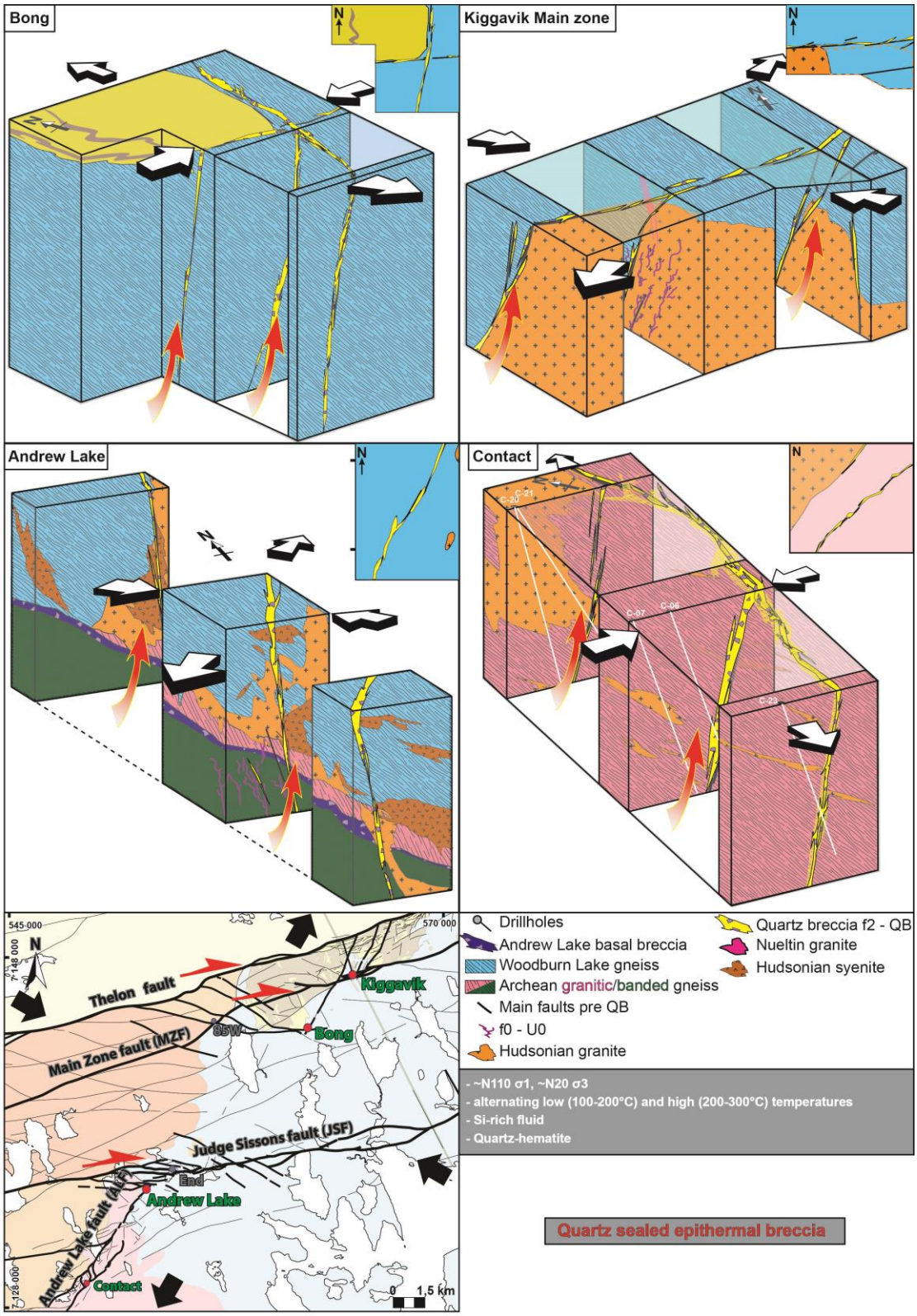

Figure 27: Quartz sealed brecciation. Pre-Thelon epithermal breccia linked to magmatism of the Kivalliq igneous suite (ca. 1750 Ma). ESE-WNW oriented compression.

This event is likely linked to magmatism of the Kivalliq igneous suite dated at ca. 1750 Ma. QB was formed under a WNW-ESE oriented main stress, well constrained by macro- to micro-scale oriented data. Fluid circulation was focused along major faults and relay zones (Fig. 27), silicifying/overprinting previously formed fault rocks. This event likely constrained, at least partly, later fracturing and fluid circulation, depending on the intensity of the quartz brecciation: Uranium mineralization is usually stronger in the hanging wall of the structure (for example at End and Contact).

(Syn?) Post-Thelon Basin fracturing events: second and third stages of uranium mineralization

(f5, U1): U1, observed in all deposits and prospects of the Kiggavik area, is characterized by monometallic to polymetallic mineralized, reduced narrow fault (core and damage) zones (Fig. 28). Illite is the main alteration product compared to sudoite. However, sudoite was observed in altered mineralized fault rocks at Jane (Miller, 1997), End (Iida, 1997), Bong, (Riegler et al., 2014; Sharpe et al., 2015) and Kiggavik Main Zone (Pacquet, 1994). Aluminum Phosphate Sulfate (aps) synchronous with uranium mineralization, were observed once at the 85W prospect, and by Riegler et al. (2014) at the Bong deposit.

U1 postdates quartz veins and dolomite veins precipitated from typical basin-derived high salinity brines (Chi et al., 2017; and Riegler et al., 2013; respectively), and is synchronous with the first generation of calcite veins. Fluid inclusions in calcite of the Kiggavik area were studied by Chi et al., (2017). Calcite generation at the End deposit were not characterized under cathodoluminescence, but it is probable that Chi et al. (2017) studied fluid inclusions of the first generation of calcite as veins of the second generation are usually too thin to allow fluid inclusions study. As this first generation of calcite precipitated from Thelon-derived basinal brines, therefore U1 synchronous with it is inferred to have precipitated from basinal brines too. This synchronicity also allows deducing that fracturing stage f5 associated with U1 formed in response to a WNW-ESE trending σ1 and NNE-SSW trending σ3 (Fig. 28). Micro-scale data on aqueous FIP also indicate that the main direction of the tectonic stress associated with brine circulation is trending WNW-ESE. Successive small tectonic events lead to the formation of quartz (rare generation of drusy quartz derived from basinal brines, not observed in this study),

dolomite and calcite veins, culminating ultimately with the precipitation of the second stage of uranium mineralization.

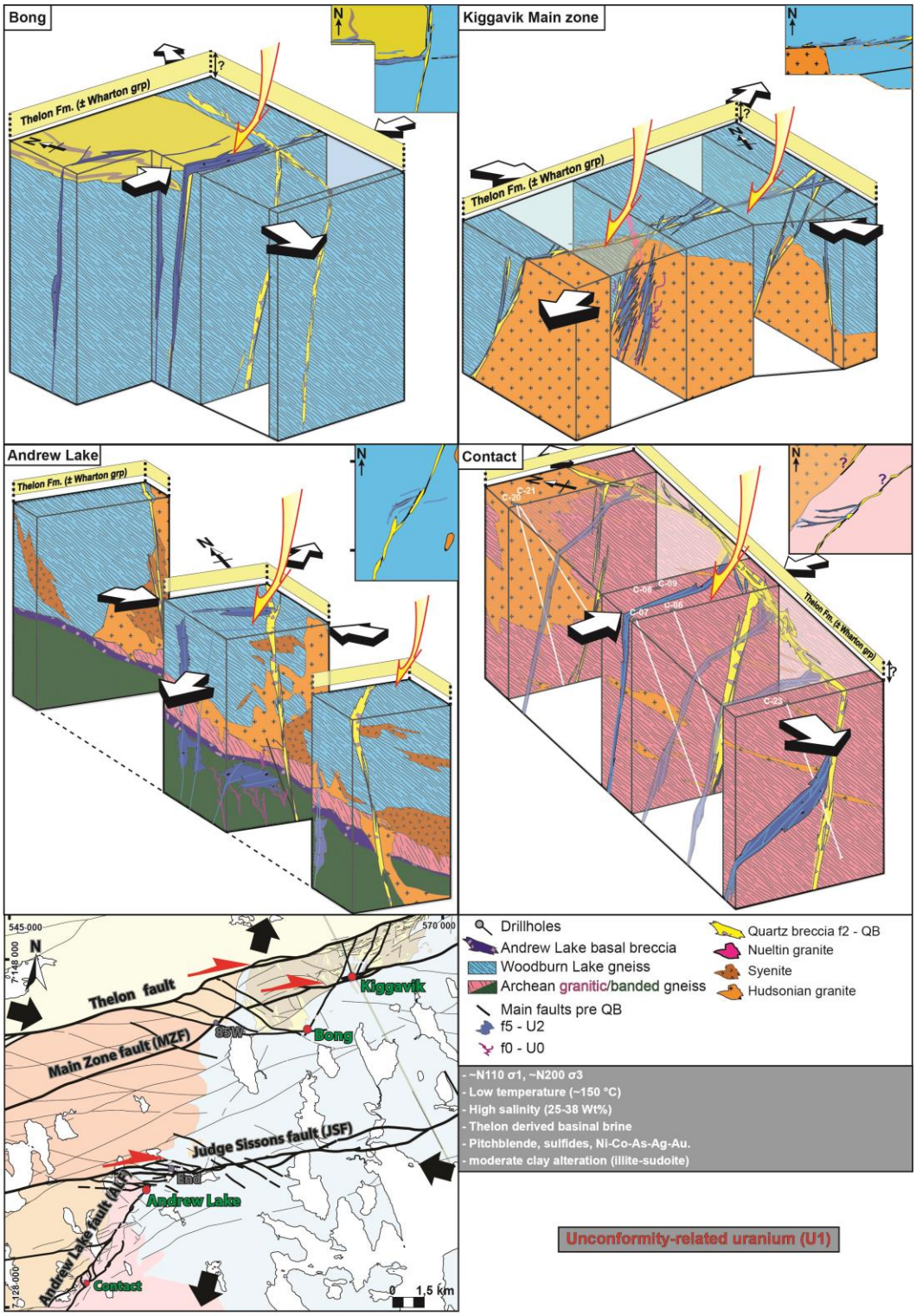

Figure 28: Second stage of uranium mineralization. Syn-Post Thelon circulation of basinal brines. "Low" temperature fluids (150-200°C). ESE-WNW oriented compression.

The E-W trending Thelon-Taltson orogeny (2100-1930 Ma) could have driven such tectonic stress during a long period of time. Reactivation of the ENE-WSW, N-dipping extensive fault system formed initially during the deposition of the Baker Lake and Wharton Groups, in dextral-normal kinematics until circulation of uranium-bearing basinal brines (U1). However Anand and Jefferson (2017) rather proposed the process associated with the younger Racklan orogeny (to the west of the Kiggavik area) to be at the origin of the WNW-ESE trending shortening. The oldest ages were obtained by Farkas et al., (1984) and Sharpe et al., (2015) at 1403±10 Ma and 1520±79 Ma respectively. Local heating and hydrothermal fluid circulation associated with emplacement of the Kuungmi lavas at ca. 1540±30 Ma (Chamberlain et al., 2010), is described as one possible resetting event of the U/Pb system in the Kiggavik area. This age was observed throughout the Thelon-Baker Lake area (Turner et al., 2003; Bridge et al., 2013). Ages at 1500-1400 Ma are comparable to ages obtained on oldest URU mineralization in Athabasca (1514±18 Ma, Cumming and Krstic, 1992; 1519±22 Ma, Fayek et al., 2002; 1540±19 Ma, Alexandre et al., 2009).

These observations on minerals that fingerprint the circulation of high salinity basinal brines (sudoite, aps), fluid inclusions characteristics (high salinity, low temperature, calcic brine), and the REE bell shape pattern of uranium oxides, along with the timing of the mineralizing event (post-Thelon formation), allow concluding on the nature of uranium mineralizing stage U1, precipitated from a Thelon-derived basinal brine, and being of the unconformity-related type.

(f6, U2): U2, observed in all deposits and prospects of the Kiggavik area, is characterized by monometallic mineralized, oxidized wide fault (mainly damage) zones (Fig. 29), formed under a ~NE-SW trending main stress that neoformed fractures and likely reactivated the previously formed and already complex fracture network of the Kiggavik area. Response of the fracture network to the tectonic stress is obviously different depending on its orientation: at Andrew Lake and Contact, hematized and mineralized damage zones of faults trending NE-SW are well developed in contrary to those associated within ENE-WSW fault zones of the Kiggavik Main Zone deposit (Fig. 29).

Aluminum phosphate-sulfate (aps) were observed in oxidized fault zones at the Contact prospect (Grare et al., 2017), and sudoite was observed more often, associated with illite, compared to U1, at Contact (Grare et al., 2017), Jane (Miller, 1997), Kiggavik Main Zone (Hasegawa, 1990), End (Iida, 1997) and Andrew Lake (Hasegawa et al., 1990; Pacquet, 1994). This monometallic mineralizing stage was also described at Andrew Lake (Shabaga et al., 2017).

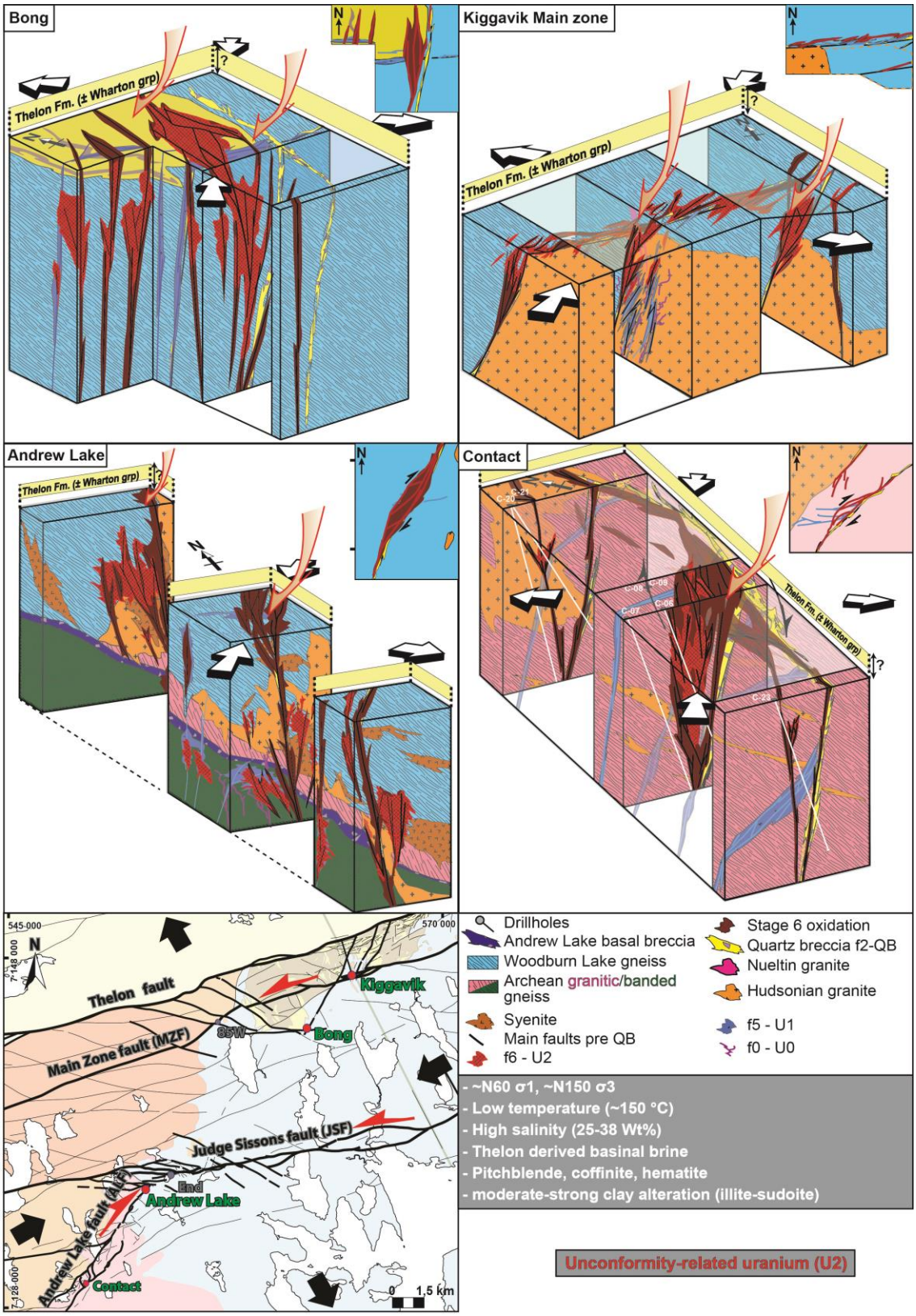

Figure 29: Third stage of uranium mineralization. Post-Thelon renewed circulation of basinal brines. "Low" temperature fluids (150-200°C). NE-SW oriented compression.

Relative chronology places the formation of U2 after the deposition of the Thelon formation but before emplacement of the Mackenzie dikes nevertheless unsupported by absolute age dating (ca. 1000 Ma, Shabaga et al., 2017; 550-300 Ma, Shabaga et al., 2017; this study). This could be due to alteration of pitchblende by a fluid of unconstrained chemistry, explaining the more or less modified REE bell-shape pattern for U2 uranium oxides. Reconstruction of the tectonic stress under which occurred U2 (NE-SW to ENE-WSW) at macro-scale allows to link it at the micro-scale to aqueous FIP and therefore to calcic brine circulation, consistent with the mineralogy and other chacracteristics described above. Changes in the mineralogy between U1 and U2 could be explained by the different tectonic stress and associated fracturation, implying a different fluid circulation and therefore fluid-rock interaction. The initial stock (in uranium and other metals) would also have been depleted by U1 formation.
Like for U1, these observations fingerprint the circulation of basinal brines: minerals (sudoite, aps), fluid inclusions characteristics (high salinity, low temperature, calcic brine), and the REE bell shape pattern (although slightly modified) of U2 uranium oxides. This, along with the timing of the mineralizing event (post-Thelon formation), allow concluding on the nature of uranium mineralizing stage U2, precipitated from a Thelon-derived basinal brine, and being of the unconformity-related type, but associated with a fracturing event occurring under a different tectonic than f5/U1. U1 and f6/U2 are bracketed between 1500 and 1300 Ma.
A main difference with the Athabasca Basin is the absence of magnesio-foitite (Mg-tourmaline also called dravite) and the sudoite being a Mg-rich sudoite rather than a Al-Mg sudoite as observed in Athabasca.

Sources of uranium for U1 and U2 are various and could be the metamorphosed epiclastic rocks of the Puqik Lake formation (Johnstone et al., 2017), rhyolitic flows of the Wharton group (Blake, 1980; Peterson, 2015), fluorapatite-cemented breccia at the base of the Thelon formation (Davis et al., 2011), ultrapotassic minette and bostonite dikes (Lecheminant et al., 1987; Miller and Blackwell, 1992; Peterson et al., 2011) of the Dubawnt igneous suite (ca. 1830 Ma), U-rich pegmatite of the Kivalliq igneous suite (Scott et al., 2012) but more specifically and as supported by the present work the previously formed uranium mineralizing stage (U0). U0 is observed in significantly mineralized brecciated rocks, and is characterized by easily leachable uranium minerals making it an efficient “provider” of U for basinal brines.

(f8): The last main fracturing event is characterized by strongly desilicified, illitized and bleached fault rocks, also reworking/offsetting previously formed ore bodies (along E-W and NW-SE faults, fig. 30). Emplacement of a mantle plume at the base of the earth crust, triggered

the emplacement of Mackenzie mafic dikes swarm at ca. 1267 ± 2 Ma. Such magmatism intruded the pre-existing extensional fractures which were active at ca. 1300 Ma, under a NW-SE compressive stress. This magmatism is likely at the origin of circulation of hot hydrothermal acidic fluids of f8 fracturing stage. This timing is supported by age dating on white micas (K-Ar and Ar-Ar) showing a altering event at ca. 1300 Ma (Fig. 24) at End, Andrew Lake, Bong and Kiggavik Main Zone. This tectonic/magmatic event was concluded by emplacement of the diabase dikes which crosscut orebodies and are almost unaltered and fractured. Along these dikes, thermal effect would have locally remobilized uranium oxides and reset the U/Pb isotopic system. Such strong clay alteration was described to be synchronous with uranium alteration in previous studies (Hasegawa et al., 1990; Riegler et al., 2014; Shabaga et al., 2017), if we don't deny that illitization is an alteration products of basinal brines circulation in the Kiggavik area (U1 and U2), white clay illitized fault zone post-date main uranium mineralizing events.

Post Mackenzie dikes fracturing events and uranium mineralization

Several ages were obtained on uranium oxides posterior to at ca. 1000 Ma and ca. 700 Ma (Fig. 24) and could correspond to far-field tectonic event such as the Grenville orogeny (Gordon and Hempton, 1986) and the initial rifting event of Rodinia (Badger et al., 2010; McClellan and Gazel, 2014) respectively. Younger ages were also obtained at ca. 500 Ma and ca. 300 Ma. Uranium precipitated at these ages (U3) display a modified bell shape pattern representing alteration of uranium oxides by meteoric-derived fluids, which is consistent with the observation of goethite in these mineralized samples, a low temperature iron oxide (in contrary to hematite observed for stage U2). This allow to conclude on the nature of uranium mineralization occurring at a post-Mackenzie stage, which are not of unconformity-related type, and likely happened when a significant thickness of Thelon, Wharton and/or basement rocks was eroded, letting supergene, low-temperature oxidizing fluids circulating in the fracture network.

Finally, we can say that the method applied in this study allowed deciphering the fracturing event in the Kiggavik area, thus proposing a structural evolution of the fracture network, which differs, thus being not incompatible from the Riedel shear system of Anand and Jefferson (2017), in which they proposed that the fracture network evolved mainly under a ~N110-N140 trending σ1 from ca. 1800 Ma to 1540 Ma. In their model, the different fault zones (ENE-WSW, NNW-SSE, NS, NE-SW, E-W) are part of the Riedel system (P, T, X, R', R). In overall the Riedel shear system could have been set up very early in the history of the area, and reactivated over time.

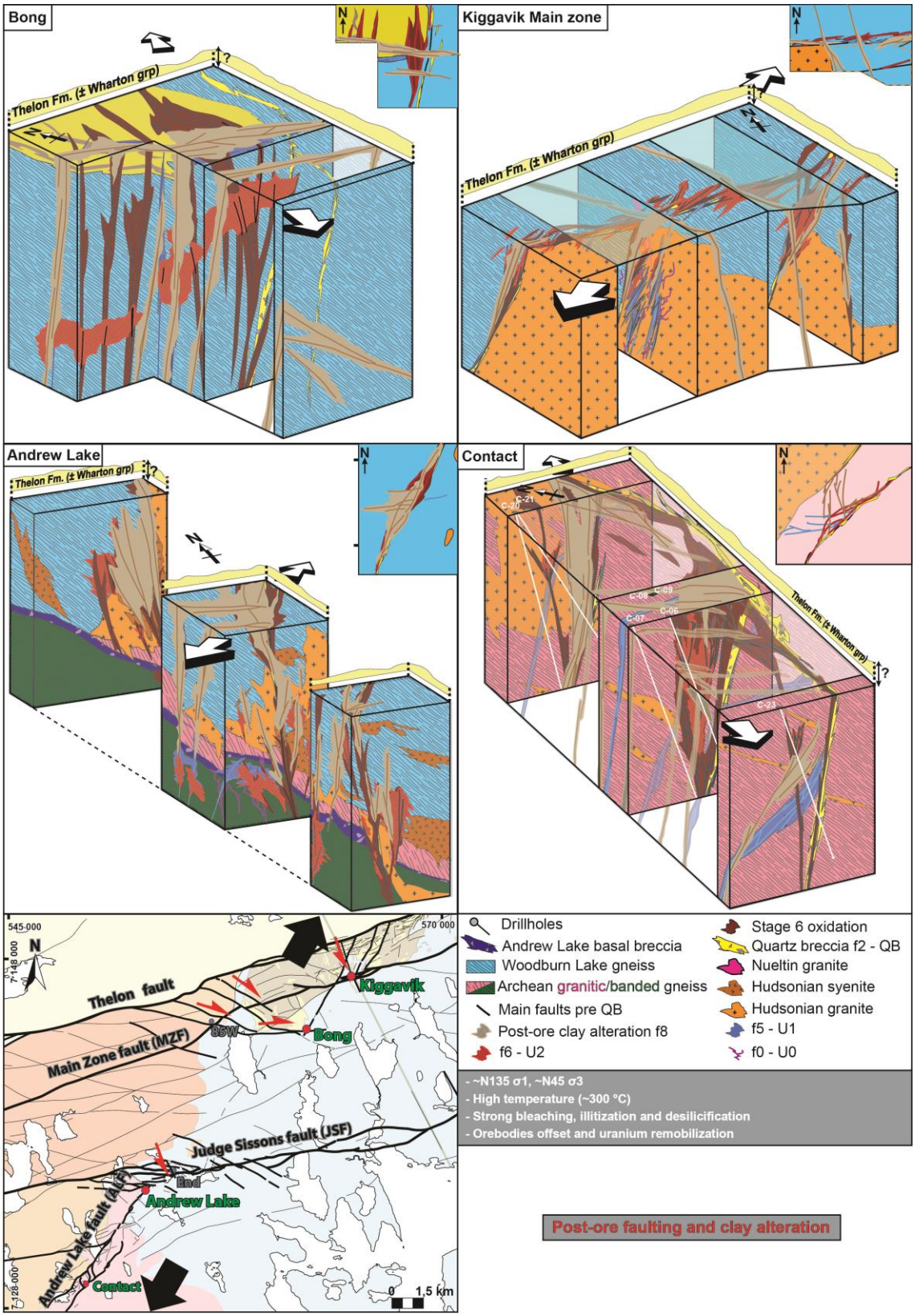

Figure 29: Post ore, Pre Mackenzie dikes (1267 Ma) illitization and desilicification, local remobilization and offsetting of orebodies. High temperature (~300 °C) fluid circulation.

Conclusions

The integrated structural and metallogenic model of the Kiggavik area gather several major conclusions.

(1) Tectono-metallogic evolution of the Kiggavik area

- The Kiggavik area is characterized by a polyphased fracture network that evolved in a brittle style from the end of the Trans-Hudsonian orogeny at ca. 1830 Ma until emplacement of the Mackenzie dikes at ca. 1270 Ma. A WNW-ESE compressive stress was active during deposition of the Thelon formation, until fracturing (f5) along E-W faults and precipitation of U1. NE-SW compressive stress of unconstrained origin was then active during the fracturing event (f6) linked with U2.

- A first stage of fracturation (f0) and uranium mineralization (U0) was observed at the deposits of the Kiggavik area and is linked with the peralkaline magmatism of the Dubawnt minette suite at ca. 1830 Ma. Such mineralized breccia constituted a first stock of uranium available for reconcentration through later circulation of oxidized basinal brines. This mineralization is magmatic-related type.

- the first stage of uranium mineralization and the QB event (f2) highlight the importance of magmatic-linked fracturing events, pre-Thelon formation, in constraining later fracturation and fluid circulation, therefore location of URU deposits.

- Posterior to deposition of the Thelon formation, controlled by ENE-WSW dextral-normal faults, after marine transgression and deposition of the Lookout Point formation, a first circulation of basinal brines occurred, likely triggered by magmatism of the kuungmi lavas, still under a WNW-ESE tectonic regime. This circulation of basinal brine precipitated U1, either in vertical or horizontal fault relay zones (End, Kiggavik Main Zone) or in zones where faults were structurally connected to the quartz breccia (Bong, Contact, Andrew Lake). Fracturation and renewed circulation of basinal brines occurred under a NE-SW compressive stress with transpressive reactivation of the previously formed fracture network. Uranium mineralization were preferentially developed in moderately altered damage zones of hematized fault zones. U1 and U2 are uranium mineralization of unconformity-related type, displaying characteristics similar to URU mineralization in Athabasca (Canada) and McArthur Basins (Australia).

- Late faulting and associated strong clay alteration and bleaching of the host rock occurred at ca. 1300 Ma as a response to locally NE-SW extension and regionally NW-SE compression linked to the push of the Grenville Ocean ridge. This fracturing event didn’t bring new influx of uranium in the system and only reworked, offset previously formed

orebodies. These fracturing events explain the formation in the Kiggavik area of strongly altered area disconnected of any uranium mineralization, which is something actually (?) un-observed in the Athabasca Basin.

- Post Mackenzie (1267±2Ma) weak reactivation of the fracture network induced mainly circulation of meteoric fluids and probably of fluids of unconstrained composition, remobilizing/reprecipitating (U3) uranium oxides and altering their geochemical signature at three different timing, at ca. 1000 Ma, ca. 550 and 350 Ma, likely linked to far-field stress associated with continent break-up and assembly.

- Uranium mineralization in the Kiggavik area are of mix types rather than being purely of unconformity-related type, in comparison to what is currently presented in actual models of uranium mineralization in the Athabasca Basin. A better comparison can be drawn with uranium mineralization in the Beaverlodge area (on the NW border of the Athabasca Basin), where magmatic-volcanic uranium mineralization are observed alongside with URU mineralization (Dieng et al., 2013, 2014).

(2) Other major conclusions

- Change in the tectonic regime can induce renewed circulation of basinal brines, through a different fracture network as the answer of pre-existing fault zone to the tectonic stress will differ compared to the previous one, also inducing a changed pathways for fluids, different fluid-rock interaction (changing characteristics of the fluid such as fO2 and pH) and therefore a different style in uranium mineralization (polymetallic reduced against monometallic oxidized in the present study).

- The most economic uranium mineralization occurred where U0, U1 and U2 crosscut each other's, making the deposits in the Kiggavik area a mixed type between magmatic related and unconformity related.

- Brines uranium concentrations are similar to those obtained for NaCl/CaCl2-rich brines in Athabasca (Richard et al., 2010), however the concentrations in other metals, especially in B and Mg, are much lower. This would explain why, in the Kiggavik area, although B-link alteration is observed (through whole rock geochemical analysis) there are no observed occurrences of Mg-foitite (dravite), typical in URU deposits. Kandasami et al. (2015) explained B is contained in micro-crystalline dravite (trigonal coordination), or contained in illite (tetrahedral coordination).

- Reconstructing the tectonic stress behind some fracturing events was done successfully through a macro- to micro-scale characterization, allowing to link precisely fracturing events and the fluid that circulated in their fracture network.

Acknowledgment

The authors thank AREVA and AREVA Resources Canada for the full financial support and access to the Kiggavik camp and exploration data. Special thanks to senior geoscientist D. Quirt, geologists R. Zerff, R. Hutchinson, K. Martin, and D. Hrabok for their help and enriching discussions during field work and data interpretation.

References

Alexandre, P., Kyser, T.K., 2005. EFFECTS OF CATIONIC SUBSTITUTIONS AND ALTERATION IN URANINITE, AND IMPLICATIONS FOR THE DATING OF URANIUM DEPOSITS. Can. Mineral. 43, 1005–1017. doi:10.2113/gscanmin.43.3.1005

Anand, A., and Jefferson, C.W., 2017. Reactivated fault systems and their effects on outcrop patterns of thin-skinned early thrust imbrications in the Kiggavik uranium camp, Nunavut, Geological Survey of Canada, Open File 7895, 2017, 9 pages (1 sheet), https://doi.org/10.4095/302776

Badger, R.L., Ashley, K.T., Cousens, B.L., 2010. Stratigraphy and geochemistry of the Catoctin volcanics: Implications for mantle evolution during the breakup of Rodinia, in: Tollo, R.P., Bartholomew, M.J., Hibbard, J.P., Karabinos, P.M. (Eds.), From Rodinia to Pangea: The Lithotectonic Record of the Appalachian Region. Geological Society of America.

Benedicto, A., Schultz, R.A., 2010. Stylolites in limestone: Magnitude of contractional strain accommodated and scaling relationships. J. Struct. Geol. 32, 1250–1256. doi:https://doi.org/10.1016/j.jsg.2009.04.020

Bloss, F.D., 1954. Microstylolites in a rhyolite porphyry. J. Sediment. Res. 24, 252–254. doi:10.1306/D42697BA-2B26-11D7-8648000102C1865D

Burma, B.H., Riley, C.M., 1955. Two unusual occurrences of microstylolite. J. Sediment. Res. 25, 38–40. doi:10.1306/D42697EC-2B26-11D7-8648000102C1865D

Bonhoure, J., Kister, P., Cuney, M., Deloule, E., 2007. Methodology for Rare Earth Element Determinations of Uranium Oxides by Ion Microprobe. Geostand. Geoanalytical Res. 31, 209–225. doi:10.1111/j.1751-908X.2007.00865.x

Cathelineau, M., Nieva, D., 1985. A chlorite solid solution geothermometer the Los Azufres (Mexico) geothermal system. Contrib. to Mineral. Petrol. 91, 235–244. doi:10.1007/BF00413350

Cathelineau, M., 1988. Cation Site Occupancy in Chlorites and Illites as a Function of Temperature. Clay Miner. - CLAY Min. 23, 471–485

Chamberlain, K.R., Schmitt, A.K., Swapp, S.M., Harrison, T.M., Swoboda-Colberg, N., Bleeker, W., Peterson, T.D., Jefferson, C.W., Khudoley, A.K., 2010. In situ U–Pb SIMS (IN-SIMS) micro-baddeleyite dating of mafic rocks: Method with examples. Precambrian Res. 183, 379–387. doi:10.1016/j.precamres.2010.05.004

Chester, F.M., Logan, J.M., 1986. Implications for mechanical properties of brittle faults from observations of the Punchbowl fault zone, California. pure Appl. Geophys. 124, 79–106. doi:10.1007/BF00875720

Chi, G., Haid, T., Quirt, D., Fayek, M., Blamey, N., Chu, H., 2017. Petrography, fluid inclusion analysis, and geochronology of the End uranium deposit, Kiggavik, Nunavut, Canada. Miner. Depos. 1–22. doi:10.1007/s00126-016-0657-9

Cook, F.A., 1992. Racklan Orogen. Can. J. Earth Sci. 29, 2490–2496. doi:10.1139/e92-195

Cuney, M., 1978. Geologic environment, mineralogy, and fluid inclusions of the Bois Noirs-Limouzat uranium vein, Forez, France. Econ. Geol. 73, 1567–1610. doi:10.2113/gsecongeo.73.8.1567

Curtis, L., and Miller, A.R., 1980. Uranium geology in the Amer-Dubawnt-Yathkyed-Baker Lake region, Keewatin district, N.W.T., Canada. In Uranium in the Pine Creek geosyncline, J. Ferguson, and A. B. Golebys (eds), 595-616. Vienna: International Atomic Energy Agency.

Davis, W.J., Gall, Q., Jefferson, C.W., Rainbird, R.H., 2011. Fluorapatite in the Paleoproterozoic Thelon Basin: Structural-stratigraphic context, in situ ion microprobe U-Pb ages, and fluid-flow history. GSA Bull. 123, 1056–1073. doi:10.1130/B30163.1

Depiné, M., Frimmel, H.E., Emsbo, P., Koenig, A.E., Kern, M., 2013. Trace element distribution in uraninite from Mesoarchaean Witwatersrand conglomerates (South Africa) supports placer model and magmatogenic source. Miner. Depos. 48, 423–435. doi:10.1007/s00126-013-0458-3

Derome, D., Cathelineau, M., Cuney, M., Fabre, C., Lhomme, T., Banks, D.A., 2005. Mixing of Sodic and Calcic Brines and Uranium Deposition at McArthur River, Saskatchewan, Canada: A Raman and Laser-Induced Breakdown Spectroscopic Study of Fluid Inclusions. Econ. Geol. 100, 1529–1545. doi:10.2113/gsecongeo.100.8.1529

Dudar, J.S., 1960. The geology and mineralogy of the Verna uranium deposit, Beaverlodge, Saskatchewan University of Michigan. Unpublished M.Sc. Thesis, 312 pp.

Eglinger, A., André-Mayer, A.-S., Vanderhaeghe, O., Mercadier, J., Cuney, M., Decrée, S., Feybesse, J.-L., Milesi, J.-P., 2013. Geochemical signatures of uranium oxides in the

Lufilian belt: From unconformity-related to syn-metamorphic uranium deposits during the Pan-African orogenic cycle. Ore Geol. Rev. 54, 197–213. doi:https://doi.org/10.1016/j.oregeorev.2013.04.003

Evoy, E.F., 1961. Geology of the Gunnar uranium deposit, Beaverlodge area, Saskatchewan. Unpublished Ph.D. Thesis, University of Wisconsin, Madison, 62pp.

Farkas, A., 1984. Mineralogy and host rock alteration of the Lone Gull deposit: Urangesellschaft internal report, 44 p.

Faulkner, D.R., Jackson, C.A.L., Lunn, R.J., Schlische, R.W., Shipton, Z.K., Wibberley, C.A.J., Withjack, M.O., 2010. A review of recent developments concerning the structure, mechanics and fluid flow properties of fault zones. J. Struct. Geol. 32, 1557–1575. doi:10.1016/j.jsg.2010.06.009

Fayek, M., Quirt, D., Jefferson, C., Camacho, A., Ashcroft, G., Shabaga, B., Sharpe, R. 2017. The Kiggavik-Andrew Lake structural trend uranium deposits: an overview. In SGA Extended Abstract proceedings. SGA 2017 Conference Quebec City, August 20-23. In press.

Fossen, H., Rotevatn, A., 2016. Fault linkage and relay structures in extensional settings-A review. Earth-Science Rev. 154, 14–28. doi:10.1016/j.earscirev.2015.11.014

Fraenkel, M.O.; Santos, R.C.; Loureiro, F.E.V.L. and Muniz, W.S. 1985. Jazida de Urânio do Planalto Poços de Caldas, Minas Gerais. In: SCHOBBENHAUS, C. and COELHO, C.E.S., coords. Principais depósitos minerais do Brasil. Brasília, DNPM/CVRD, v.1. p.89-103

Friedrich, G., Weyer, H.J., and Bechtel, A. 1989. The Lone Gull uranium deposit – New geochemical and petrological data as evidence for the nature of the ore-bearing solutions. In: Proceedings of an IAEA Technical Committee Meeting on Metallogenesis of Uranium Deposits, March 9-12 1987, IAEA TC-542/19, p. 293-306

Frimmel, H.E., Schedel, S., Brätz, H., 2014. Uraninite chemistry as forensic tool for provenance analysis. Appl. Geochemistry 48, 104–121. doi:https://doi.org/10.1016/j.apgeochem.2014.07.013

Fuchs, H., and Hilger, W., 1989. Kiggavik (Lone Gull): An unconformity related uranium deposit in the Thelon Basin, Northwest Territories, Canada: International Atomic Energy Agency Technical Committee Meeting, Saskatoon, 1–3 September 1987, IAEA TECDOC-500, p. 429–454

Fuchs, H.D., Hilger, W., and Prosser, E., 1986. Geology and exploration history of the Lone Gull property, in Evans, L., ed., Uranium Deposits of Canada: Canadian Institute of Mining and Metallurgy Special Volume 33, p. 286-292

Gall, Q., Peterson, T.D., Donaldson, J.A., 1992. A proposed revision of early Proterozoic stratigraphy of the Thelon and Baker Lake basins, Northwest Territories. Current research; Part C, Canadian Shield, Geological Survey of Canada Paper 92-01C, pp. 129–137.

Golding, H.G., Conolly, J.R., 1962. Stylolites in volcanic rocks. J. Sediment. Res. 32, 534–538. doi:10.1306/74D70D12-2B21-11D7-8648000102C1865D

Gordon, M.B., Hempton, M.R., 1986. Collision-induced rifting: The Grenville Orogeny and the Keweenawan Rift of North America. Tectonophysics 127, 1–25. doi:https://doi.org/10.1016/0040-1951(86)90076-4

Hadlari, T., and Rainbird, R.H., 2011. Retro-arc extension and continental rifting: a model for the Paleoproterozoic Baker Lake Basin, Nunavut1Geological Survey of Canada Contribution 20100436. Can. J. Earth Sci. 48, 1232–1258. doi:10.1139/e11-002

Hiatt, E.E., Palmer, S.E., Kurt Kyser, T., O'Connor, T.K., 2010. Basin evolution, diagenesis and uranium mineralization in the Paleoproterozic Thelon Basin, Nunavut, Canada. Basin Res. 22, 302–323. doi:10.1111/j.1365-2117.2009.00415.x

Hoeve, J., and Quirt, D.H., 1984. Mineralization and Host Rock Alteration in Relation to Clay Mineral Diagenesis and Evolution of the Middle-Proterozoic, Athabasca Basin, northern Saskatchewan, Canada: Saskatchewan Research Council, SRC Technical Report 187, 187 p.

Hoffman, P.F., 1988. United Plates of America, the Birth of a Craton: Early Proterozoic Assembly and Growth of Laurentia. Annu. Rev. Earth Planet. Sci. 16, 543–603. doi:10.1146/annurev.ea.16.050188.002551

Jefferson, C.W., Thomas, D.J., Gandhi, S.S., Ramaekers, P., Delaney, G., Brisbin, D., Cutts, C., Quirt, D., Portella, P., and Olson, R.A., 2007. Unconformity-Associated Uranium Deposits of the Athabasca Basin, Saskatchewan and Alberta. In: Goodfellow, W.D. (Ed.), Mineral Deposits of Canada: A Synthesis Of Major Deposit Types, District Metallogeny, The Evolution Of Geological Provinces, And Exploration Methods. Geological Assoiciation of Candada, Special Publication 5, pp. 273–305

Jochum, K., Weis, U., Stoll, B., Kuzmin, D., Jacob, D., Stracke, A., Birbaum, K., Frick, D., Günther, D., Enzweiler, J., 2011. Determination of reference values for NIST SRM 610–617 glasses following ISO Guidelines. Geostand. Geoanalytical Res. 35, 397–429.

Johnstone, D., Bethune, K.M., Quirt, D., Benedicto, A. 2017. Lithostratigraphic and structural controls of uranium mineralization in the Kiggavik East, Centre and Main Zone deposits, Nunavut. In Proceedings of the Geological Association of Canada-Mineralogical Association of Canada, Joint Annual Meeting, Whitehorse Yukon, June 1-3 2016

Kranidiotis, P., MacLean, W.H., 1987. Systematics of chlorite alteration at the Phelps Dodge massive sulfide deposit, Matagami, Quebec. Econ. Geol. 82, 1898–1911. doi:10.2113/gsecongeo.82.7.1898

Kim, Y.-S., Peacock, D.C.P., Sanderson, D.J., 2004. Fault damage zones. J. Struct. Geol. 26, 503–517. doi:https://doi.org/10.1016/j.jsg.2003.08.002

Kotzer, T.G., Kyser, T.K., 1995. Petrogenesis of the Proterozoic Athabasca Basin, northern Saskatchewan, Canada, and its relation to diagenesis, hydrothermal uranium mineralization and paleohydrogeology. Chem. Geol. 120, 45–89. doi:https://doi.org/10.1016/0009-2541(94)00114-N

LeCheminant, A.N., Leatherbarrow, R.W., and Miller, A.R., 1979. Thirty Mile Lake map area, District of Keewatin; - in Current Research, Part B, Geological Survey of Canada, Paper 79-IB, p. 319-327

LeCheminant, A.N., Miller, A.R., LeCheminant, G.M., 1987. Early Proterozoic Alkaline Igneous Rocks, District of Keewatin, Canada: Petrogenesis and Mineralization. Geol. Soc. London, Spec. Publ. 33, 219–240. doi:10.1144/GSL.SP.1987.033.01.16

Leroy, J., 1978. The Margnac and Fanay uranium deposits of the La Crouzille District (western Massif Central, France); geologic and fluid inclusion studies. Econ. Geol. 73, 1611–1634. doi:10.2113/gsecongeo.73.8.1611

Mazimhaka, P.K., Hendry, H.E., 1985. The Martin Group, Charlot Point and Jug Bay areas. In Summary of Investigations 1985. Saskatchewan Geological Survey, Saskatchewan Energy Mines, Miscellaneous Report 85-4, pp. 67–80

McClellan, E., Gazel, E., 2014. The Cryogenian intra-continental rifting of Rodinia: Evidence from the Laurentian margin in eastern North America. Lithos 206–207, 321–337. doi:https://doi.org/10.1016/j.lithos.2014.08.006

Mercadier, J., Cuney, M., Lach, P., Boiron, M.C., Bonhoure, J., Richard, A., Leisen, M., Kister, P., 2011a. Origin of uranium deposits revealed by their rare earth element signature. Terra Nov. 23, 264–269. doi:10.1111/j.1365-3121.2011.01008.x

Mercadier, J., Cuney, M., Cathelineau, M., Lacorde, M., 2011b. U redox fronts and kaolinisation in basement-hosted unconformity-related U ores of the Athabasca Basin (Canada): late U remobilisation by meteoric fluids. Miner. Depos. 46, 105–135. doi:10.1007/s00126-010-0314-7

Miller, A.R., 1979, Uranium geology in the central Baker Lake Basin, District of Keewatin, in Current Research, Part A: Geological Survey of Canada, Paper 79-1A, p. 57-59

Miller, A.R., 1980. Uranium geology of the Eastern Baker Lake basin, district of Keewatin, Northwest Territories. Geological survey of Canada, bulletin 330, 63p.

Miller, A.R., 1982. Alteration and Mineralization Types: Amer-Thelon Area, N.T.S. 66 G, H, report to Westmin Resources Limited

Miller, A.R., 1995. Polymetallic unconformity-related uranium veins in lower Proterozoic Amer Group, Pelly Lake map area, northern Thelon Basin, Churchill province, Northwest Territories: Geological Survey of Canada, Current Research 1995-C, pp. 151-161

Miller, A.R., Stanton, R.A., Cluff, G.R. and Male, M.J. 1986. Uranium deposits and prospects of the Baker Lake Basin and subbasins, Central District of Keewatin, Northwest Territories. In Uranium Deposits of Canada, edited by E.L. Evans, Canadian Institute of Mining and Metallurgy, Special Volume 33, pp.263-285.

Miller, A.R., and Blackwell, G.W. 1992. Petrology of alkaline rare earth element bearing plutonic rocks, Enekatcha Lake (65 E/15) and Carey Lake (65 L/7) map-areas, District of Mackenzie. Geological Survey of Canada, Open File 2484

Miller, A.R. and LeCheminant, A.N., 1985. Geology and uranium metallogeny of Proterozoic supracrustal successions, central District of Keewatin, N.W.T., with comparisons to northern Saskatchewan. Special Volume - Canadian Institute of Mining and Metallurgy 32: 167-185

Pinheiro, R.V.L., Holdsworth, R.E., 1997. Reactivation of Archaean strike-slip fault systems, Amazon region, Brazil. J. Geol. Soc. London. 154, 99–103. doi:10.1144/gsjgs.154.1.0099

Rainbird, R.H., Hadlari, T., Aspler, L.B., Donaldson, J.A., LeCheminant, A.N., Peterson, T.D., 2003. Sequence stratigraphy and evolution of the paleoproterozoic intracontinental Baker Lake and Thelon Basins, western Churchill Province, Nunavut, Canada. Precambrian Res. 125, 21–53. doi:10.1016/S0301-9268(03)00076-7

Ramaekers, P., Jefferson, C.W., Yeo, G.M., Collier, B., Long, D.G.F., Drever, G., et al. 2007. Revised geological map and stratigraphy of the Athabasca Group, Saskatchewan and Alberta. In EXTECH IV: Geology and Uranium Exploration TECHnology of the Proterozoic Athabasca Basin, Saskatchewan and Alberta. Edited by C.W. Jefferson and G. Delaney. Geological Survey of Canada, Bulletin 588, (also Geological Association of Canada, Mineral Deposits Division, Special Publication 4; Saskatchewan Geological Society, Special Publication 18). pp. 155–192

Richard, A., Pettke, T., Cathelineau, M., Boiron, M., Mercadier, J., Cuney, M., Derome, D., 2010. Brine – rock interaction in the Athabasca basement (McArthur River U deposit , Canada):

consequences for fluid chemistry and uranium uptake 303–308. doi:10.1111/j.1365-3121.2010.00947.x

Richard, A., Cathelineau, M., Boiron, M.-C., Mercadier, J., Banks, D., Cuney, M., 2016. Metal-rich fluid inclusions provide new insights into unconformity-related U deposits (Athabasca Basin and Basement, Canada). Miner. Depos. 51, 249–270.

Riegler, T., Lescuyer, J.-L., Wollenberg, P., Quirt, D., Beaufort, D., 2014. Alteration related to uranium deposits in the Kiggavik-Andrew Lake structural trend, Nunavut, Canada : New insights from petrography and clay mineralogy. Can. Mineral. 52, 27–45. doi:10.3749/canmin.52.1.27

Riegler, T., Quirt, D., Beaufort, D., 2016a. Spatial distribution and compositional variation of APS minerals related to uranium deposits in the Kiggavik-Andrew Lake structural trend, Nunavut, Canada. Miner. Depos. 51, 219–236. doi:10.1007/s00126-015-0595-y

Romberger, S.B., 1984. Transport and deposition of uranium in hydrothermal systems at temperatures up to 300°C: geological implications, in: De Vivo, B., Ippolito, F., Capaldi, G., Simpson, P.R. (Eds.), Uranium Geochemistry, Mineralogy, Geology, Exploration and Resources. Springer Netherlands, Dordrecht, pp. 12–17. doi:10.1007/978-94-009-6060-2_3

Rotevatn, A., Bastesen, E., 2014. Fault linkage and damage zone architecture in tight carbonate rocks in the Suez Rift (Egypt): implications for permeability structure along segmented normal faults. Geol. Soc. London, Spec. Publ. 374, 79–95. doi:10.1144/SP374.12

Rutter, E.H., 1983. Pressure solution in nature, theory and experiment. J. Geol. Soc. London. 140, 725–740. doi:10.1144/gsjgs.140.5.0725

Shabaga, B., M., Fayek, M., Quirt, D., Davis, B., Pesja, T., Jefferson, C., 2015. Geochemistry and Geochronology of the Andrew Lake deposit, Thelon Basin, Nunavut, Canada. Poster presented at 2015 GAC MAC

Shabaga, B., M., Fayek, M., Quirt, D., Jefferson, C.W., Camacho, A., 2017. Geochronology and genesis of the Andrew Lake uranium deposit, Thelon Basin, Nunavut, Canada. Poster presented at 2017 GAC MAC

Sharpe, R., Fayek, M., Quirt, D., Jefferson, C.W., 2015. Geochronology and genesis of the bong uranium deposit, Thelon Basin, Nunavut, Canada. Econ. Geol. 110, 1759–1777. doi:10.2113/econgeo.110.7.1759

Wang, K., Chi, G., Bethune, K.M., and Card, C.D., 2015. Fluid Composition, Thermal Conditions, Fluid-structural Relationships and Graphite Alteration of the Phoenix Uranium Deposit, Athabasca Basin, Saskatchewan, in Targeted Geoscience Initiative 4: unconformity-related

uranium systems, (ed.) E.G. Potter and D.M. Wright; Geological Survey of Canada, Open File 7791, p. 93–102. doi: 10.4095/295776

6.2 CHARACTERIZATION OF THE QUARTZ BRECCIA IN THE KIGGAVIK AREA: COMPLEMENTARY OBSERVATIONS AND TENTATIVE GENETIC MODEL

6.2.1 INTRODUCTION

The pre-Thelon silicification event that originated the quartz breccia (QB) has been identified along major faults in the Kiggavik area. Figure 46 presents the parts of the faults where the QB has been observed from field and drillcores observations. These faults presumably pre-Thelon major drains, as demonstrated by clay altered fault rock crosscut by the QB, acted as conduits for silica-rich fluids and are highlighted by silicification and pervasive hematisation, unlike other faults (see also cross-section of Fig. 46). In previous sections of this PhD manuscript, the QB emplacement was simplified as one event linked to magmatism of the Kivalliq igneous suite and some of the quartz textures observed within the QB were described, although their chronology remains complex with contradicting observations. Complementary observations made throughout the Kiggavik area on the QB and observations made under cathodoluminescence (on quartz spatially or not associated to quartz veins) are presented hereafter and a tentative conceptual model of formation of the QB is described at the end.

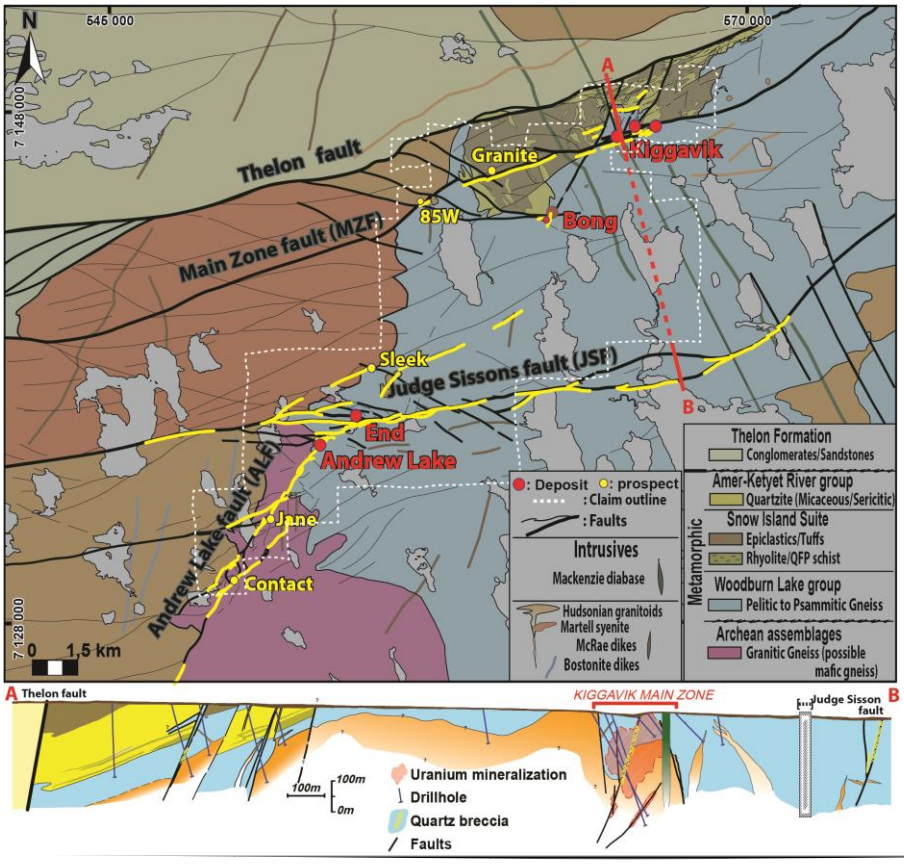

Figure 36: Simplified geological map of the Kiggavik area (AREVA internal document) highlighting the occurrence of the QB (yellow) along the major faults. Cross-section from the Thelon fault to the Judge Sisson fault. Deposits and prospects are indicated with red and yellow circles respectively.

At a first glance, the breccia consists of massive white quartz

veins crosscutting silicified cataclastic fault rocks (Fig. 47A). These quartz veins are crosscut by several fracturing events and observed as clasts in fault zones (Fig. 47B). However, having a closer look at drillcore samples from the core zone of the quartz breccia, a more complex chronology of fracturing and quartz-healing with different types of silica arises (Fig. 47C).

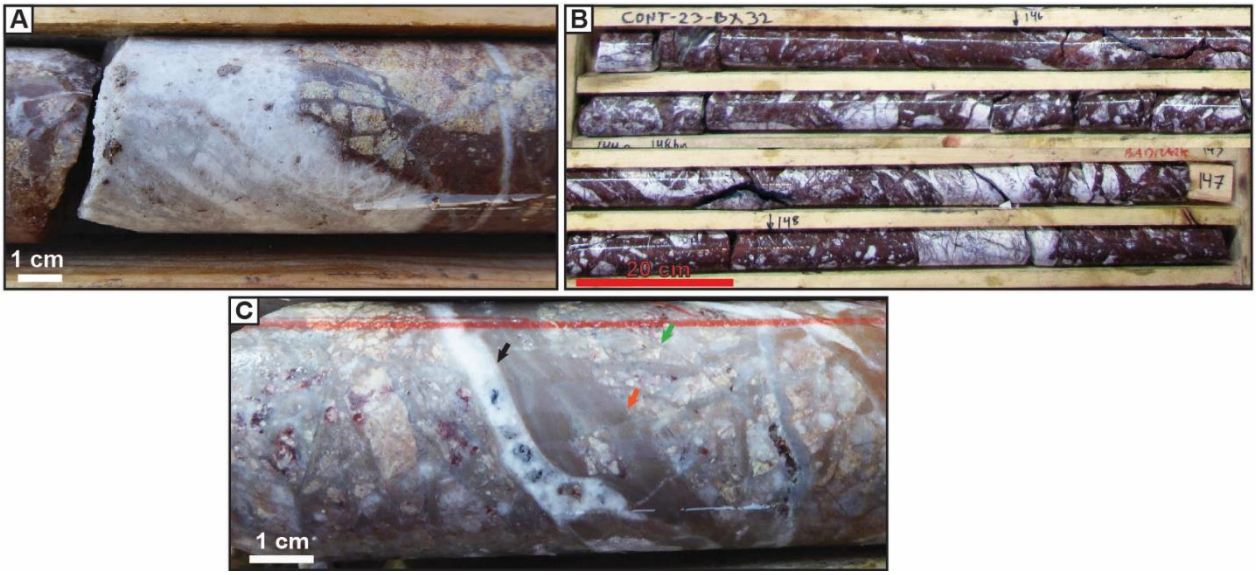

Figure 37: A) Drillcore photograph of a silicified and illitized cataclastic fault rock crosscut by white quartz and grey quartz veins of the QB. B) Drillcore photograph of a cataclastic fault rock displaying clasts of the QB. C) Drillcore photograph of a silicified and illitized cataclastic fault rock (red arrow, brownish cement with grey quartz), with clasts bearing quartz veins (green arrow) and crosscut by white quartz vein (black arrow).

6.2.2 MACRO-SCALE ORGANISATION AND MORPHOLOGY OF THE QB

At Contact, several fault core zones were crosscut by drillholes (CONT-24, CONT-16, CONT-06). These core zones are discontinuous from the SW to the NE. They are tapering toward their ends both laterally (for example, between CONT-26 and CONT-25, Fig. 48) and vertically (for example, between CONT-10 and CONT-11, Fig. 48), which supports that they have elliptical shapes, connected by quartz vein networks. This observation indicates that the structure was permeable, at least locally. Each quartz-breccia body observed in drillholes consists mainly of a complex network of quartz veins, individually up to a few cm in thickness, that surround and isolate angular fragments of the host rock (various intrusives, mainly from the Hudson igneous suite, and Archean granitic gneiss). Such observations are limited by the partial

nature of the recovered rock in drillholes. Core zones are characterized by massive (more than 10 cm thick) white quartz veins where the host-rock is barely visible, while damage zones are characterized by millimeter to centimeter-thick quartz veins. “Chloritic”, “hematitic” breccias usually characterize pre-QB silicified cataclastic to ultra-cataclastic fault rocks that are crosscut by white quartz veins.

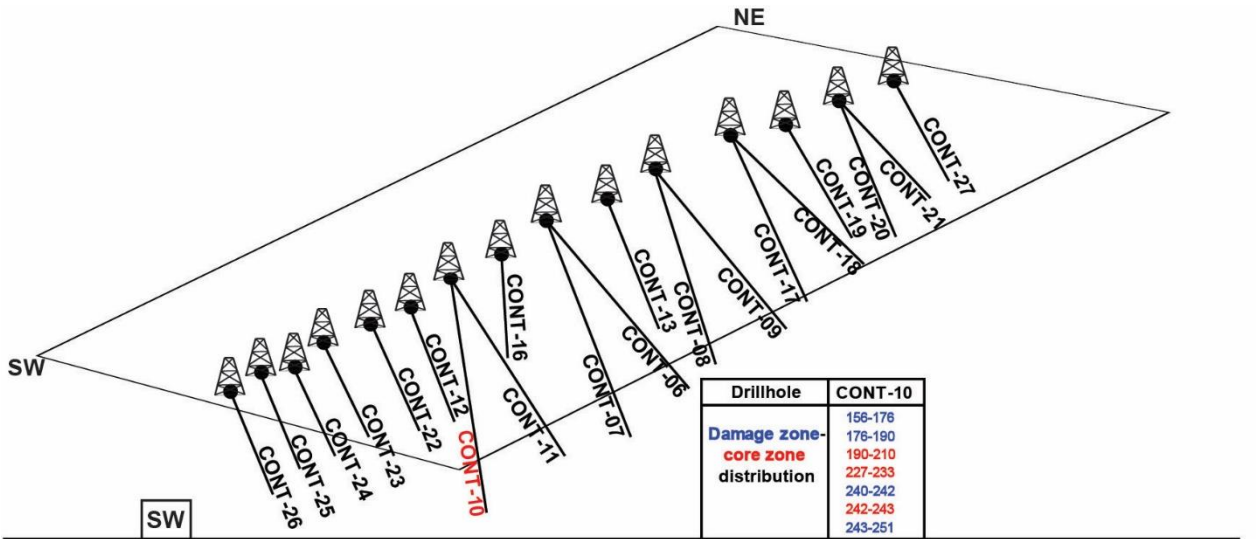

Drillhole	CONT-10
Damage zone-core zone distribution	156-176 176-190 190-210 227-233 240-242 242-243 243-251

SW

Drillhole	CONT-26	CONT-25	CONT-24	CONT-23	CONT-22	CONT-12	CONT-11	CONT-16	CONT-06
Damage zone-core zone distribution	227-234 234-238 238-245	144-148 160-161 190-192 269-290	105-114 114-125 126-128 2 veins 50cm 136-140 140-end	132-144 144-149 149-153 153-160	180-186 188-191 192-196 226-227	216-220 220-237 237-241	131-155	201-213 213-216 216-238 238-243 243-255	161-168 168-171 171-175 175-183 183-187 187-194 224-228
notes	grey breccia	2 branches chloritic breccia hematitic breccia	hematitic breccia			chloritic breccia grey breccia		2 branches chloritic breccia hematitic breccia	2 branches chloritic breccia hematitic breccia

NE

CONT-06	CONT-13	CONT-09	CONT-18	CONT-19	CONT-21	CONT-27
161-168 168-171 171-175 175-183 183-187 187-194 224-228	148-175 175-176	103-126 126-139 139-145	151-162 162-183	165-185 185-198 198-205	187-195 195-200 200-204	189-220 227-251 251-257
2 branches chloritic breccia hematitic breccia	not complete hematitic breccia chloritic breccia (?)	hematitic breccia	white quartz equal other cement hematitic breccia brown breccia	white quartz not dominant hematitic breccia chloritic breccia brown breccia	white quartz not dominant hematitic breccia	

Figure 38: Organisation of core and damage zones of the QB crosscut in drillholes at Contact.

6.2.3 MICRO-SCALE OBSERVATIONS (OPTICAL AND CATHODOLUMINESCENCE MICROSCOPES): NATURE AND CHRONOLOGY OF SILICIFYING EVENTS

At the macro-scale, quartz generations can be roughly separated into white quartz and grey quartz generations. White quartz consists of millimetric or up to tens of centimeters veins. At the micro scale white quartz cementing fractures are usually characterized by subhedral crystals up to 0.5 mm and devoid of fluid inclusions (Fig. 49A-D). Vug porosity within the vein is filled with microcrystalline quartz (Fig. 49C). Grey quartz consists of sub-angular smaller crystals, sometimes “clouded” by dense trends of pseudo-secondary fluid inclusions.

The white quartz veins are observed as one of the latest quartz generation, crosscutting micro-breccias (Fig. 49B, 49C) or other quartz textures (Fig. 49D) but the chronology is more complex, as micro-breccias are observed crosscutting white quartz veins (fig 49A). Cataclastic fault rocks are usually observed crosscut by these various quartz veins and micro-breccias (Fig. 49E).

White quartz (veins or breccias) is sometimes characterized by subhedral crystals together with fragments of former euhedral quartz crystals. .

The most recurrent colour observed under cathodoluminescence is a deep-blue to purple-blue, weak luminescence (a 20 seconds of time exposition was required in order to get enough signal). This is observed for microcrystalline quartz veins, sometimes synchronous with hematite (Fig. 50A-B), and quartz cementing microbreccias (Fig. 50C-D). On the other hand, subhedral quartz that displays dense trends of monophasic fluid inclusions on some of their growth zones are characterized by a more purplish luminescence (Fig. 50F).

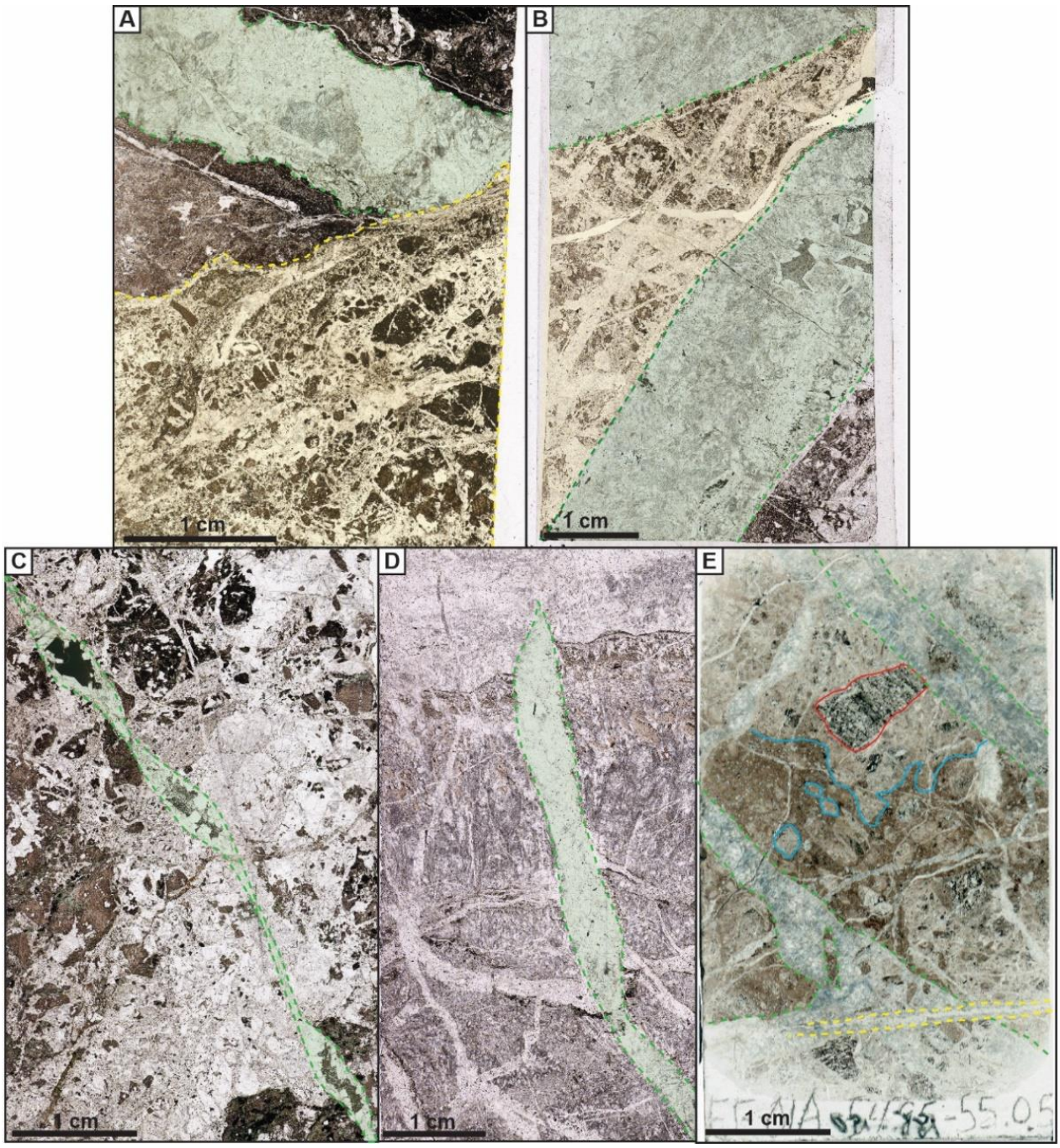

Figure 39: A) Quartz cemented microbreccia crosscutting a clear quartz vein. B) Quartz cemented microbreccia crosscutted by clear quartz vein. C) Quartz cemented microbreccia crosscutted by clear quartz vein displaying syntaxial growth, vuggy aspect and filled with microcrystalline quartz. D) Several generations of quartz (bladed, microcrystalline, xenomorphic..) crosscut by clear quartz vein. E) Two generations of cataclastic fault rocks crossscut by quartz veins.

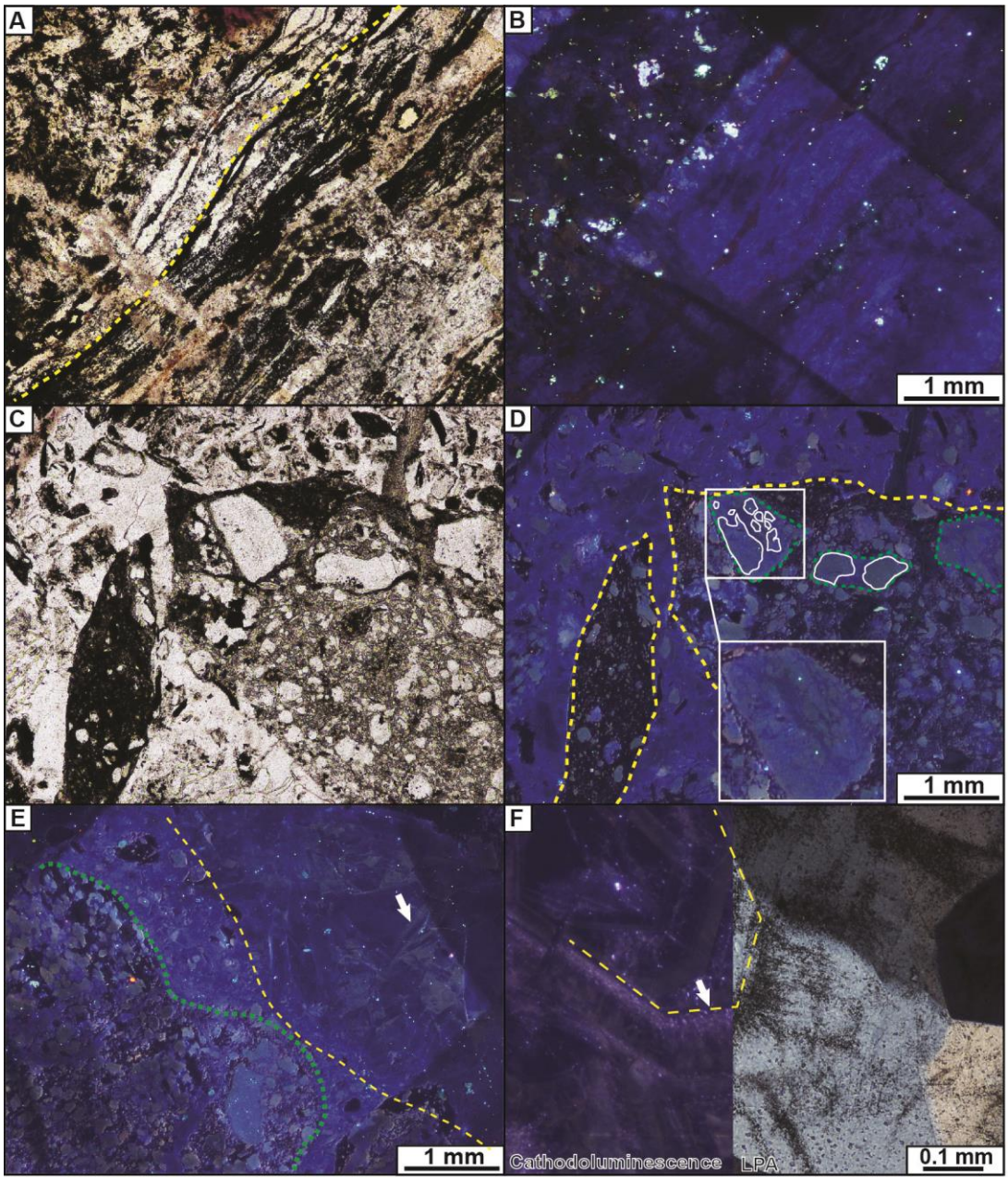

Figure 40: A and B) Optical microscope (OM) and cathodoluminescence microphotograph (CM) of crustiform microcrystalline quartz displaying blue-purple luminescence and synchronous anhedral hematite. C-D) OM and CM of reworked clasts (yellow) of a quartz cemented breccia (blue-purple luminescence) bearing reworked clasts (green) of cataclastic fault rock. Quartz of the host rock display a green-brown luminescence and were initially brecciated (white) by blue quartz. E) CM: Quartz breccia (green) cemented by subhedral, sub-millimetric blue-purple quartz, crosscut by dark blue luminescent subhedral millimetric quartz vein (yellow), the white arrow highlight brown-luminescent overgrowth. F) CM and OM of purplish luminescent euhedral quartz (sectoral zoning highlighted by the yellow line) displaying dense trends (pointed by the white arrow) of monophasic fluid inclusions.

The clear subhedral quartz crystals, usually observed as the last generation, display alternating growth zones of brown and blue luminescence (oscillatory growth-zoning, Fig. 50E, 51A, 51B). The chronology is more clearly observed (Fig. 51B), however the brown luminescence is also observed in pseudo-secondary fluid inclusions planes (Fig. 51A) and in breccias where the quartz has likely completely recrystallized, letting the breccia texture only observable under cathodoluminescence; the “cement” of the breccia displays a brown luminescence (Fig. 51C). Other evidences of fracturing, tectonic comminution and reprecipitation of quartz are exemplified by white quartz veins where subhedral quartz grains are surrounded by microcrystalline quartz and other quartz of heterogeneous sizes (Fig. 51D).

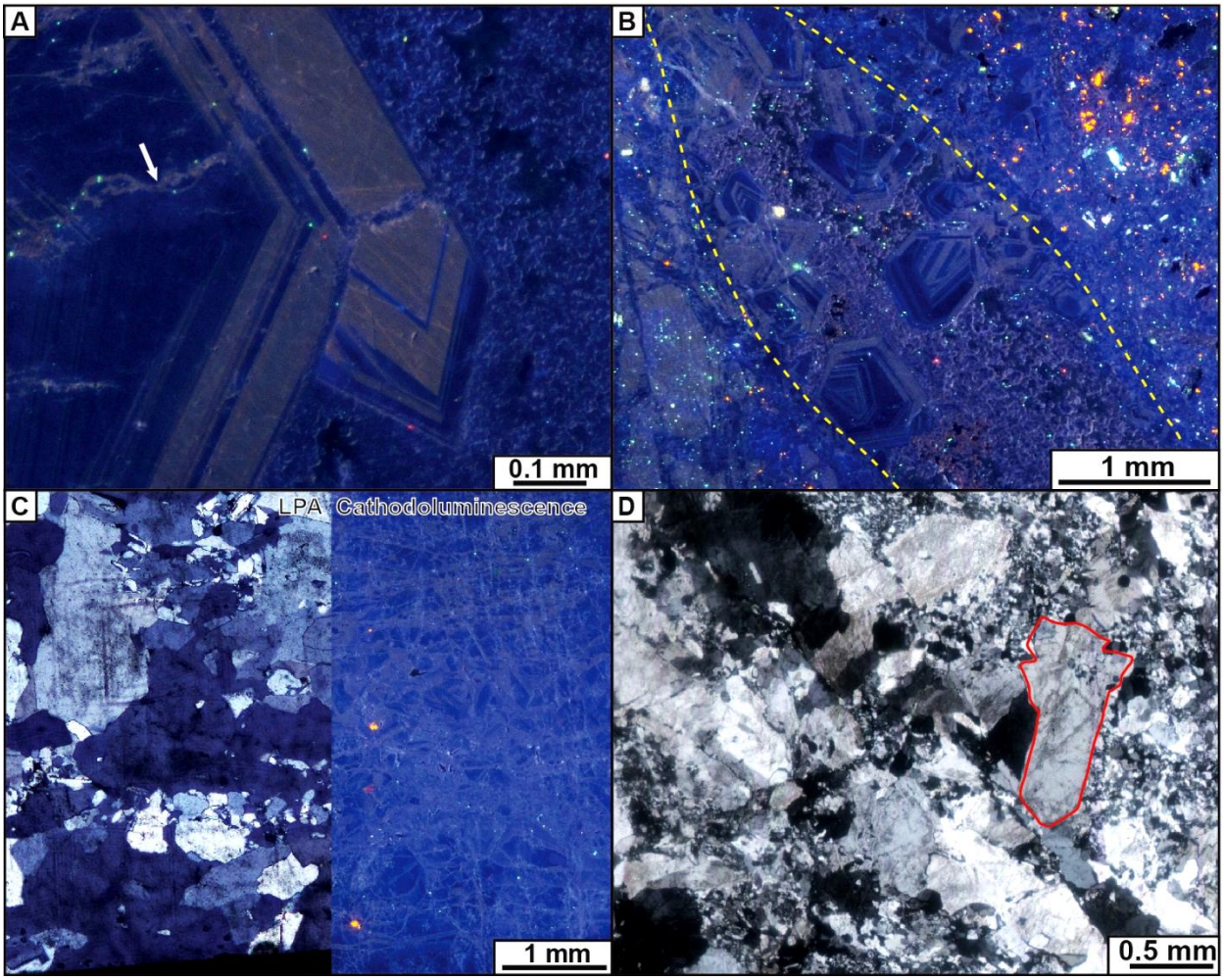

Figure 41: A) CM: Euhedral clear quartz crystal displaying alternating blue-brown coloured growth zones. A pseudo-secondary fluid inclusions trail displays a brownish luminescence (white arrow). B) CM: Fracture cemented with syntaxial euhedral clear quartz and microcrystalline quartz (blue-brown luminescence, yellow dotted line) crosscut a micro-breccia cemented by quartz displaying a deeper blue luminescence and specked with calcite crystals (orange) C) OM and CM of the same zone: subhedral and microcrystalline quartz (blue luminescence) displaying

microbrecciation/recrystallization (brown luminescence). D) OM: Coarse quartz grains engulf in a fine-grained quartz matrix (example in red)

To summarize, textures and crosscutting relationships of quartz reveal :

- episodes of brittle faulting and cataclasis, before the circulation of silica-rich fluid,
- episodes of brittle faulting and cataclasis, synchronous with the circulation of silica-rich fluids; during this period, there were stages of slow and rapid silica precipitation (boiling exemplified by arrays of monophase fluid inclusions at the tip of euhedral quartz), alternating with stages of fluid-assisted brecciation and quartz-reprecipitation.
- evolution of the chemistry of the fluid. Early quartz display deep blue to purple luminescence, while late quartz displays deep-blue/purple alternating with brown luminescence. This evolution of the luminescence and this alternance likely indicates the income of a fluid with a different chemistry in the system, however in “competition” with the previous fluid. The income of this new fluid is probably linked to deposition and diagenetic evolution of the overlying sedimentary formations (Baker-Lake basin or Thelon basin).

6.2.4 LUMINESCENCE OF QUARTZ IN PRESENCE OF URANIUM MINERALIZATION

As presented in the previous chapter, the various quartz generations are crosscut by microfractures cemented with dolomite then calcite which are sometimes synchronous with deposition of uranium and other ore minerals. Quartz which has been in contact with uranium minerals displays a characteristic luminescence: red/pink close to the uranium mineral, yellow/greenish farther to the uranium mineral (Fig. 52). This is especially well observed in quartz veins that were later orthogonally microfractured (Fig. 52A-D) and on quartz of the host rock (when they were not dissolved by circulation of the uranium-bearing fluid, for example in the case of U0 and U1, which are associated with weaker clay alteration, see Fig. 52E). This peculiar luminescence is brighter than the original luminescence of the quartz and displays a nearly uniform 35-45 µm width (Fig. 52F): it is likely due to alpha-particle-induced damage that travelled through the quartz crystal and disturbed, the atomic organisation of its lattice, as suggested by Owen (1988) and Komuro et al. (2002). Such features are observed distinctly in mineralized samples but can be observed in samples (cataclastic fault rock for example) that do not currently bear any uranium minerals.

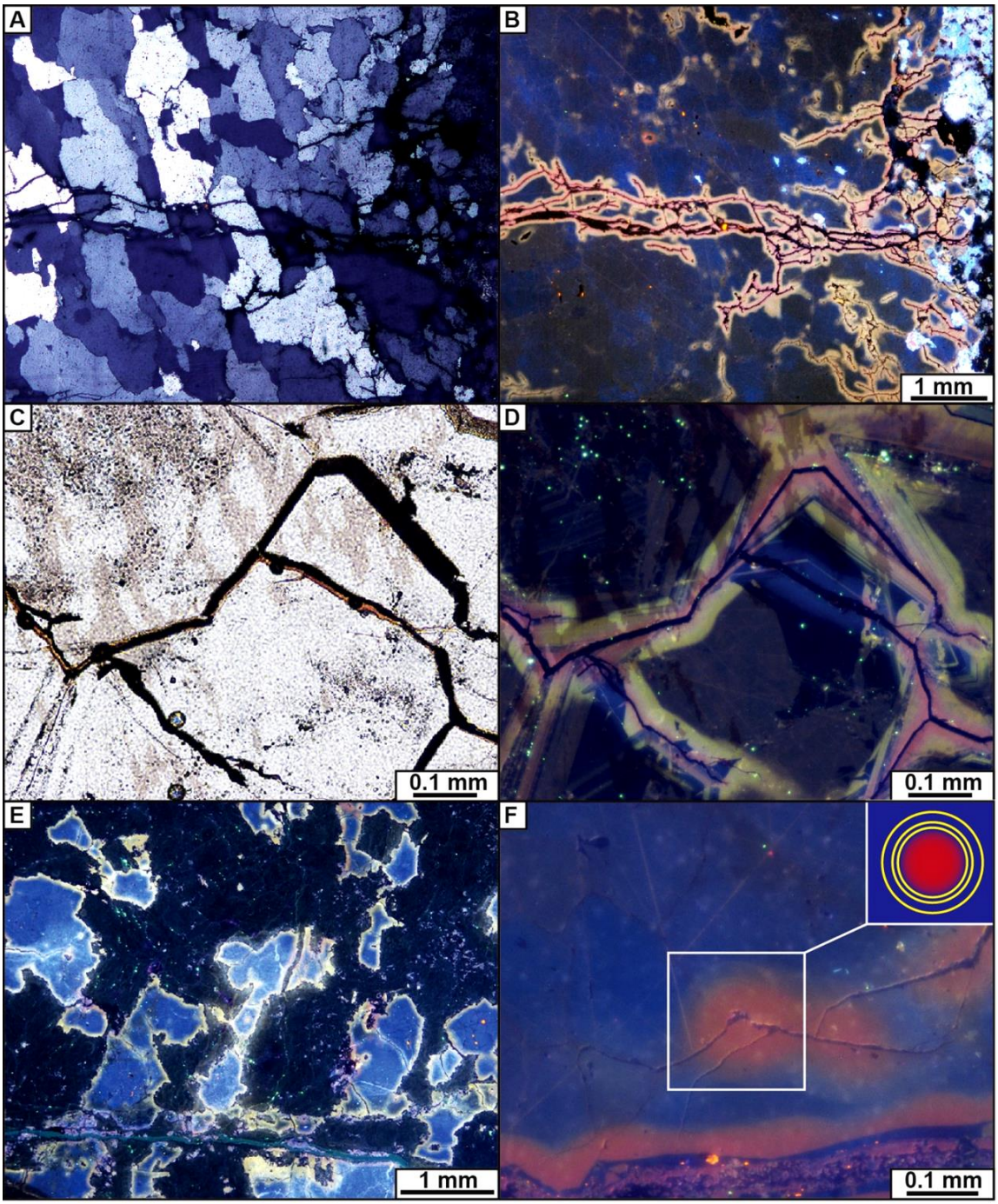

Figure 42: A-B) OM and CM: Magmatic quartz vein orthogonally crosscut by a microfracture and cemented with pitchblende. The boundaries of the microfractures display a "buffer area" where the luminescence of the quartz is modified, from pink to yellow. C-D) OM and CM: Same observations as above but closer view, in a hydrothermal quartz vein. E) CM: Uranium mineralized granitic gneiss sample, quartz are from the host rock and are irradiated on their boundaries. F) CM: Close view on a quartz displaying haloes of irradiation. The characteristic thin haloes, caused by various depth of penetration due to different energy of the emitted atom, are visible.

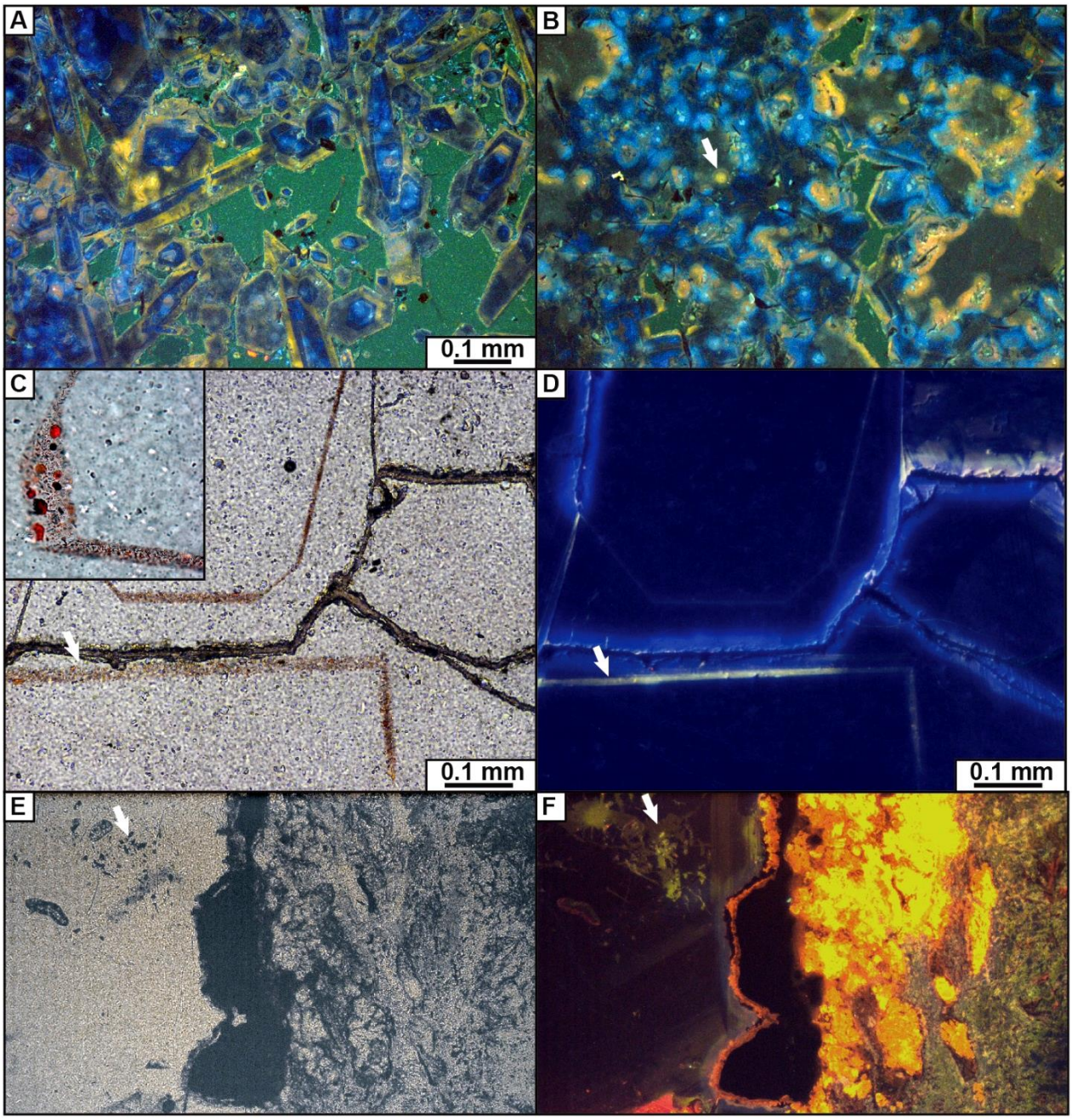

Figure 43: A) CM: Acicular quartz crystals displaying deep blue luminescence and yellowish luminescent growth zones. Numerous irradiating haloes are observed. B) CM: Same observation as A, some haloes are more visible (white arrow). C-D) OM and CM: Blue luminescent subhedral quartz and primary sub-millimetric solid inclusions (hematite crystals). The fluid inclusions trends display a weak yellowish luminescence. E-F) OM and CM: Subhedral quartz crystals displaying pseudo-secondary fluid biphase fluid inclusions. The quartz surrounding the fluid inclusion is characterized by a greenish luminescence (white arrow).

Rare samples display oscillatory growth zone with deep blue to yellowish luminescence (Fig. 53A, B) within acicular, euhedral, sub-millimetric quartz crystals. These samples are not mineralized but the characteristics halo of irradiation is observed in numerous locations within quartz (Fig. 53B). One generation of quartz was observed displaying primary solid inclusions of hematite. These solid inclusions trends also return a yellow luminescence (Fig. 53C, D). Some samples display subhedral quartz crystal with the blue-brown oscillatory growth zoning described before, these quartz can display (pseudo?) secondary biphase fluid inclusions. Quartz surrounding the fluid inclusions is characterized by a greenish-yellow luminescence (Fig. 53E, F).

6.2.5 INTERPRETATIONS OF OBSERVATIONS AND CONCLUSIONS

The luminescence observed in the Kiggavik area is most commonly observed as deep blue to purple. These colours characterize the first generations of quartz, while later generations of quartz appear to be rather deep blue to purple and light brown, with oscillatory growth zoning. Blue-purple luminescence is commonly found in magmatic/hydrothermal environments (Vollbrecht et al., 1996, 2002; Kremenetsky et al., 2005) while brown luminescence was observed in sedimentary-diagenetic environment (Kraishan et al., 2009). Tracing back the specific origin of the luminescence for a quartz is a difficult exercise, as the luminescence can be due to a great variety of factors or elemental concentration within the quartz (for example, change in aluminum content).

Quartz displaying specific luminescence associated with destabilization of the crystal lattice linked to the nearby occurrence of uranium minerals (radiation damages due to liberation of alpha particles through U^{238} decay series) has been described in deposits throughout the world (Meunier et al., 1990; Hu et al., 2008; MacRae et al., 2013; Cerin et al., 2017). Some of these authors reported the red-pink luminescence as being associated with the α particle-induced defects, while Götze et al. (2015) attributed the yellow luminescence to high oxygen deficiency and structural disorder in quartz. Mineralized as well as unmineralized samples can display quartz with radiation-damages luminescence, and both situations were observed in deposits (e.g. Meunier et al., 1990), α particle-induced defects in unmineralized samples being interpreted as a record of uranium-bearing fluids circulation.

The rare acicular euhedral quartz generation displaying yellow-blue oscillatory growth zones were observed in an unmineralized sample, cementing microfractures in the paleoproterozoic quartzite (Amer and Ketyet River group). Yellow luminescence, due to oxygen deficiency and structural disorder (Götze et al., 2015), could be associated with the presence of sub-

micrometric uranium inclusions in growth zones of the quartz, reflecting the circulation of an uranium bearing fluid. The observation that these quartz do not display any α particle-induced defect on their border would mean that neither uranium mineralization nor remobilization occurred in the microfracture, likely due to a unfavourable environment (absence of reductant ?). Yellow luminescence observed in the trends of primary solid hematite inclusions follows the previous interpretation; in addition, this type of primary inclusions in quartz was observed in Athabasca unconformity related deposit, associated with the circulation of uranium-bearing basinal brines (Richard et al., 2012). This would also be in agreement with occurrence of biphase aqueous fluid inclusions within quartz displaying yellow-greenish luminescence (Fig. 53F).

This characterization of quartz luminescence reflects the tectonic events and fluid composition evolution in the Kiggavik area. The first generations of quartz of the QB display several textures, some characteristics of epithermal environments but displaying one deep blue to purple luminescence. Associated with this luminescence we observe several episodes of brecciation of the host rock and quartz cementation, likely cyclic, since these quartz veins and breccias crosscut silicified cataclastic fault rocks. Investigations of the veins and breccias at the micro-scale reveal an intimate spatial association of all quartz structures and the lack of a simple and clear chronology of events. This suggests that the structure-forming processes occur repeatedly and, to various extents, at different locations, and demonstrates that the already complex patchwork of quartz textures observed on drillcore and in transmitted light shows a still more complex history of quartz fracturing, dissolution, reprecipitation, and recrystallization, under cathodoluminescence. These processes that led to the formation of the QB were initiated by the emplacement of the Kivalliq igneous suite (Fig. 54), and are linked to fluctuation in pressure, temperature (Okamoto et al., 2013) and (lately) fluid compositions. Such variations in fluid compositions were observed by Turner et al. (2001) in their fluid inclusions study of the Mallery Lake epithermal deposit, south to the Kiggavik area, and by Chi et al. (2017) in their fluid inclusions study of hydrothermal quartz at the End deposit. They observe low temperature (80-180°C)-high salinity (25-38 wt% NaCl) fluids, low temperature (140-200°C)-low salinity (<9wt% NaCl) fluids and high temperature (250-340°C)-low salinity (<9 wt% NaCl) fluids. Chi et al. (2017) characterized a shallow depth (<2km) for the formation of the QB.

Repeated brittle failure, dilation, pressure drop, quartz precipitation and pressure rebuilding are indicated by quartz textures and by numerous generations of reworked clasts within quartz-cemented breccias to micro-breccias. The massive white quartz mass that displays fine-grained subhedral quartz crystals together with numerous fragments of earlier aggregates

indicate they formed by precipitation from a fluid but also by cataclasis of already existing quartz veins and/or quartz lenses fragmentation during movements along the fault (Yilmaz et al., 2014). Fluids that circulated during these episodes of cataclasis were silica-rich, as indicated by the fragmentation-induced pores cemented by quartz. It is envisaged that silica-rich fluids inferred to be of igneous origin used newly-formed fault zones as conduits for flowing upward to higher levels in the Earth's crust, and that the bodies of quartz breccia resulted from the passive in-situ modification of the initial fault breccia (Fig. 54), probably in a series of pulses, as the fluid pressure evolved cyclically between hydrostatic and supralithostatic, depending on the sealing of the fault zone by quartz precipitation and likely on the difficulty to reactivate such high angle faults without overpressured fluids (Sibson, 1992; The impermeable barrier in his model would be here created by silicification along the fault), here inferred coming from the underlying igneous system.

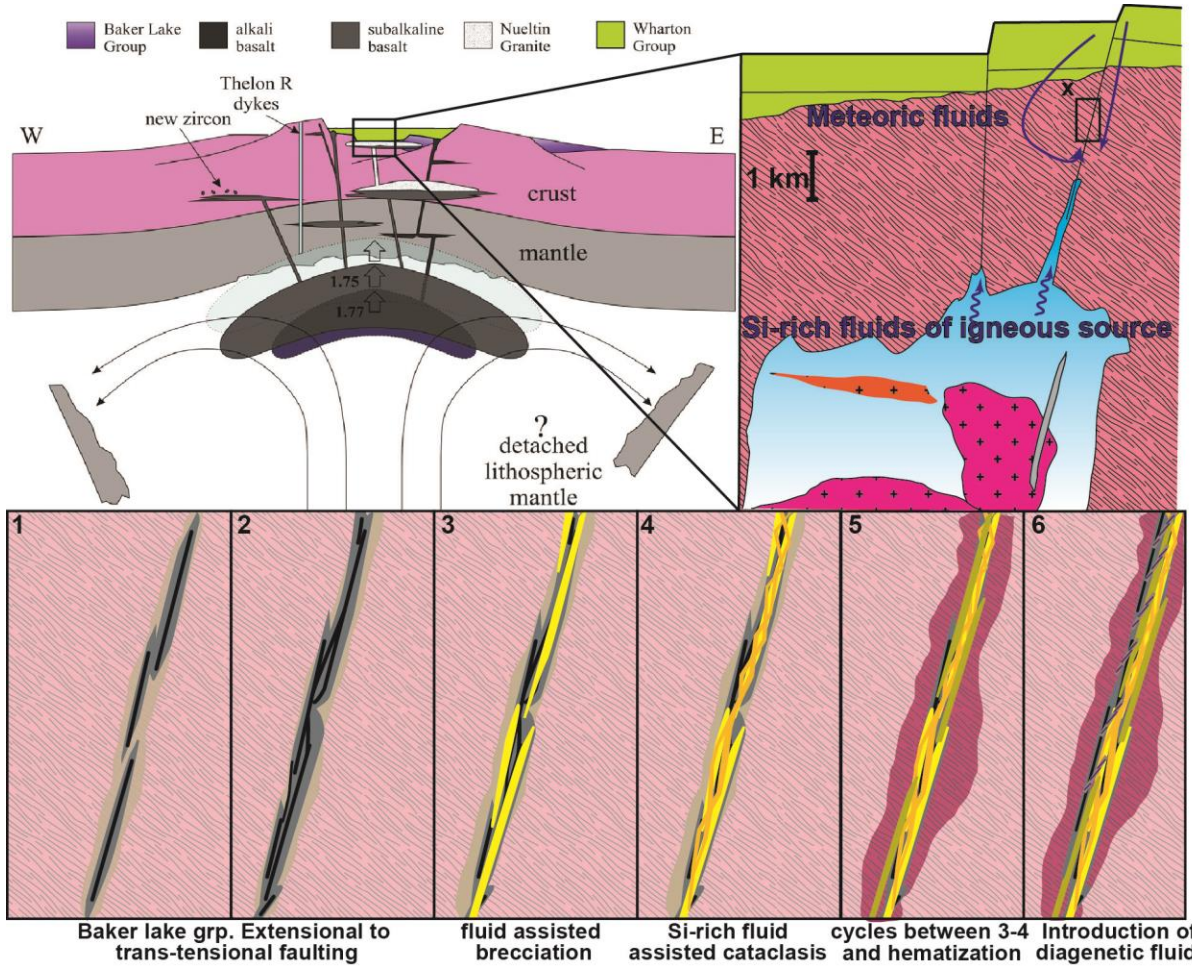

Figure 44: simplified scheme depicting the formation of the quartz breccia. (Top left synthetic cross section after Peterson et al., 2015). The X on the side of the rectangle localize the synthetic evolution (1-6) of a fault zone.

The final geometry of the quartz-breccia bodies (QB) at Contact (and likely at other deposits and prospects in the Kiggavik area) would have been controlled by a pre-existing irregular distribution of quartz breccias along the pre-existing fault zones, such features giving rise to lateral variations in hydraulic properties: certain fault segments acted as barriers to fluid flow, whereas others acted as conduits or show mixed behaviour. These characteristics would also have evolved temporally after each “increment” of silica-rich fluid circulation and quartz precipitation, leading to the building of a complex quartz-cemented breccia, up to tens of meter thick, acting as a barrier for fluid flow within its core zone, but also as a conduit within its damage zone. We can see the quartz breccia event as a kind of “resetting” of the fracture network, with the evolution of the affected fault zone into an impermeable lithology.

Fluid composition evolution is reflected by the late development of quartz displaying brown luminescence, sectoral zoning between deep blue and brown luminescence, and finally by the transition to yellow luminescence. Brown luminescence would characterize the introduction of diagenetic-hydrothermal (saline) fluids in the system, in competition with magmatic-hydrothermal fluids from the igneous suite. Such diagenetic-hydrothermal could come from the overlying Baker Lake basin, from the Thelon basin or both. Diagenetic-hydrothermal fluids chemistry would have evolved until the introduction of uranium in the system (characterized by quartz sectoral zoning displaying yellow luminescence). The observation in banded quartz veins of magnetite being altered to hematite, also characterize an evolution of the fluid from reducing to oxidizing, this support the observation of

1- reduced clay altered silicified fault rock as clasts in the core zone of the quartz breccia
2- pervasively hematized host rock more in the damage zone and in the vicinity of the quartz breccia.

This fact characterizes the pervasive hematization associated with the QB, as being a “late” event in the history of the formation of the breccia.

7 CONCLUSIONS

7.1 CONCLUSIONS AT THE SCALE OF THE KIGGAVIK PROJECT

(1) A metallogenic model is presented based on an integrated multidisciplinary and multiscale approach. The fault and fracture networks are characterized by their geometry, crosscutting relationships, and their cements, illustrating the fluid-rock interaction at each stage of deformation and mineralization. Thus, a precise link is established between the circulation of the paleo-fluid and the specific tectonic event. This integrated methodology enabled us to (1) reconstruct the local and regional tectonic history, (2) to accurately characterize the fault and fracture networks in the Kiggavik area and (3) to ultimately propose a metallogenic model for the formation of uranium deposits in the Kiggavik area. This approach highlights the importance to integrate structural, petrographical and geochemical approaches for the characterization of the mineralization events and is a powerful tool to be applied to every structurally-controlled uranium deposit.

(2) The strain field and tectonic stresses are reconstructed by combining macroscopic (kinematic indicators observed on outcrops and drillcores) and microscopic (fluid inclusion planes directions) structural observations, therefore allowing to accurately stablish the link between regional tectonic stresses and paleo-fluid flow events. This approach allows framing the long-live and polyphased tectono-fluid history of the uranium deposits in the Kiggavik (and Thelon) area.

(3) The present work shows that the fracture network in the Kiggavik area is polyphased and complex with faults that were active through a very long period of time from ca. 1830 Ma (Late Hudson orogeny) to ca. 1267 Ma (emplacement of the MacKenzie dikes). The deciphered main fracture and mineralizing events are as follows:

- a first stage of uranium mineralization at ca. 1830 Ma (f0-U0), followed by brittle tectonic activity and associated clay alteration (f1) linked to development of the Baker Lake Basin (Baker Lake group and Wharton group; and cryptocrystalline silicification and quartz cemented breccia development (QB, f2). All these events occurred prior to deposition of the Thelon formation and designed the structural template of which various portions will be later reactivated and used as pathways for fluids.

- a second (f5-U1) and third stages (f6-U2) of uranium mineralization which belong to two distinct fracturing events with associated strong bleaching and illitization of the host rock (f8). These events occurred after the deposition of the Thelon formation (ca. 1667 Ma), prior to the emplacement of the MacKenzie dikes (ca. 1267 Ma).
- Then, weak reactivation of the fracture network occurred enhancing circulation of meteoric fluids (f9) and the remobilization and re-concentration of uranium oxides (U3) along redox fronts and lately, supergene in-situ alteration of tetravalent uranium minerals to hexavalent uranium minerals (f10) when the local redox conditions changed from reducing to oxidizing.

(4) A very significant and major tectonic event occurred in the Kiggavik area marked by the development of the Andrew Lake, Main zone and Judge Sissons faults that were reactivated several times and used as drains for the circulation of silica-rich fluids. Repeated cycles of fluid assisted brecciation, cataclasis and quartz cementation led to the formation of tens of meters-thick quartz breccias and pervasive extended iron oxidation of the host rock (QB). This event occurred lately in the deposition history of the Wharton group, associated with the emplacement of the Kivalliq igneous suite at ca. 1750 Ma. This silicifying event “reset” the permeability of the fault zones and changed the behaviour of the fluid pathway with two major consequences:

- the QB acted as a mechanical barrier partitioning deformation and localizing subsequent fracture reactivation within its damage zone.
- the well-quartz-sealed core of the QB acted as a barrier for fluids while damage zones acted as conduits. In the Kiggavik area, the economically significant uranium orebodies are located within the fractured hanging wall and footwall QB damage zones.

(5) This work has characterized three out of ten (f0 to f9) fracturing events that directly controlled the circulation of uranium bearing fluids and trapping of uranium mineralization.

- As already noted, the U0 event is a pre-Thelon Basin uranium mineralizing event that occurred at ca. 1.83 Ga, linked to the pery-granitic brecciation associated with the (partly) peralkaline magmatism of the Baker Lake group, emplaced under a likely strike-slip stress regime with a WSW-ENE trending σ1 and a NNW-SSE trending σ3. Mineralogical assemblage (e.g. hydrothermal rutile), chemical compositions of uranium oxides (displaying several percent of Thorium) and temperature of chlorite synchronous with this stage attest for the high temperature (>300°C) of the uranium bearing fluids and mineralization.

- F5 (U1) and f6 (U2) are two fracturing events associated with the circulation of uranium-bearing basinal brines, inferred to be derived from the Thelon Basin formation. During f5, less mature fault zones formed as a response to a strike-slip stress regime with a WNW-ESE trending σ1 and a NNE-SSW trending σ3. The damage zone of the quartz breccia was extensively reactivated during this stage and led to the precipitation of a polymetallic ore assemblage. During f6, extensively oxidized and more mature fault zones formed as a response to a different strike-slip stress regime with a NE-SW to ENE-WSW trending σ1 and a NW-SE to NNW-SSE trending σ3. This stage was accompanied with the precipitation of a monometallic ore assemblage. However, whole rock geochemical characterization highlights the enrichment in metals that are (i) probably derived from the U1 stage of mineralization, or (ii) likely reflect a stock of metals already depleted. The greater maturation and therefore the complexity of the fracture network linked to increased permeability of the affected basement rocks, likely increased fluid circulation and fluid-rock interaction during f6-U2.

(6) The combination of the structural analysis with the mineralogical and geochemical characterization of uranium-oxides and related alteration assemblages allowed determining the typology of the uranium deposits in the Kiggavik. The uranium deposits of Kiggavik are of mixed typeThey result from the combination of a pre-Thelon Basin magmatic origin (f0-U0) and a post-Thelon Basin unconformity-related (f5-U1 and f6-U2). The confirmation that part of these deposits are of unconformity type attests for the presence, now eroded, of the Thelon formation over the Kiggavik area. Although the thickness remains unconstrained, it had to be enough to generate diagenetic-hydrothermal fluids and convection cells as suggested by Chi et al., (2013). The depth of the Kiggavik uranium deposits below the Thelon Basin unconformity remains another unconstrained parameter.

(7) After the main fracturing events that led to the formation of the uranium orebodies in the Kiggavik area (f0 to f6), the fracture network was re-activated and re-used once again under an extensional stress regime (with a strike-slip component) with a ~NE-SW trending σ3 and a ~NW-SE trending σ1, inferred to be linked to the far tectonics and stress field occurring at the boundary of the Canadian shield and the Greenville Ocean spreading (Hou et al., 2010), before the emplacement of the MacKenzie dikes. Uranium orebodies were significantly offset and the uranium mineralization was remobilized by the hot and likely acidic fluids. These fluids induced iron oxides removal and strong illitization (f8). This alteration seems to be disconnected of any uranium input into the system and its timing is supported by Ar/Ar and K/Ar ages on illite realized

at several deposits and prospects in the area (ca. 1300 Ma). Such uranium remobilization under reducing conditions is unusual but recent modelling work by Timofeev et al. (2017) suggests that uranium can be mobilized in reducing conditions. In the Kiggavik area, Shabaga et al. (2017) also pointed out such a possibility.

7.2 UPSCALING AND REGIONAL CONCLUSIONS. COMPARISONS WITH THE ATHABASCA BASIN URANIUM DEPOSITS

(1) The first stage of uranium mineralization in the Kiggavik area (U0), along with other uranium occurrences in the Thelon-Baker Lake area, make of this area an uraniferous Province initiated with the emplacement of the Hudson, Dubawnt, and Kivalliq igneous suites, from ca. 1830 Ma to ca. 1750 Ma. Uranium enriched intrusions such as U-rich pegmatites and bostonites have been commonly identified in the area and associated to this pre-Thelon magmatism. The uranium mineralized breccia (U0) in the Kiggavik area and the pitchblende-hematite-chlorite-calcite gashes of the Lac Cinquante deposit (ca. 1830 Ma, Bridge et al., 2013) are two examples illustrating that, in addition to primary uranium mineralization (U-rich intrusions, U-rich lithologies such as epiclastic of the Wharton group), secondary uranium mineralization of economic interest could occur during pre-Thelon times. These uranium occurrences are highly comparable to those from the Beaverlodge area, NW Athabasca, where the main mineralizing events are associated with metamorphic to magmatic-related fluids (Dieng et al., 2015) at ca. 1850 and 1830 Ma. Moreover volcano-sedimentary formations of the Martin Lake basin (Beaverlodge) were described to be similar to the volcano-sedimentary formations of the Baker Lake basin (Donaldson, 1968; Rainbird et al., 2003a).

(2) Geochemical characterization of the fluids from the fluid inclusions and the quantification of the metals content through LA-ICP-MS, beyond helping characterize U1 and U2 as being unconformity-related in type, bring several significant conclusions:

- The mineralizing brines are NaCl/$CaCl_2$-rich display salinity and temperatures similar to those of the brines characterized in the Athabasca's and Kombolgie's (Australia) basins, suitable for the transport of uranium.
- Brines uranium concentrations are similar to those obtained for NaCl/$CaCl_2$-rich brines in Athabasca (Richard et al., 2010), although the concentrations in other metals, especially in B and Mg, are much lower. This would explain why, in the Kiggavik area, although B-

link alteration is documented through whole rock geochemical analysis there is no observed occurrences of Mg-foitite (dravite) typical in unconformity-related uranium deposits. Kandasami et al. (2015) showed that bore is contained in micro-crystalline dravite (trigonal coordination) or contained in illite (tetrahedral coordination).

- Two late minor fluid-circulation events, associated with weak fracturing, led to the precipitation of uranium at 1073±5 Ma and ca. 550 Ma in the Kiggavik area, such ages were also obtained in Athabasca. The first event at ca. 550 Ma bears the characteristic bell-shaped REE signature of unconformity-related deposits, and is therefore interpreted as a reset of the isotopic system through the circulation of meteoric fluids. Uranium oxides neoformed at 1073 ± 5 Ma displays an unconventional REE signature moreover much more enriched in REE. This signature not observed to date in Canadian and Australian Paleoproterozoic uranium deposits, is difficult to explain and could correspond to a modified unconformity-related REE signature by a fluid of unconstrained characteristics.

(3) The fine microstructural analysis made in this work, has shown that the fracturing event (f8) which is associated with strong illitization and bleaching of the host rock postdates the main stages of uranium mineralization in the Kiggavik area. This is a significant result because such clay alteration is commonly observed in most of the Thelon and Athabasca deposits and has always been interpreted as to be synchronous of the mineralizing events in the unconformity-type deposits. In Kiggavik, this strong alteration is responsible for the low gravity anomalies that helped to discover the uranium deposit. The spatial coincidence of mineralization and alteration in many deposits attests for the common structural pathways and traps used by fluids at different times. The diachronism between mineralization events and this late strong alteration can also explain why some zones of low gravity anomalies do not display any uranium mineralization and the possibility that existing mineralization has been leached out by this alteration cannot be discarded. We wonder if this alteration episode is removing uranium from the basement and transporting it upward to the unconformity and sandstones of the overlying basin.

7.3 IMPLICATIONS FOR URANIUM EXPLORATION IN THE THELON-BAKER LAKE AREA

This PhD demonstrates the importance of accurate and integrated structural, geochemical and geochronological studies on the understanding of the formation and evolution of structurally controlled uranium deposits. This work particularly shows how much important is to properly depict and characterize all fracturing events and which ones of them control circulation of uranium-bearing fluids and formation of ore deposits. This integrated approach, including the characterization of the related paleo-fluids and the reconstitution of the strain field and tectonic stresses are of great help and support to better understand uranium deposits in the area and to improve chances and success on future exploration opportunities.
This work points out the following conclusions concerning exploration:

(1) As demonstrated all through the present work, the primary control of fluid flow and uranium mineralization in the Kiggavik area is structural in nature. As exemplified by the discoveries of mineralization hosted within the Hudsonian granites in the 85W prospect, within granitic gneiss in the Contact prospect and within the Woodburn paragneiss in all of the other deposits, uranium mineralization can be expected in every lithology in the area containing sulfurs, or maybe chlorites, as reductants. The exception is the quartzites of the Ketyet Unit that are empty of those potential reductants preventing mineralization. In structural terms, what gives to a lithology its structural “potential” is the orientation of the pre-existing fractures and/or the foliation planes to respect a given stress regime and the aptitude to amplify fault reactivation and fracture propagation enhancing permeability. Although fractures control fluid flow through fracture permeability, the combination of both the geometrical (structural) and geochemical (reductants) traps are necessary to coexist in a place for mineralization to be developed.

(2) Although depicting the Thelon-Baker Lake area as an uraniferous Province is not a new concept (Curtis and Miller, 1980; Jefferson et al., 2014), the identification of pre-Thelon mineralizing event as producing economically significant initial uranium mineralization within the basement is a new and significant output. This statement, in addition to the recent re-attribution of some sediments from the Thelon formation to the Wharton group and the presence of evaporitic formations (Aspler et al., 2004; from which pre-Thelon brines could have been generated) within the Baker Lake basin increase the exploratory interest of the Thelon-Baker Lake area and basins, even out of low gravity anomalies.

(3) Future exploration in this area can now target, first, areas with intrusions from the Dubawnt and Kivalliq igneous suites that have been covered by volcanic-sedimentary formations of the Baker Lake and/or sediments of the Thelon basin. Then, exploration via geophysical surveys or field work can focus on targets (cartographic fault inflexions and bends reflecting fault relay zones) along long-live polyphased faults underlined by quartz-cemented breccia. These types of faults are the right uranium metallotects like the Andrew Lake and Judge Sisson faults in the Kiggavik area. The present knowledge of the tectonic stresses associated with uranium mineralizing events and the geometry and orientations of the pre-existing main faults, can be used for geomechanical fault modelling in order to predict and identify high potential for reactivation and mineralization of fault zones for each given tectonic episode.

(4) Vein-related quartz recorded circulation of uranium-bearing fluids and/or the precipitation of uranium oxides by showing specific luminescence and irradiation haloes. Cathodoluminescence is therefore a cheap and powerful technique that can be analysed on thin sections in order to depict fertile structures that drove uranium-bearing fluids.

(5) The post-ore clay-alteration event (f8) could reflect a remobilizing event of uranium oxides through the circulation of reducing, hot acidic fluids as discussed above. Remobilized uranium could have travelled upward to the unconformity or to the Thelon basin and have precipitated uranium in these locations, possibly when mixing with oxidizing brines. This would lead to the formation of perched uranium mineralization in the basin posterior to the main mineralizing event occurring in the basement.

7.4 PERSPECTIVES

(1) This work has brought new insights into the structural control on the uranium deposits of the Kiggavik area and allowed characterizing (1) an early mineralizing event (U0), and (2) two fracturing events associated with the circulation of uranium-bearing basinal brines (U1 and U2). This approach can be applied to other unconformity-related deposits in order to decipher mineralizing and fracturing events, potentially leading to the characterization of the tectonic history and associated fluid circulation. Such an approach applied for example in Athabasca could also bridge the gap between macro-scale structural studies (Baudemont and Federowich;

1996; Tourigny et al., 2007; Liang et al., 2017) and micro-scale structural studies (Mercadier et al., 2012; Wang et al., 2015: Martz et al., 2017).

(2) The understanding of the 3D architecture and geometry of main fault Andrew Lake, Main Zone, and Judge Sissons faults started with the structural study made at the Contact prospect and with the construction of block diagrams at Bong, Kiggavik Main Zone, Andrew Lake and Contact. Although our understanding of the structural control on uranium deposits in the Kiggavik area has been greatly improved, a significant work is still needed in order to precisely characterize the geometry of the fault zones that host the economic uranium mineralization: fault bending zones or fault relay zones versus fault tips location, type of fault relay zones (hard-linked vs soft-linked, underlapping vs overlapping, both vertically and laterally) and their maturity (breached relay or not?)

In the continuity of the characterization of the tectonic events which started with the study of the kinematic indicators and the associated reconstruction of the tectonic stresses, the analysis of twinning in calcite crystals (generation associated with U1), which presumably result from one or several applied stress regimes, would confirm the orientations of principal stress axes but more interestingly would possibly allow to obtain associated differential stresses (Etchecopar, 1984; Parlangeau et al., 2018). Reconstruction of differential stresses would make modelling of the reactivated faults more accurate (see point 2 in exploration's perspectives).

(3) A stronger characterization of U0 in term of fracturing geometry, fluid characteristics and chronology (through characterization of uranium oxides), would led to a more accurate definition of this mineralizing stage, which would have implications in term of exploration as well. Along with the characterization of U0, other uranium occurrences in the Thelon-Baker lake area should be re-examined under the light of new genetic models (and more precise analytic tools) in order to increase the comprehension of the processes leading to uranium mineralization in this uraniferous Province.

(4) Measuring the isotopic signatures of carbon and oxygen in carbonates will help constrain the origin of the fluids that circulated in the Kiggavik area, those associated with uranium mineralization and the differences between U1 and U2, as two generations of calcite were demonstrated to be linked to these two mineralizing events.

(5) Better constraining the timing of the fracturing and mineralizing event could be done through age-dating studies of the carbonate veins (U/Pb isotopic system, e.g. Goodfellow et al., 2017) associated to U1 and U2 and coupled with age dating on hydrothermal rutiles associated with U0 and U1 (however potentially limited by the size of the crystals. e.g. Pi et al., 2017). Moreover, having now precisely deciphered the fracturing events, each faulting event associated with synkinematic illite in fractures and illitic alteration (observed throughout the whole history, from pre-QB to post uranium mineralization timing) could be dated through K-Ar isotopic analysis (e.g. Viola et al., 2016).

(5) A better characterization of the “altered” luminescence of quartz spatially associated with the uranium mineralization would be useful for calibrating the relationship between pink-reddish to deeper red, yellow and greenish colours and durations of contact between uranium oxides and quartz crystals (stronger destabilization of the crystal lattice).

REFERENCES

Alexandre, P., Kyser, K., and Polito, P., 2003. Geochronology of the Paleoproterozoic basement-hosted unconformity-type uranium deposits in northern Saskatchewan, Canada: Uranium Geochemistry 2003, International Conference, Université Henri Poincaré, Nancy, France, April 13-16, 2003, Proceedings, p. 37-40.

Alexandre, P., Kyser, K., Polito, P., and Thomas, D. 2005a. Alteration mineralogy and stable isotope geochemistry of Paleoproterozoic basement-hosted unconformity-type uranium deposits in the Athabasca Basin, Canada; Econ. Geol., v100, p1547-1563.

Alexandre, P., Kyser, T.K., 2005b. Effects of cationic substitutions and alteration in uraninite, and implications for the dating of uranium deposits. Can. Mineral. 43, 1005–1017. doi:10.2113/gscanmin.43.3.1005

Alexandre, P., Kyser, T.K., 2007. Geochemistry of uraniferous bitumen in the southwest Athabasca Basin, Saskatchewan, Canada. Econ. Geol. 101, 1605–1612.

Alexandre, P., Kyser, K., Thomas, D., Polito, P., Marlat, J., 2009. Geochronology of unconformity-related uranium deposits in the Athabasca Basin, Saskatchewan, Canada and their integration in the evolution of the basin. Miner. Depos. 44, 41–59. doi:10.1007/s00126-007-0153-3

Anand, A., and Jefferson, C.W., 2017. Reactivated fault systems and their effects on outcrop patterns of thin-skinned early thrust imbrications in the Kiggavik uranium camp, Nunavut, Geological Survey of Canada, Open File 7895, 2017, 9 pages (1 sheet), https://doi.org/10.4095/302776

Aspler, L.B., Chiarenzelli, J.R., Cousens, B.L., 2004. Fluvial, lacustrine and volcanic sedimentation in the Angikuni sub-basin, and initiation of ~1.84–1.79 Ga Baker Lake Basin, western Churchill Province, Nunavut, Canada. Precambrian Res. 129, 225–250. doi:https://doi.org/10.1016/j.precamres.2003.10.004

Barbey, P., Cuney, M., 1982. K, Rb, Sr, Ba, U and Th geochemistry of the Lapland Granulites (Fennoscandia). LILE fractionation controlling factors. Contrib. to Mineral. Petrol. 81, 304–316. doi:10.1007/BF00371685

Basson, I.J., Greenway, G., 2004. The Rössing Uranium Deposit: a product of late-kinematic localization of uraniferous granites in the Central Zone of the Damara Orogen, Namibia. J. African Earth Sci. 38, 413–435. doi:https://doi.org/10.1016/j.jafrearsci.2004.04.004

Baudemont, D., and Federowich, J., 1996. Structural control of uranium mineralization at the Dominique-Peter deposit, Saskatchewan, Canada: Economic Geology, v. 91, p. 855-874.

Baudemont, D., and Pacquet, A., 1996. The Sue D and E uranium deposits, northern Saskatchewan: Evidence for structurally controlled fluid circulation in the Athabasca Basin, inAshton, K.E., and Harper, C.T., eds., MinExpo'96 Symposium-Advances in Saskatchewan Geology and Mineral Exploration: Saskatchewan Geological Society, Special Publication No. 14, p. 85-94.

Baudemont, D., and Reilly, B., 1997. Thelon Project – 1997 Reconnaissance Mapping and Structural Geology. Cogema internal report. 97-CND-100-01. 43p.

Berman, R. G., Davis, W. J., and Pehrsson, S., 2007. Collisional Snowbird tectonic zone resurrected: Growth of Laurentia during the 1.9 accretionary phase of the Hudsonian orogeny: Geology, v. 35, no. 10, p. 911-914.

Berning, J., Cooke, R., Hiemstra, S.A., Hoffman, U., 1976. The Roessing uranium deposit, South West Africa. Econ. Geol. 71, 351–368. doi:10.2113/gsecongeo.71.1.351

Beshears, C.J., 2010. The geology and geochemistry of the Millennium uranium deposit, Athabasca Basin, Saskatchewan, Canada: Unpublished M.Sc. thesis, Winnipeg, Canada, University of Manitoba, 133 p.

Betts, P., Giles, D., Schaefer, B., 2008. Comparing 1800-1600 Ma accretionary and basin processes in Australia and Laurentia: Possible geographic connections in Columbia. Precambrian Res. 166, 81–92.

Beyer, S.R., Kyser, K., 2010. Applying the Concept of "Holistic" Basin Analysis to Unconformity-related Uranium Prospects in Under-explored Paleoproterozoic Basins 1–4.

Bosman, S.A., and Ramaekers, P., 2015. Athabasca Group + Martin Group = Athabasca Supergroup? Athabasca Basin multiparameter drill log compilation and interpretation, with updated geological map; in Summary of Investigations 2015, Volume 2, Saskatchewan Geological Survey, Saskatchewan Ministry of the Economy, Miscellaneous Report 2015-4.2, Paper A-5, 13p.

Bray, C.J., Spooner, E.T.C., Longstaffe, F.J., 1988. Unconformity-related uranium mineralization, McClean deposits, north Saskatchewan, Canada; hydrogen and oxygen isotope geochemistry. Can. Mineral. 26, 249–268.

Bright, S., Conner, G., Turner, A., Vearncombe, J., 2014. Drillcore, structure and digital technologies. Appl. Earth Sci. 123, 47–68. doi:10.1179/1743275814Y.0000000051

Bridge, N., Banerjee, N., S. Finnigan, C., Carpenter, R., Ward, J., 2009. The Lac Cinquante Uranium Deposit, Nunavut, Canada. AGU Fall Meet. Abstr.

Cerin, D., Götze, J., Pan, Y., 2017. Radiation-Induced Damage In Quartz At the Arrow Uranium Deposit, Southwestern Athabasca Basin, Saskatchewan. Can. Mineral. 55, 457–472. doi:10.3749/canmin.1700003

Chamberlain, K.R., Schmitt, A.K., Swapp, S.M., Harrison, T.M., Swoboda-Colberg, N., Bleeker, W., Peterson, T.D., Jefferson, C.W., Khudoley, A.K., 2010. In situ U–Pb SIMS (IN-SIMS) micro-baddeleyite dating of mafic rocks: Method with examples. Precambrian Res. 183, 379–387. doi:10.1016/j.precamres.2010.05.004

Cheney, E.S., 1985. Similarities between roll-front and Athabasca unconformity-type uranium deposits and the possible role of sulfides in their origin; inSibbald, T.I.I. and Petruk, W. (eds.), Geology of Uranium Deposits, CIM, Spec. Vol. 32, 268p.

Chester, F.M., Logan, J.M., 1986. Implications for mechanical properties of brittle faults from observations of the Punchbowl fault zone, California. Pure Appl. Geophys. 124, 79–106. doi:10.1007/BF00875720

Chi, G., Bosman, S., Card, C., 2013. Numerical modeling of fluid pressure regime in the Athabasca basin and implications for fluid flow models related to the unconformity-type uranium mineralization. J. Geochemical Explor. 125, 8–19. doi:https://doi.org/10.1016/j.gexplo.2012.10.017

Chi, G., Haid, T., Quirt, D., Fayek, M., Blamey, N., Chu, H., 2017. Petrography, fluid inclusion analysis, and geochronology of the End uranium deposit, Kiggavik, Nunavut, Canada. Miner. Depos. 1–22. doi:10.1007/s00126-016-0657-9

Chipley, D., Polito, P.A., Kyser, T.K., 2007. Measurement of U-Pb ages of uraninite and davidite by laser ablation-HR-ICP-MS. Am. Mineral. 92, 1925–1935. doi:10.2138/am.2007.2226

Cloutier, J., Kyser, K., Olivo, G.R., Alexandre, P., and Halaburda, J., 2009. The Millennium Uranium Deposit, Athabasca Basin, Saskatchewan, Canada: An Atypical Basement-Hosted Unconformity-Related Uranium Deposit. Econ. Geol. 104 , 815–840. doi:10.2113/ gsecongeo.104.6.815

Cloutier, J., Kyser, K., Olivo, G.R., and Alexandre, P., 2010. Contrasting patterns of alteration at the wheeler river area, Athabasca Basin, Saskatchewan, Canada: insights into the apparently uranium-barren zone K alteration system. Econ. Geol. 105 (2), 303–324.

Cloutier, J., Kyser, K., Olivo, G.R., and Brisbin, D. 2011. Geochemical, isotopic, and geochronologic constraints on the formation of the Eagle Point basement-hosted uranium deposit, Athabasca Basin, Saskatchewan, Canada and recent remobilization of primary uraninite in secondary structures; Mineral. Dep., online first, DOI: 10.1007/s00126-010-0308-5Cui, T., Yang, J., and Samson, I.M., 2012. Tectonic deformation and fluid flow: implications for the formation of unconformity-related uranium deposits. Econ. Geol. 107 (1), 147–163.

Cui, T., Yang, J., and Samson, I.M., 2012. Tectonic deformation and fluid flow: implications for the formation of unconformity-related uranium deposits. Econ. Geol. 107 (1), 147–163.

Cumming, G.L., and Krstic, D., 1992. The age of unconformity-associated uranium mineralization in the Athabasca Basin, northern Saskatchewan: Canadian Journal of Earth Sciences, v. 29, p. 1623-1639.

Cuney, M., Leroy, J., and Pagel, M., 1992. L'uranium; Que sais-je ? Presses Universitaires de France, Paris. 123p.

Cuney, M., Brouand, M., Cathelineau, M., Derome, D., Freiberger, R., Hecht, L., Kister, P., Lobaev, V., Lorilleux, G., Peiffert, C., and Bastoul, A.M., 2003. What parameters control the high grade - large tonnage of the Proterozoic unconformity related uranium deposits?: Uranium Geochemistry 2003, International Conference, Nancy, France, April 13-16 2003, Proceedings, p. 123-126.

Cuney, M., Kyser, K., 2009. Recent and Not-So-Recent Developments in Uranium Deposits and Implications for Exploration. Econ. Geol. 104, 600–601.

Cuney, M., 2011. Uranium and thorium: The extreme diversity of the resources of the world's energy minerals. In: Sinding-Larsen R, Wellmer FW (eds), Non-Renewable Resource Issues: Geoscientific and Societal Challenges, International Year of Planet Earth, Springer, 91-129

Cuney, M., 2014. Felsic magmatism and uranium deposits. Bull. la Soc. Geol. Fr. 185, 75–92.

Cuney, M., 2015. A Genetic Classification of Uranium Deposits. In SGA Extended abstract proceedings of the 12th Biennial SGA Meeting, SGA 2015 held in Uppsala, Sweden, 2013

Cuney, M., Kyser, T.K., Mineralogical Association of Canada, 2015. The geology and geochemistry of uranium and thorium deposits.

Curtis, L., and Miller, A.R., 1980. Uranium geology in the Amer-Dubawnt-Yathkyed-Baker Lake region, Keewatin district, N.W.T., Canada. In Uranium in the Pine Creek geosyncline, J. Ferguson, and A. B. Golebys (eds), 595-616. Vienna: International Atomic Energy Agency.

Dahlkamp, F., J., 1993. Uranium ore deposits. Springer-Verlag, Berlin, 460p.

Dargent, M., Dubessy, J., Truche, L., F Bazarkina, E., Nguyen-Trung, C., Robert, P., 2013. Experimental study of uranyl(VI) chloride complex formation in acidic LiCl aqueous solutions under hydrothermal conditions (T = 21 °C-350 °C, Psat) using Raman spectroscopy. Eur. J. Mineral. 25.

Davis and Zaleski, 1998. Geochronological investigations of the Woodburn Lake group western Churchill Province: preliminary results. In Radiogenic Age and Isotopic Studies, Report 11; Geological Survey of Canada, Current Research 1998-F, p89-97.

Davis, W.J., Gall, Q., Jefferson, C.W., Rainbird, R.H., 2011. Fluorapatite in the Paleoproterozoic Thelon Basin: Structural-stratigraphic context, in situ ion microprobe U-Pb ages, and fluid-flow history. GSA Bull. 123, 1056–1073.

Depiné, M., Frimmel, H.E., Emsbo, P., Koenig, A.E., Kern, M., 2013. Trace element distribution in uraninite from Mesoarchaean Witwatersrand conglomerates (South Africa) supports placer model and magmatogenic source. Miner. Depos. 48, 423–435. doi:10.1007/s00126-013-0458-3

Derome, D., Cuney M., Cathelineau, M., Fabre, C., and Lhomme, T., 2002. Reconstitution of individual fluid inclusion composition using microthermometry, Raman and Laser Induced Breakdown Spectroscopy: Application to the Shea Creek uranium deposit (Saskatchewan, Canada), in Abstracts Volume, SS18: The Athabasca Basin and Its Uranium Deposits: Geological Association of Canada - Mineralogical Association of Canada, Annual Meeting, Saskatoon, 1 p.

Derome, D., Cathelineau, M., Cuney M., and Fabre. C., 2003a. Reconstitution of the P, T, X properties of paleo-fluids in the McArthur River unconformity-type uranium deposit (Saskatchewan, Canada): Uranium Geochemistry 2003, International Conference, Nancy, France, April 13-16 2003, Proceedings, p. 141-144.

Derome, D., Cuney, M., Cathelineau, M., Fabre, C., Dubessy, J., Bruneton, P., Hubert, A., 2003b. A detailed fluid inclusion study in silicified breccias from the Kombolgie sandstones (Northern Territory, Australia): inferences for the genesis of middle-Proterozoic unconformity-type uranium deposits. J. Geochemical Explor. 80, 259–275. doi:http://dx.doi.org/10.1016/S0375-6742(03)00194-8

Derome D., Cathelineau M., Cuney M., Fabre C., Lhomme T. and Banks D. A. 2005. Mixing of sodic and calcic brines and uranium deposition at McArthur River, Saskatchewan, Canada: a Raman and laser-induced breakdown spectroscopic study of fluid inclusions. Econ. Geol. 100, 1529–1545.

Dieng, S., Kyser, K., Godin, L., 2013. Tectonic history of the North American shield recorded in uranium deposits in the Beaverlodge area , northern Saskatchewan , Canada. Precambrian Res. 224, 316–340. doi:10.1016/j.precamres.2012.09.011

Dieng, S., Kyser, K., Godin, L., 2015. Genesis of Multifarious Uranium Mineralization in the Beaverlodge Area, Northern Saskatchewan, Canada. Econ. Geol. 110, 209–240.

Diouly-Osso, P., & Chauvet, R. J., 1979. Les Gisements D'uranium de la Region de Franceville (Gabon). In Uranium deposits in Africa: geology and exploration. Proceedings of an IAEA regional advisory group meeting, Lusaka pp. 123-147.

Donaldson, J.A. 1965. The Dubawnt Group, District of Keewatin and MacKenzie; Geological Survey of Canada, Paper 64-20.

Donaldson, J.A., 1968. Proterozoic sedimentary rocks of northern Saskatchewan, Report of Activities, Part A. Geological Survey of Canada, Paper, 68-1, p. 131.

Elliott-Meadows, S.R., Appleyard, E.C., 1991. The alteration geochemistry and petrology of the Lar Cu-Zn deposit, Lynn Lake area, Manitoba, Canada. Economic Geology; 86 (3): 486–505. doi: https://doi.org/10.2113/gsecongeo.86.3.486

Eriksson, P.G., Martins-Neto, M.A., Nelson, D.R., Aspler, L.B., Chiarenzelli, J.R., Catuneanu, O., Sarkar, S., Altermann, W., Rautenbach, C.J.D.W., 2001. An introduction to Precambrian basins; their characteristics and genesis; The influence of magmatism, tectonics, sea level change and paleo-climate on Precambrian basin evolution; change over time. Sediment. Geol. doi:10.1016/S0037-0738(01)00066-5

Etchecopar, A., 1984. Etudes des états de contraintes en tectonique cassante et simulations de deformations plastiques (approaches mathématiques). Université des Sciences et Techniques du Languedoc.

Farkas, A., 1984, Mineralogy and host rock alteration of the Lone Gull deposit: Urangesellschaft Internal Report, 44 p.

Faulkner, D.R., Jackson, C.A.L., Lunn, R.J., Schlische, R.W., Shipton, Z.K., Wibberley, C.A.J., Withjack, M.O., 2010. A review of recent developments concerning the structure, mechanics and fluid flow properties of fault zones. J. Struct. Geol. 32, 1557–1575. doi:10.1016/j.jsg.2010.06.009

Fayek, M. and Kyser, K. 1997. Characterization of multiple fluid-flow events and rare-earth elements mobility associated with formation of unconformity uranium deposits in the Athabasca basin, Saskatchewan; Can. Mineral., v35, p627-658.

Fayek, M., Harrison, T.M., Ewing, R.C., Grove, M., and Coath, C.D., 2002. O and Pb isotope analyses of uranium minerals by ion microprobe and U-Pb ages from the Cigar Lake deposit: Chemical Geology, v. 185, p. 205-225.

Fayek, M., Camacho, A., Beshears, C., Jiricka, D., Halaburda, J., 2010. Two sources of uranium at the Millennium uranium deposit, Athabasca basin, Saskatchewan, Canada. Geological Association of Canada—Mineralogical Association of Canada 2010 (Calgary) Annual Conference Abstracts Volume, p. 4

Fayek, M., Quirt, D., Jefferson, C., Camacho, A., Ashcroft, G., Shabaga, B., Sharpe, R. 2017. The Kiggavik-Andrew Lake structural trend uranium deposits: an overview. In SGA Extended Abstract proceedings. SGA 2017 Conference Quebec City, August 20-23. In press.

Feybesse, J-L., 2010. Sequence of structural events in the Kiggavik district (Nunavut, Canada): The uranium mineralization in its geological and tectonic setting and structural control on the ore bodies geometry. AREVA BGM/DGS.

Flotté, N., 2009. END-grid geological observations and interpretations & 3D modeling in Gocad. ARC internal report. 108pp.

Fredrickson, J.K., Zachara, J.M., Kennedy, D.W., Duff, M.C., Gorby, U.A., Li, S-M.W., and Krupka, K.M., 2000. Reduction of U(VI) in goethite (α-FOOH) suspensions by a dissimilatory metal-reducing bacterium. Geochimica et Cosmochimica Acta, 64, 3085-3098.

Friedrich, G., Weyer, H.J., and Bechtel, A. 1989. The Lone Gull uranium deposit – New geochemical and petrological data as evidence for the nature of the ore-bearing solutions. In: Proceedings of an IAEA Technical Committee Meeting on Metallogenesis of Uranium Deposits, March 9-12 1987, IAEA TC-542/19, p. 293-306.

Fuchs, H.D., Hilger, W., and Prosser, E., 1986. Geology and exploration history of the Lone Gull property, in Evans, L., ed., Uranium Deposits of Canada: Canadian Institute of Mining and Metallurgy Special Volume 33, p. 286-292

Fuchs, H.D., Hilger, W., 1989. Kiggavik (Lone Gull): An unconformity related uranium deposit in the Thelon basin, northwest territories, Canada, Uranium resources and geology of North America

Gaboreau, S., Cuney, M., Quirt, D., Beaufort, D., Patrier, P., Mathieu, R., 2007. Significance of aluminum phosphate-sulfate minerals associated with U unconformity-type deposits: The Athabasca basin, Canada. Am. Mineral. - AMER Miner. 92, 267–280.

Gall, Q., Peterson, T.D., and Donaldson, J.A. 1992. A proposed revision of early Proterozoic stratigraphy of the Thelon and Baker Lake basins, Northwest Territories. Geological Survey of Canada Current Research Paper, 92-01C: 129–137.

Gandhi, S., Potter, E., Fayek, M., 2013. Polymetallic U-Ag veins at Port Radium, Great Bear magmatic zone, Canada: main botryoidal pitchblende stage cuts 1.74 Ga diabase dykes and has REE signatures diagnostic of unconformity-type deposits. Geological Survey of Canada, Open File 7493, 2013, 1 sheet, https://doi.org/10.4095/293118

Gatzweiler, R., 1987. Uranium mineralization in the Proterozoic Otish Basin, central Quebec, Canada. Berlin-Stuttgart, Gebrüder Borntaeger, Monograph Series on Mineral Deposits, 27, pp. 27-48.

Goodfellow, B., Viola, G., Bingen, B., Nuriel, P., Kylander-Clark, A., 2017. Palaeocene faulting in SE Sweden from U-Pb dating of slickenfibre calcite. Terra Nov. 29.

Götze, J., Pan, Y., Stevens-Kalceff, M., Kempe, U., Müller, A., 2015. Origin and significance of the yellow cathodoluminescence (CL) of quartz. Am. Mineral. . doi:10.2138/am-2015-5072

Grare, A., Benedicto, A., Lacombe, O., Trave, A., Ledru, P., Robbins, J., and Blains, M., 2017. Structural controls on uranium mineralization at the Kiggavik Project (NE Thelon area, Canada). In SGA Extended abstract proceedings of the 14th Biennial SGA Meeting,

Quebéc, Canada, Volume 2. p739. SGA 2017 Conference in Quebec City, August 20-23. ISBN: 978-2-9816898-0-1

Györfi, I., Z. Hajnal, D. J. White, E. Takacs, B. Reilkoff, I. R. Annesley, B. Powell and R. Koch, 2007, High resolution seismic survey from the McArthur River region; contributions to mapping the complex P2 uranium ore zone, Athabasca Basin Saskatchewan, EXTECH IV: Geology and Uranium Exploration Technology of the Proterozoic Athabasca Basin, Saskatchewan and Alberta, Edit. C. W. Jefferson, and G. Delaney; GSC Bull. 588; SGS Special Pub. 18; GAC (Mineral Deposits Division) Special Pub. 4; 397-412.

Hadlari, T., and Rainbird, R.H., 2011. Retro-arc extension and continental rifting: a model for the Paleoproterozoic Baker Lake Basin, Nunavut1Geological Survey of Canada Contribution 20100436. Can. J. Earth Sci. 48, 1232–1258. doi:10.1139/e11-002

Haid, T., 2014. Petrographic and fluid inclusion studies of the End uranium deposit, Kiggavik, Nunavut, Canada. Unpublished BSc.Honours thesis, University of Regina, 87p.

Hanmer, S, Williams, ML, Kopf, C., 1995. Striding-Athabasca mylonite zone: implications for the Archean and Early Proterozoic tectonics of the Western Canadian shield. CanadianJournal of Earth Sciences 32:178-196.

Hansley, P. L., Collings, S. P., Brownfield, I. K., & Skipp, G. L. (1989). Mineralogy of uranium ore from the Crow Butte uranium deposit, Oligocene Chadron Formation, northwestern Nebraska (No. 89-225). US Geological Survey.

Harvey, S.E., and Bethune, K., 2007. Context of the Deilmann orebody, Key Lake mine, Saskatchewan, in Jefferson, C.W., and Delaney, G., eds., EXTECH IV: Geology and Uranium EXploration TECHnology of the Proterozoic Athabasca Basin, Saskatchewan and Alberta: Geological Survey of Canada, Bulletin 588, (also Geological Association of Canada, Mineral Deposits Division, Special Publication 4; Saskatchewan Geological Society, Special Publication 18), p. 249-266.

Hasegawa, K., Davidson, G.I., Wollenberg, P., and Lida, Y., 1990. Geophysical exploration for unconformity-related uranium deposits in the northeastern part of the Thelon Basin. Northwest Territories, Canada: Mining Geology, 40, p. 83–95.

Heaman, L.M., LeCheminant, A.N., 1993. Paragenesis and U-Pb systematics of baddeleyite (ZrO2). Chem. Geol. 110, 95–126. doi:http://dx.doi.org/10.1016/0009-2541(93)90249-I

Hecht, L., and Cuney, M., 2000. Hydrothermal alteration of monazite in the Precambrian crystalline basement of the Athabasca Basin (Saskatchewan, Canada): implications for the formation of unconformity-related uranium deposits. Mineral. Deposita 35, 791–795.

Hiatt, E.E., Kyser, T.K. and Dalrymple, R.W. 2003. Relationships among sedimentology, stratigraphy and diagenesis in the Proterozoic Thelon Basin, Nunavut, Canada: implications for paleo-aquifers and sedimentary-hosted mineral deposits; Journal of Geochemical Exploration, 80, 221-240.

Hiatt, E.E., Palmer, S.E., Kyser, Kurt, E., O'Connor, Terrence, K., 2010. Basin Evolution, Diagenesis and Uranium Mineralization in the Paleoproterozoic Thelon Basin, Nunavut, Canada.

Hoeve, J., and Quirt, D.H., 1984. Mineralization and Host Rock Alteration in Relation to Clay Mineral Diagenesis and Evolution of the Middle-Proterozoic, Athabasca Basin, northern Saskatchewan, Canada: Saskatchewan Research Council, SRC Technical Report 187, 187 p.

Hoeve, J., and Sibbald, T.I., 1978. On the genesis of Rabbit Lake and other unconformity- type uranium deposits in northern Saskatchewan, Canada. Econ. Geol. 73 (8),1450–1473.

Hoffman, P., F., 1988. United Plates of America, The Birth of a Craton: Early Proterozoic Assembly and Growth of Laurentia. Annual Review of Earth and Planetary Sciences 16:543-603. doi: doi:10.1146/annurev.ea.16.050188.002551.

Holk, G.J., Kyser, T.K., Chipley, D., Hiatt, E.E., Marlatt, J., 2003. Mobile Pb-isotopes in Proterozoic sedimentary basins as guides for exploration of uranium deposits. J. Geochemical Explor. 80, 297–320. doi:10.1016/S0375-6742(03)00196-1.

Hou, G., Kusky, T.M., Wang, C., Wang, Y., 2010. Mechanics of the giant radiating MacKenzie dyke swarm: A paleostress field modeling. J. Geophys. Res. Solid Earth 115, n/a-n/a. doi:10.1029/2007JB005475

Hu, B., Pan, Y., Botis, S., Rogers, B., Kotzer, T., Yeo, G., 2008. Radiation-induced defects in drusy quartz, Athabasca Basin, Canada: a new aid to exploration of uranium deposits. Econ Geol 103:1571–1580

IAEA, 2014. Resources, Production and Demand. NEA No. 7209, OECD 2014, 504p.

Iida, Y., 1998. Geochemical and mineralogical studies, 1997 Sissons Project. Areva Resources Canada internal report, Cogema Library, PNC Tono Geoscience Center. 97-CAD-93-09. 169p.

Ifill, R., 1989. Mineralogical and process controls on the oxidative acid-leaching of radioactive phases in Elliot Lake, Ontario, uranium ores: I - uraninite, uranothorite and monazite. CIM Bull. 82, 65.

Jaireth, S., Roach, I.C., Bastrakov, E., Liu, S., 2016. Basin-related uranium mineral systems in Australia: A review of critical features. Ore Geol. Rev. 76, 360–394. doi:https://doi.org/10.1016/j.oregeorev.2015.08.006

Jamieson, B. W., 2000. Mining the high grade McArthur River uranium deposit. The Uranium Production Cycle and the Environment, 2, 272.

Jefferson, C.W., Thomas, D.J., Gandhi, S.S., Ramaekers, P., Delaney, G., Brisbin, D., Cutts, C., Quirt, D., Portella, P., and Olson, R.A., 2007. Unconformity-Associated Uranium Deposits of the Athabasca Basin, Saskatchewan and Alberta. In: Goodfellow, W.D. (Ed.), Mineral Deposits of Canada: A Synthesis Of Major Deposit Types, District Metallogeny, The Evolution Of Geological Provinces, And Exploration Methods. Geological Assoiciation of Candada, Special Publication 5, pp. 273–305

Jefferson, C.W., Chorlton. L.B., Pehrsson, S.J., Peterso, T.D.,. Wollenberg, P., Scott, J., Tschirhart, V., McEwan, B., Bethune, K., Calhoun, L., White, J.C., Leblon, B. LaRocque, A. Shelat, Y., Lentz, D., Patterson, J., Riegler, T., Skulski, Tobinson, S., Paulen, R., McClenaghan, M.B., Layton-Matws, D., MacIsaac, D., Riemer, W., Stieber, C., and Tschirhart, P., 2011. Northeast Thelon Region: Geomapping for Uranium in Nunavut; Geological Survey of Canada, Open File 6962, 1 CD-ROM. doi:10.4095/289037.

Jefferson, C.W., Pehrsson, S., Peterson, T., Wollenberg, P., Tschirhart, V., Riegler, T., McEwan, B., Tschirhart, P., Scott, J., Chorlton, L., Davis, W., Bethune, K., Riemer, W., Patterson, J., Morris, W.A., Anand, A., and Stieber, C. 2013. Bedrock geology of the western Marjorie-Tehek supracrustal belt and Northeast Thelon Basin margin in parts of NTS 66A and 66B, Nunavut; Geological Survey of Canada, Open File 7241

Jefferson, C.W., Peterson, T., Tschirhart, V., Davis, W., Scott, J.M.J., Reid, K., Ramaekers, P., Gandhi, S.S., Bleeker, W., Pehrsson, S., Morris, W.A., Fayek, M., Potter, E., Bridge, N., Grunsky, E., Keating, P., Ansdell, K., and Banerjee, N. 2014. LIPs and Proterozoic uranium

(U) deposits of the Canadian Shield. Geological Survey of Canada, Open File 7352. doi:10.4095/292377.

Jefferson, C.W., White, J.C., Young, G.M., Patterson, J., Tschirhart, V.L., Pehrsson, S.J., Calhoun, L., Rainbird, R.H., Peterson, T.D., Davis, W.J., Tella, S., Chorlton, L.B., Scott, J.M.J., Percival, J.A., Morris, W.A., Keating, P., Anand, A., Shelat, Y., and MacIsaac, D. 2015. Outcrop and remote predictive geology of the Amer Belt and basement beside and beneath the northeast Thelon Basin, in parts of NTS 66-A, B, C, F, G and H, Kivalliq Region, Nunavut. Geological Survey of Canada, Open File 7242, 1 sheet. doi:10.4095/296825

Johnstone, D., Bethune, K.M., Quirt, D., Benedicto, A. 2017. Lithostratigraphic and structural controls of uranium mineralization in the Kiggavik East, Centre and Main Zone deposits, Nunavut. In Proceedings of the Geological Association of Canada-Mineralogical Association of Canada, Joint Annual Meeting, Whitehorse Yukon, June 1-3 2016

Kandasami, T., 2015. Integrated geochemical fingerprinting of uranium deposits for sustainable exploration and development. Unpublished BSc.Honours thesis, University of Western Ontario, 98p.

Kerans, C., Ross, G.M., Donaldson, J.A., Geldsetzer, H.J., 1981. Tectonism and depositional history of the Helikian Hornby Bay and Dismal Lakes groups, District of MacKenzie. In: F.H.A. Campbell (Editors). Geol. Surv. Can. Pap., 81-10 (1981), pp. 157-182

Kheloufi, A. 2007. Estimation et calcul d'incertitudes des ressources géologiques en U dans la région de Kiggavik-Sissons (Canada, 49 Septembre 2007). Rapport interne: BUM/DTD/SER RT 06/025. 81pp.

Kister, P., Cuney, M., Golubev, V.N., Royer, J.-J., Le Carlier De Veslud, C., Rippert, J.-C., 2004. Radiogenic lead mobility in the Shea Creek unconformity-related uranium deposit (Saskatchewan, Canada): migration pathways and Pb loss quantification. Comptes Rendus Geosci. 336, 205–215. doi:http://dx.doi.org/10.1016/j.crte.2003.11.006

Kister, P., Vieillard, P., Cuney, M., Quirt, D., Laverret, E., 2005. Thermodynamic constraints on the mineralogical and fluid composition evolution in a clastic sedimentary basin: the Athabasca Basin (Saskatchewan, Canada). Eur. J. Mineral. 17, 325–341. doi:10.1127/0935-1221/2005/0017-0325.

Kister, P., Laverret, E., Quirt, D., Cuney, M., Mas, P.P., Beaufort, D., Bruneton, P., 2006. Mineralogy and geochemistry of the host-rock alterations associated with the Shea Creek

unconformity-type uranium deposits (Athabasca Basin, Saskatchewan, Canada). Part 2. Regional-scale spatial distribution of the Athabasca Group sandstone matrix mineral. Clays and Clay Miner. 54, 295–313.

Koeppel, V., 1967. Age and History of Uranium Mineralization of the Beaverlodge Area, Saskatchewan: Geological Survey of Canada, Paper 67-31, 111 p.

Komuro, K.H., Orikawa, Y., Toyada, S., 2002. Development of radiation-damage halos in low-quartz: cathodoluminescence measurement after He + ion implantation. Mineral. Petrol. 76, 261-266

Kotzer, T.G., Kyser, T.K., 1995. Petrogenesis of the Proterozoic Athabasca Basin, northern Saskatchewan, Canada, and its relation to diagenesis, hydrothermal uranium mineralization and paleohydrogeology. Chem. Geol. 120, 45–89. doi:https://doi.org/10.1016/0009-2541(94)00114-N

Kraishan, G., Rezaee, R., Worden, R., 2009. Significance of Trace Element Composition of Quartz Cement as A Key to Reveal the Origin of Silica in Sandstones: An Example from the Cretaceous of the Barrow Sub-Basin, Western Australia 29, 317–331.

Krauskopf, K.B., 1979. Introduction to Geochemistry. 2nd ed., McGraw-Hill, London

Kremenetsky, A.A., Maksimyuk, I.E, Yushko, N.A., Kempe, U., Poutivtsev, M., 2005. Trace elements in quartz from conglomerates in the Witwatersrand Basin (South African Republic) and its role in the understanding of the deposit formation. In: Burenko EK, Kremenetsky AA (eds) Prikladnaya Geokhimiya. IMGRE, Moscow, vyp. 7, 1 87–100 (in Russian)

Kyser, T.K, Wilson, M.R. and Rutherman, G. 1989. Stable isotope constraints on the role of graphite in the genesis of unconformity-type uranium deposits; Canadian Journal of Earth Sciences, 26, 490-498.

Kyser, K., Hiatt, E., Renac, C., Durocher, K., Holk, G., and Deckart, K., 2000. Diagenetic fluids in Paleo- and Mesoproterozoic sedimentary basins and their implications for long protracted fluid histories, Chapter 10 in Kyser, K., ed., Fluids and Basin Evolution, Short Course Series Volume 28 (Series editor Robert Raeside): Mineralogical Association of Canada, p. 225-262.

Kyser, K., Hiatt, E., Christophe, R., Durocher, K., Holk, G., Deckart, K., 2005. Diagenetic fluids in paleo- and meso-proterozoic sedimentary basins and their implications for long protracted

fluid histories. Chapter: 10, Publisher: Mineralogical Society of Canda, pp.1-38 DOI: 10.13140/2.1.1033.1847

Kyser, K., Hiatt, E., Renac, C., Durocher, K., Holk, G., and Deckart, K., 2000. Diagenetic fluids in Paleo- and Mesoproterozoic sedimentary basins and their implications for long protracted fluid histories, Chapter 10 in Kyser, K., ed., Fluids and Basin Evolution, Short Course Series Volume 28 (Series editor Robert Raeside): Mineralogical Association of Canada, p. 225-262.

Lach, P., Mercadier, J., Dubessy, J., Boiron, M.-C., Cuney, M., 2013. In Situ Quantitative Measurement of Rare Earth Elements in Uranium Oxides by Laser Ablation-Inductively Coupled Plasma-Mass Spectrometry. Geostand. Geoanalytical Res. 37, 277–296. doi:10.1111/j.1751-908X.2012.00161.x

Landais, P., Dubessy, J., Dereppe, J. and Philp, R.P. 1993. Characterization of graphite alteration and bitumen genesis in the Cigar Lake deposits (Saskatchewan, Canada); Canadian Journal of Earth Sciences, 30, 743-753.

Laversanne, J., 1978. Le Permien de Lodève (Massif Central français), évolution des dépôts autuniens et exemples de minéralisations uranif'eres diagénétiques et diagénétiques par circulation de solutions exogènes. Sci. Terre XXII: 147-166 (1978)

LeCheminant, A.N., and Roddick, J.C., 1991. U-Pb zircon evidence for widespread 2.6 Ga felsic magmatism in the central District of Keewatin, N.W.T.; in Radiogenic Age and Isotopic Studies, Report 4: Geological Survey of Canada, Paper 90-2, p. 91–99.

LeCheminant, A.N. and Heaman, L.M. 1989. MacKenzie igneous events, Canada: Middle Proterozoic hotspot magmatism associated with ocean opening. Earth and Planetary Science Letters, v. 96, p. 38-48.

Leibold, J., 2013. Geochemistry and Mineralogy of the Alteration Halo Associated with the Three Crow Roll-front Uranium Deposit. Colourado School of Mines, Nebraska, USA

Lespinasse, M., 1999. Are fluid inclusion planes useful in structural geology? Journal of Structural Geology 21, 1237–1243. doi:10.1016/S0191-8141(99)00027-9

Lespinasse, M., Désindes, L., Fratczak, P., Petrov, V., 2005. Microfissural mapping of natural cracks in rocks: Implications for fluid transfers quantification in the crust. Chemical Geology 223, 170–178. doi:10.1016/j.chemgeo.2005.05.009

Leventhal, J.S., Grauch, R.I, Threlkeld, C.N., Liche, F.E. and Harper, C.T. 1987. Unusual organic matter associated with uranium from the Claude deposit, Cluff Lake, Canada; Economic Geology, 82, 1169- 1176.

Liang, R., Chi, G., Ashton, K., Blamey, N., Fayek, M., 2017. Fluid compositions and P-T conditions of vein-type uranium mineralization in the Beaverlodge uranium district, northern Saskatchewan, Canada. Ore Geol. Rev. 80, 460–483. doi:https://doi.org/10.1016/j.oregeorev.2016.07.012

Lovley, D.R., Phillips, E.J.P., Gorby, Y.A. and Landa, E.R., 1991. Microbial reduction of uranium. Nature, 350, 413-416.

Ludwig, K.R., Grauch, R.I., Nutt, C.J., Nash, J.T., Frishman, D., Simmons, K.R., 1987. Age of uranium mineralization at the Jabiluka and Ranger deposits, Northern Territory, Australia; new U-Pb isotope evidence. Econ. Geol. 82, 857–874. doi:10.2113/gsecongeo.82.4.857

Macdonald, C.C. 1980. Mineralogy and Geochemistry of a Precambrian Regolith in the Athabasca Basin. Unpublished M.Sc. thesis, University of Saskatchewan, 151 pp.

MacLean, H., Kranidiotis, W.P., 1987. Immobile elements as monitors of mass transfer in hydrothermal alteration: Phelps Dodge massive sulfide deposit, Matagami, Quebec (Canada). Econ. Geol. 82, 951–962.

MacLean, W.H., Barrett, T.J., 1993. Lithogeochemical techniques using immobile elements. J. Geochemical Explor. 48, 109–133. doi:https://doi.org/10.1016/0375-6742(93)90002-4.

MacRae, C.M., Wilson, N.C., Torpy, A., 2013. Hyperspectral cathodoluminescence. Mineral. Petrol. 107, 429–440. doi:10.1007/s00710-013-0272-8

Mahan, K.H., Williams, M.L., 2005. Reconstruction of a large deep-crustal terrane: Implications for the Snowbird tectonic zone and early growth of Laurentia. Geol. 33 , 385–388. doi:10.1130/G21273.1

Malpas, J., Duzgoren-Aydin, N.S., Aydin, A., 2001. Behaviour of chemical elements during weathering of pyroclastic rocks, Hong Kong. Environ. Int. 26, 359–368. doi:https://doi.org/10.1016/S0160-4120(01)00013-7

Martz, P., Cathelineau, M., Mercadier, J., Boiron, M.-C., Jaguin, J., Tarantola, A., Demacon, M., Gerbeaud, O., Quirt, D., Doney, A., Ledru, P., 2017. C-O-H-N fluids circulations and graphite precipitation in reactivated Hudsonian shear zones during basement uplift of the

Wollaston-Mudjatik Transition Zone: Example of the Cigar Lake U deposit. Lithos 294–295, 222–245. doi:https://doi.org/10.1016/j.lithos.2017.10.001

Mathieu, R., Deschamps, Y., Selezneva, V., Pouradier, A., Brouand, M., Deloule, E., Boulesteix, T., 2015. Key Mineralogical Characteristics of the New South Tortkuduk Uranium Roll-Front Deposits, Kazakhstan.

Matthews, R., R. Koch and M. Leppin, 1997. Advances in integrated exploration for unconformity uranium deposits in western Canada, in Proceedings of Exploration 97: Fourth Decennial International Conference on Mineral Exploration, edited by A. G. Gubins, 1997, 993 – 1024.

McEwan, B., 2012. Structural style and regional comparison of the Paleoproterozoic Ketyet River group in the region North-Northwest of Baker Lake, Nunavut. Regina, SK. November.

McGill, B., Marlatt, J., Matthews, R., Sopuck, V., Homeniuk, L., and Hubregtse, J., 1993, The P2 North uranium deposit Saskatchewan, Canada: Exploration Mining Geology, v. 2, 4, p. 321-331.

Mercadier, J., Richard, A., Boiron, M.C., Cathelineau, M., and Cuney, M., 2010. Migration of brines in the basement rocks of the Athabasca Basin through microfracture networks (P-Patch U deposit, Canada). Lithos 115 (1), 121–136.

Mercadier, J., Cuney, M., Cathelineau, M., Lacorde, M., 2011a. U redox fronts and kaolinisation in basement-hosted unconformity-related U ores of the Athabasca Basin (Canada): Late U remobilisation by meteoric fluids. Miner. Depos. 46, 105–135. doi:10.1007/s00126-010-0314-7

Mercadier, J., Cuney, M., Lach, P., Boiron, M.C., Bonhoure, J., Richard, A., Leisen, M., Kister, P., 2011b. Origin of uranium deposits revealed by their rare earth element signature. Terra Nov. 23, 264–269. doi:10.1111/j.1365-3121.2011.01008.x

Mercadier, J., Richard, A., and Cathelineau, M., 2012. Boron-and magnesium-rich marine brines at the origin of giant unconformity-related uranium deposits: δ 11 B evidence from Mg-tourmalines. Geology 40 (3), 231–234.

Mercadier, J., Annesley, I.R., McKechnie, C.L., Bogdan, T.S., Creighton, S., 2013a. Magmatic and metamorphic uraninite mineralization in the western margin of the Trans-Hudson Orogen (Saskatchewan, Canada): a uranium source for unconformity-related uranium deposits? Econ. Geol. 108 (5), 1037–1065.

Meunier, J.D., Sellier, E., Pagel, M., 1990. Radiation-damage rims in quartz from uranium-bearing sandstones. J Sediment Petrol 60:53–58

Miller, A.R., 1980. Uranium geology of the Eastern Baker Lake basin, district of Keewatin, Northwest Territories. Geological survey of Canada, bulletin 330, 63p.

Miller, A.R., 1982. Alteration and Mineralization Types: Amer-Thelon Area, N.T.S. 66 G, H, report to Westmin Resources Limited

Miller, A.R., 1995. Polymetallic unconformity-related uranium veins in lower Proterozoic Amer Group, Pelly Lake map area, northern Thelon Basin, Churchill Province, Northwest Territories: Geological Survey of Canada, Current Research 1995-C, pp. 151-161

Miller, A.R. and LeCheminant, A.N., 1985. Geology and uranium metallogeny of Proterozoic supracrustal successions, central District of Keewatin, N.W.T., with comparisons to northern Saskatchewan. Special Volume - Canadian Institute of Mining and Metallurgy 32: 167-185

Miller, A.R., Stanton, R.A., Cluff, G.R. and Male, M.J. 1986. Uranium deposits and prospects of the Baker Lake Basin and subbasins, Central District of Keewatin, Northwest Territories. In Uranium Deposits of Canada, edited by E.L. Evans, Canadian Institute of Mining and Metallurgy, Special Volume 33, pp.263-285.

Miller, A.R., Cumming, G.L., Krstic, D., 1989. U–Pb, Pb–Pb, and K–Ar isotopic study and petrography of uraniferous phosphate-bearing rocks in the Thelon Formation, Dubawnt Group, Northwest Territories, Canada. Can. J. Earth Sci. 26, 867–880. doi:10.1139/e89-070

Mills, A.J., Berman, R.G., Davis, W.J., Tella, S., Roddick, C., S. Carr, S.H., 2007. Thermobarometry and geochronology of the Uvauk complex, a polymetamorphic Neoarchean and Paleoproterozoic segment of the Snowbird tectonic zone, Nunavut, Canada. Can. J. Earth Sci. 44, 245–266. doi:10.1139/e06-080

Neff, H., 1994. RQ-mode principal components analysis of ceramic compositional data. Archaeometry 36, 115–130. doi:10.1111/j.1475-4754.1994.tb01068.x

OECD NEA & IAEA, 2014, Uranium 2014: Resources, Production and Demand

Okamoto, A., Yamada, R., Saishu, H., Tsuchiya, N., 2017. Porosity and Permeability Evolution Induced by Precipitation of Silica under Hydrothermal Conditions. Procedia Earth Planet. Sci. 17, 249–252. doi:https://doi.org/10.1016/j.proeps.2016.12.046

Owen MR (1988) Radiation-damage halos in quartz. Geology 16(6):529–532

Plant, J.A., Simpson, P.R., Smith, B., Windley, B.F., 1999. Uranium ore deposits; products of the radioactive Earth. Rev. Mineral. Geochemistry 38, 255–319.

Pagel, M., Cavellec, S., Forbes, P., Gerbaud, O., Vergely, P., Wagani, I., Mathieu, R., 2005. Uranium deposits in the Arlit area (niger), in: Mao, J., Bierlein, F.P. (Eds.), Mineral Deposit Research: Meeting the Global Challenge: Proceedings of the Eighth Biennial SGA Meeting Beijing, China, 18--21 August 2005. Springer Berlin Heidelberg, Berlin, Heidelberg, pp. 303–305. doi:10.1007/3-540-27946-6_79

Parlangeau, C., Lacombe, O., Schueller, S., Daniel, J.M., 2018. Inversion of calcite twin data for paleostress orientations and magnitudes: A new technique tested and calibrated on numerically-generated and natural data. Tectonophysics 722. In press. https://dx.doi.org/10.1016/j.tecto.2017.09.023

Pascal, M., Ansdell, K.M., and Annesley, I.R., 2015. Graphite-bearing and Graphite-depleted Basement Rocks in the Dufferin Lake Zone, South-central Athabasca Basin, Saskatchewan, in Targeted Geoscience Initiative 4: unconformity-related uranium systems, (ed.) E.G. Potter and D.M. Wright; Geological Survey of Canada, Open File 7791, p. 83–92. doi:10.4095/295776

Pechmann, E., 1992. Mineralogy and Geochronology of U(–Au) Deposits from the Pine Creek Geosyncline, Northern Territory, Australia, and from the Athabasca Basin, Saskatchewan and Alberta, Canada. Heidelberg Universitat, Heidelberg, Federal Republic of Germany.

Pehrsson, S., Wilkinson, L., Zaleski, E., 2004. Geology of the Meadowbank gold deposit area, Nunavut. Geological Survey of Canada, Open File 4269, scale 1:20 000

Pehrsson, S., Jefferson, C.W., Peterson, T., Scott, J., Chorlton, L., Hillary, B., Patterson, Judith, Lentz, D., Shelat, Y., and Bethune, K., 2010. Basement to the Thelon Basin, Nunavut - Revisited. Special Session on Geological Environments hosting Uranium Deposits, GeoCanada 2010 - Working with the Earth, Calgary, May 10-14th, 4 p. abstract

Pehrsson S., Berman, R., Davis, W. 2013. Paleoproterozoic orogenesis during Nuna aggregation: a case study of reworking of the Archean Rae craton, Woodburn Lake, Nunavut. Precambrian Research, 232: 167-188. doi: 10.1016/j.precamres.2013.02.010

Peterson, T.D., Breemen, O. Van, Sandeman, H., Cousens, B., 2002. Proterozoic (1.85–1.75 Ga) igneous suites of the Western Churchill Province: granitoid and ultrapotassic

magmatism in a reworked Archean hinterland. Precambrian Res. 119, 73–100. doi:https://doi.org/10.1016/S0301-9268(02)00118-3

Peterson, T.D., 2006. Geology of the Dubawnt Lake area, Nunavut-Northwest Territories. Geological Survey of Canada, Bulletin 580

Peterson, T.D., Scott, J.M.J., LeCheminant, A.N., Jefferson, C.W., Pehrsson, S.J., 2015a. The Kivalliq Igneous Suite: Anorogenic bimodal magmatism at 1.75 Ga in the western Churchill Province, Canada. Precambrian Res. 262, 101–119. doi:https://doi.org/10.1016/j.precamres.2015.02.019

Peterson, T.D., Scott, J.M.J., Lecheminant, A.N., Tschirhart, V.L., Chorlton, L.B., Davis, W.J., Hamilton, M.A., 2015b. Nueltin granites and mafic rocks in the Tebesjuak Lake map area, Nunavut: new geochronological, petrological, and geophysical data. Geological Survey of Canada, Current Research (Online) 2015-5, 2015; 23 pages, doi:10.4095/296163

Pi, Q., Hu, R., Xiong, B., Li, Q., Zhong, R., 2017. In situ SIMS U-Pb dating of hydrothermal rutile: reliable age for the Zhesang Carlin-type gold deposit in the golden triangle region, SW China. Miner. Depos.

Polito, P.A., Kyser, T.K., Marlatt, J., Alexandre, P., Bajwah, Z., and Drever,G., 2004. Significance of alteration assemblages for the origin and evolution of the Proterozoic Nabarlek unconformity-related uranium deposit, Northern Territory, Australia: Economic Geology, v. 99, p. 113-139.

Polito, P.A., Kyser, T.K., Rheinberger, G., and Southgate, P.N., 2005a. A paragenetic and isotopic study of the proterozoic Westmoreland uranium deposits, Southern McArthur Basin, Northern Territory, Australia. Econ. Geol. 100, 1243–1260.

Polito, P.A., Kyser, T.K., Thomas, D., Marlatt, J., and Drever, G., 2005b. Re-evaluation of the petrogenesis of the Proterozoic Jabiluka unconformity-related uranium deposit, Northern Territory, Australia. Mineral. Deposita 40, 257–288.

Polito, P.A., Kyser, T.K., Alexandre, P., Hiatt, E.E., Stanley, C.R., 2011. Advances in understanding the Kombolgie Subgroup and unconformity-related uranium deposits in the Alligator Rivers Uranium Field and how to explore for them using lithogeochemical principles. Aust. J. Earth Sci. 58, 453–474. doi:10.1080/08120099.2011.561873

Quirt, D.., 2003. Athabasca unconformity-type uranium deposits: one deposit type with many variations: Uranium Geochemistry 2003, International Conference, Nancy, France, April 13-16 2003, Proceedings, p. 309-312

Rainbird, R.H., Davis, W.J., 2007. U-Pb detrital zircon geochronology and provenance of the late Paleoproterozoic Dubawnt Supergroup: Linking sedimentation with tectonic reworking of the western Churchill Province, Canada. GSA Bull. 119, 314. doi:10.1130/B25989.1

Rainbird, R.H., Hadlari, T., Aspler, L.B, Donaldson, J.A., LeCheminant, A.N., and Peterson, T. D. 2003a. Sequence stratigraphy and evolution of the Paleoprotezoic intracontinental Baker Lake and Thelon basins, western

Rainbird, R.H., Rayner, N., and Stern, R.A., 2003b. SHRIMP U-Pb geochronology of apatite cements and zircon bearing tuff clasts in sandstones from the Athabasca Group, Athabasca Basin, northern Saskatchewan and Alberta: Saskatchewan Industry Resources, Open House, December 1-3, 2003, Saskatoon, Proceedings, p. 6

Rainbird, R.H., Stern, R.A., Rayner, N., and Jefferson, C.W., 2007. Age, provenance, and regional correlation of the Athabasca Group, Saskatchewan and Alberta, constrained by igneous and detrital zircon geochronology, in Jefferson, C.W., and Delaney, G., eds., EXTECH IV: Geology and Uranium EXploration TECHnology of the Proterozoic Athabasca Basin, Saskatchewan and Alberta: Geological Survey of Canada, Bulletin 588, (also Geological Association of Canada, Mineral Deposits Division, Special Publication 4; Saskatchewan Geological Society, Special Publication 18) p. 193-210.

Rainbird, R.H., Davis, W.J., Pehrsson, S.J., Wodicka, N., Rayner, N., Skulski, T., 2010. Early Paleoproterozoic supracrustal assemblages of the Rae domain, Nunavut, Canada: Intracratonic basin development during supercontinent break-up and assembly. Precambrian Res. 181, 167–186. doi:https://doi.org/10.1016/j.precamres.2010.06.005

Ramaekers, P., 1981. HudsonJan and Helikian basins of the Ath-abasca region, northern Saskatchewan: Canada Geol. Survey Paper 81-10, p. 219-233.

Ramaekers, P., Jefferson, C.W., Yeo, G.M., Collier, B., Long, D.G.F., Catuneanu, O., Bernier, S., Kupsch, B., Post, R., Drever, G., McHardy, S., Jiricka, D., Cutts, C., and Wheatley, K., 2007. Revised geological map and stratigraphy of the Athabasca Group, Saskatchewan and Alberta, in Jefferson, C.W., and Delaney, G., eds., EXTECH IV: Geology and Uranium EXploration TECHnology of the Proterozoic Athabasca Basin, Saskatchewan and Alberta: Geological Survey of Canada, Bulletin 588, (also Geological Association of Canada,

Mineral Deposits Division, Special Publication 4; Saskatchewan Geological Society, Special Publication 18) p. 155-192.

Renac, C., Kyser, T.K., Durocher, K., Dreaver, G. and O'Connor, T. 2002. Comparison of diagenetic fluids in the Proterozoic Thelon and Athabasca Basins, Canada: 139 Implications for protracted fluid histories in stable intracratonic basins; Canadian Journal of Earth Sciences, 39, 113-132.

Regan, S.P., Williams, M.L., Leslie, S., Mahan, K.H., Jercinovic, M.J., Holland, M.E., 2014. The Cora Lake shear zone, Athabasca granulite terrane, an intraplate response to far-field orogenic processes during the amalgamation of Laurentia. Can. J. Earth Sci. 51, 877–901. doi:10.1139/cjes-2014-0015

Reyx, J., 1984. Report 8548. Ore minerals metallography. Sissons Schultz South Drill hole SW 72. Internal report COGEMA. 20 p.

Richard A., Pettke T., Cathelineau M., Boiron M.-C., Mercadier J., Cuney M. and Derome D. 2010. Brine–rock interaction in the Athabasca basement (McArthur River U deposit, Canada): consequences for fluid chemistry and uranium uptake. Terra Nova 22, 303–308.

Richard, A., Rozsypal, C., Mercadier, J., Banks, D. a., Cuney, M., Boiron, M.-C., Cathelineau, M., 2012. Giant uranium deposits formed from exceptionally uranium-rich acidic brines. Nat. Geosci. 5, 142–146. doi:10.1038/ngeo1338;

Richard A., Boulvais P., Mercadier J., Boiron M.-C., Cathelineau M., Cuney M. and France-Lanord C. 2013a. From evaporated seawater to uranium-mineralizing brines: isotopic and trace element study of quartz–dolomite veins in the Athabasca system. Geochim. Cosmochim. Acta 113, 38–59.

Richard A., Cauzid J., Cathelineau M., Boiron M.-C., Mercadier J. and Cuney M. 2013b. Synchrotron XRF and XANES investigation of uranium speciation and element distribution in fluid inclusions from unconformity-related uranium deposits. Geofluids 13, 101–111.

Richard, A., Montel, J.-M., Leborgne, R., Peiffert, C., Cuney, M., Cathelineau, M., 2015. Monazite Alteration in H2O ± HCl ± NaCl ± CaCl2 Fluids at 150 oC and psat: Implications for Uranium Deposits. Minerals 5, 693–706.

Riegler, T., 2013. Système d'altération et minéralisation en uranium le long du faisceau structural Kiggavik-Andrew Lake (Nunavut, Canada): Modèle génétique et guides d'exploration: Unpublished Ph.D. thesis, Poitiers, France, Université de Poitiers. 244 p.

Riegler, T., Lescuyer, J.-L., Wollenberg, P., Quirt, D., Beaufort, D., 2014. Alteration related to uranium deposits in the Kiggavik-Andrew Lake structural trend, Nunavut, Canada : New insights from petrography and clay mineralogy. Can. Mineral. 52, 27–45. doi:10.3749/canmin.52.1.27

Riegler, T., Beaufort, M.-F., Allard, T., Pierson-Wickmann, A.-C., Beaufort, D., 2017. Nanoscale relationships between uranium and carbonaceous material in alteration halos around unconformity-related uranium deposits of the Kiggavik camp, Paleoproterozoic Thelon Basin, Nunavut, Canada. Ore Geol. Rev. 79, 382–391. doi:https://doi.org/10.1016/j.oregeorev.2016.04.018

Rippert, J.C., Koning, E., Robbins, J., Koch, R., and Baudemont, D., 2000. The Shea Creek Uranium Project, West Athabasca Basin, Saskatchewan, Canada, Geological Association of Canada –Mineralogical Association of Canada, Joint Annual Meeting, Calgary, Abstract, v. 26, p. 65.

Robbins, J., Richard, Y., Carter, C., Behaegel, M., Benedicto, A., and Ledru, P., 2015. Newguidesledtonewmodels-Continuingreturnofexplorationexperience, Nunavut, Canada. In The AusIMM International Uranium Conference 2015, Abstract volume, p. 2.

Roedder, E, 1984. Fluid Inclusions in Minerals : Methods and Applications. Virginia Tech, Blacksburg, USA

Rogers, J.J.W., and Adams, J.A.S., 1969. Geochemistry of uranium. In: K.H., Wedepohl, Ed., Handbook of Geochemistry, Vol. 113, Springer, Berlin, 92-B-1 to 92-0-8 and 90-Bb-1 to 90-00-5.

Ross, G.M., Eaton, D.W., Boerner, D.E., Miles, W., 2000. Tectonic entrapment and its role in the evolution of continental lithosphere: An example from the Precambrian of western Canada. Tectonics 19, 116–134. doi:10.1029/1999TC900047

Ross, G.M., Kerans, C., 1989. Geology, Hornby Bay and Dismal Lakes groups, Coppermine Homocline, District of MacKenzie, Northwest Territories. Geological Survey of Canada, Map 1663A, Scale 1:250,000.

Roy, R., Benedicto, A., Grare, A., Béhaegel, M., Richard, Y., Harrison, G., 2017. Three-dimensional gravity modelling applied to the exploration of uranium unconformity-related basement-hosted deposits: the Contact prospect case study, Kiggavik, northeast Thelon region (Nunavut, Canada). Can. J. Earth Sci. 54, 869–882. doi:10.1139/cjes-2016-0225

Ruzicka, V.R., 1996. Unconformity-associated uranium, Chapter 7 in Eckstrand, O.R., Sinclair, W.D., and Thorpe, R.I., eds., Geology of Canadian Mineral Deposit Types: Geological Survey of Canada, Geology of Canada, v, 8, p. 197-210.

Sanborn-Barrie, M., Carr, S., Thériault, R., 2001. Geochronological constraints on metamorphism, magmatism and exhumation of deep-crustal rocks of the Kramanituar Complex, with implications for the Paleoproterozoic evolution of the Archean western Churchill Province, Canada. Contrib. to Mineral. Petrol. 141, 592–612. doi:10.1007/s004100100262

Sanford, R.F., 1994. A quantitative model of ground-water flow during formation of tabular sandstone uranium deposits. Econ. Geol. 89, 341–360.

Sangely, L., Chaussidon, M., Michels, R., Brouand, M., Cuney, M., Hualut, V. and Landais, P. 2007. Micrometer scale carbon isotopic study of bitumen associated with Athabasca uranium deposits: Constraints on the genetic relationship with petroleum source-rocks and the abiogenic origin hypothesis; Earth and Planetary Science Letters, 258, 378-396.

Scholz, M., 2006. Approaches to analyse and interpret biological profile data. PhD Universität Potsdam.

Scott, J.M.J. 2012. Paleoproterozoic (1.75 Ga) Granitoid Rocks and Uranium Mineralization in the Baker Lake–Thelon Basin region, Nunavut. M.Sc. thesis, Carleton University, Ottawa, Ont.

Scott, J.M.J., Peterson, T.D., Jefferson, C.W., Cousens, B.L., 2015. Petrology and geochronology of Paleoproterozoic intrusive rocks, Kiggavik uranium camp, Nunavut. Can. J. Earth Sci. 518, 1–80. doi:10.1139/cjes-2014-0153

Shabaga, B., M., Fayek, M., Quirt, D., Jefferson, C.W., Camacho, A., 2017. Geochronology and genesis of the Andrew Lake uranium deposit, Thelon Basin, Nunavut, Canada. Poster presented at 2017 GAC MAC

Sharpe, R., Fayek, M., Quirt, D., and Jefferson, C.W., 2015. Geochronology and Genesis of the Bong Uranium Deposit, Thelon Basin, Nunavut, Canada. Econ. Geol. 110, 1759–1777. doi:10.2113/econgeo. 110.7.1759

Sherlock, R., Pehrsson, S., Logan, A. V., Hrabi, R.B., Davis, W.J., 2004. Geological setting of the Meadowbank gold deposits, Woodburn Lake Group, Nunavut. Explor. Min. Geol. 13, 67–107. doi:10.2113/13.1-4.67

Sherman, D.M., Peacock, C.L. and Hubbard, C.G., 2008. Surface complexation of U(IV) on goethite (α-FeOOH). Geochimica et Cosmochimica Acta, 72, 298-310.

Sibson, R.H., 1992. Implications of fault-valve behaviour for rupture nucleation and recurrence. Tectonophysics 211, 283–293. doi:https://doi.org/10.1016/0040-1951(92)90065-E

Skirrow, R.G., Jaireth, S., Huston, D.L., Bastrakov, E.N., Schofield, A., van der Wielen, S.E., and Barnicoat, A.C., 2009, Uranium mineral systems: Processes, exploration criteria and a new deposit framework: Geoscience Australia Record 2009/20, 44 p.

Skirrow, R.G., Mercadier, J., Armstrong, R., Kuske, T., Deloule, E., 2015. The Ranger uranium deposit, northern Australia: Timing constraints, regional and ore-related alteration, and genetic implications for unconformity-related mineralisation. Ore Geol. Rev. 76, 463–503. doi:10.1016/j.oregeorev.2015.09.001

Skirrow, R.G., Mercadier, J., Armstrong, R., Kuske, T., Deloule, E., 2016. The Ranger uranium deposit, northern Australia: Timing constraints, regional and ore-related alteration, and genetic implications for unconformity-related mineralisation. Ore Geol. Rev. 76, 463–503. doi:https://doi.org/10.1016/j.oregeorev.2015.09.001

Sopuck, V.J., de Carla, A., Wray, E.M., Cooper, B., 1983. The application of lithogeochemistry in the search for unconformity-type uranium deposits, Northern Saskatchewan, Canada. J. Geochemical Explor. 19, 77–99. doi:https://doi.org/10.1016/0375-6742(83)90009-2

Timofeev, A., Migdisov, A., Williams-Jones, A., Roback, B., Nelson, A., White, J., 2017. Transporting Uranium in Acidic Brines Under Reducing Conditions. 27th Goldschmidt Conference, Paris.

Tourigny, G., Wilson, G., Breton, G., and Portella, P., 2002. Geology of the Sue C uranium deposit, McClean Lake area, northern Saskatchewan, in N. Andrade, G.B., C.W. Jefferson, D.J.

Tourigny, G., Quirt, D.H., Wilson, N., Wilson, S., Breton, G., and Portella, P., 2007. Basement geology of the Sue C uranium deposit, McClean Lake area, Saskatchewan, in Jefferson, C.W., and Delaney, G., eds., EXTECH IV: Geology and Uranium EXploration TECHnology of the Proterozoic Athabasca Basin, Saskatchewan and Alberta: Geological Survey of Canada, Bulletin 588, (also Geological Association of Canada, Mineral Deposits Division, Special Publication 4; Saskatchewan Geological Society, Special Publication 18) p. 229-248.

Tremblay, L.P. 1972. Geology of the Beaverlodge Mining Area, Saskatchewan; Geological Survey of Canada, Memoir 367, 265 p.

Tschirhart, V., Morris, W.A., Jefferson, C.W., 2013. Framework geophysical modelling of granitoid vs. supracrustal basement to the northeast Thelon Basin around the Kiggavik uranium camp, Nunavut. Can. J. Earth Sci. 50, 667–677. doi:10.1139/cjes-2012-0149

Tschirhart, V., Jefferson, C.W., Morris, W.A. 2017. Basement geology beneath the northeast Thelon Basin, Nunavut: insights from integrating new gravity, magnetic and geological data. Geophysical Prospecting, 65: 617-636. doi: 10.1111/1365-2478.12430

Turner, W.A., Richards, J., Nesbitt, B., Muehlenbachs, K., Biczok, J., 2001. Proterozoic low-sulfidation epithermal Au-Ag mineralization in the Mallery Lake area, Nunavut, Canada. Miner. Depos. 36, 442–457. doi:10.1007/s001260100181

Turpina, L., Clauer, N., Forbes, P., Pagel, M., 1991. U□Pb, Sm□Nd and K□Ar systematics of the Akouta uranium deposit, Niger. Chem. Geol. Isot. Geosci. Sect. 87, 217–230. doi:https://doi.org/10.1016/0168-9622(91)90022-O

Uvarova, Y.A., Kyser, T.K., Lahusen, L., 2012. The uranium potential of the north-eastern part of the Paleoproterozoic Thelon Basin, Canada. J. Geochemical Explor. 119–120, 76–84. doi:10.1016/j.gexplo.2012.06.020

Van Breemen, O., Peterson, T.D., Sandeman, H.A., 2005. U–Pb zircon geochronology and Nd isotope geochemistry of Proterozoic granitoids in the western Churchill Province: intrusive age pattern and Archean source domains. Can. J. Earth Sci. 42, 339–377. doi:10.1139/e05-007

Viola, G., Scheiber, T., Fredin, O., Zwingmann, H., Margreth, A., Knies, J., 2016. Deconvoluting complex structural histories archived in brittle fault zones. Nat. Commun. 7, 13448.

Vollbrecht, A., Ruedrich, J., Weber, K., Oberthür, T., 1996. Gefügekundliche Untersuchungen an Geröllquarzen der Witwatersrand-Lagerstätte in Südafrika. Z Angew Geol 42:156–161

Vollbrecht, A., Oberthür, T., Ruedrich, J., Weber, K., 2002. Microfabric analyses applied to the Witwatersrand gold- and uranium-bearing conglomerates: constraints on the provenance and post-depositional modification of rock and ore components. Mineral Deposita 37:433–451

Waite, T.D., Davis, J.A., Payne, T.E., Waychunas, G.A. and Xu, N., 1994. Uranium (VI) adsorption to ferrihydrite – application of a surface complexation model. Geochimica et Cosmochimica Acta, 58, 5465-5478.

Wallis, R.H., Saracoglu, N., Brummer, J.J., and Golighltly, J.P.1985. The geology of the McClean uranium deposits, northern Saskatchewan; inSibbald, T.I.I. and Petruk, W. (eds.), Geology of Uranium Deposits, CIM Spec. Vol. 32, p101-131.

Wang, K., Chi, G., Bethune, K.M., and Card, C.D., 2015. Fluid Composition, Thermal Conditions, Fluid-structural Relationships and Graphite Alteration of the Phoenix Uranium Deposit, Athabasca Basin, Saskatchewan, in Targeted Geoscience Initiative 4: unconformity-related uranium systems, (ed.) E.G. Potter and D.M. Wright; Geological Survey of Canada, Open File 7791, p. 93–102. doi: 10.4095/295776

Wasyliuk, K., 2002. Petrogenesis of the kaolinite-group minerals in the eastern Athabasca basin of northern Saskatchewan: Applications to uranium mineralization; M. Sc. Thesis, University of Saskatchewan, Saskatoon, Saskatchewan, 140 p

Weyer HJ, Friedrich G, Bechtel A, Ballhorn RK., 1987. The Lone Gull uranium deposit—new geochemical and petrological data as evidence for the nature of the ore bearing solutions. Metallogenesis of uranium deposits: Proceeding of a technical committee meeting, Vienna, p. 9–12.

Weyer, H.J., Friedrich, G., Bectel, A., Ballhorn, R.K., 1989. The Lone Gull uranium deposit - New geochemical and petrological data as evidence for the nature of the ore bearing solutions. IAEA, Tech. Comm. Metallog. uranium Depos. 293–305.

Weyer H-J (1992) Die uraniagnerstätte Kiggavik, Nordwesterritorien, Kanada Fakultät für Bergbau, Hüttenwesen und Geowissenschaften. Rheinisch-Westfälischen Technischen Hochschule, Aachen, pp 223

Wibberley, C.A.J., Yielding, G., Di Toro, G., 2008. Recent advances in the understanding of fault zone internal structure: a review. Geol. Soc. London, Spec. Publ. 299, 5–33. doi:10.1144/SP299.2

Wilde, A.R., and Wall, V.J., 1987. Geologyof the NabarlekUranium Deposit, NorthernTerritory. Australia. Econ. Geol. Vol. 82, 1152–1168.

Wilde, A.R., Mernagh, T.P., Bloom, M.S., and Hoffmann, C.F., 1989. Fluid inclusion evidence on the origin of some Australian unconformity-related uranium deposits. Econ. Geol. 84 (6), 1627–1642.

Williams, J.H., Johnson, C.D., 2004. Acoustic and optical borehole-wall imaging for fractured-rock aquifer studies. J. Appl. Geophys. 55, 151–159. doi:https://doi.org/10.1016/j.jappgeo.2003.06.009

WoldeGabriel, G., Boukhalfa, H., Ware, S.D., Cheshire, M., Reimus, P., Heikoop, J., Conradson, S.D., Batuk, O., Havrilla, G., House, B., Simmons, A., Clay, J., Basu, A., Christensen, J.N., Brown, S.T., DePaolo, D.J., 2014. Characterization of cores from an in-situ recovery mined uranium deposit in Wyoming: Implications for post-mining restoration. Chem. Geol. 390, 32–45. doi:https://doi.org/10.1016/j.chemgeo.2014.10.009

Yeo G. M. and Potter E. G. 2010. Review of reducing mechanisms potentially involved in the formation of unconformity-type uranium deposits and their relevance to exploration. In Summary of Investigations 2010, Volume 2. Saskatchewan Geological Survey. Paper A-12. 13p.

Yilmaz, T.I., Prosser, G., Liotta, D., Kruhl, J.H., Gilg, H.A., 2014. Repeated hydrothermal quartz crystallization and cataclasis in the Bavarian Pfahl shear zone (Germany). J. Struct. Geol. 68, 158–174. doi:https://doi.org/10.1016/j.jsg.2014.09.004

Li, Z., Chi, G., Bethune, K., 2016. The effects of basement faults on thermal convection and implications for the formation of unconformity-related uranium deposits in the Athabasca Basin, Canada. Geofluids 16.

Zerff, R. 2013. END-grid 3D geological and structural model. Kiggavik Project. ARC internal report. 50pp.

ANNEXES

GEOCHEMICAL CHARACTERIZATION: STUDY OF MAIN FRACTURING STAGES BY PRINCIPAL COMPONENT ANALYSIS (PCA)

1 INTRODUCTION

Macro- to micro-scale observation and study of oriented data allowed characterising the fracturing events at the Contact prospect. These fracturing events are associated with fluid circulation which interacted with the host rock, altering and forming new minerals thus changing the elemental signature of the host rock (or newly formed fault rock). One example is the difference between the first and second mineralizing stage: complex versus simple mineralogy. However minerals are not always observed at the micro-scale, and bias could be introduced by the number of samples picked, and the amount of observations made.

One way to correct this is and to get a finer appreciation of the elemental enrichment/depletion associated with fracturing stages is to use the whole rock geochemical database of Areva Resources Canada. Systematic drill core samples are analyzed by the Saskatchewan Research Council (SRC, located at Saskatoon, Canada) and their concentrations in major and minor elements are obtained and studied in this chapter in order to chemically characterize the geochemical signature of the main fracturing event occurring at Contact. First, as an exploratory data analysis, observation of the variations in major and minor elements associated to one U1 and one U2 fault zones, and comparisons of geochemical variations between these two stages are made. Second, Principal Component Analysis is run on the entire set of samples (separated by lithologies) in order to observe positive and negative correlations between minor and major elements, therefore obtaining a finer characterization and comparison of geochemical signatures of the different fracturing events at Contact.

2 METHODOLOGY

This study is based on chemical compositions of drill core from the Contact prospect determined by the Saskatchewan Research Council, using an inductively coupled plasma optical

emission spectrometer (ICP-OES) and mass spectrometry (ICP-MS, for uranium) following the partial and total digestion using acids (a mixture of $HF/HNO_3/HClO_4$ and HNO_3-HCL for uranium). Boron is determined by fusion at 650 C in a mixture of Na_2O_2/Na_2CO_3.

There are a total of 1519 samples in the dataset. Principal Component Analysis (PCA) was run on 4 different sets of samples, differentiated by their lithologies: Granitic gneiss (1230 samples), Granite/granodiorite (162 samples), lamprophyre (145 samples), syenite (35 samples). Two types of sampling are carried out on the drillcore during field campaigns at Kiggavik: Systematic samples (1SYB) and mineralized samples (1BAS); they were both used to identify geochemical signatures in PCA. 1SYB involves collecting ~5 cm chips from the end of each box row, they are composited over a 10 m length (Fig. 45) except if there is a change in the lithology. In the case of uranium mineralized zone (defined by any rock returning a scintillometer reading of 300 counts per second (cps) or more, using a portable scintillometer of Algade Brand), samples are 50 cm long, split intervals with two 50 centimetre split samples above and below the mineralized sample(s), see Figure 45. There are more mineralized samples (985) than non-mineralized samples (494 samples), indicating that mineralized fault zones are more finely characterized (statistically speaking) compared to non-mineralized ones. As observed in the previous sections, mineralization is associated with fracturing so the sampling indirectly targets (more or less) fault zones associated with uranium mineralization, but systematic samples are mixing rock chips collected over a 10m zone, though often smaller faults are lumped in with the lithology based samples.

As presented, 50 cm samples are taken above and below a mineralized sample, this 50 cm interval can characterize fault zone proximal to uranium mineralization but not associated with it.

Analyzed elements in the dataset include major and minor elements: Al, Ag, As, B, Ba, Be, Bi, Ca, Ce, Co, Cr, Cu, Dy, Er, Fe, K, La, Mg, Mo, Na, Ni, P, Pb, Pr, S, Se, Sc, Sm, Sn, Sr, Tb, Ti, U, V, W, Y, Yb, Zr and Zn. Si was not measured by the Saskatchewan Research Council and was re-calculated using concentrations of other elements. Even if it is a rough calculation, especially considering that we do not have lost of ignition (LOI) that can also vary depending on the intensity of clay alteration of the samply, it allows to have an estimation of the silicification or desilicification of the sample. Major and trace elements were studied as a whole in PCA.

After characterisation of the fracturing events and associated alteration at the Contact prospect (see previous sections), each sample was assigned to an alteration stage.

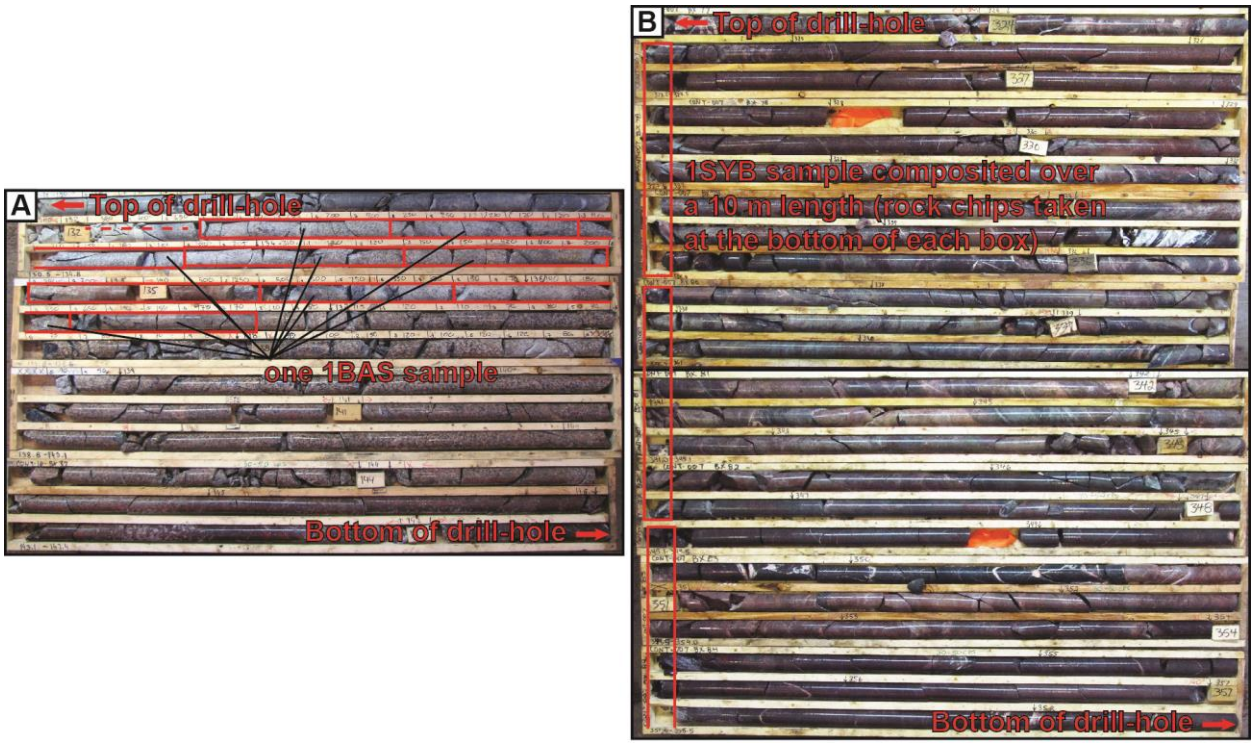

Figure 45: Geochemical sampling in the Kiggavik area. A) 1BAS geochemical sampling in uranium-mineralized zones, 50cm long half drillcore is sampled as long as the SPPγ return 300 cps or more. B) 1SYB geochemical sampling in non-mineralized zone, a sample is taken every 20m, except if there is a change in lithology.

Principal Components Analysis

Looking at the great amount of samples analyzed in geochemisty, PCA can be regarded as an optimal technique in this case: by reducing the dimensionality (the number of variables) of a data set, it simplified the description of multi-element associations that can reflect variation of mineralogy (characterizing primary rock type, hydrothermal alteration assemblages, mineralization…). Simply put, PCA involves an orthonormal transformation (rotation) of the original multivariate data space such that the axes of the new coordinate system point into the directions of highest variances of the data. The axes or new variables (Fig. 46) are termed Principal Components (PCs) and are ordered by variance: The first component, PC1, represents the direction of the highest variance of the data. The direction of the second component, PC2, represents the highest of the remaining variance orthogonal to the first component. This can be extended to PC3, PC4, etc., to obtain the required number of components in order to represent the desired amount of variance.

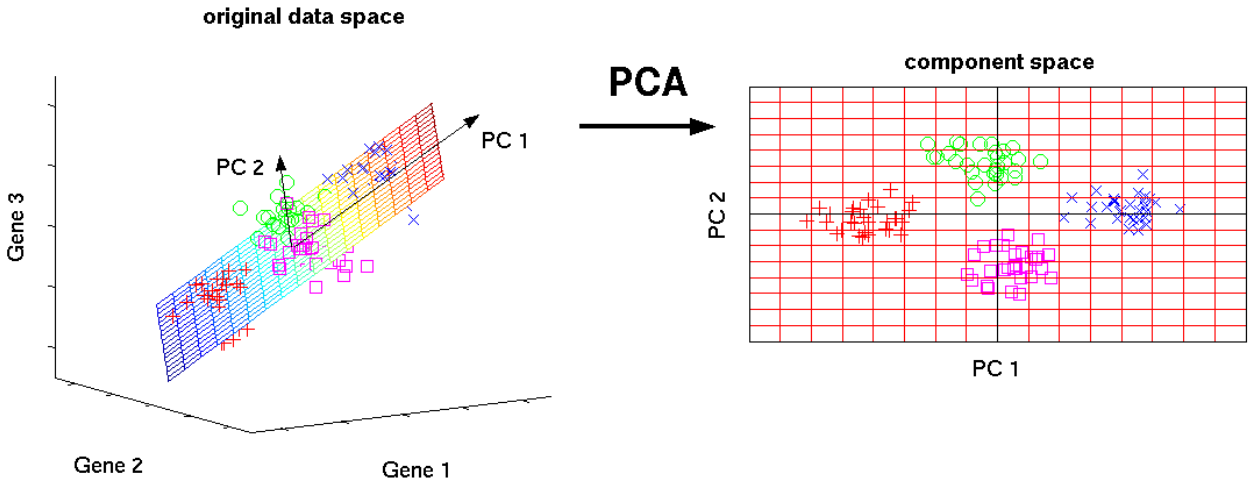

Figure 46: The three original variables (genes) are reduced to a lower number of two new variables termed principal components (PCs). Left: Using PCA, we can identify the two-dimensional plane that optimally describes the highest variance of the data. This two-dimensional subspace can then be rotated and presented as a two-dimensional component space (right). (this example is after Scholz, 2006).

There are several types of PCA (Neff, 1994). R-mode PCA is based on variables (elemental concentrations in this study); the loading of the original variables on each principal component may be inspected to obtain the desired information. It is suitable for identifying the associations of variables with a set of observations. Q-mode PCA is primarily based on observations (samples in this study); the factor scores for the original variables may be inspected. It is suitable for the characterization of multivariate observations.

For example, in the case of an exploration geologist looking to explore element associations related to uranium mineralization in a specific area, Q-mode PCA will focus on interrelationships between samples, while R-mode PCA will focus on interrelationships between variables. Something to take into account is that Q-mode calculation is more computationally intensive than R-mode PCA because the number of samples results in a large matrix that can be difficult to manipulate with statistical software.

A more direct approach is to perform a simultaneous RQ-mode analysis. In this way data points (samples) and the variables (elements) can be displayed on the same set of diagrams (called biplots).

The PCA was carried out using XLSTAT add-in for Microsoft Excel.

3 GEOCHEMICAL SIGNATURE OF FIRST AND SECOND STAGES OF URANIUM MINERALIZATION (PRELIMINARY EXPLORATION OF THE DATASET)

Fault zones representative of the fracturing event associated with the first (U1) and second (U2) stage of uranium mineralization at Contact were selected for study and to compare their geochemical characteristics. These fault zones were chosen (least affected by following fracturing stage, similar lithologies) from drill hole CONT-23 from 104 to 125 m for U1 and drill hole CONT-06 from 37 to 135 m for U2. Results of the whole rock geochemical analysis (1SYB and 1BAS samples) are plotted against depth in Fig. 47 for U1 and Fig. 48 for U2. Synthetic lithological and structural logs (damage zones in grey, fault core in black) are located on the left of the figures, major elements are in wt% oxides and minor elements are in ppm.

Fresh rock samples were taken from several drillholes to assess the mineralogy of the protolith. Several intrusions (syeno-granite to lamprophyre, dykes and sills) are observed in the Contact area, but mineralization is generally restricted to granitic gneiss. Mineralogical features indicate that the granitic gneiss underwent greenschist facies metamorphism before retrograding. For example chlorite after biotite, epidote, hematization along foliation (rimming quartz) and minor clay (illite/sericite) after plagioclase. Almost all biotites are replaced by chlorite. Sericitization of feldspars is weak to moderate. Other minerals present are quartz, with undulose extinction, potassic feldspar (microcline), titanite altered to rutile, apatite, zircon, pyrite and magnetite. Magnetite is rimmed by hematite. In some thin sections, K-feldspar displays exsolution lamellae (perthite) which are illitized. Quartz is the most prominent mineral that defines the fabric and is usually present as elongated polygranular aggregates. A number of recent studies in exploration lithogeochemistry have stressed the identification and use of elements (such as Ti and Al) that have remained immobile during hydrothermal alteration and metamorphism around ore deposits (e.g., MacLean and Kranidiotis, 1987; Elliott-Meadows and Appleyard 1991; MacLean and Barrett, 1993).

The less mobile elements thus reflect the degree of alteration of the host rock through fluid rock interaction: indirect “enrichment” in these elements indicates loss of other components usually linked to alteration of the host rock minerals (biotite, retrograde metamorphic chlorite, feldspar…).

A first observation is that uranium mineralization is observed strictly in fractured zones and as presented in the section dedicated to the fracturing event observed at the Contact prospect, the U1 fault zone is smaller than U2 fault zone; U2 is characterized by a uranium mineralization

distributed over ~100 m of mainly damage zone and narrow fault cores. Uranium mineralization in U1 presents the highest grade with several U values over 15 000 ppm, maximum at 30 000 ppm. In the case of U2, some values reach 10 000 ppm; maximum at 25 000 ppm. However, these lower grades are contained in a greater volume of rock.

3.1 Major and minor elements characterising alteration of the host rock linked to uranium mineralized fault zones

Faulted intervals returned local increased in TiO_2 up to 1.0 wt% and several values between 0.5-0.6 wt%, this increase is correlated with increases in Al_2O_3 content up to 20 wt% in the case of U1 (Fig. 47). These augmentations are the result of clay alteration of the host rock minerals; the increase in these elements is also correlated with K_2O with values up to 7 wt%, likely indicating that the clay alteration is represented by illitization $(K,H_3O)(Al,Mg,Fe)_2(Si,Al)_4O_{10}[(OH)_2,(H_2O)]$ (Riegler, 2014)**.** This interpretation is confirmed through observations under optical microscope and SEM. U2 display the same kind of positive correlations (Fig. 48) for these elements but the enrichment is stronger with TiO_2 usually reaching values above 1 wt%, Al_2O_3 20 wt%, and K_2O up to 10 wt%. Stronger increases of TiO_2, Al_2O_3 and MgO in the case of U2 could be explained by a stronger clay alteration of the host rock and/or stronger crystallization of sudoite $(Mg_2(Al,Fe^{3+})_3Si_3AlO_{10}(OH)_8)$, two interpretations which were confirmed by macro- to micro-scale observations.

Decreases in elements such as Ba, La, Sr and Ce (Fig. 47 and 48), correlated with the increase of elements named before, characterizes the clay-alteration of feldspar (Malpas et al., 2001) from the fresh host rock. Local high values in Ce, La and Sr could represent crystallization of Aluminum Phosphate-Sulfate minerals (APS); they are a group of minerals of which one end-member (named florencite) is enriched in rare earth elements, usually associated with the clay alteration assemblages of unconformity-related uranium mineralization (Gaboreau et al., 2007), this would be consistent with the observed increase in Al, S and P.

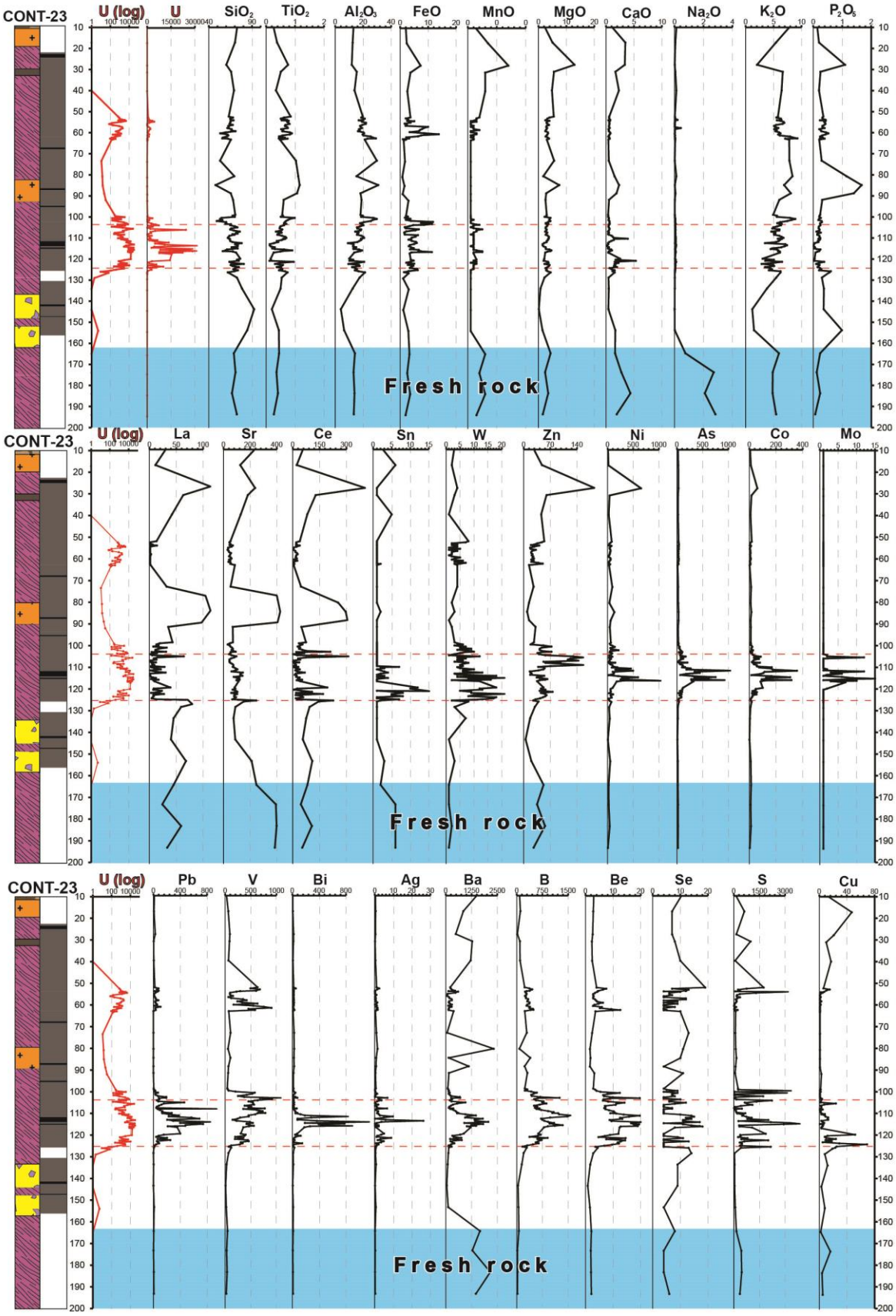

Figure 47: Profiles of the major and minor element contents of drill hole CONT-23 with the left column showing lithological (pink: granitic gneiss; orange: granite; yellow: quartz breccia) and structural log (brown: damage zone; black, core zone). The major element contents are in wt. %, minor element contents are in ppm.

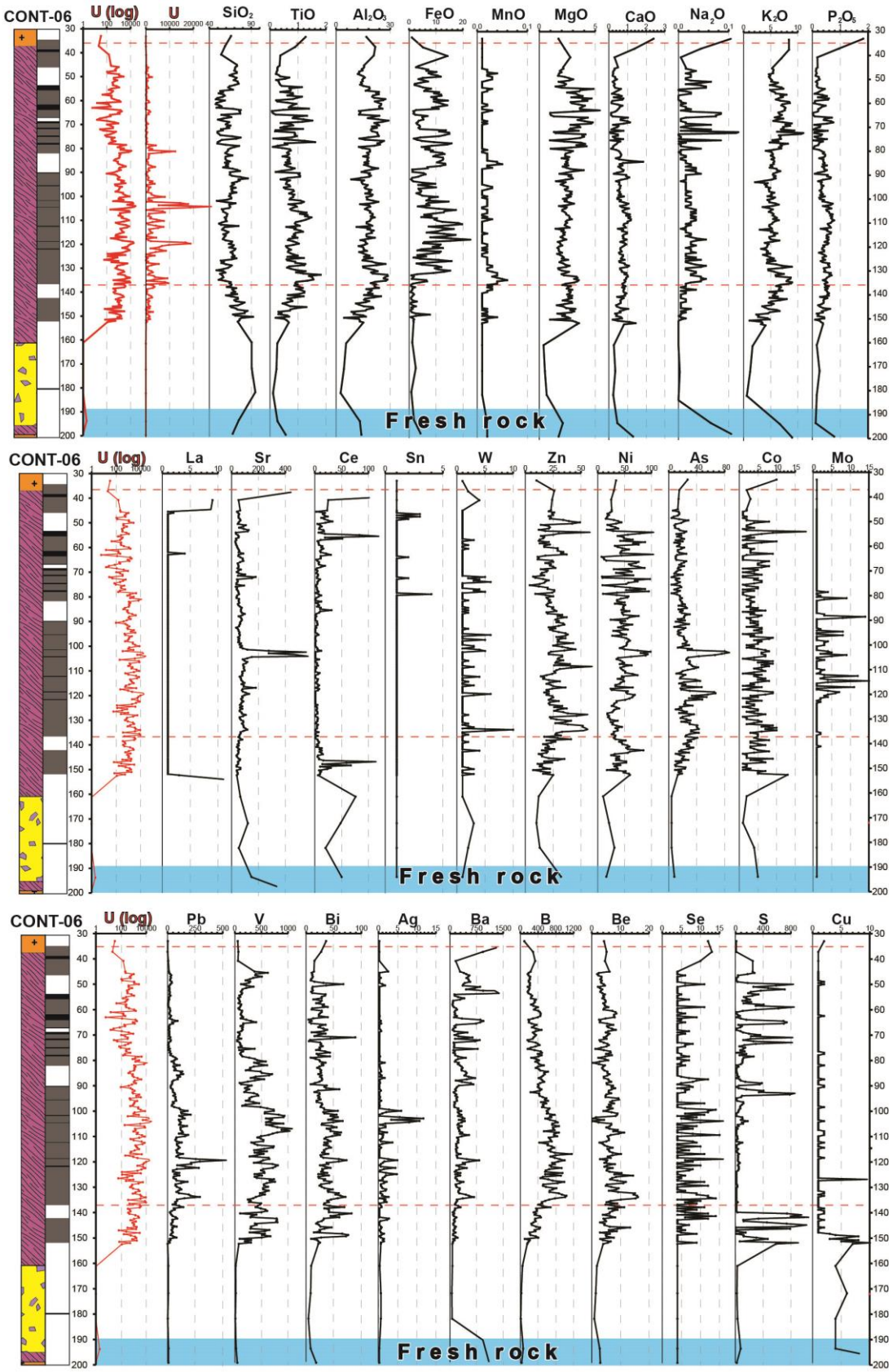

Figure 48: Profiles of the major and minor element contents of drill hole CONT-06 with the left column showing lithological (pink: granitic gneiss; orange: granite; yellow: quartz breccia) and structural log (brown: damage zone; black, core zone). The major element contents are in wt. %, minor element contents are in ppm.

APS minerals were rarely observed at the Contact prospect, only characterized under SEM once in the case of an oxidized U2 fault zone, but not in the case of U1. Peak values of Ce, Sr and La in CONT-23 at ~118 m (Fig. 47) are not correlated with increased values of Al_2O_3 and TiO_2, possibly representing a mineralized fractured zone where alteration was weaker and feldspar less clay altered.

A positive correlation is observed between B and MgO with peak values for B at 750 and 1500 ppm. This correlation (also observed for U2, although with lower peak values of B) could characterize the crystallization of dravite (Alkali-deficient Mg-foitite, where B is present in trigonal coordination); however this interpretation was not confirmed by micro-scale observations. Boron could be hosted in different, yet uncharacterized, mineral species, such as illite, in tetragonal coordination (Kandasami, 2015). Many elements (B, MgO, K_2O, Al_2O_3 and U) are positively correlated indicating that uranium mineralization is associated with increase of elements that usually represent alteration of the host rock, moreover, the association of U and B is a characteristic feature of unconformity-related uranium mineralization (Sopuck et al., 1983; Jefferson et al., 2007; Mercadier et al., 2012).

3.2 Minor elements characterizing ore minerals and uranium mineralization

In the case of U1 (Fig. 47), uranium mineralization is correlated with elevated levels of several metals such as W (5-20 ppm), Zn (30-140 ppm), Ni (200-1000 ppm), As (200-1000 ppm), Co (70-400 ppm), Mo (3-15 ppm), Pb (200-800 ppm), Ag (5-30 ppm), Bi (100-1000 ppm), V (300-1000 ppm), and Se (10-20 ppm). Ni-As-Co-Mo and Bi were analyzed under SEM in samples coming from CONT-23 fault zone, as anhedral assemblages of native elements and un-identified minerals, associated with U. Pb can be contained in pitchblende (as radiogenic lead in UO_2) or galena (PbS). Anhedral compounds containing Ag were observed once mixed with uranium associated with galena as cementing microfractures in quartz. No minerals were observed at the micro-scale for characterizing the augmentations in W, Zn, Mo and V. Increase in Zn, which also positively correlate with Cu and S, could be explained by sphalerite ((Zn, Fe)S). Sphalerite was not observed in the Contact prospect, but was at the 85W prospect. The pathfinder elementa discussed above (W, Zn, Mo, Ni, As, Ag, Pb, Se, Bi and V) are commonly associated with U in unconformity-related uranium deposits (Ruzicka et al., 1989; Hoeve and Quirt, 1984; Jefferson et al., 2007), and could be associated with non-observed nano-minerals, clays or in minerals in concentrations too low to be detected. The characterization of U1 as a

polymetallic stage (defined as such after macro- to micro-scale observations made throughout the Contact prospect, see section 5.2.1) is confirmed through these observations.
For U2 (Fig. 48), the majority of pathfinder elements also display enrichment (W (3-10 ppm), Zn (30-140 ppm), Ni (40-100 ppm), As (15-80 ppm), Co (4-15 ppm), Mo (3-15 ppm), Pb (100-500 ppm), Ag (3-12 ppm), Bi (25-90 ppm), V (200-1000 ppm) and Se (8-15 ppm) also display enrichment but – with the exceptions of Mo, V and Se - much less compared to U1. Contrary to U1, no minerals or anhedral assemblages were observed at the micro-scale to explain enrichment in these metals.

In the case of U1 fault zone, there is increased (Fig. 47) in S (750-3000 ppm), Cu (20-60 ppm), Ni (200-1000 ppm) and Co (100-400 ppm), correlated with Fe. These positive correlations are consistent with the crystallization of sulfides (pyrite (FeS_2), chalcopyrite ($CuFeS_2$) and bravoite ($(Fe,Ni,Co)S_2$) observed under optical microscope and more precisely characterized under SEM. However, chalcopyrite and bravoite are are not abundant enough to account for the anomalous values. This is especially true for the peak values of these elements witch correlate poorly with the presence of the minerals. And also in the case of Ni, Co and Cu. Ni and Co are more correlated with U as presented before. These elements are much stronger enriched in the case of U1 compared to U2, as U2 is a monometallic mineralizing stage, characterized by pitchblende, coffinite and rare sulfides (see section 5.2.1).

4 PRINCIPAL COMPONENT ANALYSIS

The variations displayed by the major oxides usually result from variations in mineralogy (clay alteration of the host rock minerals). This can be seen as an expression of primary rock type, alteration mineral assemblages, or both. PCA was conducted for four different lithologies, main results are presented hereafter for the granitic gneiss, which is the dominant lithologies at Contact, (host of most of uranium mineralization) and for intrusives (granite/granodiorite, syenite and lamprophyre, as characterized by geologists of Areva Resources Canada during exploration campaigns). Samples used for PCA were labelled with the dominant “alteration” type, after macroscopic observations: “Fresh” is for fresh rocks, “silicification” for silicified rocks (around SiO_2 90 wt%) usually due to the presence of the Quartz Breccia (QB, which could be considered as a new lithology where the brecciation is the most intense), “Grey” for the first stage of uranium mineralization (U1), “SecHem” for the second stage of uranium mineralization (U2), “Greenclay” for greenish clay-altered fault zones, “whiteclay” for post-ore clay alteration (f8).

"SecHemLight" and "Bleaching" characterize alteration hematization and iron oxides removal, respectively. In the following part F1, F2, F3… refer to components, while f1, f2, f3… refer to the fracturing stages.

4.1 Granitic gneiss

Figure 49A displays eigenvalues and % of variance explained against cumulative components. Figure 49B shows the contribution of major and minor element variances from five components that account for 72.55 % of the variation in the data. U contributes more to F2 and F3. F1 plus F2 account for 49.72% of the total variability in the granitic gneiss dataset.

A

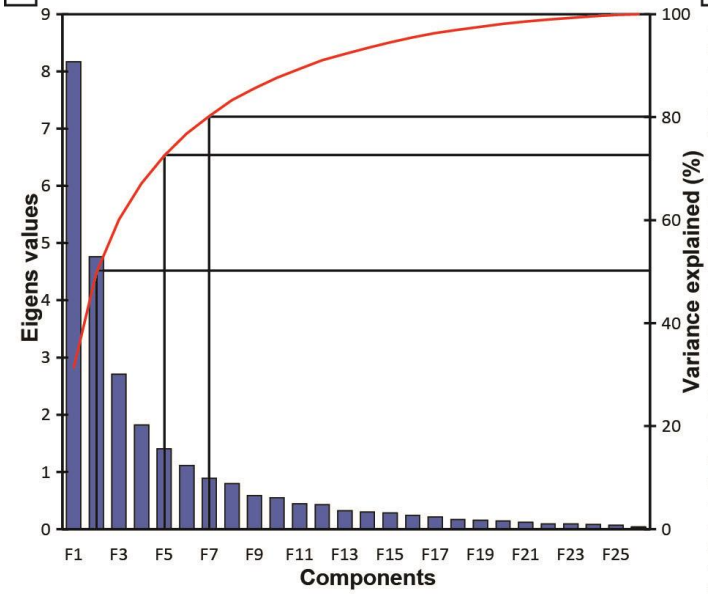

B

	F1	F2	F3	F4	F5
SiO2	8,00	0,17	0,60	10,07	1,42
TiO2	9,15	0,00	4,64	0,41	0,49
Al2O3	7,10	0,63	1,46	12,87	0,19
Fe2O3 FeO	2,58	0,00	0,01	1,60	2,71
MnO	1,65	8,50	2,49	2,68	7,73
MgO	6,01	3,79	1,71	0,00	6,97
CaO	3,09	6,91	0,36	3,81	0,12
Na2O	0,26	8,58	12,04	4,75	0,19
K2O	0,34	1,74	0,35	36,94	0,01
P2O5	6,56	0,30	4,52	0,43	1,08
B	4,59	7,48	3,42	0,43	0,25
Ce	0,48	7,73	0,15	2,04	6,03
Cr	7,37	0,00	2,88	1,45	0,65
Sr	0,04	12,95	2,72	0,53	2,73
Ni	8,11	0,03	0,75	0,71	0,08
As	5,75	0,52	0,60	0,64	9,43
Co	4,03	6,47	0,40	3,77	0,36
Ag	0,54	0,00	4,48	2,35	16,05
Zn	3,22	7,67	0,78	2,12	3,77
Mo	1,20	0,10	10,26	1,59	1,22
Pb	2,62	3,62	17,60	0,09	0,03
V	6,03	3,14	5,70	0,37	0,57
Bi	8,55	0,55	0,04	0,05	0,10
U	2,41	6,79	11,75	0,04	0,04
Zr	0,02	0,84	0,40	8,35	37,06
Ba	0,29	11,50	9,86	1,90	0,74
	100	100	100	100	100

Figure 49: A) Variability of the principal component, with five components accounting for 72.55%. Seven components account for 80.24% of the total variability. B) Contribution of each variable for components F1 to F5.

F1 to F5 are plotted against each others in figure 50A-F. The F1-F2 plot in Fig. 50A shows an association of Ca, Na, Ba and Sr (F2 positive axis), for fresh samples, consistent with observations made previously and indicating weak to no alteration of feldspars. These elements coherently display an opposite trend to elements interpreted to be associated with alteration (Al, Ti, Cr, B). This negative correlation is better observed on the F3-F1 plot (Fig.50B). "GreenClay", "SecHemLight" and "Bleaching" possibly display close resemblance to "Fresh" in term of elemental correlation because they represent only weak clay alteration of the host rock.

Alteration is also characterized by the strong negative correlation between Si, Al, and Ti (Si-loss through desilicification Al an Ti "enriched" through loss of other more mobile elements).

Grey-U1 samples are associated with Mo, U, V, Ag, Bi, As, Zn. Overall, “Grey”, “whiteClay” and “SecHem”, characterize clay alteration of the host rock, desilicification and metals enrichment associated with U1 and U2; and clay alteration and desilicification associated with “WhiteClay”. They show an opposite trend and so are not associated with “fresh”, “silicification”, “SecHemLight”, and “Bleaching”. There is a weaker association between “SecHem” and U compared to “grey” and U that can be explained by the presence of unmineralized clay altered fault zones (in the case of U2). As such, “WhiteClay” is observed in several plots (Fig. 50B, 50C, 42A, 42B) to be associated with “SecHem”. The association of U, Al, V, Pb, and B is expressed in F4-F2 and F5-F2 (Fig. 50D and 50E repectively).

differencees between U1 and U2 can be seen in when examining the relationship between U and various elements and oxides (plot F3-F1, Fig. 50B and F3-F2, Fig. 50A). that the correlation of U to Al and Ti is weaker in U1 than U2, consistent with a weaker (although still present) clay alteration of the host rock.

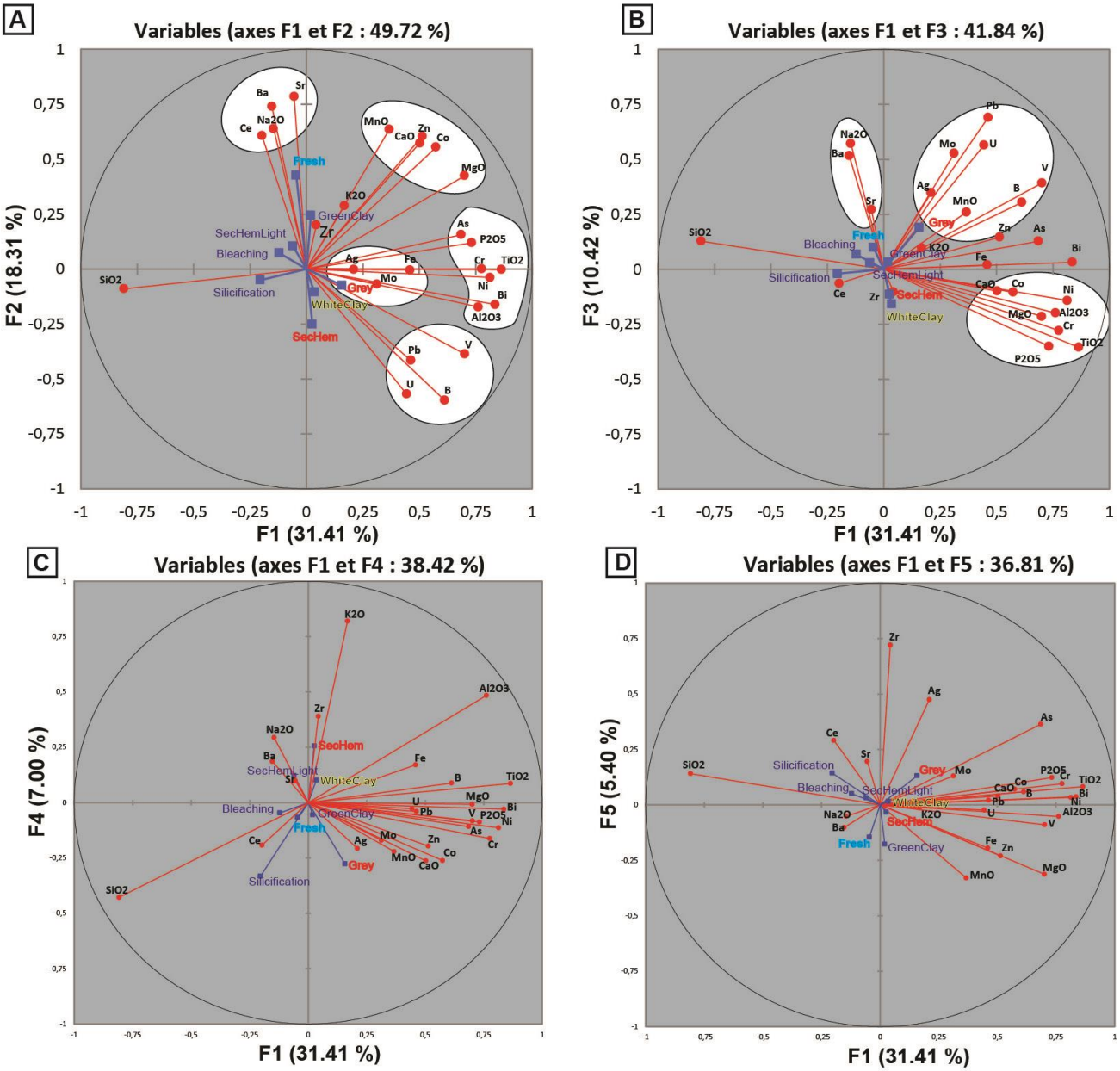

Figure 50: Correlations between loadings and factors for granitic gneiss samples.

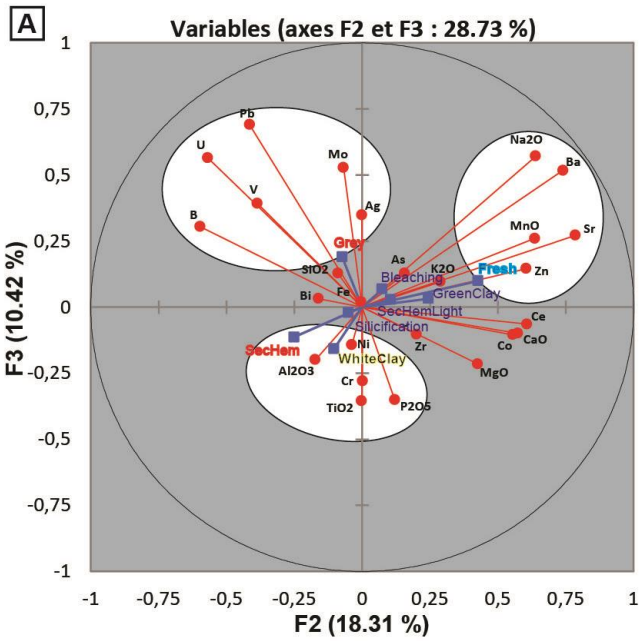
A
Variables (axes F2 et F3 : 28.73 %)
F3 (10.42 %)
F2 (18.31 %)
Pb
U
Mo
V
Ag
B
Grey
SiO2
Fe
As
K2O
Bleaching
Fresh
Zn
Bi
GreenClay
SecHemLight
Silicification
Ce
SecHem
Ni
Zr
CaO
Al2O3
WhiteClay
Co
Cr
MgO
TiO2
P2O5
Na2O
Ba
MnO
Sr

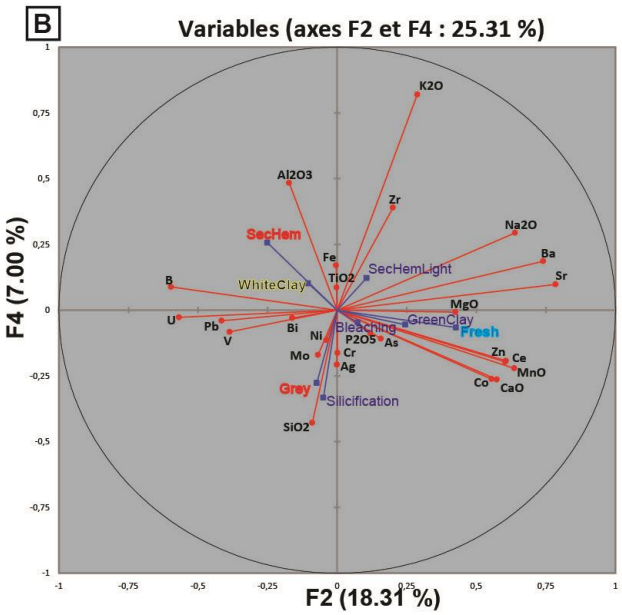
B
Variables (axes F2 et F4 : 25.31 %)
F4 (7.00 %)
F2 (18.31 %)
K2O
Al2O3
Zr
SecHem
Na2O
Fe
Ba
TiO2
SecHemLight
Sr
B
WhiteClay
MgO
U
Pb
GreenClay
V
Bi
Ni
Bleaching
Fresh
P2O5
As
Mo
Cr
Zn
Ce
Ag
MnO
Grey
Co
CaO
Silicification
SiO2

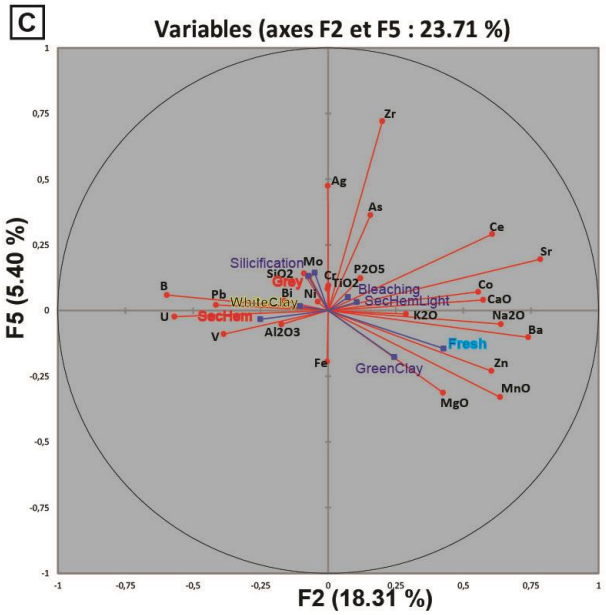
C
Variables (axes F2 et F5 : 23.71 %)
F5 (5.40 %)
F2 (18.31 %)
Zr
Ag
As
Ce
Sr
Silification
Mo
P2O5
SiO2
Cr
Grey
TiO2
Bleaching
Co
B
Pb
Bi
Ni
SecHemLight
CaO
WhiteClay
U
SecHem
K2O
Na2O
Al2O3
Ba
V
Fresh
Fe
Zn
GreenClay
MnO
MgO

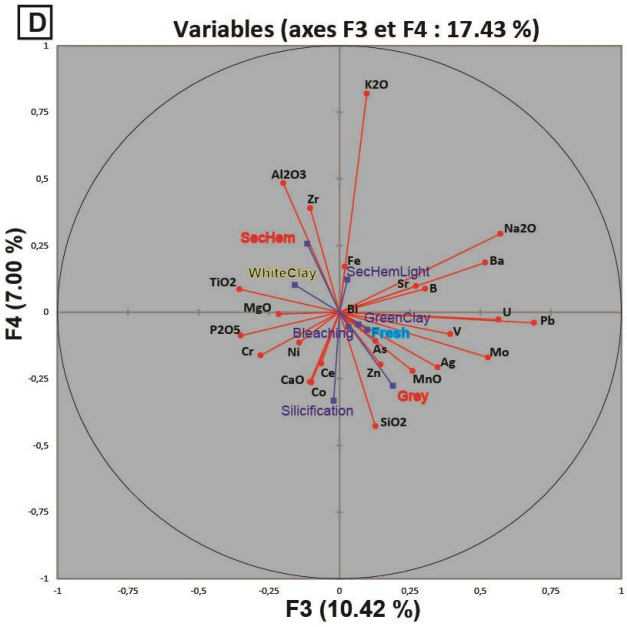
D
Variables (axes F3 et F4 : 17.43 %)
F4 (7.00 %)
F3 (10.42 %)
K2O
Al2O3
Zr
SecHem
Na2O
Fe
Ba
WhiteClay
SecHemLight
TiO2
Sr
B
MgO
Bi
U
Pb
GreenClay
P2O5
Bleaching
Fresh
V
Cr
Ni
As
Mo
Ag
Zn
CaO
Ce
MnO
Co
Grey
Silicification
SiO2

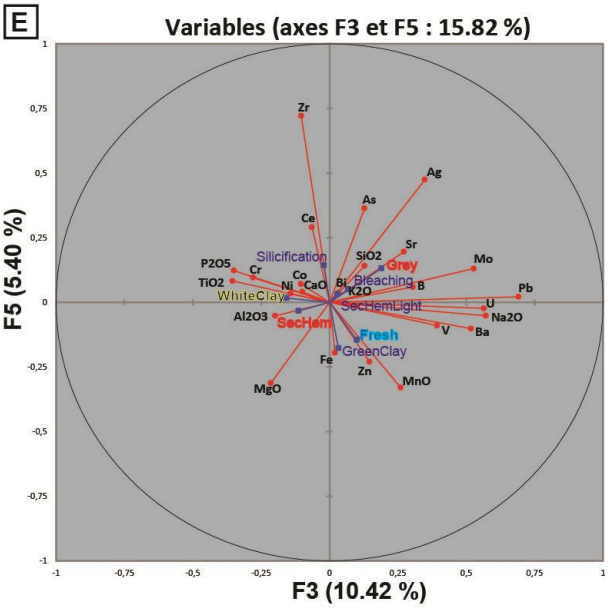
E
Variables (axes F3 et F5 : 15.82 %)
F5 (5.40 %)
F3 (10.42 %)
Zr
Ag
As
Ce
Sr
P2O5
Silicification
SiO2
Mo
Cr
Grey
Co
TiO2
Bi
Bleaching
B
Pb
Ni
CaO
K2O
WhiteClay
SecHemLight
U
Al2O3
SecHem
Na2O
Fresh
V
Ba
GreenClay
Fe
Zn
MnO
MgO

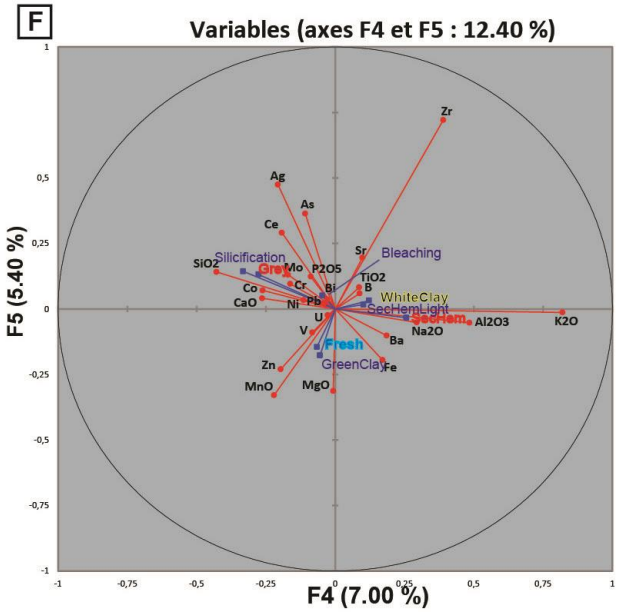
F
Variables (axes F4 et F5 : 12.40 %)
F5 (5.40 %)
F4 (7.00 %)
Zr
Ag
As
Ce
Sr
Bleaching
SiO2
Silicification
Grey
Mo
P2O5
TiO2
Cr
Co
Bi
B
CaO
Ni
Pb
WhiteClay
SecHemLight
U
SecHem
Al2O3
K2O
V
Na2O
Ba
Fresh
GreenClay
Fe
Zn
MnO
MgO

Figure 50 cont'd: Correlations between loadings and factors for granitic gneiss samples.

4.2 Intrusives

Figure 51 presents eigenvalues and % of variance explained against cumulative components, with the contribution of major and minor elements for three types of intrusive rocks: Granite/Granodiorite (77.40 % of the variation in the data explained by 5 components), Lamprophyre (80.75 % of the variation in the data explained by 5 components), and syenite (85.38 % of the variation in the data explained by 5 components). U is better explained by F3 in the case of granite/granodiorite samples, by F2 in the case of lamprophyre samples, and by F1 in the case of syenite samples.

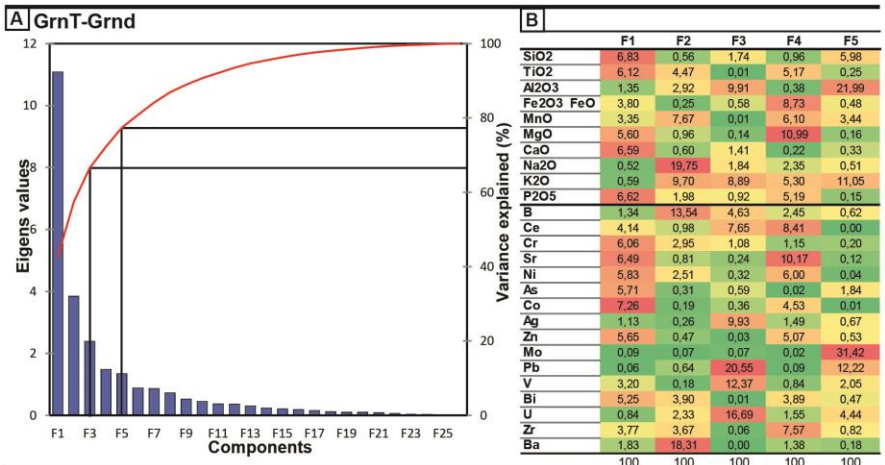

B

	F1	F2	F3	F4	F5
SiO2	6,83	0,56	1,74	0,96	5,98
TiO2	6,12	4,47	0,01	5,17	0,25
Al2O3	1,35	2,92	9,91	0,38	21,99
Fe2O3 FeO	3,80	0,25	0,58	8,73	0,48
MnO	3,35	7,67	0,01	6,10	3,44
MgO	5,60	0,96	0,14	10,99	0,16
CaO	6,59	0,60	1,41	0,22	0,33
Na2O	0,52	19,75	1,84	2,35	0,51
K2O	0,59	9,70	8,89	5,30	11,05
P2O5	6,62	1,98	0,92	5,19	0,15
B	1,34	13,54	4,63	2,45	0,62
Ce	4,14	0,98	7,65	8,41	0,00
Cr	6,06	2,95	1,08	1,15	0,20
Sr	6,49	0,81	0,24	10,17	0,12
Ni	5,83	2,51	0,32	6,00	0,04
As	5,71	0,31	0,59	0,02	1,84
Co	7,26	0,19	0,36	4,53	0,01
Ag	1,13	0,26	9,93	1,49	0,67
Zn	5,65	0,47	0,03	5,07	0,53
Mo	0,09	0,07	0,07	0,02	31,42
Pb	0,06	0,64	20,55	0,09	12,22
V	3,20	0,18	12,37	0,84	2,05
Bi	5,25	3,90	0,01	3,89	0,47
U	0,84	2,33	16,69	1,55	4,44
Zr	3,77	3,67	0,06	7,57	0,82
Ba	1,83	18,31	0,00	1,38	0,18
	100	100	100	100	100

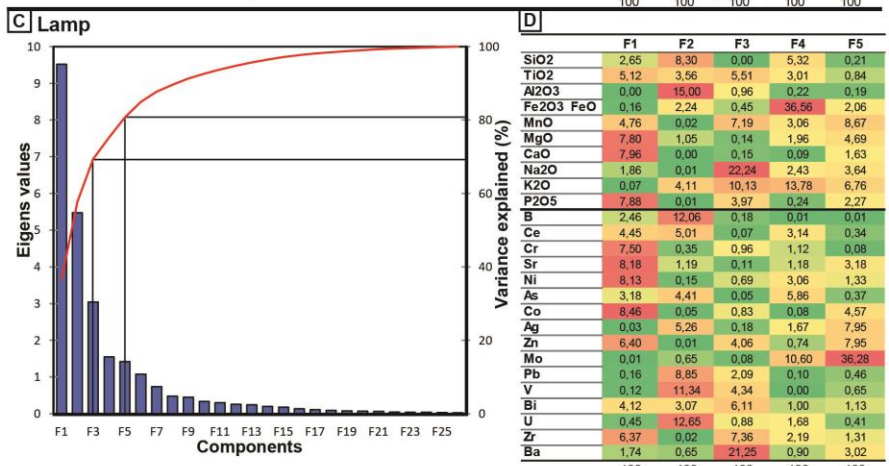

D

	F1	F2	F3	F4	F5
SiO2	2,65	8,30	0,00	5,32	0,21
TiO2	5,12	3,56	5,51	3,01	0,84
Al2O3	0,00	15,00	0,96	0,22	0,19
Fe2O3 FeO	0,16	2,24	0,45	36,56	2,06
MnO	4,76	0,02	7,19	3,06	8,67
MgO	7,80	1,05	0,14	1,96	4,69
CaO	7,96	0,00	0,15	0,09	1,63
Na2O	1,86	0,01	22,24	2,43	3,64
K2O	0,07	4,11	10,13	13,78	6,76
P2O5	7,88	0,01	3,97	0,24	2,27
B	2,46	12,06	0,18	0,01	0,01
Ce	4,45	5,01	0,07	3,14	0,34
Cr	7,50	0,35	0,96	1,12	0,08
Sr	8,18	1,19	0,11	1,18	3,18
Ni	8,13	0,15	0,69	3,06	1,33
As	3,18	4,41	0,05	5,86	0,37
Co	8,46	0,05	0,83	0,08	4,57
Ag	0,03	5,26	0,18	1,67	7,95
Zn	6,40	0,01	4,06	0,74	7,95
Mo	0,01	0,65	0,08	10,60	36,28
Pb	0,16	8,85	2,09	0,10	0,46
V	0,12	11,34	4,34	0,00	0,65
Bi	4,12	3,07	6,11	1,00	1,13
U	0,45	12,65	0,88	1,68	0,41
Zr	6,37	0,02	7,36	2,19	1,31
Ba	1,74	0,65	21,25	0,90	3,02
	100	100	100	100	100

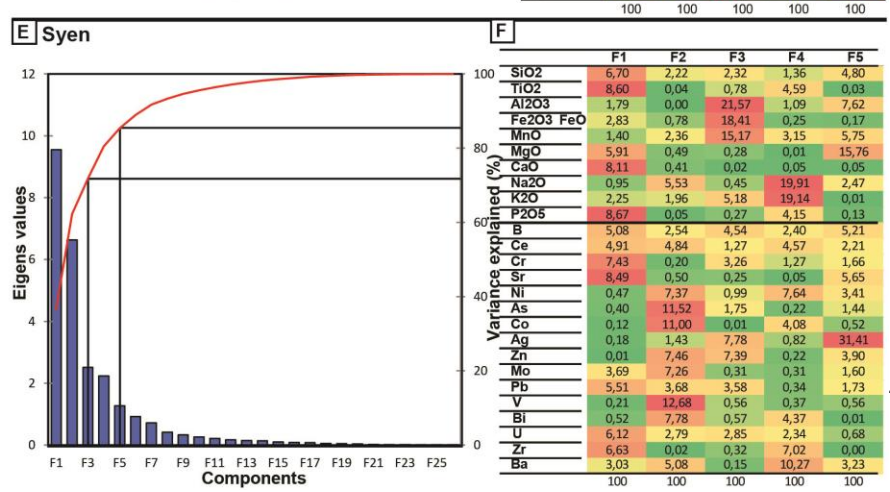

F

	F1	F2	F3	F4	F5
SiO2	6,70	2,22	2,32	1,36	4,80
TiO2	8,60	0,04	0,78	4,59	0,03
Al2O3	1,79	0,00	21,57	1,09	7,62
Fe2O3 FeO	2,83	0,78	18,41	0,25	0,17
MnO	1,40	2,36	15,17	3,15	5,75
MgO	5,91	0,49	0,28	0,01	15,76
CaO	8,11	0,41	0,02	0,05	0,05
Na2O	0,95	5,53	0,45	19,91	2,47
K2O	2,25	1,96	5,18	19,14	0,01
P2O5	8,67	0,05	0,27	4,15	0,13
B	5,08	2,54	4,54	2,40	5,21
Ce	4,91	4,84	1,27	4,57	2,21
Cr	7,43	0,20	3,26	1,27	1,66
Sr	8,49	0,50	0,25	0,05	5,65
Ni	0,47	7,37	0,99	7,64	3,41
As	0,40	11,52	1,75	0,22	1,44
Co	0,12	11,00	0,01	4,08	0,52
Ag	0,18	1,43	7,78	0,82	31,41
Zn	0,01	7,46	7,39	0,22	3,90
Mo	3,69	7,26	0,31	0,31	1,60
Pb	5,51	3,68	3,58	0,34	1,73
V	0,21	12,68	0,56	0,37	0,56
Bi	0,52	7,78	0,57	4,37	0,01
U	6,12	2,79	2,85	2,34	0,68
Zr	6,63	0,02	0,32	7,02	0,00
Ba	3,03	5,08	0,15	10,27	3,23
	100	100	100	100	100

Figure 51: Granite/granodiorite samples (A, B), Lamprophyre samples (C, D) and Syenite samples (E, F): % of variability explained by cumulative component B) Contribution of each variable for components F1 to F5.

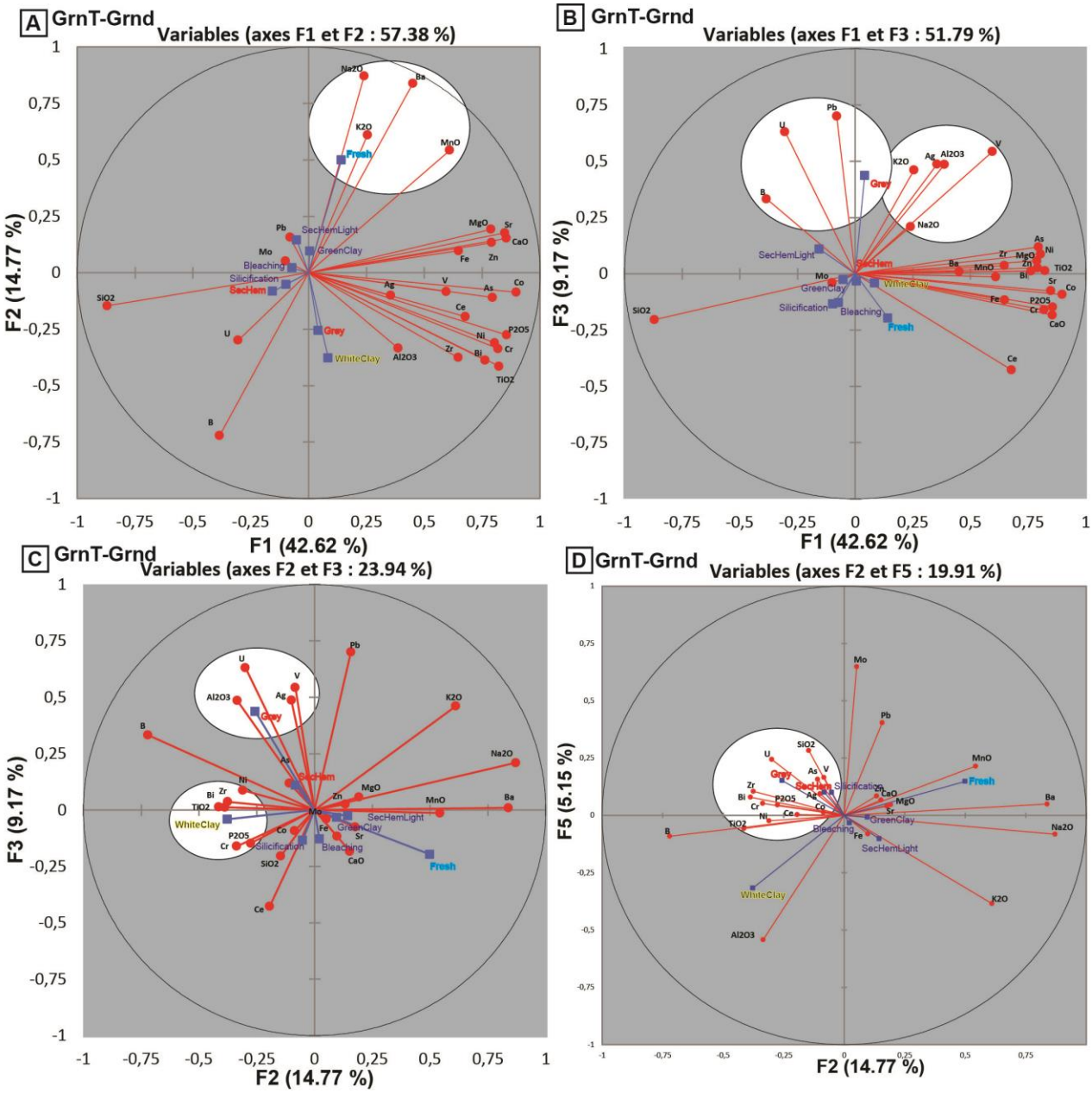

Figure 52: Selected correlations between loadings and factors for Granite/Granodiorite samples.

In overall, the same kind of element associations and positive and negative element association trends are observed for altered and/or mineralized intrusives, with only minor differences by lithology.

In granitic-granodioritic samples, fresh rocks are characterized by the K, Na, Mn and Ba association, these elements displaying an opposite trend to U and B (F2-F1, Fig. 52A; weaker negative association is displayed in Fig. 52B-D). The observation that fresh rocks are inversely associated with Si can be explained by the presence of silicified clay-altered, non-mineralized fault zones, within or in the vicinity of the Quartz Breccia. Examples of such silicified fault zones were shown in the previous section. SecHem samples display an association with U and some

metals (Ag, V, As, Co, Ni; Fig. 52C-D), but still weaker compared to Grey samples. WhiteClay alteration is well represented by a Ti and Zr association, and shows a strong inverse association with Ba (Fig. 52C-D). The association of WhiteClay with Al is weaker compared to Grey-U1, which could be explained by the crystallization of Al-rich chlorite (sudoite) during U1. GreenClay, Bleaching and SecHemLight samples don't display significant element associations, as they are not characterized either by significant clay alteration nor mineralization.

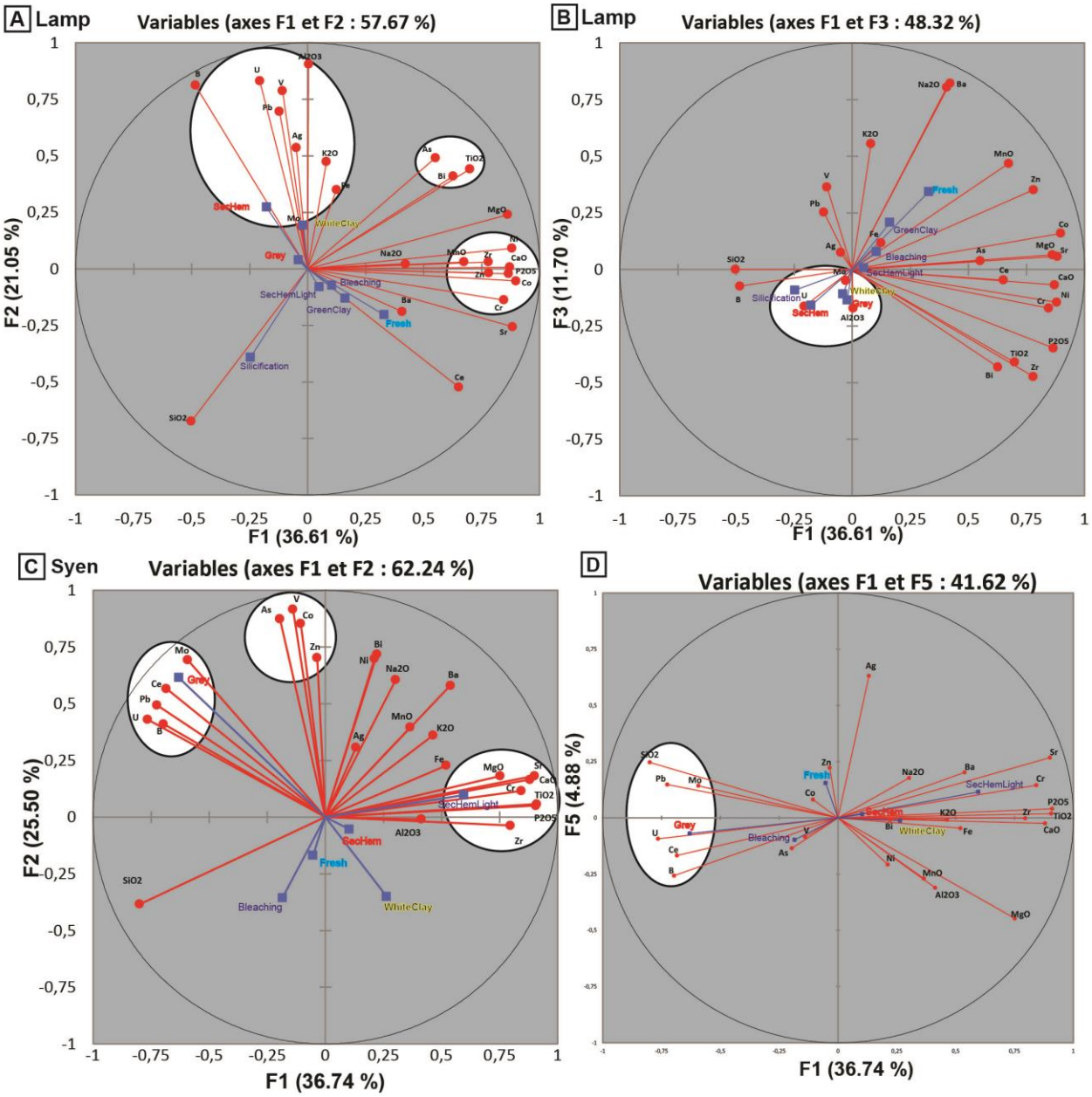

Figure 53: Selected correlations between loadings and factors for Lamprophyres (A, B) and Syenite (C, D) samples.

Element associations are stronger in the case of lamprophyre and syenite samples. For lamprophyre, Grey, SecHem and WhiteClay are characterized by association of U, Pb, Ag, Mo, and Fe metal enrichment (Fig. 53A), which is associated with clay alteration characterized by Al and K (likely illitization). Unlike granitic and granitic gneiss samples, As and Co are less associated with U. SecHem samples are better associated with U compared to Grey samples (Fig. 53A, B) which could be explained by the presence of more SecHem-mineralized fault zones in lamprophyre and less SecHem non-mineralized fault zones compared to granitic gneiss, therefore strengthening the association between U and SecHem.

For syenite samples, Grey samples are characterized by a strong association of Mo, Ce, Pb, U, and B (Fig. 53C) and a weaker association with As, V, Co, and Zn. U content is inverse to SecHem, which is weakly associated with WhiteClay (Al, Ti, K, Mg; (Fig. 53D), which could be explained by the presence of non-mineralized SecHem-bearing fault zones intersected in drill core.

In intrusive rocks, the element association(s) characterizing alteration are weaker than for the granitic gneiss. This geochemical feature is consistent with the observation of less fractured fault rock in these lithologies (Fig. 54), compared to granitic gneiss, likely explained by different responses to tectonic stress due to different rheological behaviour.

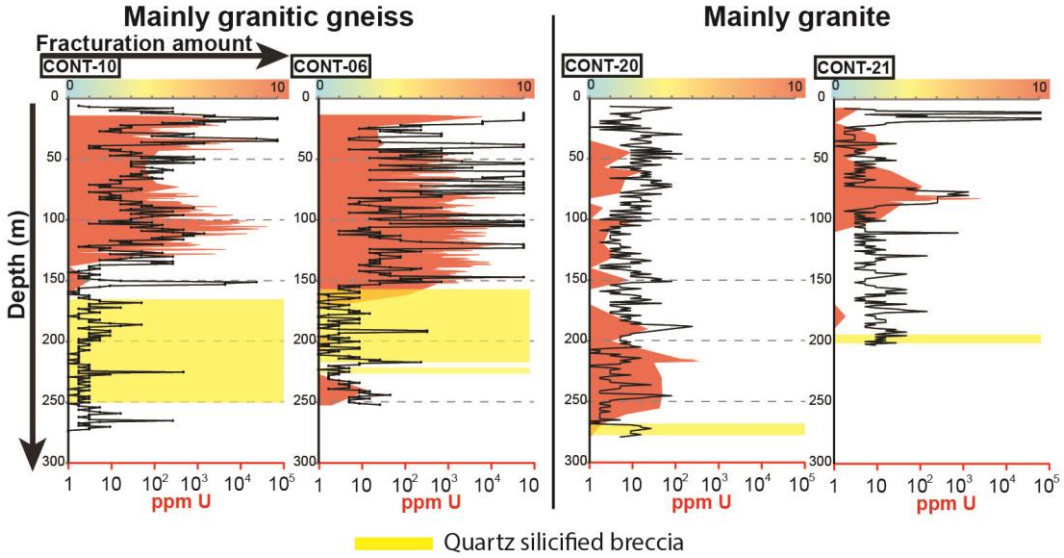

Figure 54: Fracture density and uranium content (ppm) differences between granitic gneiss and granite, for four drill holes from the Contact prospect.

4.3 Synthesis and conclusions

Geochemical characterization of fracturing events and associated host-rock alteration in faults at the Contact prospect was performed through the PCA of whole rock geochemical data of two fault zones containing the first and second stages of uranium mineralization. PCAprovided

a geochemical characterization of U1 and U2 and elemental characterization of other fracturing events.

- The First (“grey”) and second (“SecHem”) stages of uranium mineralization display different enrichment in metals. U1 displays moderate enrichment in W, Zn, Ni, As, Co, Mo, Pb, Ag, Bi, V, and Se, while U2 displays weak to moderate enrichment in the same elements, except for Mo, V and Se. These elements are usually associated with U-enrichment, which is stronger and focused around narrow fault zones in the case of U1. Local stronger associations of these metals in the case of U2 may be explained by U2-fault zones cross-cutting U1-fault zones thus redistributing and reconcentrating these elements. The differences in elemental enrichments between these two uranium mineralizing stages could imply different fluid characteristics, or simply that the stock of metals (as yet unconstrained) was depleted after circulation of fluids linked to U1.

- Grey, SecHem, and WhiteClay, as discussed in previous sections of the thesis, are the three dominant altering features at the Contact prospect. Elements related to alteration show greater associations with WhiteClay, which is the result of the main clay altering event. WhiteClay is less associated with B than are Grey and SecHem, and it is at best weakly associated with U, consistent with the conclusion made in the previous section (WhiteClay is not a mineralizing event). The association between B and uranium mineralization is a feature observed in Athabasca uranium deposits and allows an inference that the Contact prospect may be of the unconformity-related type. However the origin of the anomaly has to be explored, as no dravite was observed at the Contact prospect, it could be contained in illite, as suggested by Kandasami (2015).

- The associations of uranium and elements characterizing alteration of the host rock are less strong for the intrusive rocks, reflecting the weaker degrees of fracturing and less pervasive spread of alteration in such rocks.

Sample	n°	La	Ce	Pr	Nd	Sm	Eu	Gd	Tb	Dy	Ho	Er	Tm	Yb	Lu	Total REE	LREE	HREE	HREE/LREE
9850	1	280	510	149	1000	625	208	1120	172	685	85	154	15	76	8	5087	2772	1023	0,37
9850	2	396	576	146	940	608	197	1018	164	657	82	144	14	77	8	5027	2863	983	0,34
9850	3	811	879	125	646	354	117	506	92	382	47	84	10	53	6	4112	2932	582	0,20
9850	4	828	882	125	607	286	91	336	63	253	30	55	6	37	4	3602	2818	384	0,14
9850	5	838	911	143	693	354	75	408	81	343	41	80	10	61	6	4043	3014	540	0,18
9850	6	846	992	150	737	358	89	456	79	336	41	81	9	53	6	4232	3172	526	0,17
9568-39	1	39	297	58	361	358	182	897	195	928	127	269	28	144	12	3895	1295	1508	1,16
9568-39	2	79	439	80	453	361	169	836	172	866	117	237	24	125	11	3969	1581	1380	0,87
9568-39	3	46	332	61	370	355	173	872	182	942	123	256	26	141	12	3891	1337	1500	1,12
9568-39	4	49	337	63	398	345	169	824	179	927	117	255	26	141	11	3841	1361	1477	1,09
9568-39	5	67	400	69	397	309	149	736	158	798	100	215	21	121	9	3549	1391	1264	0,91
9568-39	6	61	387	70	393	355	163	804	170	891	115	234	24	126	11	3804	1429	1401	0,98
9568-38	1	82	451	64	330	210	102	448	106	604	79	182	19	109	10	2796	1239	1003	0,81
9568-38	2	54	318	55	315	297	136	700	159	848	115	254	26	148	12	3437	1175	1403	1,19
9568-38	3	60	382	62	361	286	136	622	133	729	93	196	21	117	12	3210	1287	1168	0,91
9568-38	4	67	408	65	357	280	127	589	131	717	95	208	22	126	12	3204	1304	1180	0,90
9568-08	1	14	148	39	279	302	127	994	255	1219	162	353	35	198	17	4142	909	1984	2,18
9568-08	2	32	205	48	324	304	131	1024	260	1353	186	369	42	209	19	4506	1044	2178	2,09
AND-15-01-05	1	182	702	148	895	622	213	1050	211	990	139	258	27	147	13	5595	2762	1573	0,57
AND-15-01-05	2	164	861	153	990	756	244	1317	267	1280	175	319	36	194	17	6772	3168	2020	0,64
AND-15-01-05	3	222	723	209	1322	1031	356	2020	424	2100	301	586	62	323	31	9711	3863	3404	0,88
AND-15-01-05	4	234	747	212	1291	1011	406	1890	412	2050	285	545	60	316	31	9491	3901	3287	0,84
9851	1	46	352	95	595	418	145	843	141	554	64	104	10	45	4	3416	1651	781	0,47
9851	2	40	320	104	692	496	182	1027	173	681	80	135	13	62	6	4010	1833	976	0,53
9851	3	44	341	94	598	416	144	834	134	518	62	102	9	42	4	3340	1637	735	0,45
9851	4	44	337	101	639	467	161	937	157	588	69	116	11	49	4	3681	1749	838	0,48
AND-15-01-04	1	185	104	15	83	110	38	303	104	562	78	157	19	107	11	1875	534	933	1,75
AND-15-01-04	2	247	152	24	151	193	71	552	189	996	136	281	34	187	19	3231	838	1652	1,97
AND-15-01-04	3	225	107	13	80	110	38	342	116	632	85	176	21	116	12	2073	573	1042	1,82
AND-15-01-04	4	155	72	10	61	85	29	285	93	491	70	145	17	91	10	1613	412	823	2,00
AND-15-01-04	5	173	97	13	83	123	38	369	135	724	95	190	24	134	13	2210	526	1181	2,25
AND-15-01-04	6	184	101	14	83	119	40	363	131	716	93	193	24	132	13	2206	541	1171	2,17

Table 1: Table of REE concentrations (in ppm), measured by ICPMS.

Location	Sample-ID	204Pb/206Pb	207Pb/206Pb	206Pb/238U	207Pb/235U	Age
Andrew Lake	9850-c1-1	0,001642	0,07751	0,014660604	0,109215234	370
Andrew Lake	9850-c1-2	0,004242	0,125555	0,068467657	0,615362026	780
Andrew Lake	9850-c1-3	0,001166	0,0738994	0,032331466	0,255804938	505
Andrew Lake	9850-c1-4	0,001728	0,08399551	0,036170349	0,296417036	582
Andrew Lake	9850-c1-5	0,001024	0,07002361	0,024899086	0,190626823	432
Andrew Lake	9850-c1-6	0,002775	0,09807715	0,0505801	0,406977857	543
Andrew Lake	9850-c1-7	0,001493	0,08057929	0,024322087	0,199249681	581
Andrew Lake	9850-c2-1	0,000524	0,0623962	0,048517706	0,368713555	416
Andrew Lake	9850-c2-2	0,000166	0,05649702	0,049776865	0,373395789	387
Andrew Lake	9850-C4-1-1	0,000120	0,06964182	0,008829534	0,08324182	878
Andrew Lake	9850-C4-1-2	0,000073	0,05664802	0,008218265	0,063425188	448
Andrew Lake	9850-C4-1-3	0,000049	0,0533411	0,008769392	0,064085108	325
Andrew Lake	9850-C4-1-4	0,000103	0,07157625	0,009047319	0,088020801	943
Andrew Lake	9850-C4-1-5	0,000030	0,05225467	0,008601531	0,061901253	290
Andrew Lake	9850-C4-1-6	0,000037	0,0500914	0,009052608	0,062292567	187
Andrew Lake	9850-C4-2-1	0,000076	0,0615693	0,008251244	0,069275913	633
Andrew Lake	9850-C4-3-1	0,000060	0,05668002	0,008196914	0,063522254	457
Andrew Lake	9850-C4-3-2	0,000136	0,0703336	0,008714792	0,082735121	892
Andrew Lake	9850-c1-8	0,001900	0,08541147	0,027414877	0,220481213	541
Andrew Lake	9850-c1-9	0,002303	0,102569	0,013581603	0,131488384	933
Andrew Lake	9850-c1-10	0,003485	0,111087	0,066734613	0,564156243	650
Andrew Lake	9850-c1-11	0,001846	0,08267321	0,031171439	0,241959239	463
Andrew Lake	9850-c1-12	0,001812	0,08473311	0,032098719	0,260861174	564
Andrew Lake	9850-c1-13	0,004619	0,13433	0,06233239	0,591935559	895
Andrew Lake	9850-c1-14	0,003437	0,117195	0,021618698	0,204435694	885
Andrew Lake	9850-c1-15	0,000582	0,06294565	0,00939346	0,071071628	404
Andrew Lake	9850-c1-16	0,001861	0,0830558	0,011670531	0,090927683	470
Andrew Lake	9850-C4-4-1	0,000083	0,06437074	0,008169324	0,071645248	726
Andrew Lake	9850-C5-1	0,000030	0,05502162	0,033302645	0,252114692	408
Andrew Lake	9850-C5-2	0,000080	0,06066902	0,009941995	0,082113454	598
Andrew Lake	9850-C5-3	0,000046	0,053962	0,033933872	0,250825397	354
Andrew Lake	9850-C5-4	0,000043	0,05535985	0,034755737	0,263820574	414
Andrew Lake	9850-C6-1	0,000217	0,06203522	0,010146345	0,082946848	575
Andrew Lake	9850-C6-02	0,000074	0,06677692	0,009307428	0,084880162	809
Andrew Lake	9850-C6-03	0,000053	0,0572022	0,007600783	0,059552441	482
Andrew Lake	9850-C6-04	0,000094	0,07768733	0,007540096	0,079906984	1115
Andrew Lake	9850-C6-05	0,000070	0,06482279	0,008599675	0,076164929	747
Andrew Lake	9850-C6-06	0,000075	0,0643322	0,007045109	0,061868066	729
Andrew Lake	9850-C6-07	0,000117	0,06675561	0,008148236	0,073600484	788
Andrew Lake	9850-C6-08	0,000068	0,05640045	0,007921137	0,060932532	441
Andrew Lake	9850-C6-09	0,000057	0,05841934	0,008506557	0,068017058	527
Andrew Lake	9850-C6-10	0,000068	0,06637461	0,010168811	0,092286459	799
Andrew Lake	9850-C6-11	0,000095	0,05805112	0,007849113	0,061762884	491
Andrew Lake	9850-C6-12	0,000065	0,06008085	0,008165605	0,06703056	584
Andrew Lake	9850-C6-13	0,000100	0,06271361	0,00814202	0,069258405	661
Andrew Lake	9850-C6-14	0,000084	0,07870979	0,010521064	0,113162872	1146
Andrew Lake	9850-C6-15	0,000071	0,06319337	0,008582426	0,07405999	692
Andrew Lake	9850-C7-1	0,000078	0,05358002	0,040510248	0,294623266	317
Andrew Lake	9850-C7-02	0,000055	0,0530424	0,039132335	0,283505324	308
Andrew Lake	9850-C7-03	0,000033	0,05396065	0,038604361	0,286312292	361
Andrew Lake	9850-C7-04	0,000026	0,0549882	0,024010869	0,18186332	408
Andrew Lake	9850-C6-14	0,000084	0,07870979	0,010521064	0,113162872	1146
Andrew Lake	9850-C6-15	0,000071	0,06319337	0,008582426	0,07405999	692
Andrew Lake	9850-C7-1	0,000078	0,05358002	0,040510248	0,294623266	317
Andrew Lake	9850-C7-02	0,000055	0,0530424	0,039132335	0,283505324	308
Andrew Lake	9850-C7-03	0,000033	0,05396065	0,038604361	0,286312292	361
Andrew Lake	9850-C7-04	0,000026	0,0549882	0,024010869	0,18186332	408
Andrew Lake	9850-C7-05	0,000040	0,05565795	0,034231082	0,261490265	428
Andrew Lake	9850-C7-06	0,000059	0,05715573	0,016651791	0,130083553	477
Andrew Lake	9850-C7-07	0,000043	0,05357185	0,036937111	0,271220034	339
Andrew Lake	9850-C7-08	0,000034	0,08389517	0,019180406	0,221904113	1290
Andrew Lake	9850-C7-09	0,000019	0,05296958	0,046436931	0,339317232	328
Andrew Lake	9850-C7-10	0,000032	0,05257657	0,037393641	0,270269931	303
Andrew Lake	9850-C7-11	0,000115	0,05665197	0,031966383	0,243793242	424
Andrew Lake	9850-C8-1	0,000342	0,06795485	0,011003999	0,096271197	721
Andrew Lake	9850-C8-2	0,000096	0,05835871	0,007802124	0,061710172	502
Andrew Lake	9850-C8-3	0,000119	0,05193232	0,006947776	0,048434298	217
Andrew Lake	15-1-5-C1-1	0,000035	0,05895518	0,018173633	0,147358372	559
Andrew Lake	15-1-5-C1-2	0,000028	0,05840362	0,028718657	0,231005648	542
Andrew Lake	15-1-5-C1-3	0,000021	0,05733913	0,032172968	0,254480449	505
Andrew Lake	15-1-5-C1-4	0,000032	0,05878612	0,029096064	0,235351343	554
Andrew Lake	15-1-5-C1-5	0,000028	0,05774577	0,030808894	0,244983476	516
Andrew Lake	15-1-5-C1-6	0,000041	0,06017628	0,026745056	0,221035065	601
Andrew Lake	15-1-5-C1-7	0,000021	0,05656	0,03212336	0,250645824	475
Andrew Lake	15-1-5-C1-8	0,000035	0,05988	0,026845443	0,221064198	593
Andrew Lake	85W-10-4-C1-1	0,000008	0,07649047	0,200883594	2,127383985	1116
Andrew Lake	85W-10-4-C1-2	0,000007	0,07674037	0,202416359	2,150863386	1123

Location	Sample-ID	204Pb/206Pb	207Pb/206Pb	206Pb/238U	207Pb/235U	Age
Andrew Lake	9851-1	0,000012	0,05314224	0,040778315	0,299516073	340
Andrew Lake	9851-02	0,000033	0,05359653	0,034196689	0,251923909	346
Andrew Lake	9851-03	0,000021	0,05254304	0,044013777	0,31881277	308
Andrew Lake	9851-05	0,000010	0,05303189	0,043982267	0,322546222	336
Andrew Lake	9851-06	0,000012	0,05257626	0,043553977	0,316502489	315
Andrew Lake	9851-07	0,000012	0,05300682	0,042921455	0,314442201	334
Andrew Lake	9851-08	0,000009	0,05258732	0,043573419	0,316996321	318
Andrew Lake	9851-09	0,000008	0,05352651	0,045952136	0,340378357	359
Andrew Lake	9851-10	0,000006	0,05302922	0,046268387	0,339655455	339
Andrew Lake	9851-11	0,000020	0,05357065	0,047551993	0,351387376	353
Andrew Lake	9851-12	0,000011	0,05275873	0,04149957	0,302704887	324
Andrew Lake	9851-13	0,000008	0,05353811	0,051557673	0,381929281	359
Andrew Lake	9851-13	0,000008	0,05353811	0,051557673	0,381929281	359
Andrew Lake	9851-14	0,000020	0,05326421	0,033220963	0,244083537	340
Andrew Lake	9851-15	0,000007	0,05281302	0,047878497	0,349949023	329
Andrew Lake	9851-16	0,000013	0,05353236	0,04484447	0,331699672	356
Andrew Lake	9851-17	0,000005	0,05253193	0,044043039	0,320364765	318
Andrew Lake	9851-18	0,000011	0,05366212	0,0422863	0,313771596	363
Andrew Lake	9851-19	0,000033	0,0545283	0,030108564	0,225697264	385
Andrew Lake	9851-20	0,000006	0,05270049	0,049471687	0,360933284	325
Andrew Lake	9851-21	0,000014	0,05260597	0,033931894	0,246589738	315
Andrew Lake	9851-22	0,000012	0,05283913	0,042644384	0,311469789	327
Andrew Lake	9851-23	0,000007	0,05317427	0,049053113	0,36103905	344
Andrew Lake	9851-24	0,000014	0,05296017	0,047166722	0,345078992	331
85W	85W-10-4-2C1-02	0,000008	0,07682263	-2,085756645	-22,21448025	1124
85W	85W-10-4-2C1-03	0,000003	0,07655954	-0,942419436	-10,00292239	1120
85W	85W-10-4-2C1-04	0,000017	0,07623523	0,871005966	9,20577157	1106
85W	85W-10-4-2C1-05	0,000011	0,07521358	0,279985877	2,919548782	1081
85W	85W-10-4-2C1-06	0,000000	0,0757392	1,527569934	16,04002959	1099
85W	85W-10-4-2C1-07	0,000006	0,07574003	1,835004959	19,26841825	1097
85W	85W-10-4-2C1-08	0,000012	0,07667468	0,689381527	7,328160342	1119
85W	85W-10-4-2C1-09	0,000014	0,07681574	3,695331492	39,35382694	1122
85W	85W-10-4-2C1-10	0,000039	0,07807997	-7,313884736	-79,17190579	1146
85W	85W-10-4-2C1-11	0,000000	0,07422823	-0,026485385	-0,27255788	1059
85W	85W-10-4-2C1-12	0,000017	0,07658109	0,366113998	3,887059842	1115
85W	85W-10-4-2C1-13	-0,000009	0,104476	0,020192639	0,292477835	1717
85W	85W-10-4-2C1-14	0,002008	0,121429	0,006718416	0,113102627	1512
85W	85W-10-4-2C1-15	0,000130	0,08246399	3,699802442	42,29862292	1223
85W	85W-10-4-2C1-16	-0,000052	0,08089331	0,327065896	3,668015972	1247
85W	85W-10-4-2C1-17	0,000019	0,07635539	-0,575799508	-6,095289514	1108
85W	85W-10-4-2C1-18	0,000023	0,07793656	#VALUE!	#VALUE!	1148
85W	85W-10-4-2C1-19	0,000135	0,08069707	0,075712442	0,847048678	1178
85W	85W-10-4-2C1-20	0,000008	0,07616247	0,225664587	2,382801041	1107
85W	85W-10-4-2C1-21	0,000068	0,0821802	0,341802241	3,894264529	1238
85W	85W-10-4-2C1-22	0,000060	0,07924395	0,01445808	0,158840078	1168
85W	AG85W-1	0,0000043	0,0754	0,14774	1,528	1069
85W	AG85W-02	0,0000074	0,0763	0,14805	1,549	1092
85W	AG85W-03	0,0000079	0,0756	0,12666	1,314	1074
85W	AG85W-04	0,0000488	0,0776	0,06786	0,717	1110
85W	AG85W-05	0,0000065	0,0758	0,14524	1,510	1079
85W	AG85W-06	0,0000110	0,0757	0,13583	1,410	1076
85W	AG85W-07	0,0000217	0,0764	0,13887	1,451	1089
85W	AG85W-08	0,0000138	0,0760	0,14621	1,522	1082
85W	AG85W-09	0,0000081	0,0758	0,14207	1,476	1078
85W	AG85W-10	0,0000090	0,0755	0,12963	1,343	1071
85W	AG85W-11	0,0000029	0,0757	0,13759	1,430	1078
85W	AG85W-12	0,0000329	0,0769	0,14868	1,561	1099
85W	AG85W-13	0,0000061	0,0757	0,14963	1,554	1077
85W	AG85W-14	0,0000074	0,0757	0,13873	1,440	1076
85W	AG85W-15	0,0000071	0,0759	0,15448	1,608	1081
85W	AG85W-16	0,0000045	0,0759	0,14942	1,556	1082
85W	AG85W-17	0,0000072	0,0757	0,15480	1,607	1076
85W	AG85W-18	0,0000062	0,0755	0,14823	1,535	1071
85W	AG85W-19	0,0000063	0,0756	0,15371	1,595	1075
85W	AG85W-20	0,0000027	0,0753	0,15342	1,587	1069
85W	AG85W-21	0,0000051	0,0756	0,15056	1,563	1076
85W	AG85W-22	0,0000060	0,0759	0,15973	1,664	1083
Andrew Lake	AND-15-1-4-1	0,0009081	0,0711	0,03328	0,265	518
Andrew Lake	AND-15-1-4-02	0,0008358	0,0714	0,03923	0,320	568
Andrew Lake	AND-15-1-4-03	0,0008466	0,0718	0,03596	0,294	577
Andrew Lake	AND-15-1-4-04	0,0008662	0,0709	0,04324	0,346	532
Andrew Lake	AND-15-1-4-05	0,0008579	0,0710	0,04031	0,324	539
Andrew Lake	AND-15-1-4-06	0,0008947	0,0712	0,03445	0,275	527
Andrew Lake	AND-15-1-4-07	0,0008783	0,0714	0,03951	0,318	544
Andrew Lake	AND-15-1-4-08	0,0008726	0,0716	0,02692	0,218	554
Andrew Lake	AND-15-1-4-09	0,0008645	0,0713	0,03494	0,282	550
Andrew Lake	AND-15-1-4-10	0,0009024	0,0727	0,03494	0,286	579
Andrew Lake	AND-15-1-4-11	0,0008916	0,0712	0,03904	0,312	530
Andrew Lake	AND-15-1-4-12	0,0008960	0,0716	0,02462	0,198	544
Andrew Lake	AND-15-1-4-13	0,0008542	0,0734	0,01925	0,161	630
Andrew Lake	AND-15-1-4-14	0,0008781	0,0724	0,02189	0,180	582
Andrew Lake	AND-15-1-4-15	0,0008780	0,0716	0,02461	0,199	552
Andrew Lake	AND-15-1-4-16	0,0008608	0,0713	0,02340	0,189	550
Andrew Lake	AND-15-1-4-17	0,0009034	0,0725	0,04249	0,346	571
Andrew Lake	AND-15-1-4-18	0,0008682	0,0714	0,03179	0,257	551
Andrew Lake	AND-15-1-4-19	0,0008213	0,0717	0,01999	0,164	587
Andrew Lake	AND-15-1-4-20	0,0008866	0,0740	0,01422	0,120	635
Andrew Lake	AND-15-1-4-21	0,0009009	0,0738	0,05555	0,464	622
Andrew Lake	AND-15-1-4-22	0,0008232	0,0708	0,03915	0,317	554
Andrew Lake	AND-15-1-4-23	0,0008415	0,0708	0,03877	0,312	542
Andrew Lake	AND-15-1-4-24	0,0008804	0,0713	0,03934	0,316	541
Andrew Lake	AND-15-1-4-25	0,0008932	0,0712	0,04343	0,347	529
Andrew Lake	AND-15-1-4-26	0,0008822	0,0719	0,03959	0,321	561
Andrew Lake	AND-15-1-4-27	0,0009010	0,0718	0,03462	0,280	549
Andrew Lake	AND-15-1-4-28	0,0008682	0,0720	0,00798	0,065	571
Andrew Lake	AND-15-1-4-29	0,0008503	0,0720	0,03738	0,306	582

Table 2: U-Pb isotopes analysis and calculated age.

TABLE DES ILLUSTRATIONS

TABLE DES TABLEAUX